SANDIA REPORT

SAND2010-8676
Unlimited Release
Printed December 2011

The Phoenix Series Large Scale LNG Pool Fire Experiments

Thomas Blanchat, Paul Helmick, Richard Jensen, Anay Luketa, Regina Deola, Jill Suo-Anttila, Jeffery Mercier, Timothy Miller, Allen Ricks, Richard Simpson, Byron Demosthenous, Sheldon Tieszen, and Michael Hightower

Prepared by
Sandia National Laboratories
Albuquerque, New Mexico 87185 and Livermore, California 94550

Sandia National Laboratories is a multi-program laboratory managed and operated by Sandia Corporation, a wholly owned subsidiary of Lockheed Martin Corporation, for the U.S. Department of Energy's National Nuclear Security Administration under contract DE-AC04-94AL85000.

Sandia National Laboratories

Issued by Sandia National Laboratories, operated for the United States Department of Energy by Sandia Corporation.

Available to DOE and DOE contractors from
U.S. Department of Energy
Office of Scientific and Technical Information
P.O. Box 62
Oak Ridge, TN 37831

Telephone: (865) 576-8401
Facsimile: (865) 576-5728
E-Mail: reports@adonis.osti.gov
Online ordering: http://www.osti.gov/bridge

Available to the public from
U.S. Department of Commerce
National Technical Information Service
5285 Port Royal Rd.
Springfield, VA 22161

Telephone: (800) 553-6847
Facsimile: (703) 605-6900
E-Mail: orders@ntis.fedworld.gov
Online order: http://www.ntis.gov/help/ordermethods.asp?loc=7-4-0#online

SAND2010-8676
Unlimited Release
Printed December 2011

The Phoenix Series Large Scale LNG Pool Fire Experiments

Thomas Blanchat, Paul Helmick, Richard Jensen, Anay Luketa, Regina Deola,
Jill Suo-Anttila, Jeffery Mercier, Timothy Miller, Allen Ricks, Richard Simpson,
Byron Demosthenous, Sheldon Tieszen, and Michael Hightower

Sandia National Laboratories
P.O. Box 5800
Albuquerque, NM 87185-1135

Abstract

The increasing demand for natural gas could increase the number and frequency of Liquefied Natural Gas (LNG) tanker imports and exports at ports across the United States. Because of the increasing number of shipments and the number of possible new facilities, concerns about the potential safety of the public and property from an accidental, and even more importantly intentional spills, have increased. While improvements have been made over the past decade in assessing hazards from LNG spills, the existing experimental data is much smaller in size and scale than many postulated large accidental and intentional spills. Since the physics and hazards from a fire change with fire size, there are concerns about the adequacy of current hazard prediction techniques for large LNG spills and fires. To address these concerns, the United States (US) Congress funded the Department of Energy (DOE) in 2008 to conduct a series of laboratory and large-scale LNG pool fire experiments at Sandia National Laboratories (Sandia) in Albuquerque, New Mexico.

This report presents the test data and results of two types of fire experiments. A series of four reduced-scale (gas burner) tests (yielding 22 sets of data) were conducted in 2007 and 2008 at Sandia's Thermal Test Complex (TTC) to assess flame height to fire diameter ratios as a function of nondimensional heat release rates for extrapolation to large-scale LNG fires. The large-scale LNG pool fire experiments were conducted in a 120 m diameter pond specially designed and constructed in Sandia's Area III large-scale test complex. Two fire tests of LNG spills on water producing pools of 21 and 83 m in diameter were conducted in 2009 to improve the understanding of flame height, smoke production, and burn rate and therefore the physics and hazards of large LNG spills and fires.

Acknowledgements

Key contributors to this report and their roles are as follows:

Tom Blanchat - principal author, investigator, and test director
Anay Luketa - LNG modeler and analyst
Jill Suo-Anttila - mid-infrared spectroscopy testing and analyst
Jeffery Mercier - FTIR spectroscopy testing and analyst
Regina Deola - Sandia meteorologist
Allen Ricks – small scale gas burner test planning and SEP data reduction methodology
Timothy Miller - video analyses
Richard Simpson - photometric and aviation operations coordinator
Byron Demothenous - lead photographer for photometric group
Paul Helmick - LNG reservoir solid modeling, mechanical systems engineering design
Richard Jensen - reservoir civil engineering design
Sheldon Tieszen - experiment design and fire analyst
Michael Hightower - program management.

The author is indebted to numerous people for contributions to this project. First and foremost was the extremely capable team of technologists in the Fire and Aerosol Science department, with Sylvia Gomez (LNG fire experiment lead), Dann Jernigan (DAS network, spectral and IR measurements), Pat Brady (reservoir systems lead), and Chuck Hanks (data acquisition lead) who installed the systems and performed the testing. Data acquisition and test support leads were provided by Bennie Belone, Randy Foster, Ciro Ramirez, Martin Sanchez, and Barry Wilt. Testing was a 24/7 operation, involving weeks of shift work. The author especially thanks Allen Ricks and Sheldon Tieszen (Fire Sciences department manager) who worked the night shift, loaded fuel, and allowed the test director a few hours of sleep.

James Arnold was the construction site supervisor, also supported by Paul Helmick and Richard Jensen in their roles as field engineers supervising Area 3 TMSS contractors. Many people were involved in video activities, including Mark Nissen (photometric video support supervisor), Michael Bejarano, Ed Bystrom, Byron Demosthenous, Amarante Martinez, J Edward Nowicki, and Richard Simpson as video support technicians. Richard Simpson was the aviation operations coordinator and lead aircraft video technician supported by Wolf Rogulja, Mark Olona, Dale Kruzic, USAF 512th RQS pilots and 58th SOW safety officers. Additional photographers included Dale Green, Bernard Pelletier, and Randy Montoya. Construction aerial photography was taken by Captain Sean "Bull" Masters. Additional construction support and wild land firefighting support was provided by TMMS contractors Mel Crow, Jeffry Chavez, Paul Codding, Randy Foster, Don McManaway, Jose Molina, Ciro Ramirez, Rafael Sanchez, Pasqual Vallejos and others working as Sandia Area 3 TMSS contractors.

Environment safety and health is an important concern, especially for large tests with hazardous materials; key personnel who provided guidance and supervision included Tim Stirrup, Stacy Medina, Stanley Haynes, and Michael Vigil (Safety Basis), Roger Shrouf (Pressure and Cryogenic Safety), Paul Giering (Confined Space), Ryann Fisher (Industrial Hygiene), Kelsey Curran (Air Quality), (Bill Wolf (Incident Commander), Randey Colgrove (Safety Engineer),

Glen Argabright (Facilities Fire Protection), Frank Stibick (ES&H coordinator), Gary Hoe (Electrical Safety), and Captain Paul Romero (Security).

The author deeply appreciates the support and resources provide by the DOE/NNSA Sandia Site Office (SSO), especially Jeff Petraglia (lead for the SSO FORECAST system effort), Susan Lacy (NEPA Compliance Officer), Michael Brown (Facility Representative), Mike Collopy (Fire Protection), John Franchere (Explosives Safety), Roy Lybarger (Transportation), Karen Agogino (Water Permits), Carolyn Holloway (Air Permits), Jose Munoz (Safety Basis), Tami Moore (Public Affairs), and Patty Wagner (SSO Manager). The SSO FORECAST system, necessary for approval of the LNG tests, ensures that medium and high hazard mission tests receive the ES&H, S&S, and other operational support to uniformly achieve mission success per the test plan

Overall LNG program management was provided by Mike Hightower. Numerous Sandia managers supported this work and removed obstacles, from Level 1 managers up to the laboratory president, Tom Hunter, for which the author is very grateful.

A voluntary advisory peer review group was formed consisting of a small number of experts in the field of LNG and other hydrocarbon pool fire tests. Members were chosen specifically for their expertise in the performance and measurements of such testing. The author thanks Dr. Jonathan Puttock (Shell Global Solutions), Dr. John de Ris (FM Global), Dr. Richard Corlett (University of Washington), and Dr. Carlos Fernandez-Pello (University of California, Berkeley) for their participation.

Thanks are due to the Sandia internal peer reviewers, Mike Hightower and Sheldon Tieszen, whose comments and suggestions greatly improved the quality of this report. In addition, the author thanks Dr. John Moorhouse, British Gas (*formerly of*), who while serving as an external peer review panel member on the Sandia's LNG Cascading Damage Research Program, provided a very thoughtful and rigorous review of this report.

Lastly, the author and program managers gratefully acknowledge personnel at the United States Department of Energy: Bob Corbin (Director, Oil and Gas Global Security and Supply, Office of Oil and Natural Gas), Christopher Freitas (Program Manager, Natural Gas Storage, Pipeline Reliability, and LNG, Office of Oil and Natural Gas), and James Slutz (Deputy Assistant Secretary, Office of Fossil Energy); who understood the importance of this work, had the vision and drive to obtain the necessary funding from Congress, and faith that Sandia National Laboratories would be able to perform the unprecedented LNG fire experiments described herein.

Briefing to management (left to right): Tom Hunter - President, Sandia National Laboratories; Mike Hightower - LNG Program Manager, Art Ratzel - Director, Engineering Sciences Center, Sheldon Tieszen - Manager, Fire and Aerosol Sciences Department, Tom Blanchat - Principal Investigator, Fire and Aerosol Sciences Department

Contents

Figures

Tables

1 Executive Summary

The increasing demand for natural gas is expected to increase the number and frequency of Liquefied Natural Gas (LNG) tanker imports and exports at ports across the U.S. Because of the increasing number of shipments and facility siting applications, concerns about the potential for an accidental spill or release of LNG have increased. In addition, since the incidents surrounding September 11, 2001, concerns have increased over the impact that accidents and other events on hazardous or flammable cargoes, such as those carried by LNG ships could have on public safety and property. The risks and hazards from an LNG spill will vary depending on the size of the spill, environmental conditions, and the site at which the spill occurs. Risks could include injuries or fatalities to people, property damage to both the LNG ship and equipment and onshore property, and economic impacts due to long-term interruptions in the LNG supply or closure of a harbor. With the growing use of imported LNG to meet increasing U.S. and regional natural gas demands, damage or disruption from a spill to LNG import terminals or harbor facilities could curtail LNG deliveries and impact natural gas supplies. Therefore, methods to ensure the safety, security, and reliability of current or future LNG terminals and LNG shipments are important from both public safety and property perspectives, as well as from a national and regional energy reliability standpoint.

As LNG imports started to increase in the U.S. in the early 2000's, a number of hazard studies were conducted that resulted in widely varying consequence and hazard estimates resulting in broad public concern over the adequacy of current hazard and consequence analysis techniques. Subsequent Sandia analysis [Hightower et al., 2004] highlighted some primary knowledge gaps that were limiting the fidelity of site-specific risk assessments due primarily to the lack of large-scale LNG spill, fire, and damage data. Experimental studies used to justify current hazard analyses were 10 to 100 times smaller in scale than potential incidents. The limiting factor in conducting the needed larger-scale experiments was that they were thought to be cost prohibitive.

While much progress has been made in LNG threat, consequence and vulnerability assessment; for example, a general approach to risk evaluation has been developed and used for a basis in site-specific risk assessments [Hightower et al., 2004]; there are still knowledge gaps for very large scale LNG pool fires [Luketa et al., 2008] that limit the fidelity of site-specific risk assessments and remain a focal point of concern. These knowledge gaps result in the need to make assumptions in hazard analysis that may or may not be warranted and could lead to over predicting or underestimating hazards and impacts to the public, property, the economy, or energy reliability.

To address these concerns, the United States Congress funded the US Department of Energy (DOE) in 2008 to conduct a series of laboratory and large-scale LNG pool fire experiments at Sandia National Laboratories (SNL or Sandia herein) in Albuquerque, New Mexico. The focus of the LNG pool fire testing efforts were to improve the understanding of the physics and hazards of large LNG spills and fires by conducting laboratory experiments and fire tests of LNG spills, on water, producing pools of up to 100 m in diameter. These tests were expected to better represent the fire behavior of spills postulated from current and future LNG carriers.

Due to its unique chemistry, methane fires behave differently compared to other hydrocarbon fuel fires, but are expected to follow the trend of heavy hydrocarbon fuel fires, where the surface emissive power (SEP) of a pool fire increases to reach a maximum value then decreases to reach a limiting value with increasing diameter. For LNG, the limiting SEP value is unknown and verifying the actual values required the improved laboratory and large-scale experiments funded by the US Congress. These large scale spreading LNG pool fire experimental datasets, combined with small-scale gas-burner experiments, support pool fire model development and validation for extrapolation to a scale of an potential LNG spill of 200-400 m or larger in diameter [Luketa, et al., 2011].

LABORATORY-SCALE EXPERIMENTS

A key technical element in establishing hazard distances from fires is establishing the view factor from the fire to the point of concern. The view factor is dependent on the flame height for a given fire diameter. One of the deficiencies of historical data acquired from gas burners is that due to the small size of burners used (< 1 m) the fires were not fully turbulent. Turbulence affects flame height and thus it is important to capture this physics. To address existing data deficiencies, Sandia tests utilized the largest gas burner to date (3 m diameter) resulting in fires that are fully in the turbulent regime. The reduced-scale experiments, conducted by burning methane gas in the FLAME test cell at the Thermal Test Complex, measured flame height at various methane flow rates to provide data for flame height correlations in fully turbulent fires burning lightly sooting fuels. The fuel flow rate was deliberately varied to cover the range relevant to LNG evaporation rates for spills onto land and water. Four separate methane experiments yielded twenty two sets of flame height vs. fuel flow rate data. A flame height correlation as a function of a dimensionless heat release rate (e.g., Q*) was developed to support recommendations on flame height for very large LNG pool fires (up to 1000 m diameter). The correlation estimates the flame height to fire diameter ratio, H/D, for a 200-400 m diameter LNG fire on water to be approximately 1.5-1.1 (with decreasing H/D for increasing diameter).

LARGE-SCALE LNG POOL FIRE EXPERIMENTS

A key technical element in establishing hazard distances from fires is establishing the surface emissive power (SEP) of the fire. One of the deficiencies of historical data is due to the small scale of the fires (10 to 100 times smaller) relative to possible spill diameters, particularly when the SEP is a strong function of fire diameter. The principal reason for the small fire diameters is cost. Cost estimates to build a facility to conduct large-scale LNG pool fire tests were prohibitive. This forced Sandia to assess ways to develop a safe, low-fabrication-cost experimental setup that could be constructed. The solution selected necessitated significant operational safety considerations including unprecedented cooperation between numerous Sandia organizations, the DOE Sandia Site Office, and Kirtland AFB agencies (including flight-operations and emergency fire-response). By focusing on the experimental objectives, and using experience in conducting large-scale experiments, the team came up with a-simple, low-cost experimental approach that enabled testing at an appropriate scale. The experimental design concept (Figure 1) included: 1) using the soil excavated from the creation of a shallow 120-m diameter pond to create a deep, 310,000 US gallon reservoir to hold the LNG while filling, 2) insulating and covering the reservoir to minimize vaporization losses, 3) using industry standard

prefabricated reinforced concrete pipes to transport the LNG from the base of the reservoir to the center of the pool, and 4) using a simple, liftable plug to allow gravity to control the flow rate.

Figure 1 The Large Scale LNG Pool Fire Experimental Site

This approach enabled high LNG spill rates onto water representative of potentially large spills, while minimizing the need for cryogenic rated high-flow rate pumps and hardware. This novel approach required significant environment, safety, and health analysis to provide confidence that the design and operations would be safe. Safety issues examined included reservoir integrity, thermal (cryogenic to fire fluxes) impacts, asphyxiation, explosion, drowning, and aviation operations (helicopter and airport traffic) issues. Advanced transient, three-dimensional transport simulations were used to estimate both the thermal performance of the reservoir and components, the transport of gaseous boil-off during the cool-down process, and in the design of the diffuser in the middle of the pool needed to translate the linear momentum of the LNG in the discharge pipes into a radially spreading pool.

The large-scale LNG spill tests were performed with liquid methane (>99.5%) as a surrogate for Liquid Natural Gas (LNG) to minimize the potential for explosive rapid phase transitions (RPTs) and minimize the parameter variations to reduce uncertainty in the analysis of the test data and for the use of present and future model development and validation. Previous historic experiments performed with typical LNG have shown that the methane burns off first, with little participation by the heavier hydrocarbons until late in the test.

Two experiments were completed obtaining fires from LNG spills with spreading pool diameters of approximately 21 m and 83 m. Extensive sets of fire data were collected for each test. Numerous cameras, spectroscopic diagnostics, and heat flux sensors were used to obtain heat flux data from the resulting fires. The spreading pool fire area was photographed with the aid of gyroscopically stabilized cameras deployed in U.S. Air Force helicopters. While three tests were proposed and attempted (to achieve spreading pool diameters at ~35 m, 70 m, and 100 m), it is believed that the data collected from the two successfully completed tests is sufficient to allow spill and fire model development and validation for use in estimating hazards and consequences for LNG pool fires on water with diameters of 200-400 m.

The data collected showed some unique and unexpected results specifically that the fire diameter was not the same as the spreading pool diameter as had been assumed by all analyses to date. Previous studies with stagnant pools in pans had resulted in fires the same size as the pool.

However, in all such studies, the pans have edges that can result in flame stabilization that would not be available on the open water. The data collected further showed that in both very light and significant cross-winds the flame will stabilize on objects projecting out of the fire, suggesting that the ship itself will act as a flame anchor.

In LNG Test 1, 58.0 m^3 (~15,340 gal) were discharged in ~510 s through a 15-inch discharge pipe. The flow rate initially was about 0.061 m^3/s (970 gpm) and increased throughout the test, reaching 0.123 m^3/s (1960 gpm) at the end of the test. During the steady-state fire interval of 390-510 s, the average flow rate from the reservoir was 0.121 m^3/s (1921 gpm), yielding an average mass discharge rate of 50.8 kg/s from the reservoir. The liquid mass flow rate from the diffuser was slightly less at 49.4 kg/s due 2-phase flow and the generation of methane vapor. The steady-state pool area yielded an equivalent circular diameter of 20.7 m. At steady-state, the average regression rate of the burning pool was 0.147 kg/m^2s.

In LNG Test 1, the average wind speed was 4.8 m/s from a direction of 331 degrees, tilting the flame plume to the South. The average length was ~70 m (as compared to an average height of ~34 m). The average tilt angle was ~50°, yielding an L/D ratio of ~3.4. Narrow view (spot) radiometers corrected for transmission losses measured a spot-average steady-state surface emissive power (SEP) of 238 kW/m^2. A flame-average SEP was determined by correlating view factor information from video analysis with the wide-angle radiometer data, yielding an average overall SEP of 277±60 (2σ) kW/m^2.

In LNG Test 2, about 198.5 m^3 (52,500 gallons) were discharged in ~144 s through the three discharge pipes. The average flow rate during the fully open period (130 s to 220 s) was 1.91 ± 0.84 m^3/s (30300 ± 13350 gpm), yielding a mass discharge rate of ~802 kg/s. The spreading LNG pool area continuously increased during the discharge interval, achieving an equivalent circular diameter of ~83 m at the end of the spill. Since the reservoir emptied prior to the pool achieving a constant area, a burn rate could not be calculated.

The test had unexpected results in that the fire did not attach to the leading edge (upwind and both sides) of the spill, hence the effective fire diameter was smaller than the spreading LNG pool diameter. The average flame width at 15 m above the pool was ~56 m and the average flame height was ~146 m during the steady-state interval from 250-300 s. This yields an H/D ratio of ~1.7 and an H/W ratio of ~2.6. The average wind speed was 1.6 m/s from a direction of 324 degrees. There was very little flame tilt; however, the wind did appear to drag the plume toward the south.

Narrow view (spot) radiometers on the North and South data collection spokes yielded spot-average steady-state surface emissive power (SEP) of 316 kW/m^2 and 239 kW/m^2, respectively. The SEP on the South spoke is believed to be low due to the presence of smoke from grass fires partially obstructing the view of the instruments. The overall flame average SEP was 286±20 (2σ) kW/m^2.

Thermal radiation spectra as a function of height and time were acquired using a scanning mid-infrared (1.3-4.8μm) spectrometer. For LNG Test 2, data reduction efforts were concentrated on spectra acquired within the quasi-steady burning period (250-300 sec). The spectra from heights

at approximately ground level to ~100 m yielded thermal radiation intensities lowest for elevations closest to the ground and then increased steadily to a maximum where they remained until the maximum scan height was achieved. There was no indication of declining intensities at the maximum scan height (103 m).

Analyzed spectra determined that the dominant contributor to the thermal radiation was from broadband soot emission. The overall thermal radiation reaching the spectrometer was attenuated by atmospheric water and CO_2 which resulted in a decrease in intensity at different wavelength bands. In LNG Test 2, at heights above ground from ~40 m to 103 m (the top of the measurement region above the pool), the data was fairly consistent, with spectra-derived flame temperatures between 1300-1600°C and emissivity between ~0.3 – 0.4.

The agreement in the surface emissive power derived from the radiometer data and the spectrometer data was found to be acceptable and within the experimental variability. Surface emissive power (from spectrometer data) was a minimum near the ground level, with approximate values of 100 kW/m^2. The heat fluxes then increased steadily from 0 to 40 m and reach peak values approaching 275 kW/m^2.

Additional spectrometer data was collected with an FTIR spectrometer, a high-speed visible camera, and a thermal imager. A two-temperature spectra fire model correlated extremely well to the measured spectra. It is postulated that the two temperature states more accurately depict the true nature of the fire by characterizing both the efficient combustion regions and those dominated by slow burning, absorbing soot.

Figure 2 plots SEP vs. LNG pool diameter for a variety of hydrocarbon fuels [Vela 2009], including the three SNL LNG pool spread tests on water (including an earlier 2005 10 m test, Blanchat, private communication, 2005). SEP for hydrocarbon fuels all have similar behaviors in that the SEP starts low (due to burning in a laminar regime), increases as the burning transitions into a fully-turbulent regime), and then tails off due to smoke shielding as soot is quenched at the flame surface. Soot quenching starts at the flame mantle, and as the fire size increases, the smoke shield progressively moves down towards the base of the burning pool. LNG is expected to follow similar trends; however, due to its unique molecular bond structure, the shape of the curve is shifted toward the right as indicated by the test data.

Figure 3 shows three LNG tests performed at SNL on water, captions indicate the effective diameter of the LNG spreading pool (all tests were performed with high-purity methane). Even though very little smoke shielding occurred in any of the tests, the trend in the data (Figure 2) does indicate that the SEP is leveling off, indicating that a SEP of ~286 kW/m^2 can be expected for spreading pools with diameters in the range of 100 m, and would be a reasonable value for use in hazard calculations for structures adjacent to or near the fire. Larger LNG fires are expected to have smoke shielding effects in the upper portions of the flame plume that will lower the SEP. This would impact hazard calculations for far-field objects but not for near-field objects relatively close to the base of the fire.

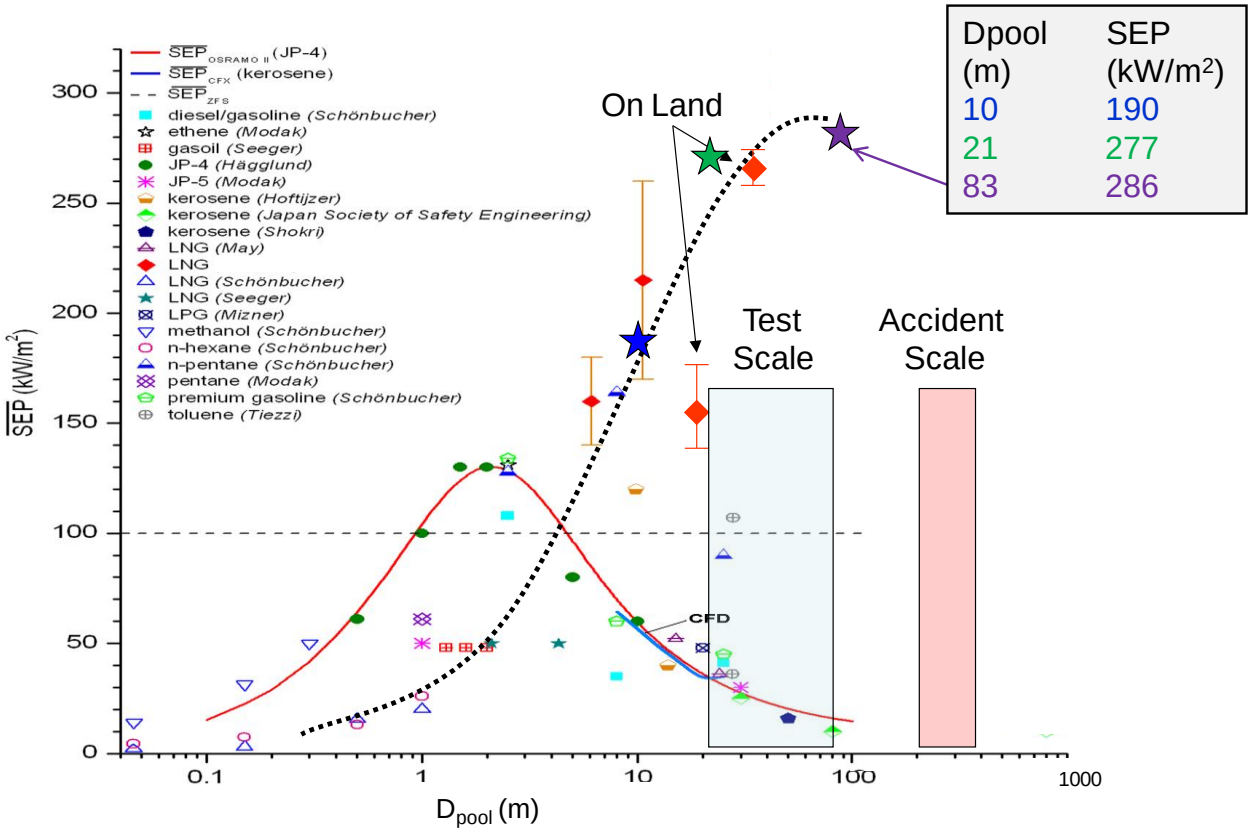

Figure 2 SEP vs. pool diameter for various hydrocarbon fuels.
(Vela, 2009, except for current data).

Smoke mantles were not evident in either test. There were a few instances when small amounts of smoke were seen in LNG Test 2 during the production of large scale vortices that "rolled up" from the base of the flame when the fire exhibited a puffing behavior, as can be seen in Figure 3.

The results from LNG Test 2 identified a number of pool fire dynamics that should be considered when modeling flame spread on the LNG pool surface, flame geometry, and smoke production for use in hazard predictions. They include 1) water entrainment and condensation in the cold region above the pool acting as a suppressant, 2) entrapment of methane in hydrates (forming with water in the pool) that limit the fuel supply rate, 3) air in-flow velocity from both air entrainment created by the intense fire and ambient wind opposing flame spread, 4) de-coupled LNG pool spreading and fire spreading, and 5) lack of flame anchoring over the water pool.

The LNG pool fire size, soot production, and SEP could vary depending on the size of a harbor and the relative congestion. Flame anchoring could change fire dynamics, behavior, and hazards. The de-coupling of the flame spread with the pool spread, i.e., lack of flame anchoring to the leading upwind edge of the spreading LNG pool over the water pool was evident in all three spreading LNG pool fire tests performed at Sandia, shown in Figure 3. Fire models that capture the above dynamics will be needed to better understand LNG fire physics and behavior over water.

LNG - 10 m SNL 2005 LNG - 21 m SNL 2009 LNG - 83 m SNL 2009

Figure 3 LNG fire dynamics at large scale.

2 Introduction

The increasing demand for natural gas is expected to increase the number and frequency of Liquefied Natural Gas (LNG) tanker imports or exports at ports across the U.S. Because of the increasing number of shipments and facility siting applications, concerns about the potential for an accidental spill or release of LNG have increased. In addition, since the incidents surrounding September 11, 2001, concerns have increased over the impact that accidents and other events on hazardous or flammable cargoes, such as those carried by LNG ships could have on public safety and property. The risks and hazards from an LNG spill will vary depending on the size of the spill, environmental conditions, and the site at which the spill occurs. Risks could include injuries or fatalities to people, property damage to both the LNG ship and equipment and onshore property, and economic impacts due to long-term interruptions in the LNG supply or closure of a harbor. With the growing use of imported LNG to meet increasing U.S. and regional natural gas demands, damage or disruption from a spill to LNG import terminals or harbor facilities could curtail LNG deliveries and impact natural gas supplies. Therefore, methods to ensure the safety, security, and reliability of current or future LNG terminals and LNG shipments are important from both public safety and property perspectives, as well as from a national and regional energy reliability standpoint.

As LNG imports started to increase in the U.S. in the early 2000's, a number of LNG hazard studies were conducted that resulted in widely varying consequence and hazard estimates resulting in broad public concern over the adequacy of current hazard and consequence analysis techniques. Subsequent Sandia analysis [Hightower et al., 2004] highlighted some primary knowledge gaps that were limiting the fidelity of site-specific risk assessments due primarily to the lack of large-scale LNG spill, fire, and damage data. Experimental studies used to justify current hazard analyses are 10 to 100 times smaller in scale than potential incidents. The limiting factor in conducting the required larger-scale experiments needed was that they were thought to be cost prohibitive.

While much progress has been made in LNG threat, consequence and vulnerability assessment, for example a general approach to risk evaluation has been developed, and used as a basis in site-specific risk assessments [Hightower et al., 2004], there are still knowledge gaps for very large scale LNG pool fires that limit the fidelity of site-specific risk assessments and remain a focal point of concern. These knowledge gaps result in the need to make assumptions in hazard analysis that may or may not be warranted and could lead to over predicting or underestimating hazards and impacts to the public, property, the economy, or energy reliability.

To address these concerns, the US Congress funded the Department of Energy (DOE) in 2008 to conduct a series of LNG experiments at Sandia National Laboratories. The efforts included three primary technical tasks to address current LNG spill and hazard assessment deficiencies:

1. Improve the understanding of the physics and hazards of large LNG spills and fires over water, including smoke shielding, and flame breakup, by conducting fire tests of LNG spills of up to 100 m in diameter,
2. Assess the possible cause, likelihood and release scenarios of a cascading failure of an LNG vessel from fire and cryogenic damage, and

3. Evaluate security and engineering mitigation techniques and options that could reduce the risks and hazards of LNG spills.

This report provides the description and final results of the experimental activities that have been performed for Task 1 above, as identified in the DOE Field Work Proposal FWP 06-013741 - Safety Hazard Testing and Modeling of Large LNG Spills over Water. Task 1 was addressed through two types of experiments.

The first was a set of reduced-scale (a few meters in diameter) fire tests in Sandia's Thermal Test Complex (TTC). The reduced-scale experiments utilized a large gas burner in the FLAME test cell at the Thermal Test Complex to measure flame height using methane fuel at various flow rates to provide data for flame height correlations in fully turbulent fires burning lightly sooting fuels. One of the deficiencies of historical data with gas burners is that due to the small size of burners used (< 1 m) the pool fires were not fully turbulent. Turbulence affects flame height and thus it is important to capture this physics. The Sandia tests utilized the largest gas burner to date (3 m diameter) and are fully in the turbulent regime. Four separate methane experiments yielded twenty two sets of flame height vs. fuel flow rate data. A flame height correlation as a function of a dimensionless heat release rate (e.g., Q*) was developed to support recommendations on flame height for very large LNG pool fires (~1000 m diameter). This data will improve estimates of fire surface areas, which will improve SEP and hazard distance estimates for large LNG pool fires.

The second part of Task 1 was conducting two large-scale LNG pool fire experiments over water in a 120 m diameter pond specially designed and constructed in Sandia's Area III large-scale test complex for these LNG pool fire tests. The experimental setup also included construction of a storage reservoir to hold up to 310,000 gallons of LNG and an extensive array of thermal spectrometers and radiometers to collect fire thermal emission data. Two fire tests of LNG spills of 21 and 83 m in diameter were conducted in February and December 2009 respectively with the specific objective to determine trends in flame height, smoke production, and burn rate.

The final results of the experimental and modeling work performed to support Tasks 2 and 3 above are not presented in this report, but are available in separate companion reports.

3 Reduced Scale (Gas Burner) Tests

The flame height is a parameter included in models used in hazard assessment studies because it relates to the total area of the fire that irradiates the surroundings. Another important feature to capture in hazard models is the transition from a coherent to a mass fire behavior. Coherent fires typically have a flame height of 1.5 to 2.0 diameters, but in very large fires the coherent structure breaks down (i.e., a 'mass' fire) and the observed height is 0.5 diameters or less. It is unknown at what diameter very large LNG fires will exhibit mass fire behavior.

It is possible to develop a correlation for the flame height to diameter ratio as a function of a nondimensional heat release rate (e.g., Q*) by utilizing gas burners in which the fuel flow rate can be controlled. This approach is based upon theoretical and experimental observations. The advantage of this approach is that the flame height of large scale pools can be investigated with a fixed pool diameter. If the fuel flow rate is reduced to a sufficiently low value the flame may exhibit mass fire behavior in which a coherent flame is not maintained, but rather multiple flames form which will significantly reduce the flame height.

3.1 Experiment Objective

The objectives of the reduced-scale experiments were to:

1. Measure the flame heights using gaseous methane fuel at various flow rates to provide data for flame height correlations in fully turbulent fires burning lightly sooting fuels
2. Determine the dimensionless fuel flow rate for transition from coherent to mass fire behavior
3. Obtain radiation emission to provide data to develop/validate soot models for these fires.

3.2 Methodology and Instrumentation

Gaseous hydrocarbon (methane) fires of meter scale were tested in a controlled environment in the Fire Laboratory for Accreditation of Models and Experiments (FLAME) / Radiant Heat (FRH) test cell in the Thermal Test Complex at Sandia National Laboratories. Figure 4 shows a representation of the FRH test cell. The main test chamber of the FRH cell is cylindrical in shape, 60 ft. (18.3 m) inner diameter with a height around the perimeter of 40 ft. (12.2 m). The ceiling slopes upwards (~18º) from the perimeter walls to a height of 48 ft. (14.6 m) over the center of the facility. A round hole at the top of the facility 16 ft. (4.9 m) diameter transitions to a 10 ft. by 12 ft. (3.0 m by 3.7 m) chimney duct. A large electrostatic precipitator downstream of FLAME collects soot prior to combustion products being sent to the exhaust stack. The outer walls are made of steel channel sections welded together and are filled with water for cooling during tests. The FRH cell is functionally airtight.

The ground level of FRH can be divided into three concentric sections. At the center of the facility is a fuel pan or gas burner. The facility can operate a gas burner (He, H_2, CH_4, etc.) or a liquid fuel pool (JP-8, methanol, etc.) from 1 m to 3 m in diameter. The test series discussed

below utilized a 3 m gaseous burner. The second section is a steel spill plate, which extends to a diameter of 12.7 m. The floor of the outer section is made of a steel grating, through which air is supplied to the FRH chamber during fire experiments.

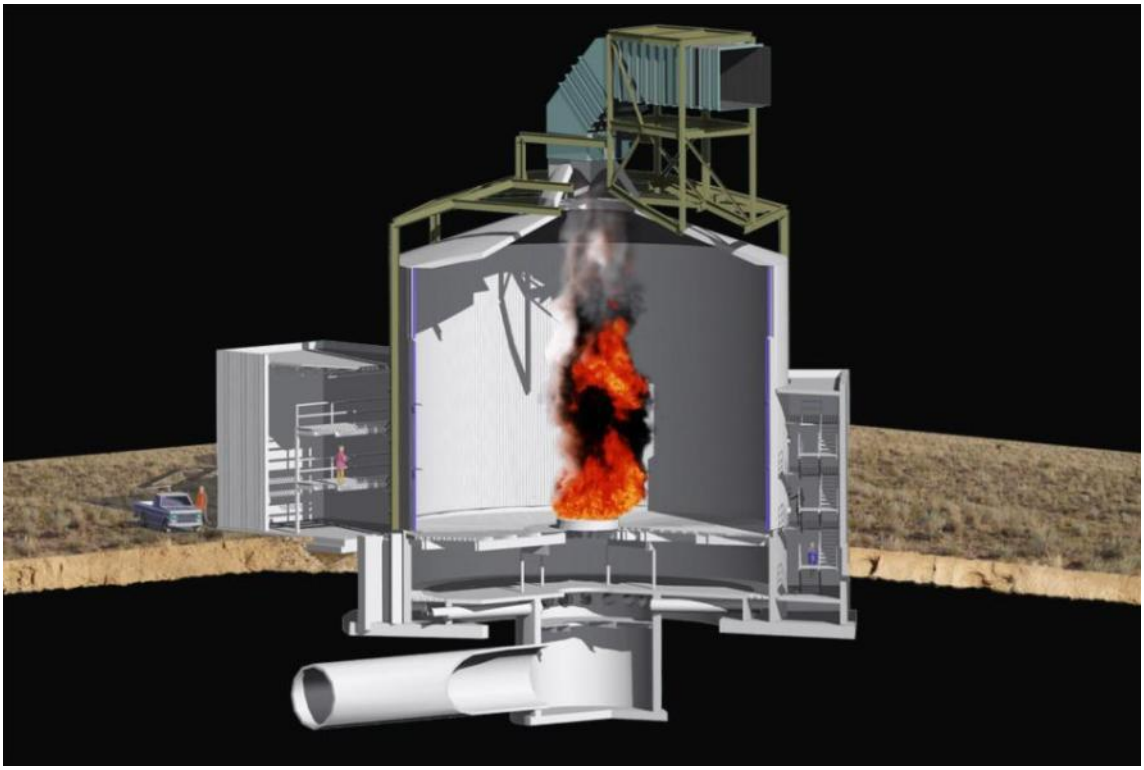

Figure 4 A cutaway view of the FRH facility.

The view shows a burner fire at the ground level, pipes supplying air flow through the basement, exhaust ductwork, and instrumentation rooms outside the FRH chamber.

Combustion air is supplied from the forced draft (FD) fan in a central utility building (not shown) through a large underground pipe (12 ft diameter) to a plenum that feeds 18 radial pipes (3 ft diameter) to a 4 ft by 4 ft annular ring in the FLAME basement. Air exits the grated top of the annular ring and enters the ground level steel grating. An induced draft (ID) fan just before the exhaust stack automatically adjusts speed to maintain the differential pressure (to ambient) across the FLAME wall to near zero.

The air flow in the absence of a fire has been characterized experimentally at the air ring in the basement and at the ground level (Ricks, 2006a). The air ring flow field (vertical upward velocities) was found to exhibit a pattern (left side of Figure 5) attributable to the 18 supply pipes carrying the air from the sub-basement plenum in the center of the facility to the annular air ring along the outer edges of the facility basement. The air flow at the ground level (vertical velocities) was found to be highest in the outer portion of the FRH cell, and exhibited a large recirculation zone in the inner portion of the facility, where mean velocities were in the negative (downward) direction (right side of Figure 5). The presence of a fire at the center of the facility is

likely to reduce the recirculation because the air flow will be drawn inwards and entrained into the buoyant fire plume.

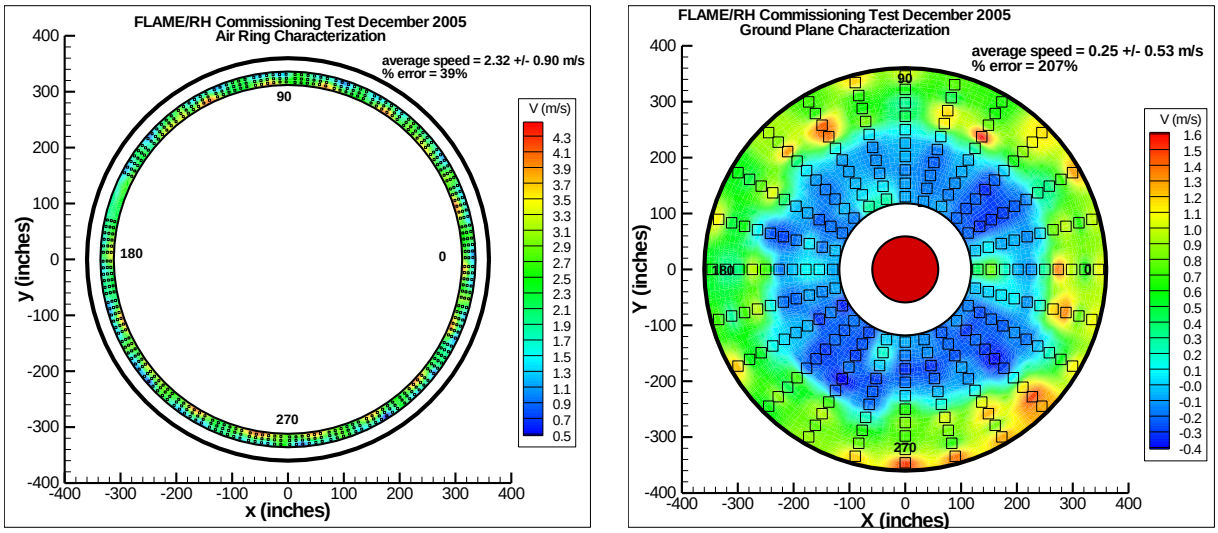

Figure 5 Combustion air at the air ring in the basement and at the ground level.

The gas burner was designed with the technical objective to provide a constant upward velocity profile of gaseous fuel (plus any diluent) over the whole of the area. In this way it was possible to closely simulate the behavior of either a gas burner or a liquid diffusion flame burning on a flat horizontal surface.

The gas burner consisted of an outer tub of mild steel 3 m in diameter and 1 m tall. An inlet pipe 6 inches (0.15 m) in diameter at the center of the base of the tub piped the fuel into the burner. The fuel first passed through a "witch's hat" diffuser at the base of the tub which was designed to direct the fuel flow outward in all directions from the inlet pipe. The witch's hat diffuser was a conical section containing 8,986 holes 1.7 mm in diameter; the total open area ratio of the diffuser is 11%. The fuel then passed through three layers of horizontal stainless steel baffle plates which served to flatten the velocity profile across the burner. Each baffle plate contained 32,345 holes of 1/8 inch (3.2 mm) diameter for a total open area ratio of 4%. The top final layer of the burner was a 3-inch stainless steel honeycomb, with the honeycomb top flush with the top lip of the burner, shown in Figure 6.

The gas burner was mounted at the center of the FRH test cell with the top of the burner positioned at the ground level of the facility, as shown in Figure 6 during commissioning [Blanchat 2006]. Figure 6 also shows an image from the 1st commissioning test (using hydrogen fuel) in the cell. The fuel was supplied to the burner from tube trailers located at the gas farm and through pipes underneath the ground level of the test cell. The gas burner flow characteristics were evaluated by Ricks [2006b].

After commissioning, the honeycomb was replaced. The final burner layer, nearly flush with the top surface of the tub, was a layer of small crushed glass pebbles ~2 inches deep intended to diffuse the gas leaving the last baffle plate. Note that the burner surface is ~1-2 inches below the ground plane of the FRH cell.

Figure 6 The 3-m diameter gas burner.

3.2.1 Fuel Mass Flux

The gaseous fuel was supplied from vendors in high pressure (3000 psi nominal) standard (38 tubes) or jumbo (8-10 tubes) tube trailers capable of supplying gas in the ranges from 60,000 to 140,000 scf (product dependent). High pressure reducing valves reduced trailer pressure to nominal manifold pressures of 25-50 psi, then a flow control valve on each gas train (A-high capacity fuel, B-high capacity diluent, C-low capacity fuel or trace gases, and D-high capacity purge-typically nitrogen) regulated the gas flow to the burner (Figure 7). Gas pressure was measured at each train manifold.

The fuel mass flux at the burner surface was measured by calibrated, independent flow meters on gas trains manifolds A, B, and C. The final low pressure (few psi) 6-inch diameter main feed line just before the burner had its own flow, pressure and temperature transmitters and provided a second measure of the flow rate.

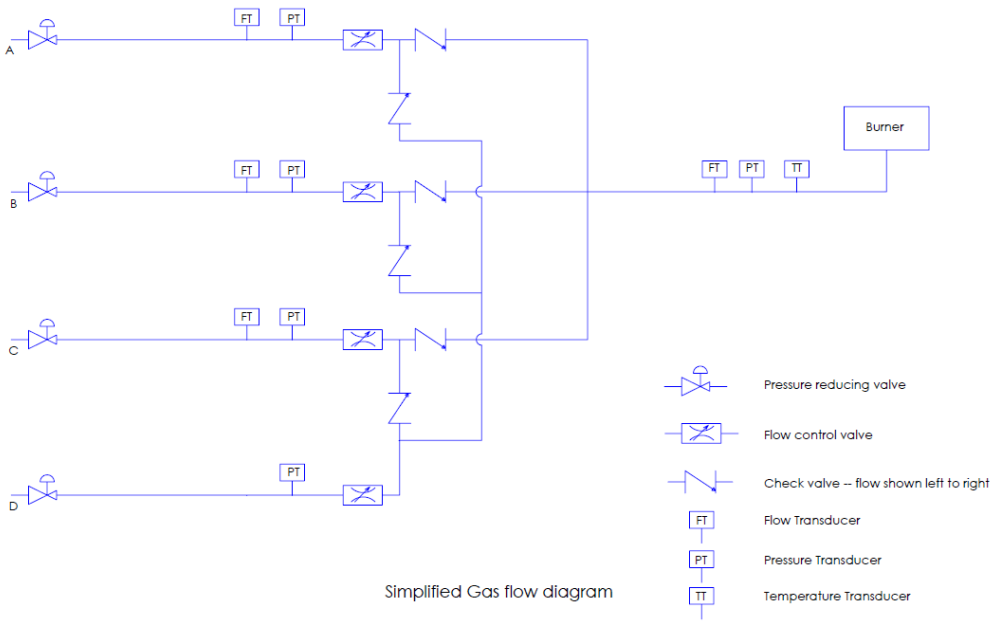

Figure 7 Simplified gas train diagram.

Uncertainty Analysis

The uncertainties at the maximum and minimum design flow rates for methane and hydrogen on gas trains A (methane), C (methane or hydrogen), and 6-inch main (hydrogen), assuming the full scale of the meter is set to the maximum for which the meter was calibrated, are shown in Table 1. Measurement error well within 10% of the reading, depending on the gas train used and the fuel type.

Table 1 Gas Train Conditions of Service and Flow Rate Uncertainty

Flow Meter	A		B		C						6-inch Main						Notes
Pressure (PSIG)	25		50		50						0 - 5						
Meter Size (in)	4		6		1.5						6						
Inside Diam (in) (Note 1)	4.026		6.065		1.61						6.065						1
Rated Capacity of Meter (SCFM Air)	1800		4000		280						4000						
Notes	7										5		6		6		
Press (PSIG)	25		50		50		50		50		0		1		1		
Gas	CH4		N2		H2		He		CH4		N2		H2		He		N2		
R (Ft-Lbf/Lbm-R)	96.3		55.1		766		386		96.3		55.1		766		386		55.1		
Correction for Specific Gravity	1.35		1.0		3.77		2.7		1.35		1.0		3.77		2.7		1.0		
Meter Full Scale (SCFM of Gas)	2430		4000		1056		756		378		280		15,080		10,800		4000		8
Density @ STP	0.0415		0.0724		0.0052		0.0103		0.0415		0.0724		0.0052		0.0103		0.0724		
Flow Condition	Max	Min	Max	Min	Max	Min	Max	Min	Max	Min	Max	Min	Max	Min	Max	Min	Max	Min	
Percent Full Flow	100%	20%	100%	20%	100%	20%	100%	20%	100%	20%	100%	20%	100%	20%	100%	20%	100%	20%	
Flow (PPH)	2,860	572	20,406	4,081	100	20	200	40	850	170	510	102	1118	224	2,783	557	5,000	1,000	
Flow (SCFM)	1,150	230	4,696	939	320	64	322	64	342	68	117	23	3,575	715	4,482	896	1,151	230	
Temp (F)	100	-20	100	-40	100	-10	100	-10	100	-20	100	-40	100	-10	100	-10	100	-40	
Density at Meter (Lb/Ft^3)	0.0993	0.1264	0.2900	0.3867	0.0209	0.0260	0.0414	0.0516	0.1661	0.2113	0.2900	0.3867	0.0041	0.0051	0.0088	0.0109	0.0615	0.0821	
Actual CFM at Meter	480	75	1173	176	80	13	80	13	85	13	29	4	4552	732	1334	230.7	1354	203	
Actual Velocity at Meter (FPM)	5,429	853	5,845	877	5,649	908	5,690	914	6,035	948	2,073	311	22,688	3646	24,823	4293	25,199	3780	
Standard Velocity at Meter (SFPM)	13,003	2,601	23,407	4,681	22,621	4,524	22,784	4,557	24,166	4,833	8,302	1,660	17,821	3,564	21,096	4,541	21,416	4,283	2
Flow % of Full Scale	47%	9.5%	117%	23.5%	30%	6.1%	43%	8.5%	90%	18.1%	42%	8.4%	24%	4.7%	42%	8.3%	29%	5.8%	3
Measurement Error (% of reading)	2.0%	6.2%	1.4%	3.1%	2.6%	9.2%	2.1%	6.8%	1.5%	3.7%	2.1%	6.9%	3.1%	11.5%	2.2%	7.0%	2.7%	9.6%	4

Notes	
1	Assumed to equal the ID of schedule 40 steel pipe
2	Limit is 20,000 or 32,000 SFPM - must confirm
3	Flow (SCFM) / Meter Full Scale (SCFM of gas)
4	Measurement Error = (0.5% of full scale / % of Full Scale) + 0.95% of reading
5	When running a combustion test using hydrogen as the fuel, use this flow meter to control FCV-57A
6	When flowing He or N2 through Gas Train D, use this flow meter to contol FCV-57D
7	This meter was specified as 3-inch, but I believe it was supplied as 4-inch.
8	Rated Capacity of Meter (SCFM Air) * Correction for Specific Gravity

The primary contributor to the uncertainty in the mass flow rate is the %full scale of the meter. The span of the meter is user-set and can be reduced to minimize the uncertainty in tests in which the maximum calibrated flow rate of the meter is not required.

Uncertainties in the actual volume flow rate of fuel gases are larger than uncertainties in the standard flow rate due to the uncertainty in the fuel density, which depends upon the local temperature and pressure. The uncertainty in the density is dominated by the uncertainty in the temperature measurement.

The ANSI standard uncertainty for Type K thermocouple wire is 2.2ºC or 0.75% of reading (in ºC), whichever is greater. This uncertainty applies to the temperature of the thermocouple junction itself. Determination of the actual desired temperature (wall temperatures of an object or fluid temperatures) is subject to additional bias errors due to mounting. These bias uncertainties are very hard to accurately quantify, are application dependent, and are often the largest errors in the measurement system. For the present tests the bias error in the fuel temperature measurements will be assumed to be small compared to the thermocouple uncertainty. The thermocouple is located in a cool duct, minimizing radiation interactions, and the high velocity of fuel ensures that convective heat transfer will dominate the energy balance for the thermocouple. The fuel temperature is expected to vary slowly compared to the thermal response time of the thermocouple.

The overall uncertainty of the fuel temperatures will be assumed to be ±3ºC, which adds some conservatism to the ANSI standard uncertainty over the expected range of temperatures. The uncertainty in the mixture gas constant is assumed to be no more than ±0.1% and the uncertainty in the pressure is assumed to be ±0.1%. The total uncertainty in the fuel density is ±1.1%. When this uncertainty is combined with the uncertainty in the fuel mass flow rate, the uncertainty in the fuel volume flow rate increases slightly (Table 1).

It is evident from the table that flow rates will be accurate within an uncertainty of 2% (maximum flow) to 6% (minimum flow) of the available range. This is regarded as a good standard and is as good as can reasonably be achieved for this type of large flow rate system.

3.3 Testing Procedures

The fire was ignited with a propane igniter and allowed to burn for approximately 5 minutes before data was taken to allow the fire and air flow in the cell to stabilize (when the burner is lit or the fuel flow rate changes, the overall gas temperature in the cell changes, this would result in a change of pressure in the cell except for the fact that the ID fan adjusts speed to maintain DP across the FRH cell to zero). Data from all instruments were taken continuously at fixed locations throughout the test. Note that a test represents a series of flow rates. The flow rate of the fuel was varied in a controlled manner during each test, with enough data logged at each desired flow rate to obtain averaged steady-state data.

3.4 Measurements

The following section describes the measurements (with initial uncertainty) necessary to meet the experimental data needs. A rigorous uncertainty analysis for all measurements was performed. The methodology typically follows Coleman and Steele [1999]. Bias errors which can be mathematically modeled, such as the bias error in thermocouple measurements in the fire, are algebraically added to the measurement and the uncertainty in the estimation of the bias is treated as a random error [Romero et al., 2005]. All reported uncertainties represent a 95% (two sigma) confidence level. Figure 8 shows a cross-section of FRH and shows the types and locations of the instrumentation.

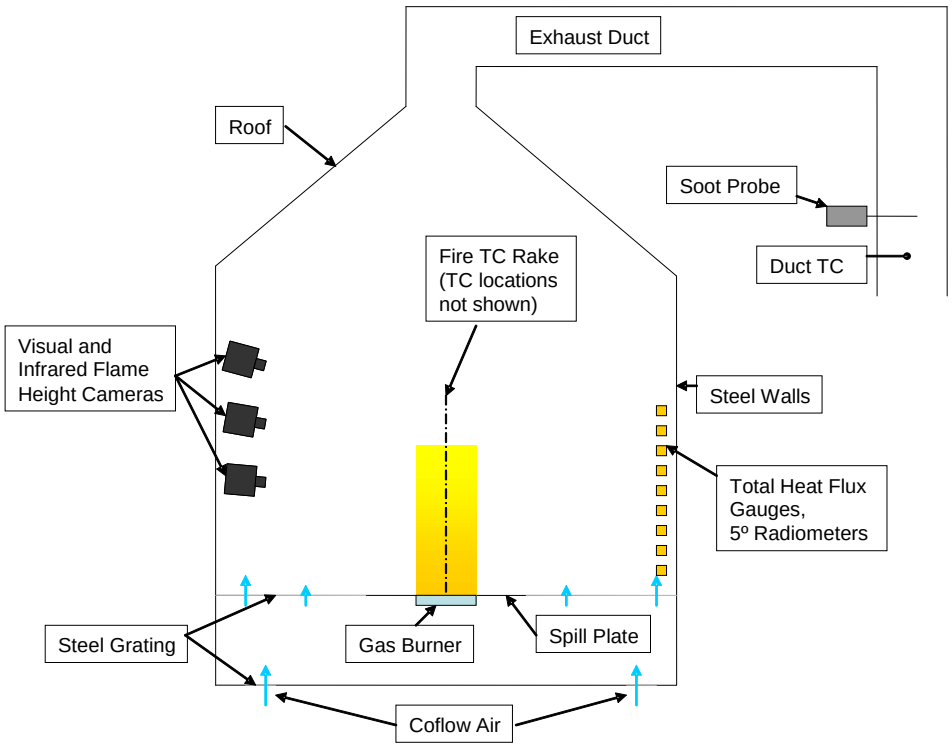

Figure 8 Locations of instrumentation for supplemental measurements.

3.4.1 Median Flame Height – Visual Data

The median flame height was determined from visual data from a video camera in the FRH test cell. Prior to the test each camera view was calibrated using vertical stadia placed at the pool centerline. The flame height was assumed to be the height at which the flame is visible at least 50% of the time. These were turbulent flames with regular cyclical (lift off); in the few images that showed "lifted" flames the highest point of the "lifted" flame was used.

Uncertainty Analysis

The flame height is defined herein as the highest point at which a flame is visible at least 50% of the time. Uncertainty in the actual height of the visible flame in an individual image is estimated to be approximately 5 cm. Uncertainty in determination of the median flame height based on a minimum of 900 video frames was assumed to be equal to the uncertainty in determining the height of the flame within the frame.

3.4.2 Temperature Data in the Flame Zone

Temperature measurements were taken along the fire centerline to supplement the visual data using a rake of 40 mil diameter mineral-insulated, metal-sheathed (MIMS) Type K thermocouples attached to a stainless steel wire hung from the ceiling. Since a variety of fuel flow rates will be studied the thermocouples were placed at heights from 10 cm to 7.5 m above the surface of the burner. The thermocouples were more tightly grouped at heights below 1 m to ensure that adequate resolution was available for fires with flame heights from 25 cm up to 6.0 m. A total of 20 thermocouples was used, at heights of 10 cm, 20 cm, 30 cm, 40 cm, 50 cm, 75 cm, 1.0 m, and then at 0.5 m increments from a height of 1.0 m to 7.5 m.

Note that the reported data can only be interpreted as the temperature of the thermocouple; these are neither flame temperatures nor gas temperatures (there are no radiation shields surrounding the thermocouples and the measurements are not gas aspirated). To use these data to obtain gas or flame temperatures, fire simulations that incorporate thermocouple models would have to be performed.

Uncertainty Analysis

The uncertainty in the thermocouple measurements is ±3ºC.

3.4.3 Air Flow Rate and Temperature

The air supplied to FRH was controlled to maintain a constant flow rate at the desired value. A forced-draft fan forced air into the chamber at the specified flow rate. An induced-draft fan in the exhaust duct was used to draw air and combustion products out of the chamber and maintained the pressure in the FRH cell at ambient levels. Both fans were computer controlled

and the flow rate, fan speed, and current for each fan was logged. The air temperature was measured by a thermocouple in the basement of the FRH facility.

Uncertainty Analysis

The air flow rate was measured by a Veltron II pressure and flow transmitter (Air Monitor Corporation, Santa Rosa, CA). The Veltron II calculated the air velocity and flow rate based on a differential pressure measurement. The differential pressure was measured to an accuracy of 0.1% of the natural span of the transmitter (10 inches of water). The uncertainty in the velocity due to the differential pressure uncertainty was approximately ±3% at a flow rate of 150,000 scfm. When the uncertainties due to non-uniformity in the velocity profile, tolerances on the duct dimensions, etc. are included the total uncertainty was approximately ±6% of the total flow rate.

The thermocouple measuring the air temperature, like the thermocouple measuring the fuel temperature, was located in a cool duct in which convection is expected to dominate the overall energy balance for the thermocouple. The uncertainty in the air temperature measurements was assumed to be the same as for the fuel measurements, ±3ºC.

3.4.4 Wall Temperatures

The temperatures of the steel walls of the FRH chamber are measured by thermocouples mounted at heights of 1 ft. (30 cm), 10 ft. (3.04 m), 20 ft. (6.08 m), 30 ft. (9.12 m), and 39 ft. (12.16 m) above the steel grating. The thermocouples are shielded from the radiation from the fire and the convective flow of the air by a small piece of metal foil to minimize bias errors in the wall temperature measurement. These measurements are duplicated at four equally-spaced angular locations around the facility. The wall temperature measurements are of interest for imposed boundary conditions in validation simulations.

Uncertainty Analysis

Wall temperature measurements are made by thermocouples mounted to the steel walls of the FRH chamber. The thermocouples are in good thermal contact with the walls, which have a very high thermal conductivity. The thermocouples will be partially shielded from radiation from the fire and convection from the cool air. Previous experience has shown that the walls remain relatively cool during tests due to their large thermal mass. The analysis of Nakos [2004] suggests that the maximum error is ±1% of the reading (in K) for temperatures up to 400K. An uncertainty of ±4ºC will be assumed for the wall temperatures in the present tests.

3.4.5 Radiant Heat Flux to Objects outside the Fire

Eight narrow-angle radiometers and eight total heat flux gauges measured the radiation intensity as a function of height. Pairs of gauges, a narrow-angle (also narrow-view, NV) radiometer (Medtherm model NVRW-15-5-360-2183, 5º view angle, 0-150 kW/m^2 range) and a wide-angle (also wide-view, WV) total heat flux gauge (Medtherm model 64-2-18 with a view angle of 180º,

0-15 kW/m^2 range), were mounted together at a distance of approximately 28 ft. (9 m) from the center of the fire. The area of view of the narrow angle gauges at a distance of 9 m is circular and close to 0.8 m in diameter. The gauge pairs were at heights of ~0.5 m to 4.0 m with a spacing of 0.5 m between gauges. The center-line of the angle of view for each gauge passed through the centerline of the fire at the height of the gauge. All of the heat flux gauges are water-cooled.

Uncertainty Analysis

The radiative heat flux measured by the narrow angle radiometers and total heat flux gauges near the walls of the facility have a manufacturer's stated uncertainty of ±3%. Calibration checks are performed on all radiometers using in-house blackbody sources when received; gauges not meeting specifications are returned to the manufacturer. However, numerous authors report greater uncertainty for radiometers, especially used in outdoor field experiments. We assume a total uncertainty of ±10% (2σ) for all radiometer measurements (to include all random and bias errors, including DAS uncertainty).

3.4.6 Data Acquisition

The data acquisition system (DAS) consisted of a PC with a 16-bit data acquisition card connected to a National Instruments (NI) SCXI-1001 chassis. It had twelve NI SCXI-1102 cards with NI SCXI-1303 blocks for TCs and four NI SCXI-1104 cards with NI SCXI-1300 blocks for analog signals. This yielded a total channel count of 384 channels if all slots are used for data acquisition. The system is upgradeable simply by adding an additional SCXI-1001 DAQ cards and more multiplexer units (MUXs).

The data acquisition system can acquire temperature, heat flux, and pressure data. The integrity of all thermocouple channels was evaluated prior to each experiment with an Ectron thermocouple simulator, which inputs a controlled signal into each channel at the thermocouple device connection point and provides a check on the integrity of the channel hardware and software from that point to the final magnetic storage location. An extensive uncertainty analysis was performed by Nakos [2004] on the use of NI DAS for fire field work at Sandia with the recommendation to use approximately ±1% for bias and ±1% for random uncertainties.

Data was sampled simultaneously for all channels, typically at 1000 Hz with an average value recorded at a rate of at least one sample per second, starting at least two minutes prior to the fuel ignition and continuing after burnout of the fire.

A formal checklist for conducting the test was created and used to record actions during the test event. The data from the instrumentation was organized via a Data Channel Summary Sheet and with sketches showing instrumentation location. This summary sheet contained a channel-by-channel listing of the instrumentation with details such as expected range, sampling rate, calibration date and source, instrument location, and the data sample rate. Post-test, all data were collected and converted to electronic format for purposes of archiving and dissemination via PC media (i.e., CD or equivalent).

3.5 Test Description and Results

Five separate experiments using methane gas as the fuel were performed in the FLAME test cell (Table 2) using a 3 m diameter gas burner yielded twenty eight sets of flame height vs. fuel flow rate data. Each data set correlates steady-state average gas flow rate data with video analysis to determine medium flame height data over a 30 second interval. Data from the test performed on 5/1/2008 are plotted in this section to demonstrate the measurement method and data acquisition used in all of the tests.

Table 2 Gas Burner Experiments

Test Date	Fuel	# of tests	# of data sets
4/21/2008	methane	1	3
4/22/2008	methane	3	9
4/30/2008	methane	1	8
5/1/2008	methane	1	8

The ID fan was set to maintain 70,000 scfm air flow into the cell for all of the methane tests. The sections below provide fuel flow rate, heat flux, temperature plots, and flame median height data for each experiment.

The methane gas tests were performed in the following manner (refer to Figure 9). A methane tube trailer was attached to the A train. The A train flow control valve (FCV) downstream of the pressure reducing (PRV) valve was set to 100% open. The burner propane igniter was lit and verified on. The PRV was opened and set to a fixed position. Following a period of time to collect steady-state data, the PRV was moved to another position and the process repeated.

Average values of trailer pressure, manifold pressure and temperature, and flow rate were determined at the time intervals marked with pairs of vertical lines (30 s duration) referred to as "cam pulls" in the legend in Figure 9. Pressure and flow rates were sufficiently steady during these intervals for valid measurements to be made and correlated with the video analyses for determining flame height.

The gas lines were back purged with nitrogen before combustible gas was introduced and after the experiment was completed. Note that the trailer pressure gauge was located on the high pressure line between the trailer and the pressure regulation valve; hence it is affected by the flowing gas and reads low during discharge particularly at the higher flow rates.

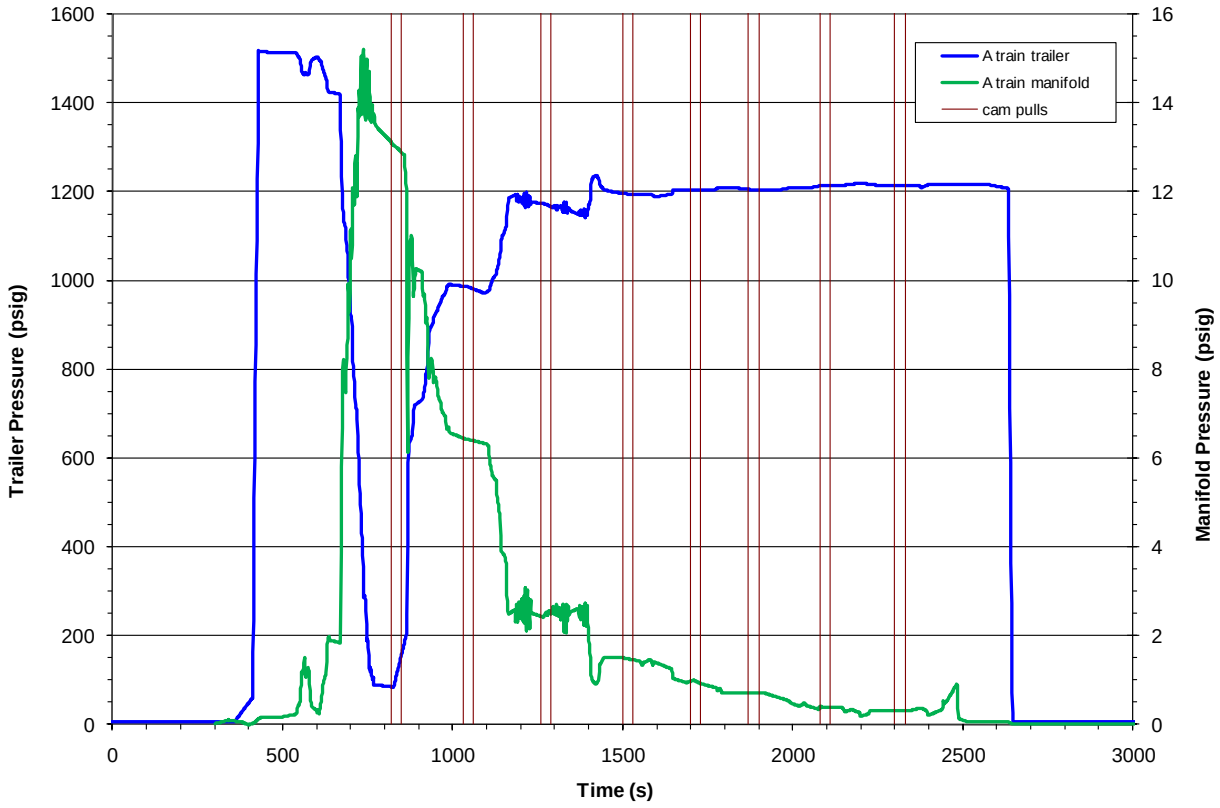

Figure 9 Trailer and manifold pressure for methane test on 5-1-08.

Fuel flow rates as measured by the primary measurement source (A train) and the main burner line (6 inch) are shown in Figure 10. There was a small difference in measured flow rate between the A train and the 6 inch line, attributed to the manifold design that probably produced non-steady flow at the flow measurement instruments. The average percentage difference over the range of flow rates was ~3% with a standard deviation of 4%. The largest difference occurred when flow rates ranged between ~200-300 scfm.

Table 3 compiles all of the steady-state flow rate measurements for each test. The start and stop times for each steady-state data set within a test are shown under the column labeled "Cam Pulls" (for data pulled from the cameras, also referred to as the video analysis times). The mass flow rates used in the Q* analyses was based on the A train flow instrumentation.

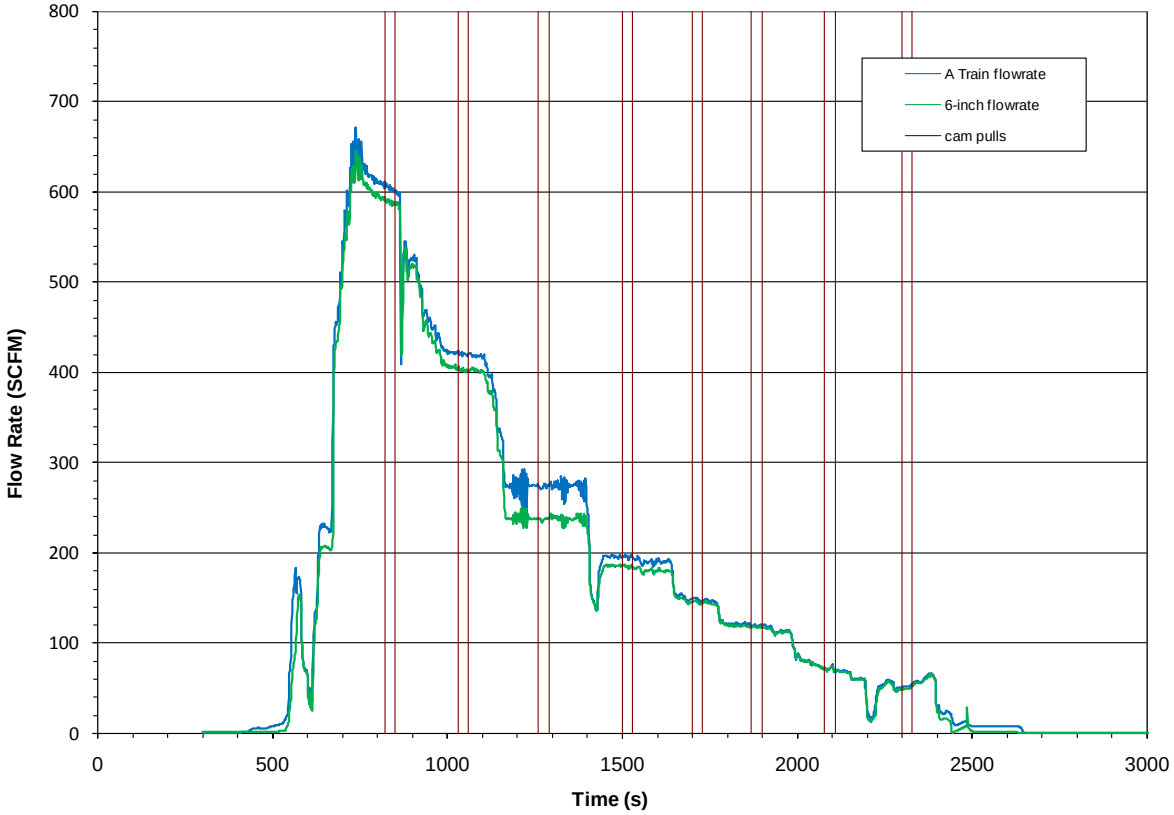

Figure 10 Fuel flow rate (5-1-08 methane test).

Table 3 Methane Gas Flow Rate Measurements

Test Date	Test #	Cam Pulls	Train A manifold pressure	Gas temp	Train A flow	Train A flow	6 inch flow	6 inch flow	flowrate % difference
		s	psig	C	scfm	st.dev.	scfm	st.dev.	
4/21/2008	1	1400-1430	3.97	29	**362**	1	356	1	2
4/21/2008	1	1900-1930	1.01	29	**202**	1	197	1	2
4/21/2008	1	2100-2130	0.52	29	**159**	2	160	1	-1
4/22/2008	1	700-730	0.49	17	**170**	1	154	0	10
4/22/2008	1	1200-1230	1.03	18	**211**	1	190	1	10
4/22/2008	1	1700-1730	3.61	19	**353**	1	326	1	8
4/22/2008	1	2100-2130	0.50	20	**169**	1	161	0	5
4/22/2008	2	900-930	3.99	30	**366**	4	356	3	3
4/22/2008	3	670-700	4.74	31	**394**	2	389	2	1
4/22/2008	3	1700-1730	9.94	31	**544**	2	550	2	-1
4/22/2008	3	1870-1900	11.71	28	**595**	2	601	2	-1
4/22/2008	3	2030-2060	14.95	27	**682**	2	688	2	-1
4/30/2008	1	900-930	19.04	27	**777**	2	759	3	2
4/30/2008	1	1000-1030	13.81	26	**635**	5	630	6	1
4/30/2008	1	1180-1210	10.26	26	**532**	2	530	2	0
4/30/2008	1	1430-1460	1.94	27	**232**	2	218	1	6
4/30/2008	1	1640-1670	0.39	29	**67**	0	68	2	-1
4/30/2008	1	1770-1800	0.65	29	**110**	1	112	1	-1
4/30/2008	1	1930-1960	0.27	30	**49**	0	46	0	8
4/30/2008	1	2050-2080	0.38	31	**76**	0	77	1	-2
5/1/2008	1	820-850	12.99	18	**604**	3	589	3	3
5/1/2008	1	1030-1060	6.42	18	**420**	2	403	1	4
5/1/2008	1	1260-1290	2.48	19	**274**	2	237	1	13
5/1/2008	1	1500-1530	1.48	20	**195**	2	184	1	6
5/1/2008	1	1700-1730	0.97	20	**148**	2	145	1	2
5/1/2008	1	1870-1900	0.72	21	**119**	1	117	1	2
5/1/2008	1	2080-2110	0.38	21	**72**	2	71	1	1
5/1/2008	1	2300-2330	0.31	22	**52**	1	49	1	6

The temperatures from the thermocouple rake above the burner are shown in Figure 11. Figure 12 shows the average and standard deviation of the thermocouple temperatures as a function of height at the times selected for flame height analysis (as indicated by the video analysis times VID1 through VID8). Note the igniter was left on for the entire test.

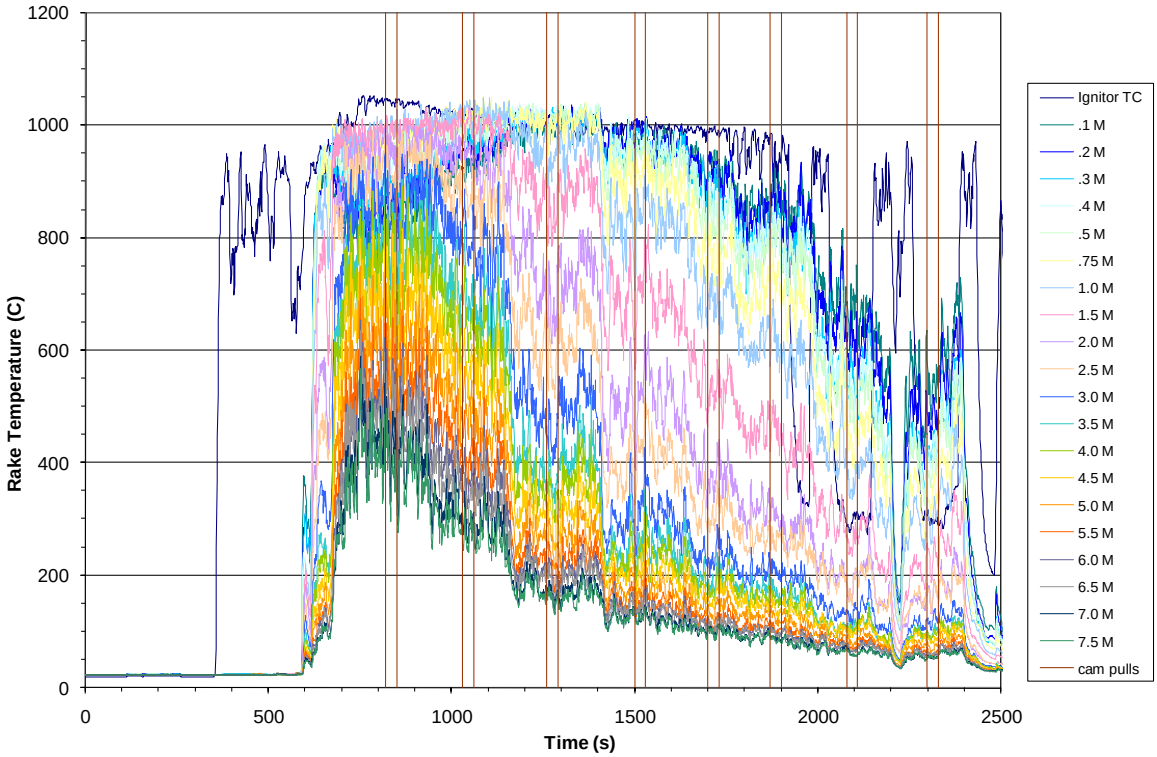

Figure 11 Temperatures above the burner at flame centerline (5-1-08 methane test).

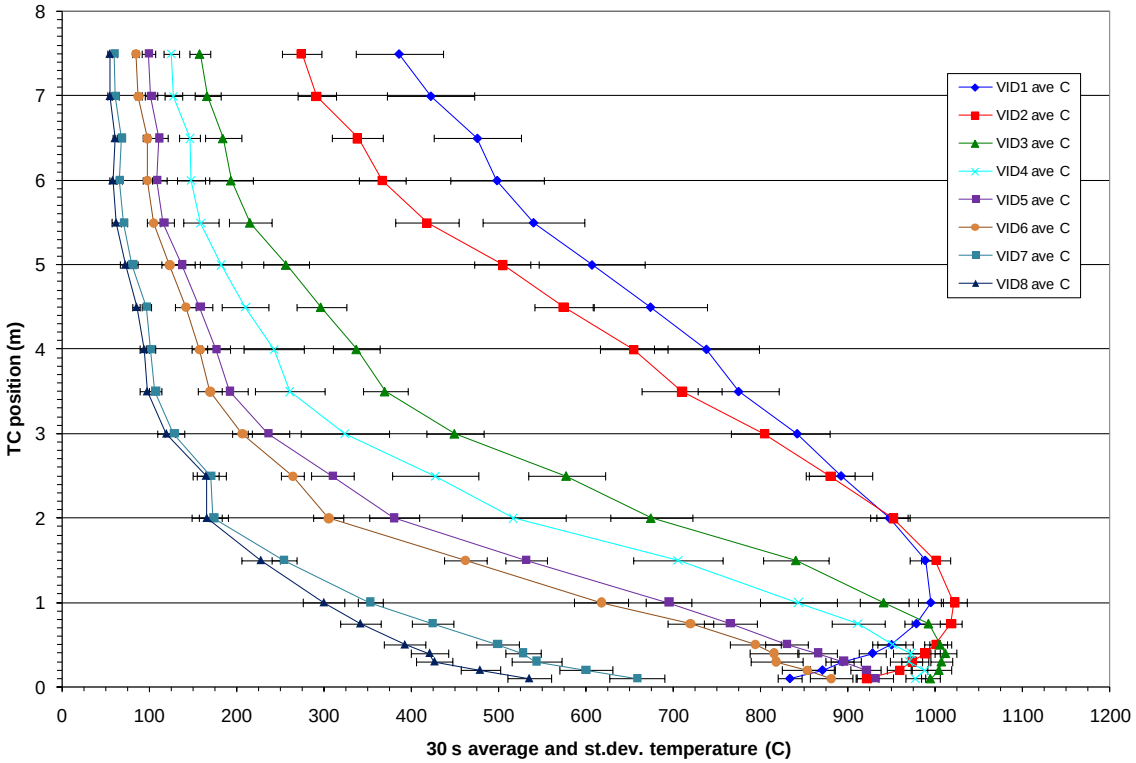

Figure 12 Average thermocouple temperatures at video analysis times (5-1-08 methane test).

Figure 13 and Figure 14 show the time dependent heat flux data from the narrow-view radiometers and the wide-view total heat flux gauges (R for narrow-view radiometer and T for wide-view total heat flux gauge in the legends). Figure 15 and Figure 16 show the 30 s average (with std.dev.) of those gauges during the video analysis times.

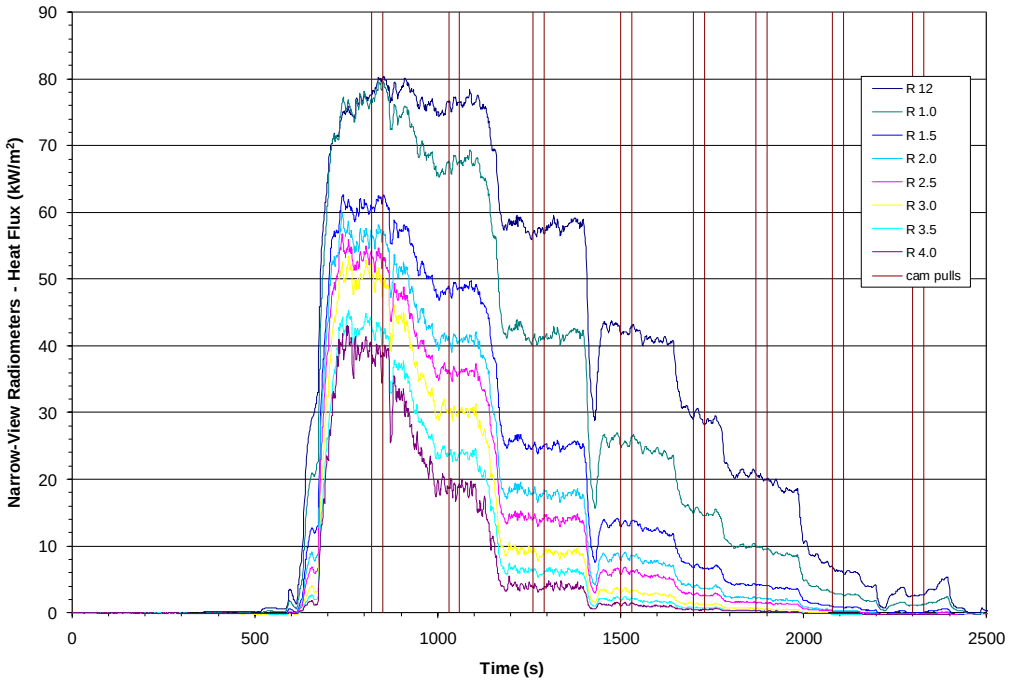

Figure 13 Narrow-view heat flux data (5-1-08 methane test).

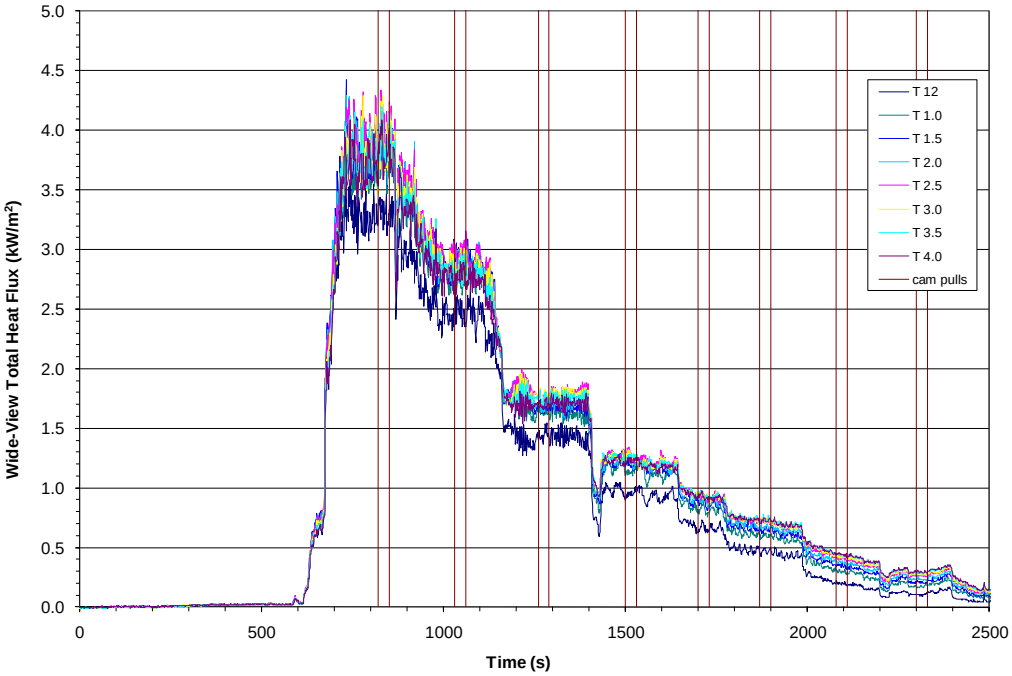

Figure 14 Wide-view heat flux data (5-1-08 methane test).

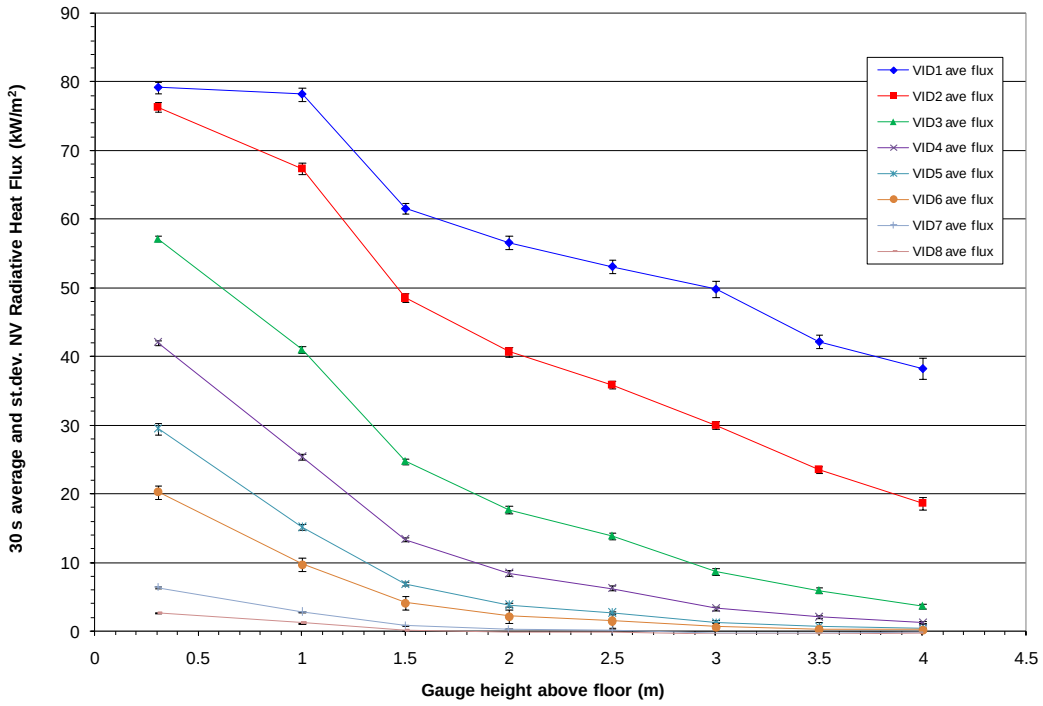

Figure 15 Average narrow view heat flux data vs. height at video analysis times (5-1-08 methane test).

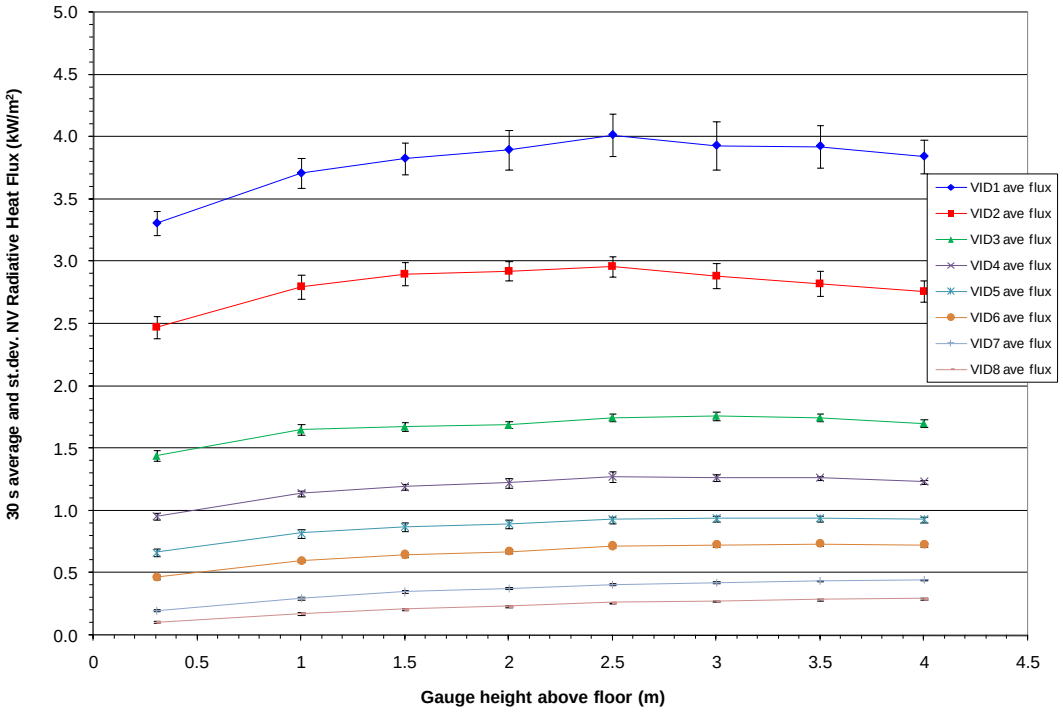

Figure 16 Average wide view heat flux data vs. height at video analysis times (5-1-08 methane test).

Figure 17 and Figure 18 show the camera calibrations and resulting curves (drawn by fitting the data with regression analysis) for reducing the flame height data for the test on 5-1-08. Note camera views and calibrations at two different levels in the FLAME facility were used to capture the flame height (certain flow rates yielded flame tops out of range of a particular field of view). For example, in the test on 5-1-08 at the 820 s video analysis time, the median flame height was extracted from the 900 frame 2nd floor camera dataset (as flame plume rose out of the 1st floor camera field of view in some frames).

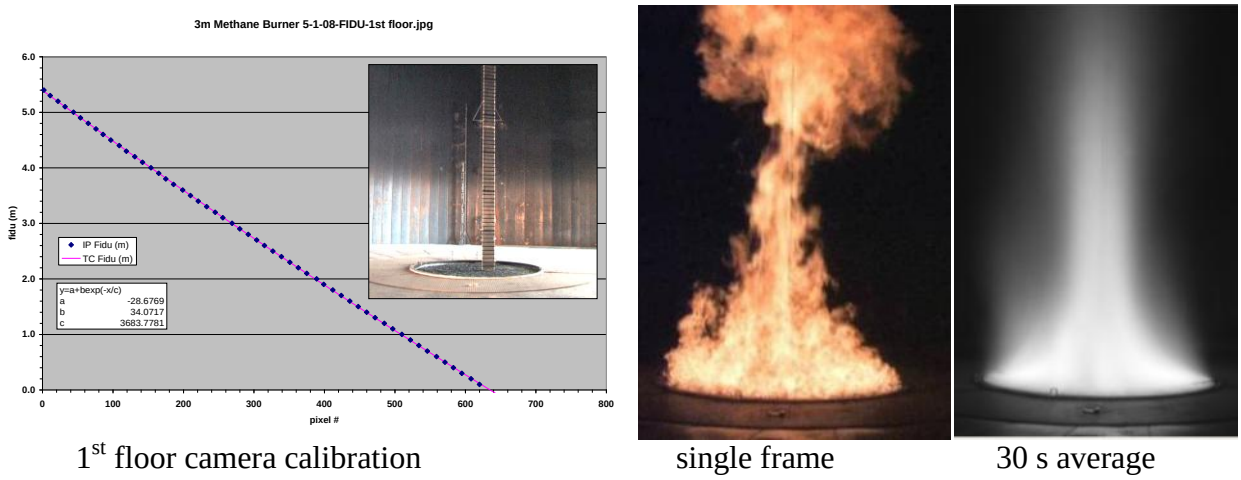

1st floor camera calibration single frame 30 s average

Figure 17 Calibration for the 1st floor camera (5-1-08 methane test).

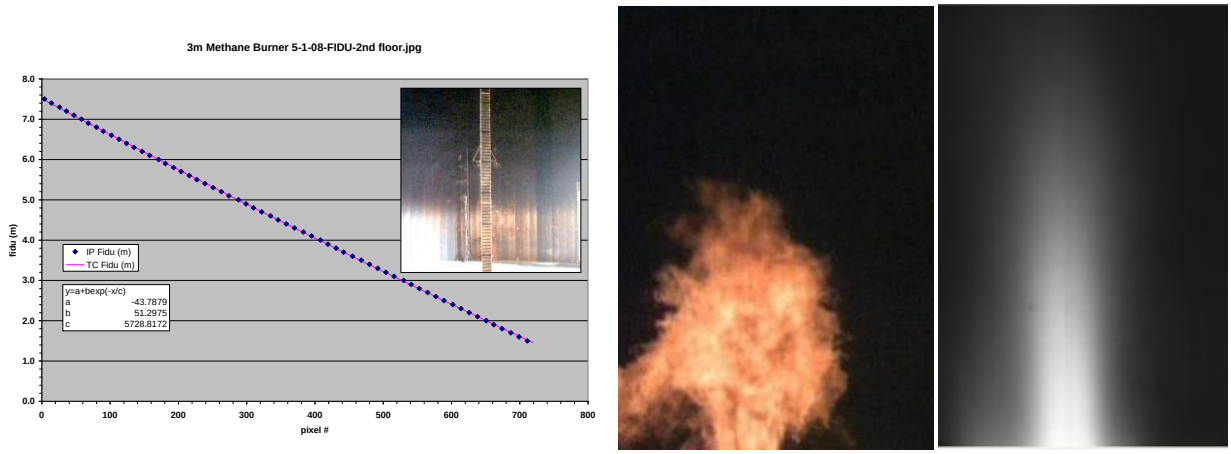

2nd floor camera calibration single frame 30 s average

Figure 18 Calibration for the 2nd floor camera (5-1-08 methane test).

For each selected averaging period within a test, thirty seconds of video data (900 frames, starting at the beginning of the steady-state time period listed in Table 3) recorded during steady state "puffing" conditions (indicating fully turbulent conditions) were analyzed to determine the

median flame height and the puffing frequency. To automate the process, imaging analyses software (ImagePro®) was used to provide the average pixel intensity at each horizontal row of a 1/3 burner diameter wide vertical line drawn through the burner centerline (line profile). Figure 19 illustrates the process, showing the average color pixel intensity as a function of vertical height (720 pixels tall).

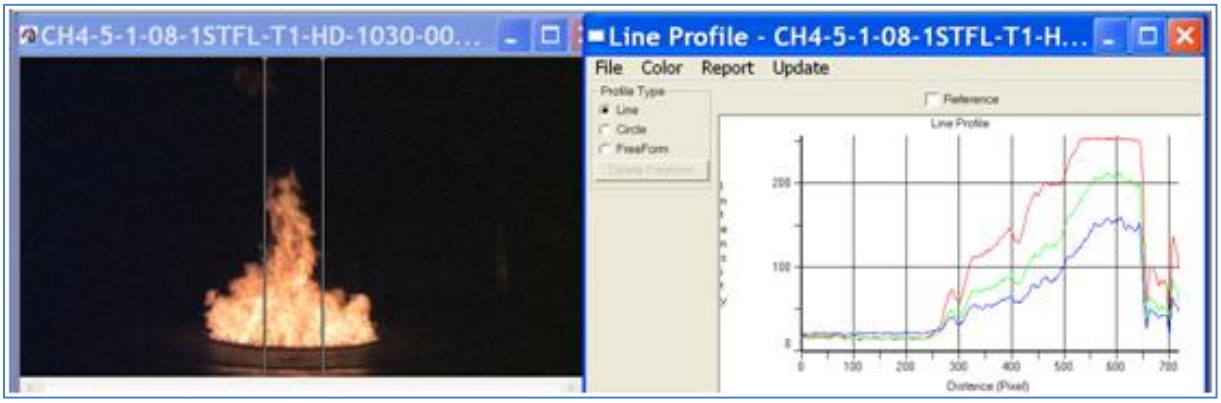

Figure 19 Intensity vs. height (line profile) for image in 5-1-08 test.

It was necessary to determine the threshold intensity to be used for each test, which changed due to differences in flame color and camera settings. A Fortran routine was used to process the vertical line profile intensity of the 900 frame dataset, varying the threshold intensity from 0 to 255 and determining the average flame height at each intensity. The result is shown in Figure 20 for all datasets in all tests. As the threshold intensity increases, a sharp drop followed by a "knee" occurs at the flame top. As the threshold intensity increases, the estimated flame height gradually decreases as the line profile progresses further down into the flame. The actual intensity used in the analysis is chosen by inspection, within ~10 units of intensity below the knee. Figure 20 shows the vertical line profiles for all tests yielding the average height as a function of threshold intensity.

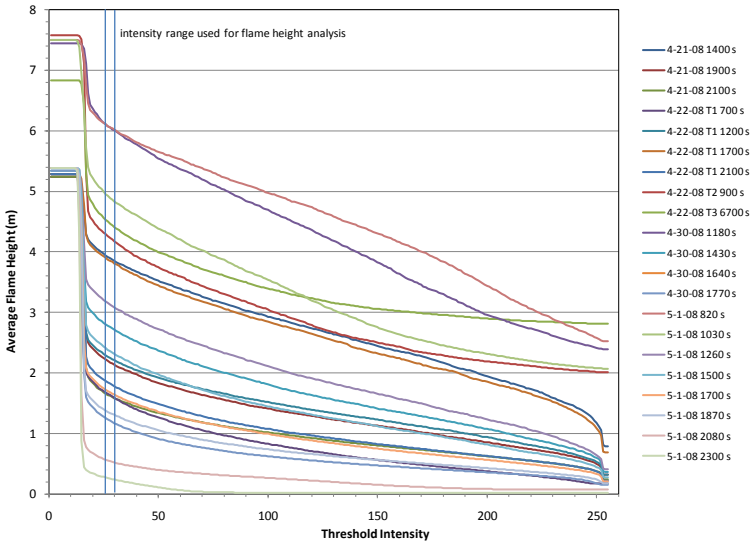

Figure 20 Average flame height as a function of threshold intensity – all datasets.

With the determination of the average threshold intensity, the medium flame height statistics can be determined. Figure 21 shows the flame height for each frame at the selected video analysis times (e.g., different flow rates) using red intensity thresholds between 28-30.

The median flame height (where the height is above and below 50% of the time) was determined for the six separate flow rates. The horizontal colored lines are drawn to represent the median flame length values. The puffing frequency for all of the methane fires ranges from ~0.9 Hz at the highest flow rates to ~0.8 Hz at the lower flow rates.

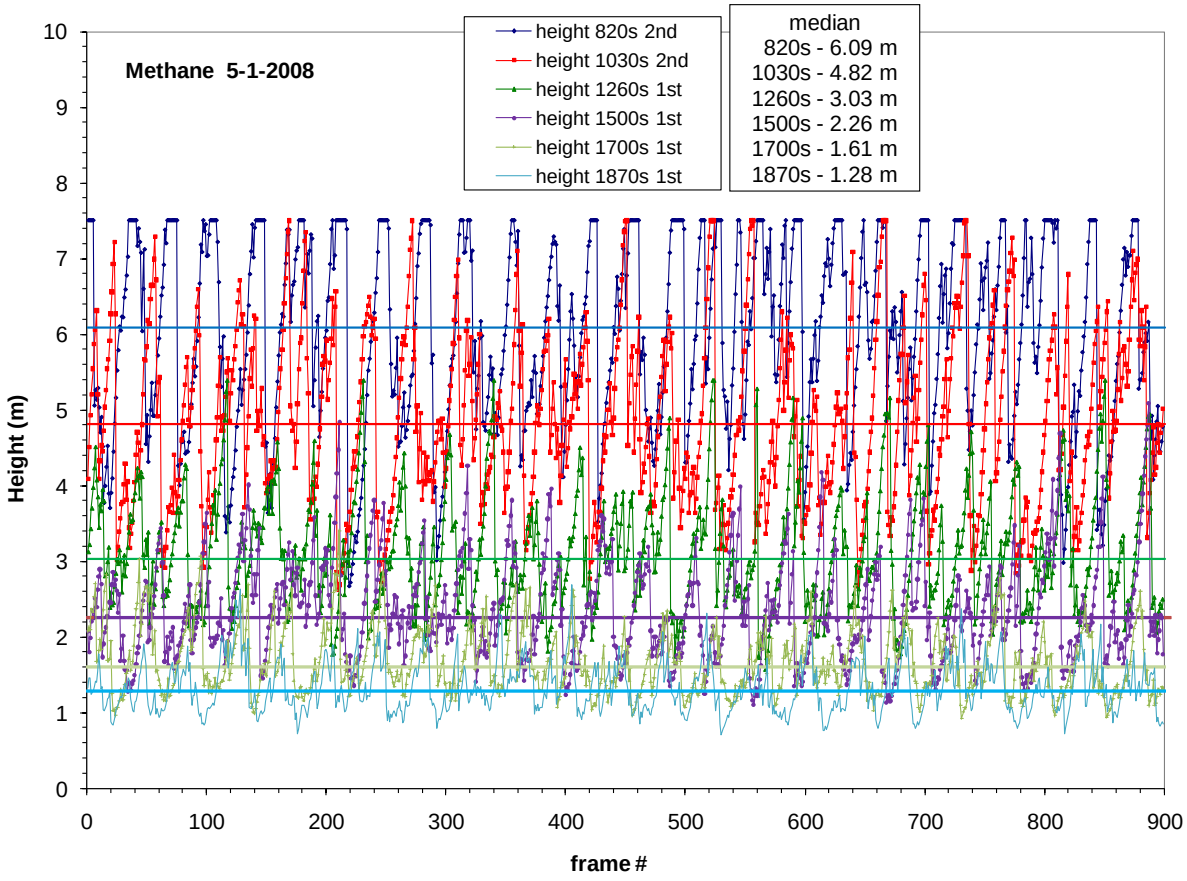

Figure 21 Individual frame flame height (5-1-08 methane test).

3.6 H/D vs. Q* - Data Reduction and Analysis

Table 4 compiles all of the datasets used in the following analyses. Ambient air temperature ranged between 15-25°C, ambient pressure for all tests was ~830 kPa, and the ambient air relative humidity ranged from 7-18%. Missing flame height data at high flow rates were caused by the flames being too tall for the camera setting. Loss of plume integrity did occur at the very low flow rates (too small of a contiguous flame to determine a height); however, it could not be determined if this was caused by a "mass fire" effect or due to imperfect operation of the burner flow straightening system at these very low flow rates.

Table 4 Compilation of the 3 m methane gas burner experimental data.

Test Date	Test #	Cam Pulls	Train A manifold pressure	Gas temp	Train A flow rate	median flame height	Flux at 1m WV	Air flow	Air temp	ambient pressure	ambient RH
		s	psig	C	scfm	m	kW/m^2	scfm	C	kPa	%
4/21/2008	1	1400-1430	3.97	29	362	3.86	2.3	70000	23	830	6
4/21/2008	1	1900-1930	1.01	29	202	2.06	1.2	70000	24		
4/21/2008	1	2100-2130	0.52	29	159	1.53	0.9	70000	24		
4/22/2008	1	700-730	0.49	17	170	1.53	0.7	70000	18	835	12
4/22/2008	1	1200-1230	1.03	18	211	2.14	1.2	70000	18		
4/22/2008	1	1700-1730	3.61	19	353	3.76	2.4	70000	18		
4/22/2008	1	2100-2130	0.50	20	169	1.74	1.0	70000	18		
4/22/2008	2	900-930	3.99	30	366	4.00	2.4	70000	23	832	7
4/22/2008	3	670-700	4.74	31	394	4.41	2.4	70000	24	832	7
4/22/2008	3	1700-1730	9.94	31	544	5.97	3.5	70000	24		
4/22/2008	3	1870-1900	11.71	28	595	6.51	4.1	70000	24		
4/22/2008	3	2030-2060	14.95	27	682	6.78	4.7	70000	24		
4/30/2008	1	900-930	19.04	27	777		4.4	70000	25	824	9
4/30/2008	1	1000-1030	13.81	26	635	6.88	4.0	70000	25		
4/30/2008	1	1180-1210	10.26	26	532	6.12	3.6	70000	25		
4/30/2008	1	1430-1460	1.94	27	232	2.63	1.5	70000	25		
4/30/2008	1	1640-1670	0.39	29	67		0.3	70000	25		
4/30/2008	1	1770-1800	0.65	29	110	1.14	0.5	70000	25		
4/30/2008	1	1930-1960	0.27	30	49		0.2	70000	25		
4/30/2008	1	2050-2080	0.38	31	76		0.3	70000	25		
5/1/2008	1	820-850	12.99	18	604	6.09	3.7	70000	17	825	17
5/1/2008	1	1030-1060	6.42	18	420	4.82	2.8	70000	17		
5/1/2008	1	1260-1290	2.48	19	274	3.03	1.6	70000	17		
5/1/2008	1	1500-1530	1.48	20	195	2.26	1.1	70000	17		
5/1/2008	1	1700-1730	0.97	20	148	1.61	0.8	70000	17		
5/1/2008	1	1870-1900	0.72	21	119	1.28	0.6	70000	17		
5/1/2008	1	2080-2110	0.38	21	72		0.3	70000	17		
5/1/2008	1	2300-2330	0.31	22	52		0.2	70000	18		

The largest contributor to the error in the height-to-diameter (H/D) calculation is the uncertainty in the flow rate. Figure 22 shows the median flame height vs. methane flow rate data as measured by the A train flow meter. A linear fit of the data is also given (x = scfm, y = medium flame height, R = goodness of fit). The uncertainty on the flow measurements is 8% (2 standard deviations) and the uncertainty on the flame height data is 10%.

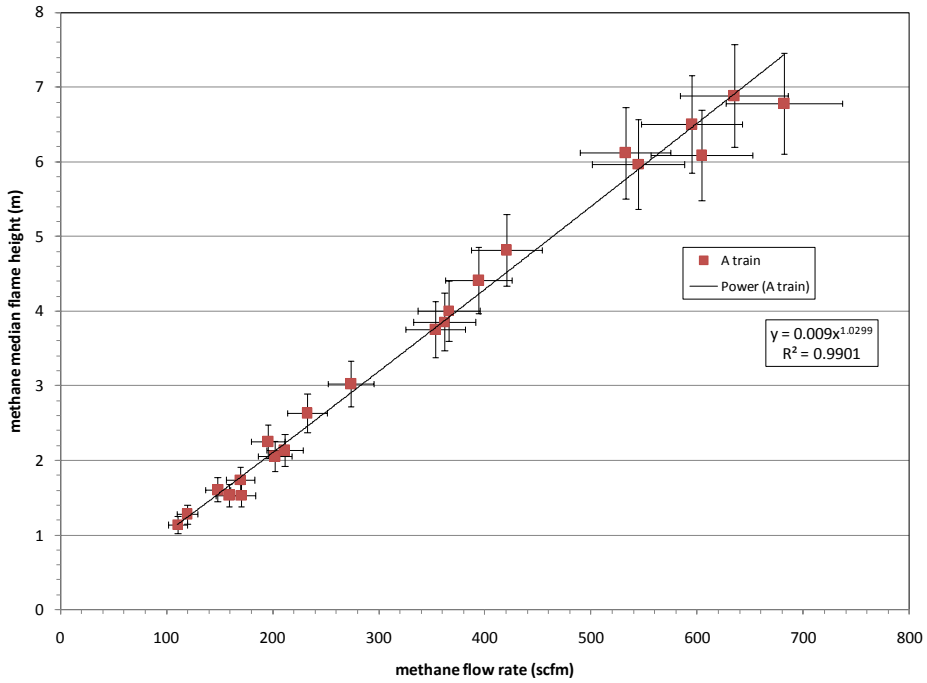

Figure 22 Flame height vs. flow rate (A train) for the methane tests.

Figure 23 shows the median flame height/diameter ratio as a function of the estimated Q* (using Eq. (1), the video median flame heights, the Train A methane flow rate values in Table 4, and properties from Table 5 for all of the tests. Several other correlations obtained with smaller burners (up to 0.5 m diameter) are also shown in Figure 23 and indicate agreement with the SNL flame height correlation at values of Q* pertinent to large-scale LNG pool fires. All correlations (cited in the reference section) are plotted over a Q* range for which they were derived.

$$Q^* = \frac{m_f \Delta H}{\rho_a T_a C_{p_a} g^{1/2} D^{5/2}} \qquad (1)$$

Table 5 Values for Q* Parameters

Parameter	symbol/units	methane
mass loss rate	m_f kg/s	-
gas density	ρ kg/m^3	0.54
heat of combustion	ΔH J/Kg	5.00E+07
air density	ρ_a kg/m^3	0.96*
air temperature	T_a K	298
air specific heat	$C_{P\ a}$ J/kgK	1.01E+03
gravity	g m/s^2	9.81
burner diameter	D m	3

*Determined by the atmospheric pressure of 82,380 Pa.

Note that mass flow of the gas was calculated by multiplying the A train flow rates (Table 4) times the gas density listed in Table 5.

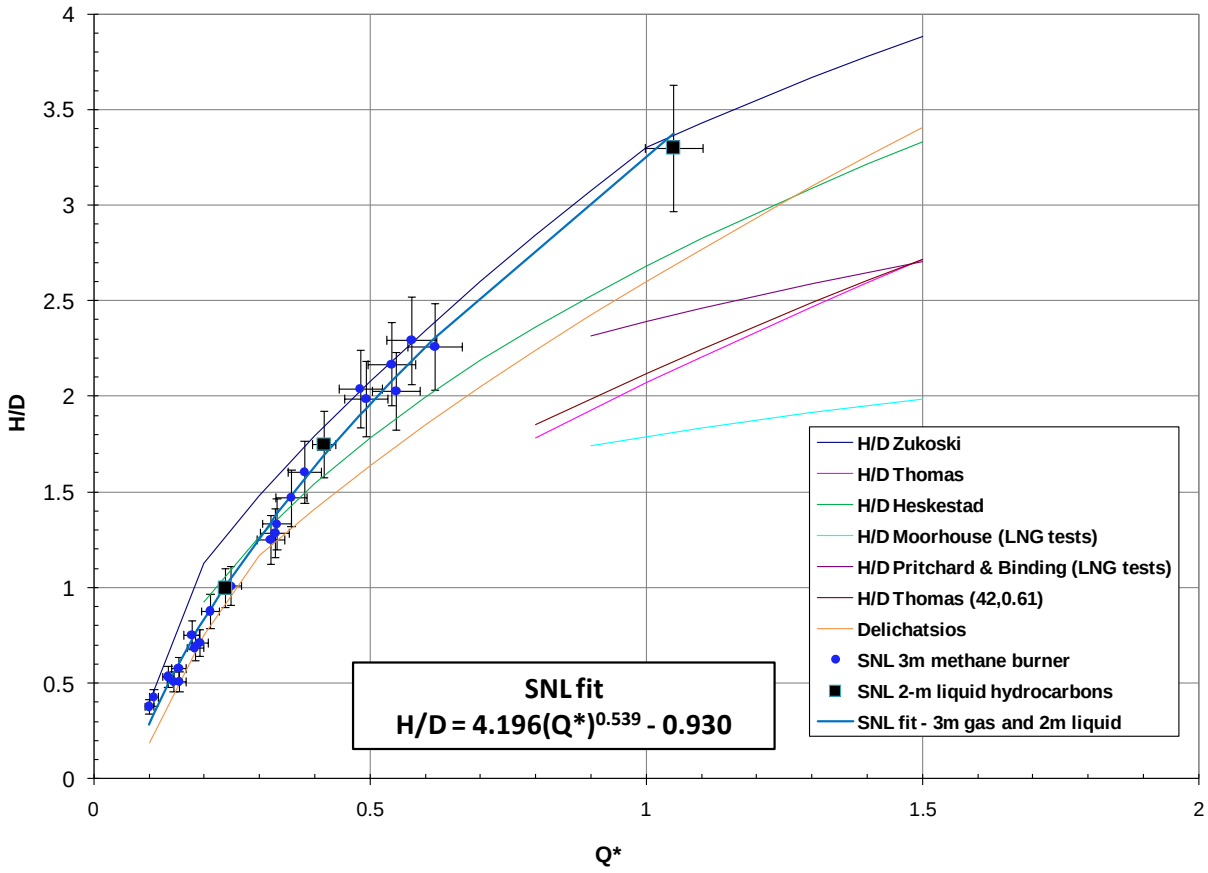

Figure 23 Flame height/diameter ratio vs. dimensionless heat release rate Q*.

Three additional data points from a previous study [Blanchat et al., 2010] were included with the methane gas data in the SNL fit shown in Figure 23. Constant level liquid pool fires (2 m diameter) utilizing various hydrocarbons (methanol, ethanol, JP8) were performed. Measurements of mass loss rates and flame heights allowed determination of Q* and H/D. The SNL H/D data and correlation shown in Figure 23 are bracketed by the correlations determined by Zukoski and Heskestad.

This data can be used to predict the ratio of flame height to diameter for very large pool fires by using Eq. (1) and a corresponding burn rate, diameter, and appropriate atmospheric conditions to determine a value of Q*. Based upon data from the LNG pool fire Test 1 it is anticipated that a regression rate of 0.147 kg/m^{2}s would result for very large LNG pool fires. The H/D value for a given Q* value can then be determined using the SNL dataset (Figure 23).

For reference, Table 6 (with values plotted in attached figure), assuming a range of pool diameters (from 25 m to 1000 m) that have a regression rate of 0.147 kg/m^{2}s, yields a range of burn rates, that then is used to determine a range of Q* values from 1.05 to 0.17, respectively. Using these Q* values, the SNL data fit shown in Figure 23 (H/D = 4.196 $Q^{*0.539}$ - 0.930)

indicates a range of H/D values of about 3.4 to 0.7. The Q* values calculated in Table 6 are based upon the standard atmospheric properties of T_a=288 K, ρ_a=1.2 kg/m^3, and C_{pa}=1006 J/kg K. Thus, a pool diameter of 300 m corresponds to a Q* value of 0.30 and the estimated H/D ratio would be ~1.3.

It is important to be aware that the pool diameter specified in the correlation (and Table 6) is a "reacting" pool diameter, i.e., the flame base diameter (if the flame is not anchored to the leading edge of the pool). Table 6 also plots the Q* and L/D or H/D data from the two large-scale LNG pool fires discussed later in this report.

Table 6 Q* and H/D values vs. pool diameters for standard atmospheric conditions.

Diameter (m)	Burn Rate (kg/s)	Q*	H/D (SNL fit)
1000	115454	0.165	0.66
900	93517	0.174	0.71
800	73890	0.185	0.76
700	56572	0.198	0.82
600	41563	0.214	0.90
500	28863	0.234	0.99
400	18473	0.262	1.11
300	10391	0.302	1.27
200	4618	0.370	1.53
100	1155	0.523	2.03
75	649	0.604	2.27
50	289	0.740	2.64
25	72	1.046	3.37

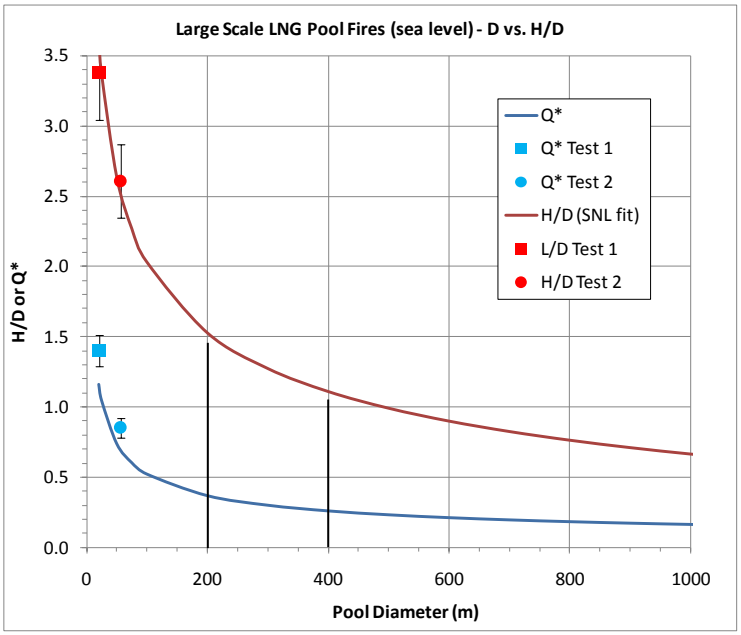

3.7 Reduced Scale (Gas Burner) Testing Summary

For application purposes Q* should be evaluated using atmospheric conditions at a specific site. For site specific analysis the diameter of interest and atmospheric values for T_a, ρ_a, C_{pa} should be substituted into equation 1 to determine a Q* value and hence an H/D value using the SNL H/D vs. Q* equation shown in Figure 23. Since any given site will have a range of conditions, in order to be conservative it is recommended that the set of conditions providing the largest Q* and hence H/D should be chosen.

Note that these results pertain to steady circular pool fires that are in quiescent surrounding conditions. If the shape is significantly different from circular and/or if there is an appreciable wind condition then the application of this data may not be appropriate. For instance regarding pool shape, consider the limiting conditions of a trench fire where the height is proportional to the shortest dimension. A very narrow trench fire would provide a much lower H/D than if it

were circular and given equivalent areas. The difference could be an order of magnitude depending on the area and trench dimensions.

With regards to the effect of wind, the existing wind tilt correlations can have wide disparity depending on the pool size and wind speed. The flame height can be reduced from 10% to 40% depending on pool size, wind speed, and what correlation is used. The range of validity of these correlations is for much smaller pool diameters. Thus, it is difficult to quantify the effect of wind on flame height for very large pool diameters. The important aspect to note is that the effect of wind will be to reduce the flame height. So, for sites requiring a wind condition a conservative answer will be provided by imposing a flame tilt and using the SNL flame height data without wind conditions.

With regards to the effect of non-steady conditions, flame height as a function of rapidly varying diameter has not been systematically studied. Additionally, data does not exist on the effect of waves. Thus, it is difficult to quantify or even qualify these effects at this time.

4 Large Scale Tests

Existing LNG pool fire data is for spills 2-3 orders of magnitude smaller than those anticipated from LNG cargo tankers caused by accidental or intentional events. Data from large-scale LNG pool fire tests will provide decision makers with information to determine best-estimate thermal hazard zones. These tests will provide a 'benchmark' for LNG pool fires much like the Burro series provided the benchmark for LNG dispersion. Thus, these tests can serve as the standard to which CFD fire codes, as well as integral-based models, are to be compared. Currently, there are no well-characterized pool fire data available for large scale LNG fires on water (order 20 m diameter and greater).

The Sandia/DOE experiments were proposed to obtain data for LNG pool fires on water for diameters up to 100 m, with the intent of extending the scale from the previous available dataset for 8 - 15 m diameter pools and have total fire durations of at least 5 minutes to allow the gathering of steady-state information.

The basic elements necessary to perform the experiment were: 1) Identify the test site, 2) Construct a 120 m diameter shallow (2 m) water pool, 3) Construct a covered, insulated reservoir to contain 1172 m^3 (310,000 gallons) of LNG, 4) Construct reservoir discharge systems to allow LNG to discharge at pool center, 5) Construct LNG reservoir fill piping, 6) Provide a nitrogen gas source and valve manifolds to provide inertion and purge gas, and 7) Install reservoir, pool, and perimeter instrumentation (flow rate, meteorology, video, infrared spectroscopy, heat flux, etc.).

4.1 Experiment Objective

The objective of the large scale tests was to obtain data to allow best estimate predictions of thermal hazard distances for large LNG pool fires. Measurements (surface emissive power, mass loss (burn) rate, luminous flame height) were desired for different pool diameters up to 100 m to obtain trends in these parameters to allow development of correlations for pool diameters greater than 100 m.

4.2 Overview of the Large Scale Tests

The major infrastructure consisted of a covered, insulated reservoir to contain the LNG, reservoir discharge valves (also called plugs) and mechanisms to empty the reservoir, and reservoir discharge piping to transport the LNG to the center of a shallow man-made water pool where it will be burned. Support infrastructure included a water line to fill the water pool, a cryogenic LNG pipeline to discharge a LNG trailer into the reservoir, a nitrogen line from a nitrogen source trailer to inert the reservoir and the discharge pipes, reservoir mixing fans, gas monitoring systems for both the reservoir and the discharge pipes, a closure mechanism for the reservoir cover vents, a CO_2 extinguisher system for fire control at the reservoir vents (in event of a

lightning strike), and igniter systems at the LNG discharge point on the water pool and also at the pool perimeter.

SNL performed engineering calculations for Sandia-designed components of the reservoir as necessary to meet form and functional design requirements. Specifications for vendor-supplied components were reviewed for applicability to meet form and functional design requirements. Materials and equipment were inspected when procured and received. Field construction activities were inspected with sufficient frequency by the site foreman and field engineers to verify construction meets design requirements.

Documentation included a formal peer-reviewed report (this document). This report describes the methodology used for test design and conduct, the parameters considered when conducting the data analysis, and the results of the pool fire experiments. The datasets (including video media) are expected to be published and available in the public domain.

The following provides a brief summary of the experiment design and construction, with a listing of all permits and approvals.

4.3 Site

The infrastructure to support the experiment was constructed at Sandia National Laboratories (Albuquerque, NM), in Tech Area III near the 'D' explosive test site. The latitude / longitude of the center of the large 120 m (394 ft) diameter pool are: North: 34° 58.517' / West: 106° 33.294', respectively. The topographical map (Figure 24) shows the location of the test (center of the two control zones, the inner yellow is for controlling hazards from a fire during LNG fill operations and the outer green is for controlling hazards for an unignited spill during testing). The yellow zone abuts against the far southwest corner of Sandia-controlled property and the green extends into property controlled by Kirtland air force base (KAFB). At no time do any potential hazards extend onto public lands. Note the airport in the upper left of the figure, a dual use facility (Albuquerque Sunport and Kirtland AFB).

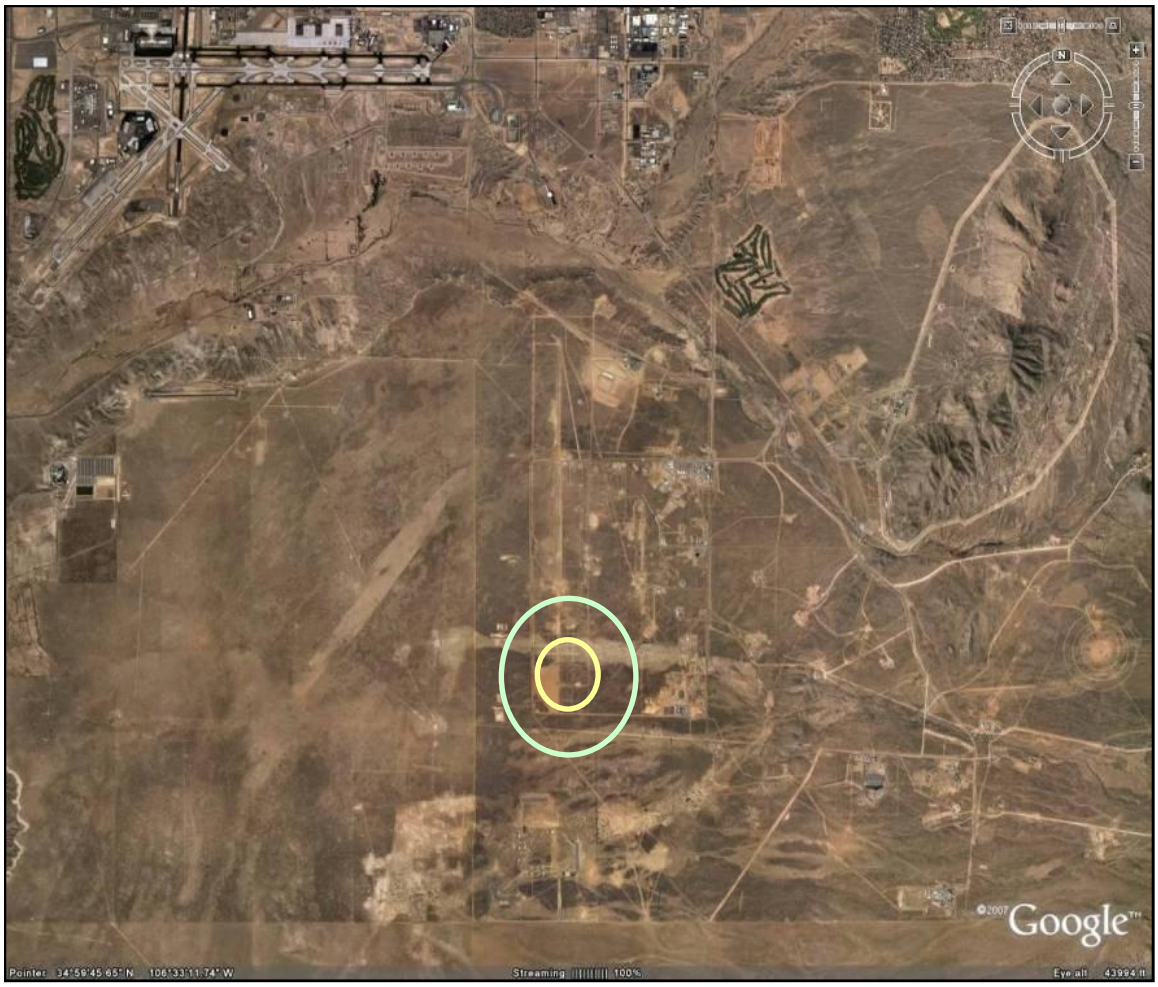

Figure 24 Test site prior to construction of the LNG pool fire experiments.
(showing 450 m and 900 m radius control zones)

Soil Analysis

A standard Proctor test, ASTM D698-00, was performed on two soil samples from the soil in the water pool area. The test determined that the maximum density of the soil was 116 lbs/ft^3 at an optimum moisture content of 12.5%.

Site Preparation and Construction

Site preparation and major construction was performed by TMSS, Inc. TMSS has provided construction and test support for SNL in the Area 3 experimental complex for over 17 years. They provided experienced heavy equipment operators to construct the earthen pool, insulated reservoir, and the process equipment for filling and draining the reservoir.

The area within the excavation limits of the water pool and reservoir was cleared of vegetation, rubbish and other foreign matter to ensure that all material that would interfere with excavation and compaction was removed. The vegetation surrounding the lake and reservoir was removed as much as possible, either through clearing and/or the use of a prescribed burn. A firebreak at a

250 m radius from the pool centerline was constructed, based on estimates of the heat flux from a 100 m diameter LNG pool fire and the heat flux necessary to combust grass and brush.

Grading was controlled to prevent surface water from running into excavated areas. Excavated material not suitable for backfill (top surface layer containing brush, etc.) was removed to a suitable site. Excavated material used for reservoir construction was either stockpiled or used immediately for reservoir construction.

4.4 LNG Reservoir Description and Construction

The reservoir exterior was constructed in the shape of a truncated cone. It was approximately 23 ft tall (from the reservoir toe to the top), had a base diameter of approximately 240 ft and a top diameter of approximately 145 ft. The exterior slope of the reservoir was approximately 2:1.

The cavity of the reservoir was an inverted truncated cone, designed to contain a minimum of 1172 m^3 (310,000 gallons) of LNG. The cavity was approximately 5.2 m (17 ft) deep. The diameter of the cavity at the top of the reservoir was approximately 29 m (95 feet). There was a 7.6 m (25 ft) wide walkway around the perimeter of the cavity at the top of the reservoir. The diameter of the cavity floor was about 6.1 m (20 ft). The interior slope of the reservoir cavity was approximately 2.25:1.

See Figure 25 and drawing set R88584-000.pdf (Appendix A) for the design layout. The field engineer used the design layout and drawings to field locate and verify specifications at time of construction.

Figure 25 Drawing of the reservoir and water pool.

The LNG reservoir was constructed per the specifications, as follows. The material used for the reservoir came exclusively from the material excavated from the water pool. This material was a

tan, clayey silt and was very uniform. Per the design specification, the soil used to build the reservoir was compacted to at least 110.2 lbs/ft^3 (95% of the maximum 116 lbs/ft^3 density) using a sheep's foot vibrating roller compactor. The soil was placed in six to eight inch layers and then rolled with the compactors. Soil moisture was controlled by adding water to the layers of the soil in the water pool as it was scarified by a grader, rolling the soil with a grader, and pushing the soil into a windrow. A scraper then picked up the soil and emptied the load onto the reservoir berm. Water was then sprayed on the loose layer followed by compaction with the sheep's foot roller. The density and water content were measured using a MC-3 Portaprobe nuclear densitometer.

The reservoir berm was divided into four equal sections and, for each lift; a measurement was taken and recorded in each quadrant. If the recorded soil density was greater than the 95% of the maximum density, the section was approved. If the recorded density was less than 95%, the section was re-rolled until the density exceeded the 95%. In six instances, the density recorded was less than 95% but greater than 94%. Since the density was very close to required and the densities recorded for the 3 of the 4 measurements in that lift were greater than 95%, those sections were given a pass per the field engineers' judgment. A total of 68 lifts were used to build up the reservoir. Therefore, each six inch thick loose lift was compacted into a layer of approximately four inches thick. For the entire reservoir, the average soil density was 122 ± 6 lbs/ft^3 and the average moisture content was 11 ± 3 %. Figure 26 shows the completed reservoir prior to lining the cavity.

Figure 26 Water pool excavation and reservoir construction.

Because the LNG is a cryogenic fluid with a saturation temperature of -160°C, the cavity wall was insulated to reduce boil-off and LNG usage. The compacted dirt face on the interior of the

reservoir cavity was covered with four inches of sprayed polyurethane foam (yellow in Figure 28), based on the below analysis.

Reservoir Insulation Analysis

Figure 27a shows the estimated quantity of LNG to yield various steady-state pool fire diameters assuming various burn rates and burn duration of 5 minutes. The reservoir capacity was designed for a nominal burn rate of $3x10^{-4}$ m/s. If the higher burn rates of $6x10^{-4}$ and $8x10^{-4}$ m/s result, then the burn duration would be reduced by about a factor of 2 and 2.7, respectively. Figure 27b gives the amount of LNG used during the initial 10-30 seconds of spreading prior to reaching the steady state pool diameter. The calculations were derived using a simple spread model in which the spreading pool is represented by circular cylinder with a given initial height and radius and allowed to evaporate as it spreads under the action of gravity. The pools reach their full dimension in roughly 1 minute with a spread rate of about 1 m/s.

Figure 27b shows that about 1000 gallons, 4000 gallons, and 10,000 gallons of LNG is used during the initial spread to obtain pool diameters of 40 m, 70 m, and 100 m, respectively, assuming a burn rate of $3x10^{-4}$ m/s. These amounts are doubled if the burn rate is $8x10^{-4}$ m/s.

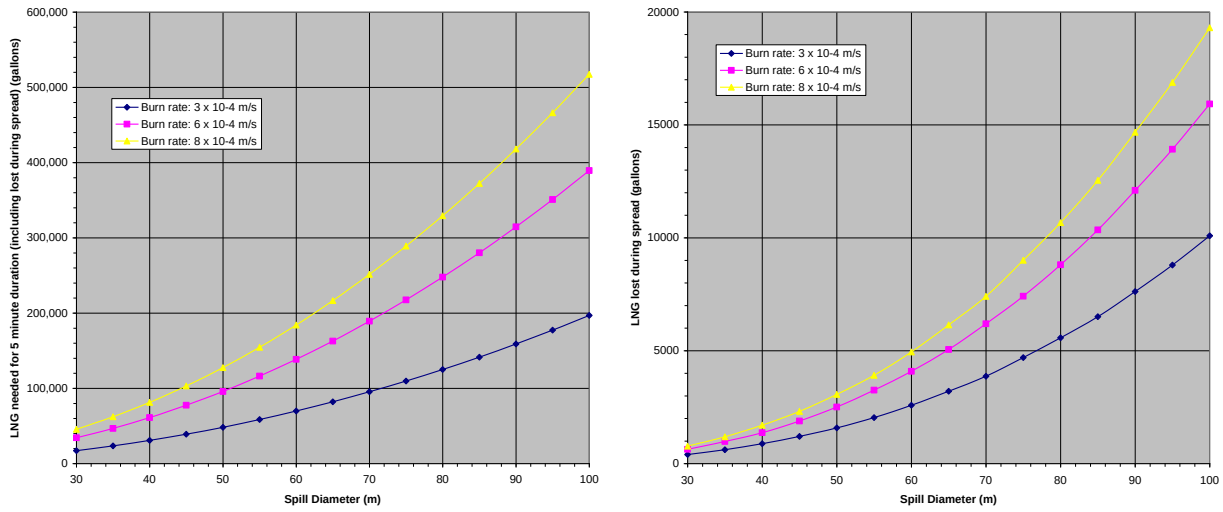

a) Total amount of LNG b) LNG used to reach steady state pool size

Figure 27 LNG required for the spill tests.

The initial plan called for LNG to also cool down the reservoir (during the fill process). Therefore, large amounts of LNG were anticipated for initial cool down of the reservoir, filling the reservoir to the desired level (maximum capacity on the order of 300,000 gallons), and maintain reserves for boil-off purposes.

The amount of LNG boiled off during reservoir fill and storage was calculated, based only on conduction losses through the walls (no losses were estimated from the top surface of the LNG pool to the roof). The diffusion equation with temperature specified at the boundaries was solved in the radial direction for temperatures of 111 K and 290 K for the LNG contact surface and outer insulation surface (assumed to be polyurethane foam insulation (PUF), respectively.

There is a period of time, approximately 1 day, in which the heat transfer through the PUF is unsteady. After this period, the heat transfer becomes relatively steady and the boil-off rate will be relatively constant. The estimated amount of LNG lost for the periods of unsteady and steady heat transfer, as well as the total is provided in Table 7 for each test. The specified duration that LNG is within the reservoir for each test is overestimated in order to anticipate worst-case conditions and to provide conservative estimates. The PUF was assumed to have thermal properties of k = 0.03 W/m K, ρ = 50 kg/m^3, and c_p= 1000 J/kg K. PUF thicknesses of 2, 4 and 6 inches were assessed as well as a case with no insulation, that is, soil contact, as indicated in Table 7. For the case assuming no insulation, a soil thickness of 6 feet, k = 1 W/m K, ρ = 2500 kg/m^3, and c_p= 850 J/kg K was assumed. It is interesting to note that it takes about 85 days to reach a steady-state condition for the soil only (no PUF) case.

Table 7 Design estimate for LNG boil-off during reservoir filling

PUF thickness (inches)	Pool diameter (m)	Volume Evaporated m^3 (gallons)			
		Duration LNG is within reservoir (days)	Unsteady period	Steady period	Total
			85 days	Mass flux: 2.0 x 10^{-4} kg/m^2 s	
0	40	3	187 (49,494)	NA	187 (49,494)
	70	5	292 (76,969)	NA	292 (76,969)
	100	8	367 (96,829)	NA	367 (96,829)
			2 hrs	Mass flux: 2.0 x 10^{-4} kg/m^2 s	
2	40	3	1.2 (304)	34 (8,876)	35 (9,180)
	70	5	1.4 (365)	68 (17,985)	70 (18,351)
	100	8	1.7 (459)	86 (22,627)	88 (23,086)
			5 hrs	Mass flux: 1.0 x 10^{-4} kg/m^2 s	
4	40	3	1.6 (417)	16 (4,248)	18 (4,665)
	70	5	1.9 (502)	33 (8,764)	35 (9,266)
	100	8	2.4 (631)	68 (17,929)	70 (18,560)
			12 hrs	Mass flux: 6.9 x 10^{-5} kg/m^2 s	
6	40	3	2.5 (658)	10 (2,536)	13 (3,194)
	70	5	3.0 (791)	21 (5,487)	24 (6,278)
	100	8	3.8 (995)	44 (11,505)	48 (12,500)

A cost-benefit study comparing amounts of insulation to LNG losses due to evaporation determined that 4 inches of PUF was about optimal. It was estimated that that 4 inches of PUF would prevent an evaporation loss of about 200,000 gallons of LNG, compared to the earth alone case (difference between the boil-off sum of the three test with 4 inches PUF vs. no PUF).

Shotcrete Cover

The foam was then covered with two inches of "shotcrete" concrete with a carbon mesh reinforcing (black mesh in Figure 28 and gray cover in Figure 29). The shotcrete mix (supplied from Vulcan concrete) was a standard 4000 psi shotcrete mix with 3/8 inch crushed aggregate. The carbon mesh used was a c50-2.9x2.9 carbon mesh manufactured by Chomarat NA.

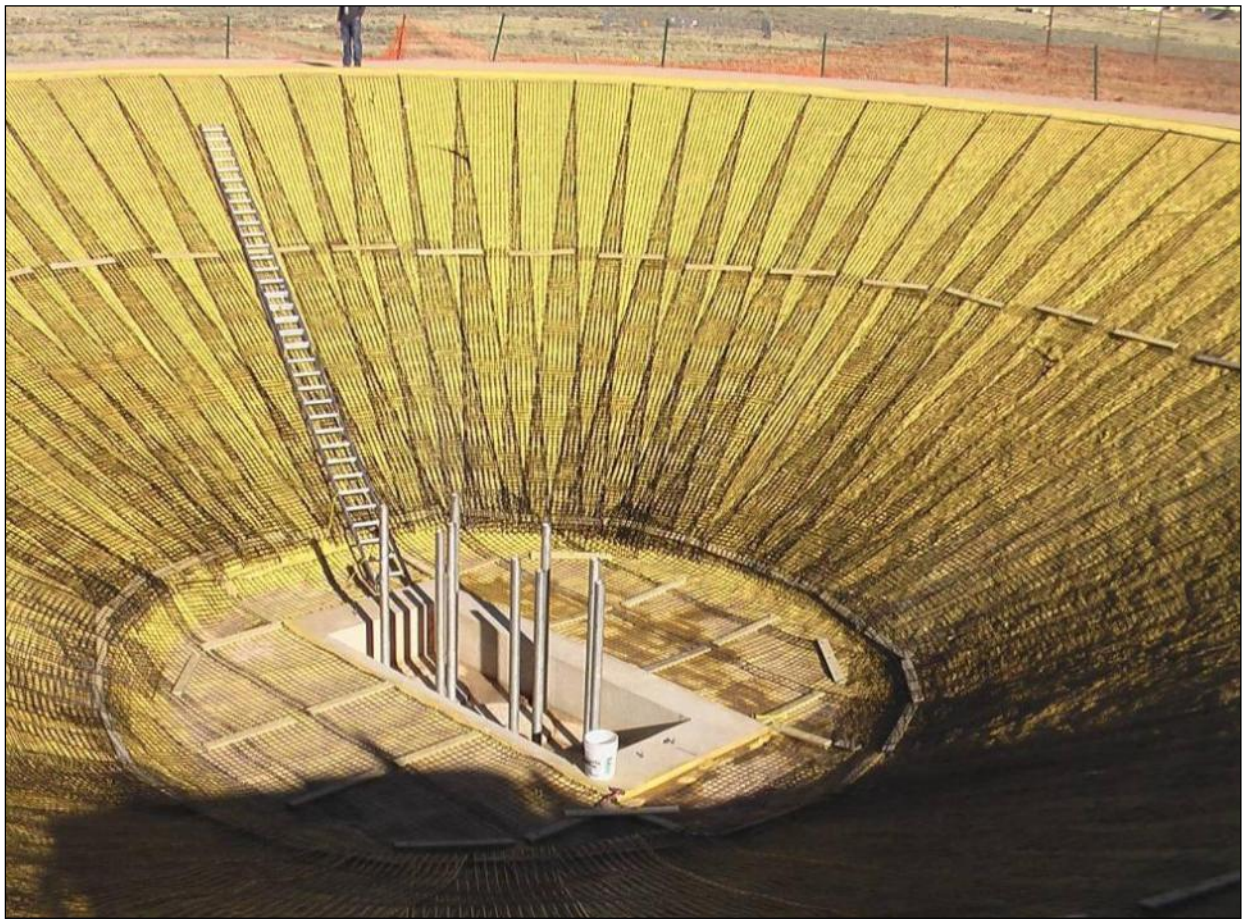

Figure 28 Cavity with polyurethane foam and carbon reinforcement mesh liner.

Figure 29 Completed reservoir cavity with shotcrete liner.

An aluminum ladder anchored to the reservoir wall provides access to the bottom of the reservoir. The ladder (not shown) was installed adjacent to one of the reservoir cover access hatches.

A concrete footer was poured around the top of the reservoir to support the reservoir cover. Teflon plates were placed between the cover “feet” and the concrete footer to allow the dome to expand and contract as needed. A number of stainless steel anchors were placed in the footer for the stainless steel wire rope used to stabilize the lifting frame for the plugs.

4.4.1 Reservoir Cover

The reservoir cover was an aluminum geodesic dome prefabricated structure manufactured by Temcor and field erected and installed by SNL (Figure 30). The dome structure was a fully triangulated all aluminum space truss complete with non-corrugated closure panels. It was clear span and designed to be self-supporting from the periphery structure; primary horizontal thrust is contained by an integral tension ring. It had full provisions to allow for thermal expansion. The dead weight of the dome structure did not exceed 3.5 pounds per square foot of surface area. The dome surface paneling was designed as a watertight system (rain and snow) under all design load and temperature conditions. Note that the liquid LNG level never exceeds the height of the dirt reservoir and never has contact with the roof.

Materials: Triangulated dome frame struts: 6061-T6 aluminum, Structural frame gussets: 6061-T6 aluminum, .375" nominal thickness, Triangular closure panels: .050" nominal thickness 3003-H16 aluminum sheet and Anchor bolts: Series 300 stainless steel.

Dome Design Loads: The dome frame and skin was designed in accordance with the "Specifications for Aluminum Structures" as published by the Aluminum Association and designed for full dead load plus live or snow load in accordance with applicable local codes:

1. Basic Live Load: 20 psf (minimum per API 650) applied per API 650-11th Edition
2. Wind Load: 120 mph velocity (default per API 650 or as otherwise specified) applied per ASCE 7-05

The aluminum panels were secured to the dome frame to withstand the following vertical loads:

1. Two concentrated loads of 250 pounds each, applied simultaneously on two separate one square foot areas of the panel.
2. A distributed load equal to the ground snow load or 60 pounds per square foot over the total panel, whichever is greater.

The cover had six 2.5 ft square access hatches on its perimeter and two 3 ft diameter vents located at the top center of the dome. The vents were equipped with a mechanical mechanism to operate and close a damper on demand. Two mixing fans that have a capacity of ~10,000 cfm each were installed inside the reservoir. The fans were operated by air motors that are mounted on the outside of the dome.

Figure 30 Installing the aluminum dome (with wire mesh) on the reservoir.

After installation, a light weight foamed concrete thermal insulation was applied to wire mesh on the cover to protect it during the LNG pool fires. The dome insulation concrete used a mix designed by Richard Jensen (SNL) and Goodson and Associates. Foam was added to each truck load (7 trucks with 4 yards concrete each) until it contained about 10 yards of concrete. The foam was created by mixing Foamcell A-100 (manufactured by Goodson and Associates) with water and running the mixture through a GFG-100 Foam Generator (also manufactured by Goodson and Associates). The concrete was then weighed (all the samples were between 50 and 65 lbs/ft^3). The concrete was then sent through a pump and spread on the dome about 1.5 to 2.5 inches thick. The mix for the foamed concrete was designed to produce a concrete with strength in the range of 400-500 psi and a thermal conductivity of ~0.1 W/mK. Since the concrete on the dome served no structural purpose, no samples of the concrete were taken to ascertain the strength.

4.4.2 Discharge Piping and Thrust Block

The experimental basis assumed one of three concrete pipes (with diameters of 15, 24, and 36 inches) with matching mating plugs would be used to achieve the desired three different sized spreading pools of LNG (three separate tests). The initial sections of the discharge pipes

penetrated the bottom of the reservoir floor and were sealed to the cavity floor using a reinforced concrete thrust block (Figure 31, Figure 32, Figure 33), designed to prevent movement of the pipes during reservoir discharge. Three discharge pipe elbows (nominal inner diameters of 15 inch, 24 inch, and 36 inch) were fabricated from Type 304 stainless steel (SS) pipe, or rolled plate, with welded flanges (machined flat after welding it ensure goodness of fit to the machined-flat plugs). The SS elbows descended from the floor of the reservoir well to a depth of approximately 6-10 feet, and had an approximate 90 degree bend to the horizontal. The stainless steel elbows and flanges were designed to mate to large aluminum plugs and form a watertight seal using flat Teflon gaskets.

A field engineer inspected all rough-in plumbing in the thrust block at time of placement and prior to pouring the floor of the reservoir. After the thrust block was poured and the forms stripped, the cavity well and the cavity floor were formed and concrete poured. The concrete used during construction (thrust block, pad around thrust block, foundation footer ring for dome, winch base, diffuser base, diffuser, etc.) was a "standard" 3000 psi mix.

The three LNG SS elbows also had mating flanges to allow attaching to reinforced concrete pipes (nominal dimensions of 15 inch, 24 inch, and 36 inch ID). Reinforced concrete pipe (8 ft sections) was used to construct pipe runs (~1% slope) approximately 300 ft long, with the first 100 ft under the reservoir and the last 200 ft on a berm constructed during the water pool excavation. The concrete pipe on the pipe berm had a dirt cover of at least 6 inches for thermal protection.

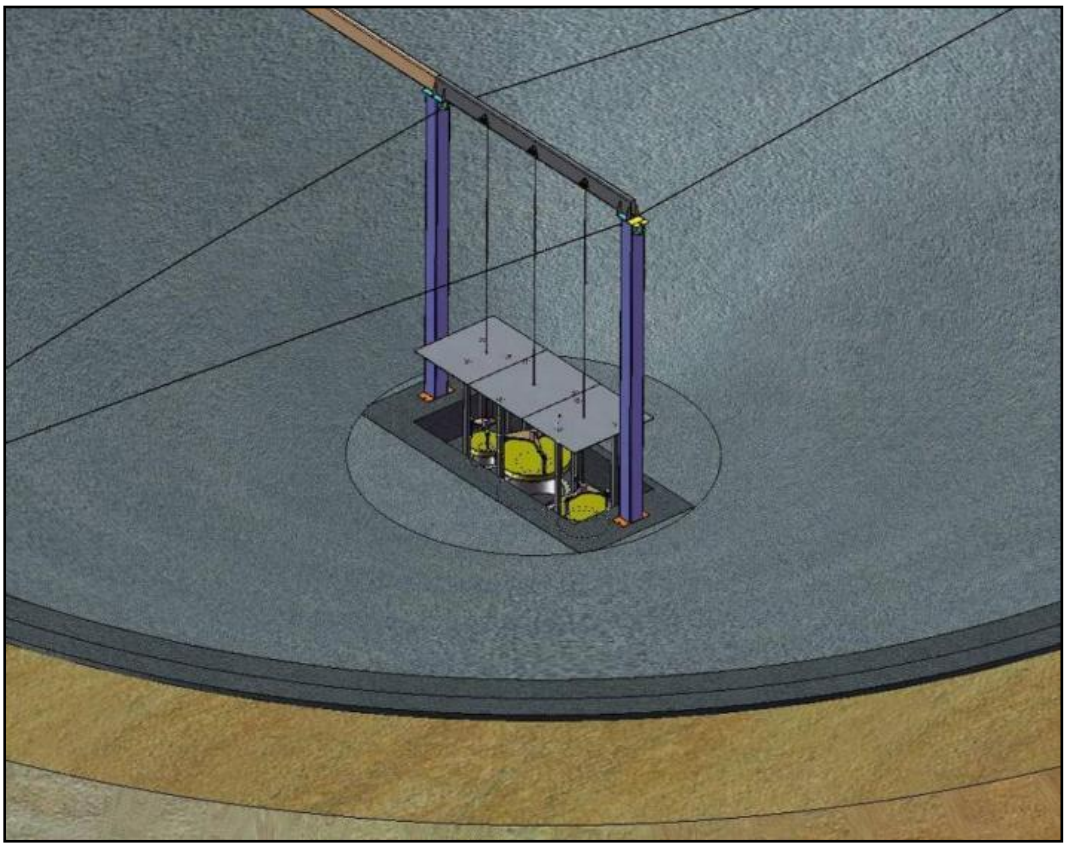

Figure 31 Diagram of the reservoir discharge pipes and plug lifting frame.

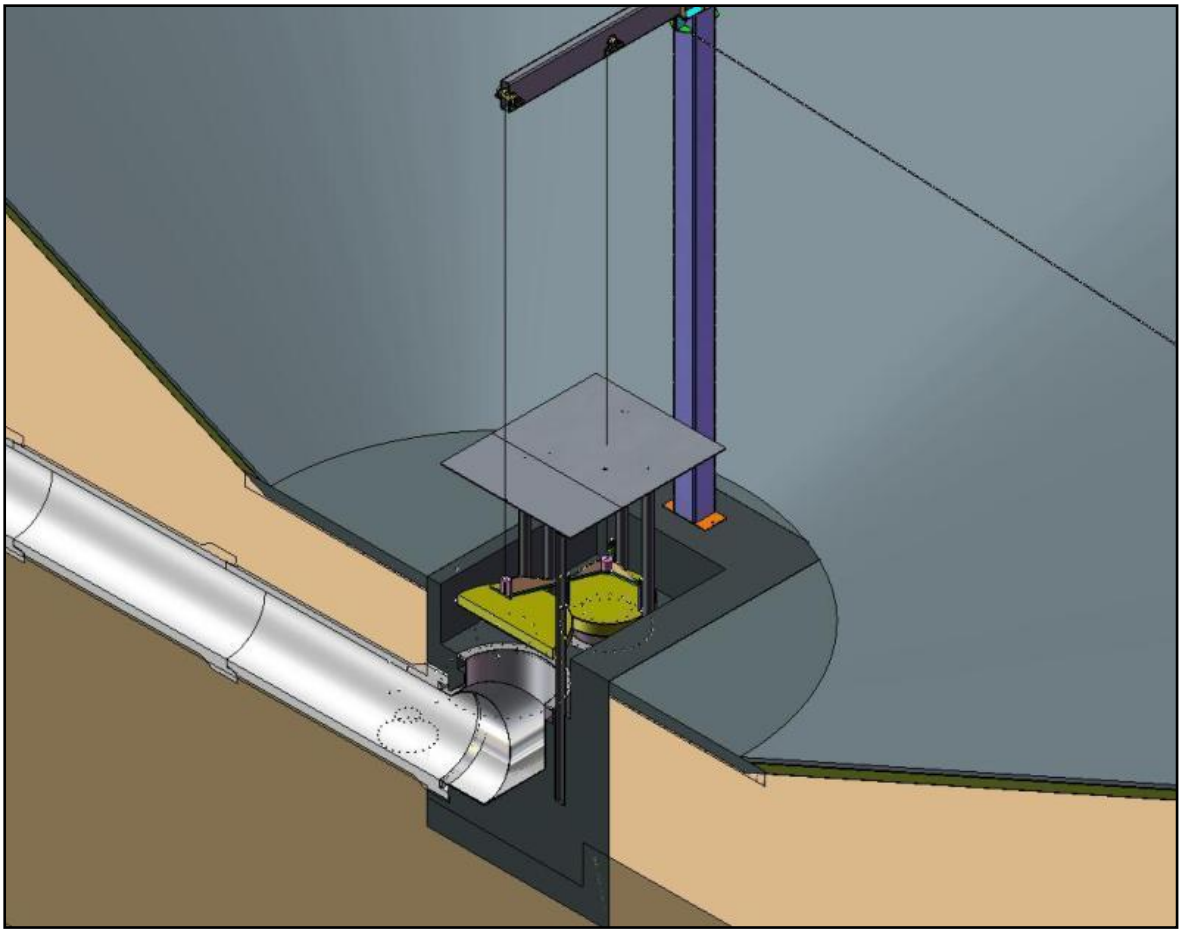

Figure 32 Cutaway diagram of the reservoir discharge pipes and plug lifting frame.

forming the thrust block around SS elbows

1st set of reinforced concrete pipe (RCP)

36 inch SS elbow mated to 36 inch RCP

concrete pour for the thrust block

laying the three rows of RCP

completed thrust block at base of reservoir

Figure 33 Construction of the thrust block and spill piping.

4.4.3 LNG Plugs

The LNG plugs were designed to withstand the dead load and the pressure load, assuming ~16 ft of liquid LNG head (~4.5 psig). Each plug, Teflon gasket (an early design not used in actual tests, see the test sections for actual design), and elbow flange assembly were modeled to predict the static von Mises stress and deflection of the assembly when subjected to a ~4.5 psig fluid pressure at the LNG Reservoir. Each part was individually modeled using SolidWorks 2007, SP4.0, and CosmosWorks, SP3.0, Date Code 2005/360, and the parts were assembled together to complete the assembly. Prototypic ambient material properties were used for each component. A ~4.5 psig pressure load was applied to the exposed surfaces of the plug, and gasket edge. The lower edge of the flange was constrained as "fixed". Contact gap constraints of "no penetration" were established between each part to simulate movement and separation of components, but no penetration of components.

The 15 inch aluminum plug was modeled at 5.0 inches thick by 22.5 inch diameter. The Teflon gasket was modeled at 21.5 inch diameter by 0.375 inch thick. The 15 inch elbow was modeled to include the top flange and approximately 5 inches of tube below the flange. Results from this analysis predict a maximum Von Mises stress for each component as follows (note that for aluminum: yield strength is ~37,000 psi and tensile strength is ~42,000 psi, for stainless steel: yield strength is ~30,000 psi and tensile strength is ~75,000 psi):

- 15 Stainless Steel Elbow: 260 psi occurs in the tube wall.
- Teflon Gasket: <~200 psi main body thickness.
- 5 in thick Plug: <~200 psi main body thickness.

The 24 inch aluminum plug was modeled at 4.0 inches thick by 32.5 inch diameter. The Teflon gasket was modeled at 32.0 inch diameter by 0.375 inch thick. The 24 inch elbow was modeled to include the top flange and approximately 5 inches of tube below the flange. Results from this analysis predict a maximum Von Mises stress for each component as follows:

- 24 Stainless Steel Elbow: 370 psi occurs in the tube wall below the flange.
- Gasket: <~100 psi main body thickness.
- 4 in thick Plug: <~100 psi main body thickness.

The 36 inch aluminum plug was modeled at 4.0 inches thick by 44.25 inch diameter. The Teflon gasket was modeled at 43.375 inch diameter by 0.375 inch thick. The 36 inch elbow was modeled to include the top flange and approximately 5 inches of tube below the flange. Results from this analysis predict a maximum Von Mises stress for each component as follows:

- 36 Stainless Steel Elbow: 382 psi occurs in the tube wall below the flange.
- Gasket: <~200 psi main body thickness.
- 4 in thick Plug: <~200 psi main body thickness.

Finite element analysis showed that the stress on the plugs at lift load was far below yield stress. Table 8 gives the lift load on the plugs, needed for design of the A-frame and lifting hardware. Figure 34 shows the installed plugs with the lifting attachments and swivel hoist rings.

Table 8 Lift Load on the Plugs

Nomenclature	**Dead Load (lbs)**	**Pressure Load (lbs)**	**Lift Load (Dead + Pressure) (lbs)**
15 inch plug	193.2	1,789.0	1,982.2
24 inch plug	323.7	3,733.0	4,056.7
36 inch plug	600.0	6,920.0	7,520.0

Figure 34 LNG plugs with lift fixtures and swivels.

4.4.4 LNG A-Frame, and Associated Hardware

A lifting frame for the plugs (the A-frame in Figure 35) (to include wire rope and guides) was designed to have a minimum load limit commensurate with the load rating necessary. To alleviate concerns about load strength and material embrittlement at cryogenic temperature, all load bearing members were constructed using aluminum or stainless steel.

All wire rope used inside the dome was type 304 stainless steel. The 36 inch diameter plug used a 5/8 in diameter rope with a minimum breaking strength of 35,000 lbs. The other two plugs used a ½ in diameter rope with a minimum breaking strength of 22,800 lbs. A 3/8 in diameter rope with a minimum breaking strength of 12,000 lb was used to stabilize the A-frame to the cover concrete footer.

The sheaves inside the dome were a custom built unit designed by Paul Helmick (SNL). The sheaves on the outside of the dome were Crosby tail board type 404. The 5/8 inch wire rope used a 6 inch diameter sheave with a minimum breaking strength of 64,000 lbs. The ½ inch wire rope used a 4.5 inch diameter sheave with a minimum breaking strength of 32,000 lbs.

The swivel hoist rings used on the plugs were 1.25 inch stainless steel with a minimum breaking strength of 37,500 lbs.

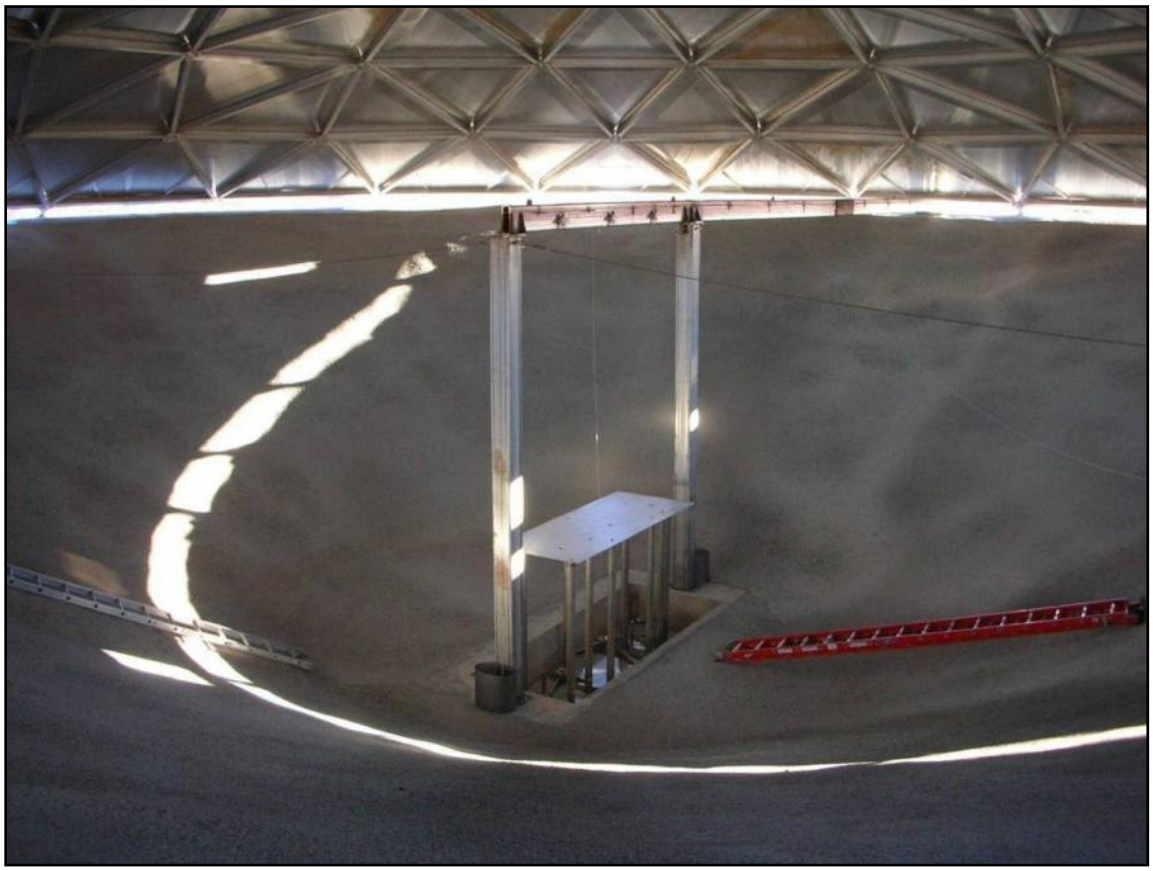

Figure 35 A-frame installation.

Static stress analysis of the SNL Large Scale LNG A-Frame main beam was performed. The A-Frame main beam was modeled per SNL drawing R92284-000 as an assembly to predict the static von Mises stress and deflection of the assembly when subjected to simulated concentrated vertical load at each Plug lift location. The stainless steel beam was modeled as an assembly to include the bearing and gusset plates at each end, and the stainless steel angle mounting plates for each plug wire rope sheave. For this analysis the attachment of each plate was modeled as full plate thickness. Each part was individually model using SolidWorks 2007, SP5.0, and CosmosWorks 2007, Date Code 2006/200, and the parts were assembled together to complete the assembly. Prototypic ambient material properties were used for each component. As a conservative approach, each concentrated applied load was applied to simulate lifting of all three (15 inch, 24 inch, and 36 inch) plugs at the same time. Each beam load bearing plate was constrained to simulate free beam end conditions. Gravity was also applied to the model simulation. The simulated loads were modeled as follows:

- ~6,920 lbs vertical downward at center wire rope mount location (simulating load from 36 inch plug).
- ~4,056 lbs vertical downward at right-hand wire rope mount location (simulating load from 2 inch plug).
- ~1,982 lbs vertical downward at left-hand wire rope mount location (simulating load from 1 inch plug).

The maximum beam deflection was predicted to be ~0.080 inch. Results from this analysis (Figure 36) predicted a maximum Von Mises stress for each component as follows (note that for stainless steel yield strength is ~30,000 psi and tensile strength is ~75,000 psi):

• Mounting Plate for 3 inch plug wire rope location: ~24,000 psi occurred as a peak stress at mounting hole locations.
• Beam: ~8,000 psi center of beam span.

Figure 36 FEA stress analysis of the A-frame.

Figure 37 Pool DAS station.

Figure 37 shows the concrete slab, transport container, and thermal shield (in construction) at the pool Data Acquisition System (DAS) station. This station houses a majority of the support systems – winches and batteries for lifting the LNG discharge plugs, propane and flare igniter systems at the diffuser, reservoir and discharge pipe gas sampling systems, gas bubbler systems for LNG liquid level, and the DAS for the pool and reservoir instrumentation.

4.4.5 LNG Diffuser

The three reinforced concrete pipes terminated in a mating stainless steel Y-connector near the center of the water pool. Field engineers inspected all Y-connector parts at time of placement and prior to pouring the diffuser. The stainless steel Y-connector terminated in a reinforced concrete diffuser located at the pool centerline. The diffuser converted the horizontal momentum of the LNG liquid discharge to a near uniform radial spread onto the water pool. The diffuser was 6 ft tall and had an inner diameter of 8 ft. The diffuser (Figure 38) was built on a reinforced concrete base that acted as a thrust block.

The diffuser foundation was constructed by inverting an eight foot long section of a ten foot diameter corrugated steel pipe and using it as a permanent form. A 9.5 ft diameter cylindrical mesh of reinforcing steel was placed just inside of the steel pipe. The pipe was then filled to the top with a 3000 psi concrete.

Similarly to the diffuser foundation, the diffuser itself was constructed using two, six foot long, corrugated steel pipes, one nine feet in diameter and one eight foot diameter, to act as a permanent form for the concrete. The nine foot diameter pipe was placed on top of the foundation, in which six, equally spaced #6 rebar had been embedded, to tie the diffuser to the diffuser foundation. The eight foot diameter pipe was placed inside the nine foot diameter pipe. A cylindrical reinforcing steel mesh was placed between the two steel pipes. Five inverted triangular slots were cut out of the bottom of both pipes. One slot (~12 inches tall, 43 inches wide at top, 20 inches wide at bottom) was located opposite the 36 inch discharge pipe at ~0º, two were located at ~45º, and two were at ~135º. The space between pipes was filled with a 3000 psi concrete. A short, cylindrical stainless steel splash plate (6 ft diameter, ~1 ft tall) was attached to the floor of the diffuser to break up the horizontal flow. A lid with a 4 ft diameter center hole was attached to the diffuser. To prevent backflow, plugs were placed in the Y-collector in those pipes not being used during a test.

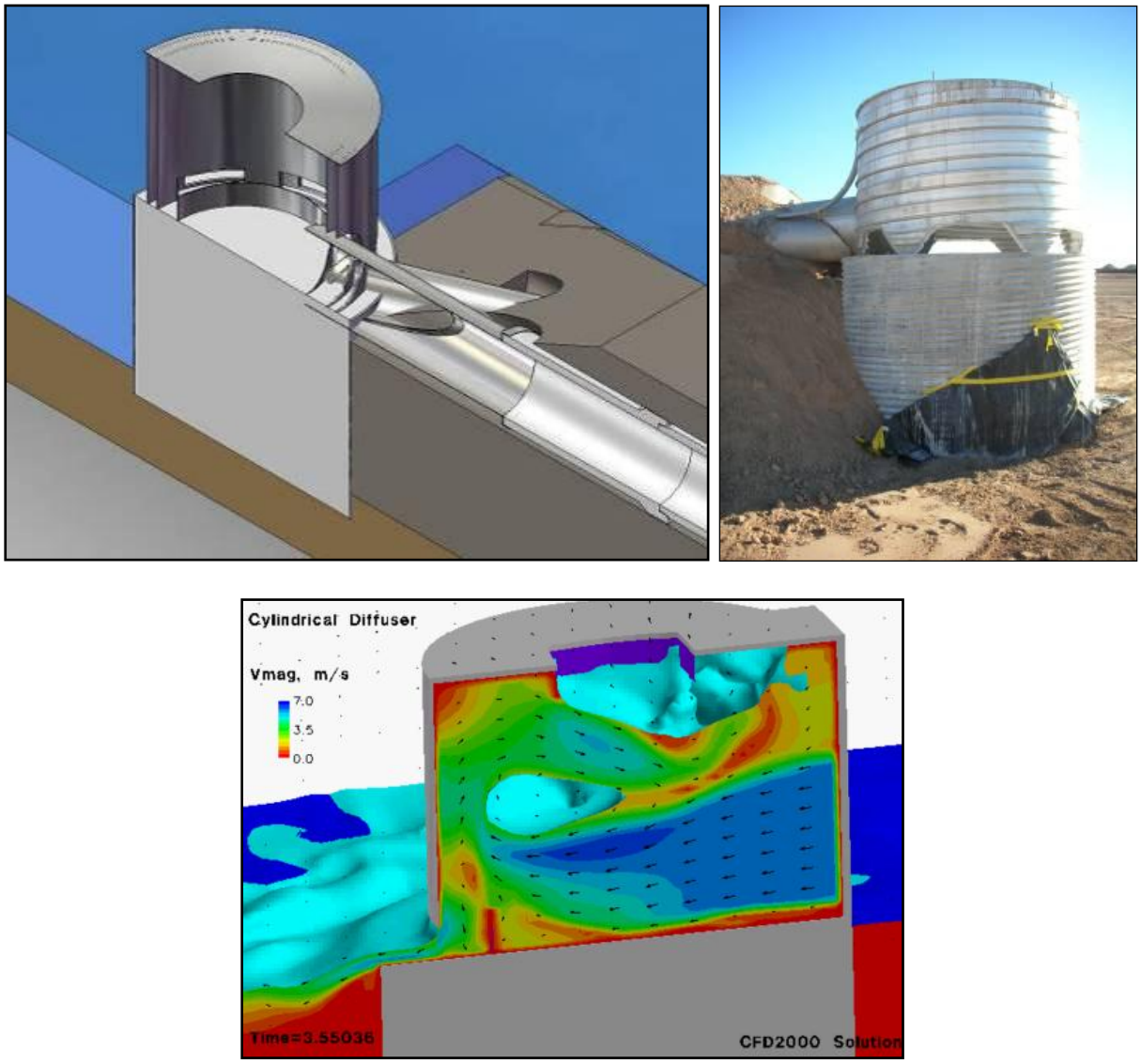

Figure 38 Diffuser conceptual layout, construction, and CFD modeling.

STORM, a free-surface computational fluid dynamics (CFD) code, was used to design the diffuser (Figure 38). STORM is a general purpose commercial computer program designed to numerically solve the Navier-Stokes equations, which consist of conservation equations for mass, momentum, and energy. STORM uses a finite-volume representation of the governing equations, whereby the continuous problem domain is decomposed into multiple control volumes, and the governing equations are applied to individual control volumes and integrated over the entire computational domain. The Free Surface option provided in STORM predicts the motion of fluid interfaces based on the solution of a conservative transport equation for the fractional volume of fluid (VOF).

4.4.6 Water Pool

The water pool was ~120 m (395 ft) in diameter with a water depth of approximately 2 m (6 feet) at the center 43 m (140 ft) radius, and then sloped upward to the pool edge. Construction of the water pool was simply an excavation; with depth based on elevation of the reservoir thrust block and the sloping pipeline draining LNG to the pool center.

The water pool was lined with a standard pond liner to prevent ground seepage (Figure 39). The pool liner was a commercial 12 mil pond liner. All joints and areas where the liner overlaps were heat sealed to be water proof. The pond liner extended from the pool edge to the edge of the pipe berm, with edges embedded in anchor trenches. Dirt or water covered any exposed pond liner to provide protection from the LNG fire.

Figure 39 Installation of the water pool liner.

4.4.7 Water Line

The source of water to fill the pool was a fire hydrant located at the nearby Gun Site facility (Bldg. 6920). Approximately 5000 ft of PVC (4 inch) irrigation tubing with ring lock couplings and a valve controlled the flow was run across the ground to the water pool (the final 700 ft was covered with soil for fire protection). The irrigation tubing was connected to the fire hydrant via a short section of flexible hose. The estimated water pool fill time was ~6 days, based on a measured flow rate through the water line of ~500 gpm.

4.4.8 LNG Fill Line

The LNG fill line was salvaged from the LNG fill pipeline that was used at the Water Impact Facility in 2005. That pipeline was fabricated from 3-inch A-312 stainless steel, type 304 Schedule 10 materials. The new field installation (Figure 40) utilized field welded joints, cryogenic-rated stainless steel flexible hose, and new and existing bolted and flanged connections with new gaskets rated for cryogenic applications. It was insulated with polyurethane foam with an integral vapor barrier, standard for cryogenic pipelines. The line extended from the fill connection at the bottom of the reservoir, up the side, and discharged into the gas space just below the top of the reservoir. The fill connection at the base of the reservoir was a 3 inch cryogenic valve with a fitting appropriate to mate to the flex hose supplied by the LNG trailer vendor (female 3 inch LNG 300 coupling).

Since the discharge end of the pipeline was open into the reservoir (no valve) there was minimal pressure cycling (only due to the liquid head (approximately 5 psig) when filling. A temporary plug was used to seal the discharge end of the pipeline and the pipeline was pressure tested to 30 psig).

The pipeline and reservoir assembly was electrically grounded according to industry and Sandia National Laboratories specifications. Prior to each experiment, SNL inspected the LNG fill line for grounding attachment and integrity, checked the electrical bond between the fill pipe and the cover, checked the electrical bond between roof and A-frame beam (used to lift the reservoir drain valves, and measured the impedance at the LNG fill pipe station to earth (verify <20 ohms).

In addition, no unrated (unclassified) electrical equipment was located inside 15 feet of locations with expected drips, drains, or vents of flammable materials (the dome vents and the LNG pipeline fill coupler).

Figure 40 LNG fill pipeline in construction.

4.4.9 Nitrogen Inertion and Purge Source

Nitrogen gas was used to inert the reservoir prior to filling with LNG and was also used to purge the reservoir of the fuel rich methane-air mixture following the test. The LNG discharge pipes were also inerted to maintain nonflammable environments in the event of leakage past the plugs. An additional benefit of the nitrogen supply to the discharge pipes was to prevent cryogenic pumping of air (with entrained water vapor) into the pipes to prevent ice formation and potentially freezing of the discharge plugs to the pipe flanges.

The gas source was provided by a liquid nitrogen Process Engineering Vessel (National Board # 7140, 3125 gallons, 250 MAWP with integral vaporizers) leased from Matheson Tri-Gas. The bulk storage vessel (Figure 41) can supply ~250,000 ft^3 of gas at a flow rate of ~1000 scfm. The vessel was on site, located on the back side of the reservoir opposite the water pool (~200 m from pool centerline) with radiant shields to protect it from the LNG fire heat flux.

A 2 inch diameter nitrogen inertion gas line was plumbed from the reservoir to a control valve on the vessel allowing operators to remotely turn on or off the nitrogen source to the reservoir. Smaller lines (1/2 inch) were plumbed to the LNG discharge pipes.

Figure 41 Nitrogen gas source trailer.

4.4.10 Ignition Mechanisms

Three igniters were installed on top of the diffuser located at the center of the water pool. The igniters were used to remotely ignite the methane exiting the LNG discharge pipe at the start of the spill. Two igniters were propane based (with glow plug ignition) and the third igniter was a 30-minute highway emergency flare (hot wire ignition). These igniters were lit before the LNG spill plug was lifted.

In addition, eight highway emergency flares were located on the perimeter of the water pool and five highway emergency flares were on the pipe berm leading to the diffuser. These flares provided additional backup ignition sources and were intended to be lit if the LNG did not ignite at the diffuser.

4.5 Measurements and Instrumentation

The following section describes the measurements (with initial uncertainty) necessary to meet the experimental data needs. The following is a summary (not inclusive) of the primary instrumentation.

- Instrument towers (12) 110 m, 160 m, and 210 m (from pool centerline)
- Data Acquisition Systems (5)
- Reservoir
  - Liquid level (2 pressure based, 1 mechanical float)
  - Internal liquid/gas temperature (8 TCs)
  - Internal wall/structure temperature (varied between tests, ~10-25 TCs)
- Pool
  - Spill area (overhead video (2))
  - Heat flux to surface (13 directional flame thermometers, DFTs)
  - Water temperature (36 TCs)
- Plume
  - Height (12 cameras) (4 high speed, 2 infrared)
  - Spectrometers (4) (400-800 nm, 1300-4800 nm)
  - Heat flux (radiometers: narrow-angle (28), wide-angle (12)
- Meteorology
  - 3D ultrasonic wind speed/direction (4)
  - ambient pressure/temperature/relative humidity (1)

4.5.1 Estimated Heat Flux for Planning Purposes

The ground level incident heat flux as a function of distance from the pool center was estimated using the following procedure.

The flame was modeled as a solid cylinder in which thermal radiation is uniformly emitted from the surface. Eq. (2) is used for the model:

$$q'' = E_p \tau F \qquad (2)$$

q'' - radiative flux incident upon an object (kW/m^2)
E_p - average surface emissive power (kW/m^2)
F - view factor
τ - transmissivity.

In order to determine the view factor F, or the amount of radiant energy that is received by an object's field of view, the flame height must be determined. The Moorhouse correlation for LNG was used to calculate flame height, found on page 3-204 of the SFPE handbook, Fire Protection Engineering, 2nd ed., (1995). The term u^* is a non-dimensional wind velocity taken to be 1 for low wind speeds.

$$H = 6.2\, D \left[\dot{m}'' / \rho_a \sqrt{gD} \right]^{0.254} u^{*-0.044} \qquad (3)$$

Eq. (3) predicts flame heights of 69 m, 126 m, and 172 m for the 35 m, 70 m, and the 100 m diameter LNG pool fires, respectively, using a 0.2 kg/m^{2}s mass loss rate (burn rate of 5 x 10^{-3} m/s) and ambient air density of 0.99 kg/m^3 (5000 ft elevation).

The view factor equations found in Mudan [1987] were used to determine the view factor as a function of distance. The surface emissive power, E_p, is based upon extrapolated conservative estimates from smaller scale data. The transmissivity was assumed to be a constant value of 0.8 which is conservative since it is expected to decrease with distance to values of around 0.6 to 0.5.

Curves of the heat flux (q'') vs. distance from the pool center were generated for pool diameters of 40, 70 and 100 meters using surface emissive powers of 300, 275, and 220 kW/m^2, respectively, for two different burn rates of 3 x 10^{-3} m/s and 8 x 10^{-3} m/s. Figure 42 shows estimated ground level incident heat flux to surfaces inclined to receive maximum flux levels as a function of distance from the pool center for pool diameters of 40, 70 and 100 meters with surface emissive powers for a burn rate of 8 x 10^{-3} m/s. Figure 42 also shows the estimated heat flux vs. distance for a fire in the reservoir.

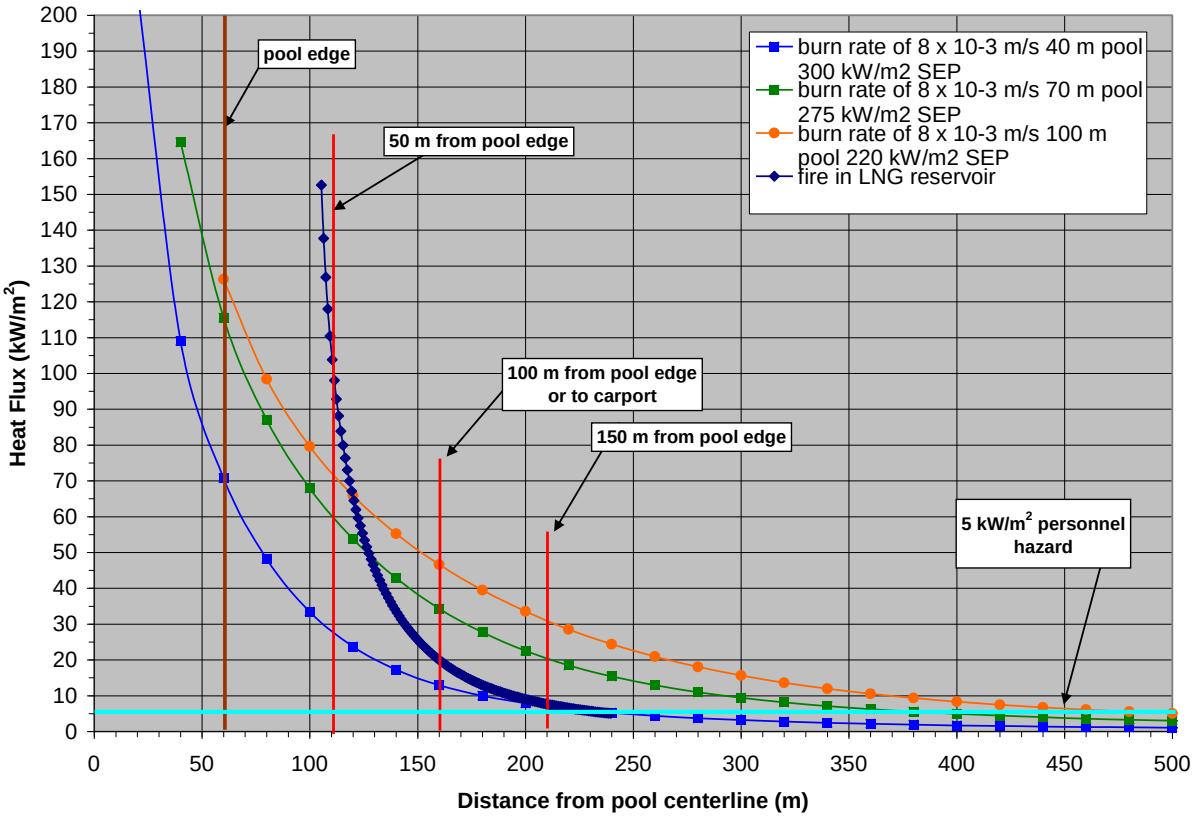

Figure 42 Pre-test design estimate for heat flux as a function of distance from the pool center. The legend indicates burn rate, pool diameter, and surface emissive power.

The flux estimates shown in Figure 42 were used to estimate the thermal insult to instrument towers and data acquisitions systems located at ~110 m, 160 m, and 210 m from pool centerline. Figure 43 shows the pool layout and tower locations.

Table 9 shows the estimated heat flux (on a surface inclined at such an angle that it will receive the maximum flux level at that distance) determined from the above procedure as a function of test and distance from the flame plume. Table 9 also shows the range of the wide-view radiometers needed to accommodate the estimated maximum heat flux (for all tests) at the particular distance.

Table 9 Estimated Hemispherical Heat Flux as a Function of Test and Distance.

Fire Diameter (m)	Flame Height (m)	Pool Edge Heat Flux (kW/m^2)	50 m from Pool Edge (kW/m^2)	100 m from Pool Edge (kW/m^2)	150 m from Pool Edge (kW/m^2)
35	69	66	26	12	7
70	126	115	58	33	18
100	172	126	73	44	28
	Max flux	**125**	**75**	**50**	**30**

4.5.2 Experimental Setup

Measurements were based on four cardinal axes or "spokes". Note that the "North" spoke (also called the 0 spoke) has a magnetic heading of 340 degrees. Figure 43, Figure 45, and Figure 46 show each spoke containing three towers upon which radiometers were mounted. The three towers were located approximately 110 m, 160 m, and 210 m from pool center. Cameras located on the end of each spoke (~226 m) focused on the pool vertical centerline. Some spokes contained additional instrumentation, such as IR cameras, spectrometers, and meteorological instrumentation, discussed in the following sections. A large firebreak at ~250 m can be seen in Figure 46. The heat flux instruments were water-cooled and the towers were insulated due the expected magnitude of the flux.

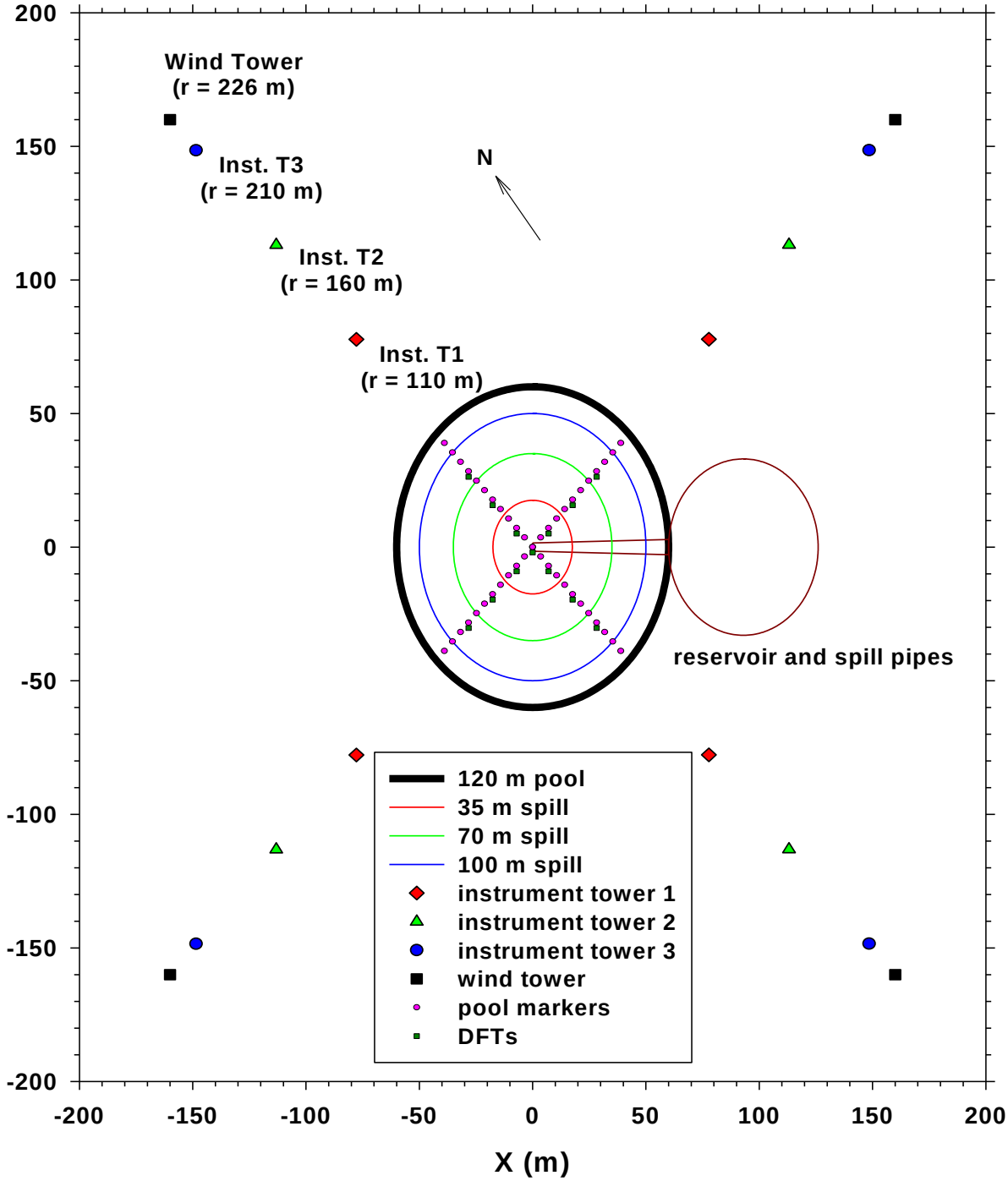

Figure 43 Experiment and instrumentation layout.

The instrument towers (approximately 1.5 m tall) were embedded in concrete slabs to provide a stable platform. Tower 1 of each quadrant was the primary tower, supporting five narrow-angle (also called narrow-view or NV) radiometers for spot intensity measurements and one-wide angle (also called wide-view or WV) radiometer for computing overall flame surface emissive power (SEP).

Towers 2 and 3 each supported one narrow-angle radiometer and one-wide angle radiometer which were used to determine variation with distance. Table 10 lists the nominal gauge positions (measured from the ground plane) on Tower 1 and the location of its measurement at the pool centerline for each planned test. The positions are also shown in Figure 44. Note that the spot diameter for the 5.5º narrow-angle gauges at a distance of 110 m (to pool centerline) is about 10.6 m, at 160 m is 15.4 m, and at 219 m is 20.2 m. The spot areas are drawn to scale in Figure 44. The additional center spots represent views seen by the Tower 2 and Tower 3 gauges. Note that these nominal values changed slightly from test to test, as indicated in the respective section describing the results of each test.

Table 10 Height of the nominal spot heat flux measurements for each test.

gauge #	Gauge height on tower (m)	Test 1 spot height above pool (m)	Test 2 spot height above pool (m)	Test 3 spot height above pool (m)
1	1	6.9	12.6	17.2
2	1.1	20.7	37.8	51.6
3	1.2	34.5	63.0	86.0
4	1.3	48.3	88.2	120.4
5	1.4	62.1	113.4	154.8

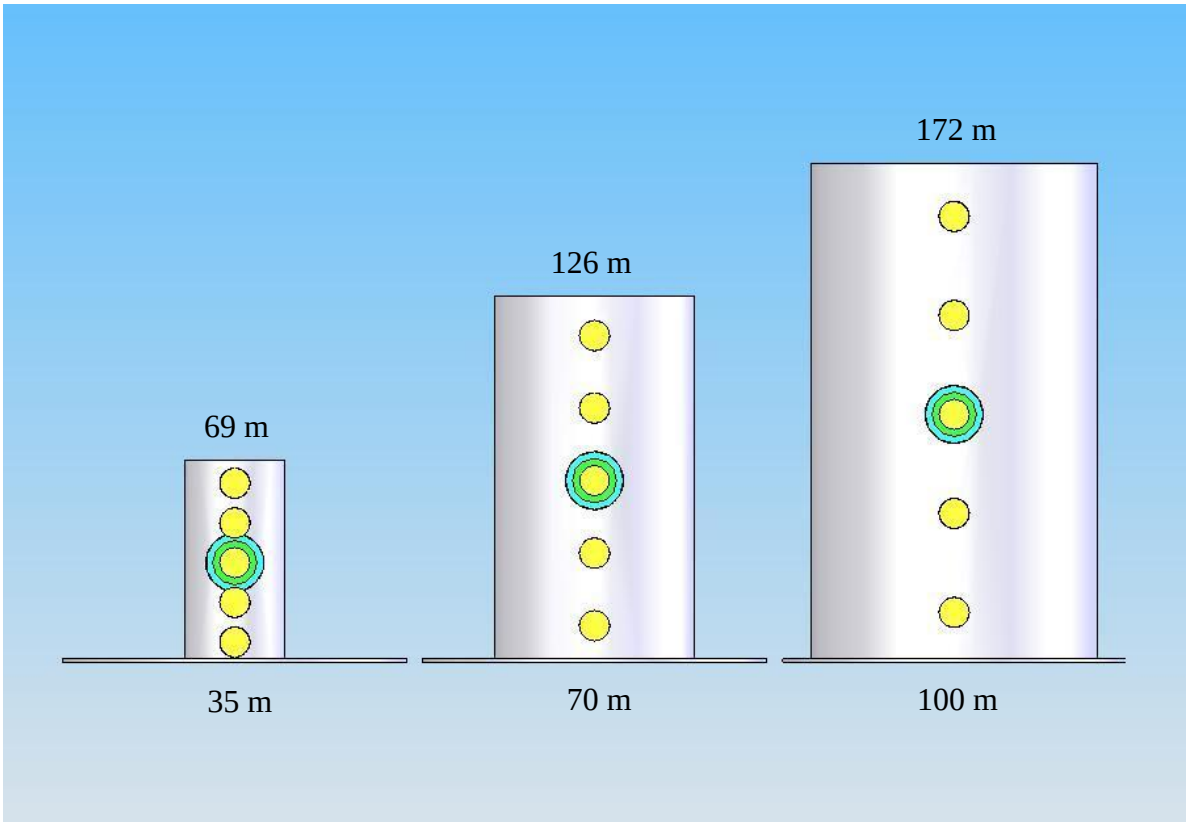

Figure 44 Initial design location and width of the spot measurements.

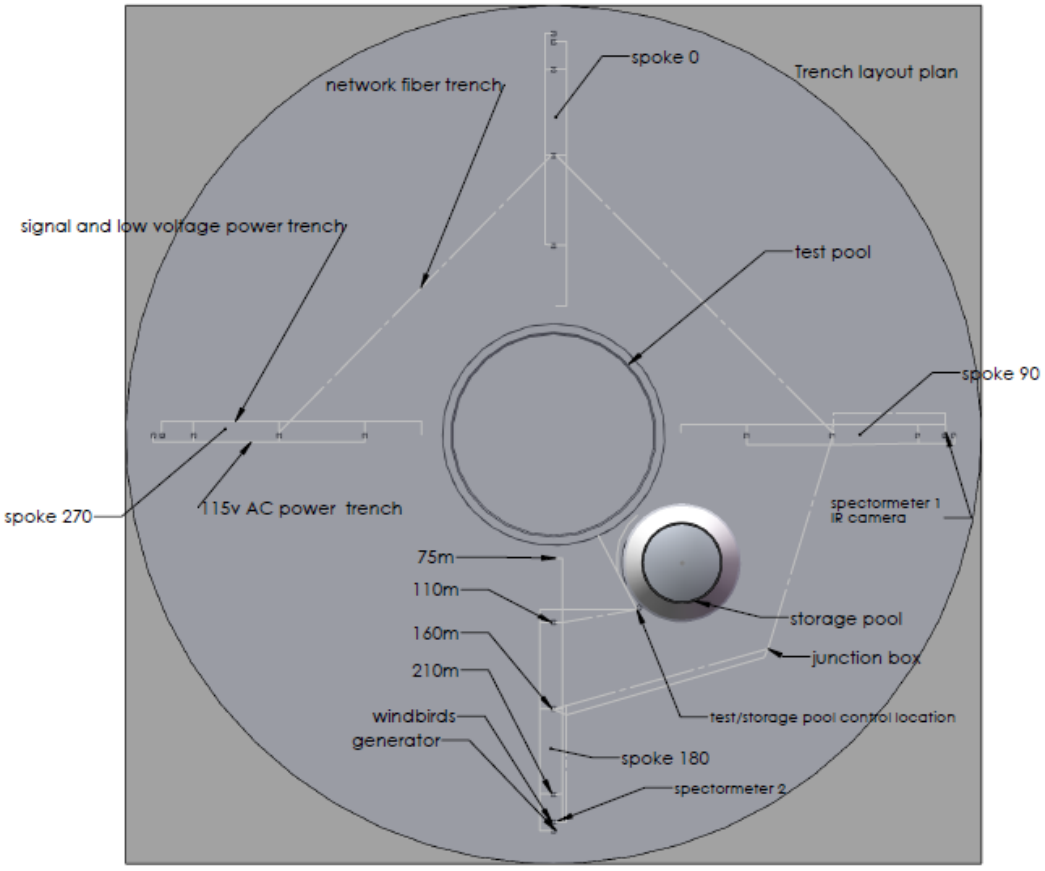

Figure 45 Power and signal lines to spokes and pool DAS.

Figure 46 Overhead view of experiment layout.

Table 11 presents the instrumentation locations (referenced to Figure 43), as measured by GPS instruments.

Table 11 Instrumentation Locations

		X (m)	Y (m)	Radial distance from center (m)
	Center of diffuser	0.00	0.00	0.00
	DFT 0-0 (top of diffuser)	0.97	0.28	1.01
	Top center of Dome	96.13	0.20	96.13
North Spoke	**DFT 0-1**	-11.21	5.11	12.32
	DFT 0-2	-21.82	17.26	27.82
	DFT 0-3	-34.42	30.63	46.07
	pido tube	-48.39	42.00	64.08
	station 1	-81.90	74.23	110.54
	station 2	-118.01	110.43	161.62
	station 3	-152.79	145.58	211.04
	camera/IR/Spectrometer station	-164.60	158.58	228.56
	tower	-170.01	163.73	236.03
East Spoke	**DFT 90-1**	-3.12	8.21	8.78
	DFT 90-2	16.54	20.40	26.26
	DFT 90-3	24.57	30.50	39.17
	pido tube	41.57	40.13	57.78
	station 1	74.47	74.74	105.51
	station 2	108.81	109.32	154.24
	station 3	144.03	145.24	204.55
	camera/IR/Spectrometer station	155.84	158.27	222.12
	tower	161.29	163.31	229.53
South Spoke	**DFT 180-1**	-1.46	-9.37	9.48
	DFT 180-2	17.36	-17.00	24.29
	DFT 180-3	28.55	-31.22	42.31
	pido tube	40.83	-48.86	63.68
	station 1	76.34	-83.33	113.01
	station 2	110.20	-116.89	160.65
	station 3	146.84	-153.03	212.08
	camera/IR/Spectrometer station	157.40	-164.54	227.70
West Spoke	**DFT 270-1**	-7.53	-5.74	9.47
	DFT 270-2	-21.01	-17.64	27.43
	DFT 270-3	-33.33	-30.09	44.90
	pido tube	-47.35	-45.97	65.99
	station 1	-81.38	-80.62	114.55
	station 2	-113.96	-115.49	162.25
	station 3	-149.48	-151.06	212.52
	camera/IR/Spectrometer station	-161.68	-164.78	230.86
	tower	-167.42	-168.95	237.85

4.5.3 Data Acquisition Systems (DAS)

The data acquisition system (DAS) consisted of a five PCs with 16-bit data acquisition cards connected to a National Instruments (NI) SCXI-1001 chassis. A typical chassis has twelve NI SCXI-1102 cards with NI SCXI-1303 blocks for TCs and four NI SCXI-1104 cards with NI SCXI-1300 blocks for analog signals. This provided the ability to increase either analog signals or TC signals. Note that the SCXI-1001 held 12 cards, yielding a total channel count of 384 channels if all slots were used for data acquisition. The system was upgradeable simply by adding an additional SCXI-1001 DAQ card and more multiplexer units (MUXs).

DAS Measurement Uncertainty Verification Procedure

The measure uncertainty of the data acquisition systems was measured using a NIST traceable calibration standard, Fluke Model 5520A. The Fluke standard was capable of simulating all major thermocouple outputs as well as AC and DC voltages.

The standard output was connected to each data acquisition channel and measurements were made to determine the channel error. The standard output was setup for the channel type, thermocouple or voltage, at steps across the channel input range. The DAS channel was configured for the measurement type and 1200 samples were taken over a 1 second interval (1200 samples/second). These readings were converted to temperature for thermocouple channels, or voltage for voltage channels. The mean and standard deviation of the samples was calculated and stored for analysis. The uncertainty was checked pre-test and in some cases post-test.

The outputs for the channel type were as follows.

Type K thermocouple

-200° to 0°C	50° step
0° to 1200°C	200° step

Type T thermocouple

-250° to 400°C	50° step

Voltage

± 50mV	10mV step	-50mV to 50mV
± 100mV	20mV step	-100mV to 100mV
0-5V	0.5V step	0V to 5V
± 5V	1V step	-5V to 5V
0-10V	1V step	0V to 10V
±10V	2V step	-10V to 10V

LabView® software interfaced with the NI cards to both control systems and record data. During pretest and post-test periods, data from all 5 field computers was sampled at 1000 Hz, averaged, and recorded on the control room computer once per second. Immediately before ignition, a 2nd

program was initiated to allow the field computers to record individual spoke and pool high-speed data locally at 200 Hz.

4.5.4 DAS Network

Due to size and remoteness (with no electrical services) of the experimental setup, and to provide robustness in the event of a single failure, the LNG electrical and DAS network system was broken down into 5 areas:

1. The patch panel at the test site
2. The IR camera network
3. The spectrometer network
4. The DAS network
5. The photometric network.

Patch panel
An existing patch panel with a 5 pair single mode fiber cable was available at the site (used by an explosive group). This single mode fiber cable was routed (~1000 m) from an existing patch panel near the liquid nitrogen bulk storage trailer to the Building 6742 control room bunker. This cable and all its lines (10 in all) was extended to a new LNG patch panel adjacent to the explosive patch panel where all the other networks discussed below were connected. Each pair of fiber wires was dedicated to each of the 4 independent networks. The spectrometer and IR instruments were added later to this network to save space, as the photometric network needed two networks (4 fibers) due to their large bandwidth.

All the field networks that feed the patch panel were multiple mode fibers to handle the internal bandwidth needed to run controls and other functions. The field networks were converted to single mode fiber for the 1000 m run to the control room. Each network required several conversions. For example, the output from a computer or laptop was a standard 10base network cable. These network cables were converted to multiple mode fiber to create the subnet for each independent network. Once all the stations on the multiple mode fiber were connected the multimode fiber was converted to single mode in the patch panel. Back in the control room, the single mode network was converted back to multiple mode for ease of control on the hub. Finally, the multiple mode fibers from the hubs in the control room were converted back to 10base network cables for use with the control computers.

IR camera and Spectrometer network
Figure 47 shows the routing of the IR camera and spectrometer network around the test site. A computer in the field controlled its own IR camera or spectrometer. Once each field laptop was connected together on one network in the patch panel those laptops could be controlled individually by another laptop in the control room inside using Windows “remote desktop.” (As each field laptop had its own unique IP address then any laptop in the control room could be used to control the field laptops.) Data on this network was stored locally, but could be viewed in the control room.

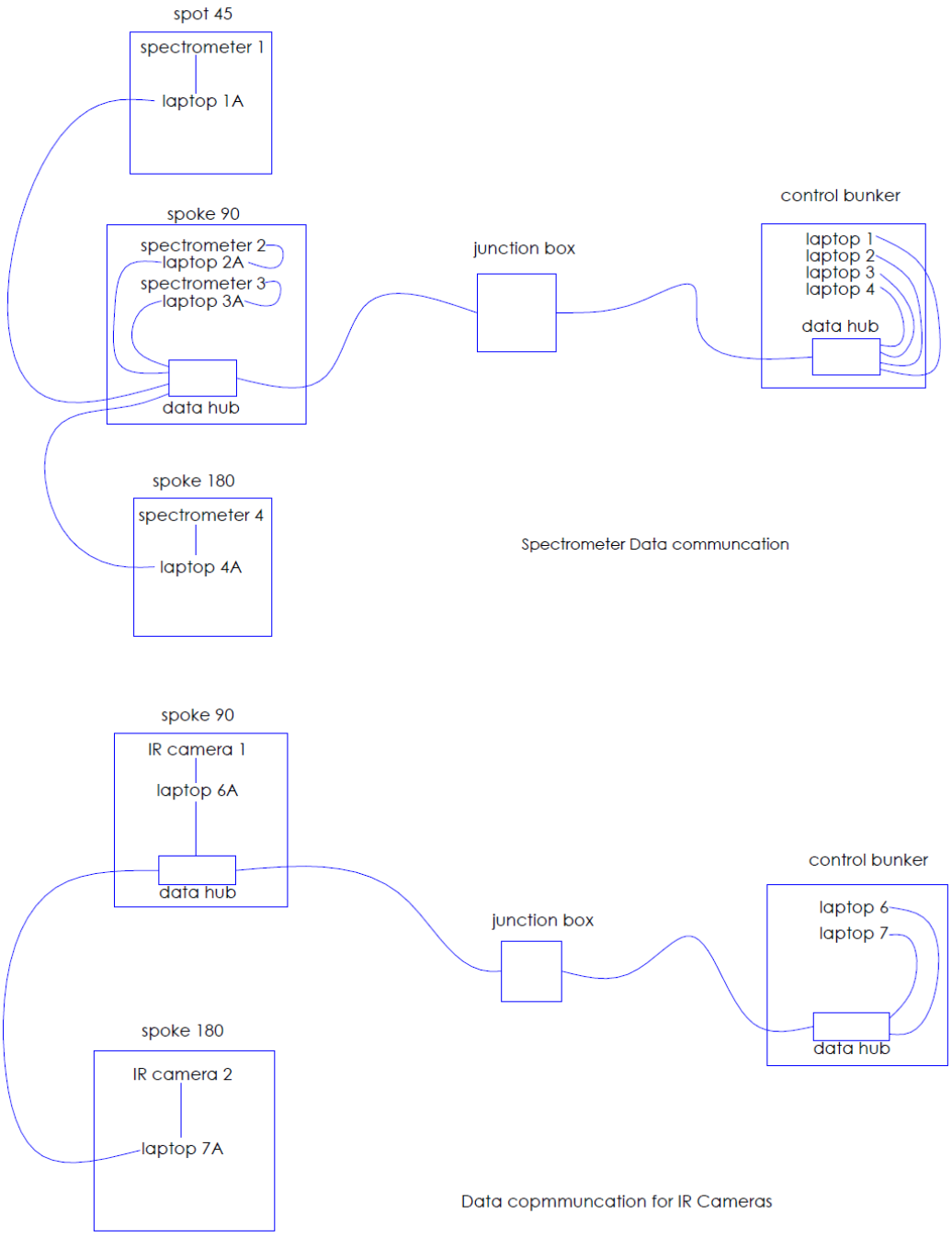

Figure 47 Spectrometer and IR camera data communication.

Data acquisition system network

The data acquisition systems (DAS) functioned similar to the spectrometer and IR networks with a few software differences. Figure 48 shows the DAS network connectivity. Again, each spoke/station computer ran its own software and collected and stored it owns data (for later download). The main data acquisition computer located in the control room was programmed to verify that each field computer (separate IP addresses) was operating, start data acquisition, collect the data from each field computer (as a backup to the field computer), and append it into one master data file. This required a complex in-house LabView® code to address timing and synchronization issues.

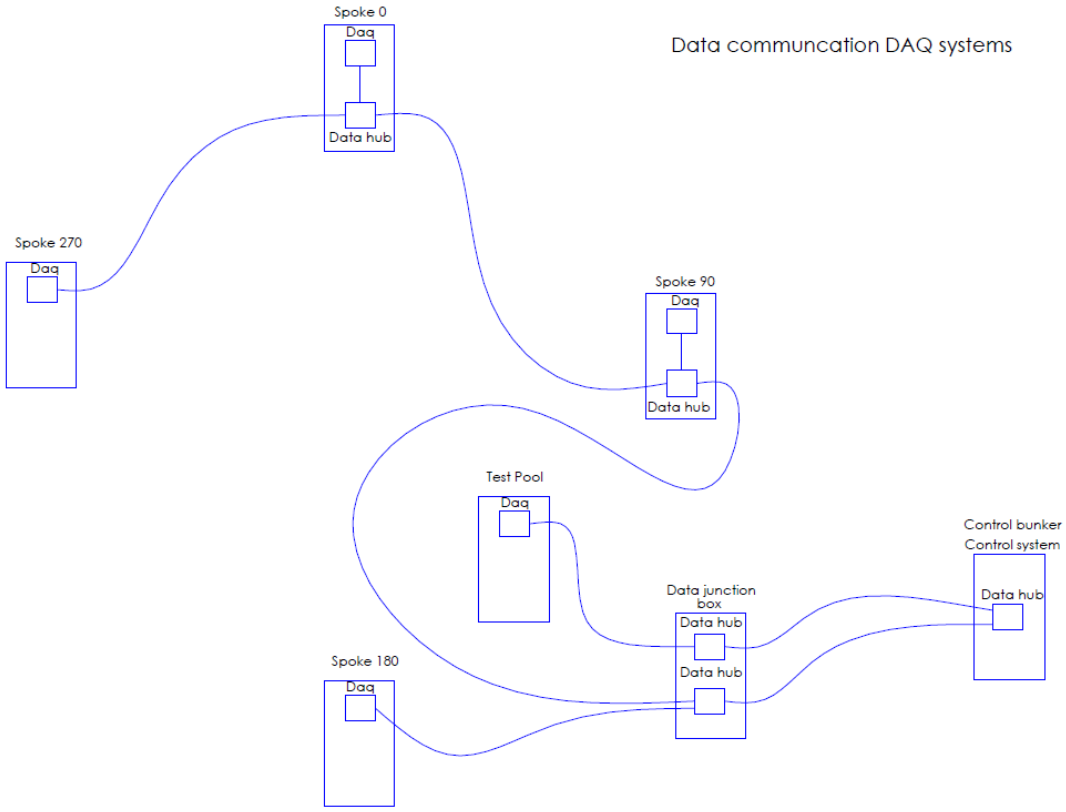

Figure 48 DAS network

Photometric Network

The photometric network was similar to the spectrometer network; each station had its own IP address. Each photo station contained several cameras and computers, each computer with a different IP address to allow personnel to remotely start cameras and verify data collection.

Power and signal routing for each spoke and the pool DAS network are shown in Figure 49.

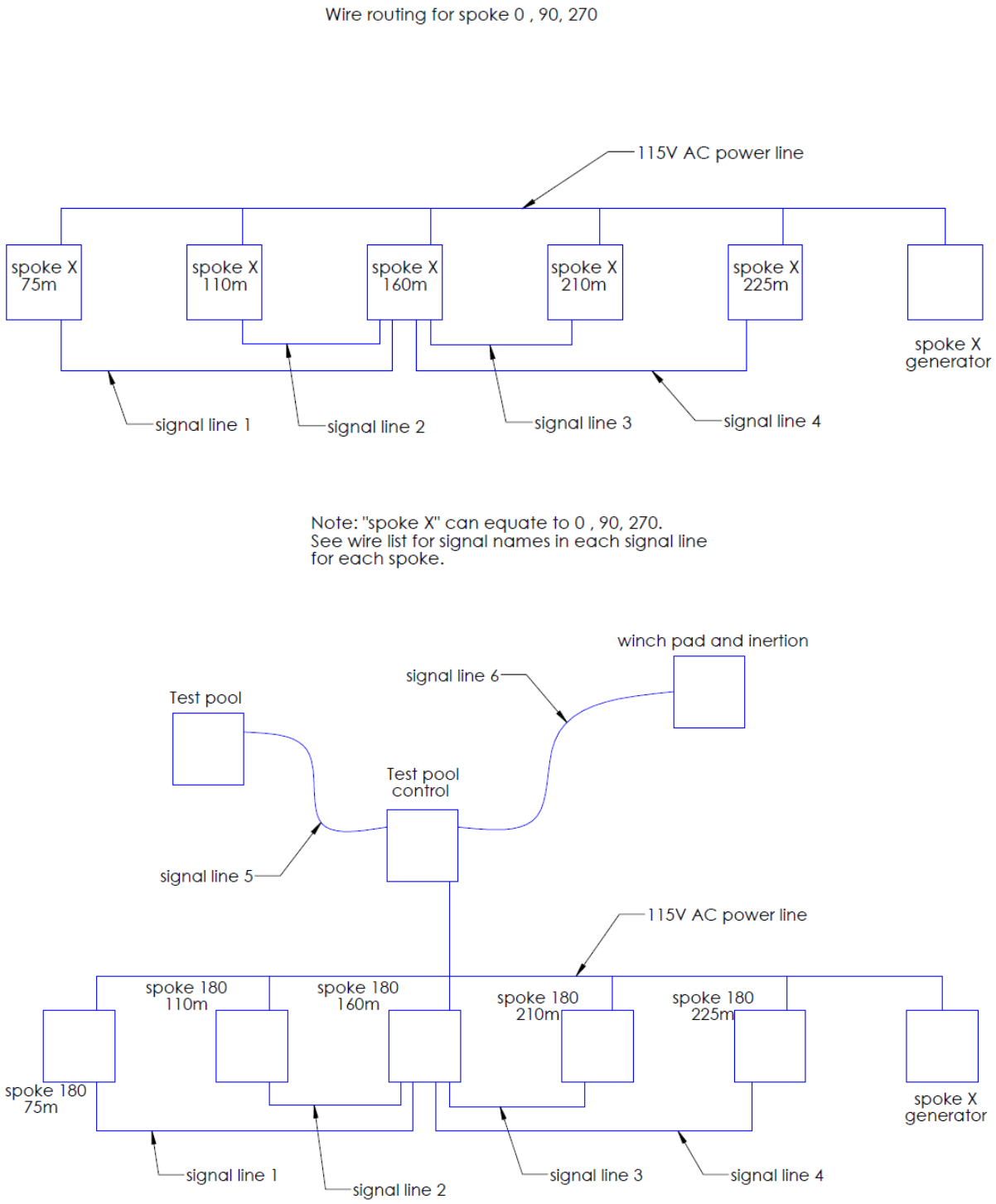

Figure 49 Power and signal routing for the spokes and pool DAS networks.

4.5.5 Flame Heat Flux - Narrow-angle Radiometers

Twenty eight (28) narrow-angle radiometers measured the "spot" incident heat flux at various heights of the flame plume surface (Medtherm Schmidt-Boelter sensors, 12 mV nominal at 300 kW/m^2, 5.5º view angle, with zinc selenide window, water cooled, 63.2% time constant is 35 ms). Due to the large variation in the flame height for the three pool diameters, the angle of mounting of the gauges varied between tests and is tabulated in each test results section. Spot diameters ranged between ~10-20 m, depending on distance of the gauge from the fire and the viewed height. Note that narrow-angle heat flux could be seen as a "spot-average" surface emissive power if the relatively small "spot" was completely filled with flame.

Five narrow-angle gauges were mounted at each of the Tower 1 locations. One narrow-angle gauge was mounted at each of the Tower 2 and Tower 3 locations. The relative angle of the narrow-angle gauges (to the ground plane) was adjusted to measure the flame plume heat flux at different heights (approximately equal spacing) with the line of sight for each gauge passing through the vertical centerline of the pool.

4.5.6 Flame Surface Emissive Power - Wide-angle Radiometers

Twelve (12) wide-angle radiometers measured the radiant heat flux (Medtherm Schmidt-Boelter sensors, view angle of 150º, with zinc selenide window, water cooled, 63.2% time constant is <500 ms). There was one gauge mounted on each tower. In order to increase signal intensity and reduce measurement uncertainty, different gauge spans were used. The ranges of the gauges were: Tower 1 – 100 kW/m^2, Tower 2 – 50 kW/m^2, and Tower 3 – 30 kW/m^2. To support the wide-angle radiometer analysis, four video cameras (one at each location) were positioned to have nearly the same view as the wide-angle radiometer in order to capture the flame plume shape and allow converting the incident heat flux to a "flame-average" SEP.

In other words, average surface emissive power measurements use wide angle radiometers and refer to an average over the flame surface and are interpreted based upon a particular geometry for the flame area.

Angular Sensitivity
It is well known that the angular sensitivity of coatings on heat flux gauges are not lambertian (i.e., do not follow a cosine law). Figure 50 [Alpert et al., 2002] shows this effect for a Medtherm Schmidt-Boelter sensor. The data shows the coating maintained the Lambertian response beyond 70° (1.22 radians) but well below the 90° (1.57 radians) ideal.

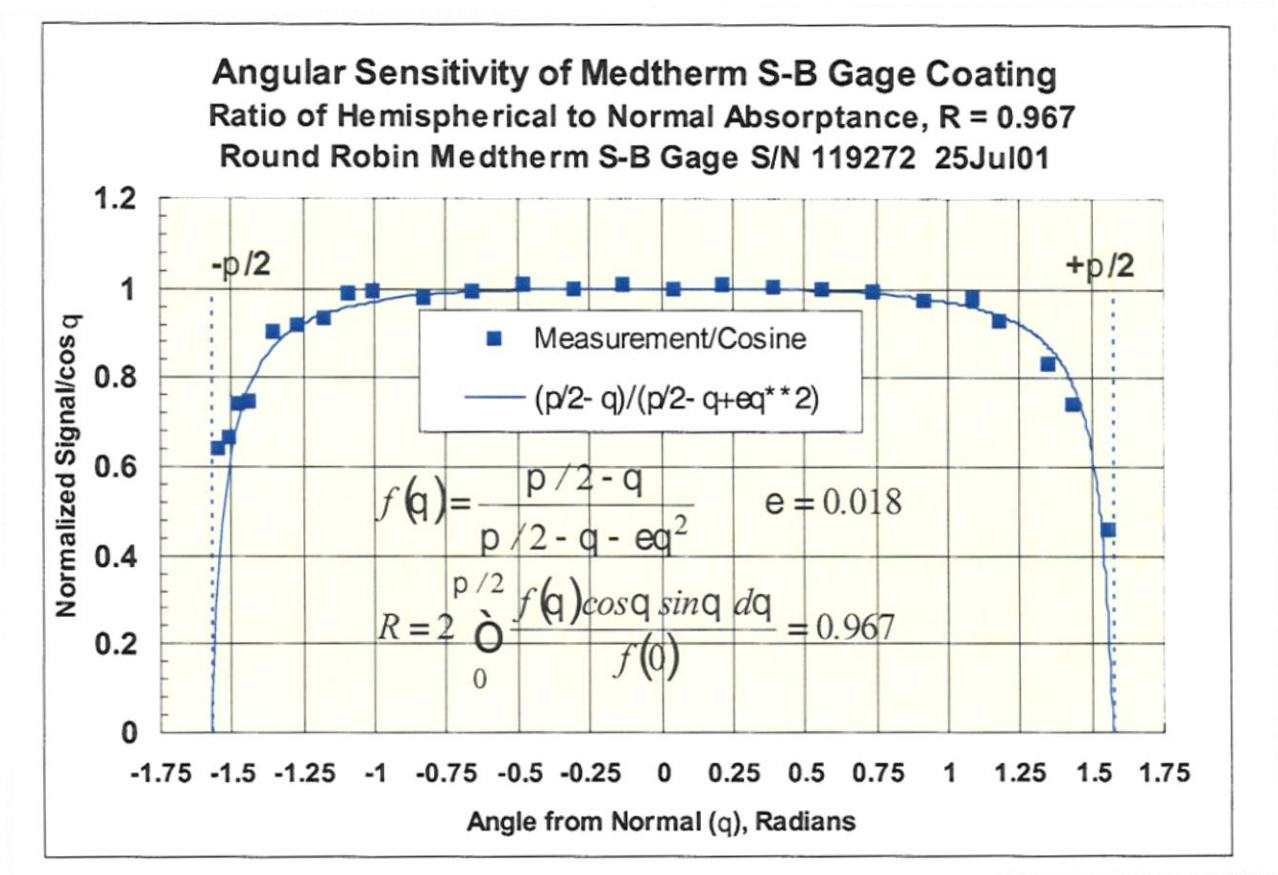

Figure 50 Angular Sensitivity of Medtherm Schmidt-Boelter Gauge Coating.

Table 12 computes the half angle of the three planned test fires (from normal, in radians), as seen at the location of the towers supporting the wide-angle radiometers. The largest fire angle (from normal) is 0.4 radians (for the largest fire diameter and the closest tower). This is well below 1.22 radians; therefore, the angular sensitivity of the wide-angle radiometers should not compromise the validity of the wide-angle radiometer measurements.

Table 12 Half angle subtended by the fire plume when viewed from a distance.

Dpool (m)	**fire angle (deg) @ TW1 (110m from fire)**	**fire angle (deg) @ TW2 (160m from fire)**	**fire angle (deg) @ TW3 (210m from fire)**	**fire angle (radians) @ TW1 (110m from fire)**	**fire angle (radians) @ TW2 (160m from fire)**	**fire angle (radians) @ TW3 (210m from fire)**
35	9.0	6.2	4.8	0.2	0.1	0.1
70	17.7	12.3	9.5	0.3	0.2	0.2
100	24.4	17.4	13.4	0.4	0.3	0.2

Atmosphere Attenuation

It is necessary to understand the effect of radiant attenuation by atmospheric species on the heat flux measurements. A correlation reported by Fuss and Hamins [2002] was used for preliminary estimates; the correlation is based on a narrow band statistical model used to estimate the uncertainty introduced into radiative heat flux measurements from fires which is attributable to attenuation by atmospheric H_2O and CO_2. The correlation gives transmittance as a function of path length (10-200 m), source temperature (1000-1600°C), atmospheric temperature (19-35°C), and relative humidity (0.25-1.0). Note the correlation pressure is fixed at 101 kPa (sea level). Table 13 presents the estimated transmittance (calculated as the ratio of the spectrally integrated intensity at a distance, L, from the fire versus the spectrally integrated intensity at L = 0) for the three tests (with Tair = 20°C, Tschmidt = 1300°C, and RH = 0.25).

Table 13 Pre-test estimate of the transmittance as a function of path length.

L (m)	transmittance
110	0.83
160	0.81
210	0.79

The correlation shows about a 20% attenuation can be expected in the radiant flame measurements at the respective distances from the fire.

Uncertainty Analysis

Uncertainty of the radiometers, per the manufacturer, is ±3% of the responsivity, corresponding to a measurement uncertainty of ±3% of the measurement across the calibration ranges [Nakos 2005].

4.5.7 Pool Heat Flux

The total incident (radiative and convective) heat flux to the pool surface was monitored at twelve locations (see Figure 43 and Figure 51) using directional flame thermocouples (DFTs) [Keltner 2007] attached to a stand in the pool that placed the DFT ~6-12 inches above the water surface. Note that the DFTs closest to the diffuser on the East and South spokes are not as closely aligned with the others on their respective slopes due to interference with the base of the pipe berm (Figure 51).

Figure 51 DFTs in pool the morning of Test 1.

Thermal simulations were performed on a typical configuration to assess performance. The solid model (an accurate representation of the instrument shown in Figure 52) consists of two inconel plates (6 inch x 6 inch, 1/16 inch thick) sandwiching a lightly compressed, ceramic fiber blanket insulation (8 lb/ft^3, 1 inch nominal thickness compressed to ¾ inch). Ungrounded junction, metal sheathed thermocouples are attached to the center of the *unexposed faces* (i.e., touching the insulation) of the metal plates by forming thin Nichrome foil tightly over the tip of the thermocouple and spot welding it around the thermocouple. In the test data, the thermocouple labeled top faces up (towards the fire) and the thermocouple label bottom faces down (into the stand).

A transient thermal analysis was performed using CosmosWorks. A 20°C initial temperature was specified for all components. The front face of one inconel plate was provided a radiation boundary condition equivalent to a 220 kW/m^2 incident heat flux (surface to surrounding ambient temperature of 1130°C, a view factor of 1, and a plate emissivity of 0.85). All other faces were assumed adiabatic. The simulation employed temperature-dependent thermal properties for both the metal and the insulation (see DFT Properties section). The model grid and a snapshot of the temperature at 1 s are also shown in Figure 52.

Four sensors were located in the model, one on each side of both inconel plates, all on the DFT centerline. Note that sensor 2 and sensor 3 represent the two attached thermocouples on the plate inside faces. Figure 53 gives the temperature response of the model. Note that is takes approximately 100 s for the thermal front to reach the back inconel plate. The front inconel plate reached 1117°C at 600 s. The temperature gradients across the thin metal plates are quite small

throughout the test (the inside plate temperatures are almost identical to the outside plate temperatures).

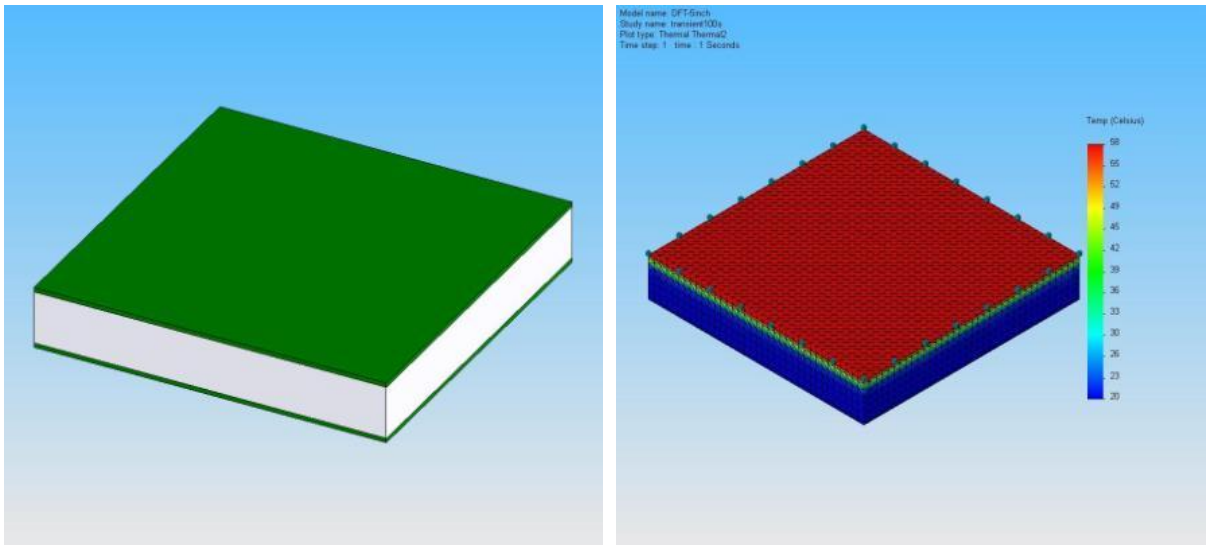

Figure 52 DFT solid model and temperature results at 1 second.

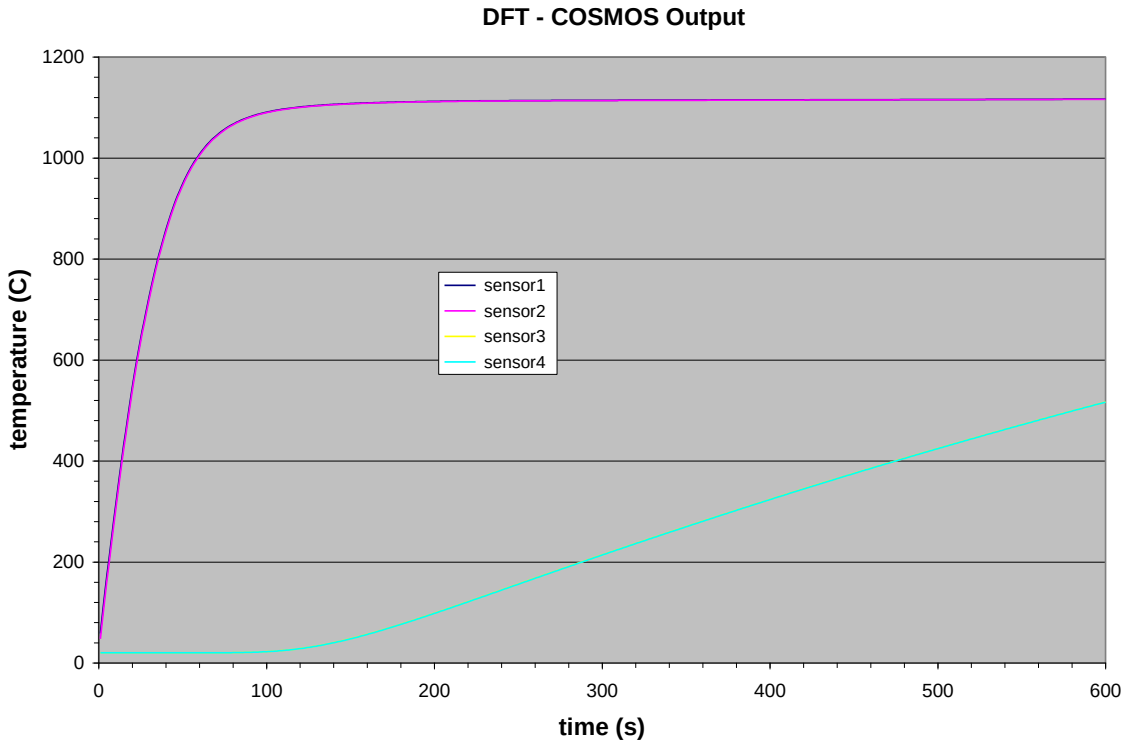

Figure 53 Temperature response of the DFT.

An inverse heat conduction analysis was performed to verify the proposed DFT geometric configuration was adequate. IHCP [Beck, 1999] was used with the identical geometric

configuration, thermal property data, and the CosmosWorks simulation temperature results for sensors 2 and 3. IHCP returns the net flux at the surface (shown as SURFACE qabs in Figure 54) and the surface temperature.

The radiated heat flux (kW/m^2) , SURFACE qrad, is computed from the IHCP-calculated surface temperature (K) (=5.67e-11 x $T_{surface}^4$).

Eq. (4) shows the incident heat flux at the surface (SURFACE qinc in Figure 54) is the net flux divided by the plate emissivity plus a radiation term (SURFACE qrad). Note that the incident heat flux calculated by Eq. (4) does indeed return the thermal simulation 220 kW/m^2 input boundary condition, shown in Figure 54.

$$q_{incident} = q_{net} / \varepsilon + \sigma T_{surface}^{4} \qquad (4)$$

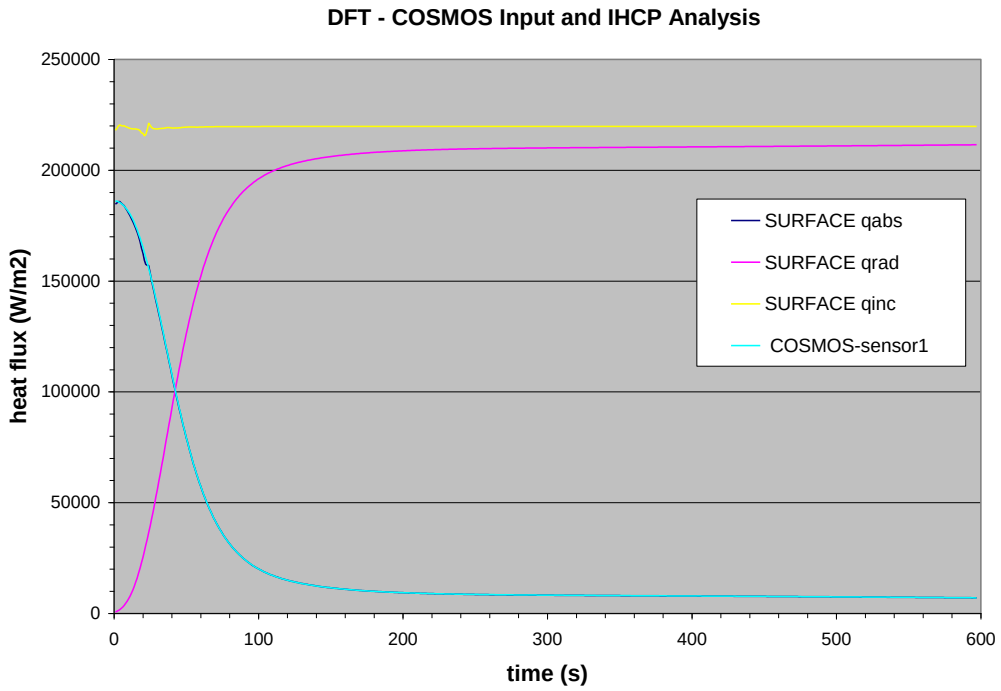

Figure 54 Comparison of net and incident flux from COSMOS and IHCP.

DFT Properties

The properties for the DFT are listed in Table 14 and Table 15 and also shown in Figure 56 and Figure 57. Cerablanket (Kaowool) properties were obtained from manufactures brochures. Manufacturer's values are determined from ASTM Method C201 that uses three thermocouples in variable thickness samples and reports the results in effective conductivity versus mean wall temperature. This is consistent with industrial use of product but inconsistent with SNL transient use. Beck, Keltner, and Oxford converted the effective values to point (local, temperature dependent) values for Thermal Ceramics providing results that are consistent with SNL use in

thermal models. Note that the corrected values are higher by as much as 30%. High temperature properties of Inconel 600 were obtained from Blumm et al. [2005].

Operational Checks

Operational checks of the DFTs were performed using a small radiant heat facility (Penlight). The cavity was preheated to ~800ºC. The DFT was placed at the entrance and a shutter removed to expose the gauge. Figure 55 shows the temperature response of DFT 0-1 (typical of all gauges) and the reduced heat flux data.

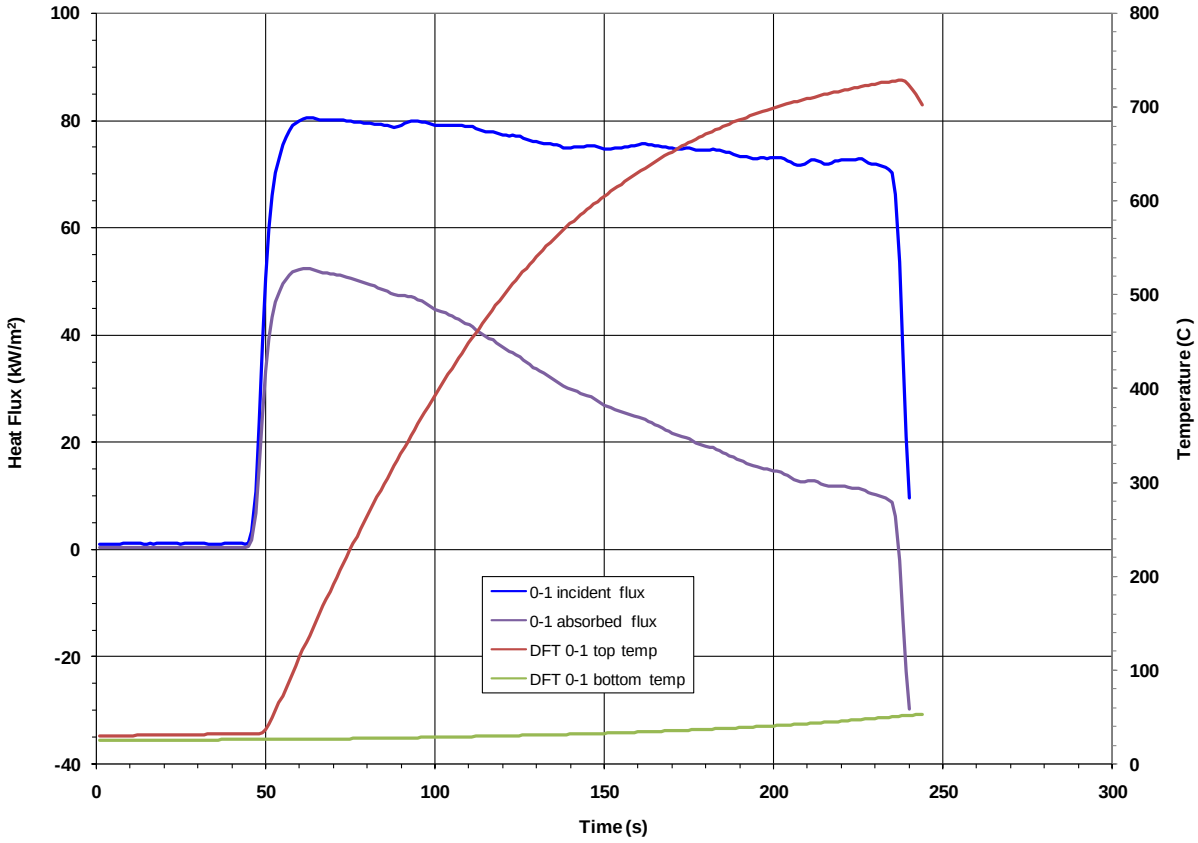

Figure 55 Operational check of a pool DFT.

Table 14 Cerablanket (Kaowool) 8PCF nominal density (128 kg/m^3) properties
8PCF nominal density (128 kg/m^3)
(1"compressed to 3/4" = x1.333 = 170.7 kg/m^3)

Temperature (K)	Thermal Conductivity – local (W/mK)	Temperature (K)	Specific Heat (J/kgK)
293.4	0.0340	273.2	788.1
295.3	0.0342	373.2	826.3
299.6	0.0345	473.2	862.3
301.5	0.0348	573.2	896.1
303.3	0.0349	673.2	927.8
414.1	0.0463	773.2	957.2
505.5	0.0581	873.2	984.5
603.4	0.0737	973.2	1009.6
778.9	0.1096	1073.2	1032.6
810.6	0.1174	1173.2	1053.3
918.3	0.1468	1273.2	1071.9
1023.9	0.1810	1373.2	1088.3
1046.7	0.1890	1473.2	1102.5
1177.8	0.2405	1657.2	1122.9
1307.8	0.3012		
1657.2	0.4857		

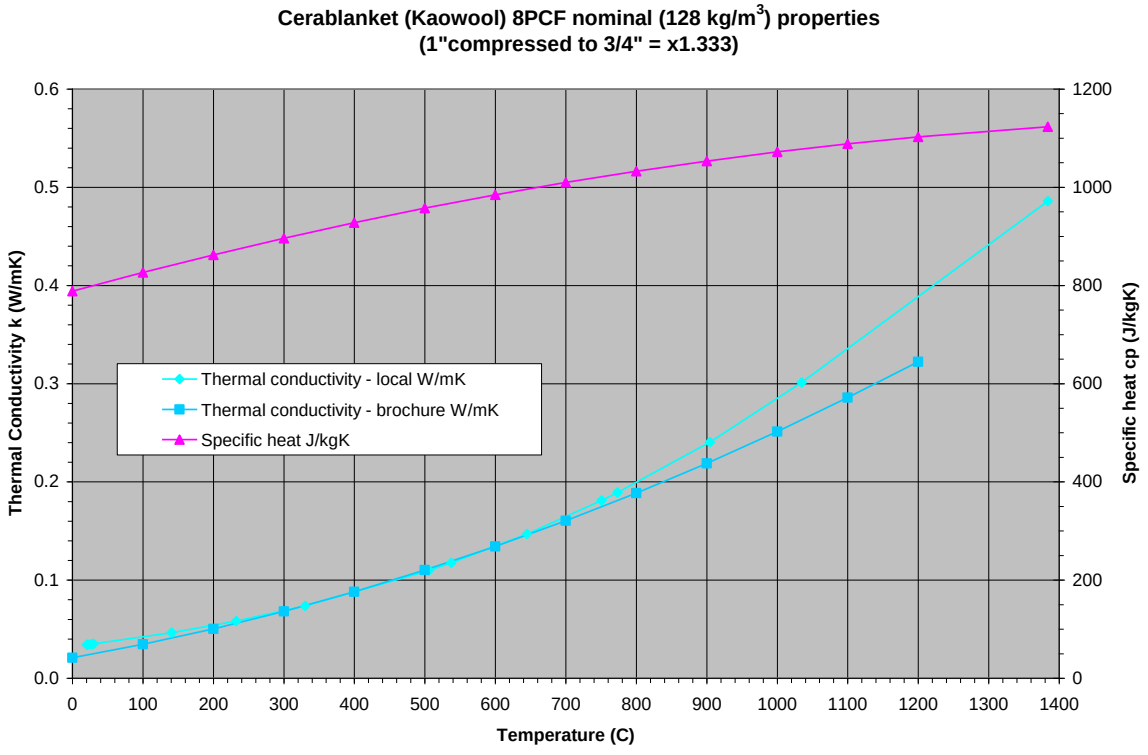

Figure 56 DFT insulation thermal properties.

Table 15 Inconel 600 Thermal Properties

Temperature (K)	Thermal Conductivity (W/mK)	Specific Heat (J/kgK)	Density (kg/m^3)
148.15	10.961	344	8383
173.15	11.207	374	8377
223.15	11.704	411	8363
273.15	12.364	436	8348
298.15	12.694	444	8340
323.15	13.283	453	8332
373.15	14.184	467	8315
423.15	15.016	477	8297
473.15	15.98	489	8279
523.15	16.842	497	8261
573.15	17.678	503	8242
623.15	18.488	511	8223
673.15	19.229	517	8203
723.15	19.957	524	8183
773.15	20.617	528	8164
823.15	21.902	546	8143
873.15	24.35	589	8122
923.15	25.22	588	8100
973.15	25.705	592	8078
1023.15	25.648	599	8056
1073.15	26.25	606	8034
1123.15	26.871	608	8011
1173.15	27.788	615	7987
1223.15	28.805	625	7963
1273.15	29.689	638	7937
1657.15	36.53	704	7798.5

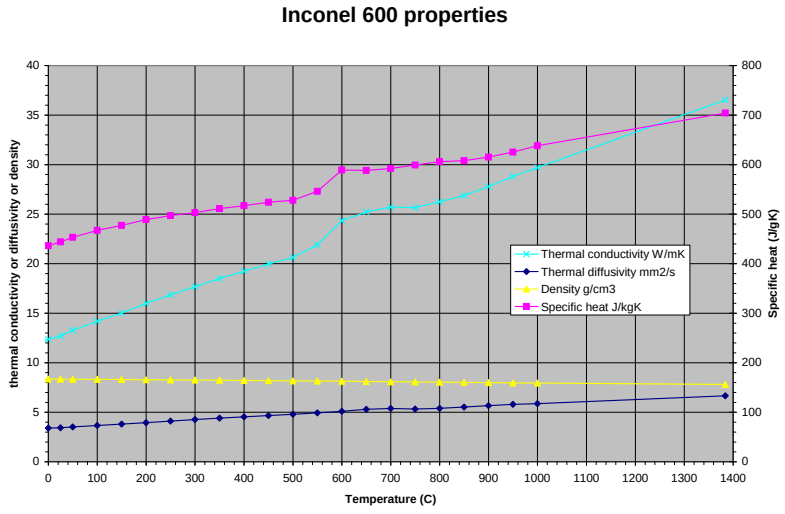

Figure 57 DFT inconel plate thermal properties.

4.5.8 Fuel Regression Rate

The fuel regression rate (sometimes referred to as the burn rate) has two major contributors; relatively hot (compared to the LNG) water upon which it is spreading and also radiative flux from the combustion of the gaseous methane evaporating preferentially from the liquid. The combined fuel regression rate (from both components) is a calculated parameter determined by dividing the measured transient mass flow rate from the reservoir by the measured transient liquid pool area and this represents an average value over the whole area of the pool.

4.5.9 Mass Flow Rate from the Reservoir

Change in liquid level vs. time in conjunction with as-built reservoir dimensions can be used to determine mass flow rate from the reservoir. A diptube system employing two independent pressure-based liquid level sensors was used to measure the height of LNG in the reservoir. The system consisted of two stainless steel tubes (1/4 inch) that ran from the pool data acquisition station (DAS) (see Figure 58) up the reservoir side, into the reservoir along the top of the A-frame, and then down the A-frame support almost to the bottom of the reservoir floor (inside perforated metal baskets), that provided a slow, constant flow rate purge of dry gas (nitrogen in LNG Test 1, helium in LNG Test 2). The dip tubes location on the outside of the south support leg stopped approximately ¼" from the floor of the reservoir in Test 1. In Test 2, one diptube ran down the north A-frame leg into the drain valve recess (reservoir well) and stopped about ¼" from the floor of the recess.

The inlet to each independent sensor system has a manual adjustable precision pressure regulator (Bellofram type 10, 2-25psi range, 0.125 inch WC sensitivity). The flow was metered by a vernier metering valve (Swagelok SS-4MG-MH) and monitored by a precision rotameter (Omega model 0/200) with the flow set to 90 units. This translates to 218.9 mL/min of nitrogen. The pressure in the diptube required to displace the head of liquid in the tube was sensed using a pressure tap downstream of the metering valve, leading to a sensitive pressure transducer scaled for 100 inches of water column (Omega model 264, 0-100 inch water column , accuracy +/- 0.4 %FS). The output from the transducer was recorded on the control DAS at 1 Hz and the pool DAS at 200 Hz. Calibrations of the dip tubes were carried out prior to each experiment using known depths of water.

Figure 58 Diptube instrument setup and tube exit locations near the reservoir floor.

4.5.10 Photometric Coverage

Pool Area

Overhead video was used to determine the real-time extent of the spreading pool fire. The overhead video utilized manned four-axis LSG-2 gyro-stabilized mounts (Figure 59) by Aerial Exposures™. They were flown in two Kirtland AFB 58th/SOW UH-1N helicopters hovering opposite each other to obtain video from a near directly overhead view (1500 ft horizontal, 1000 ft vertical from pool centerline). The helicopter hover positions were set and maintained over a pre-scaled GPS coordinate radius identified by 10' white x-markers. The axis of aircraft positioning was determined real-time by the pilots, dictated by wind direction. Attached to the stabilized mounts were two primary Sony™ HDW-750 high definition video camcorders. These cameras are 3 CCD, 2/3" color format and used Fujinon™ HA22-7.3 BERM telephoto lenses. The 1080 lines resolution x 1920 pixels produce a 16:9 aspect ratio image. The field-of-view (FOV) of these cameras was adjusted to document the full width of the spill pool at the base of the fire, and the aperture maintained to highlight the LNG-water interface at the spill front. Docked to each stabilized primary camera or hand-held, was a secondary Panasonic HDC-SD9, 3 CCD, HD MiniDV cameras with the zoom factor of the 3.0-30 mm lens adjusted to provide a full-view of the fire.

Figure 59 Kirtland AFB 58th/SOW UH-1N helicopter and gyro-stabilized camera.

Two Elmo SUV-Cam II Micro Video Camera Systems with 3 mm lenses were attached to the helmets of a helicopter pilot and flight engineer to provide aircraft cabin interior documentation during the fire test flight. Additionally, one still photographer per aircraft acquired high resolution pictures using Nikon still cameras with image stabilized optics. One still camera captured wide view and the other camera was zoomed to high magnification for LNG-water interface and other detail.

In order to calibrate the camera images (both horizontal and vertical pixels) of the spreading LNG pool to yield accurate measurement of the pool area, a grid of uniformly spaced markers (6 inch diameter stainless steel floats, 5 m spacing, at 4 radii from the diffuser to the pool edge,) were placed within the pool. Eight fire resistant, 24" quad stadia boards were placed pool-side to provide additional dimensional measurement calibration for the aerial view.

Photometric Coverage - Flame Height

Setup

A total of ten cameras were installed on the four instrumentation spokes by the Photometrics Group technicians in Org 1534. One high-speed, plus one HD real-time camera was installed per spoke, in addition one Firewire IEEE-1394b CCD camera was mounted behind both the North and West stations. Also, 2 Bosch single color CCD cameras were stationed on the top edge of the northwest face of the LNG reservoir berm. The high-speed and HD flame height cameras were mounted into protective weather enclosures which include an IR reflective window to guard the camera optics from the fire. These enclosures were attached to cast iron Palmgren heads and located on concrete pads ~225 m from the pool center. The cameras were further protected by a 6' x 4' steel heat shield with a 4' rear overhang. A steel NEMA enclosure was also be placed at each camera station and positioned within the shadow of the heat shield to further protect electro-mechanical trigger boxes, IRIG generators and power supplies. The two Firewire 800 pool area cameras were also placed into protective weather enclosures and mounted on the top of 30' posts positioned directly behind the concrete pads ~230 m from pool center.

Color high-speed digital cameras

Two of the high-speed cameras were high-resolution Phantom V10, by Vision Research™, capable of 2400 x 1800 pixels. The 12 GB of volatile internal memory in the V10 with the 8 bit option provides a frame rate of 4 frames per second for 11 minutes. The remaining two cameras were the color V7 model with an 800 x 600 pixel array. They have one third of the pixel array in comparison to the V10 and can easily capture a 10 minute burn in its entirety running at 5 - 10 Hz using the full 12 bit depth. The Phantom cameras were triggered together at T = - 5 seconds before the test fiducial signal (fidu) to capture synchronous data during the entire test. Camera positions and lens selection were optimized for prime lenses with estimated focal lengths of 28 mm and 18 mm resulting in the appropriate field of view to accommodate an expected 200 m flame height. The high-speed cameras were linked by a buried fiber-optic network and triggered remotely using a laptop running Vision Research™ software. The high-speed cameras were time-synced with GPS IRIG receivers which allowed video frame synchronization. All of the high-speed cameras were set up on their sides to optimize the maximum number of pixels with the vertical orientation of the fire.

High-definition real-time cameras

The four real-time cameras were Canon Vixia HD MiniDV real time camcorders (30 Hz). The 6.1-61 mm zoom lenses were identically adjusted for anticipated flame height. A 0.7x Panasonic wide angle lens was attached to each camera to accommodate for the expected 100 m base width of the LNG fire. The HD real-time cameras have a total record time of 83 minutes and were manually started when the hazard area was cleared. External microphones contained in protective enclosures provided audio for each of these cameras. These cameras, paired with the with the wide-angle radiometers on each spoke, were used to determine the average surface emissive power of the fires.

Firewire IEEE-1394b CCD camera

The Firewire 800(b) cameras are 5 megapixel CCD models (Point Grey) capable of a frame rate of 1 fps at a resolution of 1200 x 400. The cameras were connected to a local laptop using a 50' Firewire 800 extender. The FlyCapture® Software Development Kit provided a software interface to control the Point Grey Imaging Products. Software triggering was conducted remotely and common timing provided by the test fidu.

Additional Photometric Coverage

Reservoir berm cameras

Two Bosch color CCD cameras were mounted adjacent to one another in a heat protective enclosure and placed on the top edge of the northwest face of the LNG reservoir berm. They provided a combined low-angle, full-width view of the spill pool. These cameras used an S-video (Y/C) to Ethernet converter to relay the video signal 50' away to MiniDV decks positioned inside the winch control DAQ box at the southern base of the reservoir. The cameras were started manually and recorded to 85 minute MiniDV tapes.

Infrared cameras

Infrared data was acquired using FLIR Systems™ model S-60 and SC-660 infra-red cameras with uncooled microbolometer detectors, utilizing 450 FOV lens. The S-660 (640 x 480 pixel array) was located on the 90 spoke and the S-60 (320 x 240 pixel array) was located on the 180 spoke, both at a distance of 214 m from pool center. These cameras are sensitive to the wavelength band of 7.5-13 micrometers. The cameras were triggered remotely the recording media is local to the camera.

Flame Height / Smoke Plume cameras

One Sony™ HDW-750, one Sony 3 CCD PRO SD camcorder, one Sony HVR-Z1U HD DV camcorder and two Sony HDV camcorders were manned outside the fence line of Bldg 6639, X-Ray Facility in Area 3. This location is at a range of 1160 m from pool center. The cameras were set to record when the helicopters assumed position prior to ignition. Camera's FOV's captured full-flame height imagery, extreme wide view to acquire smoke plume characteristics, and documentation of helicopter flight envelope.

Site Surveillance / Reservoir Float Pole cameras

Three COHU 3960 Series Integrated Camera Positioner and Control systems were fielded to accomplish site surveillance and safety functions. These are 35x day/night cameras with image stabilization and a ¼", 768 x 494 pixel array. The pan/tilt/zoom controller communication link for each of the three cameras is via fiber optic network from the Bldg 6742 control room. The cameras were powered by portable generators. One camera unit was located ~300 m from pool center on the approximate 190 axis. This camera was heat shielded on an elevated platform to provide a full view of the southern side of the LNG test site. The second camera unit was heat

shielded on an elevated platform, located ~300 m from pool center on the approximate 75 axis. This camera provided an unobstructed view of the northern end of the test site including the reservoir fill station and the dome vent caps. The third camera was positioned under a metal heat shield, at a low profile in the shadow of the dirt berm adjacent to the LN_2 trailer. It also provided a close-up view of the reservoir float pole increments. These cameras also adjust for close-up views of the reservoir fill station and the LN_2 trailer. The diffuser microphone signal was patched to be recorded with these video signals. All cameras recorded in the Bldg 6742 test control room.

270 Spoke – Long Range Full Plume Capture cameras

To capture long range imagery of the smoke plume extension, two cameras were located 4 miles due west of the test site. One was a Canon, XHA1 HDV camcorder with 1/3" CCD x 3 acquiring 1080 x 1920 pixels. The second was a secondary Panasonic HDC-SD9, 3 CCD, HD MiniDV camcorder with the zoom factor of the 3.0-30mm lens and a 2x telephoto adapter. The 1/6" CCD x 3 can acquire 1080 x 1920 pixels. This perspective was back lit by early daylight and provided a less distorted full view of the smoke plume size and altitude.

Bldg 6742 Bunker Control Room Activities

Two Panasonic MiniDV camcorders were activated during final systems checks and test conduct. The cameras were mounted at both ends of the control room to capture audio and physical activities of key test personnel.

Camera calibration methods – Stadia boards / SS float array / Helium balloons

In order to calibrate the aerial video imagery of the spreading LNG pool and for accurate measurement of the pool area, a grid of uniformly spaced markers was placed in the water pool. The markers (described earlier) were 6" stainless steel float-balls strung along the spoke axes at specified locations. The grid center was coincidental with the pool center at the diffuser.

On each spoke axis and at 45 degrees between each, at the perimeter of the pool, were dual-use, 24" quad stadia boards. The boards were placed vertically to calibrate the spoke cameras, and then laid flat on the pool edge for the aerial views. A duplicate, temporary stadia board was positioned on top of the diffuser for a half-pool width measurement during spoke camera calibration. This half measurement was required due to the obstruction of the pool edge by the reservoir from the 90 degree and 180 degree spoke camera views.

To calibrate the vertical axis of the spoke and long range cameras used to measure flame height, a tethered linear array of helium balloons was deployed prior to reservoir fill operations. The array consisted of an 8' diameter balloon at a height of 460' above the diffuser with 26" diameter marker balloons at 100' spacing on the tether (starting at 50' below the 8' diameter balloon). A 10' leader followed the last 100' section and was attached from the lower most marker balloon to the main tether anchor. This 10' leader provided for full visibility of the lowermost marker balloon from all camera angles. The total height of the 8' main balloon was 460' above the top of the diffuser. Three guy lines were attached to the large balloon and anchored at the pool perimeter to stabilize the balloons during camera calibrations.

Generally, once measurements have been obtained for the purpose of scale calibration, it is always preferable to leave calibrated cameras in place prior to a test. However, the period of time between camera calibration and test conduct may be lengthy and unstable weather may be a factor. Ideal wind conditions were required in order to achieve an accurate vertical calibration using the balloon array. During the initial vertical camera calibration, photometric technicians imaged the various balloon setup using the different cameras and camera lenses and documented lens focal lengths, camera inclination angles, etc. The real-time HD DV camera zoom factors were set on full-wide for all tests.

A Meggaflash bulb located at the diffuser, remotely fired, provided a visual frame-synchronization of all cameras and fiducial signals to the control room DAS, the pool DAS, and all four spoke DASs.

4.5.11 Mid-Infrared Spectral Radiation Measurements

The objectives of mid-infrared spectral radiation measurements were to:

1. Provide thermal radiation spectra from gaseous fires in the 1.3-4.8 micron range
2. Determine the variation in spectral data with burn time
3. Determine the variation in spectral data with location in the flame
4. Determine the relative contributions of soot and gas band emissions (CO_2, H_20)
5. Determine the flame temperature and emissivity based upon fits to the soot emission
6. Determine the flame emissive power including the correction for atmospheric absorption if required
7. Determine the flame height (by vertically over scanning the flame plume), and
8. Compare data with radiometers.

A number of improvements over historical data include:

1. Increased sampling rate 2.5 ms vs. 0.5 s
2. Decreased viewing angle to reduce the potential for being influenced by areas outside the flame zone (0.27 degrees vs. 7 degrees), also reduces misalignment issues
3. Ability to scan vertically to determine variation with height and provide an assessment of flame height if over scanning is achieved.

Spectroscopy Instrumentation

Mid-infrared spectral radiation intensity measurements were taken by an imaging spectrometer (Figure 60, model ES-200, Spectraline, Inc., West Lafayette, IN).

The ES-200 measures spectral radiation intensity at 390 Hz in the 1.3 to 4.8 micron wavelength range and each of the pixels looks at a wavelength of 22 nm. The total wavelength range accounts for 75% of the emitted radiation energy from a blackbody source at 1420K, which is approximately the effective radiation temperature from a large hydrocarbon fuel fire as determined by Kearney [2001]. The view angle of the stationary spectrometer is ±0.27 degrees.

The ES200 spectrometer was equipped with a 1D scanner. The scanner is capable of measuring a line with 128 pixel resolution in just 0.32 seconds. A schematic of the internal optics of the spectrometer is shown in Figure 61.

Figure 60 Spectraline ES200, laptop, and data acquisition system

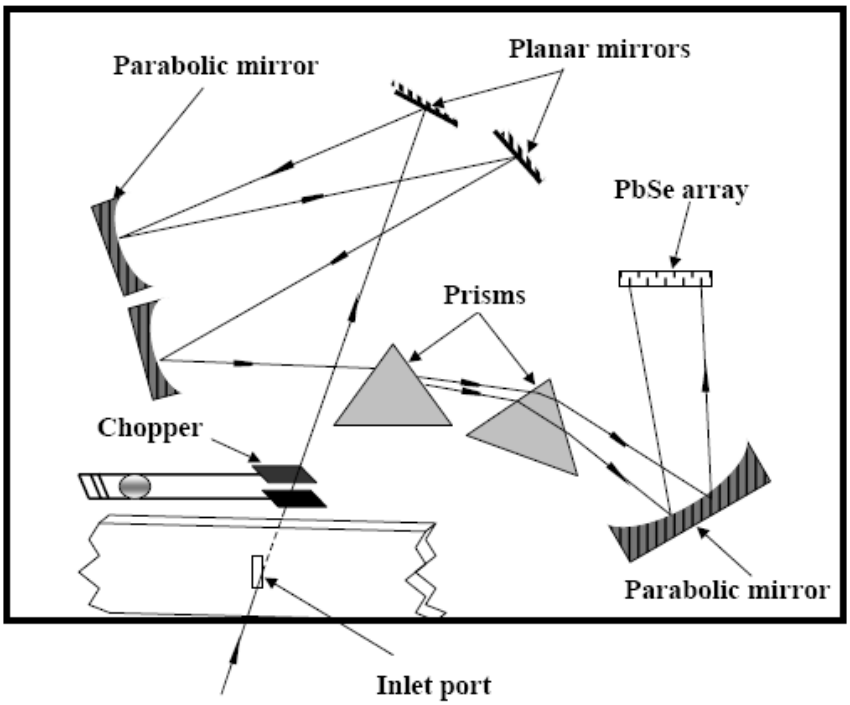

Figure 61 Internal optics for the spectrometer

Table 16 provides the specifications for the ES-200. Radiation enters the inlet port of the ES 200 through a sapphire window mounted on the interface plate. It is then chopped by a tuning fork chopper oscillating at a specific frequency. The chopped radiation falls on a set of mirrors and off-axis parabolas that collimate the beam. The beam then passes through a set of calcium fluoride prisms that disperse it into its component wavelengths. The dispersed beam falls on another parabolic mirror that reflects it on to the detector array. The detector is an array of 256 Lead Selenide elements arranged in a linear fashion. These pixel elements respond to the

incident radiation by producing an output current. The built-in multiplexer reads these currents at 1 MHz and provides it at the camera output. The proprietary drive circuit converts these currents to voltages, amplifies them and sends them to the data acquisition board. The Infraspec software reads the data acquisition board and writes the data to memory. The software then calculates the intensities corresponding to each voltage and plots it against the corresponding wavelength. When referenced with calibrations obtained using a black body, the data provides the absolute values of radiation intensities recorded by the detector array.

Table 16 ES-200 Technical Specifications

Imaging Spectrometer	
Detector	256 pixel PbSe array
Pixel size	33 x 100 microns
Cooling	Thermoelectric cooler
Nominal wavelength range	1.3 to 4.8 microns (7692 - 2083 cm-1)
Entrance slit size	1/0.5/0.25 mm x 8 mm
F Number	3.5
Acceptance angle	+/- 0.27 degrees
Spectral resolution	0.014 microns (14 nanometers)
Accuracy	0.5 % of full range
Responsivity	6e8 volts/watt
Sensor dynamic range	> 2000: 1
Frame acquisition rate	4680 / 15840 Hz
Frame sampling rate	390 / 1320 Hz
Size	11" x 10.5" x 4.5" (28 x 26 x 11 cm)
Weight	15 lbs (6.8 kg)
Housing	Cast Aluminum, sealed
Operating range	0 - 40 deg C (32 - 104 deg F)
Output	12 bit video
Power	120 VAC, 60 Hz
Environmental	Moisture, dust, corrosion proof
Mounting	Bench, tripod, cart, slide, hard mount
Configurations	Desktop, Laptop, Data logger, Mobile
System requirements	200 MHz CPU, 64 Mb RAM, Win 9X, NT, 2000, XP
User interface	*Infraspec* Windows based GUI

Four spectrometers were fielded at the following locations; however, only Unit 2 on the 189 spoke yielded useable data due to the tilt and movement of the fire plume:
1. Unit 2 - 180 spoke at 226 meters to the center of the pool
2. Unit 1 - 90 spoke is 226 meters to the center of the pool
3. ND - 45 spoke is 228 meters to the center of the pool
4. Ocean Optics - on the 90 spoke.

Calibration Results

The data files were read into the Infraspec software and were converted from raw voltages to intensities ($kW/m^2/\mu m/sr$) using a calibration file. The calibration was performed in a laboratory environment using an Infrared Systems IR-301 blackbody and IR-364 controller. The calibration file was created by performing a second order fit of the six temperature scan files (600^oC, 750^oC,

900°C, 1000°C, 1100°C, and 1200°C). The calibration was performed frequently to determine that there was no shift in the instrument and that the appropriate calibration would be applied to reduce the data. Figure 62 shows that the intensity calibration file used in LNG Test 2 to reduce the data was valid in that it accurately converted voltages obtained from a blackbody source to closely match theoretical blackbody intensities.

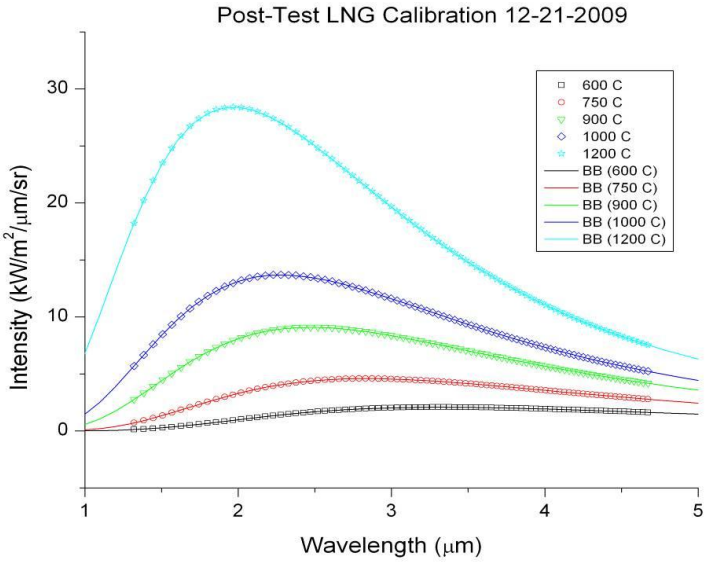

Figure 62 Spectrometer calibration showing intensity vs. wavelength

In addition to an intensity calibration, a wavelength calibration was also performed by placing narrow bandpass filters in front of the blackbody source to determine where the peak intensity was within the linear array. This allows the instrument pixels to be calibrated for actual wavelengths. A plot of the filter wavelength calibration is shown in Figure 63.

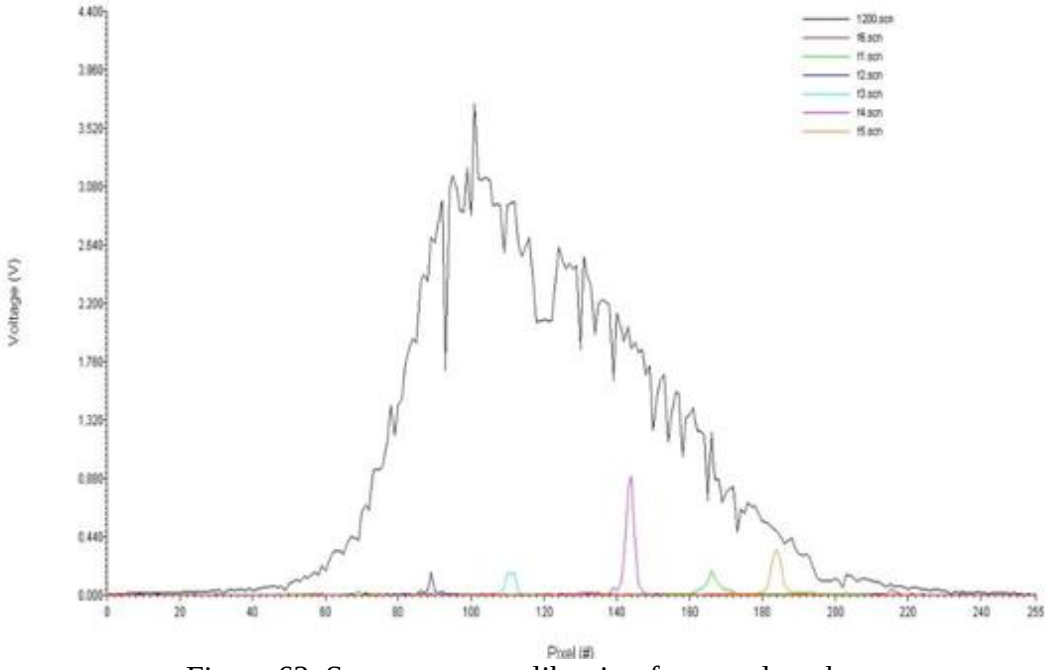

Figure 63 Spectrometer calibration for wavelength.

Uncertainty Analysis

The manufacturer's stated uncertainty for the Spectraline ES-200 spectrometer is ±0.5% of full range of the signal (0 to 10 Volts), which corresponds to the random error in the measurement. The accuracy of the intensity measurement is then a function of the accuracy and appropriateness of the calibration. A linear calibration is employed. A sensitivity of 5000 $W/m^2/sr/\mu m/V$ is typical, corresponding to a typical uncertainty of 250 $W/m^2/sr/\mu m$ due to random error in the voltage measurement. With expected typical voltage signals of 0.1 V to 1.5 V for the minimum and maximum intensities, respectively, the uncertainty due to the random measurement error is ±4% to ±50% of the measured intensity. If the uncertainty in the calibration is assumed to be ±5%, the overall uncertainties rise to ±6% and ±50% for the maximum and minimum recorded intensities, respectively.

Scan Angle Calibration

The scan angles of three Spectraline mid-infrared spectrometers were determined at the Thermal Test Complex on January 12, 2009. Two of the spectrometers (Unit 1 and Unit 2) are owned by Sandia Labs and are ES200 models. A rented ES100 model spectrometer (called ND) was also used and evaluated. The ES100 model operates at 1320 Hz, while the ES200 models operate at 390 Hz.

A blackbody source with a 1" aperture at a fixed distance was used for the radiation source. The experimental configuration is shown in Figure 64.

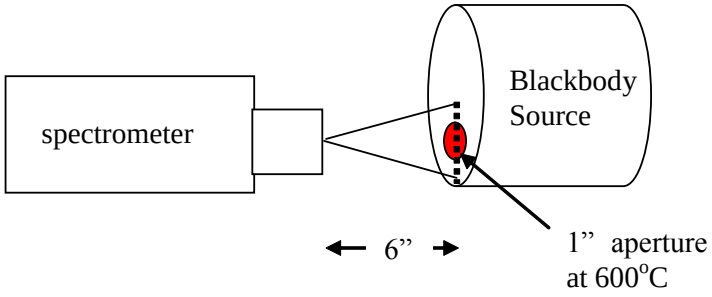

Figure 64 Experimental configuration for determining the scan angle

The blackbody was held at a fixed temperature of 600°C and distance of 6" from the spectrometer scanner. The scanner was set to acquire a 1D vertical scan of the blackbody aperture which is 1" in diameter. A plot of the scan location (from 0-127) as a function of voltage was observed. The scan angle and scan offset were adjusted (via set screws in the power supply box) until the scan was centered on the aperture (i.e. center of the aperture was at approximately location 64) and the scan angle spanned the desired amount of the aperture (Figure 65).

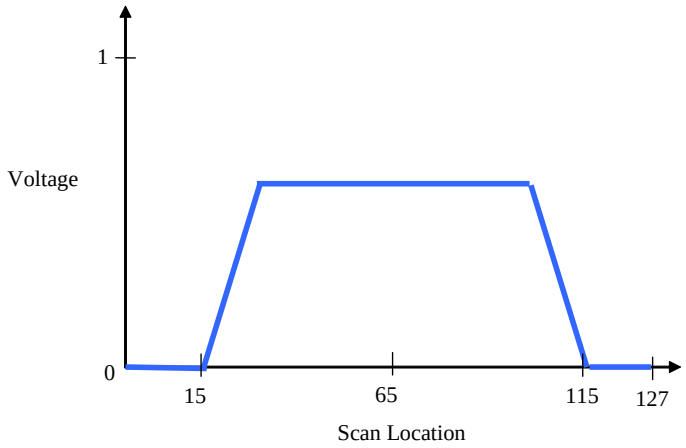

Figure 65 Example of a scan of the blackbody aperture

As shown roughly above, the aperture of the blackbody was between locations 15 and 115 and was approximately centered in the scan. The total number of points in the scan is 128. The calculation of the scan angle based upon the experiments is shown below.

$$\frac{1inch}{100\,pts} = 0.01\frac{in}{pt}$$

$$0.01\frac{in}{pt} \times 128\,pt = 1.28inches$$

Given the total scan distance of 1.28 inches and the distance from the blackbody to the spectrometer of 6 inches, the scan angle can be calculated.

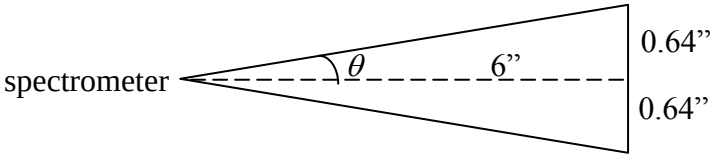

$$\tan\theta = \frac{0.64''}{6''}$$

$$\theta = 6.1^{o}$$

Therefore, the total scan angle of the spectrometer is 12.2°. Note that all spectrometers calibrated were adjusted to obtain the same calibrated scan angle. Given the 12.2° scan angle, the vertical scan distance for the LNG fires can be calculated. Nominal measured distance from spectrometer to the pool centerline = 226 m (distance was measured at the site, as built)

Therefore, half vertical distance per line scan is:

$$\tan(6.1^{o}) = \frac{x}{226m}$$

$$x = 24m$$

And the vertical scan distance total (2x) ~ 48 m

Spot size based upon published acceptance angle of ±0.27^{o}.

$$\tan(0.27^{o}) = \frac{x}{226m}$$

$$x = 1.1m$$

Therefore, the spot size is (2x) = 2.2 m

Sampling Rates:

Unit 1 and 2 operates at 390 Hz, yielding 2.5ms per spectra x 128 ~ 0.32 sec per line scan

ND operates at 1320 Hz, yielding 0.75 ms per spectra x 128 ~ 0.1 sec per line scan

4.5.12 Long-Range, High-Resolution Infrared Spectroscopy

Three separate optical instruments were fielded by the Monitoring Systems Center (5700) to collect information on the large scale LNG fire. The main instrument was a single element Fourier Transform Infrared (FTIR) Spectrometer. The other two instruments were fielded to provide contextual and ancillary information to support the spectrometer. They included a fast framing visible camera and a video rate thermal camera. A technical description of each instrument along with the calibration routine for the FTIR is provided.

FTIR Spectrometer

The FTIR is a Fourier Transform Interferometer manufactured by ABB – Bomem in Québec. The MR304 can be configured with two separate channels, one with a mercury-cadmium-telluride (MCT) detector and the other with an InSb detector. With both channels, the instrument is capable of measuring the spectral region from 1.0 to 15.0 μm with a spectral resolution of up to 1 cm^{-1}. The instrument was used with the narrow angle telescope to have a field of view (FOV) of 4.9 mrad, and can be seen in that configuration in Figure 66. The nearest focusing range for the narrow angle telescope is 30 meters and the range for the field collect was over 1 km.

Figure 66 ABB - Bomem FTIR radiometer.

The FTIR also has a medium angle telescope (28 mrad) and a wide angle telescope (75 mrad) which were not used. The instrument communicates with the PC over a 100 Mb Ethernet protocol using a standard CAT5 cable. The instrument is capable of collecting anywhere from 10 to 107 scans per second depending on the spectral resolution selected.

Thermal Imager

The thermal imager is a microbolometer based camera that has a broadband response from 8-12 μm. The field-of-view of the instrument is approximately 26° by 19.6°. The camera can output images at a rate of 30 frames per second. A LabView® GUI and data acquisition software application was developed to allow streaming of video straight to hard disc over an IEEE 1394 interface. The thermal camera and a sample image collected by the camera can be seen below in Figure 67.

Figure 67 Thermal Imager and a LNG pool fire image.

Visible Imager

A moderate speed visible imager with an extended focal length lens was exactly co-boresighted with the FTIR (using the FTIR beam splitter). The thermal imager was adjusted to provide the same view as the visible image. The camera model is a Pike and is manufactured by AVT. The digital VNIR camera has a field of view of 1.4° x 1.0° with the extended lens installed, which is larger than any of the FTIR telescope FOV. This setup allows for contextual information about the target to be collected along with providing knowledge of where in the target the FTIR FOV is centered. The frame rate of the VNIR camera is adjustable from about 1 to 900 frames per second. The VNIR camera and an image of the fire taken by the camera can be seen in Figure 68.

Figure 68 Visible Imager and panchromatic VNIR image.

FTIR Calibration

The FTIR requires that a baseline calibration measurement be done either before or after taking a measurement of the target. The standard practice is to use a calibrated blackbody source placed at the collimator input of the FTIR. In general, it's best to take at least two calibration measurements with one that is a higher temperature than the target and one that is at a lower temperature. Typically in the field, the calibration is done without the telescope installed on the instrument since it would be difficult to have a calibrated source with sufficient temperature that could overfill the 10 inch telescope. Therefore, in the laboratory environment, the losses from the telescope must be measured.

In order to calibrate the system, two separate groups of measurements were made. One without the telescope installed on the FTIR and one with the narrow field telescope installed. This technique allows for the radiometric losses associated with telescope to be computed. To provide the narrow field telescope with a calibrated radiometric source, the high temperature black body was used as the input source at the focal point of a large 12" laboratory collimator as seen in Figure 69.

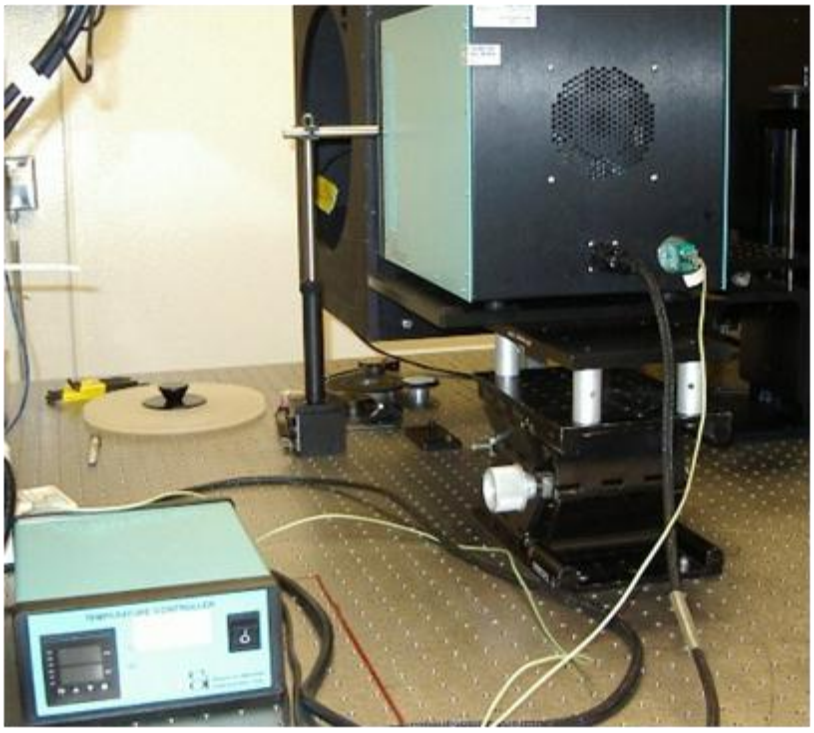

Figure 69 Blackbody source at input of the collimator.

The laboratory set up of the telescope on the FTIR in alignment with the large collimator and blackbody source can be seen in Figure 70, along with the instrument control laptop and power supply. The two sets of measurements that were made in the laboratory were repeated twice, once for the narrow telescope which has an obscuration and once for the medium angle telescope which does not have an obscuration. First, with the narrow telescope, the calibration was performed as if in the field with the radiometric reference at the input aperture at two different temperatures. Next, two calibration collects were done with radiation going through the

collimator, overfilling the telescope. Finally a scene was collected with the blackbody going through the collimator at a temperature between the two calibration temperatures.

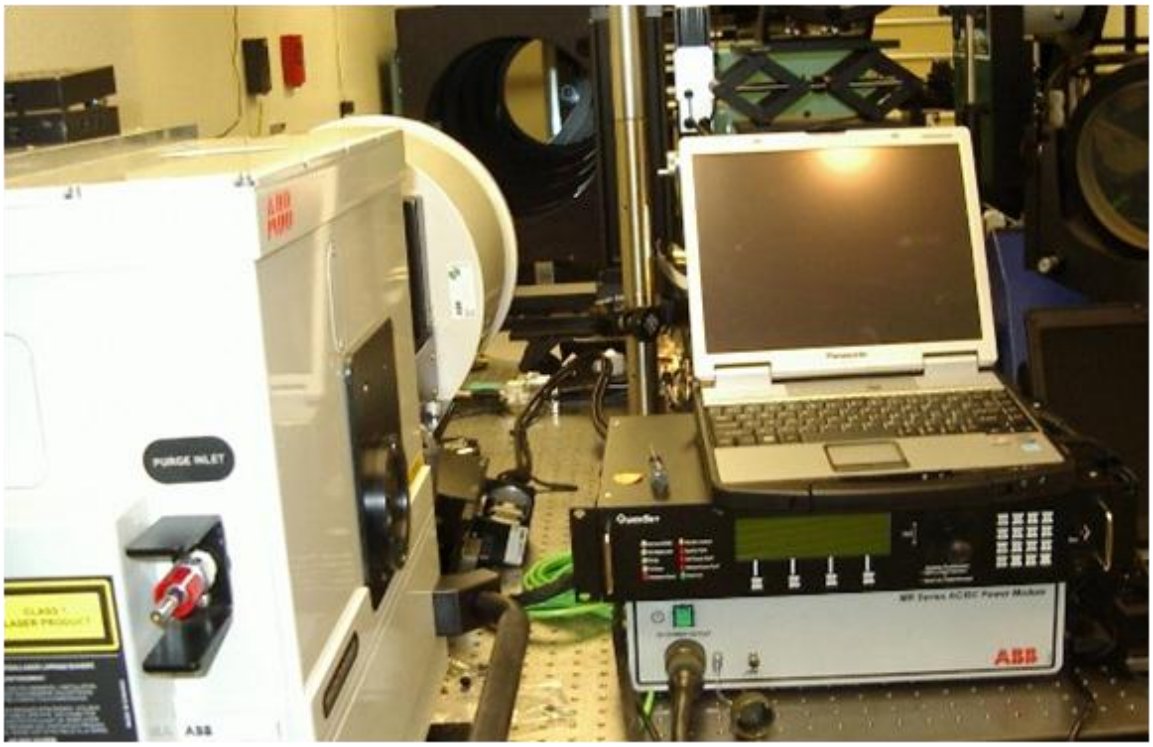

Figure 70 FTIR with narrow telescope aligned with collimator.

In order to evaluate the losses of the telescope, the calibrated scene radiance using the two different calibration techniques were compared. The theoretical spectral radiance for the 750ºC blackbody along with the measurements taken with and without the narrow angle telescope can be seen below in Figure 71. The measured radiance curve (Using Collimated Calibration) using the calibration files collected with the collimator (without telescope) can be seen to line up very well with theoretical blackbody radiance. The radiance curve (Using at Aperture Calibration) for the scene using the calibration files with the source input at the telescope aperture can be seen to have a significant reduction in signal. The final curve is the calculated fractional reduction in signal between the two calibration techniques. The vertical scale can be used for this curve as well, but is in percent instead. When looking at this curve, a significant amount of apparent noise is observed, most notably between 5.5 and 7.5 micron. The change in signal is not actually noise, but rather a change in signal due to atmospheric path absorption differences. Both CO_2 and H_20 in the atmosphere introduce a significant amount of absorption and re-emission in both the short 0.25 meter path with the source at-aperture, and the 7 meter path with the collimator in between the source and instrument. For the purposes of this calibration the atmospheric absorption regions will be ignored. This calculation accounts for not only the losses associated with the telescope obscuration and reflection, but also any reflection losses associated with the collimator. Separating the losses from the telescope and the losses from the collimator is a difficult measurement, but repeating the same measurements with the medium telescope which is not obscured can provide some additional information.

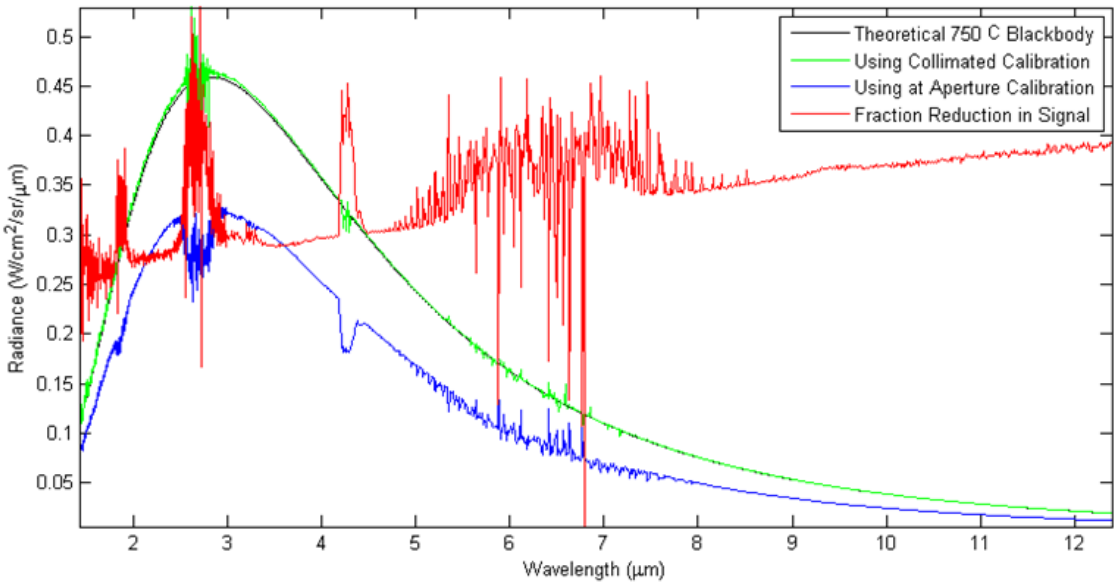

Figure 71 Narrow telescope calibration.

The same calibration technique was used with the medium angle telescope, the measurements can be seen below in Figure 72. The medium telescope shows a much smaller reduction in signal primarily due to the lack of an obscuration in the telescope.

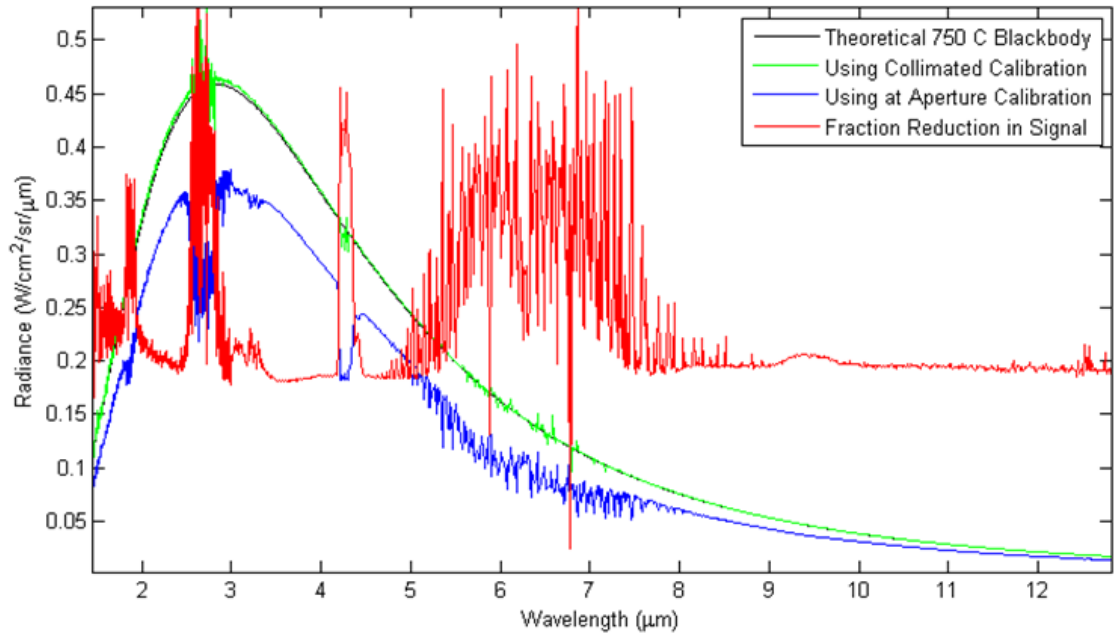

Figure 72 Medium (unobscured) telescope calibration.

To estimate the losses associated with the two telescopes, a comparison of the reduction in signal was completed by neglecting the atmospheric absorption regions. A straight line approximation was made for the losses associated with both telescopes as seen as dashed lines in Figure 73. The medium telescope with the collimator displays a spectrally flat loss with an average of

approximately 17.5%, and the narrow telescope and collimator setup displays a stronger spectral dependance with a minimum loss of approximately 26%.

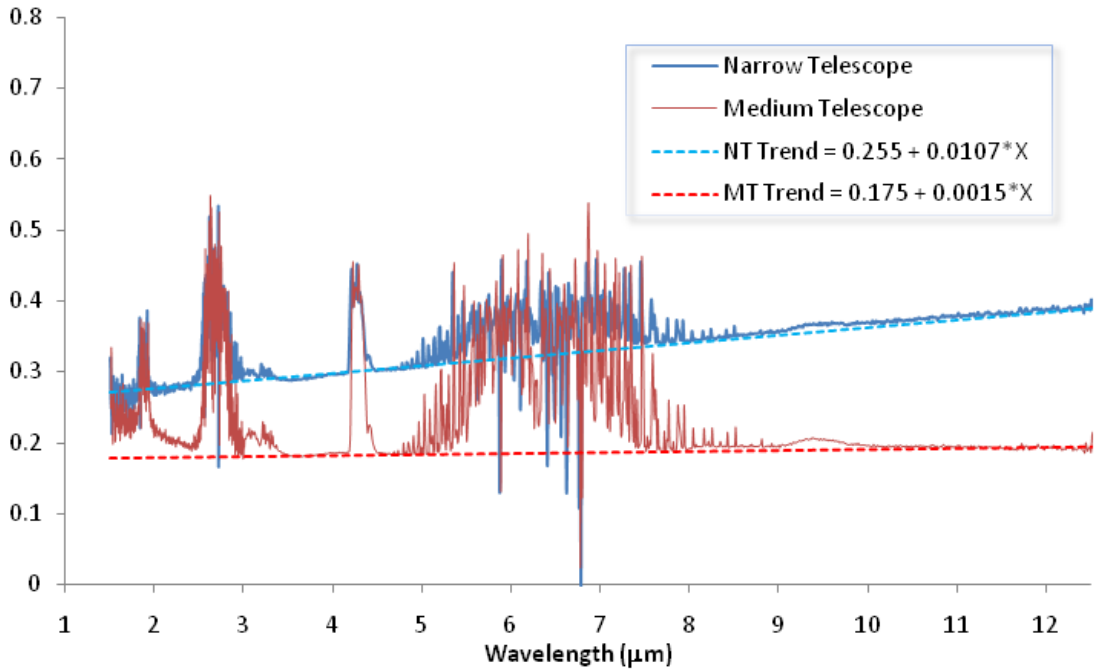

Figure 73 Comparison of narrow and medium angle telescope losses.

As previously stated, the above reductions in signals also include reflection losses associated with the collimator in the setup. Using the spectrally flat medium telescope loss of 17.5% is more appropriate because there is no loss due to obscuration. There are 4 reflection losses associated with the measurement, two reflections within the telescope off both the primary and secondary mirrors, and two associated with the collimator. Assuming all surfaces have approximately the same reflection loss and yields a total transmission of 0.825, each surface is estimated as $0.825^{0.25}$ or 95.3% which is typical for protected silver in the LWIR. This indicates that the medium telescope has an approximate loss of signal of $1-0.953^2$ or 9.17%. This would imply that any measurements made with the medium telescope if calibrated with the radiometric reference at the aperture should be increased by up to 10% (1/1-.0917).

The narrow telescope has not only the reflection losses off of two mirrors, but also a loss due to the obscuration of the secondary mirror. The obscuration and associated spiders to support the mirror obscure approximately 12% of the primary mirror further reducing the signal. This indicates that the narrow telescope has an approximate average loss of signal of 21%. Therefore, any measurements made with the narrow FOV telescope if calibrated with the radiometric reference at the aperture should be increased by up to 26.5% (1/1-.21). These calibration measurements are not being used to correct the hyperspectral data collected by the FTIR but rather provide a maximum error bar on the measurements taken in the field. In order to produce a calibration that could be used to correct the data, a more involved test setup would need to be designed such that the coupling losses associated with the large collimator and the telescope

could be accurately separated. Detailed modeling of the test setup should also be completed to better understand where the losses in the system are being introduced.

The calibration routine that was performed demonstrates that the maximum error associated with the FTIR field measurements taken with the narrow telescope is -21%.

Instrument Setup

The Sandia remote sensing group fielded all of the above described instrumentation in a data acquisition trailer shown in Figure 74. The trailer and all of the FTIR instrumentation were located ~30° North of the East spoke and at a range of ~1100 meters from the center of the pool fire, shown in Figure 75. The trailer and the LNG test pool were at approximately at the same elevation and the measurements were taken through a nearly horizontal path.

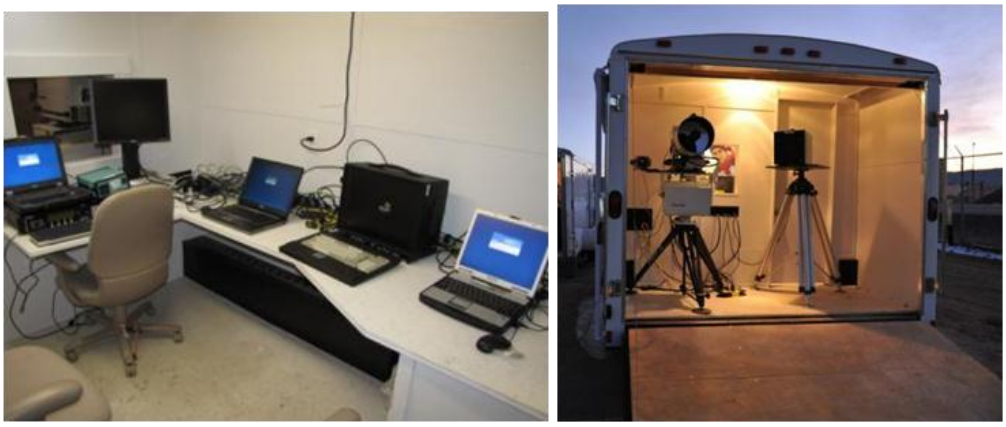

Figure 74 Remote instrumentation trailer setup.

Figure 75 LNG pool fire and FTIR measurement locations.

4.5.13 Meteorology

Meteorological data (wind direction and velocity, temperature, relative humidity and barometric pressure) were measured and recorded with near-field instruments fielded by the Fire and Aerosol Department and with instruments fielded by the Meteorological Monitoring Program at Sandia.

The Large Scale LNG pool fires required meteorological support to assist with minimizing potential unanticipated environmental effects, and identifying optimal burn conditions. Operational support for the LNG tests included the collection, analysis, and forecasting of meteorological data, ambient weather conditions, and weather criteria prior, during, and after the fire. The Environmental Programs and Assurance Department provided data acquisition and collection of near field meteorological information and weather forecasts to support the tests. The activities included:

- Prognostic Meteorological Forecasts (various forecasts windows)
- Near field measurements of meteorological conditions (LNG 30 meter tower and SODAR). See Figure 76 for the layout of the field instruments.

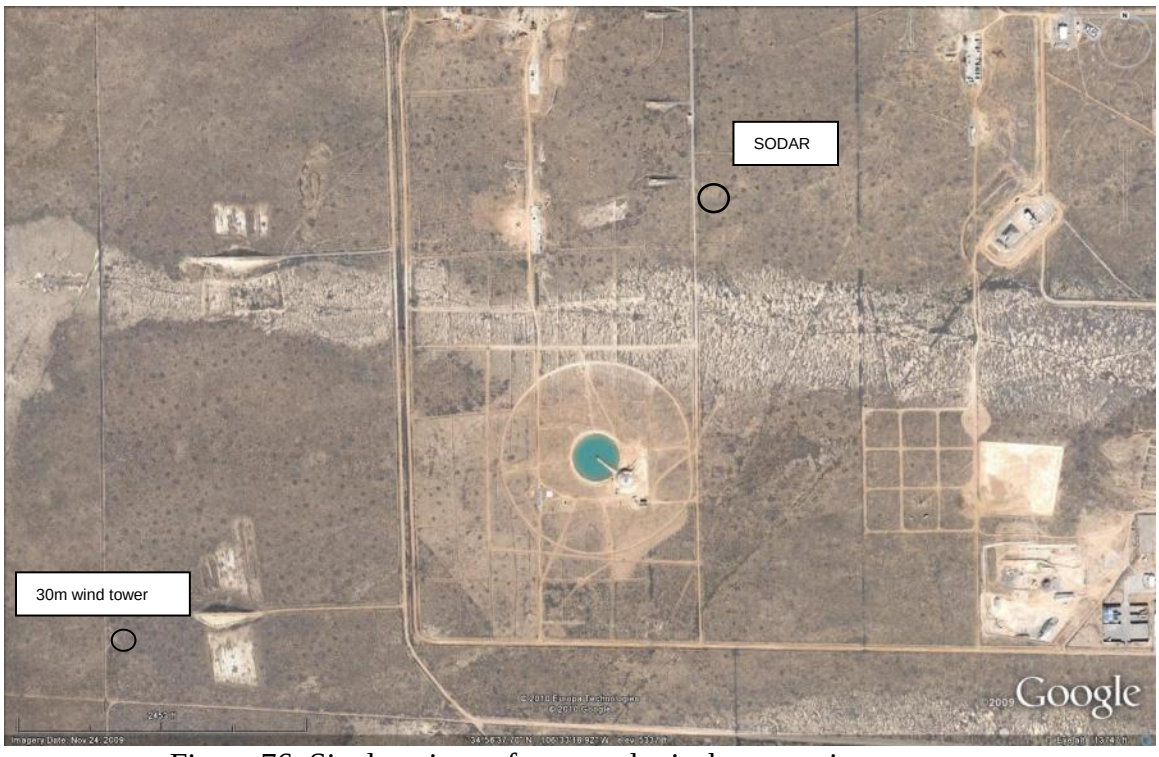

Figure 76 Site locations of meteorological support instruments.

SODAR Data Approximate Location: 34 58’ 52.62 “N 106 33’ 6.24” W

The SODAR operating frequency was 4504 Hz and the maximum height setting for this support was a nominal 200 meters. During neutral atmospheric conditions and periods when the relative humidity is below 20%, the maximum height for which valid data can be acquired is lower than

160 meters. For this support the SODAR transmitted a pulse every 1.7 seconds along each beam axis, resulting in one data point every 5 seconds. The system was operated to collect and average information at 5 minute intervals during the morning of the burn. A five minute interval is the shortest interval that produces high quality data with good statistical representation.

LNG Tower Data Approximate Location: 34 58' 16.48 "N 106 34' 6.54" W

The LNG tower was instrumented to measure temperature, relative humidity, wind, and atmospheric pressure. Wind and temperature was available at both the 10 meter and 29.3 meter levels. The tower was instrumented with the same type of instruments that are used in the CAN Meteorological Tower Network at SNL/NM. The LNG tower was operated to sample atmospheric variables once a second and record the information in 5 minute averaging intervals the morning of the LNG test.

Near Pool Wind Measurements on the North and East Wind Towers (~210 m from pool centerline)

Wind speed and direction was measured at 2 m, 5 m, and 10 m heights on the North tower and at 10 m on the East tower using YOUNG 81000 Ultrasonic Anemometers. Wind speed accuracy: ±1% rms ±0.05 m/s (0 to 30 m/s). Wind direction resolution: 0.1 degree, accuracy: ±2° (1 to 30 m/s).

Barometric Pressure on the East Wind Tower

Barometric pressure was measured using a Setra Model 278 Barometric Pressure Sensor (or equivalent). The accuracy of the Model 278 is specified over the full temperature range of -40º to +60ºC (-40º to +140ºF), rather than as a percent of full scale, with accuracies to within ±0.3 kPa/Mb of the Full Scale pressure range (500-1100 Mb).

Relative Humidity on the East Wind Tower

Relative humidity was measured using a CS HMP45C Temperature and RH probe (or equivalent) with integral radiation shield. Measurement Range: 0.8 to 100% RH, non-condensing, -39.2° to +60°C. RH Accuracy at 20°C: against factory reference: ±1% RH. Temperature Dependence: ±0.05% RH/°C. Temperature accuracy: ±0.5º

4.5.14 Flame Temperature

An insulated stainless steel pole was attached to the side of the diffuser upon which nine 1/16th inch diameter MIMS (mineral-insulated, metal-sheathed (inconel)) type-K thermocouples (TCs) and 2 DFTs were attached. The TCs were located at 0.2 m, 0.7 m, 1.3 m, 1.9 m, 2.5 m, 3.1 m, 3.7 m, 4.3 m, and 4.9 m measured from the top of the diffuser. Note the top of the diffuser is 1.8 m above the water surface. The two DFTs were located near the 2.5 m and 4.9 m heights with sensing surfaces in a vertical orientation.

4.5.15 Water Temperature

The temperature of the pool water (approximately 2 m (79 inch) depth) was measured using 1/16th inch diameter MIMS type-K thermocouples. Three TCs were attached to each of the 12 DFT stands; one at 6 inches below the water surface (TC3), one at approximately water midline at about 40 inches from the pool bottom (TC4), and one at about 6 inches above the pool bottom (TC5).

4.5.16 LNG Liquid / Gas / Reservoir Wall Temperature

The temperature of the LNG was measured using 1/16th inch diameter type-T MIMS thermocouples. In LNG Test 1, the LNG liquid or reservoir gas temperatures were measured using nine TCs located at 0.8 m, 1.6 m, 2.4 m, 3.2 m, 4.0 m, 4.8 m, 5.2 m, 5.6 m, and 6.1 m above the reservoir floor. Two TCs were attached to the concrete and the A-frame mounting plate at the reservoir floor.

Additional TCs were added during the reservoir modifications prior to LNG Test 2. TCs were added at 1 in, 6, in, 12 in, and 18 in above the floor to monitor liquid depth in the discharge plug well. Two TCs were added for monitoring gas temperature above the suspended ceiling, at 7.0 m and 7.9 m above the reservoir floor.

Additional structure temperature monitoring was desired. TCs were embedded ~3/4 inches in the reservoir wall shotcrete cover, along two paths (one path directly in line under a spray nozzle and one path between spray nozzles). The TC were located at slant distances of 5 ft, 10 ft, 20 ft, 30 ft, and 40 ft measured from the reservoir floor. This translates to vertical heights of 0.3 m, 0.9 m, 2.3 m, 3.7 m, and 4.8 m from the reservoir floor. One additional TC was attached to the aluminum skin on the inside surface of the reservoir roof.

4.5.17 Reservoir Gas Monitoring

Oxygen gas concentrations in the reservoir were measured (Mil-Ram Tox-Array 2100) for oxygen (0-25%). In LNG Test 1, an LEL monitor (Mil-Ram Tox-Array 2100) was used to measure gas flammability inside the reservoir. The concentration of methane inside the reservoir was expressed as percentage LEL, with 0-100% LEL corresponding to 0-5% methane (note that the LEL reading flat-lined at 100% when the methane concentration exceeded 5%. A vacuum pump and valve arrangement allowed switching between two sample points, one low point near the floor (that was disabled when the reservoir was being filled) and one high point near the roof. For LNG Test 2, the LEL instrument was replaced with an instrument (Net Safety Millennium Infrared Combustible Gas Detector) to directly measure methane concentration (0-100% by volume). The low sample point was relocated to sample gases directly under the suspended ceiling, close to the reservoir wall.

For both tests, the discharge pipes were sampled for gas flammability expressed as percentage LEL (0-100%) and oxygen (0-25%) concentrations, each with dedicated systems (Mil-Ram Tox-Array 2100) that included separate instruments with integral vacuum pumps.

4.6 Reservoir Volume and LNG Discharge Flow Rate

In order to predict the discharge rate for each test, an accurate measurement of the as-built volume as a function of the vertical height was required. Figure 77 compares the LNG reservoir cavity design (height as a function of volume) to that obtained by interpolation of a set of 2305 laser measurements of the as-built cavity.

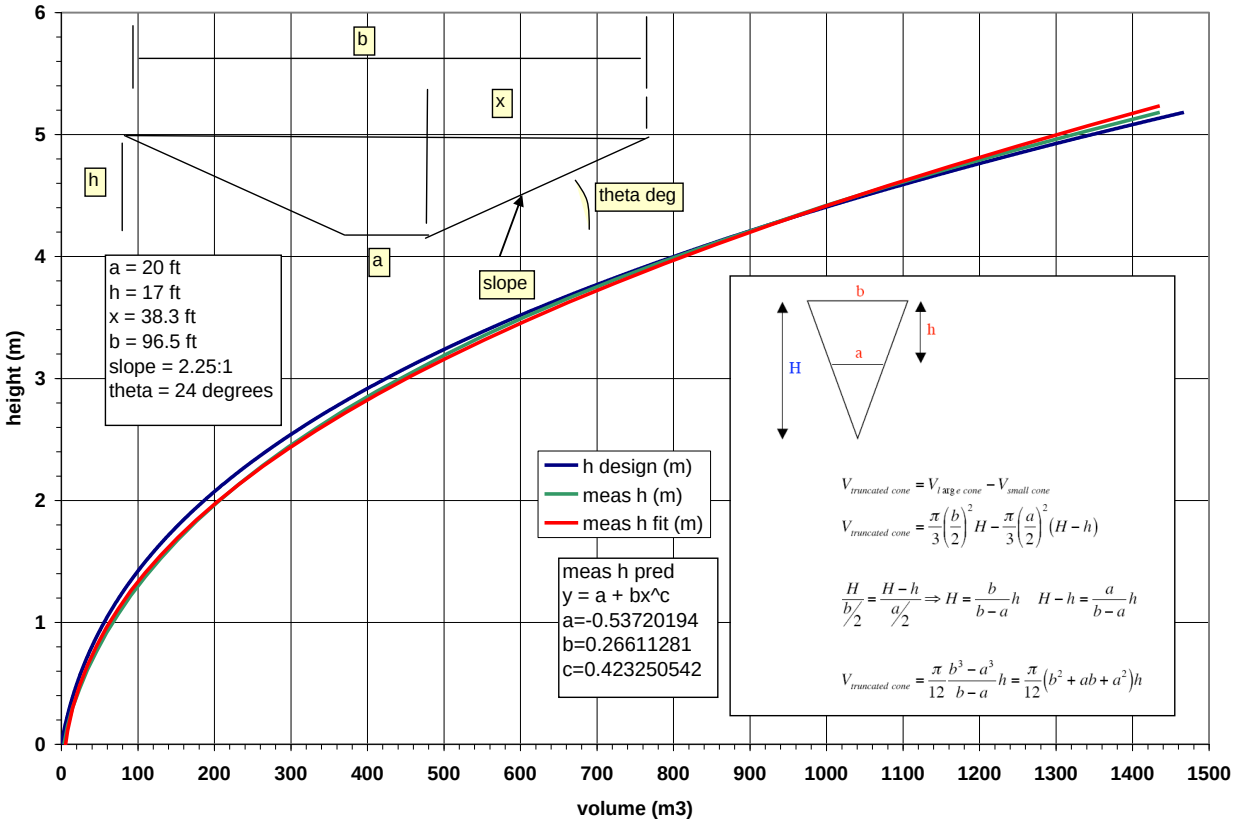

Figure 77 Reservoir design: height vs. volume compared to as-built.

Figure 78 shows the solid model of the cavity based on the laser measurements and the curve (drawn by fitting the data with regression analysis) for the reservoir liquid volume as a function of liquid height. The designed liquid volume of 1172 m^3 is achieved when the liquid height reaches ~4.75 m.

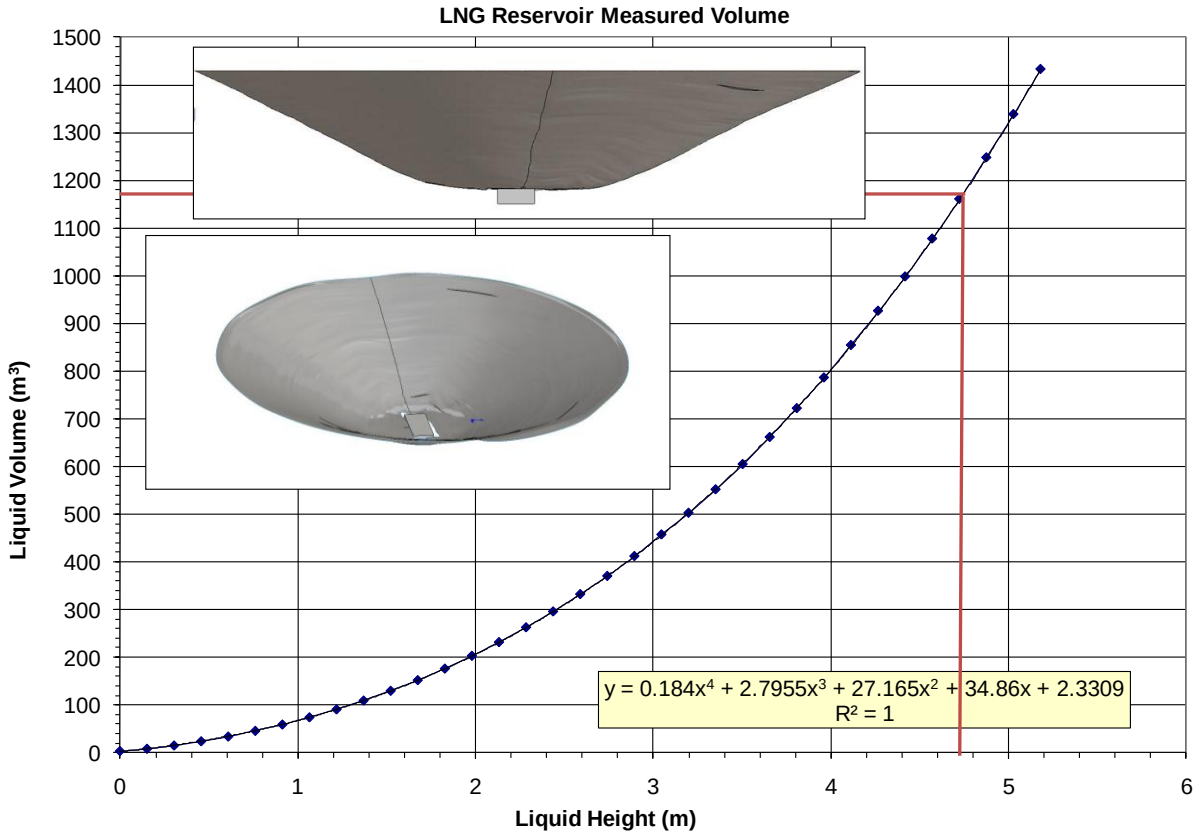

Figure 78 Reservoir volume as a function of vertical liquid height.

With the as-built volume vs. liquid height data, the best estimate for the gravity-driven flow rate from the reservoir was revisited. Determination of efflux through a hole in the side of a reservoir is a classic problem solved with the Bernoulli Equation. Use of Torricelli's Theorem, which assumes pressure at the reservoir liquid surface and at the discharge point are equal, provides the velocity of the discharge, $v = (2gh)^{1/2}$, where h is the height of the liquid head.

A Fortran program was written to study and identify parameter variation for each test to achieve the required LNG fire diameter. The inputs to the code are the estimated LNG burn rate, the desired pool diameter and spill duration, reservoir dimensions to include liquid head height at the reservoir outlet, LNG density, and pipe flow loss coefficients. Single phase liquid flow was assumed.

The velocity of the liquid draining out of the reservoir is based on the time-dependent height of the liquid, computed in an iterative loop. For example, Figure 79 provides the reservoir liquid height, the total volume discharged, and the flow rates as a function of time for the 100 m design spill. Figure 80 shows the liquid height versus time for the three design spills. The design calculations predict LNG spills with duration of approximately 5 minutes and pool fires with diameters of approximately 33 m, 70 m, and 101 m can be achieved. This is based on the key assumption that the burn rate is 0.212 kg/m^{2}s. A higher burn rate would yield smaller diameter fires.

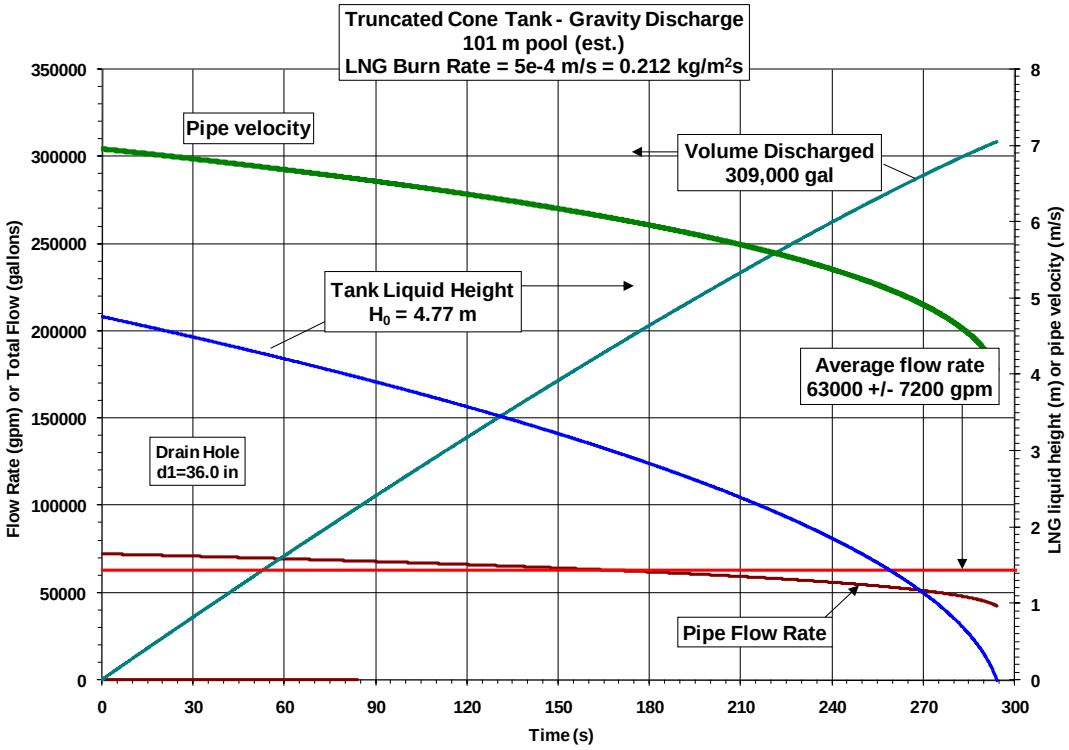

Figure 79 Pre-test predictions of reservoir flow parameters to achieve a 100 m diameter pool.

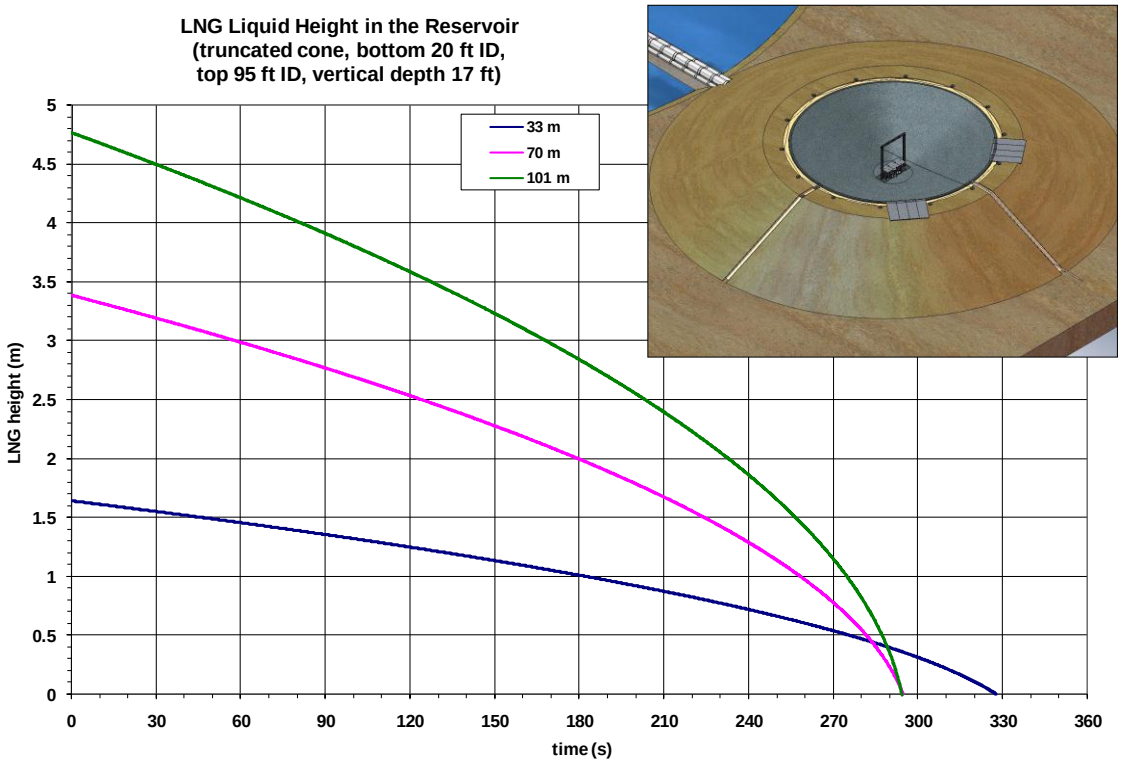

Figure 80 Pre-test predictions of reservoir liquid height vs. time for the three spills.

4.7 LNG Procurement

The large-scale LNG spill tests were performed with liquid methane (>99.5%) as a surrogate for Liquid Natural Gas (LNG). The purpose of using this grade was two-fold; 1) minimize the potential for explosive rapid phase transitions (RPTs) that could damage or destroy the experimental setup and 2) minimize the parameter variations to reduce uncertainty in the analysis of the test data and for the use of present and future model development and validation. It is recognized that LNG can have a wide range in composition (depending on the source), from almost pure methane to mixtures composed primarily of methane (typically, at least 90 percent), but may also contain ethane, propane and heavier hydrocarbons and small quantities of nitrogen, oxygen, carbon dioxide, sulfur compounds, and water. However, previous historic experiments performed with typical LNG have shown that the methane burns off first, with little participation by the heavier hydrocarbons until late in the test.

SNL submitted request for quotes for the purchase of the LNG product in accordance with Sandia procurement policies. On October 1, 2008, Sandia awarded the contract (PO#860315) to Clean Energy Corporation (4955 Peoria St. Denver, CO, 80239). Clean Energy would deliver ~590,000 gallons of liquid methane (>99.5% purity) for an estimated price of ~$1,450,000.00. The actual price per delivery was based on a fixed delivery cost ($1.29/gal) plus the published index (Houston Ship Channel or SoCal Border Commodity) for the day of order.

Clean Energy would delivery product to SNL within three days of notice. The LNG was delivered in 10,000 gallon contractor furnished trailers. The following estimates were assumed for delivery for the three design tests. A minimum of six trailer loads per day was required. For the 35 m diameter test, Clean Energy would deliver at least 60,000 gallons (six trailers) in 1 day. For the 70 m diameter test, Clean Energy would deliver at least 170,000 gallons (seventeen trailers) in 3 days. For the 100 m diameter test, Clean Energy would deliver at least 340,000 gallons (thirty-four trailers) in 7 days. Only one trailer offload at a time was allowed for safety and security purposes (and only during daylight hours). Based on a trailer nominal 300 gpm discharge rate, the offload and turnaround time was expected to be about one hour. Fuel composition data sheets would be supplied with each fuel delivery.

4.8 Peer Review Group

The technical design review was performed by a peer review group (PRG) consisting of members from both industry and academia. This voluntary advisory panel was formulated to consist of a small number of experts in the field of LNG and other hydrocarbon pool fire tests. Members were chosen specifically for their expertise in the performance and measurements of such testing. The role of the PRG was to provide advice to SNL with regards to the Sandia/DOE Large Scale LNG pool fire tests. The scope of the PRG was to review the test plan, witness some of the tests, and also review the final report. All comments from the PRG were considered and formal responses prepared and documented. The members of the PRG with a brief description of their areas of expertise are provided below.

Dr. Jonathan S. Puttock - Senior Consultant, HSE Consultancy, Shell Global Solutions. Ph.D. Cambridge University. Involved in planning, execution and analysis of the Maplin Sands LNG experiments and member of the research center which performed the Montoir LNG experiments. Leads the Major Hazards Management research and development team (sponsored by Shell's LNG business) that has produced a wide range of tools for the prediction of gas hazards, including release rate, evaporation, dispersion, jet fires, pool fires and explosions, as well as risk integration.

Dr. John L. de Ris - Principle Research Scientist - Assistant Vice President FM Global. Ph.D. Harvard University. Physical and theoretical modeling of fires, flame heat transfer, fire spread, wall burning, pool fires, laminar and turbulent combustion, flame radiation, as well as soot formation and oxidation.

Dr. Richard C. Corlett - Professor Emeritus - University of Washington. Ph.D. Harvard University. Expert in heat transfer, thermodynamics, fluid dynamics. Research focused on fire flow and thermal modeling.

Dr. Carlos Fernandez-Pello - Professor - University of California, Berkeley. Ph.D. University of California, San Diego. Specializing in combustion, heat and mass transfer, and thermodynamics. Research focused on ignition, flame spread, and explosive burning of droplets and boiling of liquid hydrocarbon fuel pools.

4.9 Safety Analyses, Permits, Reviews, and Approvals

The key enabling concept for success was that an operational NFPA59A facility was not required, just a safe, low-fabrication-cost experimental apparatus. The creative solution necessitated significant operational safety considerations including unprecedented cooperation between numerous Sandia organizations, the DOE Sandia Site Office, and Kirtland AFB agencies (including flight-operations and emergency fire-response).

The use of such novel methods required significant, first-principals-based, environment, safety, and health analysis to provide confidence that the unique design and operations were safe. Safety during testing was primarily ensured through limited access and extended hazard zones to 900 m surrounding the pool. Safety issues examined included reservoir integrity, thermal (cryogenic to fire fluxes), asphyxiation, explosion, drowning, and aviation operations (helicopter and airport traffic). Advanced transient, three-dimensional transport simulations were used to evaluate both the thermal performance of the reservoir & components, the transport of gaseous boil-off during the cool-down process, and design of the diffuser in the middle of the pool used to translate the linear momentum of the LNG in the pipes to a radially spreading pool.

4.9.1 Hazard Analyses

The identified hazards for the Large-Scale LNG Spill Test were evaluated using a "what-if" analysis technique. The purpose of a what-if analysis is to identify hazards, hazardous situations,

or specific hazardous events that could produce an undesirable consequence. The what-if analysis technique is described in detail in Guidelines for Hazard Evaluation Procedures [AIChE 1992].

Potential hazards include asphyxiation from the filling/stored LNG and thermal hazards from the burning of LNG. Potential hazards from off-normal conditions are a deflagration/fire in the reservoir (overpressure/fragmentation and subsequent fire), deflagration/fire of an unignited, dispersed plume (overpressure and subsequent fire), and asphyxiation from inadvertent release of an unignited LNG vapor plume. These events (discussed below in greater detail) were evaluated further using advanced analyses to quantify the potential impacts to potential receptors and to identify safety controls.

Where necessary, a computational fluid dynamics (CFD) model was used to complete the advanced analysis; the CFD model has been validated against results of previous unignited LNG experimental releases. The final advanced analysis determined that a deflagration event with subsequent overpressure and fragmentation is credible but that a detonation event in either the pipe or reservoir is not credible.

The 900 m test control area was based on the unignited plume subsequently igniting at the distance to the lower flammability limit (LFL) and the 450 m pretest control area is based on the thermal impact from the LNG fire in the test pool as well as from a deflagration in the reservoir resulting in an overpressure and fragmenting of the reservoir cover. The 250 m firebreak area is based on the heat flux distance from the pool fire.

Thermal Impact Analysis – Ignited LNG Normal Test Operations

During testing operations, the LNG is gravity feed from the reservoir to the center of the water pool area. The LNG vapor is ignited at the water pool area discharge point by an ignition source. The heat impact from the ignited LNG was estimated using techniques identified in large hydrocarbon pool fire literature. As provided in literature, a significant thermal impact is defined as 5 kW/m^2. The worst case release for thermal impact was defined by the bounding 310,000-gal release of LNG. The worst case impact was estimated to be 5 kW/m^2 at 450 m from the LNG discharge point at the center of the water pool area [Luketa, 2008a]. The thermal impact from the LNG fire during these normal test operations was considered acceptable at the 450 m control area. In addition, a separate analysis calculated the thermal hazard distance and potential consequences from a fireball from LNG reservoir [Luketa, 2008b].

Thermal Impact Analysis – Unignited, Dispersed, and Subsequently Ignited Plume

During testing operations, the LNG is gravity fed from the reservoir to the center of the water pool area. The LNG vapor is ignited by an ignition source. If the LNG is not ignited, the LNG will vaporize and form an unignited plume that may move away from the water pool area.

Results obtained from the CFD model indicated that an unignited plume of LNG vapor exists out to a 700 m distance before dropping below the LFL for methane (5%). If the plume crosses an ignition source, the plume will ignite/deflagrate and a flash fire would result. The fire would

quickly burn back to the LNG spill, consuming the vapors. The fire ignited at the 700 meter distance could produce a heat flux of 5 kW/m^2 at 200 m away (extending the hazard zone from 700 m to 900 m) [Luketa, 2008a]. This would significantly impact any workers located within the 900 m control area but pose little hazard beyond the control area. The hazards analysis credited access control with keeping workers, collocated workers, and public out of the 900 m control area. Because workers are not present in the 900 m control area, no impact to the workers is expected. The thermal impact from potential vapor cloud deflagration/fire was considered acceptable outside the 900 m control area.

Asphyxiant/Toxicological Analysis

LNG vapors in sufficient concentration can lower the atmospheric oxygen level to a value where asphyxiation is a concern. Because the reservoir is at atmospheric pressure and vented, vaporization of LNG will occur. An inadvertent spill of LNG during filling would also result in vaporization. In addition, if the LNG is not ignited during the normal release of LNG and a vapor cloud forms, the vapor plume may move away from the water pool area. Small, localized spills during filling and vaporization of stored LNG are only a concern for the immediate worker. Access control limits the number of workers within the immediate area during filling operations. In addition, the area is monitored for oxygen deficiency in the filling area with audible/visual alarms to indicate an inadvertent release of LNG vapor above levels of concern. In general, a small open air release of LNG vapor was not expected to pose a significant impact to the immediate worker.

During the fire experiments, the LNG is gravity fed from the reservoir onto the water surface at the center of the water pool area. The LNG is ignited by an ignition source. If the LNG is not ignited, the LNG could vaporize and form an unignited plume that may move away from the water pool area. A worst case asphyxiant/toxicological impact is represented by 100% release of the reservoir contents with no ignition. The release from the reservoir was modeled with a CFD model to the Emergency Response Planning Guideline (ERPG) 3 toxicological endpoint (50,000 ppm). The release scenario reflects 100% of the LNG from the reservoir flowing into the water pool area with subsequent boiling off of the natural gas vapor and no ignition of the vapor. The CFD results showed that the gas concentration did not exceed the endpoint outside the 900 m control area.

Overpressure/Fragmentation Analysis

During filling, the boil-off of the LNG quickly places the reservoir atmosphere above the upper flammability limit (UFL), with the atmosphere reaching 100% methane as the boil-off displaces the nitrogen purge gas. The reservoir is continuously vented to prevent overpressure.

However, when the LNG is released from the reservoir, air is drawn into the reservoir to replace the volume of LNG released into the test pool. The quantity of air drawn into the reservoir is not sufficient to bring the entire reservoir below the UFL; however, small pockets of methane/air concentrations between the LFL and UFL may exist for a short time. Immediately following the release of the LNG from reservoir, these small pockets of flammable concentrations will dissipate rapidly as the methane and air continue to mix. The flammable mixture is not detonable

but could be ignited resulting in a deflagration (i.e., burning) of the methane gas. Methane burns with a slow, subsonic flame velocity and will not detonate without confinement and/or added equivalent explosive energy.

When a low-speed deflagration occurs within a closed vessel or structure, pressure effects can produce damage due to expansion of gases resulting in atmospheric overpressure. The net result is that the volume of the vessel or structure needs to contain, expand, vent, or fail to accommodate the hot combustion gases. The reservoir is not designed to relieve the pressure associated with the potential deflagration of the LNG vapor and the cover was expected to fail in this event.

A deflagration event in the reservoir was evaluated to assess overpressure and fragmentation hazards. The event assumed that there was an ignition source as well as air/methane concentrations between UFL and LFL. Precautions were taken in the operations and experimental facility design to minimize the potential for the event. By design, no ignition or electrical sources were located in the reservoir and no ignition sources are located within the immediate area (i.e., 15 ft). Nitrogen gas was used to inert the atmosphere within the reservoir prior to filling with LNG and following the LNG release to the water pool area.

A worse-case event was represented by a post-drainage, emptied reservoir with LNG vapor at the upper flammability limit (UFL). An overpressure was calculated based on the pressure from the deflagration of LNG vapor in the reservoir. The ground distance from the center point to an acceptable overpressure endpoint (i.e., less than 0.25 psig) was calculated to be within 770 ft [Mathews 2008].

If an overpressure from a deflagration occurred, the overpressure would be large enough that the structure of the reservoir cover would fail. Overpressures from deflagrations have a limited potential for fragmentation of materials and do not typically result in a high number of fragments. A fragmentation analysis was completed to determine potential impacts to the worker and/or collocated worker. Impacts from the reservoir deflagration with subsequent overpressure resulted in the fragmentation of the reservoir cover with a fragment throw distance of 520 ft [Mathews 2008]. This event also bounded a deflagration within the discharge piping.

Detonation Evaluation

A detonation event in the spill piping or reservoir was evaluated as part of the PrHA advanced analysis. A detonation event in either the spill piping or reservoir was determined to be noncredible because of the design of the experiment (i.e., reservoir, piping), the extreme difficulty in achieving and sustaining detonations in methane/air mixtures, and the lack of an ignition source with enough energy to propagate a detonation.

One identified mechanism for initiating a detonation is a deflagration-to-detonation transition (DDT) in the discharge pipe. DDT is when a flame front inside a deflagrating fuel/air mixture reaches and exceeds the speed of sound inside a confined chamber (e.g., pipe). In a normal combustion situation, the flame front in a burning fuel/air mixture does not exceed the speed of sound, classifying it as a deflagration. DDT can only occur if conditions exist for flame

acceleration. The first condition is that the mixture be within detonability limits which are narrower than flammability limits. Detonability limits have not been determined for air/methane mixtures because of the extreme resistance to detonation. Generally, flame acceleration (i.e., DDT) will only occur via two specific mechanisms: long length-to-diameter ratio configuration and favorable geometries with repeated obstacles.

In long, narrow combustion chambers with one end open and the other closed, and have gases ignited near the closed end; the gas flow in front of the flame will be accelerated by the pressure rise behind the flame. There are no ignition sources at the closed (reservoir) end of the discharge pipe and acceleration of a flame front is therefore not possible from the closed end. In addition, a DDT in the LNG discharge pipe would require a perfect stoichiometric mixture in nearly the entire length of the discharge pipe. Given that a stoichiometric mixture in the entire length of the pipe is not credible, a DDT was not credible [Melof 2008].

For a detonation to occur in the reservoir, an equivalent explosive charge would be needed [Cooper 2008]. Nowhere on site, including in the discharge pipes and reservoir, was there an equivalent explosive charge present that would initiate a detonation. A DDT in the reservoir was not credible because the geometry of the reservoir is not conducive to a detonation because of the open, unrestricted interior space. There are no repeat obstacles to cause turbulent acceleration, nor is there a long run distance for flame acceleration. Without an acceleration mechanism in the larger reservoir, a DDT is not credible in the reservoir [Melof 2008].

Seismic Stability Analysis

A seismic deformation and stability analysis was also performed. A 2.5 factor of safety (FS) was computed for the slope stability of an earth berm using the method described in the Appendix E of the Slope Stability Engineer Manual published by the US Army Corps of Engineers. It was concluded that the embankment would withstand any level of seismic activity that might reasonably be expected to occur within the Albuquerque area [Jensen, 2008].

4.9.2 Permits and Reviews

Table 17 presents a list the permits and approvals for both the construction and the operation of the experimental activity.

Table 17 Permits, Reviews, and Approvals

Title	Status
NEPA – SNA07-0195 – Large Scale LNG Spill Tests	Complete – DOE Approved for Categorical Exclusion – July 5, 2007
LNG Experiment Industry Review - 19 Industry technical experts on LNG operations	February 21, 2007
Congressional Research Service (CRS) Project Review	November 7, 2007
Biological Survey	Complete – March 5, 2008
Excavation Permit	Complete – March 11, 2008
Fugitive Dust Permit – 10090626-3732	Complete - Issued May 29, 2007
Storm Water Pollution Prevention Plan	Complete - Issued April 24, 2008
PHS - SNL07A00147-001 - Large Scale LNG Tests	Complete – Moderate Hazard Classification
Burn Permits: 07-0064 (40,000 gal) 07-0065 (150,000 gal) 07-0066 (310,000 gal)	Complete - Approved by City of Albuquerque
Aviation Operations - requests for aviation support and aviation safety plans	Complete - Approved by NNSA and FAA, MOA with KAFB 58th/SOW
Water Discharge – City (Albuquerque) and State	Complete - Sanitary sewer discharge for pool water – April 3, 2007
DOE ISMS - IWP1662 - Large Scale LNG Pool Fire Experiments	Complete with Management Operational Review October 30, 2008
Meteorological Support	Complete - On Call
PrHA	Complete – December 11, 2008
Management Self Assessment	Complete – January 5, 2009
PSM Pre-Startup Safety Review	Complete – January 6, 2009

Process Hazard Analysis (PrHA)

Because the quantity of flammable material in these tests exceeds the Occupational Safety and Health Administration (OSHA) Process Safety Management (PSM) rule threshold for flammable materials of 10,000 pounds, this experiment falls under the PSM rule [PSM 29 CFR 1910.119] and a process hazard analysis (PrHA) was required to meet PSM requirements. This experiment was also classified as a Moderate Hazard activity from the SNL Primary Hazard Screening (PHS) for this activity, i.e., PHS Number: SNL07A00147, Large-Scale LNG Tests [PHS SNL 2008]. From the PHS, a Safety Assessment (SA) document was identified as necessary to provide Sandia safety basis documentation for this activity.

In order to satisfy both of the above safety documentation requirements (i.e., a PrHA for PSM and an SA for Sandia safety basis) the PrHA document was developed by Sandia Organization 1532 that meets the requirements for an SA safety basis document, as specified in MN471017, Safety Basis Manual [SBM SNL 2008]. The PrHA is a graded-approach safety basis document that addresses the requirements of the SB Manual and OSHA PSM.

The purpose of the PrHA is to assess the potential hazards to provide a basis for the protection of workers, collocated workers, and the public; to provide supporting documentation for the hazard classification of the experiment; and to derive a Safety Envelope based on the credited safety controls from a hazard analysis. The PrHA uses PSM rule recommended hazard identification and hazard evaluation techniques as described by the AIChE Guidelines for Hazard Evaluation Procedures. Following these accepted practices, the PrHA was completed by a team made of interdisciplinary subject matter experts that included experiment, operations, and ES&H support personnel. The scope of the PrHA included the filling of the reservoir, release of LNG from the reservoir to the water pool area, ignition/burning of the LNG vapor, and post-test operations. The PrHA also addressed potential natural phenomena hazards (NPHs) and potential external events that could have an impact on the hazards defined herein.

Management Self Assessment (MSA)

A Management Self Assessment (MSA) was performed the week of December 15, 2008. The MSA reviewed the completion of the line organization documentation, experiment construction, and credited controls implementation (e.g., training, testing, etc.). Readiness for construction and operation included obtaining required permits including NEPA, burn, fugitive dust control, Storm Water Pollution Prevention Plans, excavation, biological surveys, etc.

PSM Pre-Startup Safety Review (PSR)

A PSR must be conducted when the flammable material amount exceeds 10,000 pounds in a process, in accordance with 29 CFR 1910.119, Process Safety Management (PSM) [PSM 29 CFR 1910.119]. DOE-HDBK-1101-2004, Process Safety Management for Highly Hazardous Chemicals, provides the following regarding the focus of a PSR. The purpose of a PSR is to ensure the following: 1) New or modified facilities and equipment are built and installed in accordance with design requirements, 2) All process procedures and related process operator training are adequate and completed prior to the introduction of hazardous materials into the process, 3) Adequate safety reviews are conducted, and 4) All PrHA safety recommendations are complete prior to startup.

A site-specific Pre-Startup Safety Review was performed on January 6, 2009 using internal SNL safety basis (SB) and external independent subject matter experts followed by a recommendation to DOE to proceed.

Congressional Research Service (CRS) Review

A project review was performed on December 11, 2007 by a specialist at the Congressional Research Service (CRS), the non-partisan policy research and analysis agency of the U.S.

Congress, where his areas of expertise include energy infrastructure development, critical infrastructure protection, and terrorism threat analysis.

4.10 Costs and Schedule

Funding for the LNG pool fire activities was provided by DOE and the USCG. Planning commenced in the summer-fall 2006; a preliminary design was presented to DOE, USCG, CLNG, Industry, and International Participants in February 2007, and test plans finalized and peer-reviewed by May 2008. Construction started in June 2008 and was completed by December 2008. Safety reviews and documentation were completed in January 2009. LNG Test 1 was performed on February 19, 2009 and LNG Test 2 was performed on December 10, 2009.

5 LNG Test 1 – Test Goal

The goal of the test was to achieve a steady-state pool fire with a diameter in the range of 30 to 40 meters. Figure 81 shows the predicted reservoir response designed to achieve a 33 m diameter pool fire with a 330 s duration, assuming single-phase flow from the reservoir to the diffuser and that the LNG burn rate was 0.212 kg/m^{2}s. For this desired pool fire, approximately 138 m^3 (36600 gallons) of LNG was estimated, filling the reservoir to a 1.64 m initial liquid height. An average flow rate of 0.42 m^3/s (6700 gpm) was also estimated.

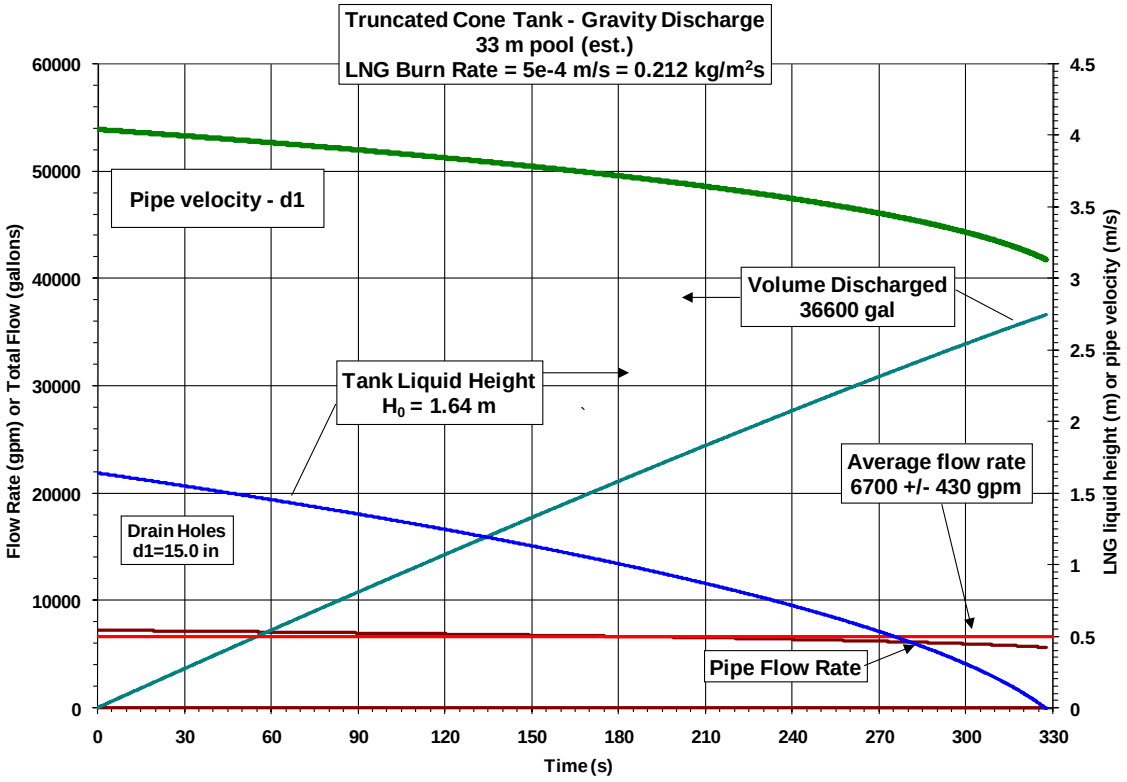

Figure 81 Predicted reservoir response for a 33 m diameter pool fire.

5.1 LNG Test 1 - Preparations

Preparations for the 1st LNG pool fire experiment commenced on Monday, February 16, 2009.

The initial configuration had the nitrogen purge nozzle pointing down and both vent dampers open. The reservoir nitrogen purge valve (see Figure 82) was opened at approximately 11 AM, by approximately 6 PM the reservoir oxygen content was reduced from 20.9% to about 7.5% (both low and high sample points). Approximately 175000 scf of nitrogen was used in the purge process. Note the 2650 gallon (250000 scf) liquid nitrogen trailer has about a 10 hr flow capacity at the maximum discharge rate of about 415 cfm.

Purging of all reservoir discharge pipes (~3 cfm/pipe) also commenced at about 11 AM and continued until the test was completed.

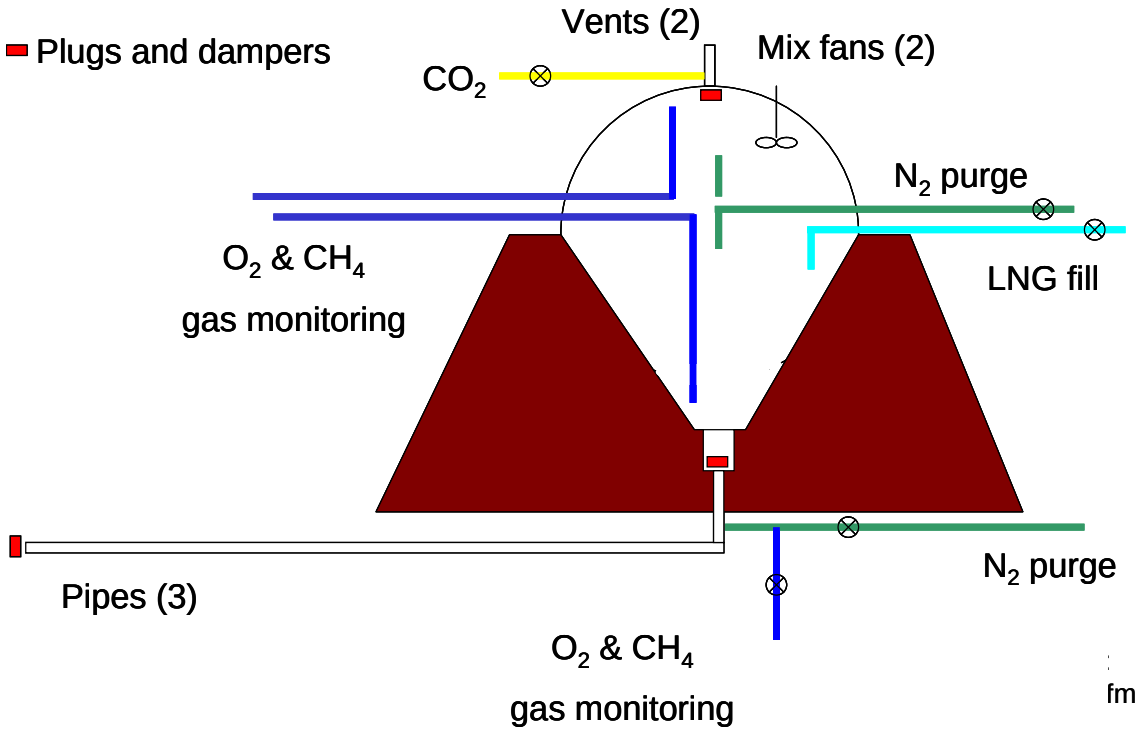

Figure 82 Reservoir systems in LNG Test 1.

Filling the reservoir with LNG (~99.9% liquid methane) commenced the following morning (on Tuesday, February 17). Five trailers (10,000 gallon capacity) were offloaded in approximately five hours, as indicated in Table 18, the reservoir fill log. Reservoir liquid height as measured by the two dip tubes and the mechanical float in the reservoir before and after each fill is also given.

Table 18 Reservoir fill log in LNG Test 1

Test #	**1**			LNG Requirements (gal)			**50000**		Expected height (ft)	**6.2**		
Spill Diameter (m)	**33**			(boiloff)			**10000**		(after boiloff)	**5.5**		
							Prefill			**Postfill**		
Date	Time	Trailer #	Trailer Weight full (lbs)	Trailer Weight empty (lbs)	Trailer Gallons	Total Gallons	Bubbler#1 Prefill Height (ft)	Bubbler#2 Prefill Height (ft)	Float Prefill Height (ft)	Bubbler#1 Postfill Height (ft)	Bubbler#2 Postfill Height (ft)	Float Postfill Height (ft)
2/17/2009	10:37	1	78200	43820	9822	9822	-0.05	-0.05	0.50	1.05	1.05	1.25
2/17/2009	11:45	2	78880	44500	9822	19645	0.89	0.90	1.25	1.90	1.90	2.00
2/17/2009	13:00	3	78580	44140	9840	29484	1.76	1.75	2.25	2.68	2.69	2.92
2/17/2009	14:26	4	78180	45100	9451	38935	2.68	2.69	2.80	3.48	3.48	3.50
2/17/2009	15:26	5	78140	44120	9720	48655	3.45	3.45	3.50	4.04	4.03	4.08
2/19/2009	6:11	6	79400	44100	10085	58740	0.90	1.00	1.40	2.06	2.11	2.25
2/19/2009	7:21	7	79120	43720	10114	68854	2.02	2.05	2.25	3.06	3.10	3.25
The post fill height will not be the same from day to day due to evaporation of the LNG												
Gallons = (trailer weight full - trailer weight empty) * 0.286												

Figure 83 shows the liquid height as measured by the two dip tubes during the fill operation. The reservoir vents were closed between the 3rd and 4th trailer to attempt to reduce the boil-off (winds were 30-40 mph during fill; large vapor plumes were seen at the vents and at the downstream door covers. Closing the reservoir vents caused the reservoir to pressurize slightly due to the boil-off. The vents were left closed until just before the test drain.

Assuming no boil-off, 5 trailers should have yielded about 6.2 ft of liquid head. Assuming a boil-off of 10,000 gallons to cool down the reservoir during the fill operation, the liquid head should have been about 5.5 ft after the fill. Figure 83 shows the actual liquid height was about 4 ft.

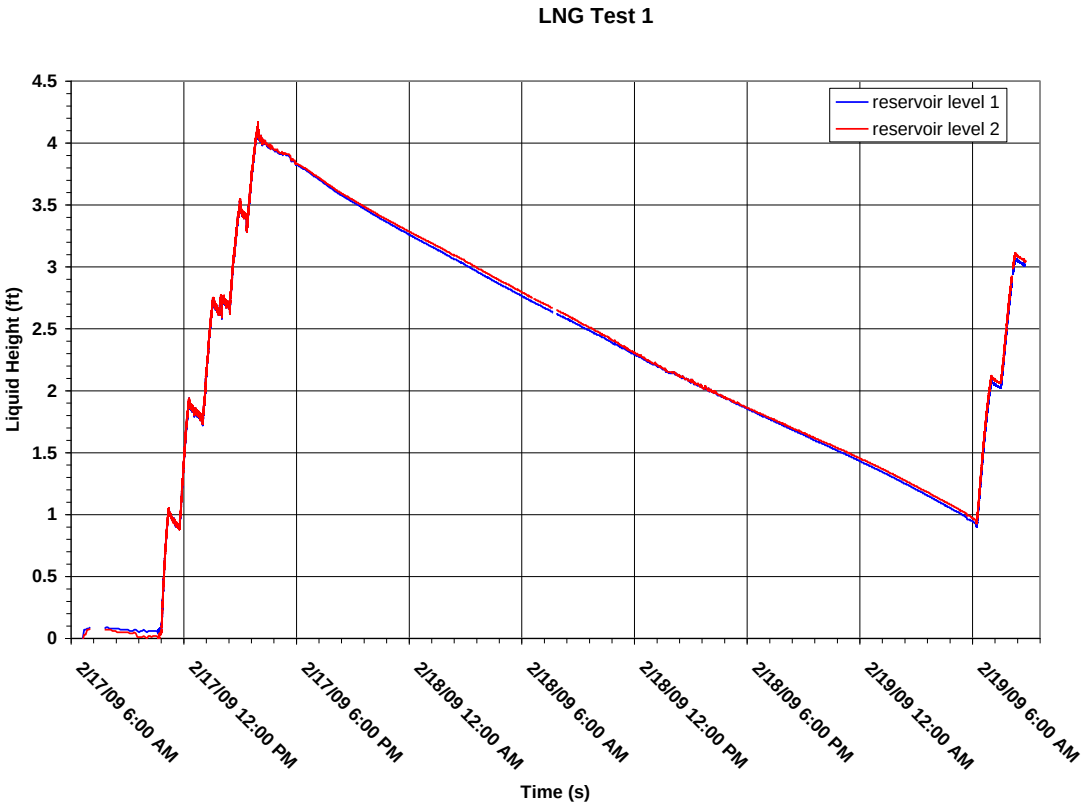

Figure 83 Reservoir liquid level during the fill operation in Test 1.

There was indication that the discharge plugs leaked. Oxygen concentration decreased in one pipe (before that pipe purge was started) when nitrogen was introduced into the reservoir. In addition, methane gas (100% LEL in the 24 and 36 inch, 10% LEL in the 15 inch) was also measured in all pipes the day after LNG was placed in the reservoir.

The aluminum plugs were sealed to the stainless steel flanges using two concentric gaskets (Figure 84). The outer gasket was fabricated using a cryogenic adhesive-backed Kapton tape wrapped around an expanded-TFPE (Teflon core (1/8 inch diameter). The inner gasket was formed using a cryogenic butyl rubber elastomer sealant. Both gaskets (tested separately) had shown no leakage when tested at small scale in a prototypic rig that was immersed in liquid nitrogen.

Figure 84 Formed gaskets on the 36 inch discharge pipe flange in Test 1.

It is believed that the process of purging the pipes lifted the 24 inch and the 36 inch plugs and broke the gasket seals. A late modification to the experiment setup placed steel blockage plates (with small vent holes) at the 24 inch and the 36 inch discharge pipe outlets to prevent back flow of the LNG into those pipes when flowing out of the 15 inch pipe. Those pipes probably pressurized during the pipe purge which broke the gaskets seals. (The nitrogen source for the discharge pipes was regulated to 40 psi; 1 psi was sufficient to lift the largest plug.)

This did not explain the methane in the 15 inch pipe. One possibility is that liquid methane leaked into the dirt berm at the joints in the concrete pipe sections; the pipes are in close proximity and the saturated soil may have allowed methane gas to seep into the 15 inch pipe.

It was not practical to install in the field the spectrometers and the cameras on Tuesday (February 17) due to the high winds; hence a hold was declared and the test was set for Thursday morning (February 19). Based on the meteorological forecast, the test was planned for 8:15 to achieve the best (lowest) wind condition. The reservoir loss rate appeared to be ~16,000 gal/day. Clean Energy was contacted Tuesday evening and they were able to provide two additional trailers for Thursday morning. Reservoir fill operations commenced at daybreak per the operational procedure; however, the fill operation took longer than anticipated due to the trailers arriving with 2-inch discharge hoses (3-inch hoses were needed to meet the test target time) and the test window was missed by one hour. Table 18 and Figure 83 show reservoir levels during the trailer off load. The LNG level in the reservoir just prior to the test was about 3 feet.

Figure 85 gives the reservoir temperatures during the fill operation. Thermocouple (TC) 1 is embedded in the concrete at the top of the well and TC 2 is attached to the steel footer plate for the winch hoist frame. TC 3 is at the 2.6 ft elevation. TC heights are listed on Figure 85. TC 10 is approximately level with the top of the reservoir and TC11 (at 18 ft) is low is the dome space (top of dome is ~31 ft). Note that during off load operations all of the gas temperatures are quite low due to the mixing and boil-off, but the temperature of the gases in the vapor space of the reservoir show highly stratified behavior within a few hours after offloading the LNG.

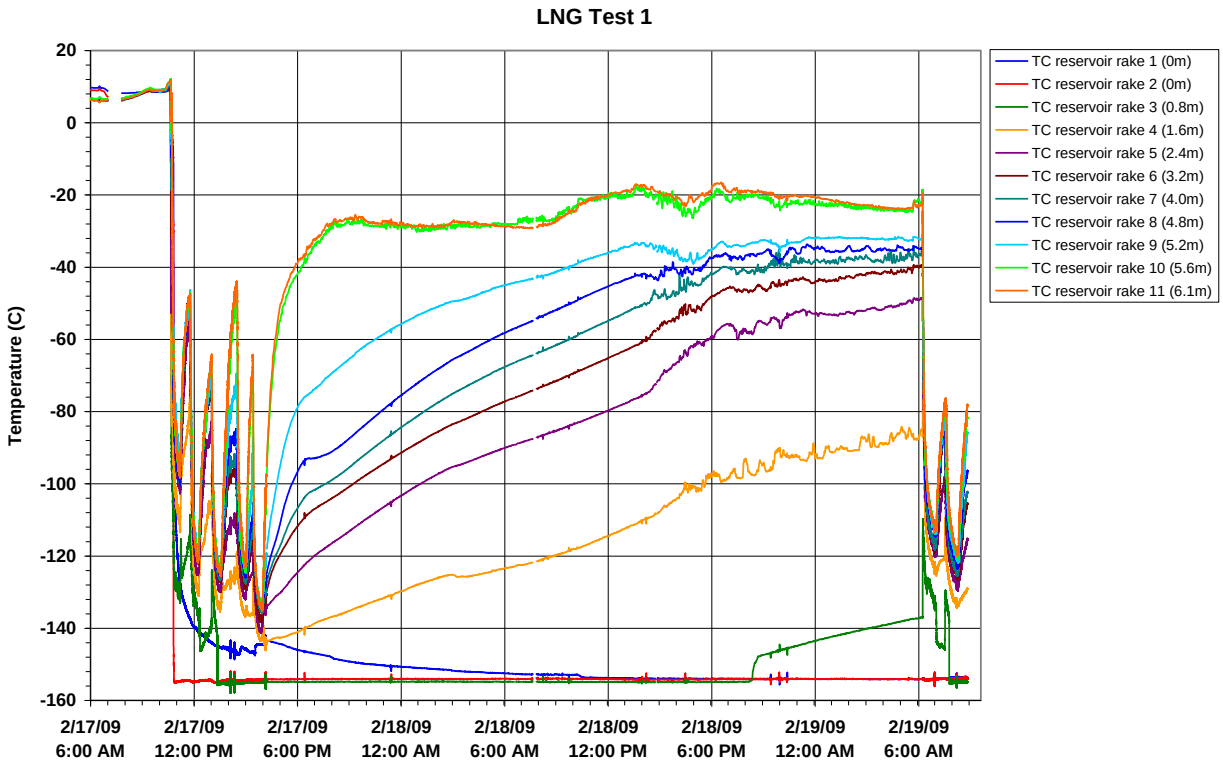

Figure 85 Reservoir temperatures during fill in Test 1.

5.2 LNG Test 1 - Execution and Measurements

The test commenced at approximately 9:15 AM on Thursday, February 19. Refer to Figure 43 in the following measurement discussions. Note there are four cardinal axes or "spokes" (note that the 0º or "North" spoke is actually located at a magnetic heading of 340º. Each spoke contains three towers, nominally at 110 m, 160 m, and 210 m from the pool center, upon which radiometers are mounted. Cameras located on the end (~226 m) of each spoke focus on the pool vertical centerline. Some spokes contain additional instrumentation, such as IR cameras, spectrometers, and meteorological instrumentation.

5.3 Meteorology

The target wind speed was <2.5 m/s, with a forecast time of 8:15 AM for that condition.

The ambient pressure was 12.32 psia, air temperature was 4°C, and the relative humidity was 32%. The water temperature was 4°C and the water depth was ~2 m at the pool center.

SODAR Data Approximate Location: 34 58' 52.62 "N 106 33' 6.24" W
(700 m NE of pool centerline)

LNG Tower Data Approximate Location: 34 58' 16.48 "N 106 34' 6.54" W
(1300 m SW of pool centerline)

As described previously, the LNG tower was instrumented to measure temperature, relative humidity, wind, and atmospheric pressure. Wind and temperature were available at both the 10 meter and 29.3 meter levels. The LNG tower was operated to sample atmospheric variables once a second, and record the information in 5 minute averaging intervals the morning of the LNG burn. Due to the data-logger size and storage space, approximately 24 minutes of 1 second data can be stored before the oldest data is overwritten. All 1 s data was logged. Due to safety concerns and hardware limitations (access to the tower was prohibited for a few days after the test), the 5 minute data during and after the burn were overwritten by the time the data was collected at the site on the morning of Tuesday, February 24th.

Figure 86 is a graph of the SODAR and tower measured wind speed data in the vicinity of the LNG burn area the morning of the burn. SODAR winds depicted are the winds in the lowest 50 meters above the ground. The desired minimum winds speeds at the surface were achieved for the anticipated time window, however, the wind speeds increased more abruptly than anticipated. Wind speeds were within burn condition criteria until approximately 8:40 AM. Wind speeds in the vicinity of LNG during the burn time between 9:16 AM and 9:26 AM were generally between 3.5 and 5.5 m/s. The wind directions were generally from the north.

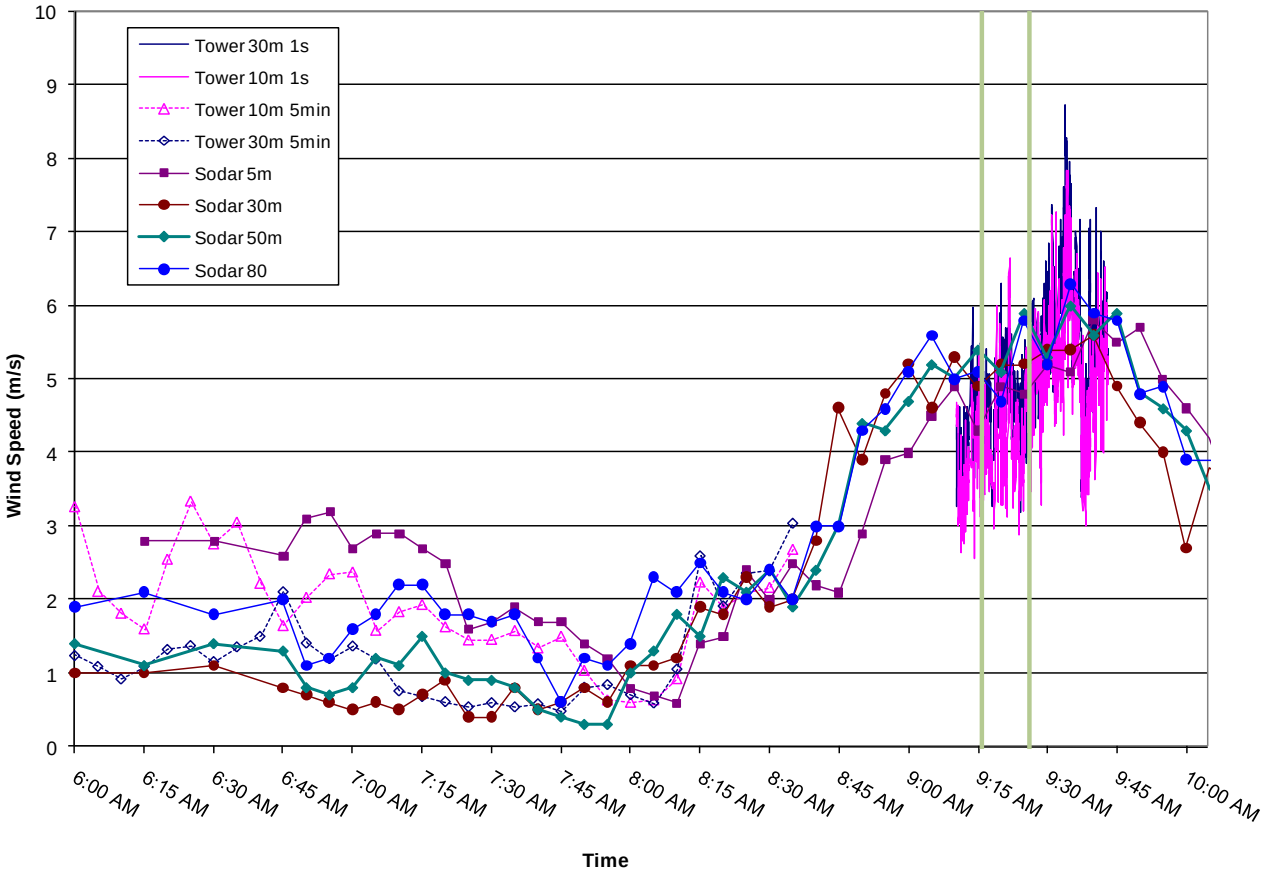

Figure 86 Wind speed meteorological data in the vicinity of the LNG Test 1.

Figure 87 and Figure 88 present the wind data from the 3D ultrasonic anemometers mounted on the wind towers located approximately 230 m from the pool centerline. The North tower has instruments at 2 m (US3), 5 m (US2), and 10 m (US1) above the ground surface. The East tower has one instrument located at 10 m (US4) above the ground. Average wind speed was 4.8±0.8 m/s at 331±13 degrees (magnetic north). This wind (from North to South), was almost parallel to the North-South spoke axis.

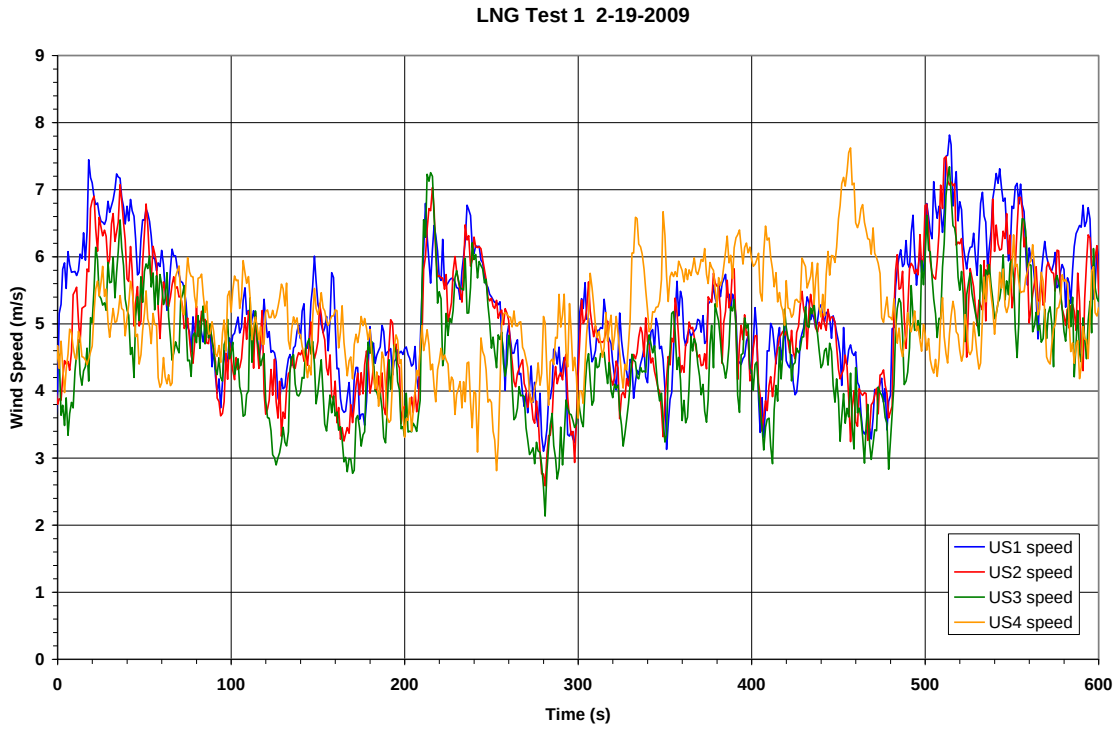

Figure 87 Test 1 wind speed at the LNG test site.

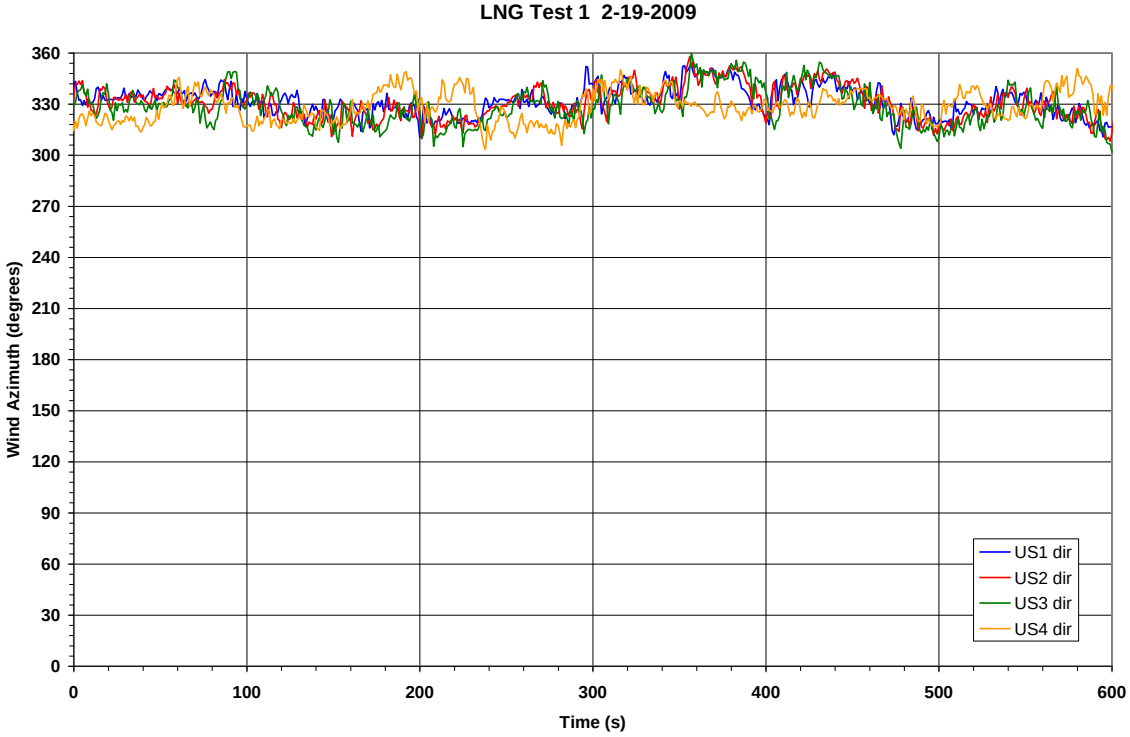

Figure 88 Test 1 wind direction at the LNG test site.

5.4 Reservoir Liquid Discharge

Time zero (0 s) on the following figures is the fiducial time logged on all data acquisition systems and is also the signal that fired the high-intensity photo flash bulb on the diffuser (for camera synchronization). The 15 inch discharge valve was opened 10 s after the fidu signal.

Figure 89 shows the methane liquid level and flow rate from the reservoir and compares it to the predicted level *based on a 2-phase flow model*, as post-test analyses determined that the single phase discharge model was inadequate. The LNG liquid level started at about 0.905 m (3 ft), yielding about 58.0 m^3 (~15,340 gal) inside the reservoir.

The measurements of discharge rate are based on pressure head from a dip tube and the laser-determined volume vs. liquid height measurements shown in Figure 90, they are basically mass flow rates that have been converted to volume flow using a methane density of 420 kg/m^3.

The flow rate initially was about 0.061 m^3/s (970 gpm) and increased throughout the test, reaching 0.123 m^3/s (1960 gpm) at the end of the test. Between the steady-state fire interval of 390-510 s, the average flow rate from the reservoir was 0.121±0.001 m^3/s (1921±21 gpm), yielding an average mass discharge rate of 50.8±0.6 kg/s.

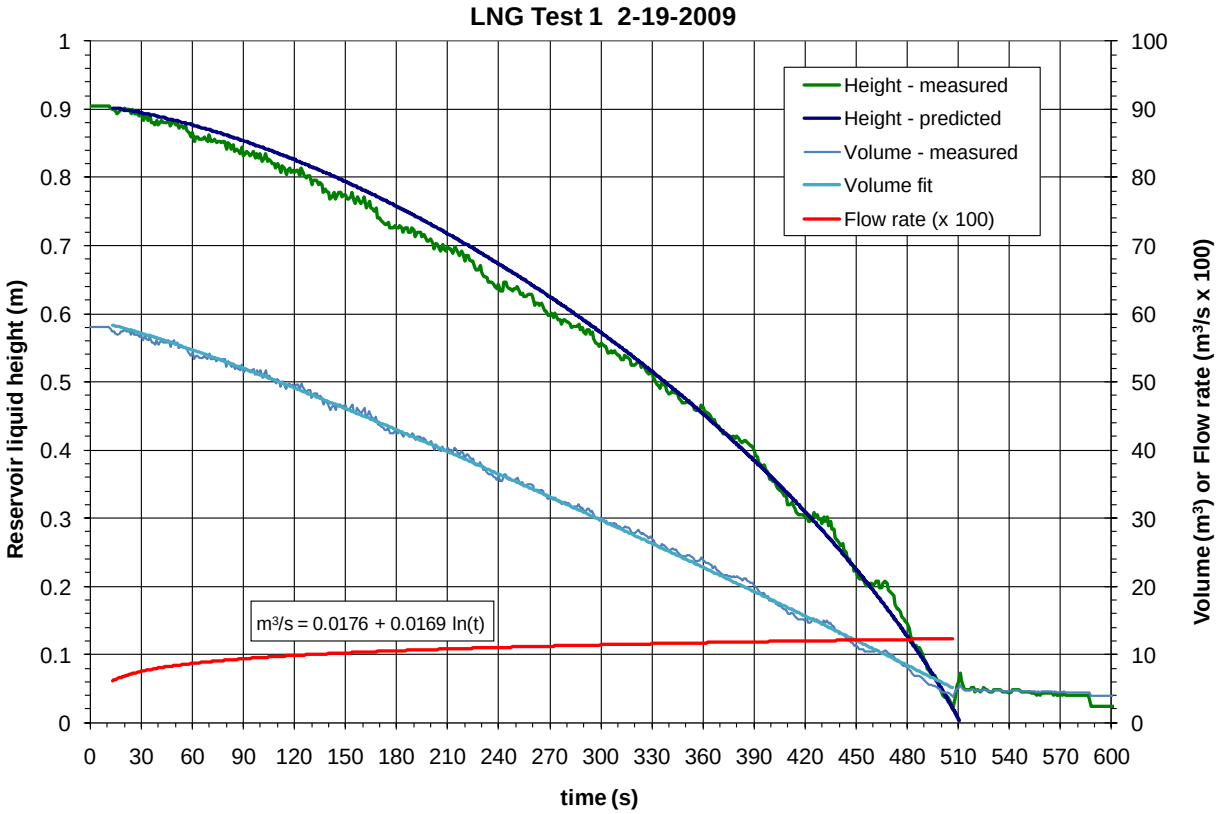

Figure 89 Reservoir level and flow rate during Test 1.

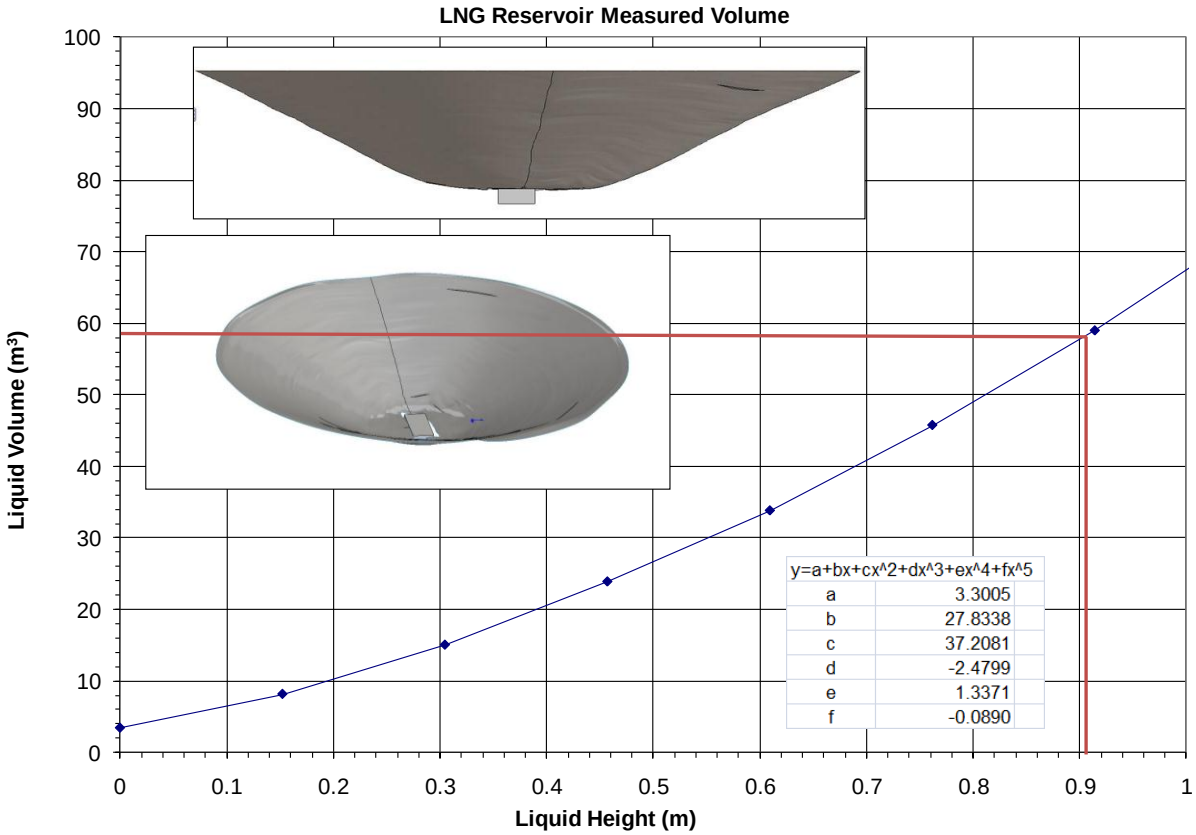

Figure 90 Reservoir volume vs. liquid height.

5.5 Pool Area and Effective Diameter

Figure 91 shows a highly manipulated, aerial high resolution (width = 3872 pixels x height = 2592 pixels at 300 dpi), lens stabilized image taken at a 34 degree angle above the pool surface at 420 seconds (Figure 92 shows a 30 s interval sequence) into the spill that was used to determine the spill area. Adobe Photoshop CS3 extended, a graphics editing program developed and published by Adobe Systems was used for the purpose of quantitative data extraction and image analysis. A tool was used to align a rectangular perspective plane, with the stadia markers present in the image. The image was then conformed to this virtual vanishing perspective grid, rotated then scaled into a corrected flat axis plane.

Figure 91 Test 1 aerial view at 420 s used to determine spreading pool area.

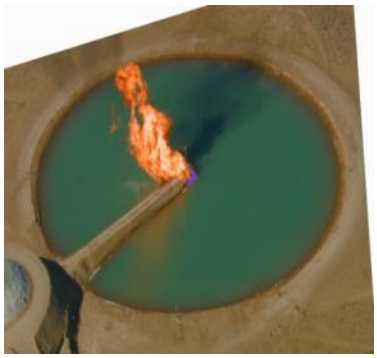

30 s

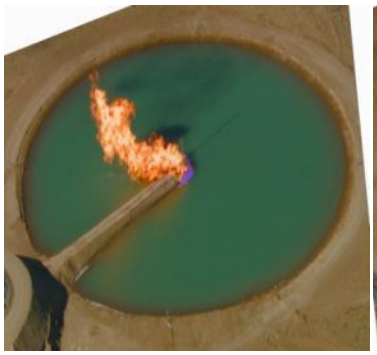

60 s

90 s

120 s

150 s

180 s

210 s

240 s

270 s

300 s

330 s

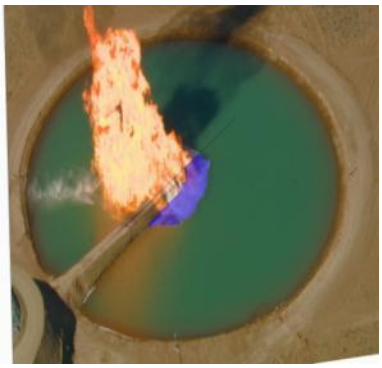

360 s

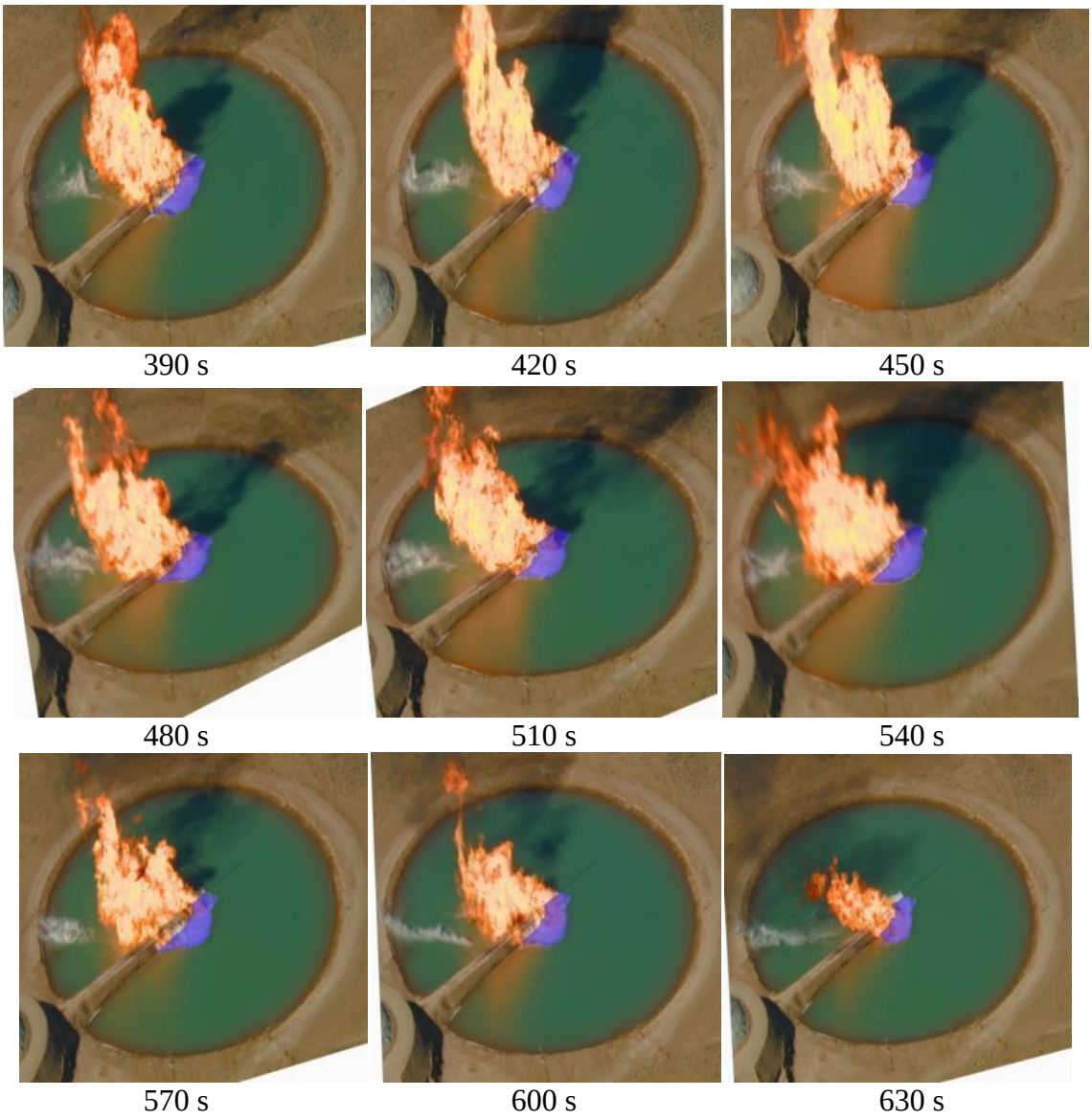

Figure 92 Sequence of aerial images in LNG Test 1

A measurement scale was developed by setting a specified number of pixels to represent known lengths in the image (scale factor: 1 pixel = 0.078 ± 0.002 m). Boundary edge measurements made using this scale were then used to calculate the area occupied by the spreading LNG on the water surface.

As the West side of the LNG pool was obscured from overhead viewing by flames, the LNG pool area was determined based on the East side (90° aerial view) spreading pool (footprint illustrated in blue) and multiplying by a scale factor of 1.75, based on data from LNG Test 2 (discussed further in the regression rate uncertainty section).

5.6 LNG Mass Loss Rate

Figure 93 compares measured reservoir discharge flow rates and liquid levels to predicted values. The 2-phase LNG flow model also predicted the vapor fraction of the liquid being discharged at the diffuser. The measured flow rate from the reservoir was multiplied by the time-dependent liquid fraction (1 minus the vapor fraction at diffuser) to yield the liquid flow rate at the diffuser. The mass loss (or regression) rate was determined by dividing the estimated liquid spill rate *at the diffuser* by the pool area. The predicted vapor fraction at the diffuser was 3% during the interval from 390-510 s.

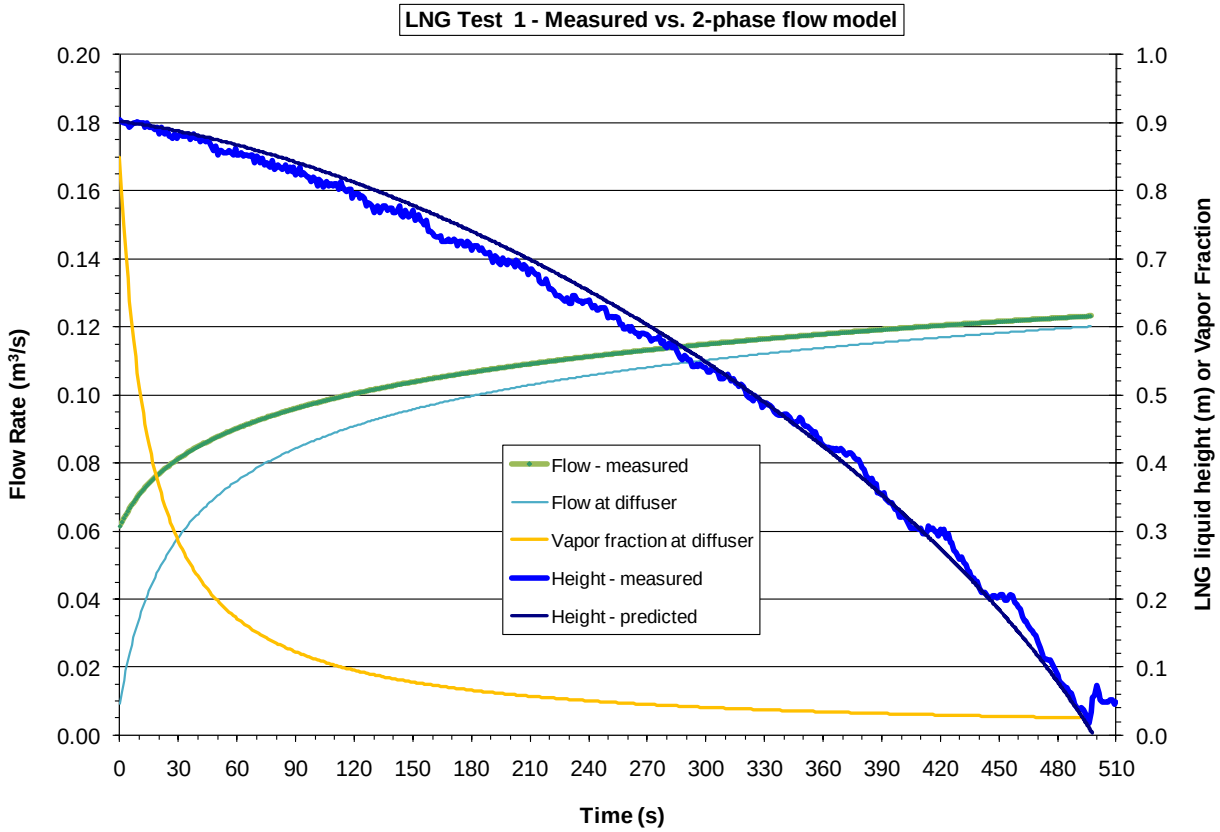

Figure 93 Measured liquid height and flows vs. 2-phase flow model predictions.

Figure 94 shows the time-dependent pool area, equivalent pool diameter, spill rate from the diffuser, and regression rate. A regression rate can only be calculated from the discharge rate and the pool area if the quantity of LNG in the pool is constant. This cannot be done while the pool is spreading. Thus the calculation of *transient regression rate* is not valid at <300 s.

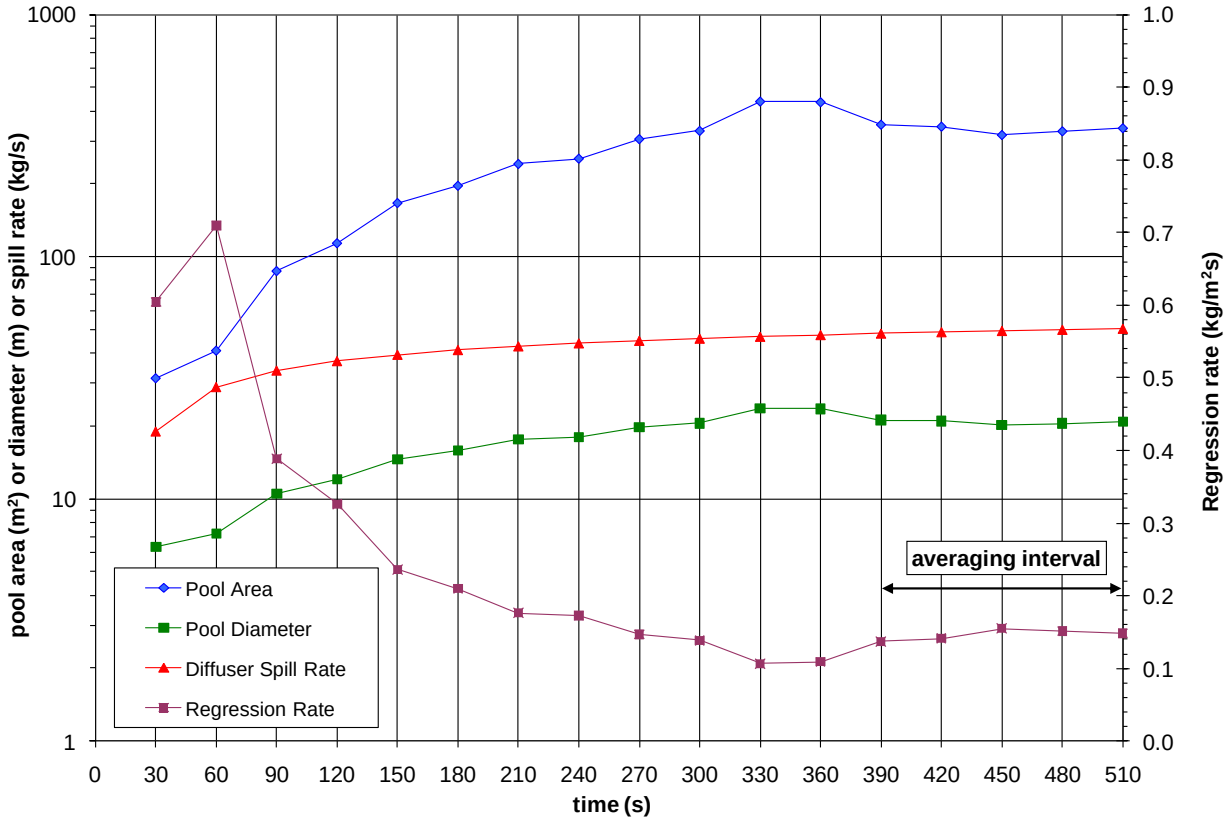

Figure 94 LNG flow rate, pool diameter, and regression rate in Test 1.

Between 390-510 s, the steady-state pool area of 337.4±12.9 m^2 yields an equivalent circular diameter of 20.7±0.4 m. Based on a calculated liquid spill rate of 49.4±0.9 kg/s at the diffuser, the regression rate was 0.147±0.01 kg/m^2s or 3.5 x 10^{-4} m/s, dividing by the liquid density of 420 kg/m^3.

The only other experiment able to derive burn rate data for LNG pool fires on water are the tests funded by the USCG [Raj 1979]. Using reported values for spill rate divided by the pool area, burn rates in the USCG tests vary between 2.6 x10^{-4} to 9 x10^{-4} m/s.

Table 19 tabulates the data and presents average and standard deviation for the steady-state period between 390-510 s.

Table 19 Regression rate for LNG Test 1

Time (s)	90° Aerial Pool Area (m^2)	Pool Area (m^2)	Pool Diameter (m)	Diffuser Spill Rate (kg/s)	Regression Rate (kg/m^2s)
30	17.9	31.4	6.3	19.0	na
60	23.3	40.8	7.2	28.9	na
90	49.8	87.2	10.5	33.9	na
120	64.9	113.6	12.0	37.1	na
150	95.3	166.7	14.6	39.4	na
180	112.3	196.5	15.8	41.2	na
210	138.3	242.0	17.6	42.7	na
240	145.5	254.6	18.0	43.9	na
270	175.3	306.7	19.8	45.0	na
300	189.5	331.6	20.5	45.9	0.138
330	250.8	438.8	23.6	46.8	0.107
360	249.2	436.0	23.6	47.5	0.109
390	201.1	351.9	21.2	48.2	0.137
420	197.4	345.4	21.0	48.8	0.141
450	182.3	319.0	20.2	49.4	0.155
480	188.8	330.4	20.5	50.0	0.151
510	194.4	340.2	20.8	50.5	0.148
540	227.1	397.4	22.5		
570	225.0	393.7	22.4		
600	191.7	335.4	20.7		
630	154.4	270.3	18.5		
average 390-510s	**192.8**	**337.4**	**20.7**	**49.4**	**0.15**
sd. dev.	**7.4**	**12.9**	**0.4**	**0.9**	**0.01**

The ground plume cameras provide a secondary means to check the analysis. Assume for this fire that the cross-sectional area of the fire near the pool surface represent the area of the burning liquid pool. At the height of the flame CG (a term commonly used in video analysis to denote the center of area of an image), the flame plume has an average length of 20.8 m across the N-S axis and a length of 27.0 m across the E-W axis during the 390-500 s steady state interval. Assuming an ellipse (440.3 m^2), and subtracting the area of the berm (74.8 m^2) and the diffuser (19.6 m^2); the pool area is determined to be 345.9 m^2. This yields an equivalent circular diameter of 21.0 m, comparable to the pool diameter listed in Table 19.

Uncertainty Analysis for Regression Rate Measurements

The time-averaged and space-averaged regression rate *RR*, is estimated using Eq. (20)

$$RR = \frac{W_f}{A} \tag{20}$$

where W_f is the time-averaged flow rate of liquid methane at the diffuser and A is the time-averaged area of the pool. The time-averaged liquid methane flow rate is found from the change in liquid volume in the reservoir (ΔV) over the interval of time averaging (Δt), the density of liquid aluminum, and the quality X_0 (the mass fraction of the methane mass that is in vapor form at the diffuser).

$$W_f = \frac{\Delta V}{\Delta t}\rho_{CH_4,liquid}(1 - X_0) \tag{21}$$

In this analysis we will assume that the uncertainty in the flow rate is dominated by the uncertainty in the volume change and the quality.

The volume measurements found from the curve shown in Figure 90 are not in a convenient form for uncertainty analysis of the volume change. In this section we will develop an alternate volume change measurement methodology based on the same laser measurements as the volume fit. This form can be shown to give very similar results but is much easier to analyze to assess the effects of uncertainties. The uncertainty in the volume change is estimated as follows. The volume change is found from the equation

$$\Delta V = \int_{h_2}^{h_1} A(h)dh \tag{22}$$

where h_1 is the initial height, h_2 is the final height, and $A(h)$ is the area of a horizontal cross-section of the reservoir at height h. The horizontal cross-sectional area can be found from the equation

$$A(h) = \int_0^{2\pi} \frac{1}{2} r^2(\theta, h)d\theta \tag{23}$$

where θ is the angle about the central axis of the reservoir. If the reservoir were a perfect frustum, then there would be no variation of $r(\theta,h)$ with θ, but laser measurements of the surface of the reservoir indicate that there is a small amount of variation. If we model the variation with a probability distribution, then the integral over all angles in Equation (23) can be recast as an integral over all possible radii, as

$$A(h) = \pi \int_0^{\infty} r^2(h)P(r(h))dr(h) \tag{24}$$

where $P(r(h))$ is the probability density function of the radius at height h. Expressed in words, this equation states that the area at height h is equal to the mean of the squares of the radii at that height, which we will approximate by curve fitting $r^2(h)$. Writing the mean of the squares for the radii as $(r^2(h))_{mean}$, the equation for area as a function of height in the reservoir is

$$A(h) = \pi\left(r^2(h)\right)_{mean}. \tag{25}$$

The unknown $(r^2(h))_{mean}$ in Equation (25) can be estimated from laser measurements of the surface of the reservoir as built. Here we will approximate $(r^2(h))_{mean}$ with a polynomial curve fit of the form

$$\left(r^2(h)\right)_{mean} = a h^4 + b h^3 + c h^2 + d h + e. \tag{26}$$

Substituting Eq. (26) into Eq. (25), then evaluating the integral of Eq. (22) yields the following expression for the volume change:

$$\Delta V = \pi\left[\frac{a}{5}\left(h_1^5 - h_2^5\right) + \frac{b}{4}\left(h_1^4 - h_2^4\right) + \frac{c}{3}\left(h_1^3 - h_2^3\right) + \frac{d}{2}\left(h_1^2 - h_2^2\right) + e\left(h_1 - h_2\right)\right]. \tag{27}$$

There are several sources of uncertainty in the volume measurement arising from original measurements of reservoir heights and coordinates on the surface of the reservoir and data manipulations required to obtain the transfer function for volume as a function of height. These sources of uncertainty are:

1. uncertainties in the laser measurements from which the relationship of radius to height is derived
2. uncertainties that arise from data manipulation (a coordinate system transformation which identifies the central axis of the reservoir)
3. uncertainties due to representing the mean square radius as a function of height with a curve fit through a collection of data points
4. uncertainty due to possible mismatch in coordinate system zero between liquid height measurements and the reservoir model curve fit
5. inherent uncertainty in the liquid height measurements due to gage uncertainty
6. changes in reservoir from time of measurements to time of test

The uncertainty due to the original laser measurements will be assumed to be negligible compared to other sources of error, so we will simply use a conservative estimate of the error in approximating the mean-square radius to account for both the uncertainty due to the original measurements and the uncertainty due to curve fitting. An estimate of this uncertainty is obtained by comparing differences between curve fits based on different intervals or with different orders in the polynomial approximation. Examination of the differences over the range of heights of interest shows that most of the fits are within ~400 square inches of the 4th order fit used here at all heights except at the extremes of the fit range. Here we will take the uncertainty to be piecewise linear, with a value of 800 square inches at a height of 3", decreasing to 400 square inches at a height of 10", and remaining constant at that value above that height. The curve fit should not be used outside of the range it was developed for, which in this case is 3" $\leq h \leq$ 80". The uncertainty in the volume measurements due to the laser measurements and curve fitting can then be written as

$$\delta(\Delta V)_{curve\ fit} = \pm\pi\int_{h_2}^{h_1} \delta\left(r^2(h)\right)_{curve\ fit}\, dh. \tag{28}$$

The instrument used to take the laser measurement is capable of finding the "level frame" normal to the gravity vector to a claimed accuracy of 2 arc seconds. The error due to misalignment of

the model for the reservoir and gravity is therefore negligible compared to other sources of error. The center of the reservoir, from which the mean-square radius is measured, is approximated by simply taking the average of the x and y locations of all data points collected. This may not be the true center of the reservoir because the measurement locations are not spaced precisely the same way all around the reservoir. The uncertainty in the volume due to the coordinate system transformation is estimated by examining different fits with different offsets applied to the laser measurements. This source of uncertainty is found to be small, since the offset has a greater role in changing the variance of the radius measurements than changes in the mean-square radius, which is the parameter needed to estimate the area. The uncertainty due to the methodology for finding the center of the reservoir will be rolled into a conservative estimate of the uncertainty in the curve fit.

The uncertainty due to the potential misalignment between the h=0 locations in the liquid height measurements and the model for the reservoir is a bias error. The effect is determined by introducing an additional variable into the volume equation. If the difference in these h=0 locations is written as h_0, then the volume equation translated into the liquid level gage coordinate system is

$$\Delta V = \pi \left[\begin{array}{l} \frac{a}{5}\left((h_1+h_0)^5-(h_2+h_0)^5\right)+\frac{b}{4}\left((h_1+h_0)^4-(h_2+h_0)^4\right)+ \\ \frac{c}{3}\left((h_1+h_0)^3-(h_2+h_0)^3\right)+\frac{d}{2}\left((h_1+h_0)^2-(h_2+h_0)^2\right)+e(h_1-h_2) \end{array} \right] \tag{29}$$

where h_0 is nominally zero, but there is some uncertainty in the actual value. Taking the derivative with respect to h_0, the sensitivity to this parameter is

$$\frac{\partial(\Delta V)}{\partial h_0} = \pi \left[\begin{array}{l} a\left((h_1+h_0)^4-(h_2+h_0)^4\right)+b\left((h_1+h_0)^3-(h_2+h_0)^3\right)+ \\ c\left((h_1+h_0)^2-(h_2+h_0)^2\right)+d(h_1-h_2) \end{array} \right]. \tag{30}$$

The uncertainty due to the h=0 mismatch is then

$$\delta(\Delta V)_{h_0} = \pm \pi \left[\begin{array}{l} a\left((h_1+h_0)^4-(h_2+h_0)^4\right)+b\left((h_1+h_0)^3-(h_2+h_0)^3\right)+ \\ c\left((h_1+h_0)^2-(h_2+h_0)^2\right)+d(h_1-h_2) \end{array} \right] \delta h_0 . \tag{31}$$

The sensitivities to the liquid level gage uncertainties can be found by taking the partial derivatives of the volume change equation with respect to h_1 and h_2, yielding

$$\frac{\partial(\Delta V)}{\partial h_1} = \pi\left[a h_1^4 + b h_1^3 + c h_1^2 + d h_1 + e\right] = A(h_1) \tag{32}$$

and

$$\frac{\partial(\Delta V)}{\partial h_2} = -\pi\left[a\,h_2^4 + b\,h_2^3 + c\,h_2^2 + d\,h_2 + e\right] = -A(h_2). \tag{33}$$

The uncertainties due to the gage measurements are then

$$\delta(\Delta V)_{h_1} = \pm A(h_1)\delta h_1 \tag{34}$$

and

$$\delta(\Delta V)_{h_2} = \pm A(h_2)\delta h_2 \tag{35}$$

where δh_1 and δh_2 are the uncertainties in the two liquid level measurements.

Another possible source of uncertainty is the changes in the reservoir shape between the time the reservoir was measured and the time of the test. The physical process most likely to cause a change is thermal contraction caused by the cold temperatures in the reservoir during the test. We believe that what actually happens when the reservoir is cooled is that the concrete liner in the reservoir cracks rather than contracting as an integral piece, so we will assume here that the change in area due to the temperature changes is small compared to the uncertainty in the area we are already accounting for in the mean-square fit.

The combined uncertainty in the volume change is found by the root-sum-square method,

$$\delta(\Delta V) = \pm\sqrt{\left(\delta(\Delta V)_{curve\,fit}\right)^2 + \left(\delta(\Delta V)_{h_0}\right)^2 + \left(\delta(\Delta V)_{h_1}\right)^2 + \left(\delta(\Delta V)_{h_2}\right)^2}\,. \tag{36}$$

The analysis of the uncertainty will take the time period of interest to be t = 300 s to t = 478 s to cut off the time period when the liquid level is very near the floor and the correlation of mean-square radius with height becomes uncertain. If the gage uncertainty is assumed to be ±1% of the measurement (increased from the manufacturer's claimed 0.4% uncertainty), h_0 is taken to be 3" and the uncertainty in h_0 is taken to be ±3", then the total volume change from t = 300 s (h_1=1.83 ft = 22.0") to t = 478 s (h_2=0.50 ft = 6") is 6087 gallons and the uncertainty in the volume change is 625 gallons (10.3% uncertainty). The percentage uncertainty is larger for cases with smaller differences in height or ending at lower elevations in the reservoir. The curve fits for volume as a function of height give very similar results for the estimated volume change over this time period, well within the estimated uncertainty.

The other major uncertain parameter in determining the mass flow rate of liquid methane at the diffuser is the quality, X_0. This factor evolves over the time period taken for averaging, but a value of 0.05 is a good approximation of the predicted value, time-averaged over the period of interest. Here we will simply take this value as the quality and will assume that the uncertainty in this value is 50%. This results in an uncertainty of approximately 2.6% in the mass flow rate of liquid methane.

Neglecting any additional uncertainty due to the time measurements at the beginning and end of the averaging period, uncertainty in the density of liquid methane, and any other factors, the uncertainty in the flow rate of liquid methane can be estimated from the uncertainties due to volume measurements and the quality. If these uncertainties are combined using the root-sum-squares method, the total uncertainty in the flow rate of liquid methane is 10.6%.

$$\delta W_f = \sqrt{\left(\delta(\Delta V)\frac{\partial W_f}{\partial(\Delta V)}\right)^2 + \left(\delta X_0 \frac{\partial W_f}{\partial X_0}\right)^2} \tag{37}$$

$$\delta W_f = \sqrt{(0.103\, W_f)^2 + (0.026\, W_f)^2} \tag{38}$$

The uncertainty in the area comes from two sources. First, the area of the pool is partially obscured by the fire. In Test 2 two camera views are available and the area on both sides of the fire can be approximated. In that test it appears that the area of the pool on the side of the diffuser that the fire was shifted towards was approximately 25% smaller than the area of the pool on the opposite side of the diffuser. The area of the pool in Test 1 will be found from the visible area (as determined from the outlines of the pool on the side of the fire that is visible) with a scaling factor to account for the area that cannot be seen. Based on the data from Test 2, the scaling factor used here is 1.75.

$$A = K\, A_{visible} \tag{39}$$

where K is the scaling factor, K=1.75.

The uncertainty in the visible area on the exposed side of the fire is assumed to be ±10%. The uncertainty in the scaling factor is assumed to be ±0.25. The total uncertainty in the area is then

$$\delta A = \sqrt{\left(\delta K \frac{\partial A}{\partial K}\right)^2 + \left(\delta A_{visible} \frac{\partial A}{\partial A_{visible}}\right)^2} \tag{40}$$

$$\delta A = \sqrt{(0.25\, A_{visible})^2 + (0.1\, A_{visible}\, K)^2} = \sqrt{\left(\frac{0.25}{K} A\right)^2 + (0.1A)^2} \tag{41}$$

which gives an uncertainty in the area equal to 17.4% of the total area for the assumed value of the scaling factor.

The uncertainty in the regression rate is then found using the root-sum-square method.

$$\delta RR = \sqrt{\left(\delta W_f \frac{\partial RR}{\partial W_f}\right)^2 + \left(\delta A \frac{\partial RR}{\partial A}\right)^2} \tag{42}$$

$$\delta RR = \sqrt{\left(0.106 W_f \frac{1}{A}\right)^2 + \left(0.174 A \frac{W_f}{A^2}\right)^2} = \sqrt{(0.106\,RR)^2 + (0.174\,RR)^2} \qquad (43)$$

so the relative uncertainty in the regression rate under the conditions of Test 1 is estimated to be 20.4%.

5.7 Plume Heat Flux

Table 20 gives the inclination angles above horizontal, shift from centerline, radiometer heights above the pool surface, spot heights, spot diameters (actually ellipses), and distance from pool centerline for the radiometers. Note that gauges 1-5, 7, and 9 are narrow view (5.5 degree view angle) radiometers (ZeSe windows) and gauges 6, 8, and 10 are wide view (150 degree) radiometers (ZeSe windows). Note that the inclination angles and focus points are not consistent; post-test checks showed some of the gauges had shifted from nominal values (in particular, the gauges on tower 2 and tower 3 on the North and East spokes). See Appendix B for radiometer alignment procedures.

Table 20 Radiometer parameters for LNG Test 1

Type	gauge #	inclination angle	North CL shift (deg)	inclination angle	East CL shift (deg)	inclination angle	South CL shift (deg)	inclination angle	West CL shift (deg)
NV (300 kW/m^2, 5.5°)	1	3.14	2.9 West	3.15	0.3 North	3.07	0.0	3.45	0.5 South
NV (300 kW/m^2, 5.5°)	2	10.10	0.0	11.00	1.0 South	11.00	0.5 West	10.60	0.5 North
NV (300 kW/m^2, 5.5°)	3	17.00	0.5 East	16.60	3.3 North	16.90	0.5 East	17.10	0.3 South
NV (300 kW/m^2, 5.5°)	4	23.30	2.6 West	23.30	0.0	23.20	0.5 West	23.40	0.5 South
NV (300 kW/m^2, 5.5°)	5	29.00	0.0	29.20	1.5 South	28.90	2.3 East	28.90	0.0
WV (75 kW/m^2, 150°)	6	18.90	0.5 East	18.10	3.9 North	19.50	3.1 East	18.50	0.3 South
NV (300 kW/m^2, 5.5°)	7	46.70	0.4 West	31.30	0.7 South	13.30	1.4 West	12.10	0.0
WV (50 kW/m^2, 150°)	8	46.70	0.0	34.80	0.4 South	12.40	1.6 East	12.80	1.4 North
NV (300 kW/m^2, 5.5°)	9	32.30	23.2 West	9.23	0.8 South	9.43	0.5 West	9.82	2.7 North
WV (30 kW/m^2, 150°)	10	27.80	17.9 West	22.00	0.3 South	9.51	1.1 West	9.71	0.8 South

gage height above water (m)

Gage height on tower m		Test 1 N TW1	Test 1 N TW2	Test 1 N TW3	Test 1 E TW1	Test 1 E TW2	Test 1 E TW3	Test 1 S TW1	Test 1 S TW2	Test 1 S TW3	Test 1 W TW1	Test 1 W TW2	Test 1 W TW3
1		1.6			3.2			1.5			1.0		
1.1		1.7			3.3			1.6			1.1		
1.2		1.8			3.4			1.7			1.2		
1.3		1.9			3.5			1.8			1.3		
1.4		2.0	1.8	1.5	3.6	4.0	4.6	1.9	1.6	1.4	1.4	0.8	-0.1
1.5		2.1	1.9	1.6	3.7	4.1	4.7	2.0	1.7	1.5	1.5	0.9	0.0
survey height above water (m)		1.6	1.8	1.5	3.2	4.0	4.6	1.5	1.6	1.4	1.0	0.8	0.0

spot center above water (m)

Gage height on tower m		Test 1 N TW1	Test 1 N TW2	Test 1 N TW3	Test 1 E TW1	Test 1 E TW2	Test 1 E TW3	Test 1 S TW1	Test 1 S TW2	Test 1 S TW3	Test 1 W TW1	Test 1 W TW2	Test 1 W TW3
1		7.6			9.4			7.4			7.6		
1.1		21.2			24.9			23.1			21.6		
1.2		35.4			36.6			35.3			35.0		
1.3		49.2			51.4			49.2			48.9		
1.4		62.9	171.4	134.0	65.7	101.1	38.7	63.0	39.4	36.3	62.1	35.1	36.2
1.5		39.7	171.5	112.1	40.1	115.1	89.5	41.2	36.9	36.7	38.3	37.2	35.9

5.5

spot diameter (m)

Gage height on tower m		Test 1 TW1	Test 1 TW2	Test 1 TW3	Test 1 E TW1	Test 1 E TW2	Test 1 E TW3	Test 1 S TW1	Test 1 S TW2	Test 1 S TW3	Test 1 W TW1	Test 1 W TW2	Test 1 W TW3
1		10.6			10.7			10.6			10.6		
1.1		10.7			10.9			10.8			10.8		
1.2		11.0			11.1			11.1			11.1		
1.3		11.5			11.6			11.6			11.5		
1.4		12.1	22.4	23.9	12.2	18.0	20.4	12.1	15.8	20.5	12.1	15.7	20.5
1.5		867	1741	1769	872	1454	1689	877	1223	1588	866	1225	1589

		Test 1 N TW1	Test 1 N TW2	Test 1 N TW3	Test 1 E TW1	Test 1 E TW2	Test 1 E TW3	Test 1 S TW1	Test 1 S TW2	Test 1 S TW3	Test 1 W TW1	Test 1 W TW2	Test 1 W TW3
distance from pool edge m		109.9	159.8	209.6	111.1	159.7	209.8	110.7	159.9	209.8	110	159.8	209.8

Figure 95, Figure 96, Figure 97, and Figure 98 give spoke HD camera stills at selected times with an overlay for the narrow-view radiometer view factors. Refer to the visual data during discussions of the plume heat flux data.

Figure 95 LNG Test 1 0° spoke HD camera stills with NV radiometer overlays.

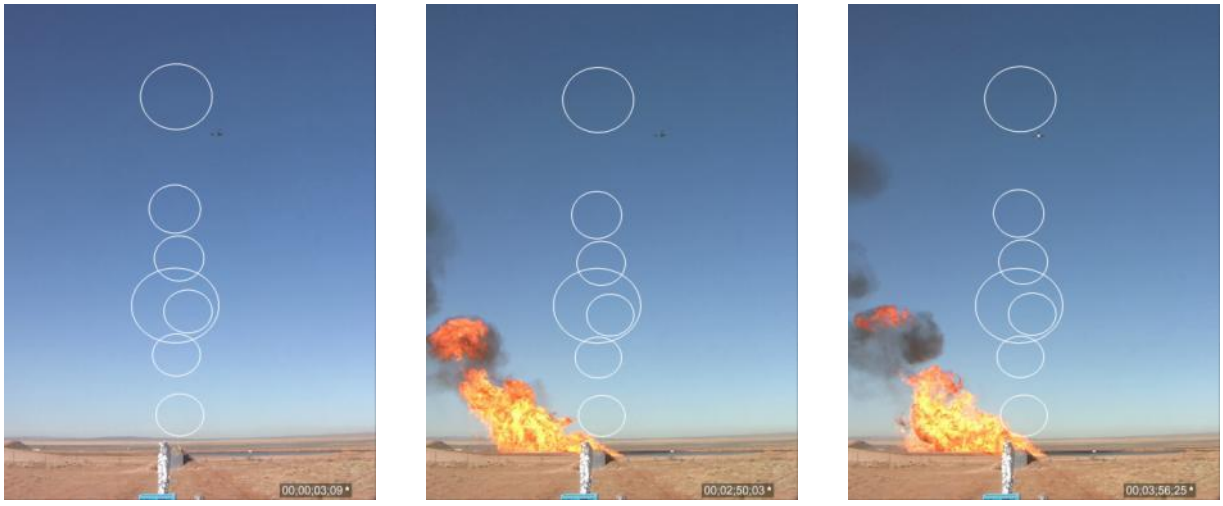

Figure 96 LNG Test 1 90° spoke HD camera stills with NV radiometer overlays.

.

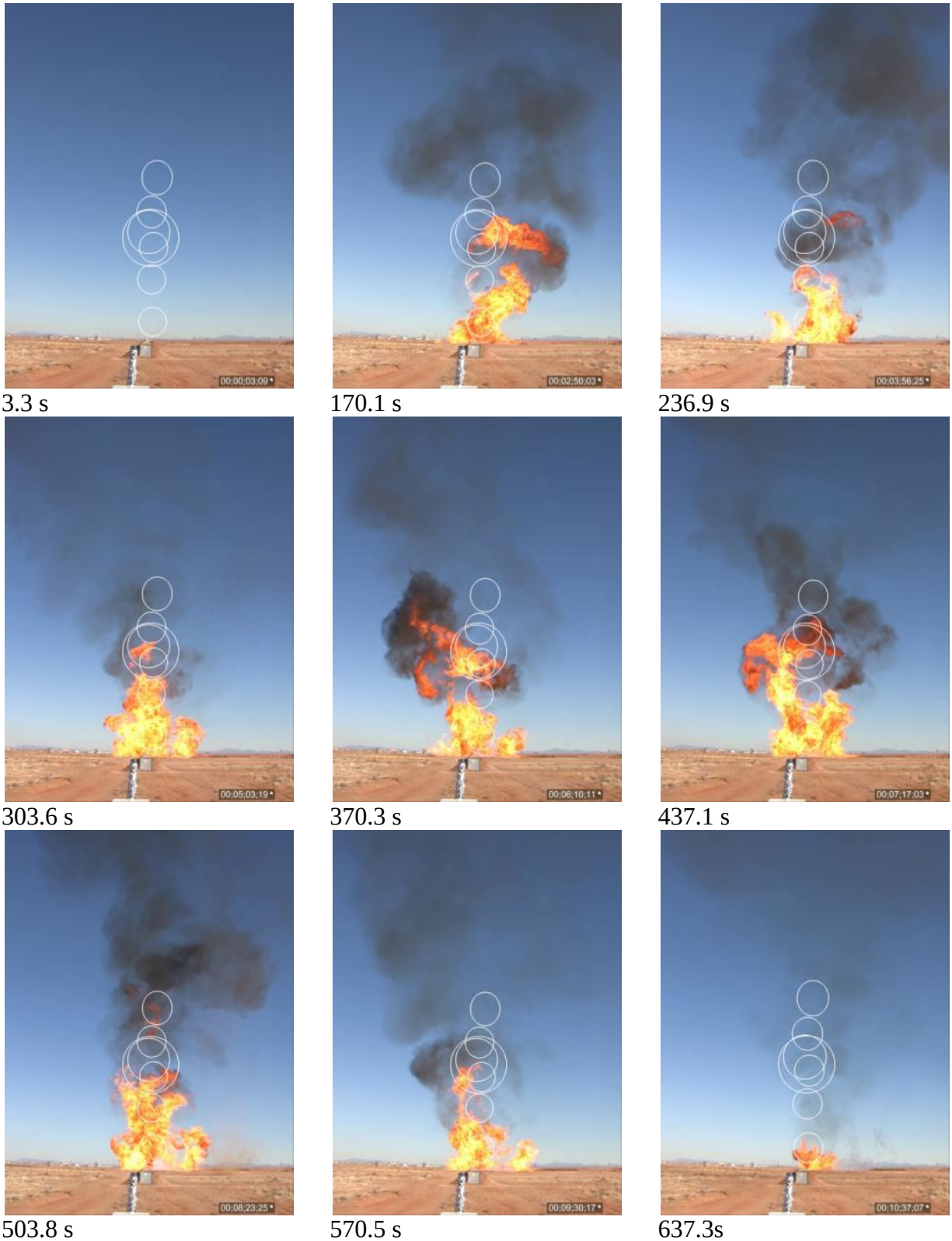

Figure 97 LNG Test 1 180° spoke HD camera stills with NV radiometer overlays.

3.3 s 170.1 s 236.9 s

303.6 s 370.3 s 437.1 s

503.8 s 570.5 s 637.3s

Figure 98 LNG Test 1 270° spoke HD camera stills with NV radiometer overlays.

Figure 99, Figure 100, Figure 101, and Figure 102 show the heat flux from the narrow-view radiometers attached to the towers closest to the pool centerline (110 m). Plots showing the measured heat flux versus time have not been adjusted for atmospheric transmission losses. The fire plume had a strong tilt from North to South, and little flux was seen by the radiometers on the 90 and the 270 degree spokes (even for the gauges looking at the lowest position (~8 m above the pool) in the fire.

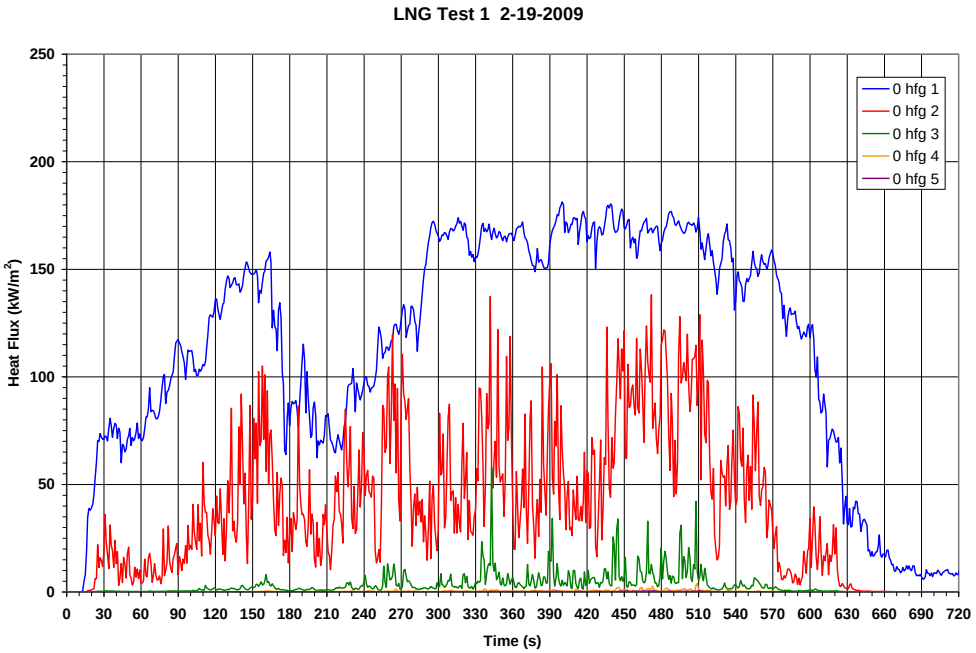

Figure 99 Test 1 NV radiative heat flux at the 110 m tower on the 0° spoke.

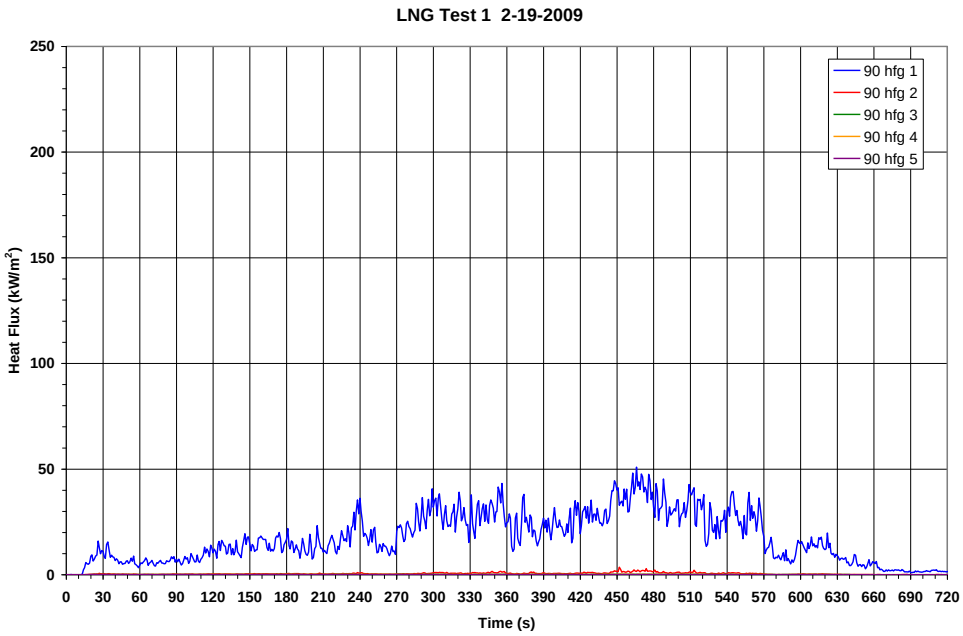

Figure 100 Test 1 NV radiative heat flux at the 110 m tower on the 90° spoke.

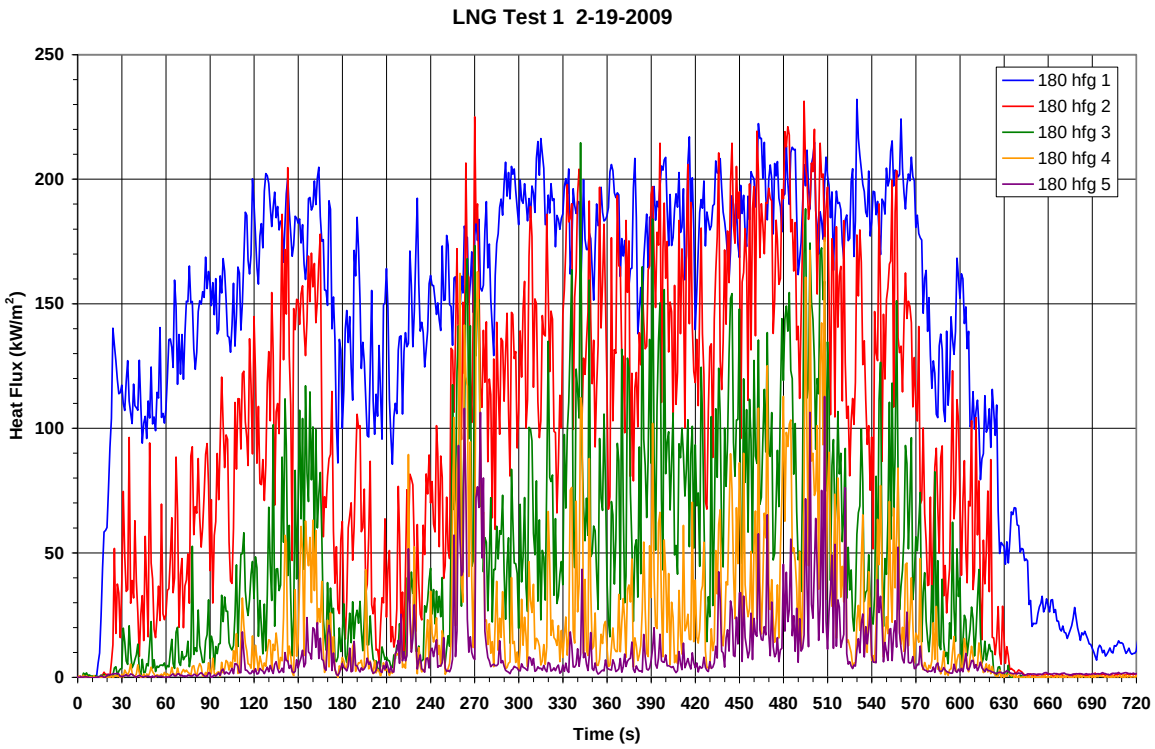

Figure 101 Test 1 NV radiative heat flux at the 110 m tower on the 180° spoke.

The spot fill analysis (discussed in Section 5.14) determined that only gauge 1 on the South tower 1 spoke (180 hfg 1) was fully viewing the flame during the steady-state period.

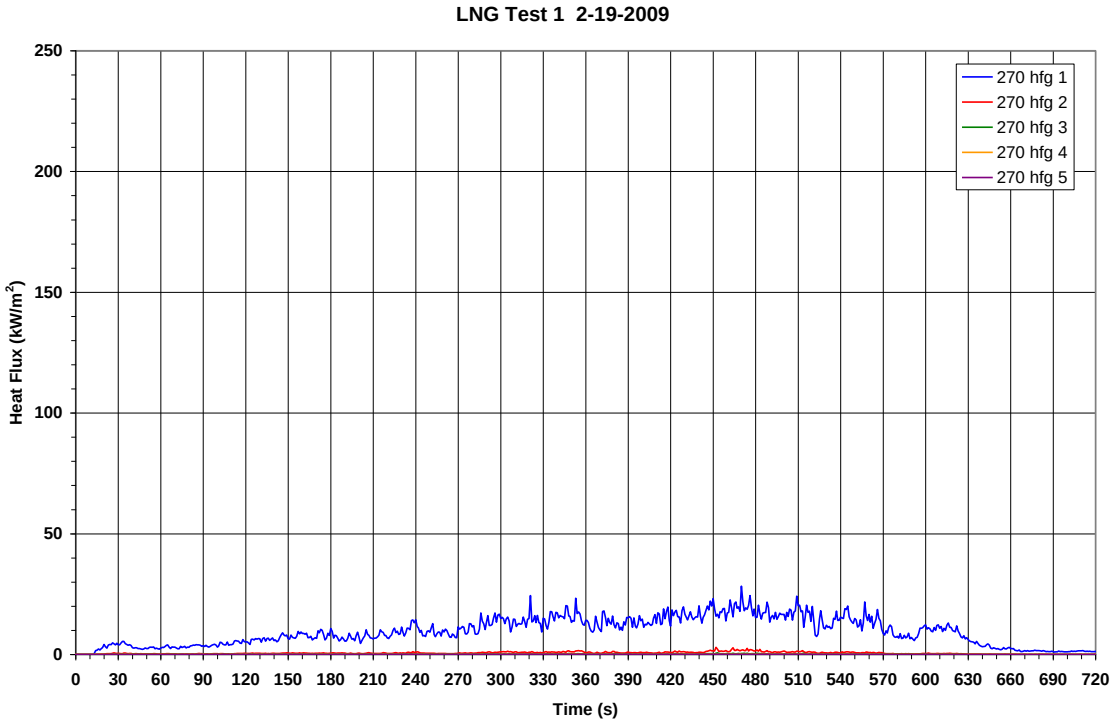

Figure 102 Test 1 NV radiative heat flux at the 110 m tower on the 270° poke.

The wind tilted the flame almost normal to the 180 degree spoke, hence those radiometers saw the highest heat flux. Figure 103 plots the flux from the gauges on the three towers on the 180 degree spoke that were positioned to look at ~53 m above the pool, estimated to be near the flame center. The gauges on the 110 m and the 160 m (from pool centerline) showed good agreement (the gauges further back should read less due to atmosphere attenuation; with the transmission at ~80% at these distances). Note that the spot analysis determined that none of these gauges had their field of view (FOV) completely filled; therefore, they will read low as they see only a portion of the flame.

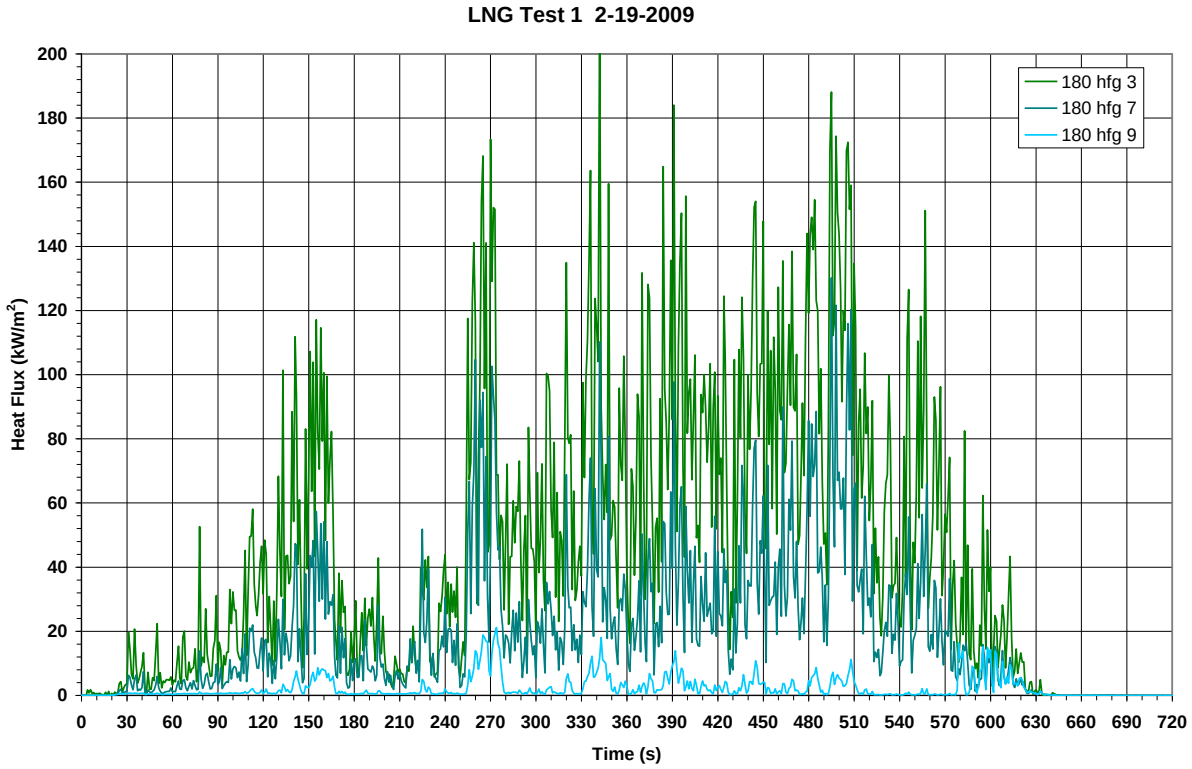

Figure 103 Test 1 NV radiative heat flux (mid-height gauges) on the 180° spoke.

Figure 104 and Figure 105 show the strong north to south tilt of the flame. Close inspection shows the thermocouple rake (16 ft tall) extending from the top of the diffuser.

Figure 104 Wide angle view from the west (~t+30s) in Test 1.

Figure 105 Close up view from the west (~t+7min) in Test 1.

Figure 106, Figure 107, Figure 108, and Figure 109 give the flux from the wide view radiometers. The data is consistent with increasing distance from pool centerline (hfg 6 is 110 m, hfg 8 is 160 m, and hfg 10 is 210 m from pool centerline).

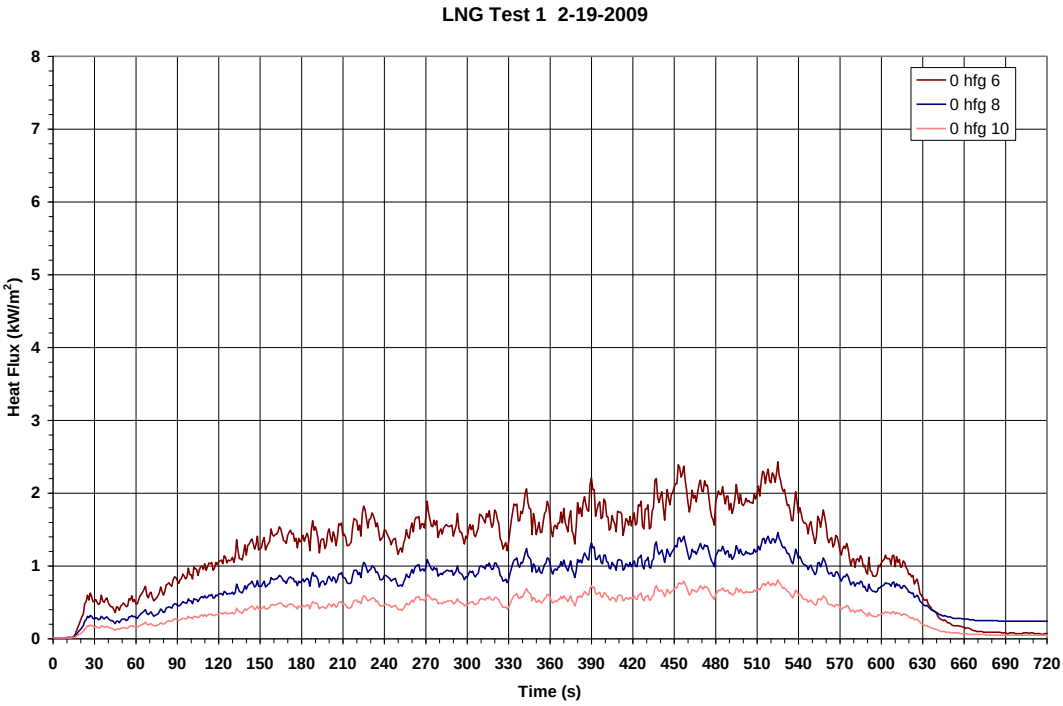

Figure 106 Test 1 heat flux from the WV (150°) radiometers on the 0° spoke.

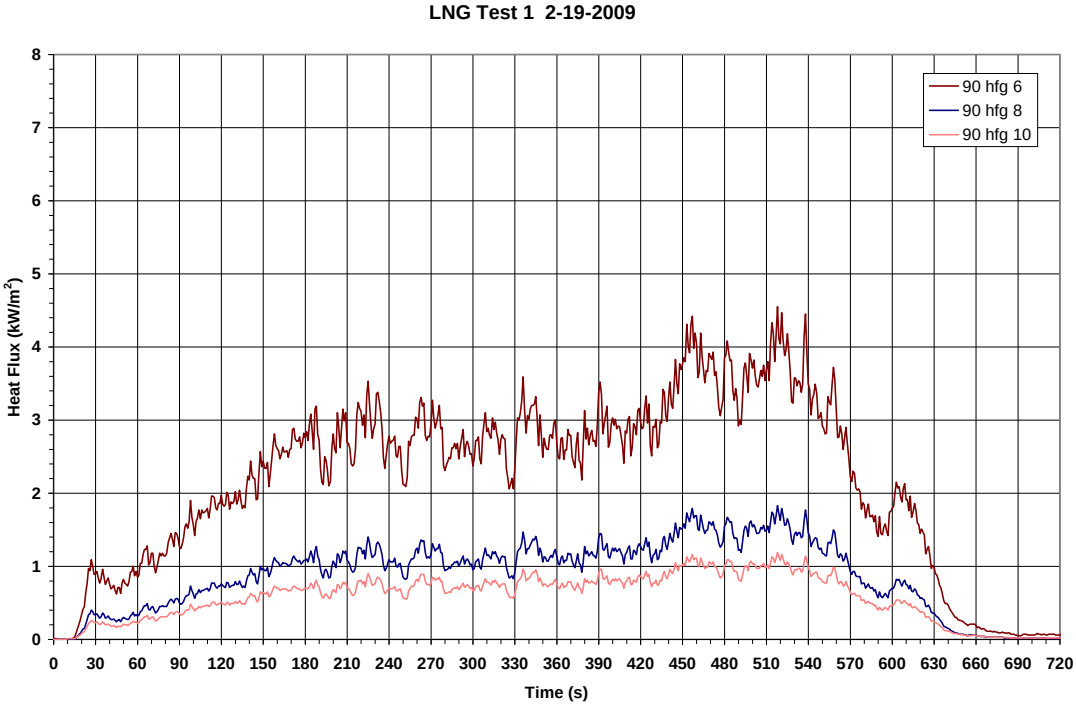

Figure 107 Test 1 heat flux from the WV (150°) radiometers on the 90° spoke.

Note that the 90 and the 270 spoke radiometers have similar views (both views are approximately normal to the tilted flame).

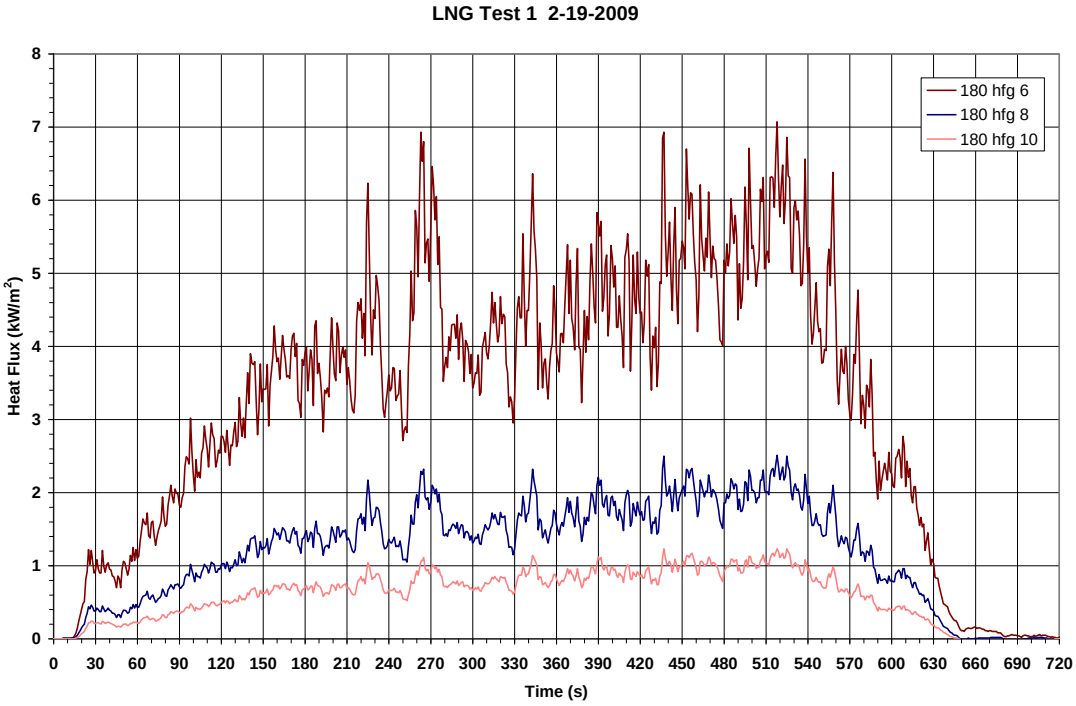

Figure 108 Test 1 heat flux from the WV (150°) radiometers on the 180° spoke.

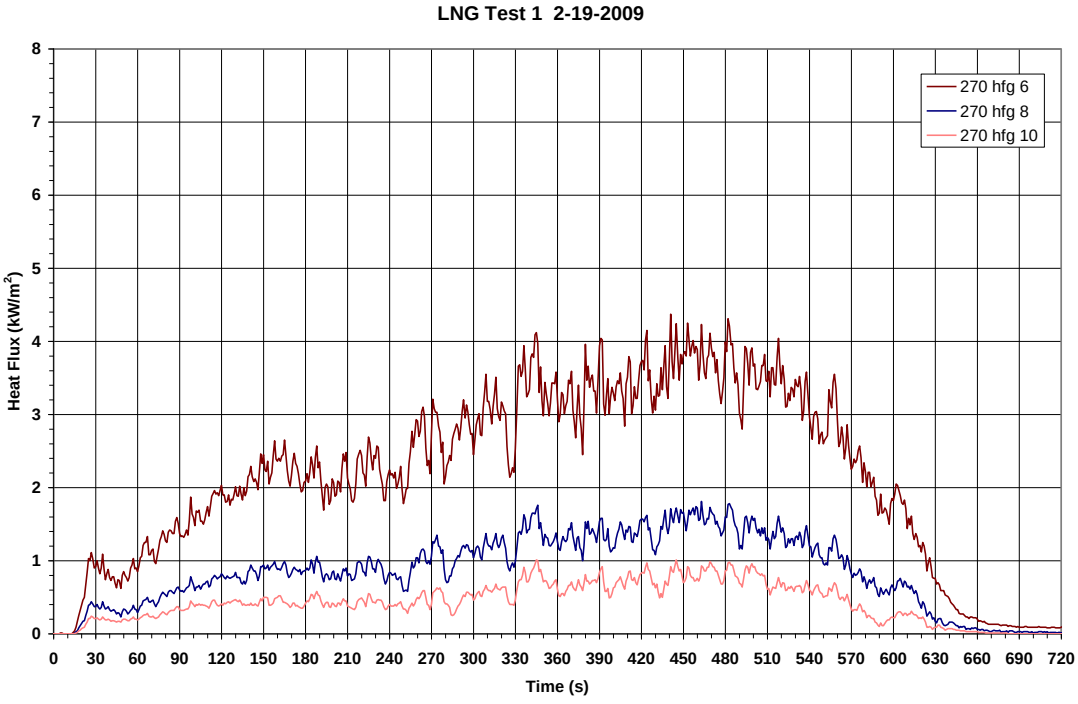

Figure 109 Test 1 heat flux from the WV (150°) radiometers on the 270° spoke.

A review of the radiometer data shows that the fire was steady and consistent between about 390 to 500 s into the spill. This time duration will be used to present average data for the remainder of the report. Table 21 presents the average and standard deviation (between 390-500 s) of radiometer data uncorrected for transmission losses. East and West spoke narrow view (or angle) radiometer data are not shown since little was measured.

Table 21 Average Test 1 radiometer data (uncorrected) between 390-500 s.

	narrow-angle radiometers							wide-angle radiometers		
nominal spot height above pool (m)	7	21	35	48	62	35	35	35	35	35
nominal distance from pool center (m)	110	110	110	110	110	160	210	110	160	210
North spoke	**0 hfg 1**	**0 hfg 2**	**0 hfg 3**	**0 hfg 4**	**0 hfg 5**	**0 hfg 7**	**0 hfg 9**	**0 hfg 6**	**0 hfg 8**	**0 hfg 10**
average kW/m^2	169.9	73.6	8.3	0.7	0.2	1.4	0.8	1.9	1.1	0.6
st.dev.	5.9	33.6	8.7	0.5	0.1	1.1	1.0	0.2	0.1	0.1
South spoke	**180 hfg 1**	**180 hfg 2**	**180 hfg 3**	**180 hfg 4**	**180 hfg 5**	**180 hfg 7**	**180 hfg 9**	**180 hfg 6**	**180 hfg 8**	**180 hfg 10**
average kW/m^2	191.0	164.1	93.2	43.8	15.9	5.0	41.5	5.0	1.9	1.0
st.dev.	16.7	41.1	47.1	42.5	20.6	0.8	29.3	0.8	0.2	0.1
East spoke								**90 hfg 6**	**90 hfg 8**	**90 hfg 10**
average kW/m^2								3.3	1.4	0.9
st.dev.								0.5	0.2	0.1
average kW/m^2								**270 hfg 6**	**270 hfg 8**	**270 hfg 10**
average								3.6	1.5	0.8
st.dev.								0.4	0.2	0.1

5.8 Pool Heat Flux

Figure 110 shows an aerial photograph taken at ~460 s into the spill. The wind is tilting the flame plume over the directional flame thermometers (DFTs) that are in the pool facing upward on the 180° spoke axis (~1 ft above the pool surface). The arrow points to the middle DFT located on the North axis (DFT 0-2).

Figure 110 Aerial view of LNG Test 1 (~midpoint of the spill).

An inverse heat conduction analysis was performed with the geometric configuration, thermal property data, and the measured plate (inside) temperatures. The average emissivity of the pre-oxidized inconel plates was 0.666. The inverse heat conduction analysis yields the net flux and the surface temperature (from which the radiative flux (qrad) is calculated). The incident heat flux is calculated from Eq. (4).

Figure 111 shows the incident heat flux from the DFTs located on top of the diffuser. DFT 0-0 is about 0.3 m (1 ft) above the diffuser surface, facing upward. DFT 8-1 is 2.4 m (8 ft) above the diffuser and DFT 16-1 is 4.9 m (16 ft) above the diffuser; they both face normal to the east and west directions.

Figure 112 shows the incident heat flux from the DFTs located on the 180° spoke axis. DFT 180-1 is about 9 m from the diffuser, DFT 180-2 is about 24 m from the diffuser, and DFT 180-3 is about 42 m from the diffuser.

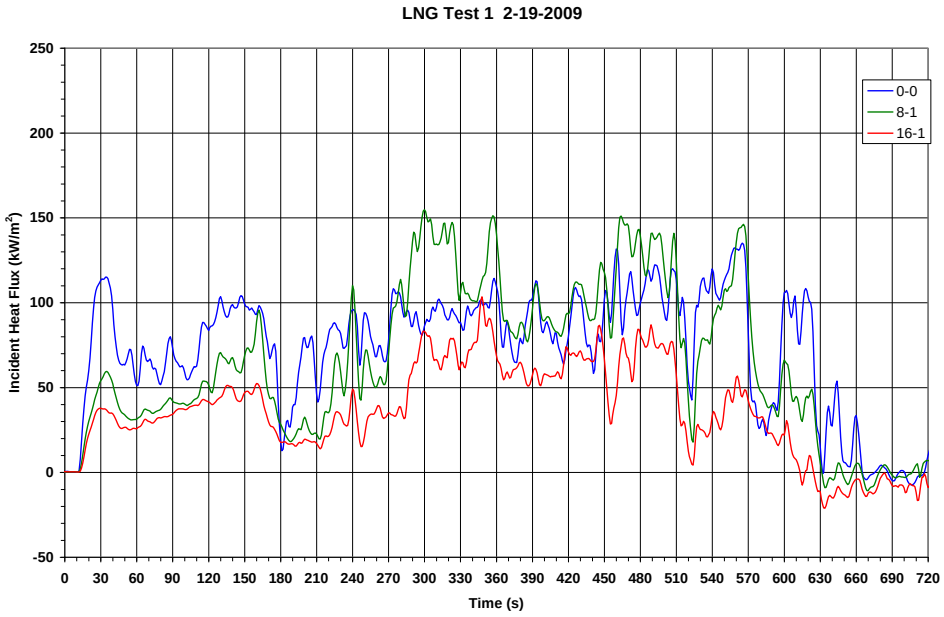

Figure 111 Incident heat flux at the DFTs above the diffuser in Test 1.

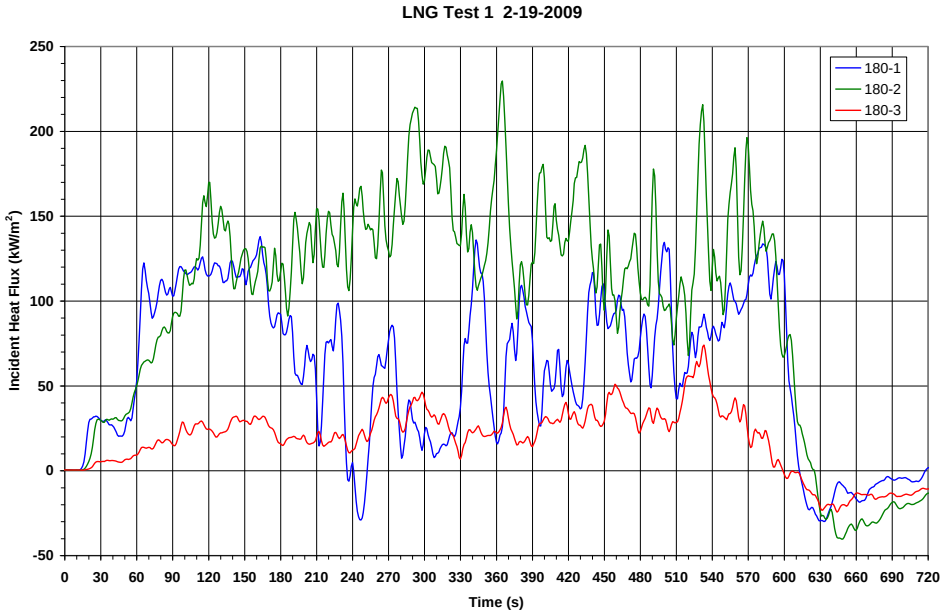

Figure 112 Incident heat flux at the pool DFTs on the 180° spoke in Test 1.

5.9 Pool Water Temperature

Figure 113 presents the pool water temperatures as measured by the type-K thermocouples attached to the three DFT stands on the North spoke. The twenty-seven thermocouples from the other 9 DFT stands show very similar temperatures. The average water temperature from all thirty-six water thermocouples was approximately 4°C, and steady throughout the test.

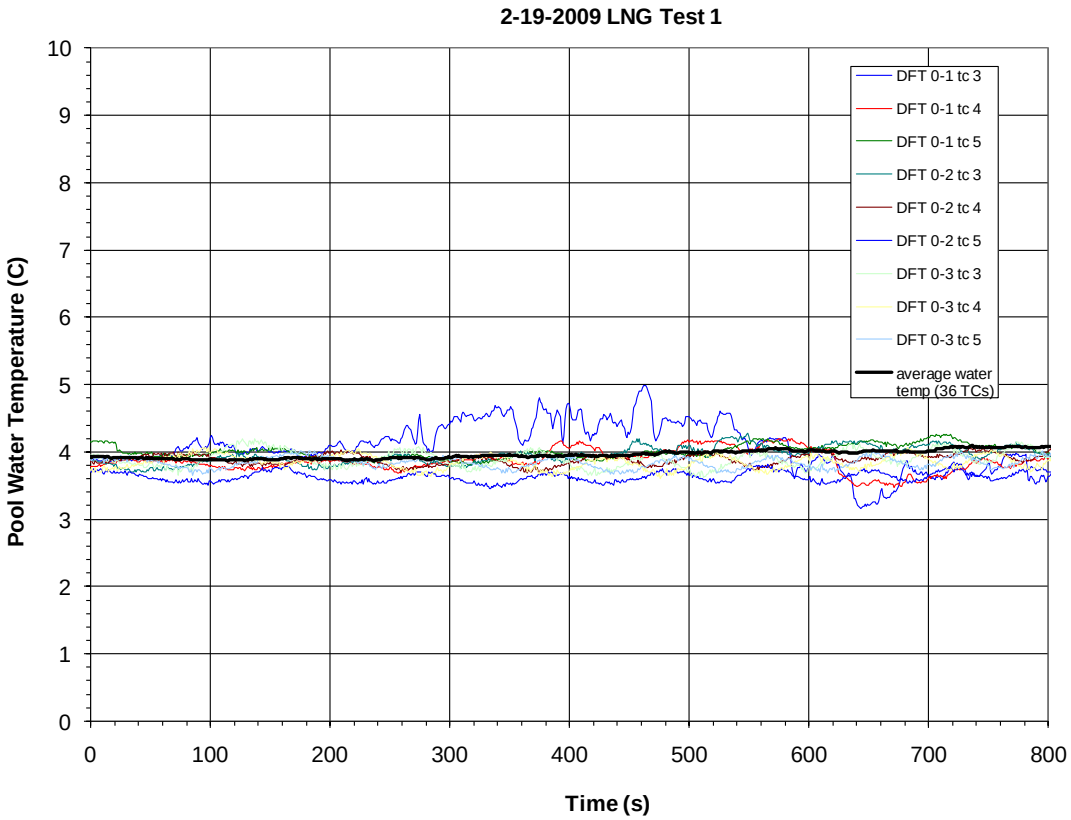

Figure 113 Pool water temperatures in Test 1.

5.10 Flame Temperature

Figure 114 presents the temperatures as measured by the type-K thermocouples attached to a 4.9 m (16 ft) tall rake located on top of the diffuser (note that the diffuser top surface is about 1.8 m above the pool surface). Thermocouples 1 and 2 were in the flame zone the majority of the duration of the fire, with measured temperatures ranging between 800-1000°C.

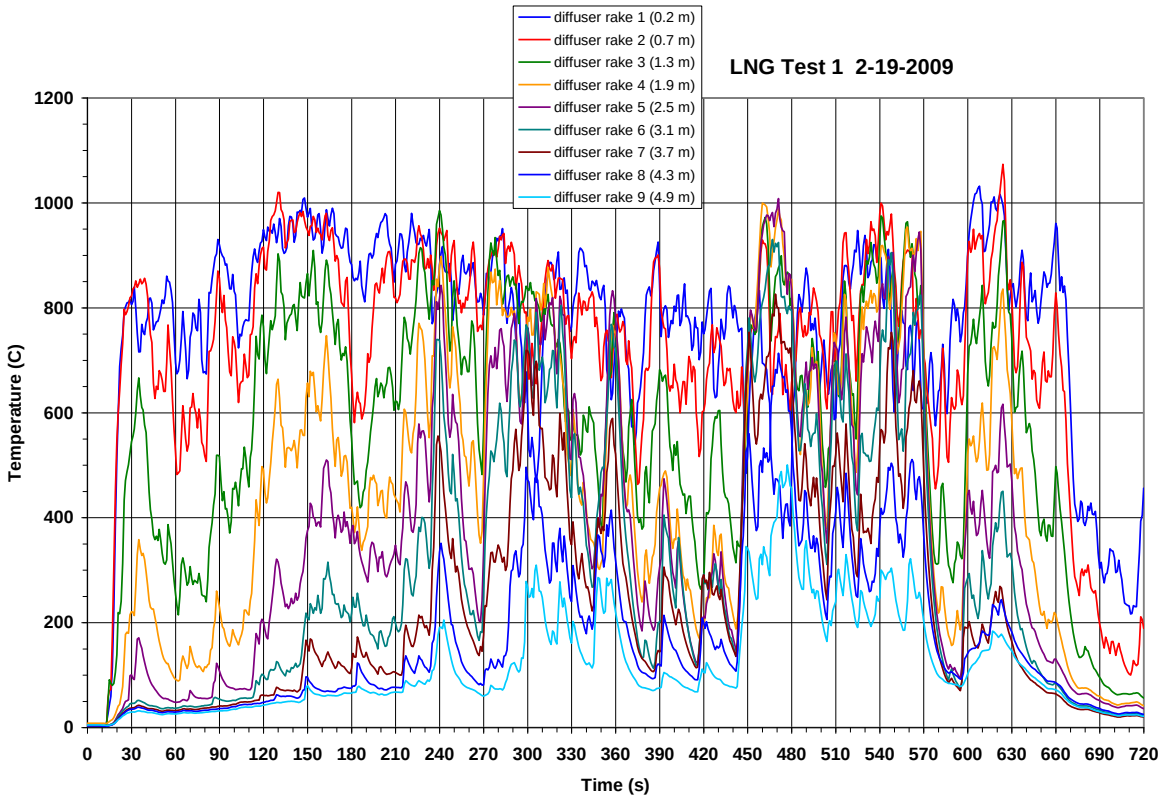

Figure 114 LNG flame temperatures in Test 1.

Figure 115 presents two images obtained at 420 s taken from the IR video cameras located on the East and South spokes. Figure 116 plots the peak temperatures from the IR cameras at 20 s intervals. Note that the temperatures are measured with the IR camera emissivity set to 1. If the emissivity of the flame (ε) and the atmospheric transmission (τ) are known, dividing the measured temperature by $(\tau\varepsilon)^{1/4}$ will yield a corrected temperature [Doebelin 1990]. Over the steady-state interval from 300-520 s, the East and South IR average peak temperatures were 1179±33°C and 1181±41°C, respectively.

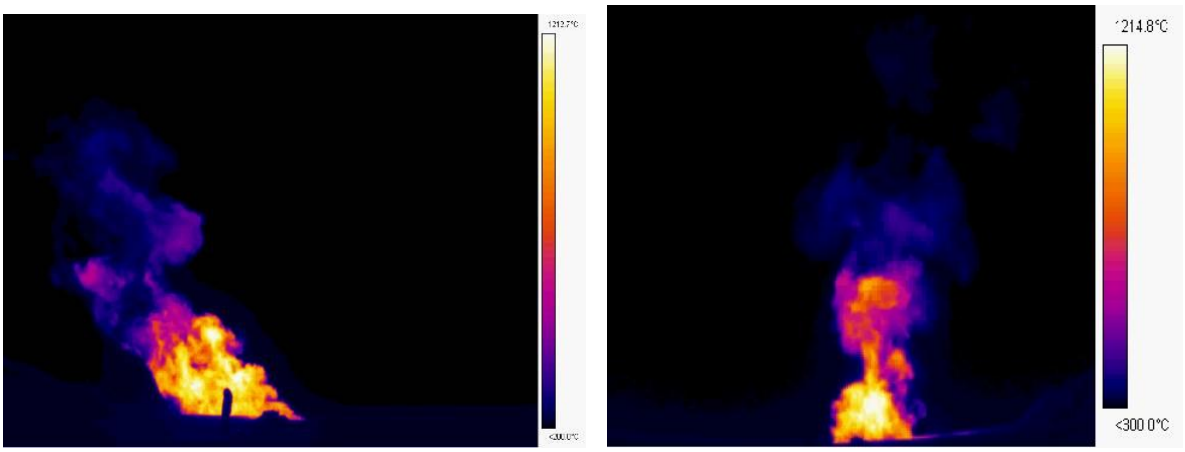

90° spoke 180° spoke

Figure 115 IR camera images at 420 s in Test 1.

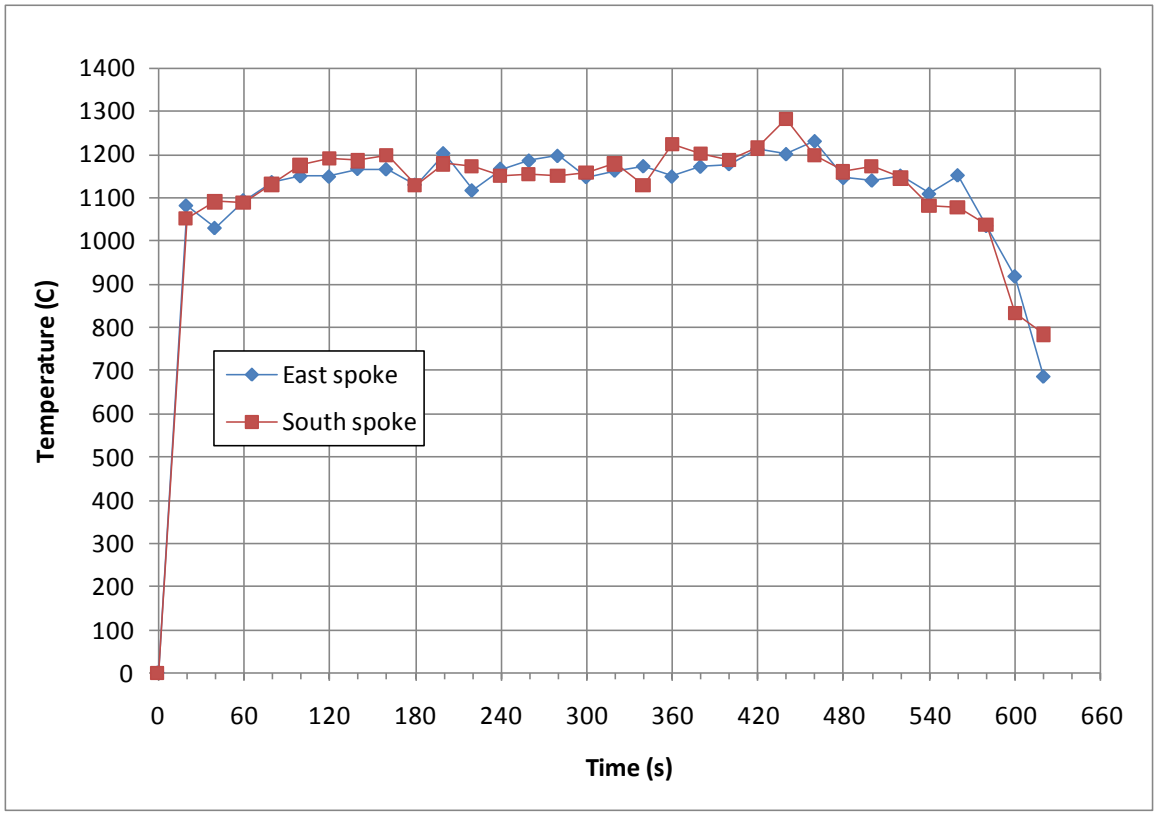

Figure 116 IR image-based peak temperature in Test 1.

5.11 Flame CG, Width, Height, and Area

Extensive MatLab® programs were developed to reduce the video data (camera calibration and image scaling discussion provided in Appendix C) to determine fire morphology (width, height, flame area, etc.). In addition, the video analyses provide information to allow corrections of radiometer data for atmospheric transmission effects, inform on the narrow-view radiometer "spot" results, and determine a time-dependent flame-average surface emissive power (SEP) from the wide-range radiometer data.

The flame plume horizontal center-of-gravity (CG) was determined to determine a time-dependent path length for use in later analyses, especially important in the correction of transmission losses for the narrow view angle radiometers and also used to correct the wide view angle radiometer data to obtain average flame SEP results. The CG (a term commonly used in video analysis to denote the center of area of an image) is calculated based on the calibrated video data from the cameras at each spoke. Figure 117 provides a diagram of a representative flame outline showing the CG, CG shift from pool centerline, flame height, CG height, and flame width at the CG height.

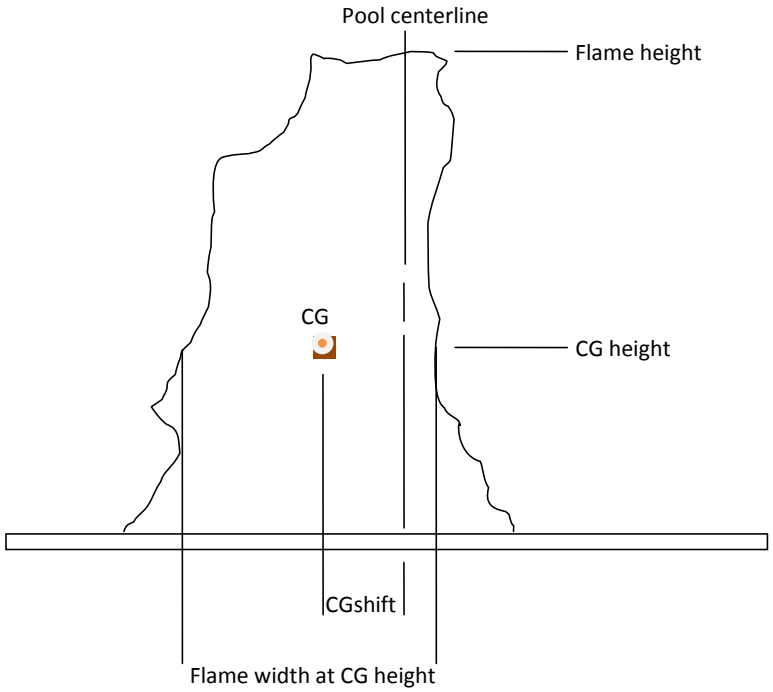

Figure 117 Representative flame morphology.

A color intensity threshold (pixels with red intensity >230±5, depending on camera view) determined those pixels that were determined to be "fire", refer to the analysis for LNG Test 2 that shows images with those pixels covered by a green mask. For example, the flame height was based on the row (scanning from top to bottom) where the fire (green mask) was first encountered.

Figure 118 shows the flame plume CG as determined by data from the east and west cameras showing a shift (from pool center) toward the south camera as a result of the wind predominately from the north. A curve (drawn by fitting the data with regression analysis) showing the average of the east and west shift is also shown.

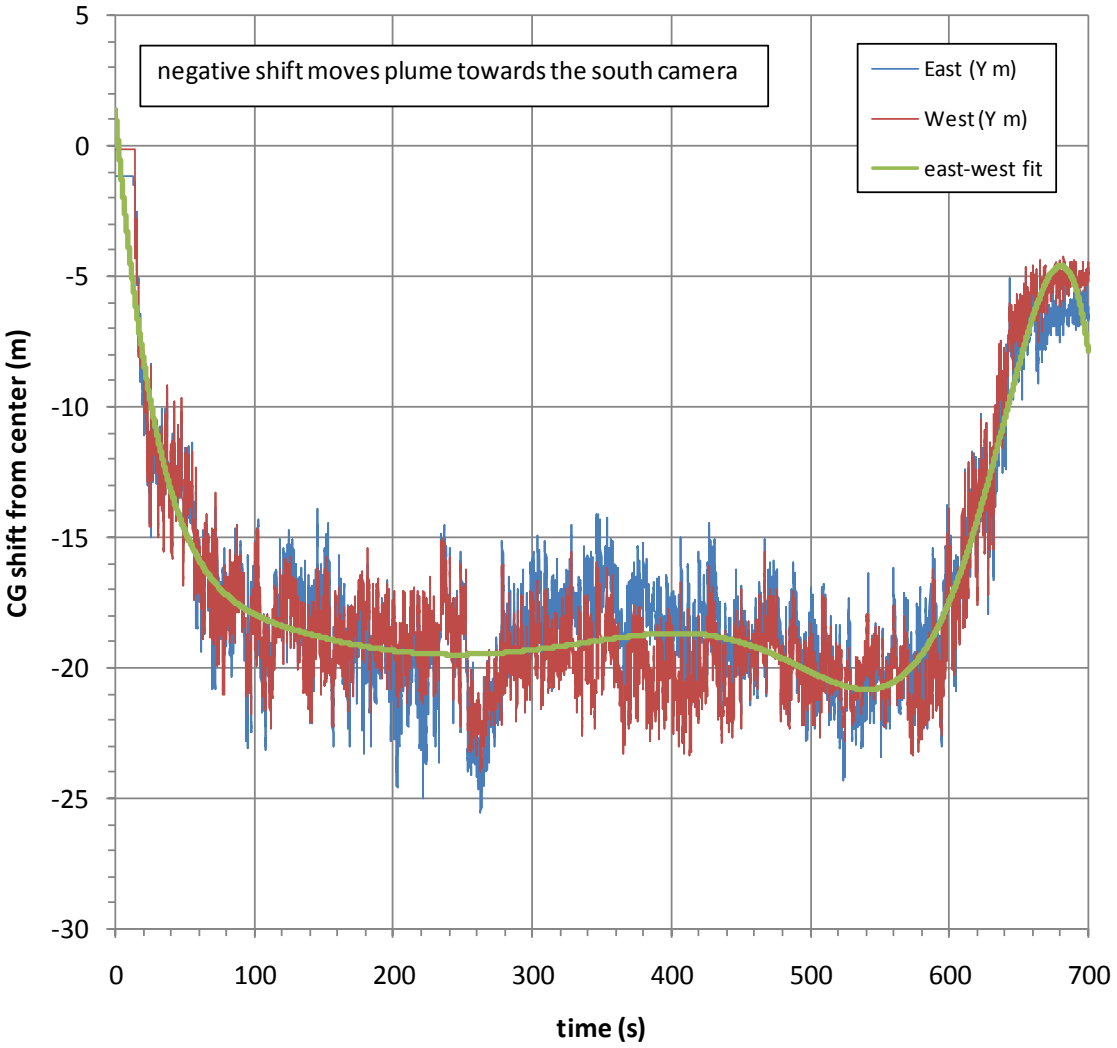

Figure 118 LNG Test 1 flame CG along the N-S axis.

Figure 119 shows the flame plume CG as determined by data from the north and south cameras showing a slight shift toward the east camera, again as a result of the wind predominately from the north as it interacted with the discharge pipe berm. A curve (drawn by fitting the data with regression analysis) showing the average of the east and west shift is also shown.

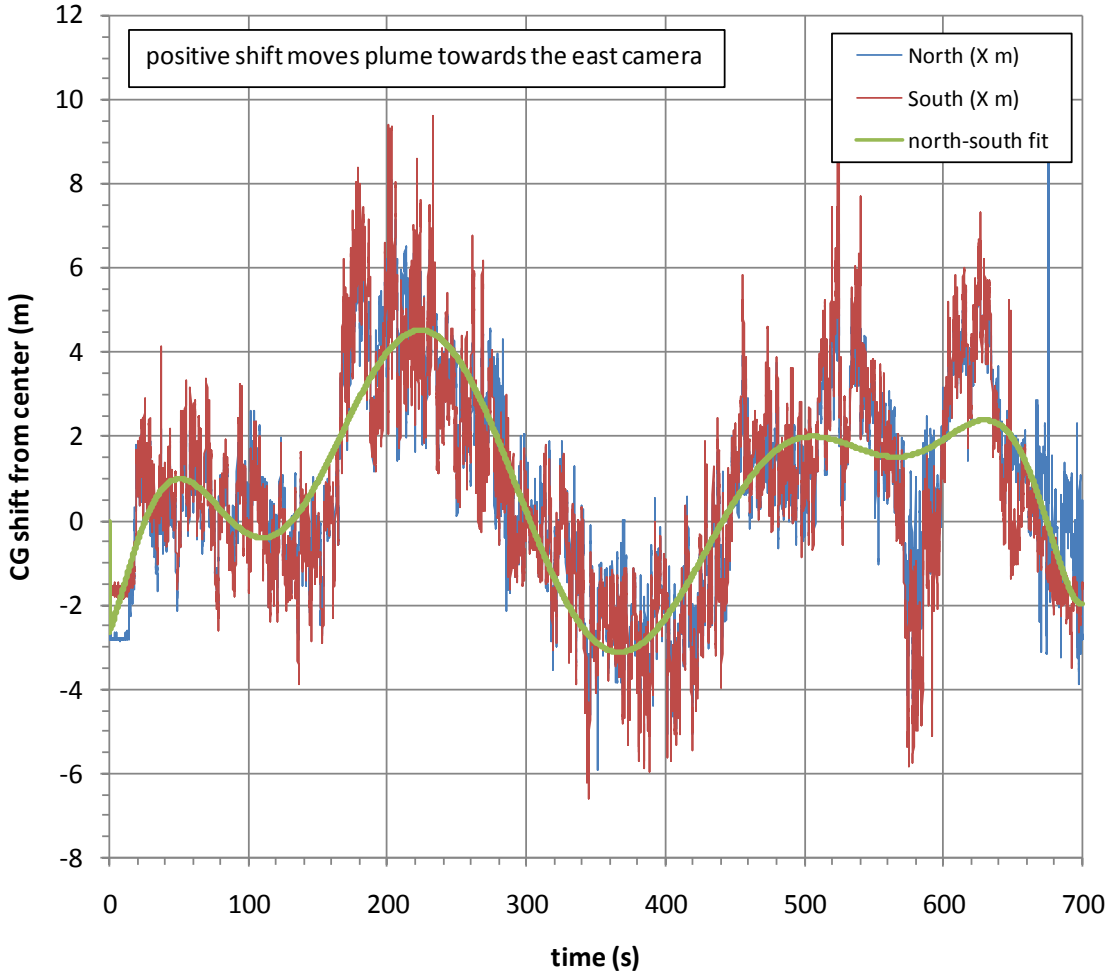

Figure 119 LNG Test 1 flame CG along the E-W axis.

Table 22 presents the average and standard deviation (between 390-500 s) of the shift in CG as determined from the video analyses.

Table 22 Average shift in CG at 390-500 s in Test 1.

390-500 s	North (X m)	South (X m)	East (Y m)	West (Y m)
average	-0.4	-0.2	-18.7	-19.9
st. dev.	1.9	2.3	1.4	1.4

Figure 120 and Figure 121 present the flame height at the CG location and the peak flame height, respectively. Figure 122 and Figure 123 present the flame plume widths at both the vertical CG height and at 15 m (an arbitrary choice) above the pool surface. Finally, the flame area as determined from each camera view is presented in Figure 124.

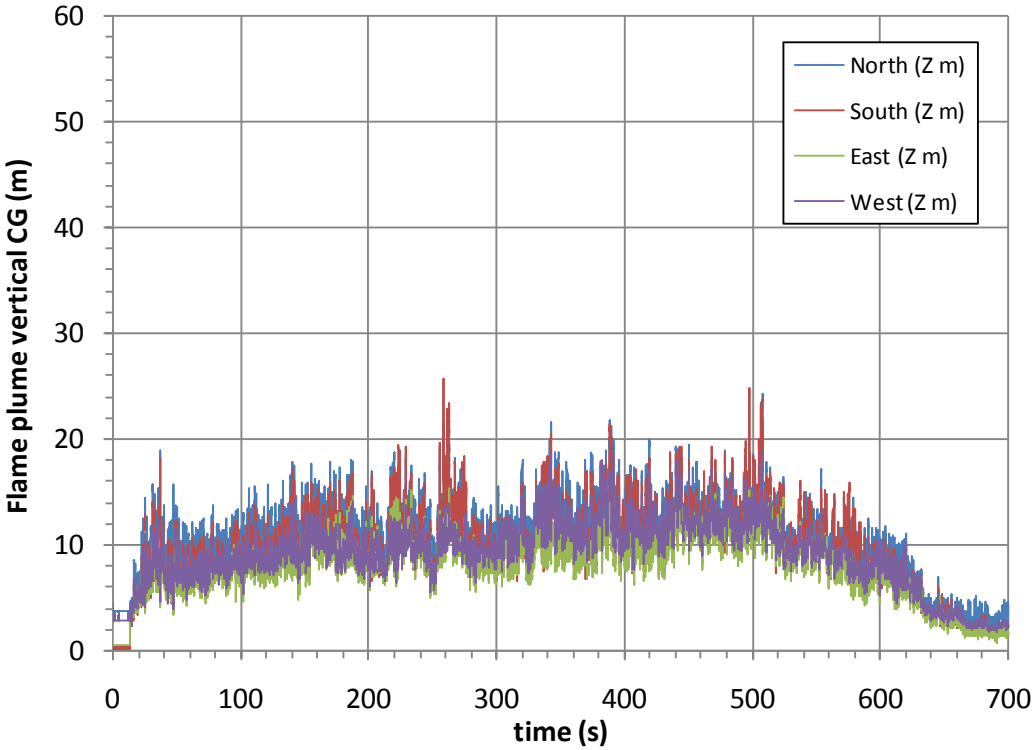

Figure 120 LNG Test 1 CG height.

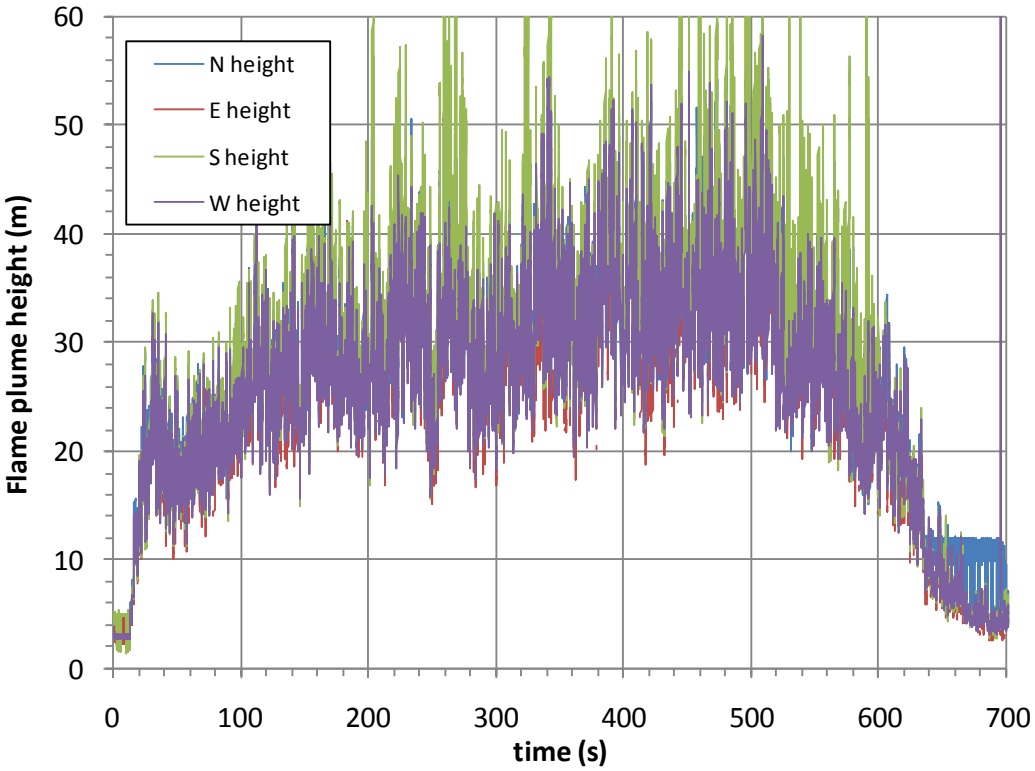

Figure 121 LNG Test 1 flame peak height.

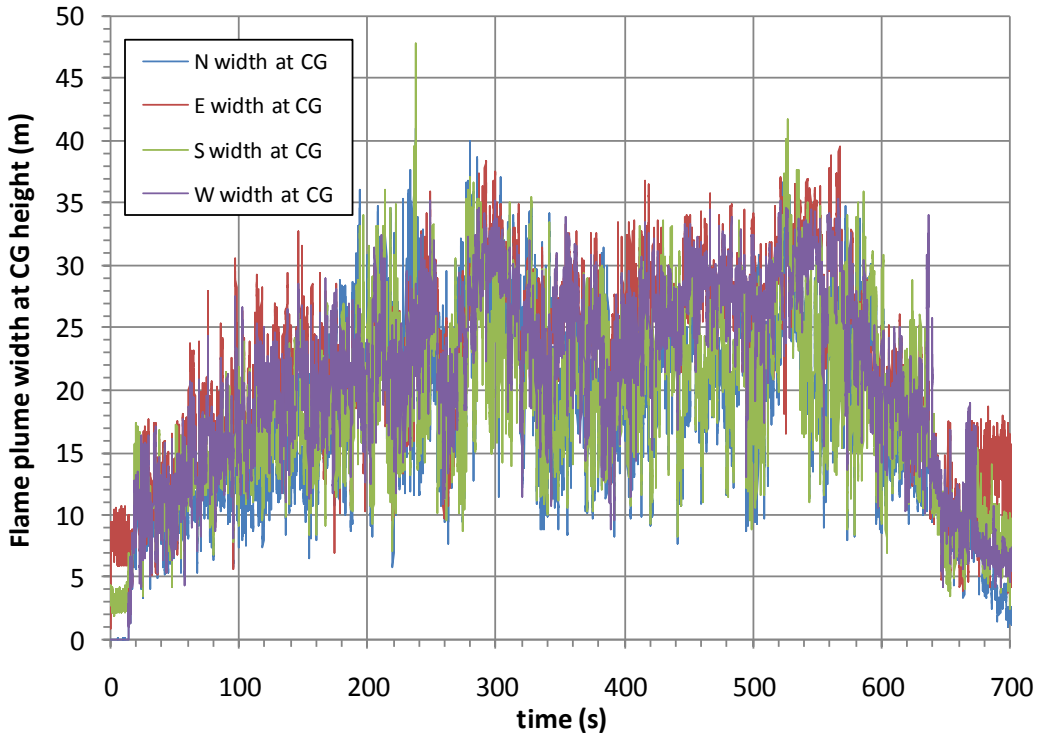

Figure 122 LNG Test 1 flame width at the CG height.

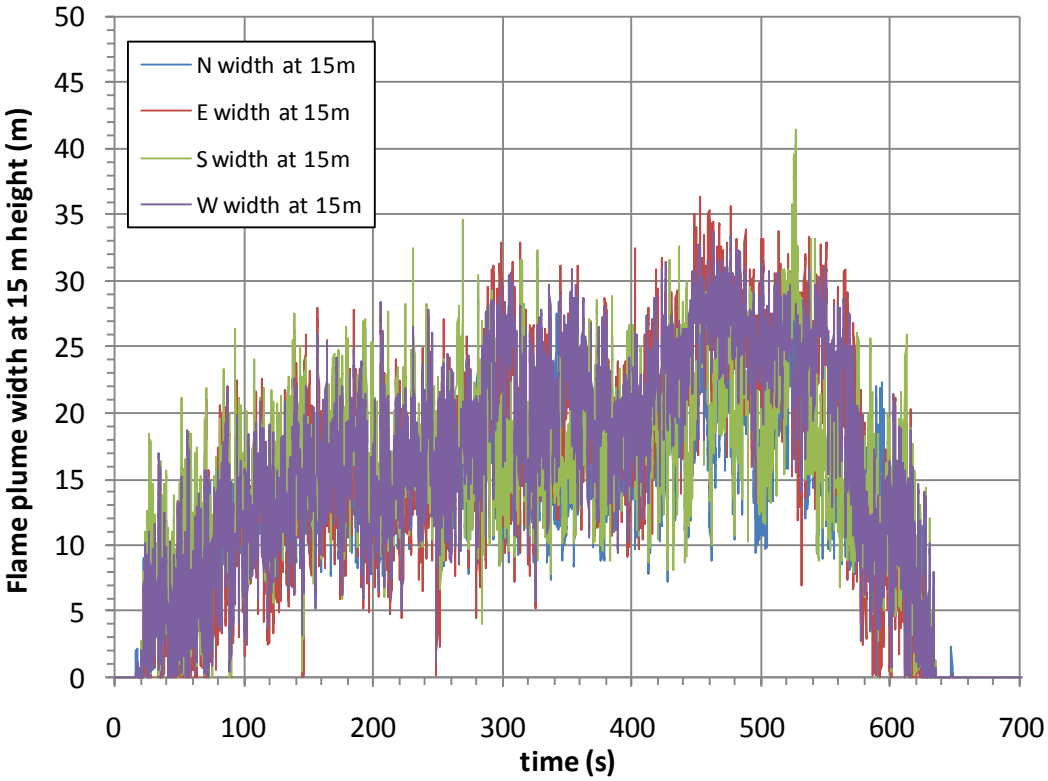

Figure 123 LNG Test 1 flame width at 15 m vertical height.

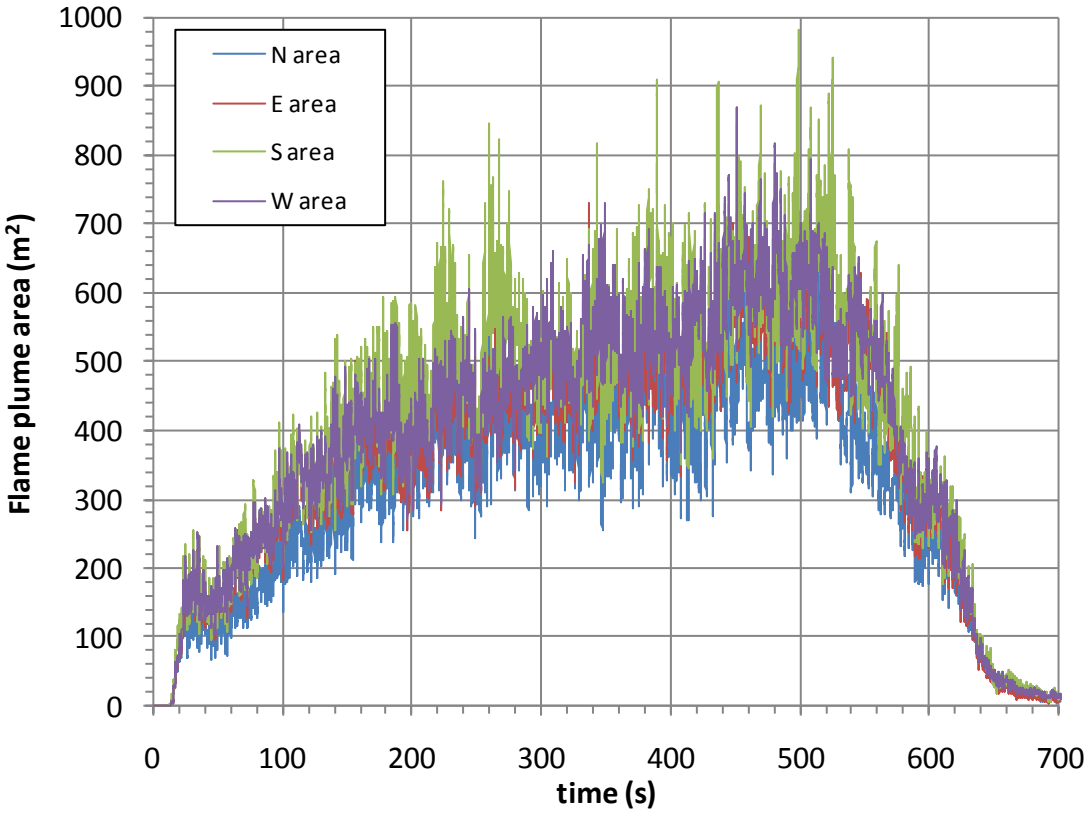

Figure 124 LNG Test 1 flame plume area.

Table 23 presents the average and standard deviation of the flame plume video analysis results (widths and heights in m, area in m^2) during the interval between 390 and 500 s.

Table 23 Flame plume average video analysis results at 390-500 s in Test 1

300-500 s	N width at CG	E width at CG	S width at CG	W width at CG	average width at CG
average	19.6	27.4	22.0	26.5	23.9
st. dev.	4.3	3.6	5.0	3.6	3.7
	N width at 15m	**E width at 15m**	**S width at 15m**	**W width at 15m**	**average width at 15m**
average	18.1	23.7	20.5	24.4	21.7
st. dev.	4.0	5.3	4.7	4.3	2.9
	N height at CG	**E height at CG**	**S height at CG**	**W height at CG**	**average height at CG**
average	13.5	10.6	12.4	12.1	12.2
st. dev.	2.0	1.7	2.4	1.7	1.2
	N height	**E height**	**S height**	**W height**	**average height**
average	36.0	31.8	38.0	34.6	35.1
st. dev.	6.5	5.8	8.1	6.0	2.6
	N area	**E area**	**S area**	**W area**	**average area**
average	456	550	589	589	546
st. dev.	70	77	94	72	63

The wind tilted the flame plume to the South. The average length (not including flame liftoff) was visually determined to be ~70 m (as compared to an average height of ~34 m shown above. The average tilt angle from the vertical axis was ~50°, as indicated in Figure 125. The effective pool diameter was 20.7 m, similar to the average flame width of 23.9 m (at the CG height of 12.2 m) and the average flame width of 21.7 m (at a height of 15 m). This yields a L/D ratio of ~3.4.

410 s 411 s

412 s 428 s

Figure 125 Flame tilt in LNG Test 1.

5.12 Atmospheric Transmission Effects on Radiative Measurements

MODTRAN [Berk, 2000], with a custom desert aerosol atmosphere model, was used to estimate the effects of atmospheric absorption on the radiometer measurements. The input parameters used for MODTRAN were measured just before the test with a local weather station and were recorded as follows:

Altitude: 1627 meters
Temperature: 1°C
Relative Humidity: 35%
Pressure: 12.34 psia (25.13 inHg)

The data were sampled evenly in wave number space (0.5 cm^{-1}) with a spectral range of 650-12500 cm^{-1} (~0.8-15.0 um) and at 8 horizontal path lengths. The MODTRAN spectral transmission vs. path length output is shown in Figure 126.

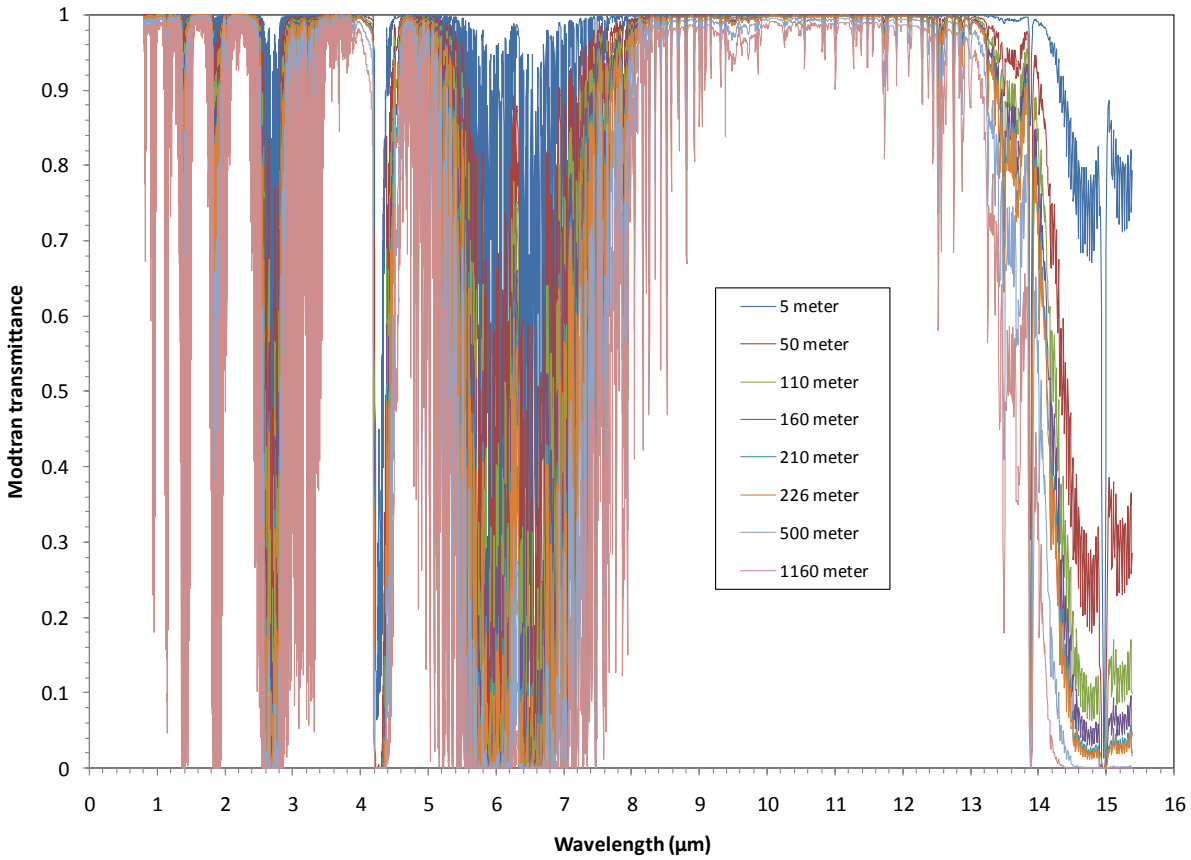

Figure 126 MODTRAN spectral transmission vs. path length for LNG Test 1.

An estimate of the in-band average transmission was determined by first weighting the MODTRAN transmission by the spectral source radiance (using an appropriate blackbody curve). Figure 127 shows the spectral radiance as a function of wavelength at three blackbody

temperatures (1400K, 1500K, and 1600K). Figure 127 also provides the radiance (the spectral radiance times the small change in wavelength between spectral radiance values) at these temperatures.

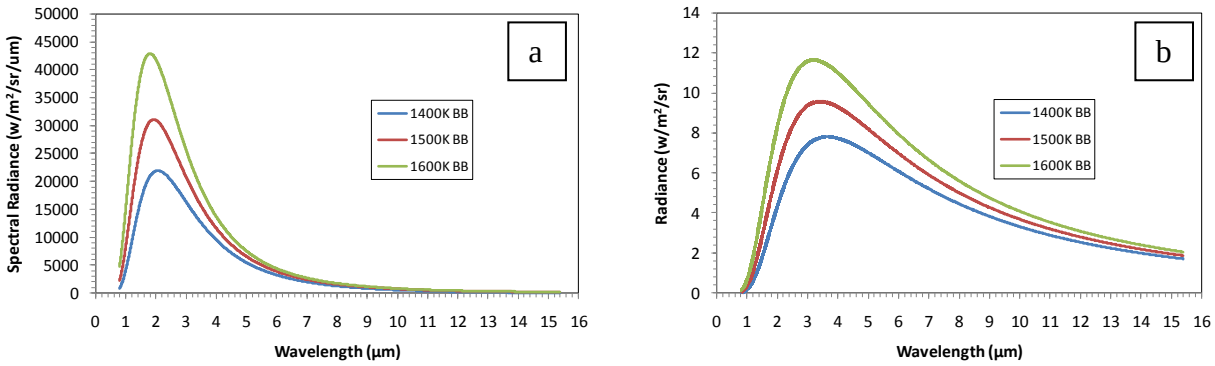

Figure 127 Spectral radiance (a) and radiance (b) vs. wavelength at three blackbody temperatures.

Next, the apparent radiance (the source radiance times the MODTRAN path transmission) as a function of distance was calculated for each blackbody temperature. Figure 128 shows the apparent and source radiance for a 1400K blackbody.

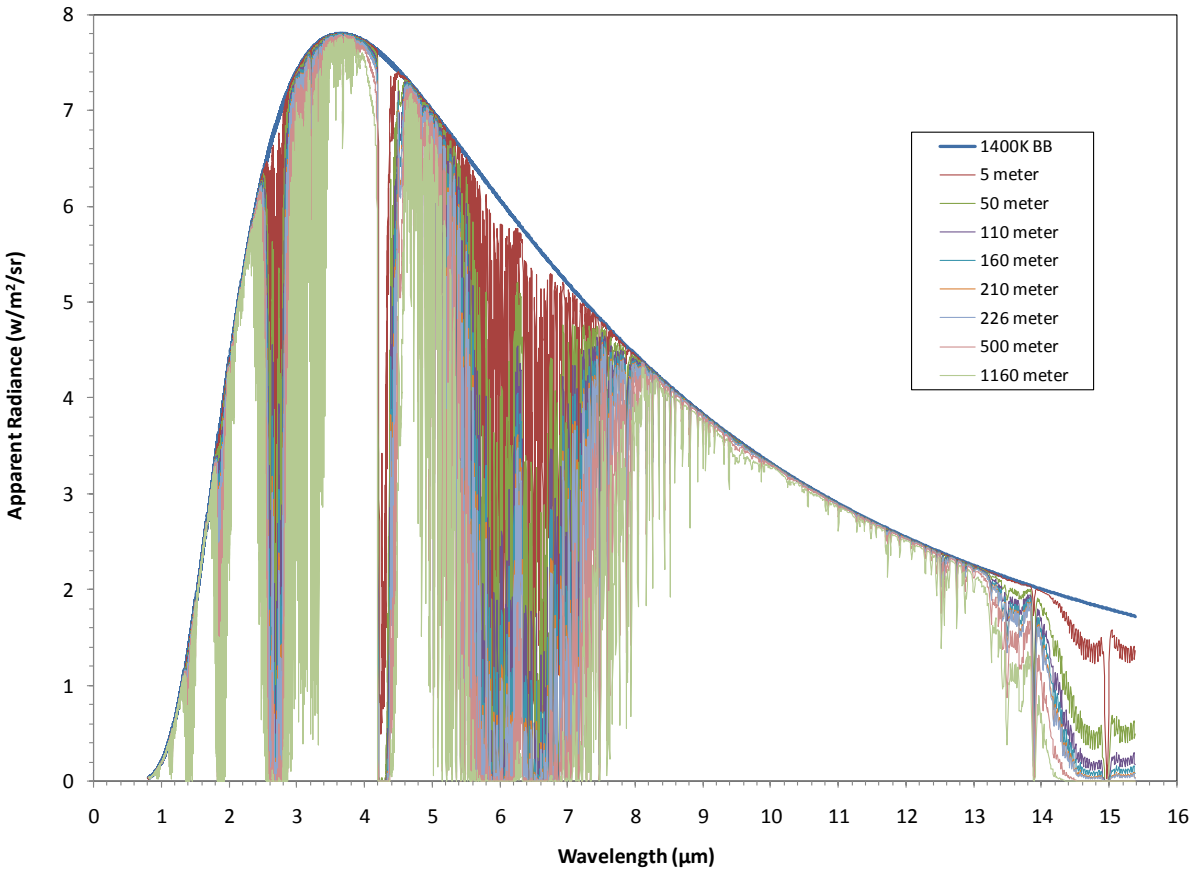

Figure 128 Apparent radiance vs. wavelength for a 1400K blackbody source.

Finally, the in-band average transmission as a function of path length and source temperature was determined by summing up the apparent radiance and dividing by the sum of the source radiance.

The integrated average transmission as a function of path length is given in Figure 129 for the three blackbody source temperatures at the 8 specified path lengths. Spectral analyses (shown later) determined LNG fire temperatures in the range of ~1400-1700K; a fit of the transmission at 1400K was performed for use in correcting measured heat flux data.

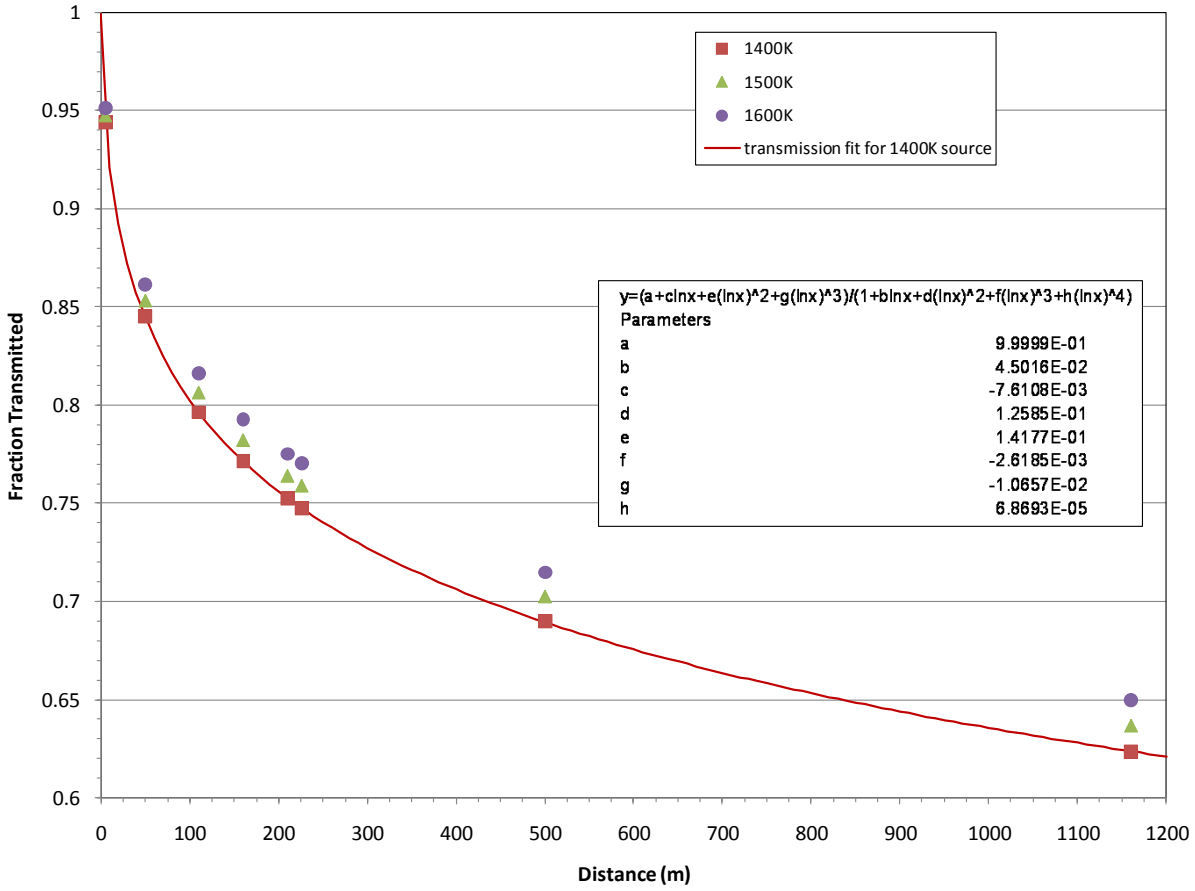

Figure 129 Integrated transmission vs. horizontal path length for LNG Test 1.

The fraction of energy transmitted to each instrument can now be estimated. Table 24 and Table 25 tabulate the distance from the flame CG to the instruments on the North-South and East-West spokes, respectively. These distances, combined with the MODTRAN atmospheric transmission curve (drawn by fitting the data with regression analysis), yielded the transmission fractions for each gauge.

Table 24 Test 1 CG distance and transmission - North and South spoke gauges

time (s)	CG shift (m)	distance to flame CG (m)							fraction transmitted						
		south tow 1	south tow 2	south tow 3	south spec	north tow 1	north tow 2	north tow 3	south tow 1	south tow 2	south tow 3	south spec	north tow 1	north tow 2	north tow 3
0.00	0.0	110.7	159.9	209.8	227.7	109.9	159.8	209.6	0.796	0.772	0.753	0.747	0.797	0.772	0.753
33.00	-11.8	98.9	148.1	198.0	215.9	121.7	171.6	221.4	0.803	0.777	0.757	0.751	0.790	0.767	0.749
66.00	-16.4	94.3	143.5	193.4	211.3	126.3	176.2	226.0	0.806	0.779	0.759	0.752	0.787	0.765	0.748
99.00	-17.9	92.8	142.0	191.9	209.8	127.8	177.7	227.5	0.807	0.780	0.759	0.753	0.787	0.764	0.747
132.00	-18.6	92.1	141.3	191.2	209.1	128.5	178.4	228.2	0.808	0.780	0.759	0.753	0.786	0.764	0.747
165.00	-19.0	91.7	140.9	190.8	208.7	128.9	178.8	228.6	0.808	0.780	0.759	0.753	0.786	0.764	0.747
198.00	-19.3	91.4	140.6	190.5	208.4	129.2	179.1	228.9	0.808	0.780	0.760	0.753	0.786	0.764	0.747
231.00	-19.5	91.2	140.4	190.3	208.2	129.4	179.3	229.1	0.809	0.780	0.760	0.753	0.786	0.764	0.747
264.00	-19.5	91.2	140.4	190.3	208.2	129.4	179.3	229.1	0.809	0.780	0.760	0.753	0.786	0.764	0.747
297.00	-19.3	91.4	140.6	190.5	208.4	129.2	179.1	228.9	0.808	0.780	0.760	0.753	0.786	0.764	0.747
330.00	-19.1	91.6	140.8	190.7	208.6	129.0	178.9	228.7	0.808	0.780	0.760	0.753	0.786	0.764	0.747
363.00	-18.9	91.8	141.0	190.9	208.8	128.8	178.7	228.5	0.808	0.780	0.759	0.753	0.786	0.764	0.747
396.00	**-18.7**	**92.0**	**141.2**	**191.1**	**209.0**	**128.6**	**178.5**	**228.3**	**0.808**	**0.780**	**0.759**	**0.753**	**0.786**	**0.764**	**0.747**
429.00	-18.8	91.9	141.1	191.0	208.9	128.7	178.6	228.4	0.808	0.780	0.759	0.753	0.786	0.764	0.747
462.00	-19.2	91.5	140.7	190.6	208.5	129.1	179.0	228.8	0.808	0.780	0.760	0.753	0.786	0.764	0.747
495.00	-20.0	90.7	139.9	189.8	207.7	129.9	179.8	229.6	0.809	0.781	0.760	0.754	0.786	0.764	0.746
528.00	-20.7	90.0	139.2	189.1	207.0	130.6	180.5	230.3	0.809	0.781	0.760	0.754	0.785	0.763	0.746
561.00	-20.5	90.2	139.4	189.3	207.2	130.4	180.3	230.1	0.809	0.781	0.760	0.754	0.785	0.763	0.746
594.00	-18.3	92.4	141.6	191.5	209.4	128.2	178.1	227.9	0.808	0.780	0.759	0.753	0.786	0.764	0.747
627.00	-13.2	97.5	146.7	196.6	214.5	123.1	173.0	222.8	0.804	0.777	0.757	0.751	0.789	0.766	0.749
660.00	0.0	110.7	159.9	209.8	227.7	109.9	159.8	209.6	0.796	0.772	0.753	0.747	0.797	0.772	0.753

Table 25 Test 1 CG distance and transmission - East and West spoke gauges

time (s)	CG shift (m)	distance to flame CG (m)						fraction transmitted					
		east tow 1	east tow 2	east tow 3	west tow 1	west tow 2	west tow 3	east tow 1	east tow 2	east tow 3	west tow 1	west tow 2	west tow 3
0.00	0.0	110.7	159.9	209.8	109.9	159.8	209.6	0.796	0.772	0.753	0.797	0.772	0.753
33.00	0.5	111.2	160.4	210.3	109.4	159.3	209.1	0.796	0.771	0.753	0.797	0.772	0.753
66.00	0.7	111.4	160.6	210.5	109.2	159.1	208.9	0.796	0.771	0.753	0.797	0.772	0.753
99.00	-0.3	110.4	159.6	209.5	110.2	160.1	209.9	0.796	0.772	0.753	0.796	0.772	0.753
132.00	0.0	110.7	159.9	209.8	109.9	159.8	209.6	0.796	0.772	0.753	0.797	0.772	0.753
165.00	1.9	112.6	161.8	211.7	108.0	157.9	207.7	0.795	0.771	0.752	0.798	0.772	0.754
198.00	3.9	114.6	163.8	213.7	106.0	155.9	205.7	0.794	0.770	0.752	0.799	0.773	0.754
231.00	4.5	115.2	164.4	214.3	105.4	155.3	205.1	0.794	0.770	0.751	0.799	0.774	0.754
264.00	3.1	113.8	163.0	212.9	106.8	156.7	206.5	0.794	0.770	0.752	0.798	0.773	0.754
297.00	0.5	111.2	160.4	210.3	109.4	159.3	209.1	0.796	0.771	0.753	0.797	0.772	0.753
330.00	-2.0	108.7	157.9	207.8	111.9	161.8	211.6	0.797	0.772	0.754	0.795	0.771	0.752
363.00	-3.1	107.6	156.8	206.7	113.0	162.9	212.7	0.798	0.773	0.754	0.795	0.770	0.752
396.00	**-2.5**	**108.2**	**157.4**	**207.3**	**112.4**	**162.3**	**212.1**	**0.798**	**0.773**	**0.754**	**0.795**	**0.771**	**0.752**
429.00	-0.7	110.0	159.2	209.1	110.6	160.5	210.3	0.797	0.772	0.753	0.796	0.771	0.753
462.00	1.0	111.7	160.9	210.8	108.9	158.8	208.6	0.795	0.771	0.753	0.797	0.772	0.753
495.00	1.9	112.6	161.8	211.7	108.0	157.9	207.7	0.795	0.771	0.752	0.798	0.772	0.754
528.00	1.9	112.6	161.8	211.7	108.0	157.9	207.7	0.795	0.771	0.752	0.798	0.772	0.754
561.00	1.5	112.2	161.4	211.3	108.4	158.3	208.1	0.795	0.771	0.752	0.797	0.772	0.753
594.00	1.8	112.5	161.7	211.6	108.1	158.0	207.8	0.795	0.771	0.752	0.798	0.772	0.754
627.00	2.4	113.1	162.3	212.2	107.5	157.4	207.2	0.795	0.771	0.752	0.798	0.773	0.754
660.00	0.0	110.7	159.9	209.8	109.9	159.8	209.6	0.796	0.772	0.753	0.797	0.772	0.753

There was little variance in the CG shift from the pool center during the steady-state interval. Therefore, the atmospheric transmission fraction values at t = 396 s, presented in Table 26, were used for correcting the radiometer data to obtain the average SEP values for the interval between 390-500 s.

Table 26 Atmospheric transmission fraction for correcting Test 1 radiometer data.

spoke	tower 1	tower 2	tower 3
north	0.786	0.764	0.747
south	0.808	0.780	0.759
east	0.798	0.773	0.754
west	0.795	0.771	0.752

Table 27 presents the average radiometer NV and WV heat flux data (units in kW/m^2) corrected by the transmission fractions (uncorrected data divided by the transmission fraction listed in Table 26.

Table 27 LNG Test 1 radiometer data (corrected) for the interval between 390-500 s.

	narrow-angle radiometers							wide-angle radiometers		
nominal spot height above pool (m)	7	21	35	48	62	35	35	35	35	35
nominal distance from pool center (m)	110	110	110	110	110	160	210	110	160	210
North spoke	**0 hfg 1**	**0 hfg 2**	**0 hfg 3**	**0 hfg 4**	**0 hfg 5**	**0 hfg 7**	**0 hfg 9**	**0 hfg 6**	**0 hfg 8**	**0 hfg 10**
average kW/m^2	216.1	93.6	10.5	0.9	0.3	1.8	1.0	2.4	1.5	0.8
st.dev.	7.4	42.7	11.0	0.7	0.1	1.4	1.3	0.3	0.1	0.1
South spoke	**180 hfg 1**	**180 hfg 2**	**180 hfg 3**	**180 hfg 4**	**180 hfg 5**	**180 hfg 7**	**180 hfg 9**	**180 hfg 6**	**180 hfg 8**	**180 hfg 10**
average kW/m^2	236.3	203.1	115.4	54.2	19.7	6.5	54.6	6.2	2.4	1.3
st.dev.	20.6	50.9	58.3	52.6	25.6	1.0	38.5	0.9	0.3	0.1
East spoke								**90 hfg 6**	**90 hfg 8**	**90 hfg 10**
average kW/m^2								4.2	1.8	1.2
st.dev.								0.6	0.2	0.2
West spoke								**270 hfg 6**	**270 hfg 8**	**270 hfg 10**
average kW/m^2								4.5	1.9	1.0
st.dev.								0.5	0.2	0.2

5.13 Flame Radiant Fraction

Engineers performing hazard analyses can estimate remote radiant fluxes starting from estimates of pool areas and surface mass transfer rates together with radiant fractions (for nearby targets engineers can calculate fluxes using values of the SEP). Note that radiant fractions, defined as the fraction of the total chemical heat release that is radiated to the surroundings, and treating the flame as a point source, tend to be independent of the fire size in the absence of a smoke mantle.

The 4π radiant fraction, χ_{rad}, can be estimated using Eq. 44:

$$\chi_{rad} = \frac{4\pi r^2 \left(q''/\tau\right)}{m_b h_c} \tag{44}$$

where r is the CG distance (m) from the fire, q''/τ is the wide-view heat flux (kW/m^2) corrected for the transmission loss (τ), and $m_b h_c$ is the average total heat release by combustion (m_b is the mass burning rate (kg/s, assumed equal to the reservoir mass flow rate) and h_c is methane heat of combustion (55687 kJ/kg)).

Figure 130 presents the time-dependent radiant fraction using the wide-view radiometer data from all spokes (corrected for transmission losses) and also shows the LNG mass flow rate from the reservoir.

Table 28 presents the average radiant fraction from each gauge during the steady-state interval from 390-500 s. The listed standard deviation is due to the variability over the interval. The average radiant fraction from all measurements and one standard deviation is 0.21±0.04 (2 sigma).

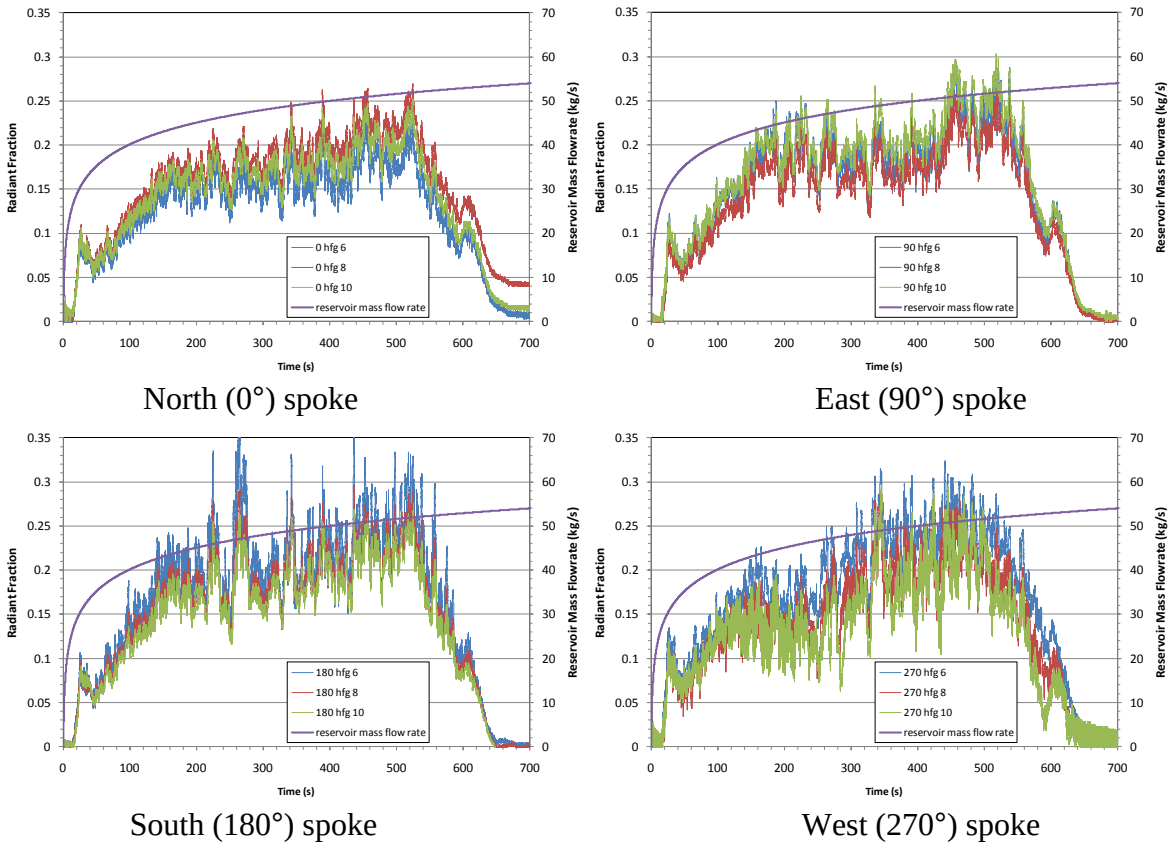

North (0°) spoke

East (90°) spoke

South (180°) spoke

West (270°) spoke

Figure 130 Test 1 radiant fraction from the WV radiometers.

Table 28 LNG Test 1 Radiant Fraction

	Wide-View Heat Flux	**Distance to CG**	**Radiant Fraction**	
Duration 390-500s	kW/m^2	m	average	st.dev.
N Tower 1	2.4	128.6	0.17	0.02
N Tower 2	1.5	178.5	0.21	0.02
N Tower 3	0.8	228.3	0.20	0.02
S Tower 1	6.2	92.0	0.23	0.04
S Tower 2	2.4	141.2	0.22	0.03
S Tower 3	1.3	191.1	0.21	0.02
E Tower 1	4.2	108.2	0.22	0.03
E Tower 2	1.8	157.4	0.20	0.03
E Tower 3	1.2	207.3	0.23	0.03
W Tower 1	4.5	112.4	0.25	0.03
W Tower 2	1.9	162.3	0.22	0.03
W Tower 3	1.0	212.1	0.21	0.03

5.14 Flame Surface Emissive Power

The video data was used in conjunction with the wide-view radiometers to determine a time-dependent flame surface emissive power (SEP). The following discussion provides some background theory on radiometers and the methodology used to determine the SEP.

Radiometers and their Calibrations

Radiometers are measuring devices which respond to incident radiation. Radiometers may have a view angle of 180° or less, where a 180° view angle implies that the gauge sees radiation in the entire hemisphere in front of the gauge. It is important to note, however, that gauges respond differently to heat flux that is incident on the gauge in a nearly normal direction as compared to the same level of source radiation that is incident at a sharply off-normal direction. Some of the reasons for this can be understood from a review of the basics of radiation heat transfer.

The sensing element inside a radiometer responds to heat flux through the element. The radiometer is constructed in such a way as to minimize convective and conductive heat transfer to the sensing element, so that the radiation is the dominant term. Radiometers are typically used in applications in which the radiation emitted from the sensing element is much smaller than the amount absorbed at the sensing element, such that the heat flux through the element can be assumed to be directly proportional to the incident radiation reaching the surface of the element. With these assumptions, we can express the heat flux through the sensing element in terms of the incident radiation over the field of view of the radiometer. Since the incident radiation may vary dramatically over the field of view, we will write the heat flux to the element in integral form:

$$q_{sensor} = \alpha_{sensor} \int_{\Omega_{gage}} I \cos\theta \, d\Omega \tag{45}$$

where q_{sensor} is the heat flux through the sensing element, α_{sensor} is the absorptivity of the sensor, I is the total radiation intensity from a given direction, θ is the angle between the surface normal and the incident radiation vector, and Ω_{gauge} is the solid angle seen by the radiometer. The direction cosine arises because energy incident at sharp angles does not "see" the surface as much as energy incident nearly normal to the surface. The gauges are typically calibrated against a blackbody source. If an isothermal blackbody source which fills the entire view angle is used for the calibration, then the incident intensity is uniform,

$$I_{b,cal} = \frac{1}{\pi} \sigma T_b^4 \tag{46}$$

and may be taken outside the integral. The heat flux through the sensing element can then be found by integration,

$$q_{sensor,cal} = \frac{1}{\pi} \sigma T_b^4 \, \alpha_{sensor} \int_{\Omega_{gage}} \cos\theta \, d\Omega \, . \tag{47}$$

For radiometers which see a round field of view, the integral over the solid angle yields

$$\int_{\Omega_{gage}} \cos\theta \, d\Omega = \int_0^{2\pi} \int_0^{\theta_{\max}} \sin\theta \cos\theta \, d\theta \, d\varphi = \pi\left(1 - \cos^2 \theta_{\max}\right) \tag{48}$$

where $\theta_{\max}$ is half of the view angle (i.e., $\theta_{\max}$ is 90° for a gauge with a 180° field of view) and φ is the azimuthal angle. Substituting Eq. (48) into Eq. (47) and writing in terms of the emissive power of the blackbody ($E_{b,\,cal} = \pi\, I_{b,\,cal} = \sigma\, T_b^4$), the heat flux through the sensor is

$$q_{sensor,\,cal} = \alpha_{sensor}\left(1 - \cos^2 \theta_{\max}\right) E_{b,\,cal} \,. \tag{49}$$

Note from this equation that the heat flux through the sensing element is equal to the emissive power of the blackbody only if the sensor absorptivity is unity and the sensor has a 180° field of view. If what is desired from the calibration, regardless of sensor absorptivity and view angle, is a correlation between the gauge response and the emissive power of a surface, then the factors related to the absorptivity and view angle can be absorbed into the calibration for the gauge response. In this scenario, the gauge output is an averaged emissive power of its surroundings (with some sensitivity to the view angle for non-uniform environments),

$$E_{environment} = \frac{q_{sensor}}{\alpha_{sensor}\left(1 - \cos^2 \theta_{\max}\right)} \,. \tag{50}$$

The relationship between the gauge output via its calibration ($E_{environment}$) and the heat flux absorbed by the sensor surface (q_{sensor}) then depends upon the gauge's field of view. This explains why narrow-angle radiometers far from a high-temperature source may report values of emissive power that are greater than the total heat flux reaching that location. A radiometer, used in this manner, is not reporting the incident heat flux but rather the average emissive power of the environment as seen through its field of view. The narrow-angle gauge may be reporting the average emissive power of the high-temperature source, while a wide-angle radiometer adjacent to it is reporting the average emissive power over a view angle that also includes a large amount of cold background. In theory the average emissive power reported by the radiometer would approach the incident heat flux as the field of view of the radiometer goes to 180°, but with narrow-angle gauges these values may differ by an order of magnitude or more.

Finding the Emissive Power of a High-Temperature Source within a Radiometer's Field of View

While the average emissive power of the surroundings may be of interest in itself, in other scenarios we wish to know the average emissive power of only a portion of the radiometer's field of view. This can be determined when video of the surroundings is available, if the heat flux is dominated by the portion of the field of view that is of interest, in the following manner.

Assume that there is a high-temperature radiation source which dominates the radiation heat transfer to the radiometer, and that this source occupies only a fraction of the radiometer's field of view. If the incident energy can be assumed to be entirely from the high-temperature source, then the integral over the field of view of the gauge is the same as the integral over the solid angle subtended by the high-temperature source

$$q_{sensor} = \alpha_{sensor} \int_{\Omega_{source}} I \cos\theta \, d\Omega \qquad I_{source} >> I_{background} \tag{51}$$

where Ω_{source} is the solid angle of the high-temperature source as seen from the radiometer ($\Omega_{source} < \Omega_{gauge}$). The gauge calibration returns $E_{environment}$, an average emissive power of the environment seen through the entire field of view of the gauge (Ω_{gauge}). We wish to compute the average emissive power over Ω_{source}. As shown in Eq. (50), the average emissive power can be determined by dividing the heat flux through the sensor by the product of the sensor absorptivity and a factor related to the view angle from the gauge to the source. A similar method can be used to determine the average emissive power of the high-temperature source, denoted E_{source}. We assume that I_{source} is a constant over Ω_{source} such that it can be taken outside the integral in Eq. (51), and that the emission from the source is diffuse such that $E_{source} = \pi \, I_{source}$. With these assumptions, Eq. (51) can be written as

$$E_{source} = \frac{q_{sensor}}{\alpha_{sensor} \frac{1}{\pi} \int_{\Omega_{source}} \cos\theta \, d\Omega} . \tag{52}$$

Comparing Eqs. (50) and (52), the average emissive power of the high-temperature source can be related to the gauge output ($E_{environment}$) by applying a correction factor based on the ratio of the view factors,

$$E_{source} = E_{environment} \frac{\pi \left(1 - \cos^2 \theta_{\max}\right)}{\int_{\Omega_{source}} \cos\theta \, d\theta} . \tag{53}$$

In applications in which the high-temperature source may have an irregular and possibly time-varying shape, the integral in the denominator must be determined from photos or videos of the environment. For this discussion we will assume that the pixels from a photograph or video have been mapped to a plane roughly at the location of the high-temperature source, that pixels within the high-temperature source region have already been identified for each image, that the radiometer is located at a known distance from the plane, that the orientation of the radiometer relative to the image plane is known, and that the location of the projection of the sensing element's surface normal onto the image plane is known. The integral is approximated by summing the contributions from all pixels identified as being within the high-temperature source region,

$$\int_{\Omega_{source}} \cos\theta \, d\Omega \approx \sum_{pixels\,in\,source} \cos\theta \frac{\cos\phi \; dA_{pixel}}{S^2} , \tag{54}$$

where dA_{pixel} is the area of each pixel on the image plane, S is the distance from the radiometer to the pixel, θ is the angle between the radiometer's surface normal and the ray from the radiometer to the pixel, and ϕ is the angle between the image plane's surface normal and the ray from the pixel to the radiometer (refer to Figure 131).

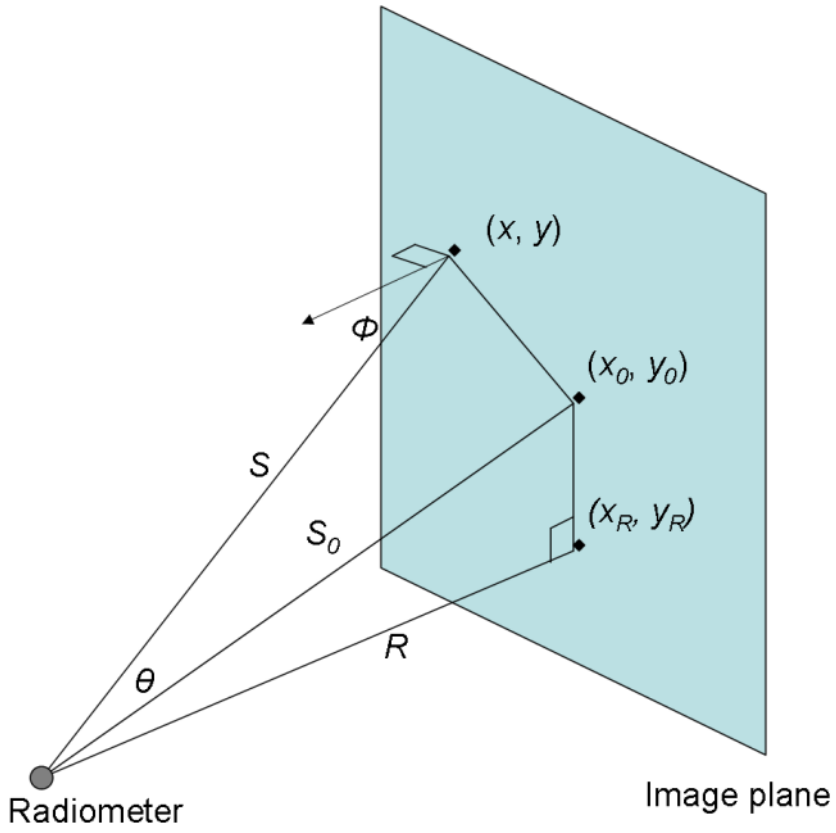

Figure 131 Sketch of geometry from radiometer, image plane, and pixels.

Assume that the plane onto which the photograph is projected is the *x*-*y* plane. Assume that the radiometer is located a distance R from the plane. Let the location on the plane nearest the radiometer be (x_R, y_R). Let the location on the image plane that the surface normal of the radiometer projects onto be denoted (x_0, y_0), which need not be the point on the plane nearest the radiometer. Then, the distance S_0 from the radiometer to the point (x_0, y_0) is

$$S_0 = \sqrt{R^2 + (x_0 - x_R)^2 + (y_0 - y_R)^2} \tag{55}$$

and the distance from any location on the image plane to the radiometer is given by

$$S = \sqrt{R^2 + (y - y_R)^2 + (x - x_R)^2}\,. \tag{56}$$

The cosine of θ can be found from the law of cosines,

$$\cos\theta = \frac{S_0^2 + S^2 - (x - x_0)^2 - (y - y_0)^2}{2 S_0 S} \tag{57}$$

while the cosine of ϕ can be found from its definition,

$$\cos\phi = \frac{R}{S}. \tag{58}$$

Substituting Eqs. (55) through (58) into Eq. (54) yields the scaling factor used in Eq. (53). The equation relating the emissive power of the high-temperature source to the gauge output at a particular time can be written as

$$E_{source} = E_{environment} \frac{\pi\left(1-\cos^2\theta_{\max}\right)}{\sum_{pixels\,in\,source} \cos\theta \frac{\cos\phi\ dA_{pixel}}{S^2}} \tag{59}$$

where the expression in the denominator has been left in terms of the direction cosines and distance for compactness and clarity in reading. For applications in which the high-temperature source is time-varying in size or intensity, the scaling factor can be applied on a frame-by-frame basis using video images and the radiometer output corresponding to the image.

Figure 132 and Figure 133 present the transmission corrected incident heat flux (green curve) from the wide-view radiometers on all spokes. These figures also show the view factor multiplier (blue curve) for the $E_{environment}$ term shown in Eq. (59). Finally, these figures also present the time-dependent overall flame SEP (red curve), the result of multiplying the transmission-corrected incident heat flux times the view factor multiplier.

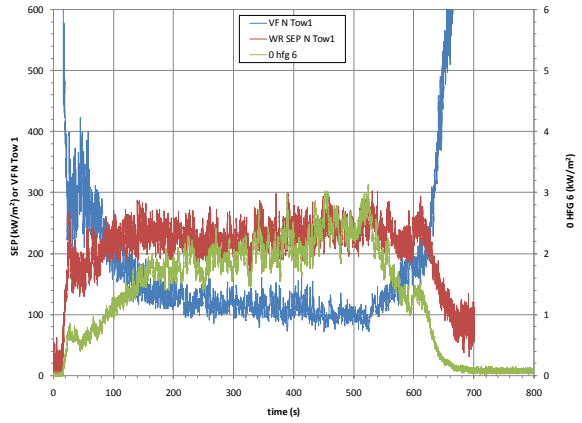

North Tower 1

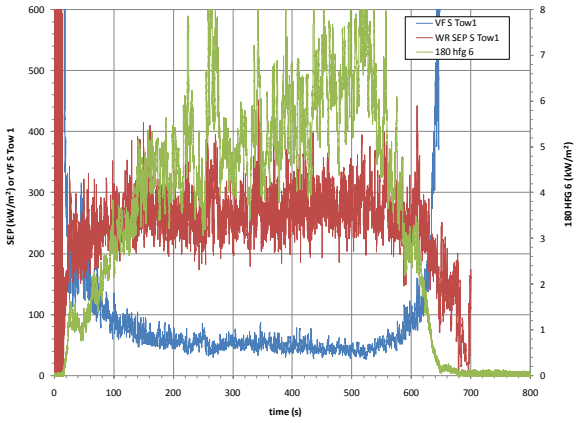

South Tower 1

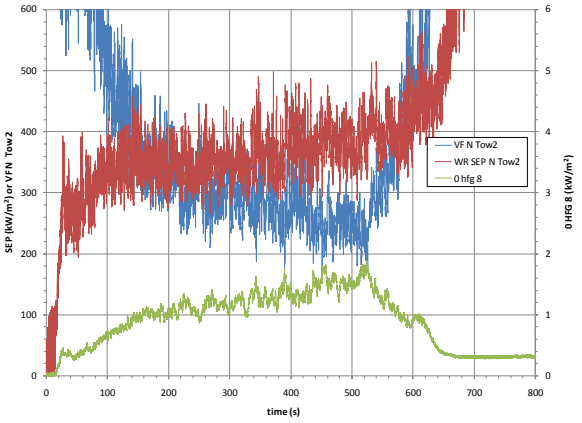

North Tower 2

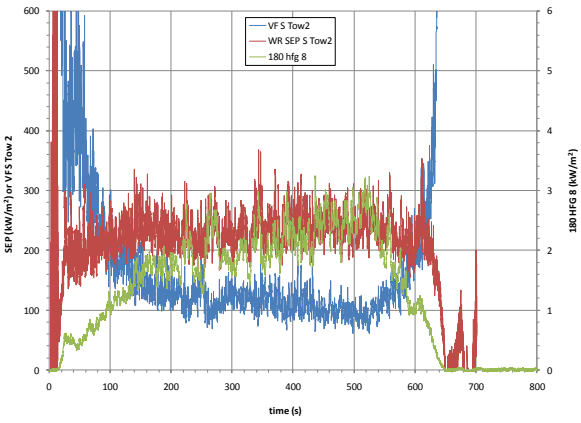

South Tower 2

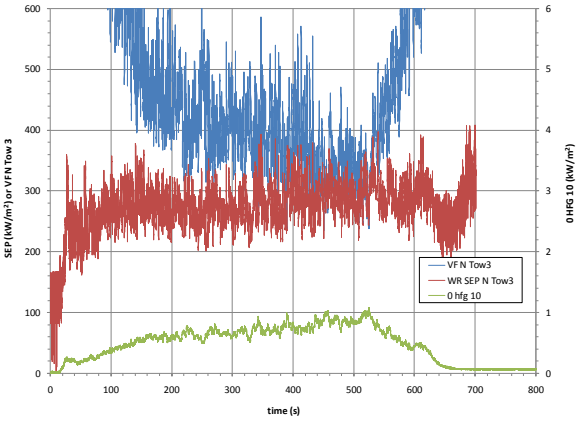

North Tower 3

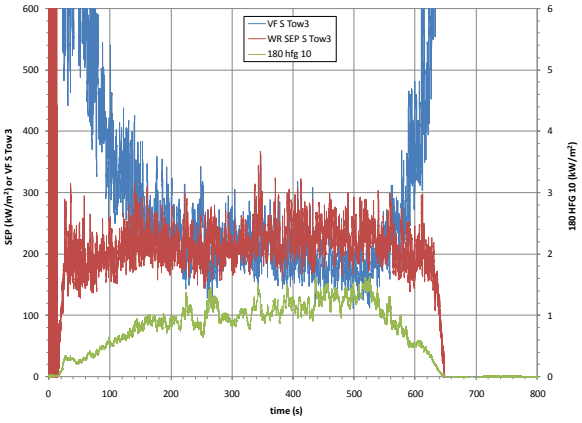

South Tower 3

Figure 132 SEP results from the North and South WV radiometers in LNG Test 1.

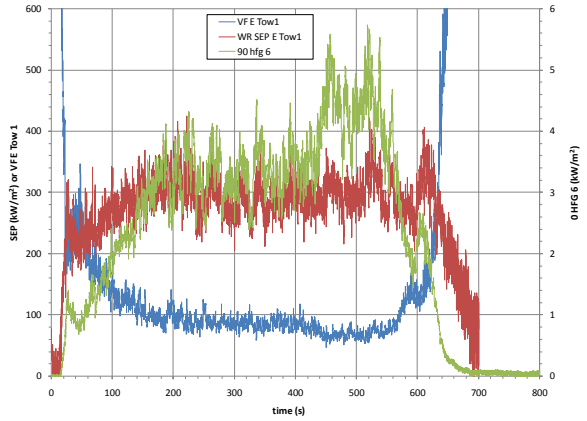

East Tower 1

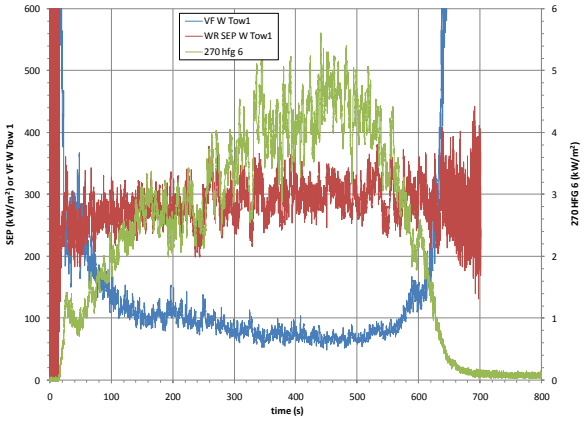

West Tower 1

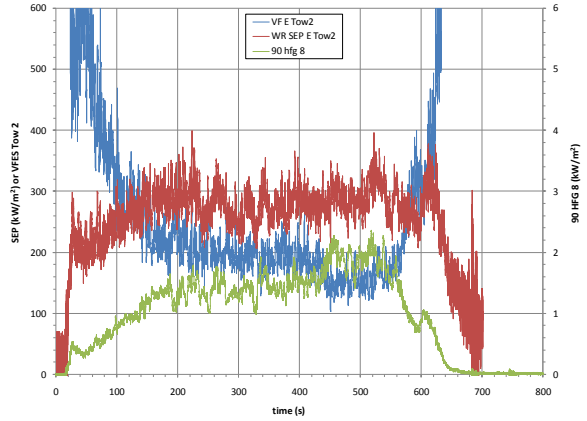

East Tower 2

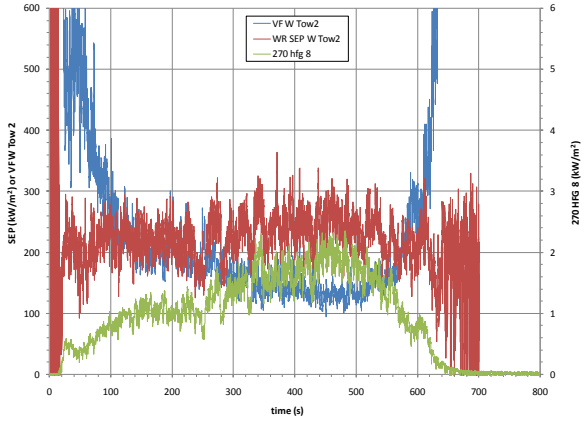

West Tower 2

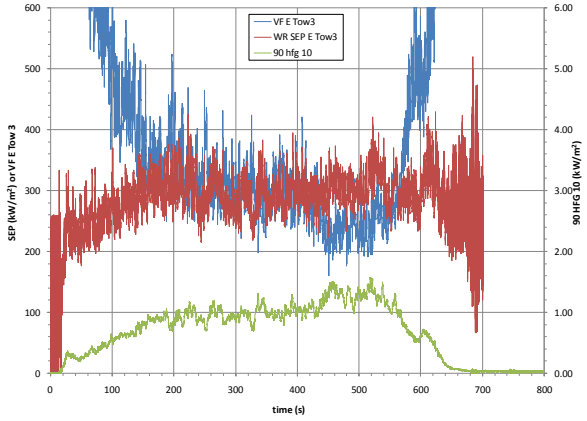

East Tower 3

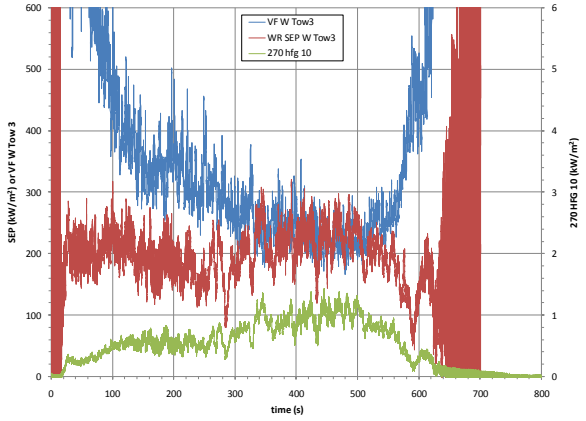

West Tower 3

Figure 133 SEP results from the East and West WV radiometers in LNG Test 1.

Table 29 presents the average and standard deviations over the interval from 390-500 s of the wide-angle incident heat flux (corrected for the atmospheric transmission loss), the view factor, and the flame SEP.

The average overall SEP is 277 ± 60 kW/m^2 (2 sigma) (average of the 11 individual SEP data points, discounting the suspect N Tower 2 gauge as it did not return to zero at test end).

Table 29 LNG Test 1 heat flux (corrected), view factor, and flame SEP (390-500 s).

	Wide-View Heat Flux (kW/m^2)		View Factor Multiplier		Surface Emissive Power (kW/m^2)	
Duration 390-500s	average	st.dev.	average	st.dev.	average	st.dev.
N Tower 1	2.4	0.3	106	15	247	19
N Tower 2	1.5	0.1	266	39	395	35
N Tower 3	0.8	0.1	363	54	303	29
S Tower 1	6.2	0.9	47	8	286	32
S Tower 2	2.4	0.3	105	18	252	26
S Tower 3	1.3	0.1	189	32	239	28
E Tower 1	4.2	0.6	75	11	305	22
E Tower 2	1.8	0.2	167	25	293	22
E Tower 3	1.2	0.2	260	39	312	25
W Tower 1	4.5	0.5	69	8	310	21
W Tower 2	1.9	0.2	137	16	260	27
W Tower 3	1.0	0.2	230	27	236	32

5.15 Narrow-View Radiometer Analysis

The video analysis routines also determined a time-dependent "fill fraction" for each narrow-view radiometer, based on the nominal gauge parameters (gauge height, view angle, inclination angle, and the distance to fire CG) in order to determine validity of the gauge data. This information determined a location and area on the flame surface (a "spot") that provided the field of view for each narrow view radiometer. Each video frame was then interrogated to count the number of pixels that were determined to be "fire" (a red threshold >230±5) that lay within this "spot" (see Section 7.8 for a visual representation).

Figure 134 shows a video frame from the North spoke cameras at t = 403.7 s. Figure 135 shows the time-dependent fill fraction for each gauge on tower 1 (110 m distance) on the North spoke. Figure 136 compares the fill fraction to the heat flux (corrected for the transmission loss) for the North gauge HFG1 (7.6 m height at 110 m distance). Note that the as fill fraction changes a corresponding change in heat flux follows after a small delay (63.2% time constant for the HFGs is 35 ms). Similar figures are presented for the NV radiometers on South spoke tower 1. The embedded image is frame 12100, taking at ~403.7 s.

Figure 134 North spoke camera view with NV radiometer field of view overlay (t=403.7 s).

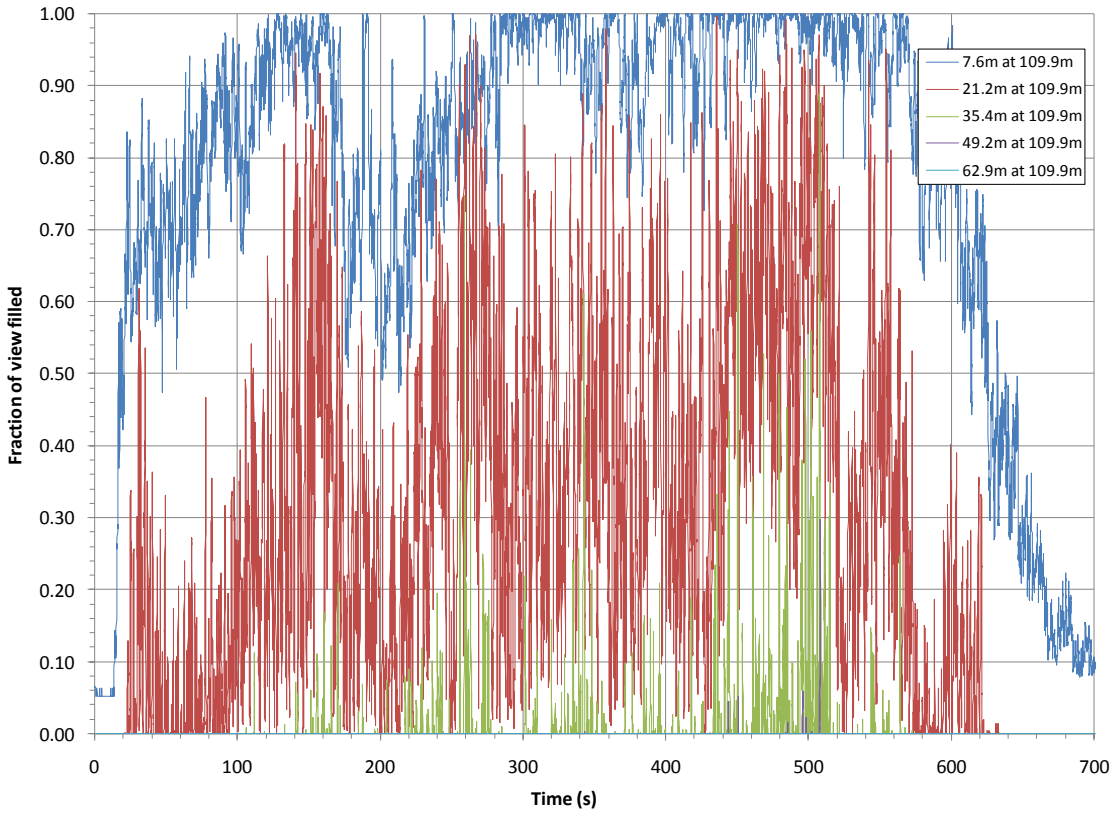

Figure 135 LNG Test 1 North HFGs fill fractions for the radiometer field of view.

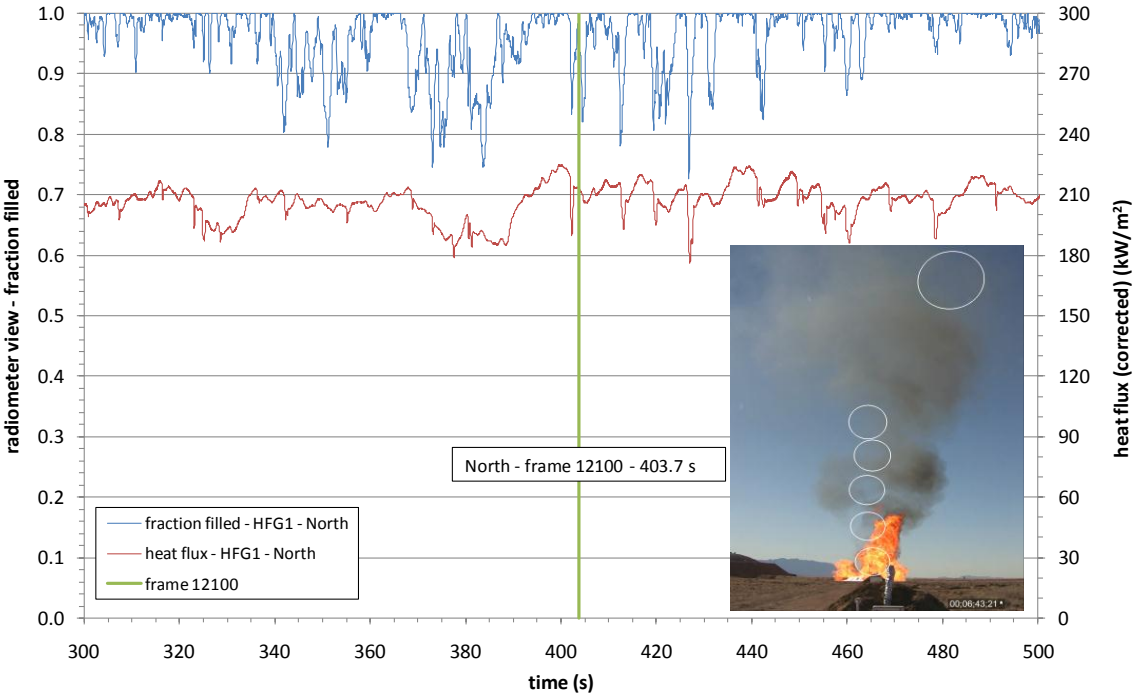

Figure 136 LNG Test 1 heat flux and fill fraction for the North NV radiometer (HFG1). (7.6m height at 110m distance)

Figure 137 South spoke camera view with NV radiometer field of view overlay (t = 403.7 s).

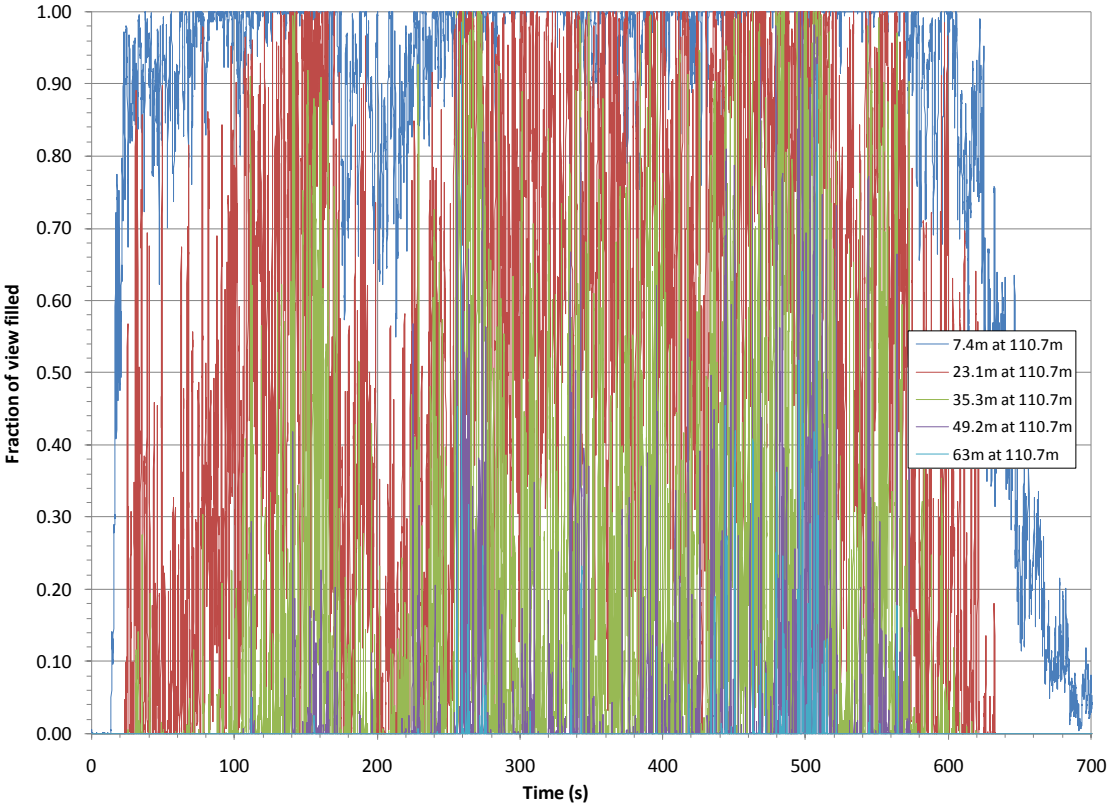

Figure 138 LNG Test 1 South HFGs fill fractions for the radiometer field of view.

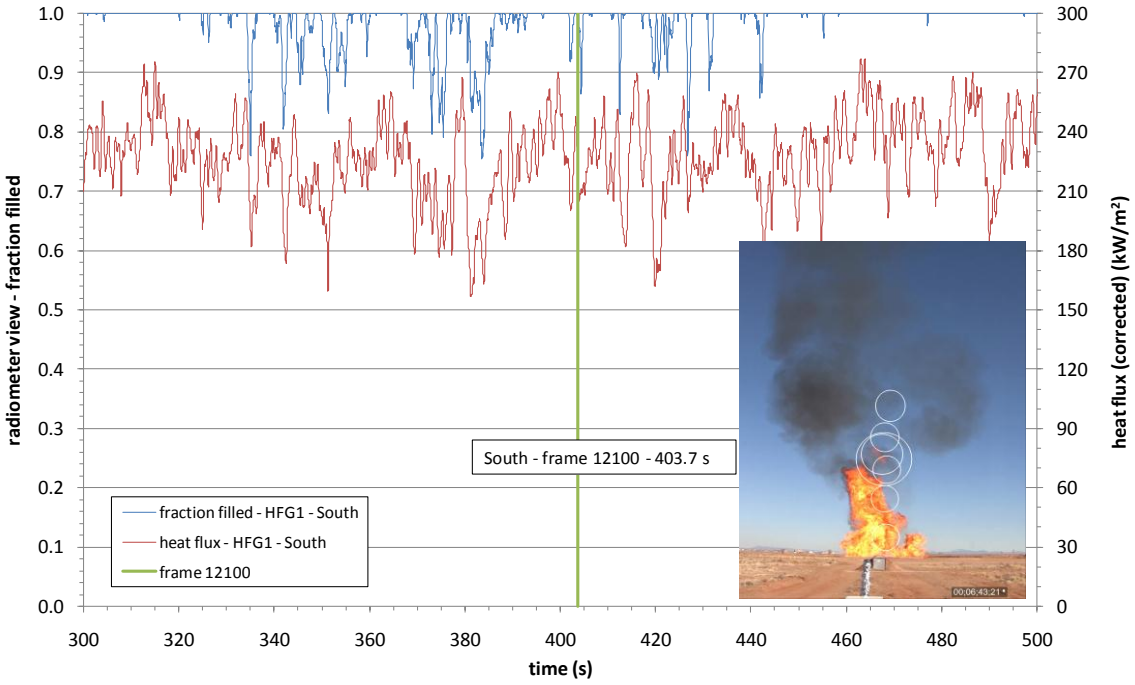

Figure 139 LNG Test 1 heat flux and fill fraction for the South NV radiometer (HFG1). (7.4m height at 110m distance)

Table 30 present the average and standard deviation of the fill fraction over the 390-500 s interval for all gauges. Table 31 shows the North and South narrow-view radiometer heat flux data corrected for transmission losses and compares that to their respective fill fraction over the 390-500 s interval.

Table 30 LNG Test 1 radiometers field of view – fill fraction

fill fraction	North Towers		South Towers		East Towers		West Towers	
390-500s	average	std.dev.	average	std.dev.	average	std.dev.	average	std.dev.
7m at 110.7m	0.97	0.04	0.99	0.02	0.09	0.06	0.28	0.06
21m at 110.7m	0.49	0.22	0.80	0.22	0.00	0.00	0.00	0.00
35m at 110.7m	0.03	0.08	0.33	0.31	0.00	0.00	0.00	0.00
35m at 159.9m	0.00	0.00	0.17	0.21	0.00	0.00	0.00	0.00
35m at 209.8m	0.00	0.00	0.21	0.18	0.00	0.00	0.00	0.00
48m at 110.7m	0.00	0.00	0.07	0.17	0.00	0.00	0.00	0.00
62m at 110.7m	0.00	0.00	0.01	0.05	0.00	0.00	0.00	0.00

Table 31 LNG Test 1 HFG fill fraction and corrected incident heat flux

fill fraction			0 hfg 1	0 hfg 2	0 hfg 3	0 hfg 4	0 hfg 5	0 hfg 6	0 hfg 7	0 hfg 8	0 hfg 9	0 hfg 10
spot height at			7m at	21m at	35m at	48m at	62m at	35m at	35m at	35m at	35m at	35m at
distance		390-500s	110.7m	110.7m	110.7m	110.7m	110.7m	110.7m	159.9m	159.9m	209.8m	209.8m
	North	ave	0.97	0.49	0.03	0.00	0.00	WV gauge		WV gauge		WV gauge
		sd dev	0.04	0.22	0.08	0.00	0.00		0.00		0.00	
	South	ave	0.99	0.80	0.33	0.07	0.01		0.17		0.21	
		sd dev	0.02	0.22	0.31	0.17	0.05		0.21		0.18	
	East	ave	0.09	0.00	0.00	0.00	0.00		0.00		0.00	
		sd dev	0.06	0.00	0.00	0.00	0.00		0.00		0.00	
	West	ave	0.28	0.00	0.00	0.00	0.00		0.00		0.00	
		sd dev	0.06	0.00	0.00	0.00	0.00		0.00		0.00	
HFG flux transmittance corrected		**390-500s**	**0 hfg 1**	**0 hfg 2**	**0 hfg 3**	**0 hfg 4**	**0 hfg 5**	**0 hfg 6**	**0 hfg 7**	**0 hfg 8**	**0 hfg 9**	**0 hfg 10**
kW/m^2												
	North	ave	216.1	93.6	10.5	0.9	0.3	2.4	1.8	1.5	1.0	0.8
		sd	7.4	42.7	11.0	0.7	0.1	0.3	1.4	0.1	1.3	0.1
	South	ave	236.3	203.1	115.4	54.2	19.7	6.2	6.5	2.4	54.6	1.3
		sd	20.6	50.9	58.3	52.6	25.6	0.9	1.0	0.3	38.5	0.1
HFG flux / fill fraction	North	ave	222.4									
kW/m^2												
	South	ave	238.0	252.3								

HFG1 on the North spoke tower 1 and HFG1 and HFG2 on the South spoke tower 1 were the only gauges with their field of views essentially filled during the entire averaging interval. It is possible to adjust some of the gauges to account for the partial fill by dividing the average flux by the average fill fraction (for those gauges with fill fractions ≥0.8). These adjusted values for the North HFG 1 and the South HFG 1 and HFG 2 are also shown in Table 31.

Note that the highlighted gauges that see 100% flame (or are corrected to allow for this) and are corrected for transmission losses represent surface emissive power values.

The "spot" average SEP was 238 ± 30 kW/m^2 (2 sigma).

Figure 140 compares the "spot" SEP from the narrow view HFG 1 on the South spoke to the full-field "flame" SEP as calculated using the wide view heat flux gauge (HFG 6) and the video data from the South spoke. Both data sets were corrected for transmission losses. Results show good agreement and fall within the uncertainty of each method.

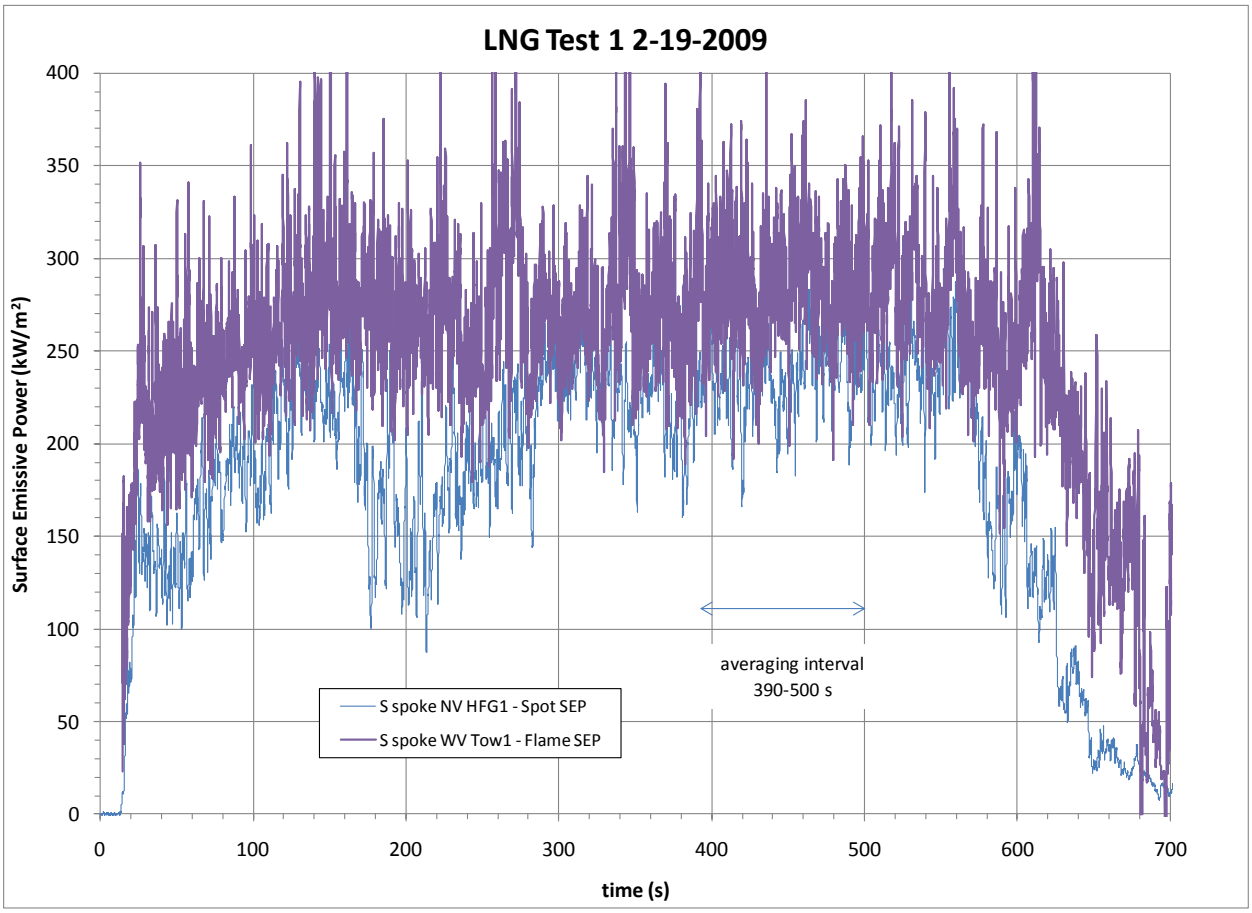

Figure 140 "Spot" SEP compared to the full-field "Flame" SEP in LNG Test 1.

5.16 LNG Spectra – Mid-Infrared

Introduction

Mid-infrared spectral radiation intensity measurements were obtained from a Model ES-200 spectrometer (Spectraline, Inc., West Lafayette, IN). The ES-200 measured spectral radiation intensity at 390 Hz in the 1.3 to 4.8 micron wavelength range and each of the pixels looks at a wavelength of 22 nm. The total wavelength range accounts for 75% of the emitted radiation energy from a blackbody source at 1420K, which is approximately the effective radiation temperature from a large hydrocarbon fuel fire as determined by Kearney. The ES200 spectrometer was fielded with a one-dimensional (1D) scanner capable of measuring 128 points along a line in 0.32 sec. At each point, the spectrometer viewed an area of the flame with a diameter of ~2.2 m. Although three spectrometers were fielded, only one spectrometer captured data due to a shift in the flame zone with unexpected winds.

The unit 2 spectrometer was located on the 180^{o} spoke and it acquired data throughout the fire. Variability in the spectra resulted from wind shifts during the experiment. The spectrometer was positioned on a tilt table, which obtained data from two different 1D scans (nominally 1-49 m and 49-100 m). The 49-100 m scan (tilt angle #2) did not collect any data as the flame height was below the field of view of the spectrometer (i.e., the spectrometer over scanned the fire). Good data were collected for all the scans for tilt angle #1 (~1-49 m). This resulted in 15 data files in times of 83, 109, 140, 173, 210, 263, 293, 322, 350, 382, 468, 542, 574, 605, and 642 seconds after ignition.

Figure 141 shows 4 images (1 sec apart) of the fire starting at the three selected times corresponding to spectrometer data collection (10 scans were performed during this 3 s interval; the average of the 10 measurements at each of the 128 heights was recorded for later analysis). A box overlay with scale information is also shown representing the width and height of the spectrometer field of view (FOV) with the tilt table at position 1.

Figure 141 LNG Test 1 images with the South spoke spectrometer FOV overlay.

Calibration

The spectrometer was calibrated before and after the experiment using an Infrared Systems blackbody source at temperature between 600-1200°C. The acquired spectra were used to create a calibration file that was used to convert measured voltages to intensities. To determine the adequacy of the calibration file over the entire spectral region, a plot of the intensities measured by the spectrometer at different blackbody temperatures is shown in Figure 142 along with the theoretical intensities from the Planck function. Only every other pixel from the spectrometer is displayed to allow the theoretical curve to be seen, but all of the pixels were perfectly aligned with the curves indicating that the calibration file was suitable.

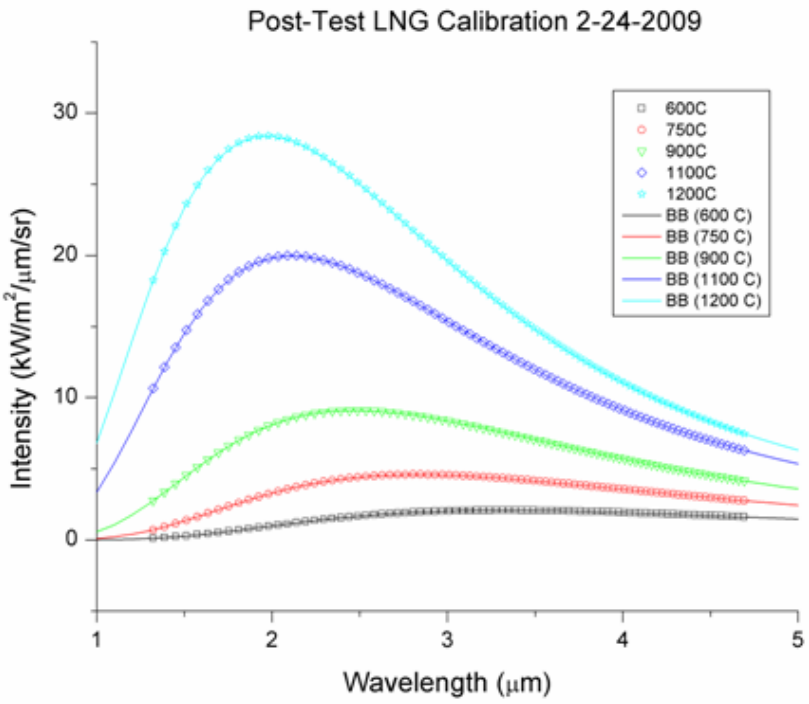

Figure 142 LNG Test 1 post-test spectrometer calibration.

Overview of Experimental Data

An example of the spectra collected at different times at various heights above the liquid surface is shown in Figure 143. The lines represent the average of 100 spectra (~3 sec) at each location.

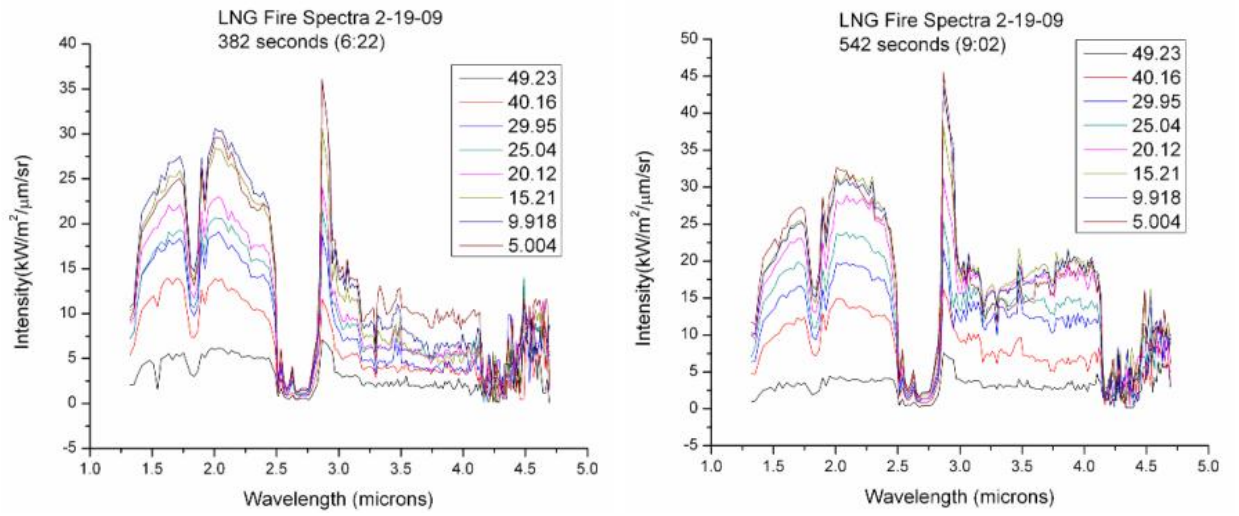

Figure 143 LNG Test 1 spectra at 382 and 542 sec for different heights.

Figure 144 displays the spectra intensity as a function of wavelength and height (127 locations) at 382 s and 542 s after ignition. The spectra (colors indicate magnitude of intensity) show low intensities near the base of the fire that increase with height up to ~15m and then decline at the higher elevations.

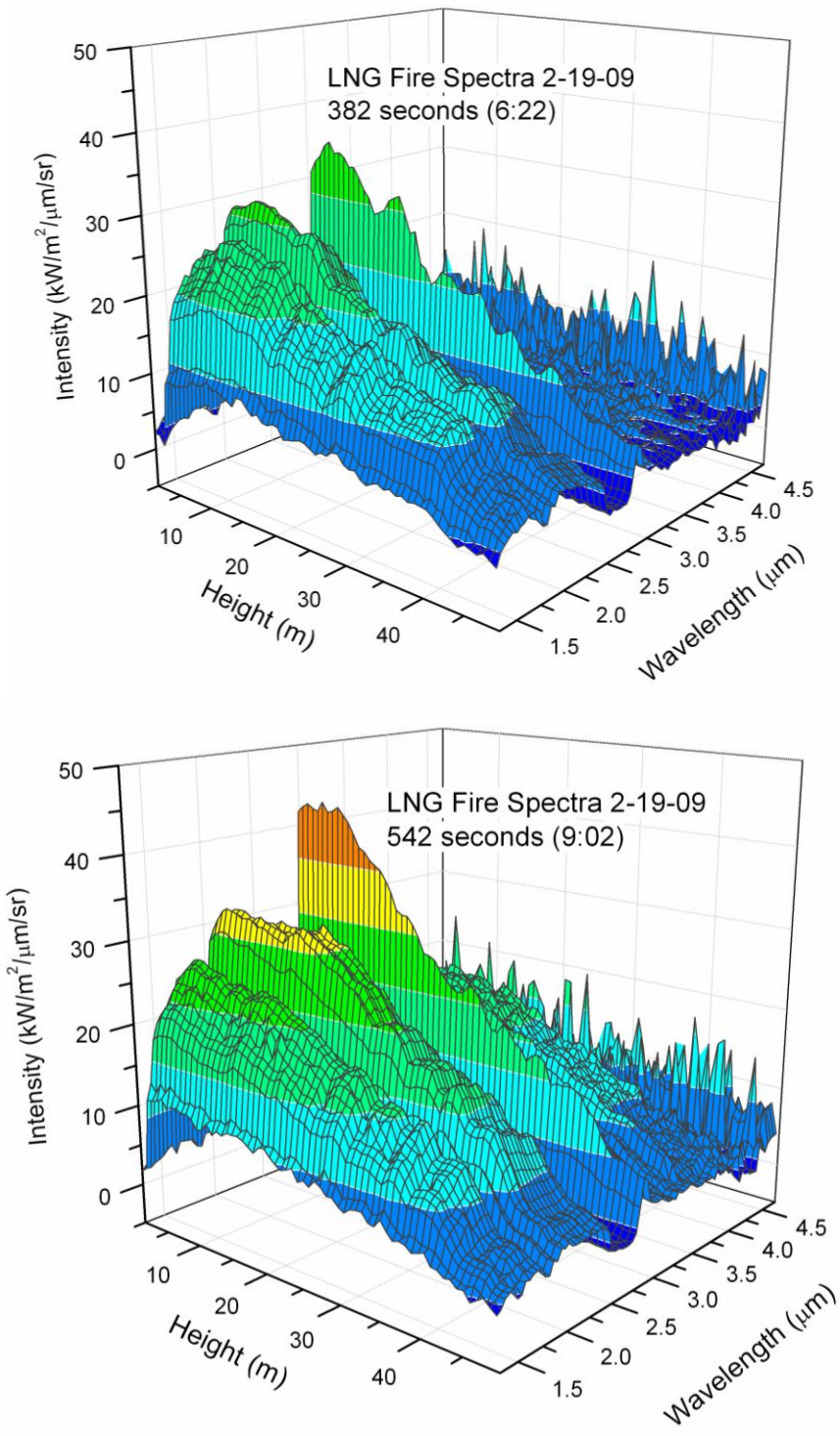

Figure 144 LNG Test 1 spectra intensity vs. height and wavelength.

Spectra were integrated over the wavelength range and multiplied by π [Incropera & DeWitt, 2nd ed.] to obtain surface emissive power as a function of height. A transmissivity fraction of 0.75 (yielding a transmission loss of 0.25) at a distance of 226 m (refer to Section 5.11) was used to

correct for transmission effects. It has been determined that approximately 22% of the emission was outside of the spectrometer wavelength range (See Section 7.16 for details). Therefore, a multiplier of 1.71 (1/1-.25) x (1/1-0.22) was used to correct the spectrometer data. Figure 145 shows the surface emissive power reduced from the 15 scans of spectrometer data. In addition, Figure 145 shows the average of the 5 SEP scans from 293 s to 468 s.

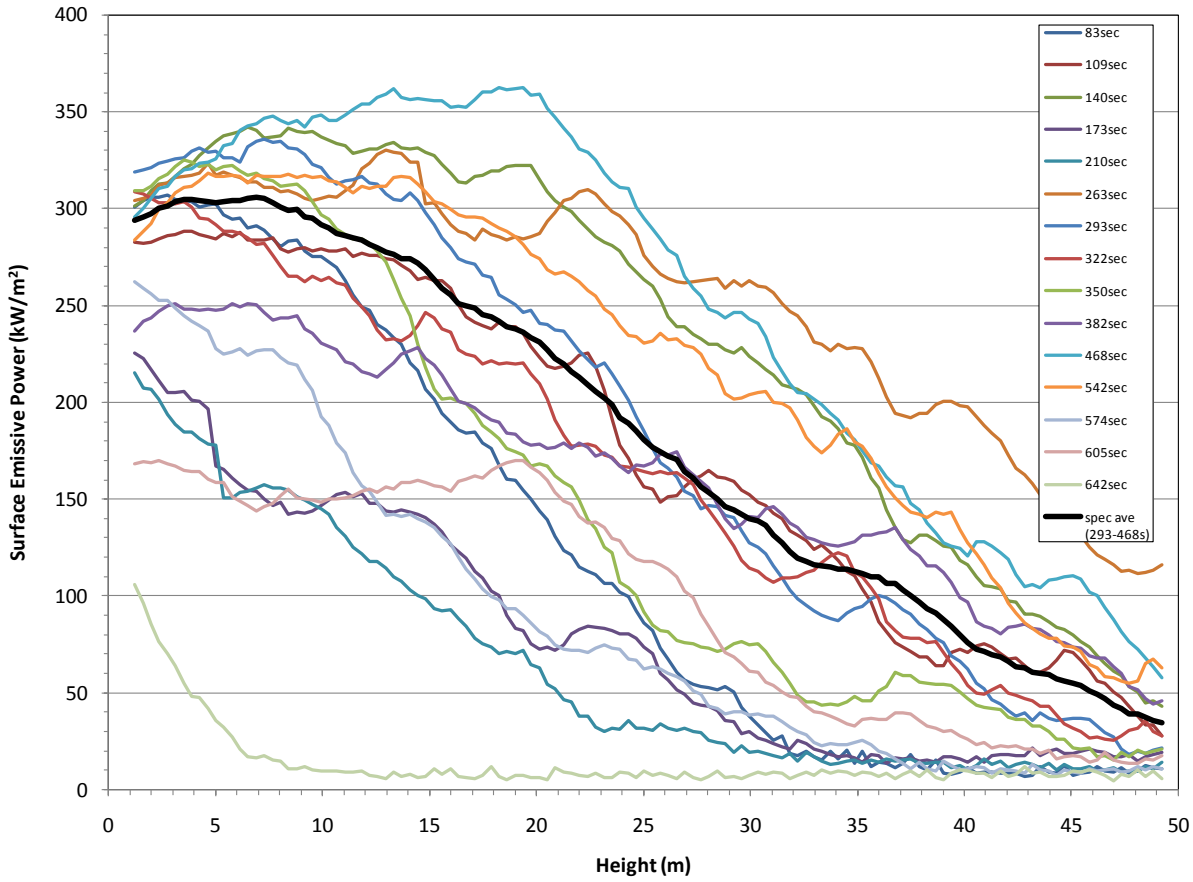

Figure 145 LNG Test 1 spectrometer-derived surface emissive power vs. height.

Figure 146 compares the spectrometer-derived surface emissive power to the transmission corrected average heat flux data (same 3 s interval as with the spectrometer) from the South narrow-view radiometer collecting data at 7.4 m and 23.1 m. The heat flux data was also adjusted to account for the average fill fraction over the 3 s interval. The decrease in intensity and corresponding heat flux with increasing height is likely due to over-scanning the fire. The video images show many instances where the overlay is not engulfed in flames. Smoke production near the flame mantle could also contribute to the decrease in intensity. In addition, Figure 146 shows the average of the 5 SEP scans from 293 s to 468 s.

Figure 146 shows variability associated with temporal scans as filled symbol error bars. Agreement between radiometer data and the spectroscopic flux is acceptable.

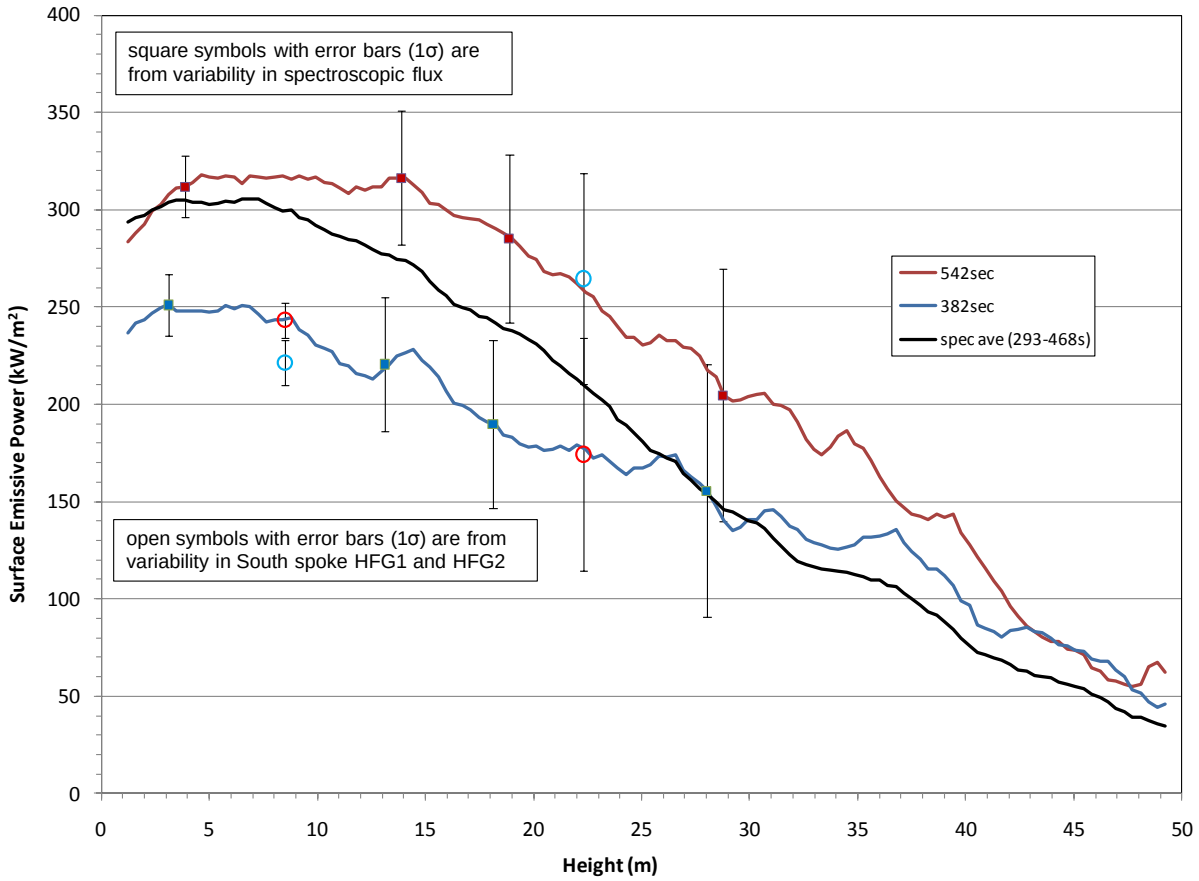

Figure 146 Comparison of LNG Test 1 spectrometer-derived SEP to radiometer data.

Results from the 382sec Scan

A trigger signal was sent to the spectrometer at 382 sec after ignition. As mentioned previously, the spectrometer completed 100 line scans during the 3 seconds following the trigger. Therefore, a total of 1280 spectra were acquired (10 at each of 128 heights) and the 100 spectra from each height were averaged to provide an average spectrum for that time period in the fire at each height. Those data are shown in Figure 147. It is evident that some features of the spectra are consistent with the paper by Raj [2007], such as the atmospheric absorption of thermal radiation by H_2O and CO_2 (1.87 um, 2.7 um, and 4.3 um).

The data were then further analyzed to determine the approximate temperature and emissivity at each location in the fire. Similar to the method of Raj [2007], wavelength bands that were free of gas band emission and atmospheric absorption (1.48-1.75 and 2.08-2.34 micron bands) were assumed to only contain emission from soot radiation. A two parameter fit of the Planck function was performed to determine an approximate soot temperature and emissivity. It was assumed that the soot was a gray (i.e. emissivity did not vary with wavelength). An example of the fits for a few spectra at 382 s are shown in Figure 147. The Planck function (using the fit temperature and emissivity values) was multiplied by the atmospheric transmission in the comparison to provide a better assessment of the accuracy of the fit. The data are shown with symbols and the fits are the semi-transparent lines of like color.

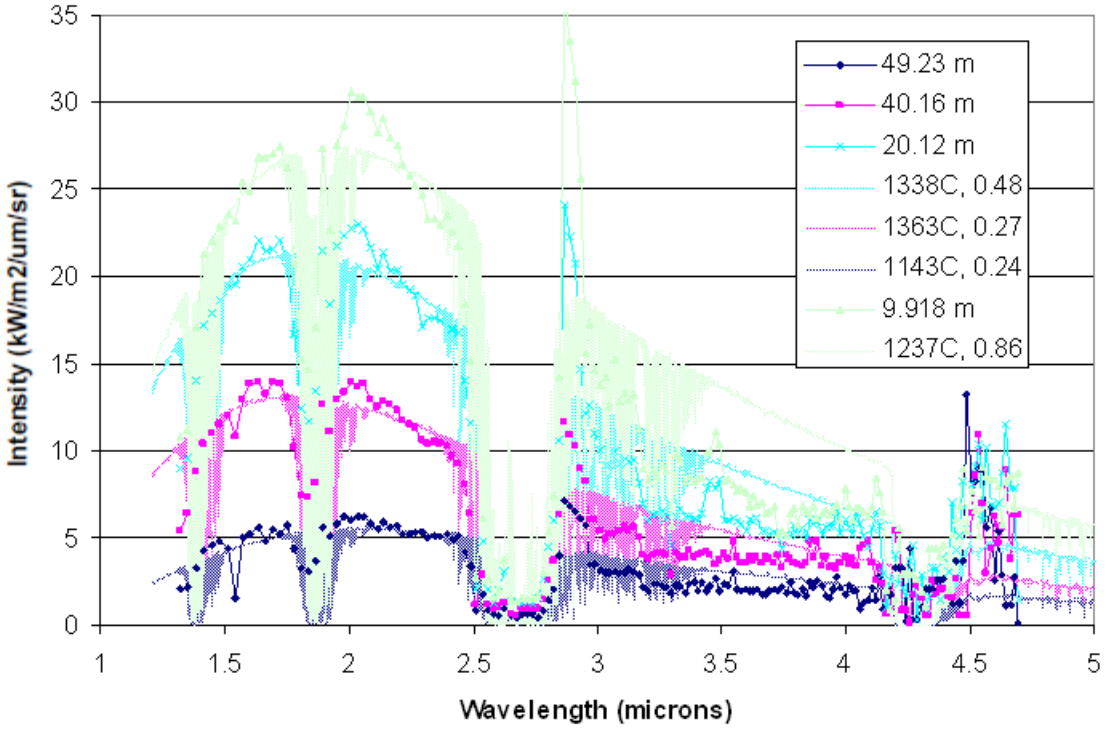

Figure 147 LNG Test 1 spectra with 2-parameter fit of the Planck function.

Table 32 from Raj [2007] provides a summary of the infrared emission bands. This table and the MODTRAN results were used to select the bands for the fit. It is also evident that the significant deviations from the fit are likely a result of gas band emission and absorption.

Table 32 IR emission bands in combustion gases

Infrared emission bands from molecular species in combustion gases

Gas	Principal bands centered at wavelengths, λ_B (μm)	Remarks
H_2O	1.88, 2.66 and 6.27	Strong emission/absorption bands
	0.94, 1.14, 1.38, 2.74 and 3.17	Weak emission/absorption bands
CO_2	2.69, 2.77 and 4.26	Strong emission/absorption bands
	1.96, 2.01, 2.06, 4.68, 4.78 and 4.82	Weak emission/absorption bands
CO	1.573, 2.345 and 4.663	
HCl	1.198, 1.764 and 3.465	
NO	2.672 and 5.3	Weak emission/absorption bands
NO_2	4.5, 6.17 and 15.4	
N_2O	2.87, 3.9, 4.06, 4.54, 7.78, 8.57 and 16.98	
SO_2	4.0, 4.34, 5.34, 7.35 and 8.69	

Source: Wolfe [10].

The results of the temperature and emissivity fits as a function of height at four scan times during steady-state portion of the fire are shown in Figure 148. The temperature in the fire appears to vary from approximately 1100°C to 1600°C. Note that the average flame height was ~34 m; puffing or lack of the fire above this height would have had an impact on the spectrometer measurements. Table 33 presents the average and standard deviation of the spectrometer-derived temperature and emissivity at the 4 scan times (only between heights of 1.2-34.5 m). The overall average temperature and emissivity is 1262°C and 0.68, respectively.

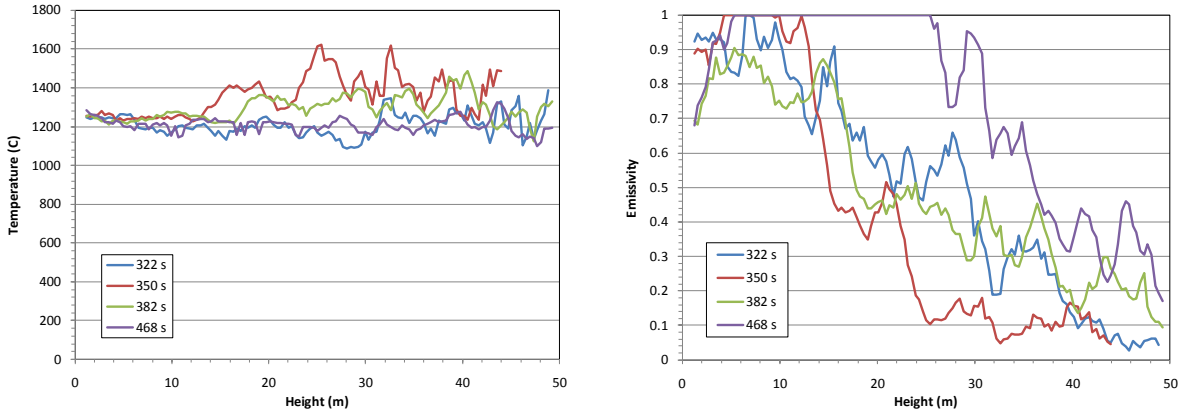

Figure 148 Temperature and emissivity fit as a function of height in LNG Test 1.

Table 33 Spectrometer-derived average temperature and emissivity in LNG Test 1.

		Temperature (C)		Emissivity	
Scan time (s)	Height Range (m)	average	st.dev.	average	st.dev.
322	1.2 - 34.5	1197	52	0.67	0.22
350	1.2 - 34.5	1354	107	0.53	0.36
382	1.2 - 34.5	1289	54	0.60	0.21
468	1.2 - 34.5	1209	28	0.92	0.13
	overall	**1262**	**73**	**0.68**	**0.17**

5.17 LNG Spectra - Long Range, High Resolution

Introduction

The spectral signature of the LNG pool fire was measured from a significant distance with a manually scanning spectrometer. The spectrometer that used was an ABB Bomem MR Series 304. The spectrometer is an FTIR instrument that can be operated in a number of different configurations. The ABB spectrometer was fielded in a high resolution configuration, with a spectral resolution of 1 cm^{-1}. In this mode, the spectrometer can collect data at a rate of 10 scans per second, scanning from the short-wave infrared (1.0 μm) all the way out to the long-wave infrared (15.0 μm). The spectrometer was fielded in a manual scan mode, where an operator controls the azimuth and elevation manually. In this mode, a co-boresighted, high speed visible

camera with a slightly larger field of view records the event simultaneously to provide contextual information about what the spectrometer is viewing.

The duration of the LNG pool fire test was nearly 10 minutes. The first 60 seconds of the test, the spectrometer was collecting on the central region of the flame. The field of view of the narrow angle telescope was 4.9 mrad. The spectrometer was approximately 1160 meters from the center of the fire, to the east. That field of view correlates to a circular area with a diameter of approximately 6 meters at the fire. Because of the massive size of the fire, the field of view of the spectrometer was completely filled by the event. After approximately 60 seconds, the spectrometer was pointed south (left) of the event, outside of the flames, and then slowly scanned through the active region of the fire, and ending outside of the active region to the north (right). This maneuver took approximately 90 seconds. Following that spatial scan, a second spatial scan was taken in the vertical direction, starting at the base of the fire, scanning to top, and ending above the active area. The second spatial scan also acquired data for approximately 90 seconds. At this point, several hundred frames of data were collected at the top of the fire plume. For the final minutes, the spectrometer was operated in still mode focusing at the flame center.

The high-resolution spectrometer was calibrated both before and after the event at two separate black body calibration source temperatures of 750 and 950 degrees Celsius. By calibrating the spectrometer to known values in the field with the test conditions, the data collected can produce the absolute values of spectral radiation over a very wide spectral region.

At the start of the test, immediately before the LNG was released, a flash bulb was illuminated on a pole just above the diffuser in the center of the pond. This flash provided a time stamp to temporally align all of the instruments. The flash bulb was captured by the VNIR camera as shown in Figure 149. There is also a red circle in the image that has been superimposed to indicate the size and location of the FTIR FOV within the visible image.

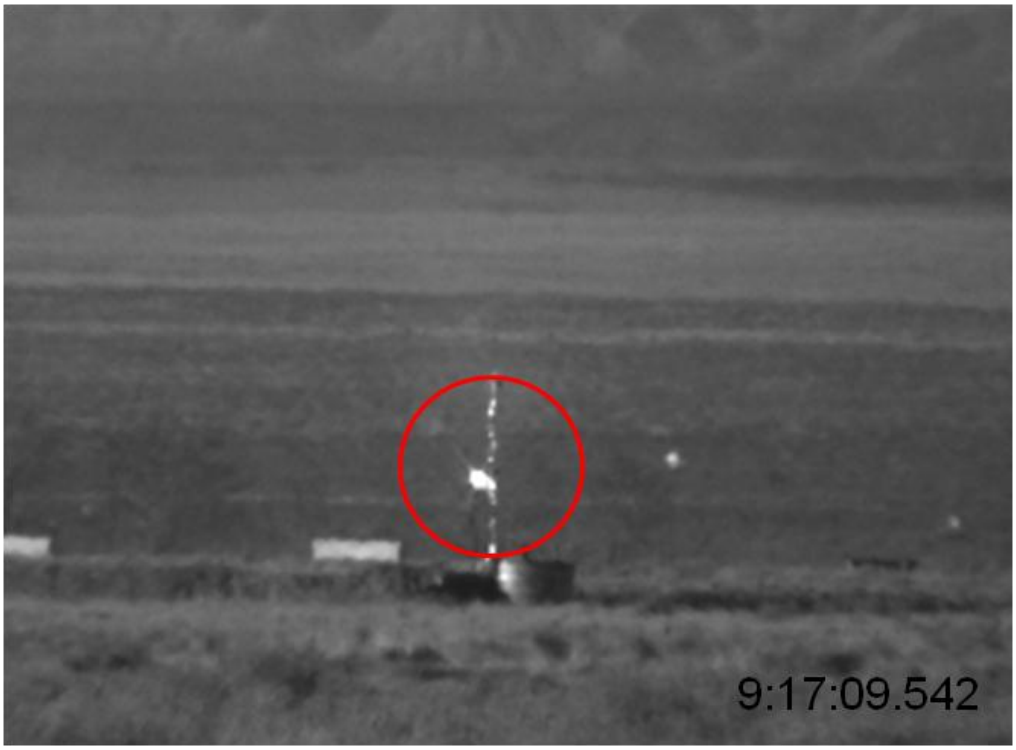

Figure 149 VNIR image of fiducial flash and FTIR bore sight in LNG Test 1.

Figure 150 shows the LNG pool fire from the location of the data acquisition trailer. The still image was taken with a standard digital camera. The red circle indicates the size of the FTIR FOV at the distance of the fire. The location within the fire was manually set so that the FTIR FOV would be completely inside the flame region just above the base of the fire.


Figure 150 LNG Test 1 fire view from the FTIR data acquisition trailer.

Hyperspectral Measurements

The FTIR hyperspectral (high resolution) data collected during the LNG Test 1 was spectrally sampled at 1 wave number. The instrument inherently collects and stores interferograms which then must be post processed to calculate calibrated spectral radiance. Once the datasets are converted to spectral radiance, they can be exported to ASCII format text files within the software provided with the instrument. MATLAB® routines have been developed to import and perform some rudimentary processing on the datasets. The spectral radiance at six different times throughout the LNG fire evolution, with respect to the burn initiation, can be seen in Figure 151. There appears to be additional radiance in the 1-2 μm range, likely due to solar radiance, as the radiance should have peaked at ~2 μm. The radiance measurements were averaged over approximately 1 second and were not corrected for the losses due to the narrow telescope (refer to Section 4.5.12 for a description of the losses). From the curve magnitudes it appears that the fire was increasing in intensity with time, except for the last time at 544 s. The decreased spectral radiance seen at the last temporal point is likely due to a lower fire combustion rate since this measurement occurred near the end of the burn.

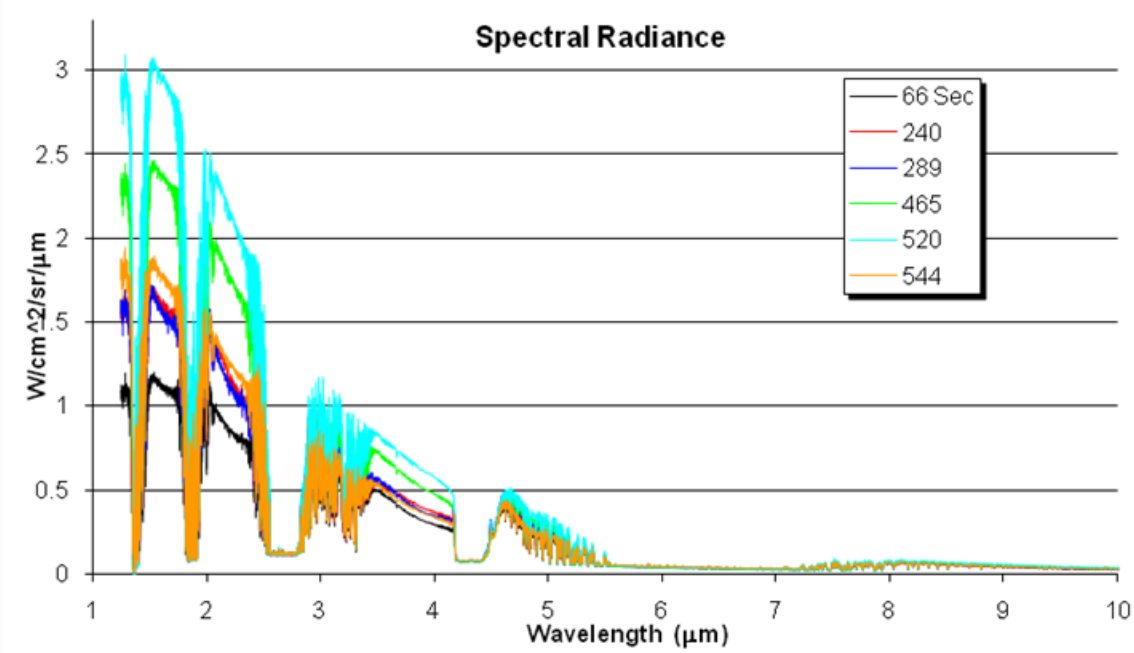

Figure 151 Time varying LNG Test 1 fire spectral radiance.

Signature Modeling

There are several phenomenological codes that can predict the spectral output from combustion. One code that was readily available, easily executable, and contained sufficient fidelity for this study was the FLAMES code developed by Spectral Sciences Inc. for the Phillips Laboratory. Distribution of the code is export controlled and limited to government agencies and their contractors and handled through the AFRL PRSA at Edwards AFB. The FLAMES code computes line-of-sight spectral radiance arising from the specified hot gas emission path. It handles emission from gases that are in local or non-local thermodynamic equilibrium. A full discussion of the FLAMES model is given be Bernstein et al. [1990].

The molecular emission bands supported by the current version of FLAMES are: Soot, H_2O, CO_2, CO, HCL, HF, OH and NO. The FLAMES code calculates soot emission with spectrally varying emissivity and constant temperature. The underlying physics enable very fast, but somewhat approximate (~±10% error) spectral predictions. One of key assumptions that limit the accuracy of the results is that all bands of same symmetry have same shape. The code has been validated against other equilibrium codes and used to analyze many chamber and field measurements of rocket plume spectra.

The FLAMES code only predicts the spectral radiant exitance of the target. In order to predict the apparent radiance reaching the aperture of the FTIR, the source radiance has to propagate through the atmosphere to the instrument. In order to accomplish this, the path transmission was predicted by MODTRAN. Table 34 lists the atmospheric conditions that were measured just before the test took place and were used as the input parameters to MODTRAN.

Table 34 LNG Test 1 atmospheric property values.

Property	**Value**
Altitude	1627 meters
Pressure	25.13 in. Hg
Temperature	33.1° F
Relative Humidity	35%
Horizontal path length	1160 meters

The simulated path spectral transmission for the test conditions can be seen in Figure 152.

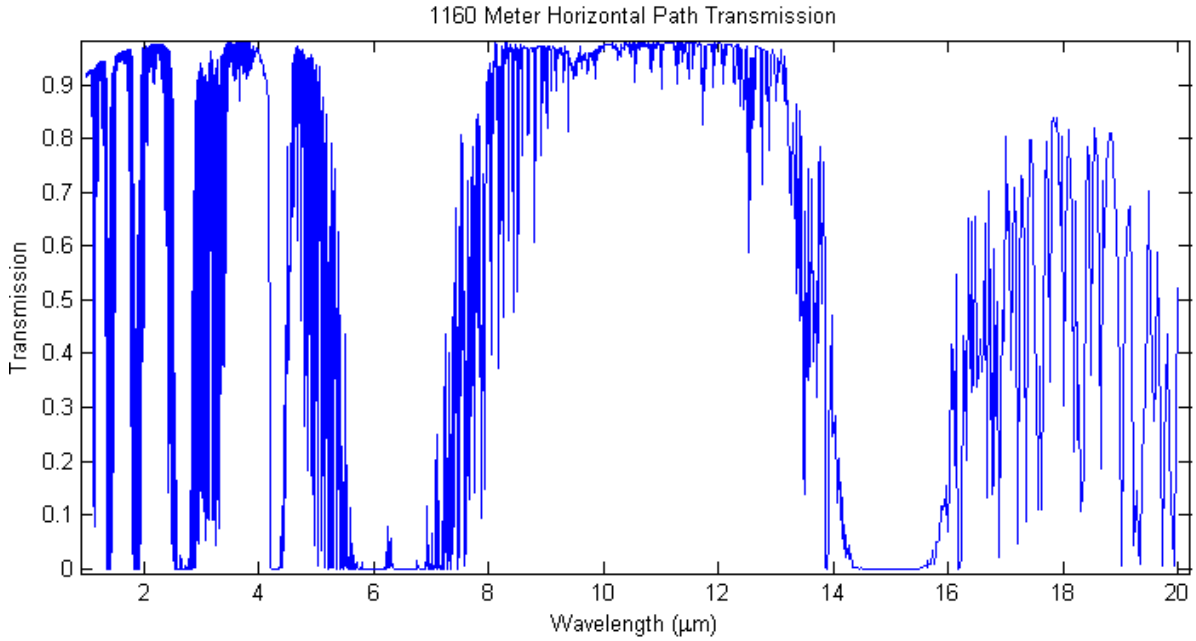

Figure 152 MODTRAN predicted path spectral transmission for LNG Test 1.

The output of the FLAMES code was reduced by the simulated path radiance as seen in Figure 153. To accurately model the observed spectra, the modeled apparent spectral intensity is then compared to measured radiance. Inputs to the FLAMES code were methodically adjusted until the predicted spectra matched that of the measurements. This method allows for a physics-based model to be used to predict the combustion conditions of the fire.

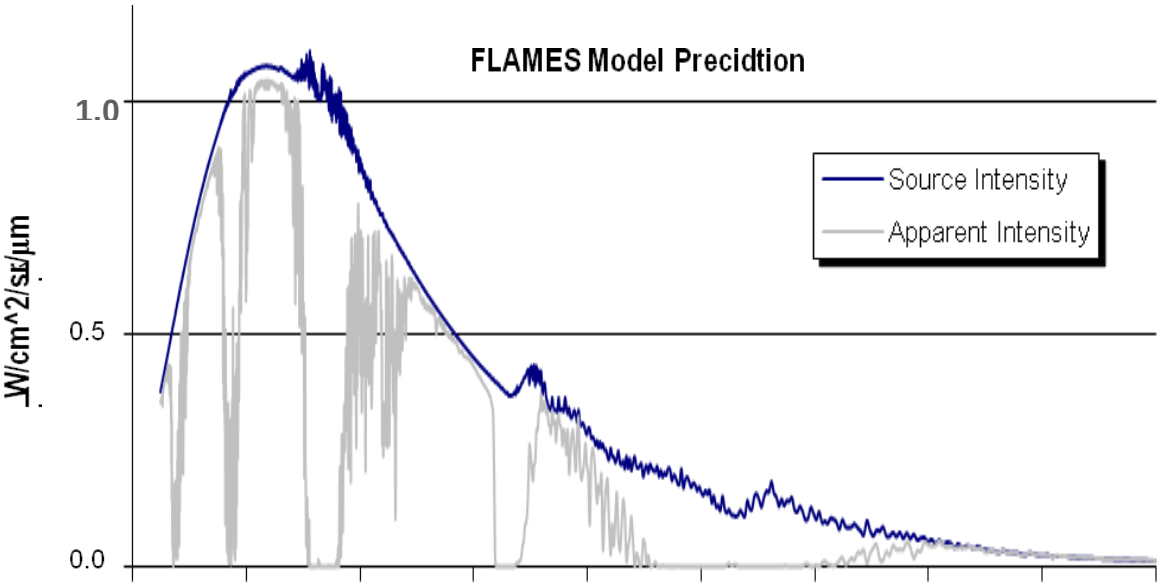

Figure 153 FLAMES output with MODTRAN predicted transmission in LNG Test 1.

The FLAMES code only predicts a single temperature at a time, as shown below in Figure 154; it provides a close but not exact fit to measured spectra. The model predicts the observed spectra well in spots, but underestimates the radiance at wavelengths less than 2 microns as well wavelengths between 3.3 µm – 4.2 µm.

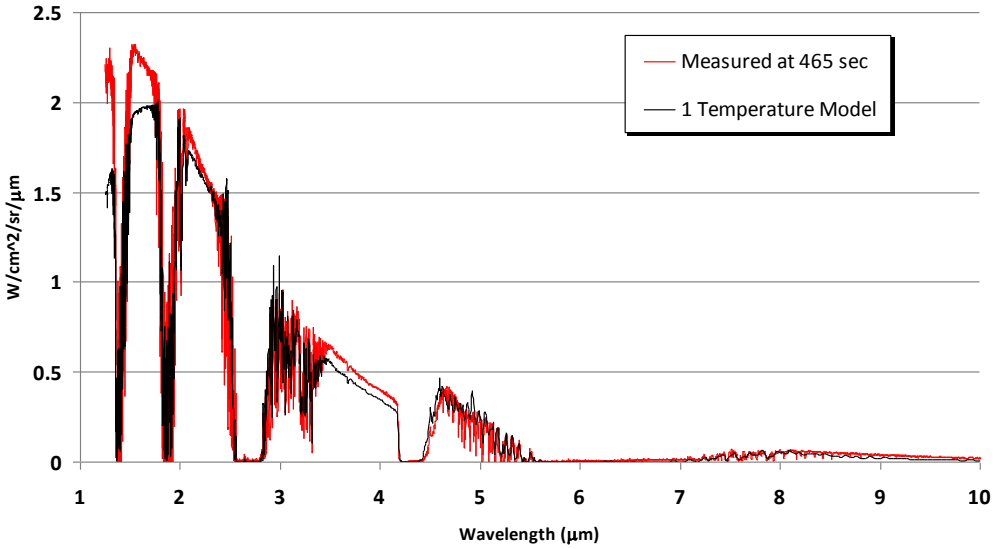

Figure 154 Single temperature signature simulation for LNG Test 1.

The FLAME code input parameters that were used for the best fit are given in Table 35.

Table 35 List of the FLAME code inputs of the 1-Temperature model

FLAME Code Input	Value
Flame Temperature	1290ºC
Emissivity at 4 microns	0.28
H_2O Mole Fraction	0.05
CO_2 Mole Fraction	0.005
CO Mole Fraction	0.05

To more closely approximate the spectral signature, a two temperature linear mixing model was used to combine two separate FLAMES simulations. This allows for the simultaneous simulation of a hotter cleaner burning portion of the flame along with a cooler more soot filled portion. The comparison of the two-temperature model to the measurement at 465 seconds can been seen below in Figure 155.

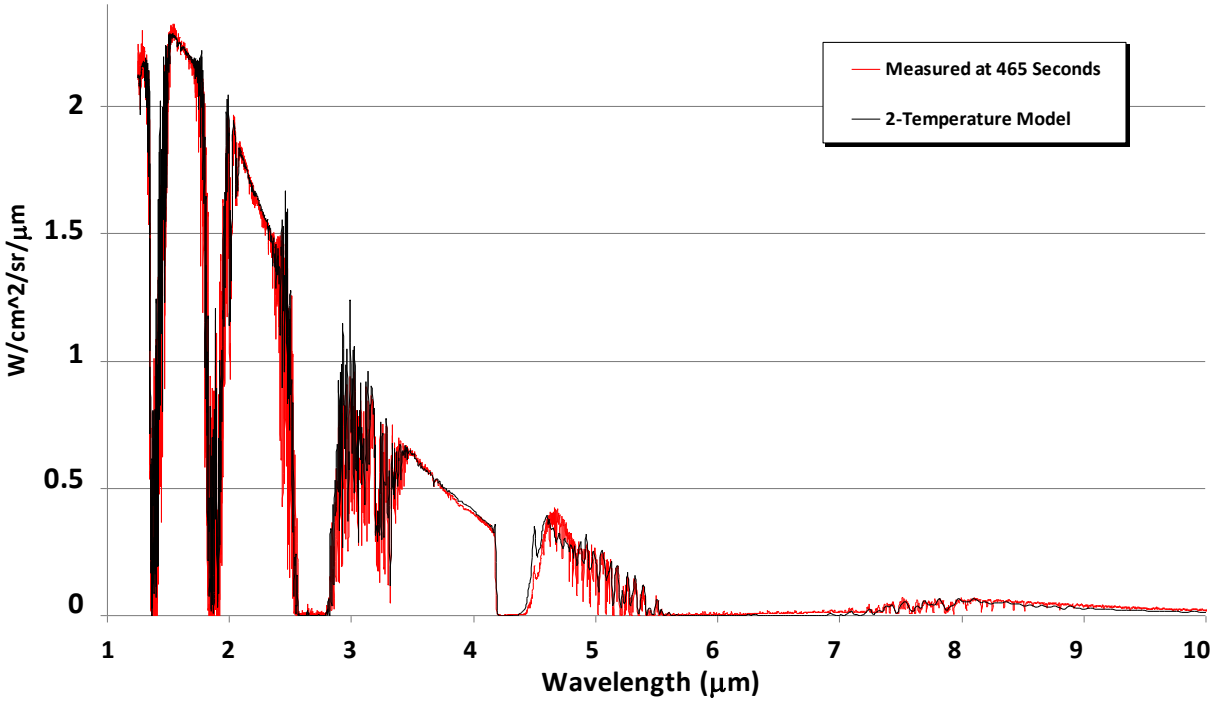

Figure 155 Two-temperature linear mixed signature model for LNG Test 1.

The 2-temperature scheme does a much better prediction of the measured spectral radiances in that both the shorter and longer wavelengths are accurately estimated. This is also a more realistic representation of the flame condition. The FLAME code input and mixing parameters that were used for the 2-temperature modeled best-fit curve are given in Table 36.

Table 36 List of the FLAME code 2-temperature model inputs for LNG Test 1

FLAME Code Input (data at 465 seconds)	High Temperature More Complete Combustion	Low Temperature Soot Rich Combustion	Weighted Average
Fractional Weight of Total	40%	60%	
Flame Temperature	1670ºC	970ºC	1250ºC
Emissivity at 4 microns	0.18	0.65	0.462
H_2O Mole Fraction	0.05	0.05	0.05
CO_2 Mole Fraction	0.001	0.005	0.003
CO Mole Fraction	0.002	0.05	0.031

FTIR Measurement Summary

Data was collected by three main instruments: a FTIR spectrometer, a high-speed visible camera, and a thermal imager. Initial laboratory and field calibration was performed that made it possible to obtain quality data. Each instrument took data at different integration times. In order to coordinate the instrument data streams and make sense of the raw data a good deal of post-processing was performed. The FTIR instrument had its own conversion files that allowed spectral radiance to be calculated. Initial start times for each data stream were established to coincide with the actual burn ignition. Algorithms were developed to import and temporally co-register the data. This registration of the instrument data allowed easy determination of the FTIR FOV at all times with respect to the location of the flame and plume.

Further calibration of the FTIR spectrometer was performed in the laboratory. Measurements were made of a blackbody source with and without telescopes mounted in front. In order to enhance the amount of radiation through the telescope, a collimator was utilized to redirect the blackbody energy. These tests allowed the transmission of the telescope-collimator system to be defined. Further, more time-consuming, testing would need to be performed in order to separate the effects of the collimator from those of the telescope. Using the wider angle telescope without the obstructing assemblies, an estimate of energy loses were made due to the reflecting mirrors. This provided a better approximation for the narrow-FOV telescope transmission. As a result, using the collimator-telescope total transmittance estimation, a maximum spectral error was calculated to be 26%. The maximum measured spectral intensity error was then quantified to be -21%. These corrections were not applied to the data since they still contain the collimator effects, but are used as an uncertainty measure.

The FLAMES combustion model was used to simulate the source fire intensity. Using the meteorological conditions measured right before ignition, the MODTRAN radiative transfer program was run to calculate the spectral atmospheric transmittance so that simulated at-sensor radiance spectra could be determined and compared to the measurements. Both a 1-temperature and a 2-temperature fire model were created, tuned, and input into the FLAME-MODTRAN simulation code. The 2-temperature modeled spectra correlated extremely well to the measure spectra. It is postulated that the two temperature states more accurately depict the true nature of the fire by characterizing both the efficient combustion regions and those dominated by slow burning, absorbing soot.

5.18 LNG Test 1 - Post-test Operations

At the end of the drain, the 15 inch discharge valve was closed, the dome vent dampers were closed, and the mixing fans were turned on for about 10 minutes to ensure the reservoir was non-flammable (fuel-rich). All discharge pipes were continuously purged with nitrogen during post-test operations. The 15 inch valve was reopened and the nitrogen purge of the reservoir commenced at about 11:30 (there was a 2-hour delay due to a problem with the limit switch on the 15 inch valve).

For the next six hours, a large fire was anchored to the diffuser as the methane was pushed out of the reservoir, through the 15 inch pipe, and mixed with air. Large amounts of concrete were spalled from the diffuser floor. In hindsight, it would have been better to leave the 15 inch plug closed until the fire extinguished (due to the methane dilution from the continuous nitrogen purge in the pipe). Once the fire was out, the methane in the reservoir could have been expelled through the 15 inch pipe with little damage to the diffuser.

As Thursday evening approached, the on-site bulk storage nitrogen trailer (initially contained 250,000 scf) was close to empty. To conserve inertion gas, the 15 inch valve closed to minimize air infiltration and nitrogen purge was secured until 3 AM Friday morning.

The trailer was refilled on Friday morning, and the nitrogen purge continued. At about 13:45 Friday afternoon, the 15 inch valve was opened. With the dome vent dampers open, the reservoir was now open at both the top and bottom, and by 14:00, methane concentration decreased below 100% of LEL; this indicated that the methane concentration was below 5%. At the same time, the oxygen concentration started to increase (from 8%).

The nitrogen trailer emptied at about 19:40. The post-test purge operation was secured at midnight on Friday (2-20-2009). Oxygen levels were between 12.7-18.4 % (upper vs. lower sample point) and methane concentrations were between 20.3-12.2 % of LEL (upper vs. lower sample point). The temperature of the concrete at the reservoir well was -57°C and the gas temperatures were in the range of -6°C to -23°C.

Two full trailers of nitrogen (500,000 ft^3 total) were required to purge the reservoir (100,000 ft^3) that had been essentially 100% pure methane at the end of the drain.

On Monday morning (2-23-2009), oxygen was ~20%, methane concentration was ~4% of LEL, and the concrete temperature was -20 C.

Figure 156 and Figure 157 provide the post-test reservoir temperatures and the oxygen and methane concentration measurements (in % of LEL).

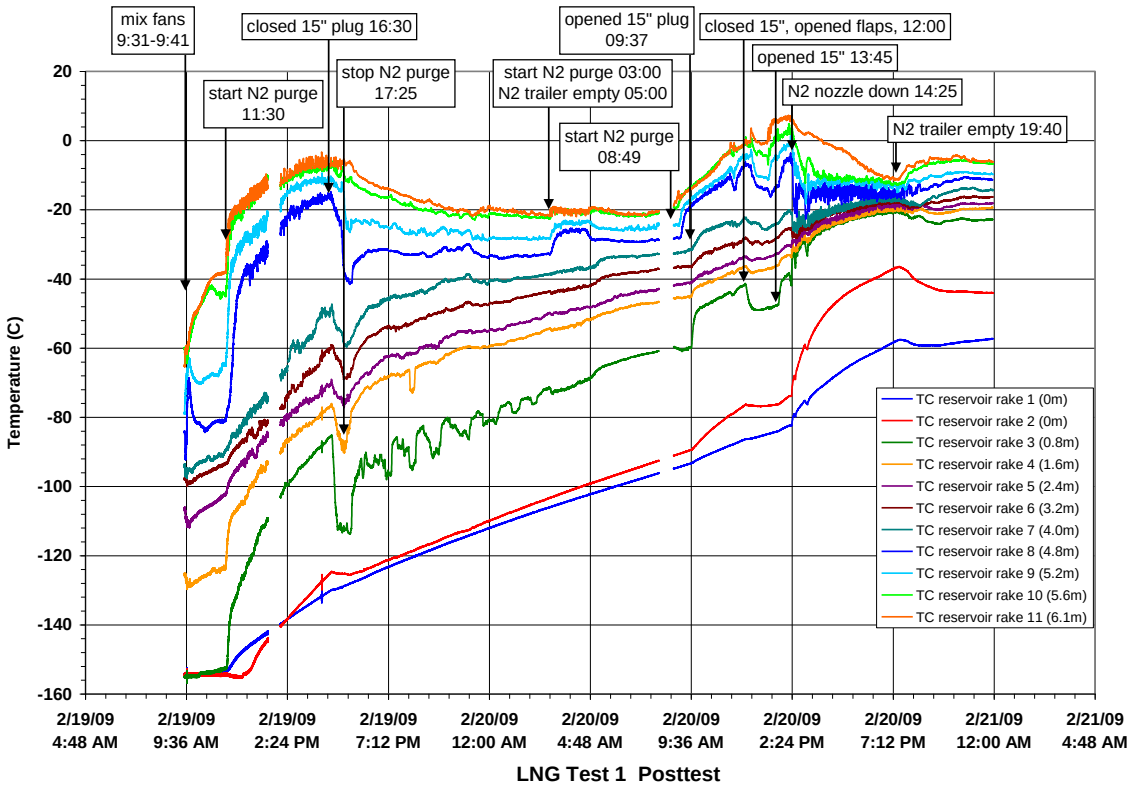

Figure 156 Post-test reservoir temperatures in LNG Test 1.

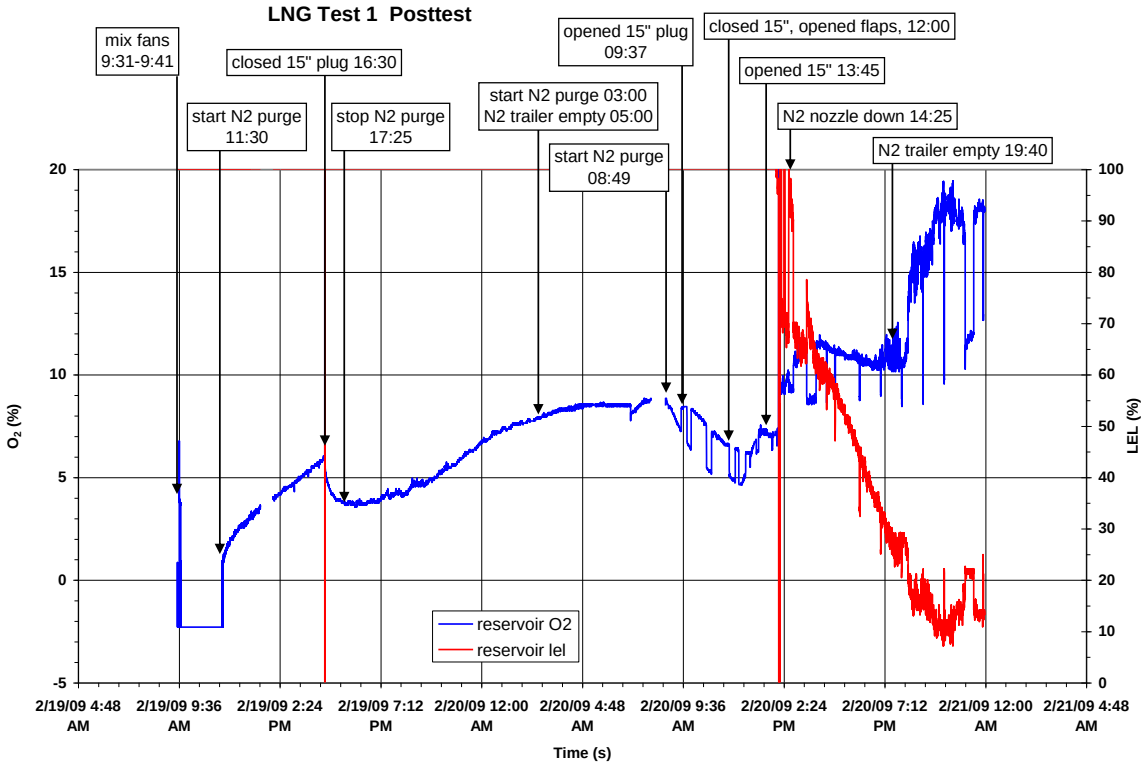

Figure 157 Post-test reservoir oxygen and LEL measurements in LNG Test 1.

5.19 LNG Test 1 - Summary

About 58.0 m^3 (~15,340 gal) were discharged in ~510 s through the 15 inch discharge pipe. The flow rate initially was about 0.061 m^3/s (970 gpm) and increased throughout the test, reaching 0.123 m^3/s (1960 gpm) at the end of the test. Between the steady-state fire interval of 390-510 s, the average flow rate from the reservoir was 0.121±0.001 m^3/s (1921±21 gpm), yielding an average mass discharge rate of 50.8±0.6 kg/s.

Average wind speed was 4.8±0.8 m/s at 331±13 degrees (magnetic north). During the steady-state interval from ~390-510 s, the steady-state pool area yielded an equivalent circular diameter of 20.7±0.4 m. Using an average liquid spill rate of 49.4±0.7 kg/s at the diffuser (based on a vapor fraction of 3%), the regression rate was 0.15±0.01 kg/m^2s.

For the Montoir land test the burn rate was about 0.07 kg/m^2s for the lowest wind speed of 2.7 m/s. The burn rate doubled for a wind speed of 9 m/s. Additionally, the 20 m land based tests by Mizner and Eyre measured a burn rate of 0.1 kg/m^2s for a wind speed of almost 7 m/s. These tests indicate that there is a trend - the higher the wind speed, the higher the burn rate.

On land the cooled ground adds little to the total evaporation rate (a function of the fire heat flux); however, boiling LNG on water will provide an additional another heat source to increase the total evaporation rate. A figure of 0.05 kg/m^2s is often used but higher figures (up to 0.2) have been suggested depending upon whether the water is confined or free.

The USCG China Lake LNG fire on water tests by Raj showed burn rates for the longest duration tests of 0.11 kg/m^2s (2.2 m/s) and 0.16 kg/m^2s (calm) (which for some reason indicate a reversed trend). Given the data from these past tests and the SNL test, the burn rate under calm conditions is probably bound by an upper limit of 0.2 kg/m^2s and is closer to 0.15 kg/m^2s.

The wind tilted the flame plume to the South. The average length was ~70 m (as compared to an average height of ~34 m. The average tilt angle from the vertical axis was ~50°. The effective pool diameter was 20.7 m, similar to the average flame width of 23.9 m at the CG height of 12.2 m and the average flame width of 21.7 m at a height of 15 m. This yielded an L/D ratio of ~3.4.

Narrow view (spot) radiometers yielded an average steady-state (between 390-500 s) surface emissive power of 238±30 kW/m^2. Surface emissive power (SEP) was also determined by correlating view factor information from video analysis with the wide-angle radiometer data, this determined an average overall flame SEP of 277±60 kW/m^2. A smoke mantle was not evident.

Surface emissive power values determined from spectroscopy correlated well with the narrow-view radiometer data. The 2-temperature model of the spectra correlated extremely well to the measured spectra. The 2-temperature model more accurately depicts the true nature of the fire by characterizing both the efficient combustion regions and those dominated by slow burning, absorbing soot. Based on user-specified (chosen to give the best fit) fractional weights of 40% for high-temperature, more complete combustion and 60% for low-temperature, soot-rich combustion; the model determined a weighted-average flame temperature of 1250°C with an emissivity of 0.46.

6 LNG Test 2 - Pretest Preparations

A number of modifications to the reservoir were implemented to reduce the high loss rate that was seen in the LNG Test 1 and another test that was attempted in June 2010 (aborted after two days of filling). Extensive peer-reviewed calculations and design reviews were performed to investigate the cause for the high loss rate. These resulted in the following modifications to the reservoir and associated systems:

1. A suspended insulated ceiling was installed to reduce the heat gain from the dome
2. A LN_2 spray cooling loop was installed at the top perimeter of the reservoir to precool the walls
3. The LNG discharge line was extended to discharge into the well to provide a bottom liquid fill (low-velocity and low mixing vs. high pressure and droplets into gas space)
4. The LNG discharge plugs seal mechanism was redesigned to ensure no leakage, and
5. Cracks in the well surface and interface to the reservoir floor were sealed with concrete sealants and a reinforced ice shield.

The first four modifications were tested for effectiveness with liquid nitrogen (LN_2) in tests performed in October 2009. These cool down tests determined that there was leakage at the well/reservoir floor interface; this led to the requirement to seal the reservoir floor using a reinforced-ice shield. This final modification was tested during the cool down for LNG Test 2 (LNG was not ordered until this test showed satisfactory results, as shown in the following section).

Figure 158 and Figure 159 show the modifications to the discharge line. The 3 inch diameter delivery line was originally near the top of the reservoir in contact with the wall. At 330 gal/min delivery rates, the flow out of the nozzle is at jet conditions (4 m/s). This condition coupled with the long distance to the reservoir bottom (5.18 m) provided a high LNG vaporization potential. A flexible stainless steel cryogenic extension line was added and placed to discharge into the discharge plug well, based on discussions and recommendations from a SIGTTO representative.

Figure 158 Original LNG discharge point and flexible hose extension.

Figure 159 Hose extending to floor and discharging into well.

Many in-ground storage tanks use a suspended deck with glass wool insulation. Stainless-steel cable (1/8 inch diameter) was strung between the roof tension ring at 3 ft centers. Insulation (duct wrap, 2 layers, 3 inch thick glass fiber blanket with foil-scrim jacket, R-value = 10) was attached on top of the cables. Analyses showed this modification is effective both for reducing heat flux (order of magnitude) and stopping convective mixing between the hot dome region and the cold reservoir region. Figure 160 shows the modifications to implement a suspended ceiling.

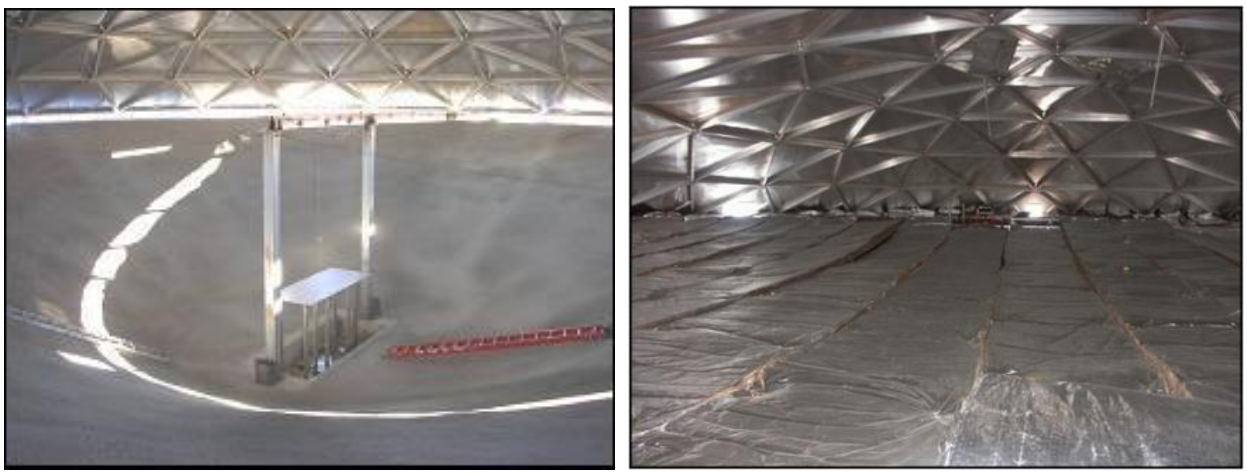

Figure 160 Reservoir without ceiling and reservoir with ceiling.

Figure 161 shows the modifications to close gaps and provide positive pressure control to address air in-leakage under low boil-off conditions (both for safety and boil-off purposes). Analysis showed that a positive pressure (a 5 inch water column) was maintained with closed dampers, 400 cfm N2, and a 7000 gpd boil-off. The nitrogen gas purge system was aligned to provide gas flow above the suspended ceiling and the dampers at the dome vents were modified to allow adjustment in their position to control and maintain positive pressure in the reservoir. A differential pressure gauge was added to monitor the pressure across the dome to ambient. Additional layers of plastic and dirt berm covered the flashing at the dome/reservoir interface.

Closed-cell foam insulation was placed at gaps in the flashing. In addition, the six hatches were also sealed with closed-cell foam insulation at final closure before the test.

Figure 161 Minimizing air leakage at dome/reservoir interface and at flashing gaps.

Analyses were performed to determine LN_2 requirements to cool down the reservoir. One-dimensional heat conduction analyses yielded the temperature gradient in the walls assuming a 24 hr contact with liquid nitrogen at 77K. The minimum amount of LN_2 needed to achieve this cooling was ~35,000 gallons (includes 10% loss due to flashing).

A spray ring was designed and installed to spray the walls below the suspended ceiling; analyses determined that a ~23 gpm flow rate was needed to cool down the reservoir walls in ~24-48 hrs (based on a useable supply of 6000 gallons of LN_2 every 4 hrs.).

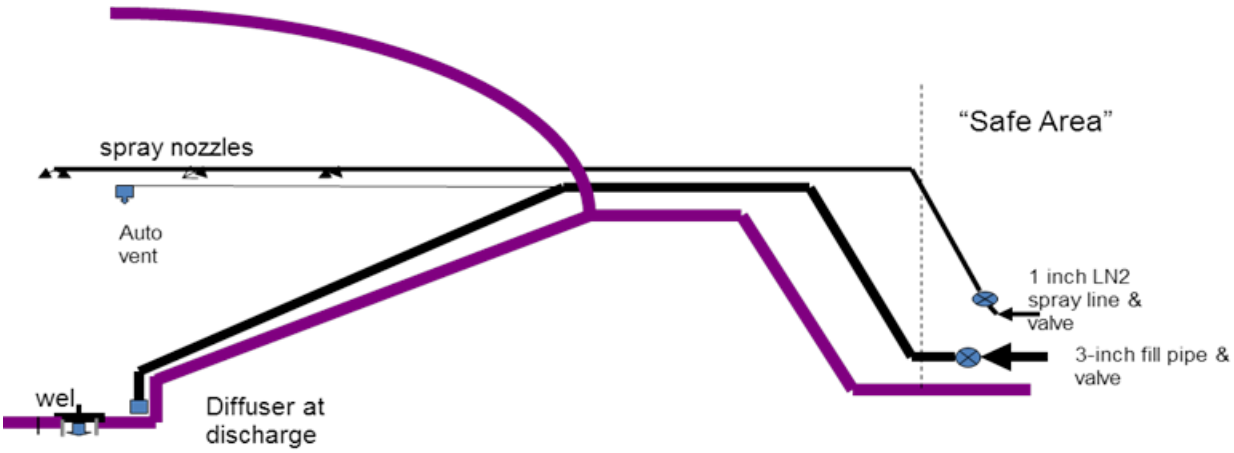

Figure 162 LN_2 spray ring concept.

The LN_2 spray ring design concept, shown in Figure 162, was based on available trailer pressure head and drops (vertical head and copper friction losses). The main fill line used 2 inch ID copper tube with LN_2 fittings. The spray circular-ring header placed at the top of the reservoir

(below the suspended ceiling) used 1.5 inch ID copper tube comprised of 10 ft sections, brazed couplings, and 1-gpm spray nozzles (23) placed every 10 feet. Figure 163 and Figure 164 show the LN_2 spray line (external) and ring (internal).

Figure 163 Building the LN_2 spray line coupler and pipe external to reservoir.

Figure 164 Fabrication of LN_2 spray ring with nozzles internal to reservoir.

There appeared to be small amount of LNG leakage past the plugs in LNG Test 1 and the aborted test in June. The LNG discharge plugs were modified to meet a no leak design criteria using 0.003 inch thick Kapton film and clamping rings. The Kapton film was placed on top of the lower plug (below couplers that attach a new lower plug to the upper original plug). The film extended to the outside of the pipe flange, where it was clamped using a clamp ring, gasket, and bolts to the pipe flange. This provides a mechanical seal at the interface of the plug and the pipe flange. Figure 165 shows the assembly on the 15 inch pipe plug after opening the plug (thereby breaking the Kapton film) following the cool down and leak test performed with LN_2 in October 2009.

Figure 165 The 15 inch plug after the October LN_2 cool down and leak test.

As mentioned previously, the October LN_2 cool down tests determined that there was leakage at the well/reservoir floor interface; this led to the requirement to seal the reservoir floor using an ice shield. Figure 166 shows a wooden dam (~6 inch tall) constructed on the top perimeter of the well. One of the reservoir liquid level dip tubes was extended into the well to monitor for water leakage into the well during the LNG Test 2 pretest cool down (which would have frozen the plugs in place). Carbon-fiber mesh was attached to the dam to ensure forming a robust ice shield when the water froze. Figure 166 also shows water on the floor prior to the LNG Test 2 pretest cool down.

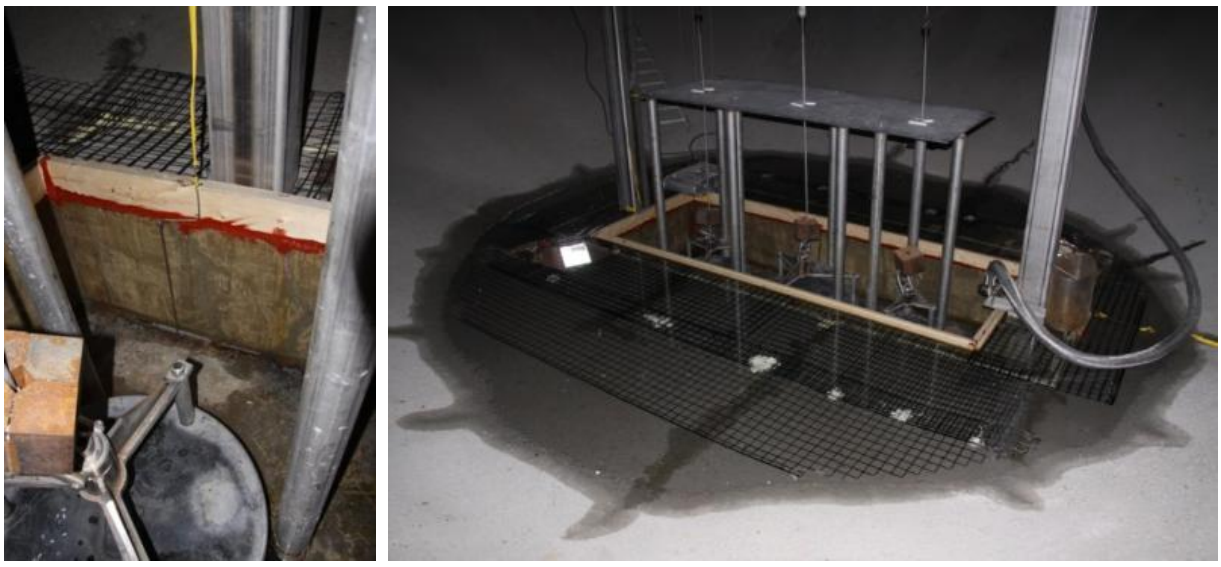

Figure 166 Construction and installation of the ice shield on the reservoir floor.

7 LNG Test 2 - Test Goal

The goal for the 2nd test was to produce a very large LNG spreading pool fire (~100 m diameter) with a steady-state duration of ~3 minutes. It was estimated that 1417 m^3 (375,000 gallons) of LNG (pure methane) would be needed, 1172 m^3 (310,000 gal) for the test and 246 m^3 (65,000 gal) to account for flashing and boil-off during filling operations. The fuel was to be delivered by 37 cryogenic road trailers (10,000 gal capacity).

It is believed that two-phase flow effects in LNG test 1 caused the spill rate to be lower than predicted. The spill rate estimate in Test 1 was based on pressure head and pressure drop assuming single-phase flow. Models for frictional pressure drop for cryogenic gas-liquid two-phase flow were reviewed and implemented that yielded reasonable comparisons to the LNG Test 1 data. Note that the pressure drop is directly related to the vapor fraction which is a function of the pipe diameter to area ratio. Two-phase flow effects should be reduced for tests using the larger pipes due to the lower vapor fraction.

Figure 167 shows the predicted reservoir response when filled with 1134 m^3 (300,000 gallons) of LNG, filling the reservoir to a 4.7 m initial liquid height, and then drained. Cryogenic gas-liquid two-phase flow models were used in the calculation. The planned method of operation was to partially open (a few inches) both the 24 inch and 36 inch plugs for about 2 minutes to cool the 100 m long discharge pipes, then fully open the plugs (an instantaneous step change in flow rate was assumed). With both plugs fully opened, an average flow rate of ~3.2-3.8 m^3/s (50,000-60,000 gpm) was predicted to occur. Figure 168 shows that the predicted pool diameter would be greater than 100 m for ~300 s, assuming the LNG burn rate was 0.15 kg/m^2s.

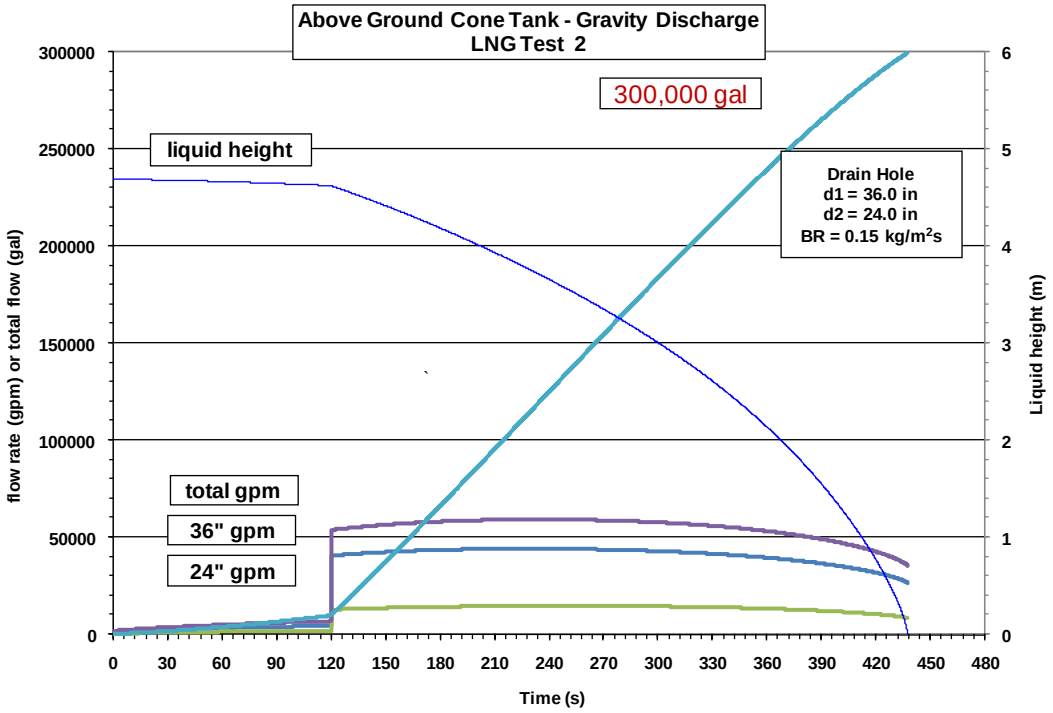

Figure 167 Predicted flow rate for a 300,000 US gallon test.

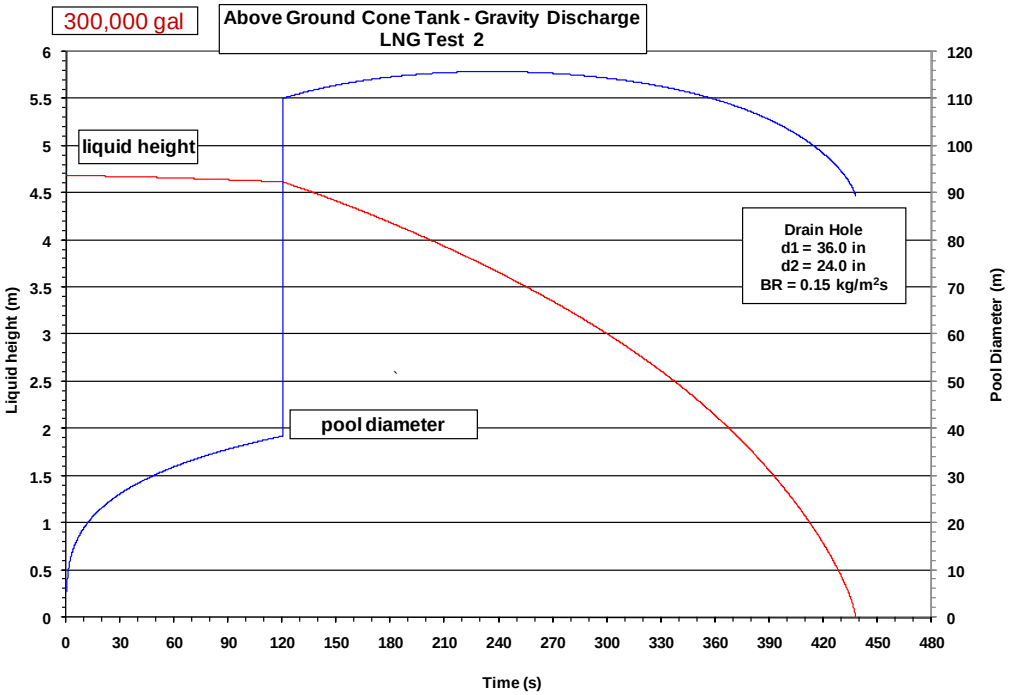

Figure 168 Predicted pool diameter for a 300,000 US gallon test.

7.1 LNG Test 2 - Reservoir Cool Down and LNG Fill

The reservoir cool down for the 2nd LNG pool fire experiment commenced on December 1, 2009. All hatches were closed and sealed. All data acquisition systems were on-line to monitor reservoir gas and wall temperatures, and also to monitor reservoir oxygen concentrations, as the LN_2 had a dual purpose as to purge the air from the reservoir.

At ~11:50, the first LN_2 trailer (6000 gal capacity) was connected to the LN_2 cooling line for spray cooling. Purging of all reservoir discharge pipes (~3 cfm/pipe) with gaseous nitrogen also commenced at about 11 AM and continued until the test was completed. The on-site bulk liquid nitrogen storage trailer (2650 gallon capacity (250000 scf)) was used for this purpose and also to provide make-up purge gas for the reservoir as necessary. Note the bulk storage trailer has about a 10 hr flow capacity at the maximum discharge rate of about 415 cfm.

Table 37 shows that a total of 12 LN_2 trailers were used in the conduct of the test. The times listed indicated the start of offload of each trailer. For many trailers, offload was intermittent, especially after the initial cool down.

Figure 169 and Figure 170 show the reservoir gas and wall temperatures and the liquid levels (well and reservoir floor) over the course of the 10 days. Note that the reservoir gas 5.2 m thermocouple is located at the suspended ceiling. Note also that the well fills to ~30 inches before it overflows onto the reservoir floor.

Table 37 Liquid nitrogen deliveries in LNG Test 2

Liquid Nitrogen Deliveries				Liquid Volume		Gas Volume	
Date	Time	Trailer #	Trailer #	Trailer Gallons	Total Gallons	Trailer scf	Total scf
12/1/2010	11:50	1	9074	6000	6000	558720	558720
12/1/2010	17:18	2	9065	6000	12000	558720	1117440
12/2/2010	1:10	3	9074	6000	18000	558720	1676160
12/2/2010	9:52	4	9105	6000	24000	558720	2234880
12/2/2010	17:45	5	9102	6000	30000	558720	2793600
12/4/2010	0:28	6	9105	6000	36000	558720	3352320
12/4/2010	11:36	7	9087	6000	42000	558720	3911040
12/5/2010	0:38	8	9074	6000	48000	558720	4469760
12/5/2010	22:09	9	9087	6000	54000	558720	5028480
12/8/2010	16:46	10	9074	6000	60000	558720	5587200
12/9/2010	11:15	11	9065	6000	66000	558720	6145920
12/10/2010	13:14	12	-	6000	72000	558720	6704640

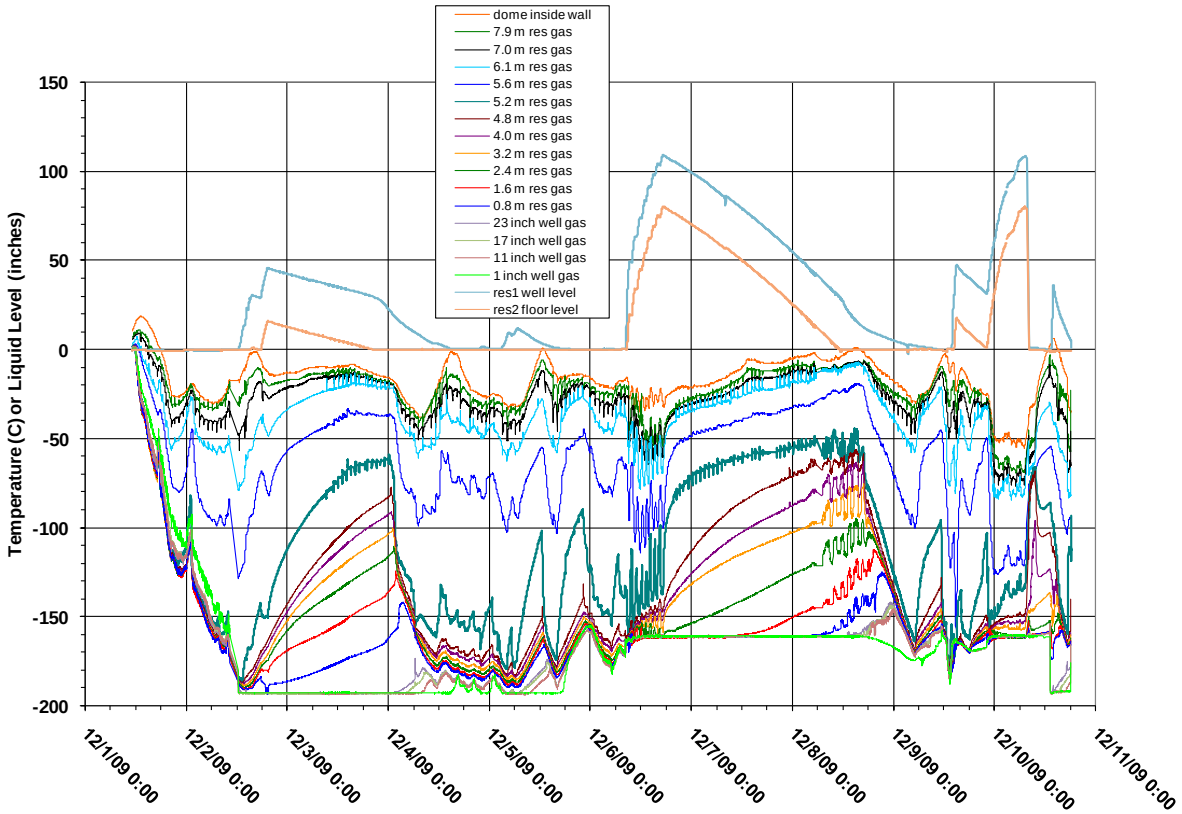

Figure 169 Gas temperatures during the LNG Test 2 cool down and fill.

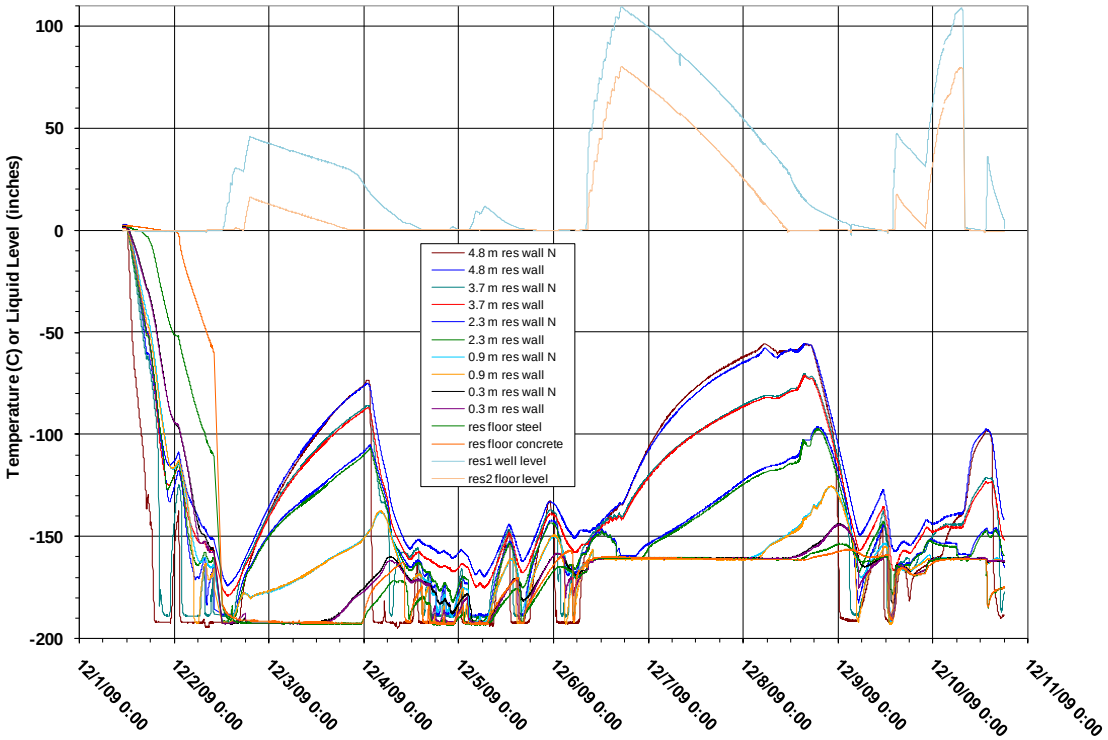

Figure 170 Wall temperatures during the LNG Test 2 cool down and fill.

It took about 24 hrs to cool the walls with the spray ring, by 1230 on 12/2/09 liquid level in the well started to increase (the water on the reservoir floor was well frozen at this time). A LN_2 trailer was connected to the LNG fill pipe and the well was overfilled to spill onto the reservoir floor (to a height of ~15 inches) to determine a loss rate. Figure 171 shows the loss rate versus time. The loss rate decreased from ~5 gpm to ~2gpm over the 24 hrs it took to boil-off the LN_2.

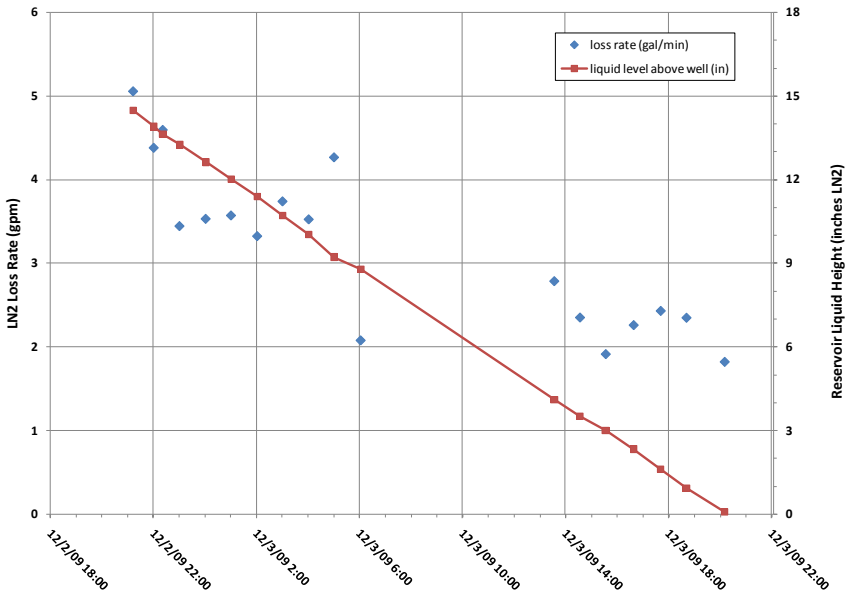

Figure 171 LN_2 loss rate from reservoir floor in LNG Test 2.

Figure 172 shows that by ~4 PM the reservoir oxygen content was reduced from 20.9% to 0% (both low and high sample points). In this 1st four hours of spray, approximately 1 trailer of LN_2 (6000 gal, 559000 scf of nitrogen gas) was used which indicates the plug flow (cold nitrogen gas slowly filling the reservoir and displacing the warm ambient air out the vents) was very efficient. The periodic dips in the gas concentrations are caused by switching the sample point between the high location (just below the vents) and the low location (just below the suspended ceiling).

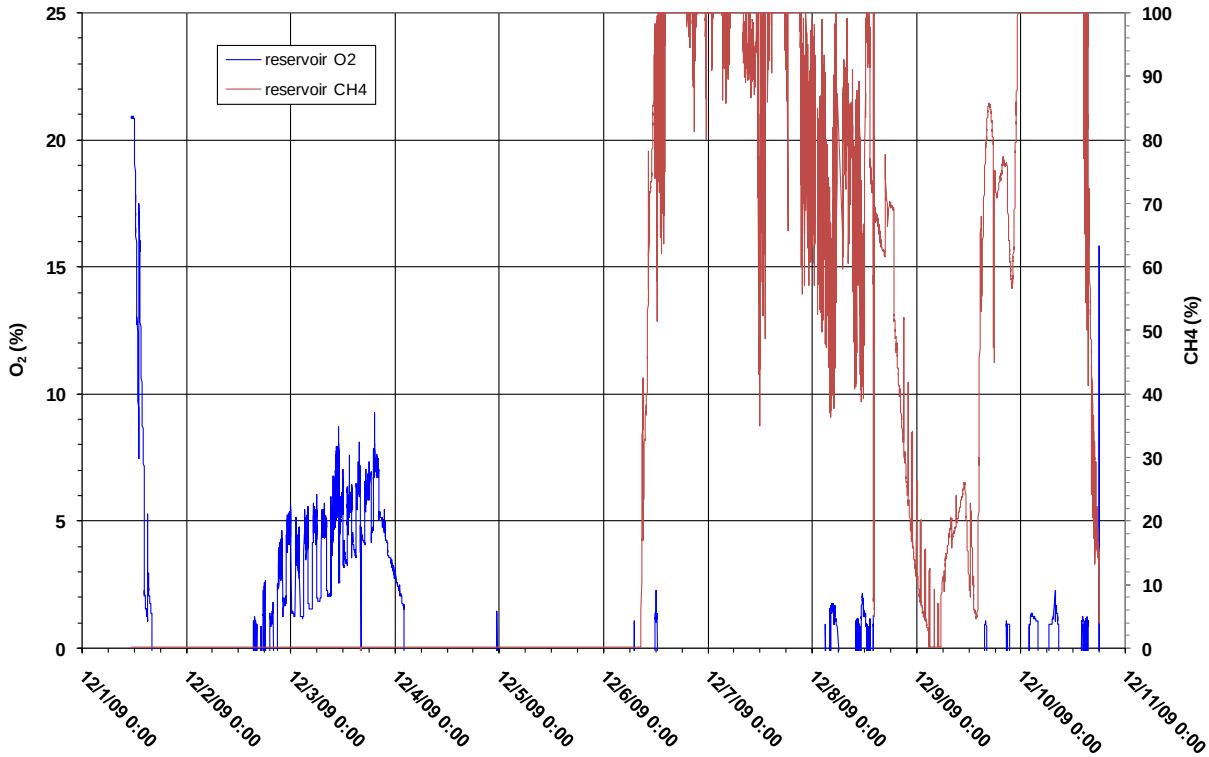

Figure 172 Oxygen and methane concentration during LNG Test 2 cool down and fill.

With the success of the cool down and boil-off test, the contractor for the LNG was given the go-ahead to start deliveries. The schedule called for ten trailers (10,000 gal capacity) to be delivered each day for three successive days (starting on Sunday, December 6), and ~4-6 trailers to be offloaded on the fourth day if needed, based on the measured boil-off during the course of the fill. The delay between the end of the LN_2 boil-off test and the loading of the reservoir was due to a contractual obligation to give the supplier a 3-day notice. The reservoir was maintained in a cold state through intermittent use of the LN_2 spray cooling system.

Filling the reservoir with LNG (~99.9% liquid methane) commenced on December 6 at ~0800 and was stopped after the offload of the 8th trailer at ~1700 the same day. Figure 173 shows the increase in levels in both the well and the reservoir (note the reservoir differential pressure to ambient in inches water is also given in Figure 173). Table 38, the reservoir LNG fill log, shows the time commencing offload of each trailer, and the initial and final values (uncorrected for baseline shifts) of the liquid level instrumentation. Reservoir liquid height is measured by the two dip tubes and the mechanical float before and after each fill.

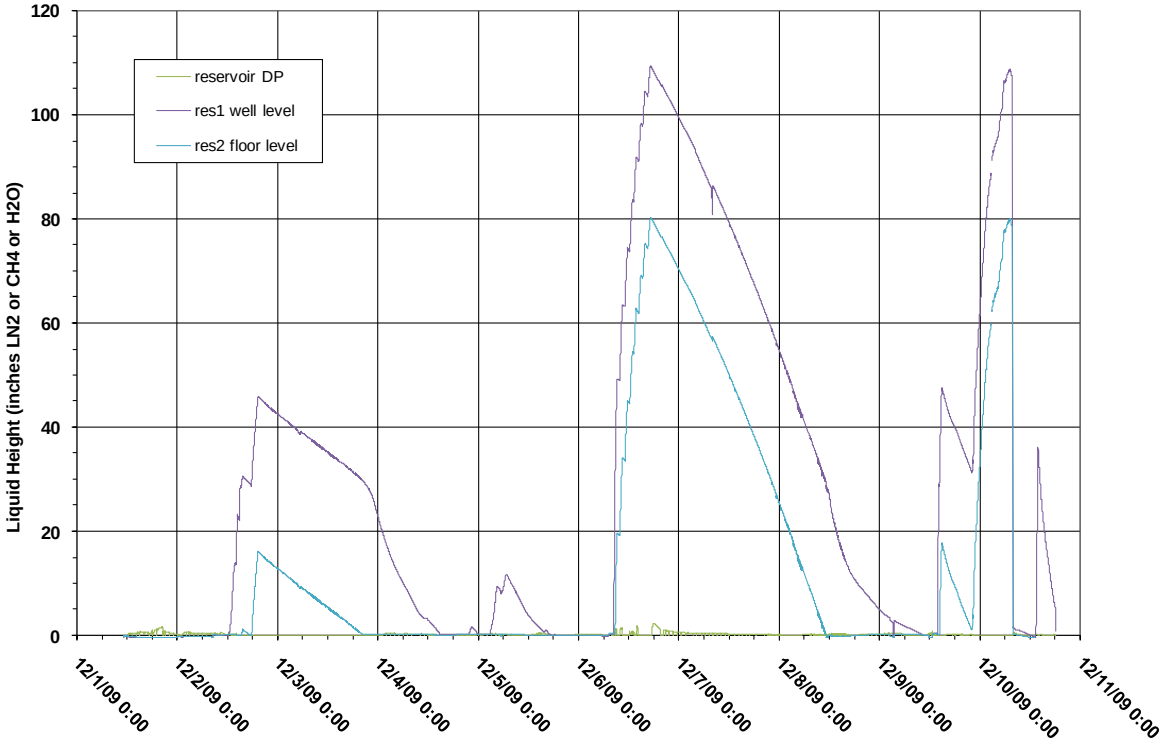

Figure 173 Liquid levels in the reservoir in LNG Test 2.

Table 38 LNG Test 2 reservoir fill log

					Prefill			Postfill			
Date	Start Time	Trailer #	Gallons Delivered	Total Gallons	Bubbler#1 Prefill Height (in)	Bubbler#2 Prefill Height (in)	Float Prefill Height (in)	Stop Time	Bubbler#1 Postfill Height (in)	Bubbler#2 Postfill Height (in)	Float Postfill Height (in)
12/6/2009	8:00	1	9863	9863	6.50	6.30	12.00	9:17	55.3	25.4	12
12/6/2009	9:45	2	10206	20069	55.20	25.10	29.00	10:29	69.7	40.0	33
12/6/2009	10:59	3	10061	30130	69.20	39.50	33.00	11:44	80.4	50.7	54
12/6/2009	12:14	4	10286	40416	80.40	50.70	54.00	12:54	90.3	60.8	61
12/6/2009	13:12	5	10434	50850	90.60	61.10	61.00	13:48	97.8	68.4	71
12/6/2009	14:12	6	10343	61193	97.20	67.20	71.00	14:58	104.2	74.9	77
12/6/2009	15:20	7	10254	71447	103.80	74.30	78.00	15:56	110.5	81.1	84
12/6/2009	16:33	8	10269	81716	109.30	79.90	84.00	17:14	115.2	85.9	89
12/9/2009	13:47	9	10229	91945	6.60	6.20	12.00	14:53	53.6	23.6	28
12/9/2009	22:02	10	10200	102145		6.97	12.00	23:04	55.4	25.7	27
12/9/2009	23:05	11	10200	112345	55.70	25.90	27.00	23:56	67.6	38.2	40
12/9/2009	23:59	12	10200	122545		38.00	40.00	0:44	77.6	48.3	48
12/10/2009	0:47	13	10200	132745	77.50	48.20	48.00	1:29	86.0	56.9	59
12/10/2009	1:29	14	10200	142945	86.20	56.90	59.00	2:25	92.9		63
12/10/2009	2:25	15	10200	153145	93.00	63.90	63.00	3:13	99.1	70.0	71
12/10/2009	3:14	16	10200	163345	99.00	70.00	71.00	4:23	102.0	72.7	74
12/10/2009	4:23	17	10200	173545	102.00	72.60	74.00	5:11	106.9	78.0	79
12/10/2009	5:15	18	10200	183745	106.80	77.80	79.00	5:52	112.4	83.7	84
12/10/2009	5:57	19	10200	193945	112.20	83.30	84.00	7:14	114.5	85.7	87

Figure 174 presents the methane liquid level in the reservoir during the off load of the 8 cryogenic trailers. Approximately 55,000 gallons was in the reservoir at the end of the off load, with an average trailer off load of ~7500 gal. Between each off load, a loss rate was calculated. Figure 174 shows these point measurements. With increasing loss rates seen at the end of each off load, it became evident that the plan to off load 10 trailers/day was not viable and the off loads was stopped. Figure 174 also shows the long-term boil-off (~30 gpm) over the next two days (the large transients in the boil-off were due to changing gas bottles and adjusting power supplies for the dip tube instrument). It is postulated that the large and increasing loss rates that were seen when the liquid level increased in the reservoir was due to cracks in the PUF insulation lining the reservoir allowing LNG to seep into the compacted dirt, as there was no indication that the discharge plugs were leaking.

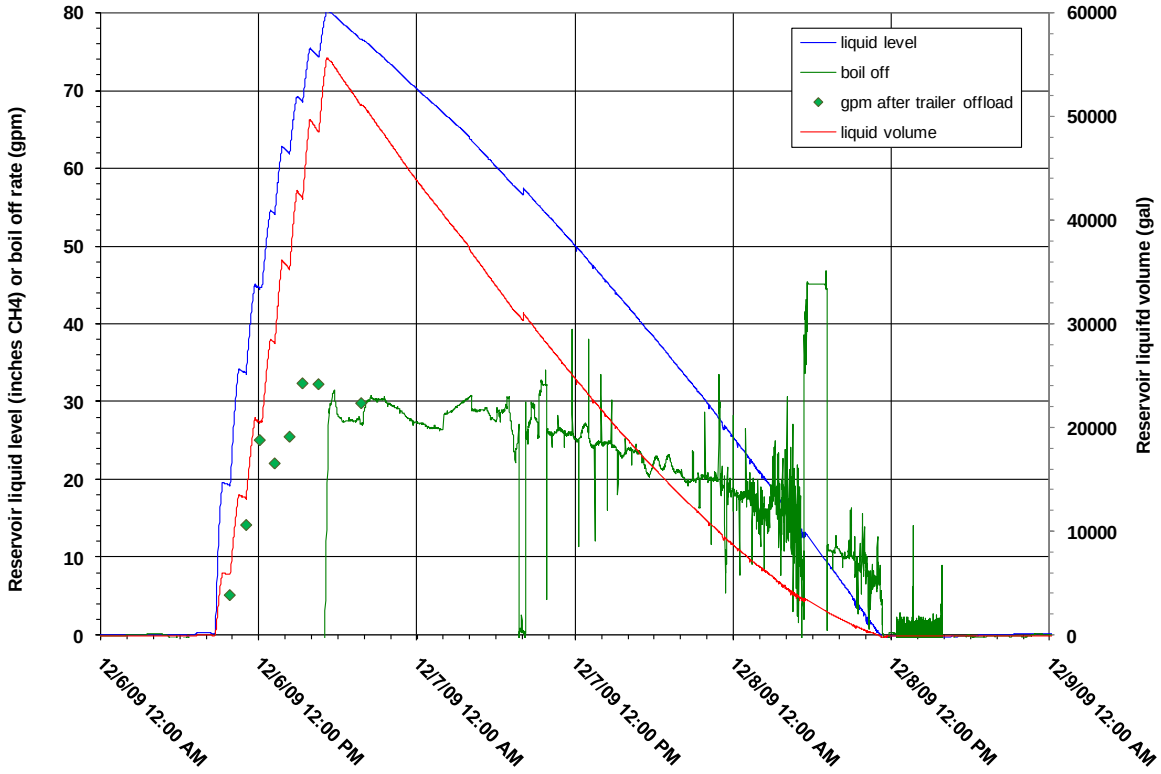

Figure 174 Reservoir liquid level during the fill operation on December 6.

Due to the large boil-off rates, it was decided to queue as many trailers as possible and then off load as quickly as possible before the test. CleanEnergy initially thought they could provide 14 trailers, but due to unexpected extremely cold weather in the Southwest, they had to pull 3 trailers to supply fuel for other customers and have us discharge 1 trailer early in order to meet other commitments. Figure 175 shows the results of the off load operations immediately before the test. One trailer was discharged at ~2PM on 12/9/2010. Off load of the remaining 10 trailers commenced at ~10 PM on 12/9 and was completed at ~7AM on 12/10.

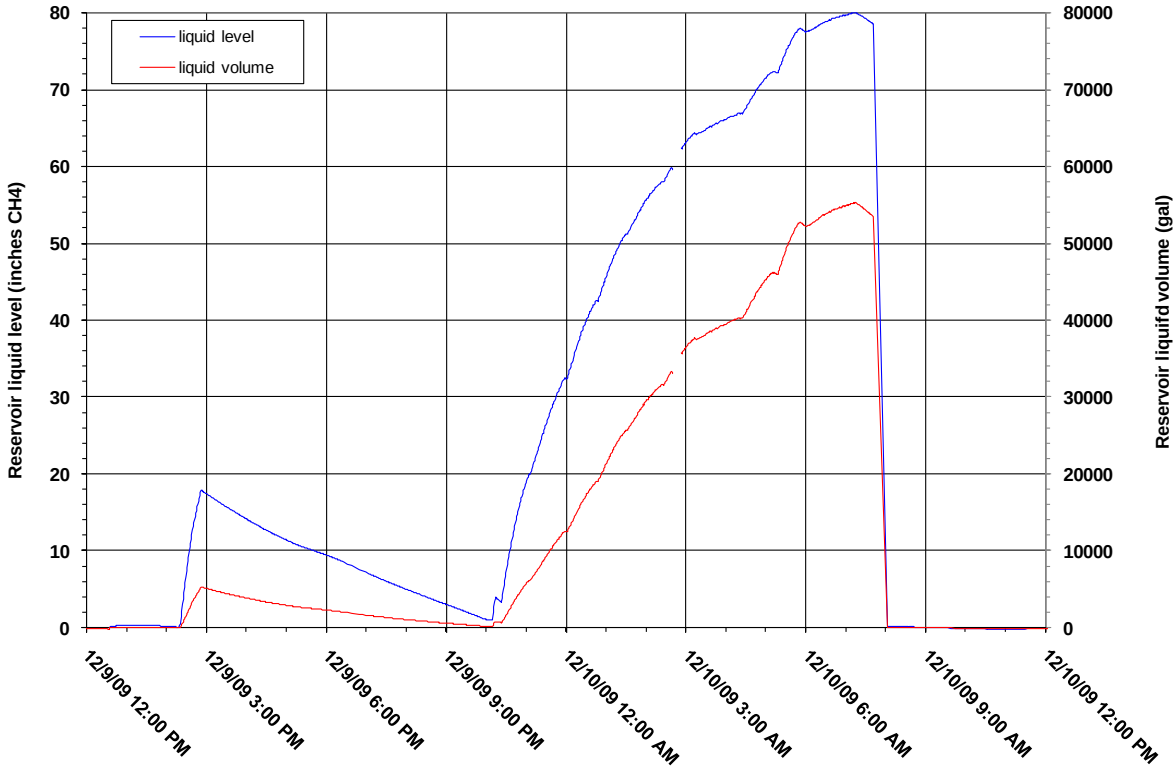

Figure 175 Reservoir liquid level during the fill operation on December 9.

With less fuel and a lower pressure head, the discharge plan was modified to maximize the discharge rate. Figure 176 shows the predicted reservoir response when filled with 208 m^3 (55,000 gallons) of LNG, filling the reservoir to a 2.0 m initial liquid height. The method of operation was to partially open (~2 inches) all plugs for about 30 seconds to cool the discharge pipes, and then fully open the plugs. It was predicted that an average flow rate of 1.89 m^3/s (30,000 gpm) should be achieved with all plugs fully open. Figure 177 shows the predicted pool diameter exceeding 80 m, with the reservoir emptied in 150 s. Note that the calculation assumed an instantaneous step change in flow and a constant regression rate of 0.15 kg/m^2s, therefore yielding a step change in pool diameter.

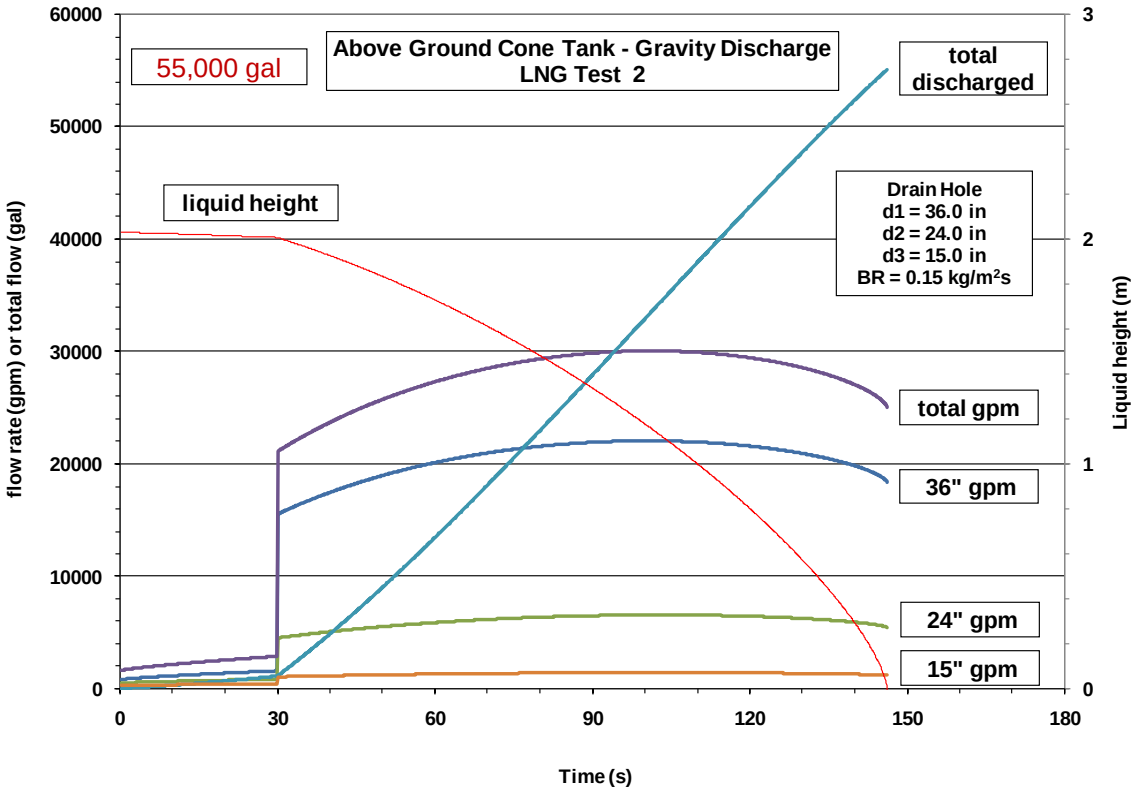

Figure 176 Predicted flow rate for a 55,000 gal test.

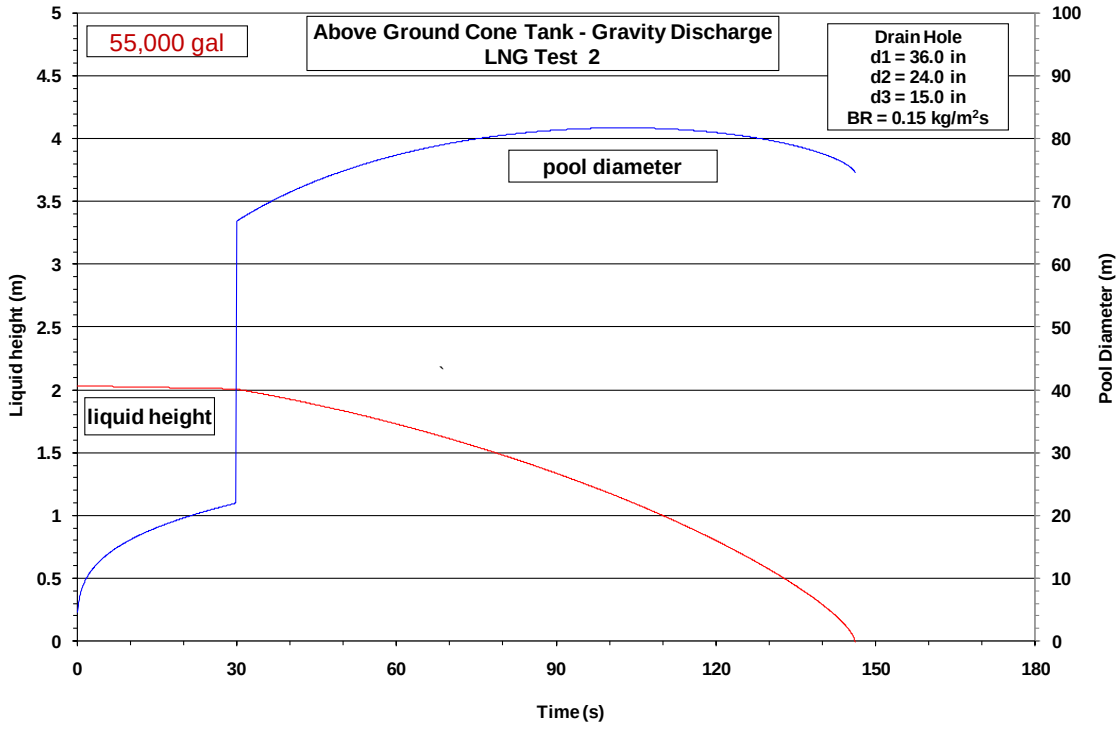

Figure 177 Predicted pool diameter for a 55,000 gal test.

7.2 LNG Test 2 - Test Execution and Measurements

The test commenced at approximately 7:49 AM on Thursday, December 10, 2009 and lasted about 10 minutes. Refer to Figure 43 in the following discussion of the various measurements.

7.3 Meteorology

The network communications with the meteorology tower were limited the morning of the test. This problem with communications prevented the recording of the higher speed data (1 Hz sample rate). Therefore, 1 second data for wind and temperature was not recorded (it was available for on-line viewing) from the LNG 30 m tower (see Figure 36 for location) during the morning of the burn. The five minute averaging interval trace was available for recording.

Qualitative visual observations of the 1 second data seemed to indicate a general trend of decreasing winds after about 0730, which was confirmed by the 5 minute data averages, standard deviations and 1 second maximum gust recorded at the tower. Most observations during the 0750 through 0755 time period seemed to be less than 1 m/s, with the directions varying from NW to E to S. Variable wind directions are expected when the wind is light.

Figure 178 is a graph of the SODAR and tower wind speed data in the vicinity of the LNG burn area the morning of the burn (x-axis indicates time of day in Mountain Standard Time (MST)). Winds depicted are those in the lowest 90 meters above ground level (AGL) in increments of 20 meters starting from the height of 10 meters (data is available in 10 meter increments). Figure 179 is a graph of the wind direction.

The sampling results in Figure 178 show winds were just about calm at the tower near and below 30 meters AGL between 740 and 0800. The SODAR showed slightly higher wind speeds, but still below 2.5 m/s below 50 meters AGL. Winds at and above 70 meters AGL were above 3 m/s at the SODAR site.

Note the data shows there can be different wind speeds and directions within a few miles, with different drainage flows in the surface layer. Winds at and above 50 meters AGL were fairly steady and generally from the NW through N consistent with the morning Rio Grande drainage flow and the synoptic pressure gradient for Thursday December 10th, 2009.

The tabulated data is given in Table 39, provides 5-minute averages of wind speed (m/s) and wind direction (degrees) at the listed end time. The table shows that between 0745 and 0800 MST the winds at 60 meters above ground were from the NNW, while the winds below were light and variable. These results are supported by the coarse data (not shown) from the Clean Air Network meteorological 60 meter A36 tower, located approximately 2 miles NE of the LNG area.

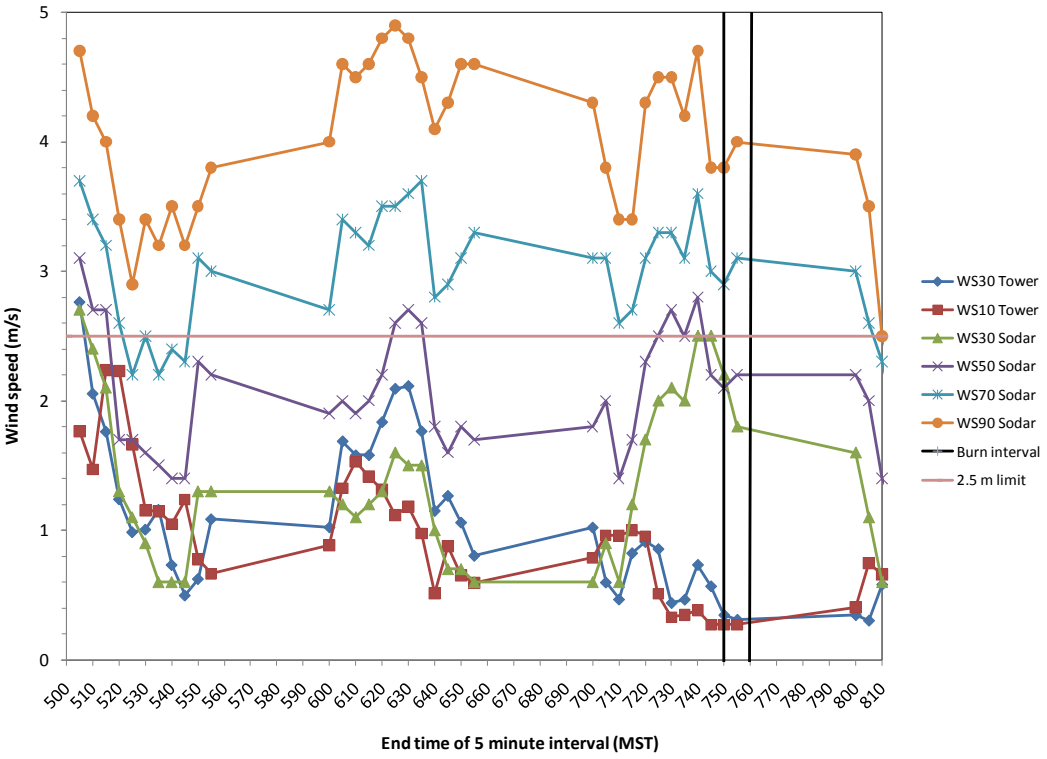

Figure 178 Wind speed data in the vicinity of LNG Test 2.

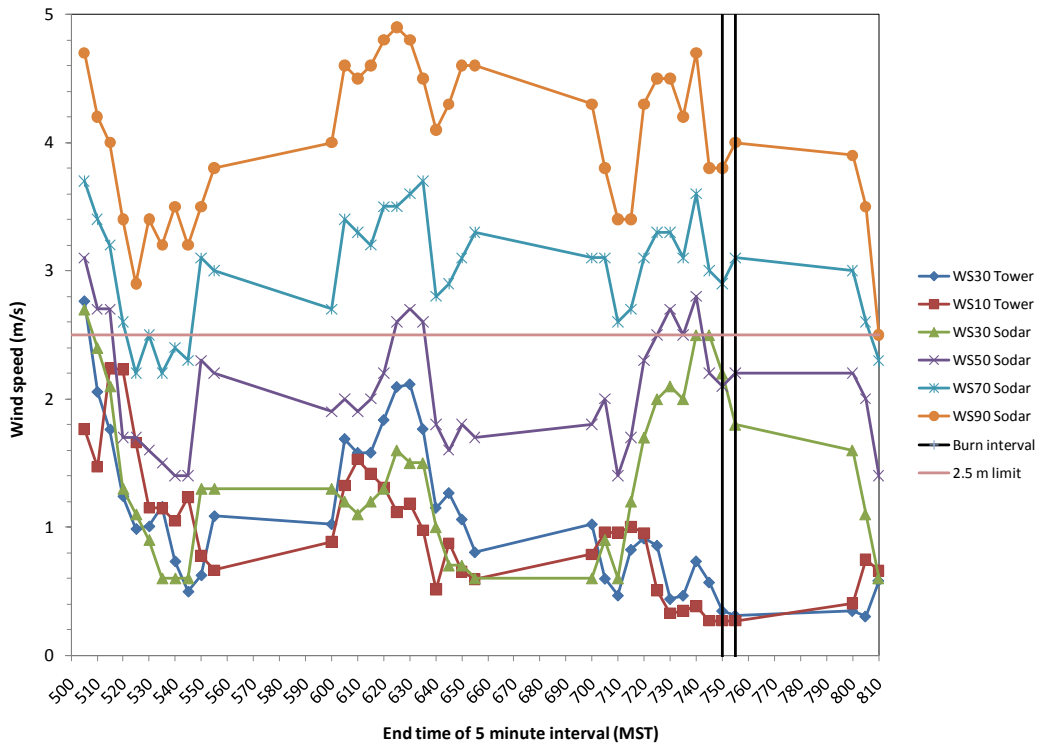

Figure 179 Wind direction data in the vicinity of LNG Test 2.

Table 39 Wind speed and direction from the LNG 30m Tower and SODAR at test execution.

End Time	WS 10m Tower (m/s)	WS 30m Tower (m/s)	WS 30m Sodar (m/s)	WS 50m Sodar (m/s)	WS 70m Sodar (m/s)	WS 90m Sodar (m/s)
745	0.3	0.6	2.5	2.2	3.0	3.8
750	0.3	0.3	2.2	2.1	2.9	3.8
755	0.3	0.3	1.8	2.2	3.1	4.0
800	0.4	0.3	1.6	2.2	3.0	3.9
End Time	WD 10m Tower (degrees)	WD 30m Tower (degrees)	WD 30m Sodar (degrees)	WD 50m Sodar (degrees)	WD 70m Sodar (degrees)	WD 90m Sodar (degrees)
745	62	18	342	353	360	357
750	90	7	347	2	359	353
755	112	16	355	1	356	351
800	250	17	346	350	348	344

In conclusion, *winds in the vicinity of the LNG s*ite below 30 meters AGL were light, while winds above 50 meters were consistent with the pressure gradient and Rio Grande drainage flow and increased gradually to over 3.5 m/s at 90 meters above ground.

Figure 180 and Figure 181 present the wind data from the 3D ultrasonic anemometers mounted on the North spoke (340º magnetic heading) wind tower located approximately 236 m from the pool centerline. The North tower has three instruments, at 2 m (US3), 5 m (US2), and 10 m (US1) above the ground surface. At ignition, the wind speed was <1 m/s.

Subsequent analysis of the heat flux data will show that the fire was at a near steady-state (SS) condition from 200 to 300 s. Most of the following averages are determined for this duration. At SS, for the anemometer at 10 m height, the average wind speed was 1.6±0.2 m/s at 324±9 degrees (magnetic north).

The ambient pressure was 12.19 psia, air temperature was -2°C, and the relative humidity was 59%. The water temperature was 1°C and the water depth was ~2 m at the pool center.

The water was quite cold, and likely contributed to the formation of ice and/or methane hydrates during the course of the test. Luketa [2011] discusses the formation of a hydrate layer during the liquid methane spill and the potential consequences on the test results. The amount of methane encased in the hydrate for the 83 m test was uncertain (upper bound estimate was about 5% of the methane spilled) but there are indications that the ice/hydrate layer was mostly comprised of ice since the duration of late-time burning was relatively short and the burn area was very limited. Note that this same hydrate formation would likely have occurred if a mixture of methane, ethane, and propane (representative of liquefied natural gas) had been spilled.

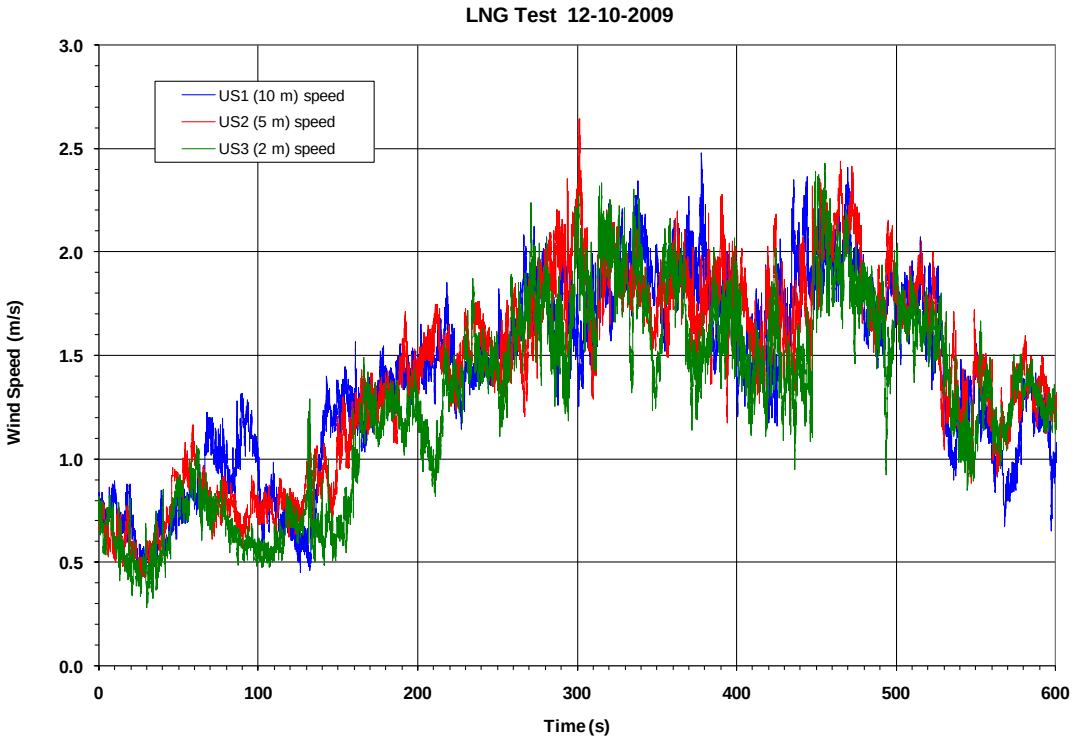

Figure 180 LNG Test 2 wind speed at the LNG test site (North spoke).

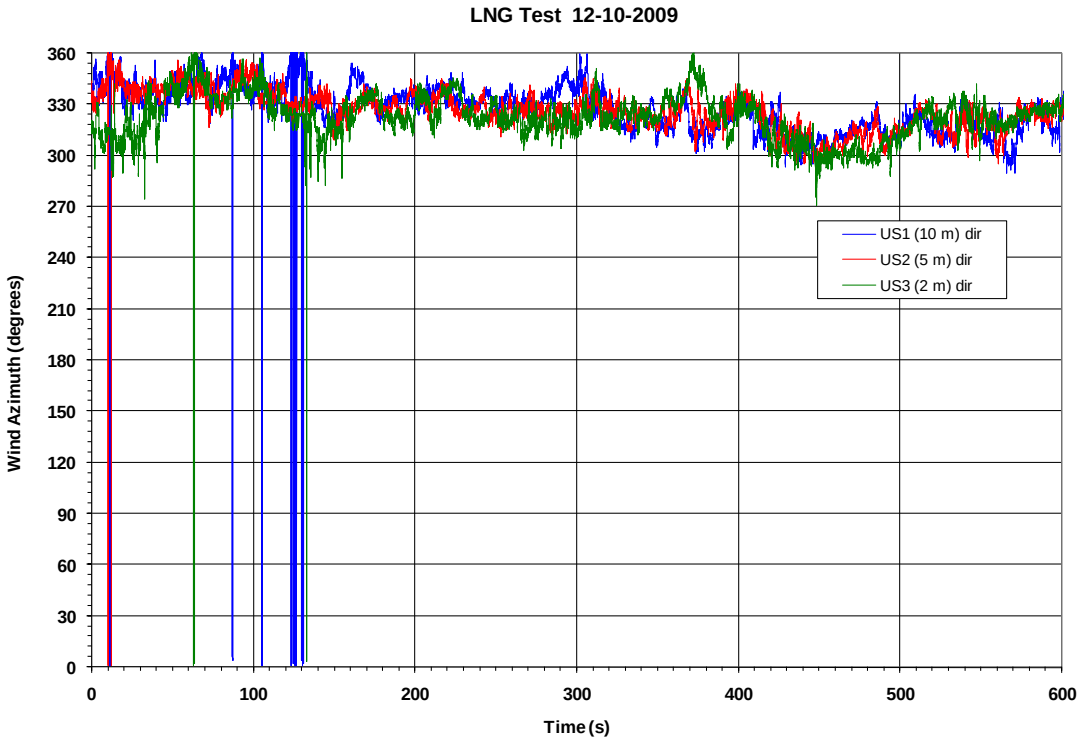

Figure 181 LNG Test 2 wind direction at the LNG test site (North spoke).

7.4 Reservoir Liquid Discharge

Figure 182 shows the methane liquid level and flow rate from the reservoir and compares it to predicted values using a discharge of 198.5 m^3 (52,500 gallons). Note that the actual level started slightly less than 2 m, and the time that the valves were partially open was ~40 s. Note also the prediction assumed an instantaneous full opening of the plugs, whereas the actual opening (for all 3 plugs) was on the order of 10 s. The flow out of the reservoir was initially oscillatory, likely caused by waves affecting the pressure gauge when the plugs were lifted.

The measurements of discharge rate are based on pressure head from a dip tube and the laser-determined volume vs. liquid height measurements shown in Figure 183 and using a methane density of 420 kg/m^3.

The measured average flow rate during the partial open period (83 s to 123 s) was 0.16 ± 0.14 m^3/s (2550 ± 2260 gpm). At the start of the fully open period the flow rate increased to 3.78 m^3/s (60000 gpm) for a short interval (~10-15s).

The measured average flow rate during the fully opening period (130 s to 220 s) was 1.91 ± 0.84 m^3/s (30300 ± 13350 gpm). Note that the predicted flow rate for the fully open period was about 1.80 ± 0.11 m^3/s (28600 ± 1700 gpm), shown in Figure 182. During the fully open period, the measured average mass discharge rate was ~802 kg/s, based on a methane density of 420 kg/m^3.

At the commencement of the test, prior to lifting any plugs, a cold gas methane plume was already exiting the diffuser. It is postulated that methane gas was diffusing through the dirt and into the concrete pipes at the pipe joints at the base of the reservoir. Time zero (0 s) on the following figures is the time that the glow plugs were energized to ignite the propane burners on the top of the diffuser. This immediately ignited the methane gas exiting the diffuser; the resulting fire plume was recorded by all cameras and allowed synchronization with the data acquisition systems (DASs). The time of day corresponding the time zero was 7:49 AM (0749 MST).

A fiducial signal was sent to all DASs at t = 30.6 s that also sent a signal to fire the high-intensity photo flash bulbs on the diffuser (also used for camera and DAS synchronization).

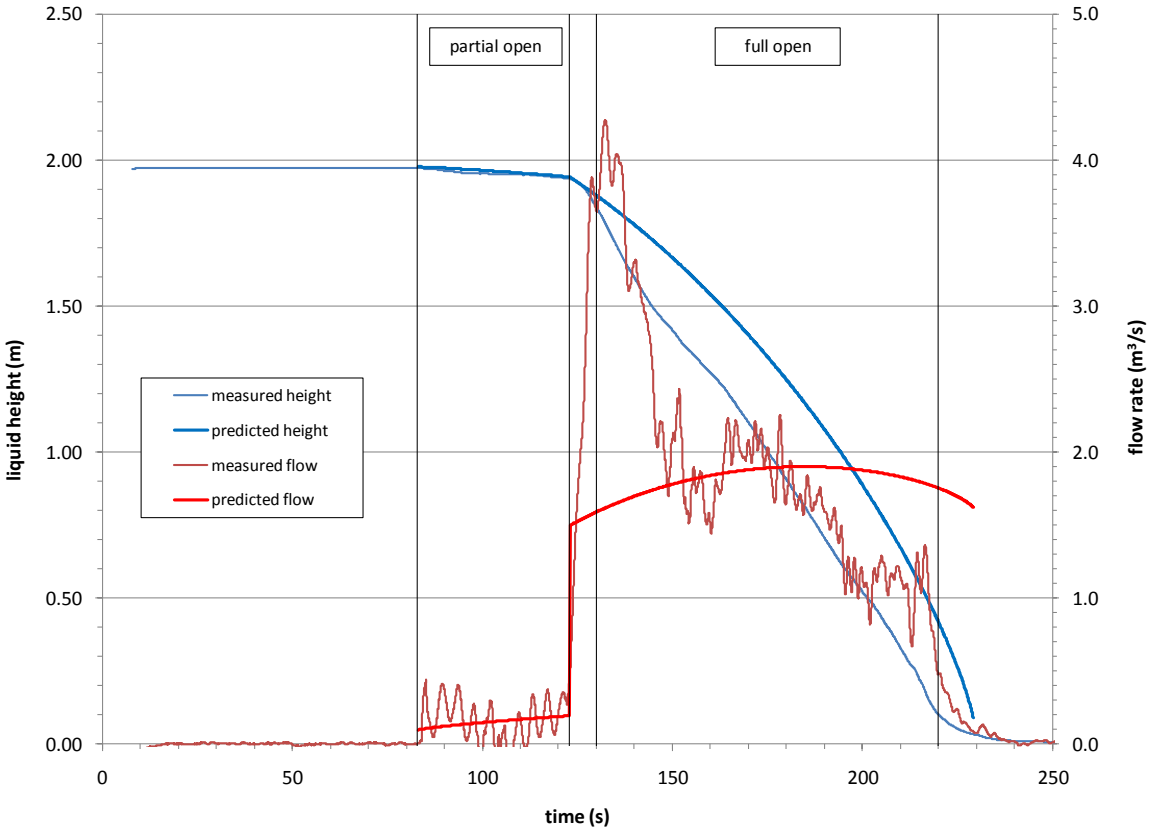

Figure 182 Reservoir level and flow rate during LNG Test 2.

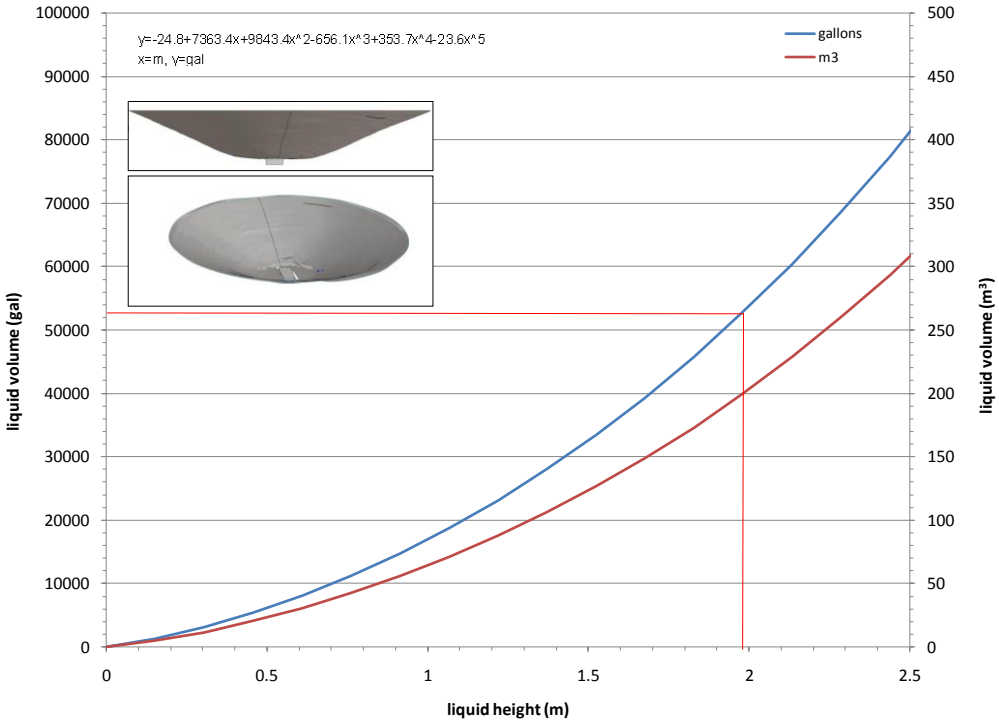

Figure 183 Estimated reservoir volume vs. liquid height in LNG Test 2.

7.5 Pool Area and Effective Diameter

Figure 184 through Figure 191 show highly manipulated, aerial, high resolution (3872 x 2592 pixels at 300 dpi) lens-stabilized still images that were used to determine the spill area. These images were extracted from video taken by the overhead helicopters above the West and East spokes at an ~34 degree angle above the pool surface from pool center.

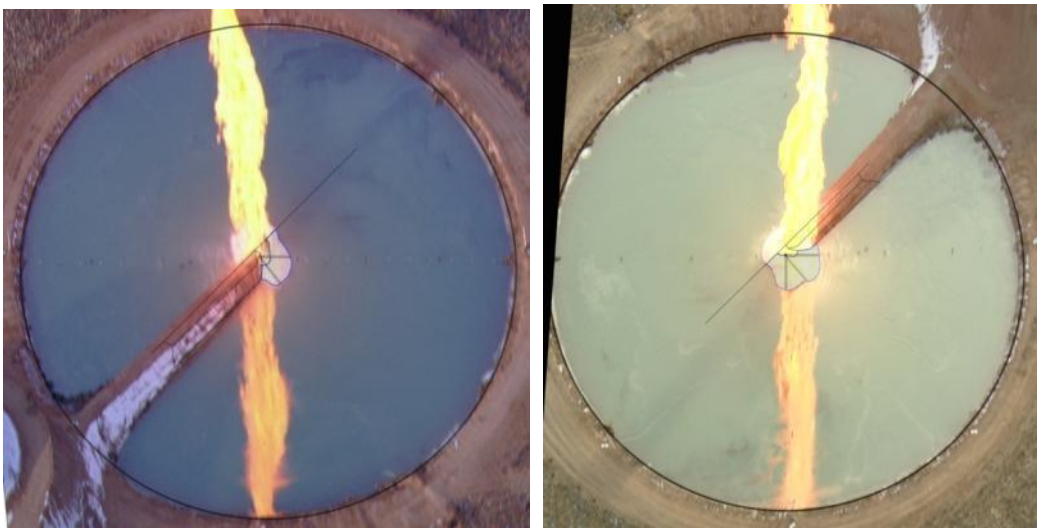

Figure 184 Aerial stills at 120 s in LNG Test 2 (left-90º view, right-270º view).

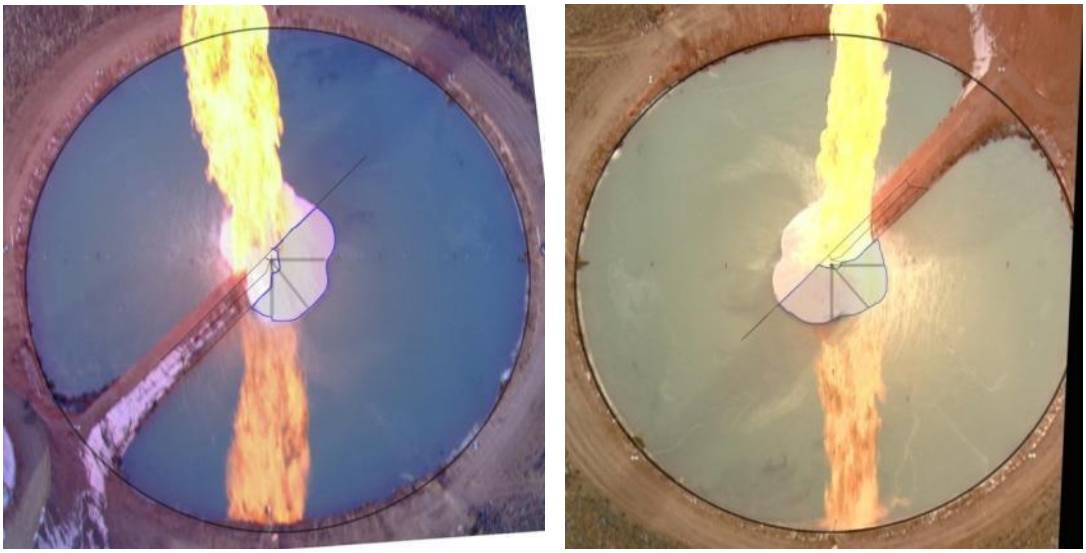

Figure 185 Aerial stills at 150 s in LNG Test 2 (left-90º view, right-270º view).

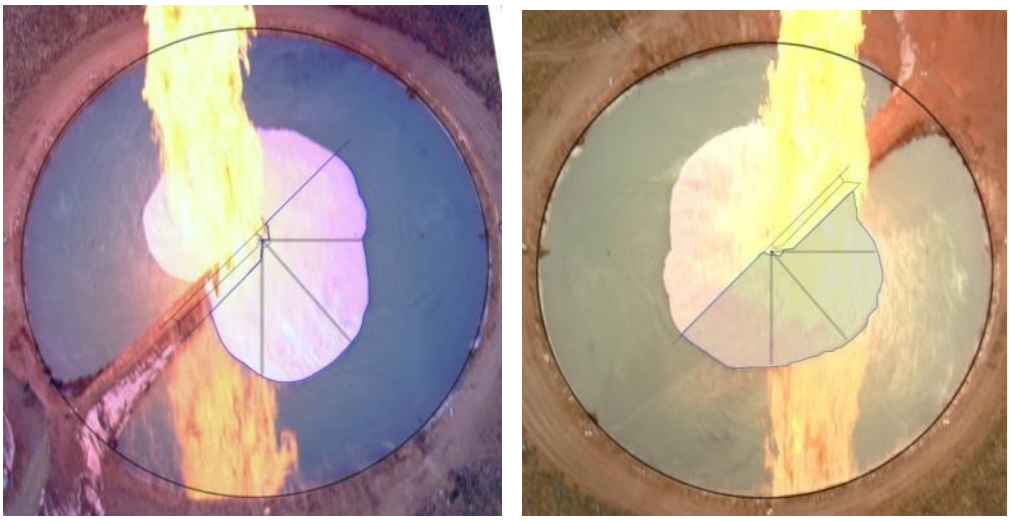

Figure 186 Aerial stills at 180 s in LNG Test 2 (left-90º view, right-270º view).

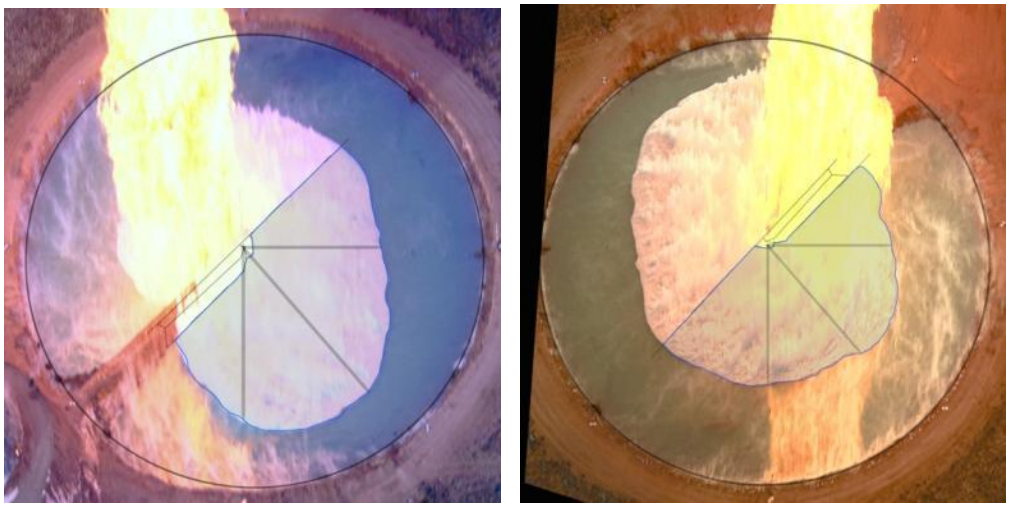

Figure 187 Aerial stills at 210 s in LNG Test 2 (left-90º view, right-270º view).

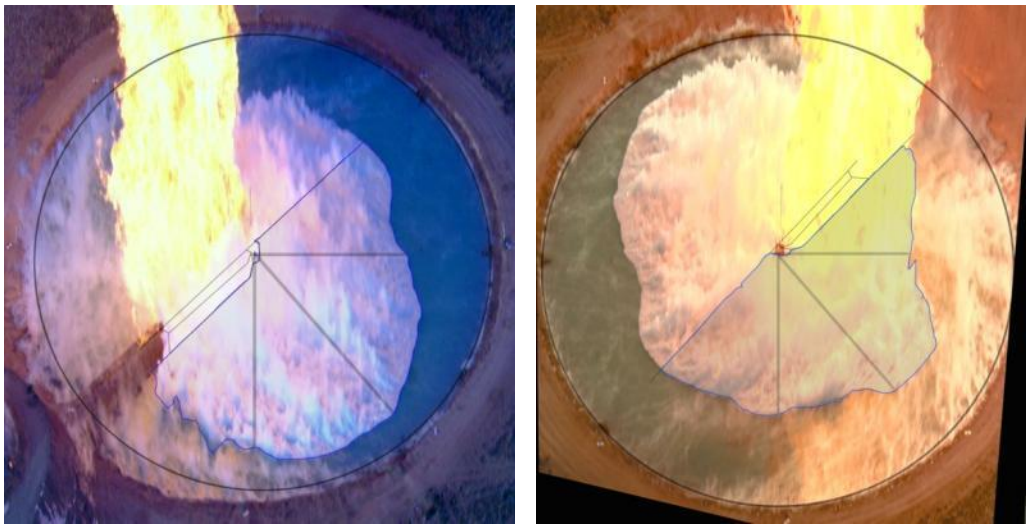

Figure 188 Aerial stills at 240 s in LNG Test 2 (left-90º view, right-270º view).

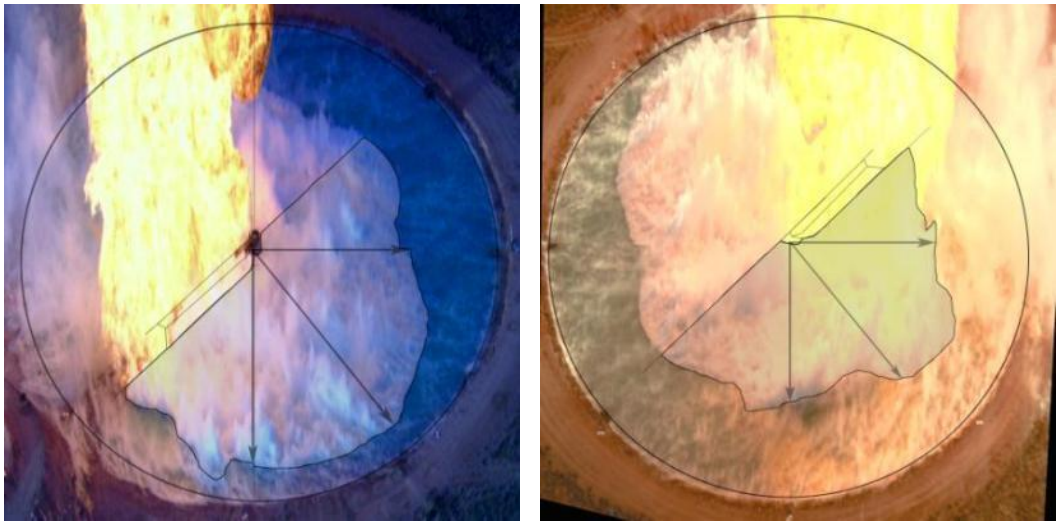

Figure 189 Aerial stills at 270 s in LNG Test 2 (left-90º view, right-270º view).

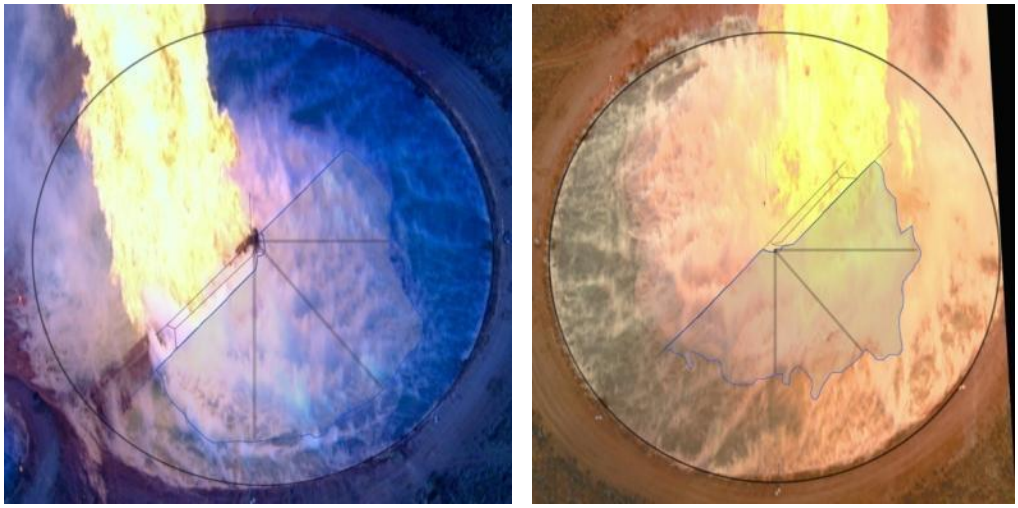

Figure 190 Aerial stills at 300 s in LNG Test 2 (left-90º view, right-270º view).

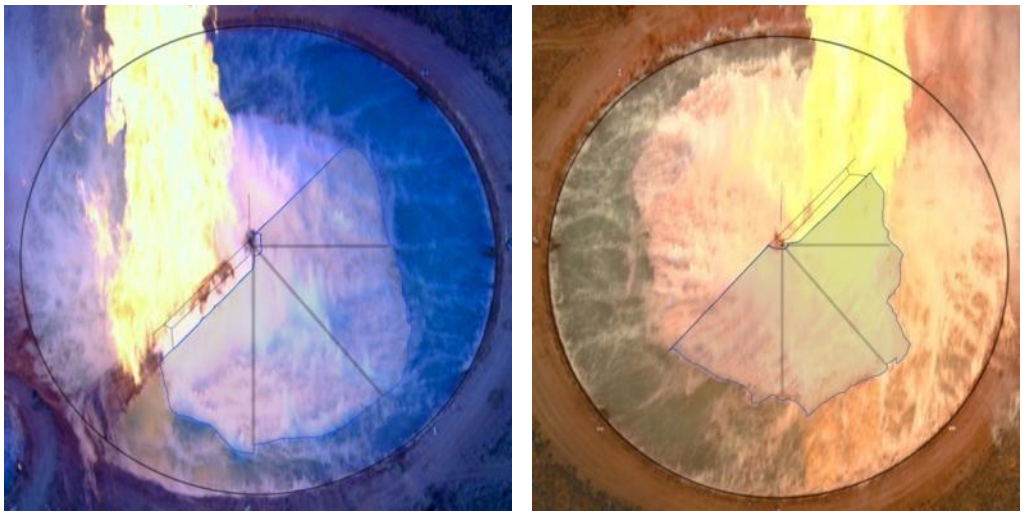

Figure 191 Aerial stills at 330 s in LNG Test 2 (left-90º view, right-270º view).

A graphics editing program (Adobe Photoshop CS3 extended) was used to align a rectangular perspective plane, with the stadia markers present in the image. The image was then conformed to this virtual vanishing perspective grid, rotated then scaled into a corrected flat axis plane. A measurement scale was developed by setting a specified number of pixels to represent known lengths in the image.

The visible outline of the pool has been drawn on the images with radial lines at 45 degrees for use in subsequent determinations of the mean pool radius versus time. The manipulated images from the two cameras are shown side by side at identical times to demonstrate the high degree of correspondence. Table 40 provides measurements derived from selected aerial stills.

Table 40 LNG Test 2 pool diameter extracted from selected aerial stills.

	90 Aerial View				270 Aerial View					
Time (s)	1/2 Pool Area (m^2)	Radius (m) (North Edge)	Radius (m) (East Edge)	Radius (m) (North East Edge)	1/2 Pool Area (m^2)	Radius (m) (South Edge)	Radius (m) (West Edge)	Radius (m) (South West Edge)	Pool Area (m^2)	Pool Diameter (m)
120	55	7.2	6.9	7.6	94	8.4	9.2	9.2	149	13.8
150	289	12.9	13.1	13.5	270	13.2	13.3	13.6	559	26.7
180	1420	25.4	34.7	34.9	1399	26.1	33.7	33.0	2819	59.9
210	2423	35.0	44.7	48.3	2196	32.1	41.3	41.9	4619	76.7
240	3220	37.4	50.3	54.9	2431	33.7	40.9	43.2	5651	84.8
270	3429	43.6	55.7	55.9	2299	37.4	40.2	44.3	5728	85.4
300	2831	33.5	50.3	49.4	1966	34.2	38.6	38.7	4797	78.2
330	2830	34.3	53.1	49.5	2032	31.6	38.7	43.4	4862	78.7
average	3160	38	52	53	2232	35	40	42	5392	82.8
st.dev.	303	5	3	3	240	2	1	3	517	4.0

Boundary edge measurements made using this scale were then used to calculate the area occupied by the fire on the half of the pool surface that is seen in each view. Selected radii are also presented. An approximate pool diameter was calculated by adding each half area and assuming the spreading pool was circular. The average pool area (using the steady pool size determined from the three data points at 240 s, 270 s, and 300 s) was 5392±517 m^2 with an equivalent circular diameter of 82.8±4.0 m. This averaging interval corresponds closely with the steady plume heat flux at 250-300 s, shown later. Figure 192 compares the growth of the spreading LNG pool area to the reservoir discharge rate as the reservoir drains.

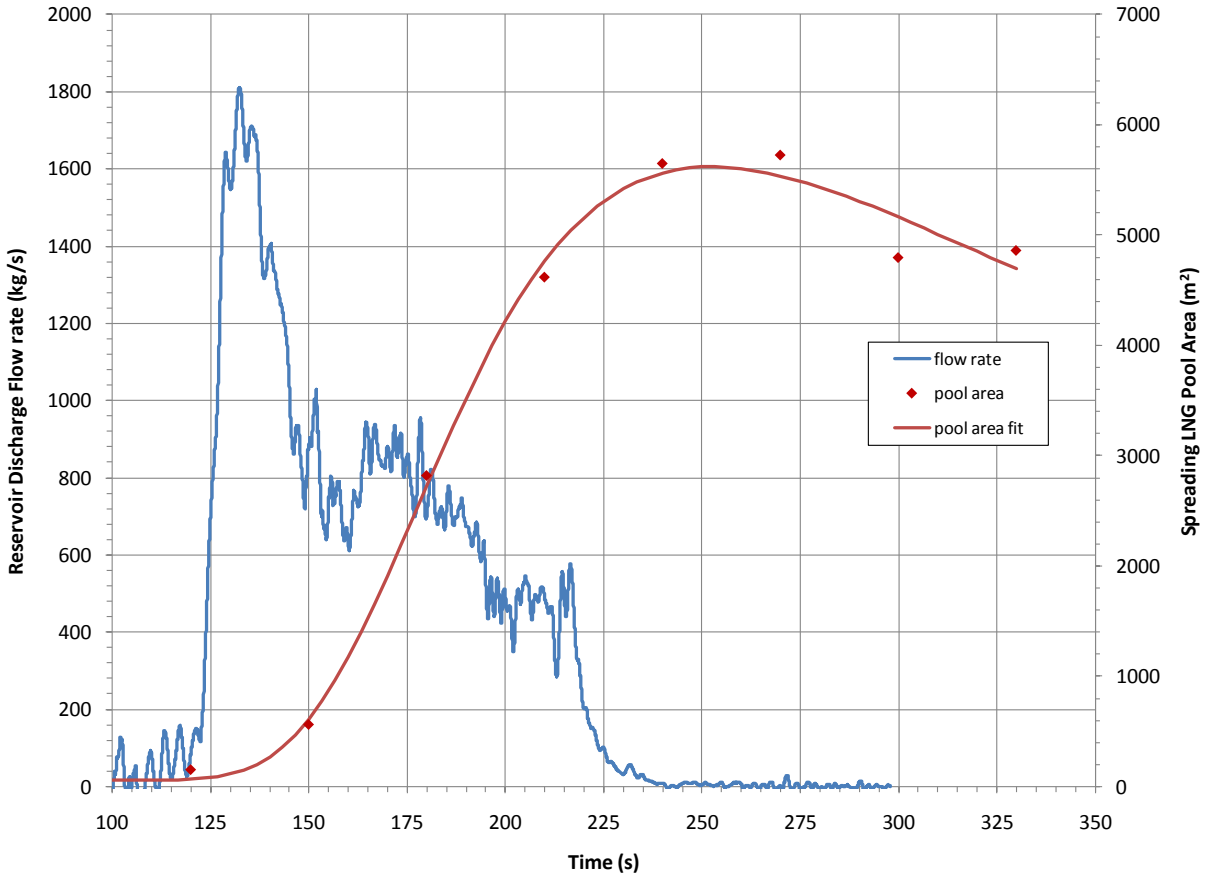

Figure 192 LNG Test 2 pool area compared to the flow rate from the reservoir.

7.6 LNG Mass Loss Rate

The mass loss rate or regression rate (RR as determined by dividing the spill rate by the pool area) could not be realistically applied in LNG Test 2. A very high flow rate coupled with a relatively small amount of fuel produced a steadily increasing spreading pool even after the reservoir had emptied, as shown in Figure 192.

In LNG Test 2, the reservoir emptied before the steady-state pool area was reached. In addition, a large portion of the spreading LNG pool did not ignite, which leaves the question as to exactly what area should be used in the mass loss rate calculation. It is worth noting that dividing the measured release rate of 802 kg/s by the regression rate of 0.147 kg/m^{2}s determined in LNG Test 1 would have given an equivalent circular diameter of 83.3 m, very close to the 82.8 m that was measured.

7.7 Plume Heat Flux

Table 41 gives the spot heights, ellipse dimensions, and distance from pool centerline for the North spoke radiometers (the other spokes are nearly identical). For reference purposes, Table 42 and Table 43 provide the radiometer heights above the pool surface and the inclination angles of the radiometers located on their respective towers. Note that gauges 1-5, 7, and 9 are narrow view (NV - 5.5 degree view angle) radiometers (with ZeSe windows) and gauges 6, 8, and 10 are wide view (WV - 150 degree view angle) radiometers (with ZeSe window).

Figure 193, Figure 194, Figure 195, and Figure 196 give spoke HD camera stills at selected times with an overlay for the narrow view radiometer view factors (note the five "spots" from the Tower 1 gauges arranged in a vertical array, and the spots from the Tower 2 and Tower 3 gauges centered on the tower 1 middle gauge spot. In addition, a color intensity threshold (pixels with red intensity >230±5) determined those pixels that were determined to be "fire", these pixels are shown by the green mask. Refer to the visual data during discussions of the plume morphology and heat flux data. For example, the flame plume area was determined simply by summing the area of each "green" pixel identified as fire in each image (after first calculating the length and width of the pixel given by the camera calibration). Plots showing the measured heat flux versus time have not been adjusted for atmospheric transmission losses.

Table 41 LNG Test 2 spot size parameters for narrow-view radiometers

Spot Height above Pool (m)	N TW1 spot major/minor length (m)	N TW2 spot major/minor length (m)	N TW3 spot major/minor length (m)
15.0	10.7 / 10.6		
30.0	11.3 / 10.9		
55.0	13.0 / 11.7	17.1 / 16.2	21.5 / 20.8
85.0	16.6 / 13.2		
120.0	22.8 / 15.5		
Spot Distance from Pool Centerline (m)	109.9	159.8	209.6

Table 42 LNG Test 2 radiometer heights above water surface (m)

gauge #	Gage height on tower m	Test 2 N TW1	Test 2 N TW2	Test 2 N TW3	Test 2 E TW1	Test 2 E TW2	Test 2 E TW3	Test 2 S TW1	Test 2 S TW2	Test 2 S TW3	Test 2 W TW1	Test 2 W TW2	Test 2 W TW3
1 NV	1	1.56			3.24			1.45			0.95		
2 NV	1.1	1.66			3.34			1.55			1.05		
3 NV	1.2	1.76			3.44			1.65			1.15		
4 NV	1.3	1.86			3.54			1.75			1.25		
5,7,9 NV	1.4	1.96	1.83	1.49	3.64	4.04	4.63	1.85	1.61	1.44	1.35	0.80	-0.08
6,8,10 WV	1.5	2.06	1.93	1.59	3.74	4.14	4.73	1.95	1.71	1.54	1.45	0.90	0.02

Table 43 LNG Test 2 radiometer inclination angles (degrees)

gauge #	Test 2 spot height above pool	Test 2 N TW1	Test 2 N TW2	Test 2 N TW3	Test 2 E TW1	Test 2 E TW2	Test 2 E TW3	Test 2 S TW1	Test 2 S TW2	Test 2 S TW3	Test 2 W TW1	Test 2 W TW2	Test 2 W TW3
1 NV	15.0	7.0			6.0			7.0			7.3		
2 NV	30.0	14.5			13.5			14.4			14.7		
3 NV	55.0	25.8			24.9			25.7			26.1		
4 NV	85.0	37.1			36.3			36.9			37.3		
5,7,9 NV	120.0	47.0	18.4	14.3	46.3	17.7	13.5	46.9	18.5	14.3	47.2	18.7	14.7
6,8,10 WV	55.0	25.7	18.4	14.3	24.8	17.7	13.5	25.6	18.4	14.3	26.0	18.7	14.7
	from pool CL m	109.9	159.8	209.6	111.1	159.7	209.8	110.7	159.9	209.8	110	159.8	209.8

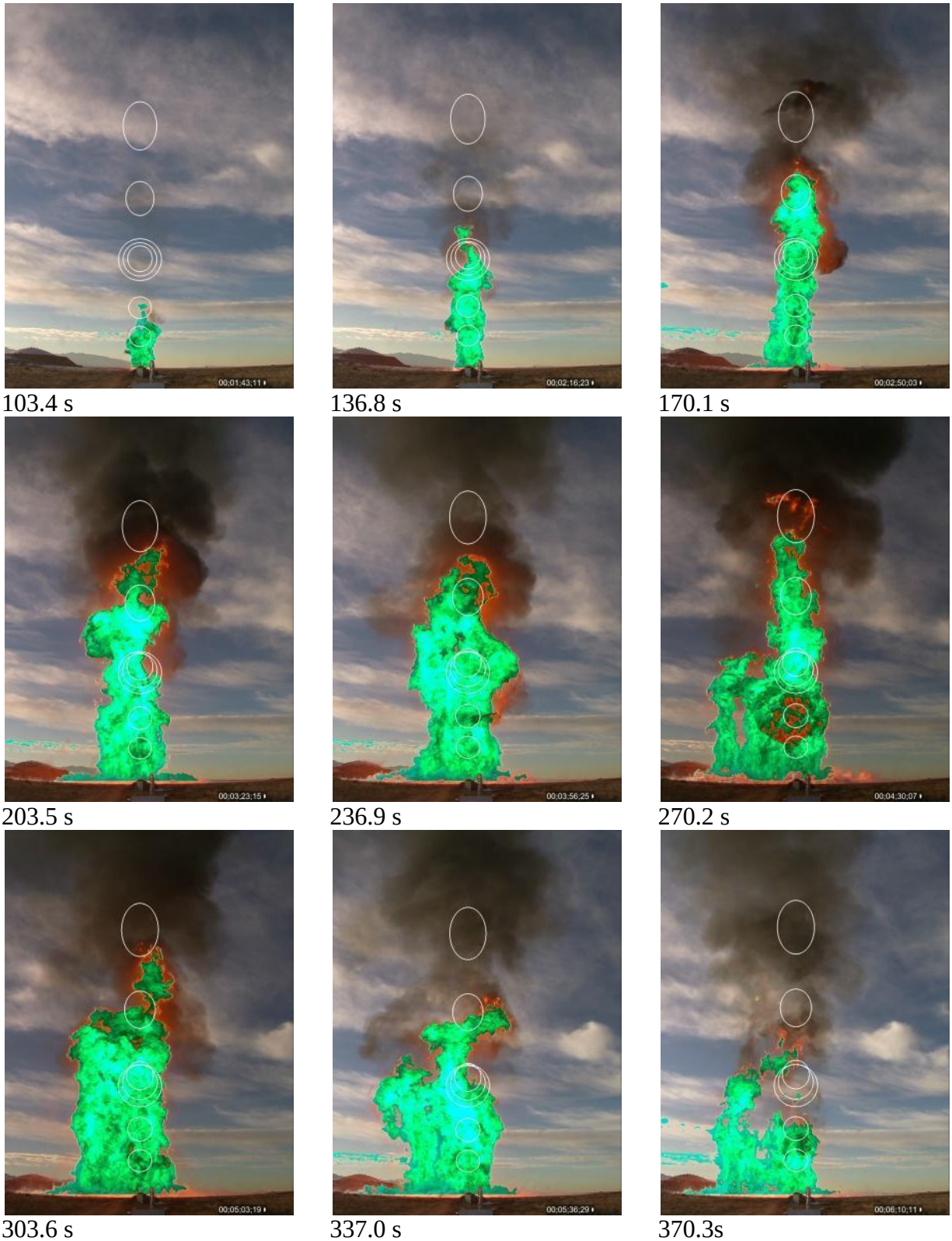

Figure 193 LNG Test 2 0° spoke HD camera stills with NV radiometer overlays.

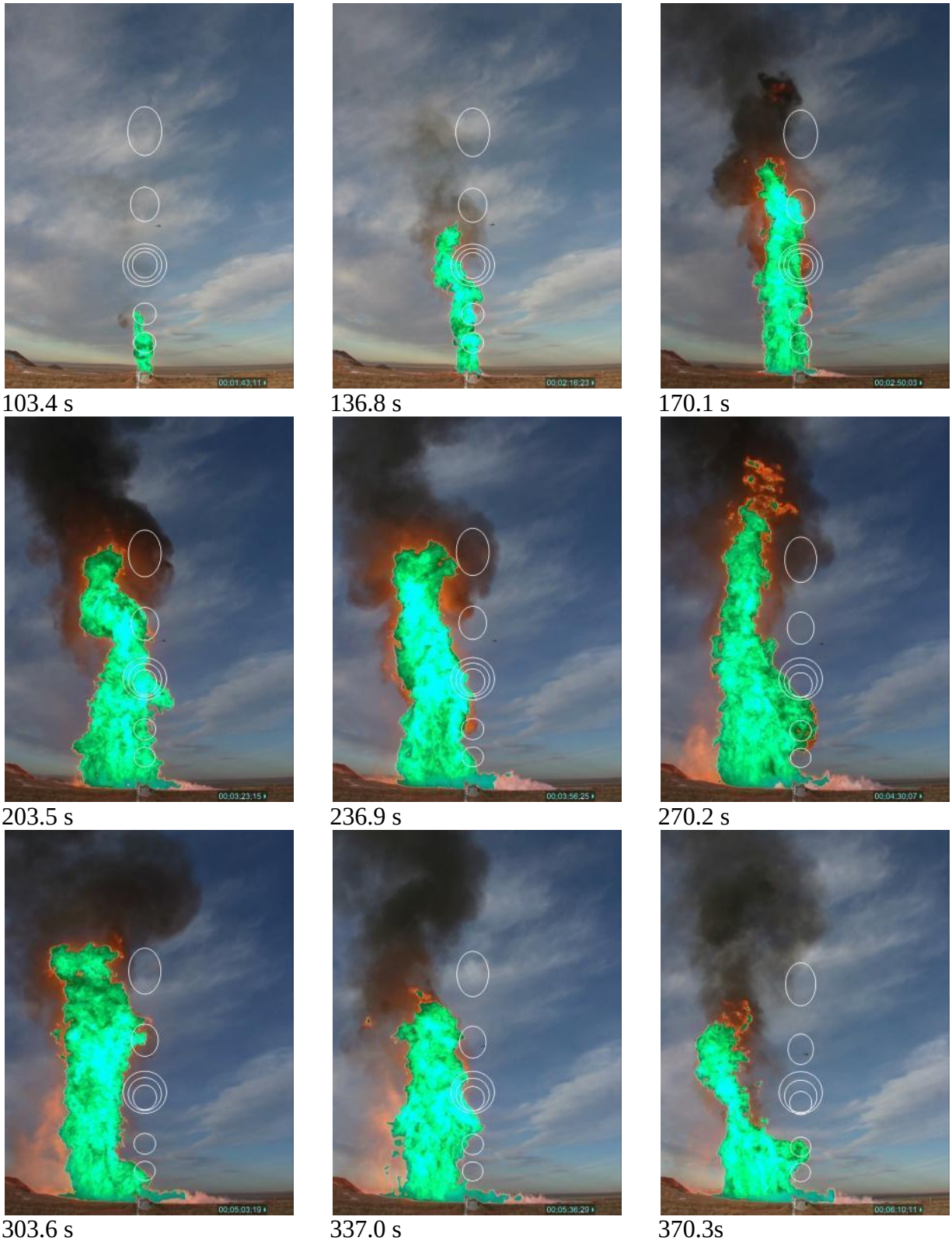

Figure 194 LNG Test 2 90° spoke HD camera stills with NV radiometer overlays.

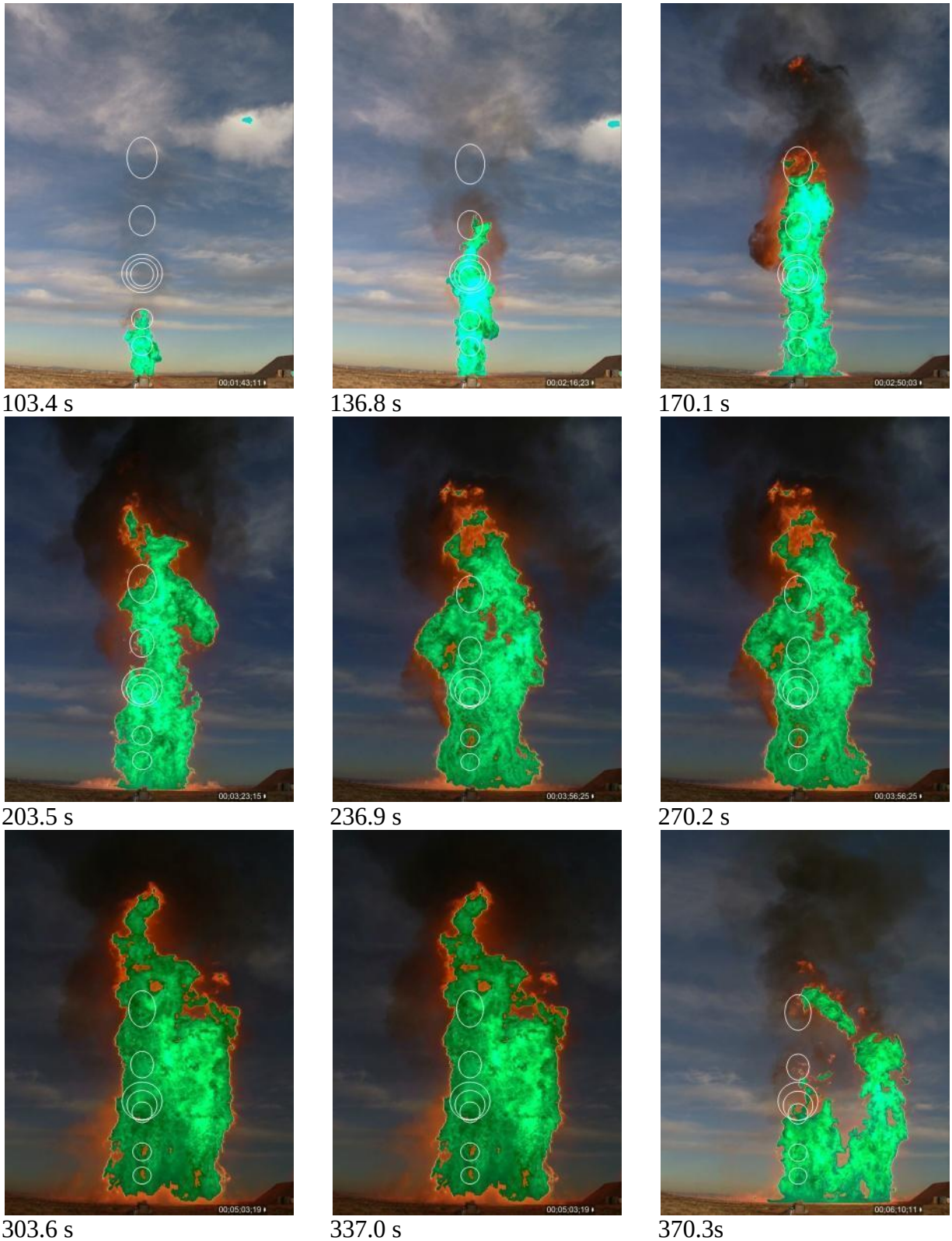

Figure 195 LNG Test 2 180° spoke HD camera stills with NV radiometer overlays.

Figure 196 LNG Test 2 270° spoke HD camera stills with NV radiometer overlays.

Figure 197 and Figure 198 show the heat flux from the five narrow view angle radiometers attached to the towers on the North spoke. Figure 197 shows the flux at 110 m distance (all heights) (the reservoir drainage is also shown) and Figure 198 shows the flux from 110 m, 160 m, and 210 m (looking at a spot 55 m above the pool).

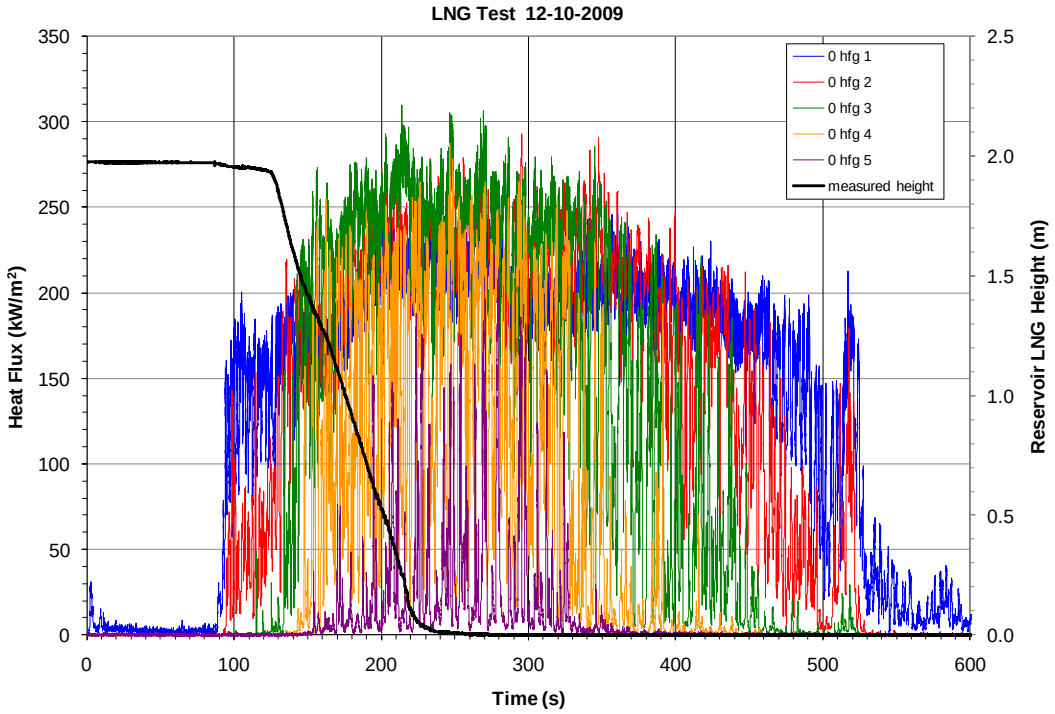

Figure 197 LNG Test 2 NV radiative heat flux at the 110 m tower on the 0° spoke.

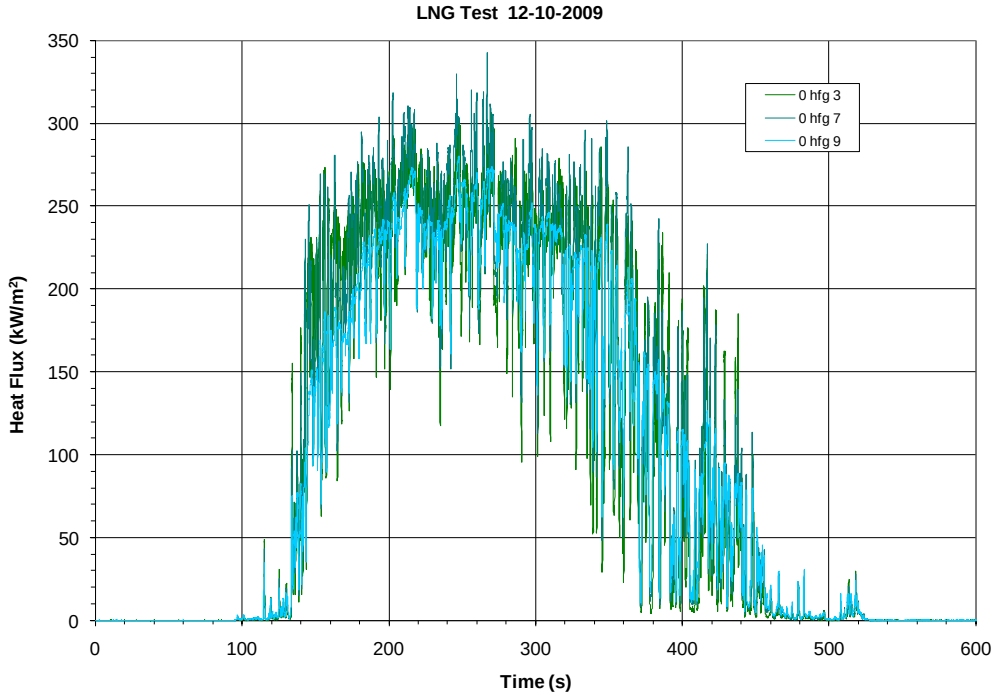

Figure 198 LNG Test 2 NV radiative heat flux on the 0° spoke at 55 m above the pool.

The wind direction, combined with the layout and orientation of the discharge pipe berm, caused the flame to drag toward the south and also attach somewhat to the pipe berm. The fire plume quickly moved out of the view of the narrow view radiometers on the east and west spokes, as evident in Figure 194 and Figure 196, and no data will be presented from those gauges.

Figure 199 presents the narrow view radiometer data from five NV radiometers on Tower 1 on the south spoke. The narrow view radiometers on Towers 2 and 3 on the south spoke failed prior to the start of the test and no data is given for those instruments.

Small fires were started in scrub grass that produced small amounts of intermittent white smoke near the south pool edge, almost directly between the south spoke radiometer towers and the flame. This may have resulted in the lower flux values seen on the lower south narrow-view radiometer gauges as compared to the north gauges.

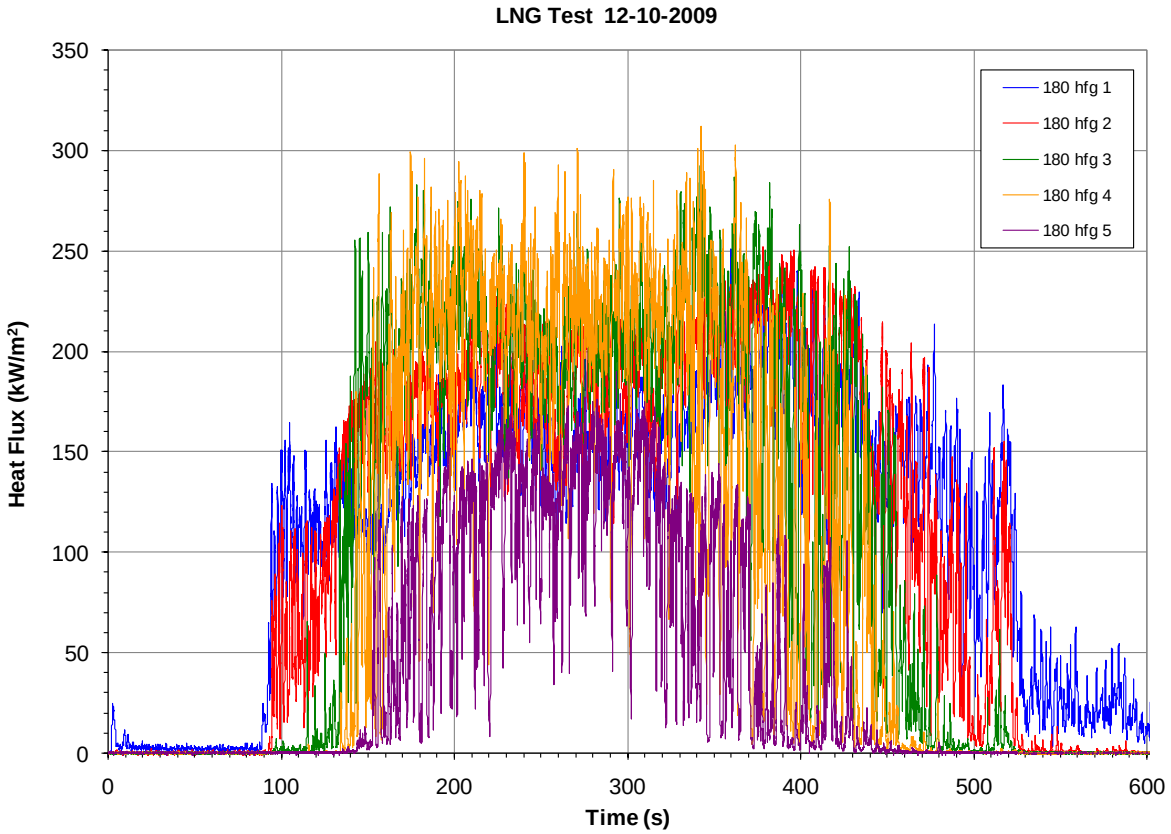

Figure 199 LNG Test 2 NV radiative heat flux at the 110 m tower on the 180° spoke.

Figure 200, Figure 201, Figure 202, and Figure 203 plot the flux from the wide view (WV) angle (150º view factor) gauges on the three towers on each spoke (gauge 6 on the East spoke failed prior to the test). Every gauge was positioned to look at the pool centerline and a spot 55 m above the pool. The data is consistent with increasing distance from pool centerline (6 is 110 m, 8 is 160 m, and 10 is 210 m). In addition, the 90 and the 270 spoke both have a similar view (normal to the dragged/tilted flame).

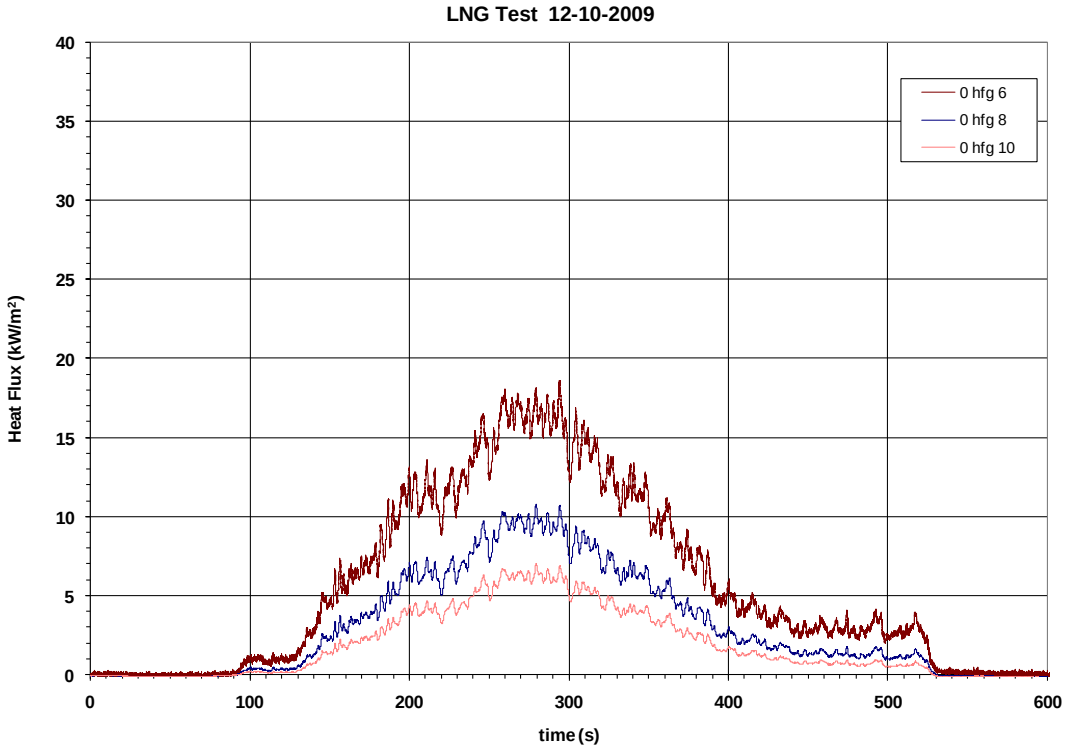

Figure 200 LNG Test 2 heat flux from the WV radiometers on the 0° spoke.

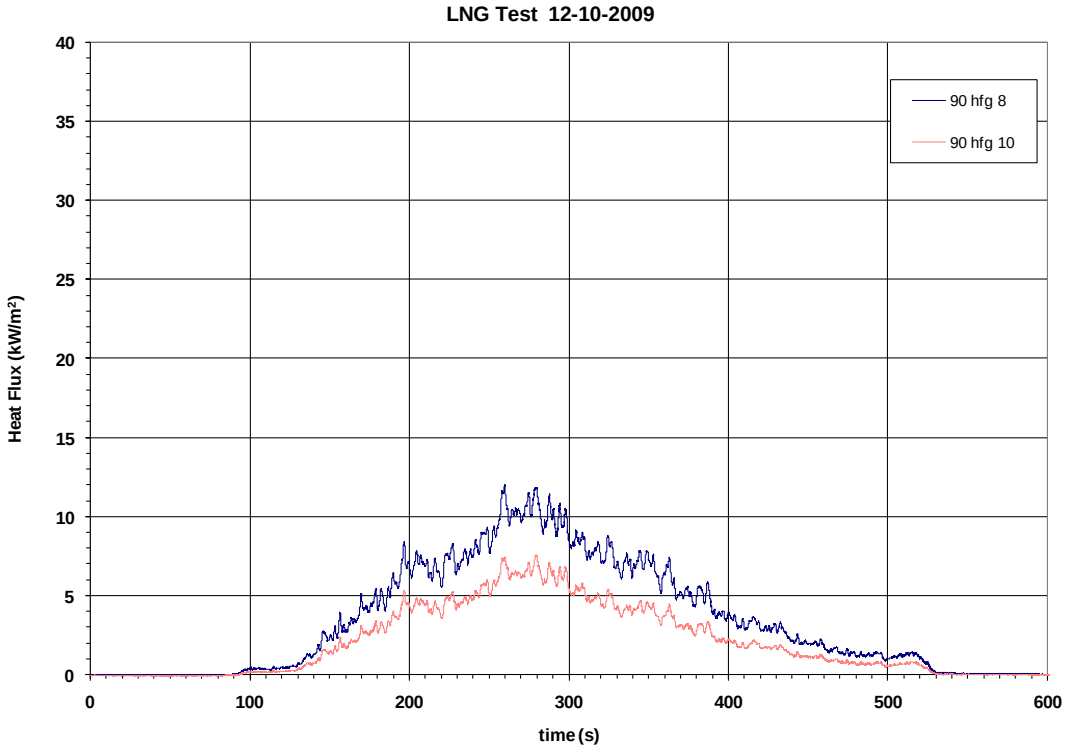

Figure 201 LNG Test 2 heat flux from the WV radiometers on the 90° spoke.

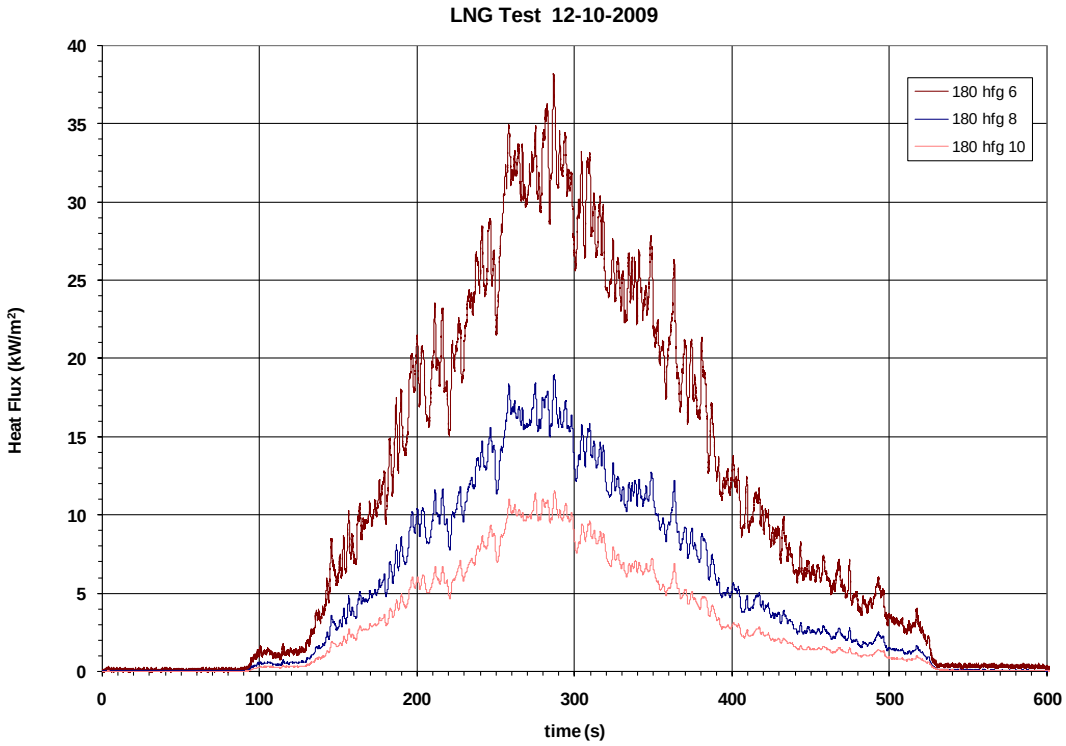

Figure 202 LNG Test 2 heat flux from the WV radiometers on the 180° spoke.

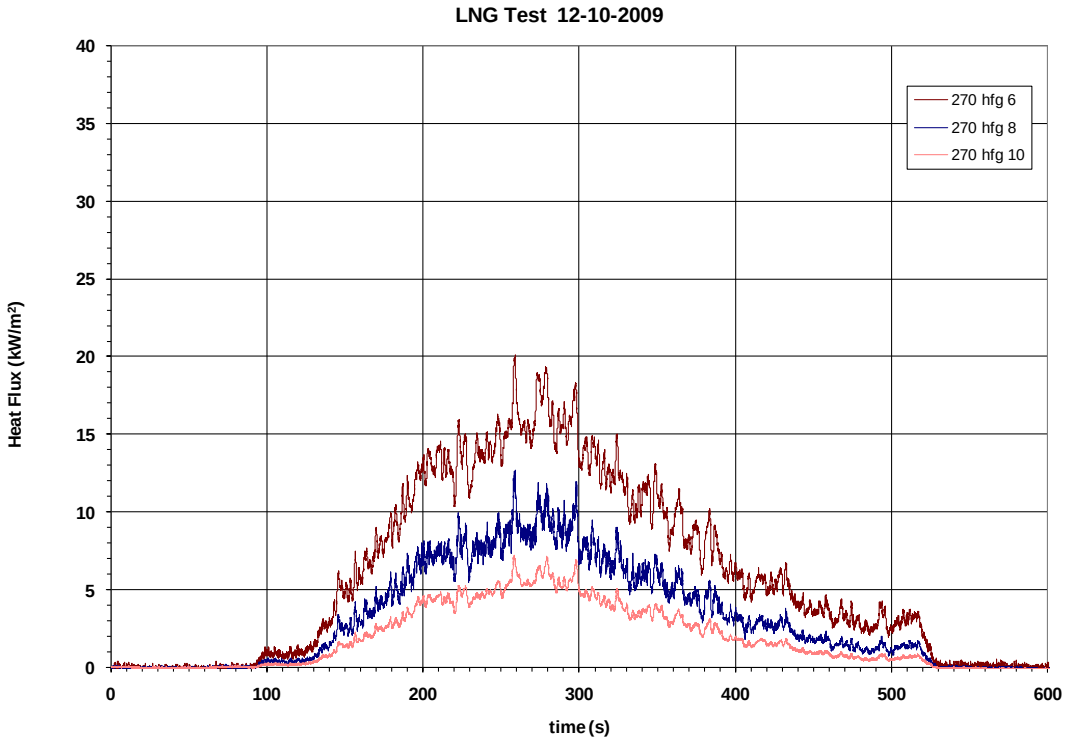

Figure 203 LNG Test 2 heat flux from the WV radiometers on the 270° spoke.

The wind dragged and elongated the flame (almost elliptical versus a typical cylindrical shape). The wide-angle gauges on the south spoke recorded the highest flux levels, likely due to the flame edge being closer to the gauges, in addition to the elliptical shape and greater flame area (discussed in the video analysis section).

A review of the radiometer data shows that the fire was steady and consistent between about 250 to 300 s into the spill. This time duration will be used to present average data for the remainder of the report. Table 44 presents the average and standard deviation (between 250-300 s) of uncorrected (for transmission losses) radiometer data.

Table 44 Average LNG Test 2 radiometer data (uncorrected) between 250-300 seconds.

	narrow-angle radiometers							wide-angle radiometers		
spot height above pool (m)	15	30	55	85	120	55	55	55	55	55
nominal distance from pool center (m)	110	110	110	110	110	160	210	110	160	210
North spoke	**0 hfg 1**	**0 hfg 2**	**0 hfg 3**	**0 hfg 4**	**0 hfg 5**	**0 hfg 7**	**0 hfg 9**	**0 hfg 6**	**0 hfg 8**	**0 hfg 10**
average	213.0	219.2	236.5	152.2	45.2	245.2	238.0	16.5	9.7	6.4
st.dev.	15.4	29.0	33.8	70.9	50.5	35.6	22.4	1.2	0.7	0.4
South spoke	**180 hfg 1**	**180 hfg 2**	**180 hfg 3**	**180 hfg 4**	**180 hfg 5**	**180 hfg 7**	**180 hfg 9**	**180 hfg 6**	**180 hfg 8**	**180 hfg 10**
average	150.3	181.5	200.3	217.1	131.0			31.5	16.1	9.9
st.dev.	19.6	22.8	23.7	34.6	28.5			2.7	1.4	0.9
East spoke								**90 hfg 6**	**90 hfg 8**	**90 hfg 10**
average									10.1	6.4
st.dev.									0.9	0.5
West spoke								**270 hfg 6**	**270 hfg 8**	**270 hfg 10**
average								18.1	9.2	5.9
st.dev.								1.5	1.0	0.6

7.8 Pool Heat Flux

Figure 204 shows an aerial still taken approximately in the middle of the fire period. The flame appears to be attached or anchored to the diffuser and the discharge pipe berm. The wind is tilting the flame plume over the directional flame thermometers (DFTs) that are in the pool facing upward on the 180° spoke axis. Note that the sensing surface of all the DFTs in the water pool is approximately 0.15 to 0.3 m (~6-12 inches) above the pool surface.

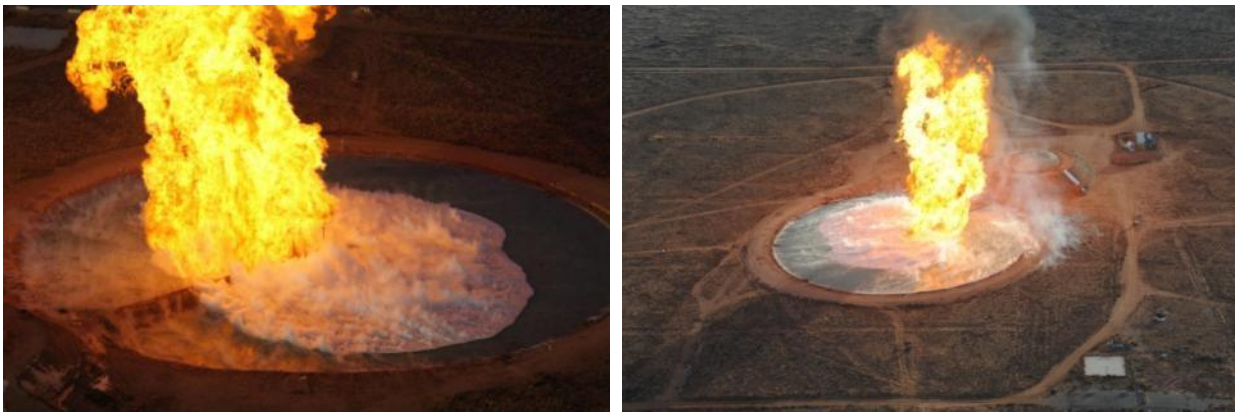

Figure 204 Aerial stills at ~250 s in LNG Test 2 (left-90º view, right-270º view).

An inverse heat conduction analysis was performed with the geometric configuration, thermal property data, and the measured top and bottom plate temperatures. The average emissivity of the pre-oxidized inconel plates was 0.67. The inverse heat conduction analysis yields the net flux and the surface temperature. Eq. (4) was used to calculate the incident heat flux.

Figure 205 shows the plate temperature and calculated incident heat flux from the DFT located on top of the diffuser. DFT 0-0 is about 1 ft above the diffuser surface, facing upward (note the top of the diffuser is ~6 feet above the water surface).

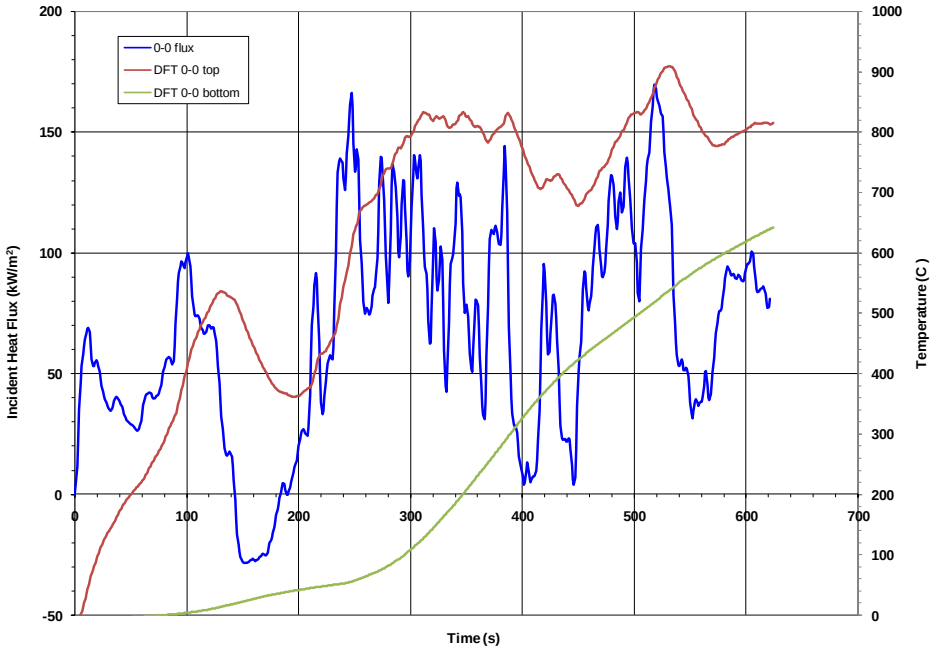

Figure 205 Incident heat flux at the DFTs above the diffuser in LNG Test 2.

Figure 206 through Figure 209 show the flux from the DFTs located on each spoke as compared to DFT 0-0. Compared to the other spokes, the South spoke DFTs measured the highest flux. Also, a large spike in heat flux was recorded on many of the DFTs at the end of the test. DFT 180-1 is about 10 m from the diffuser, DFT 180-2 is about 25 m from the diffuser, and DFT 180-1 is about 42 m from the diffuser.

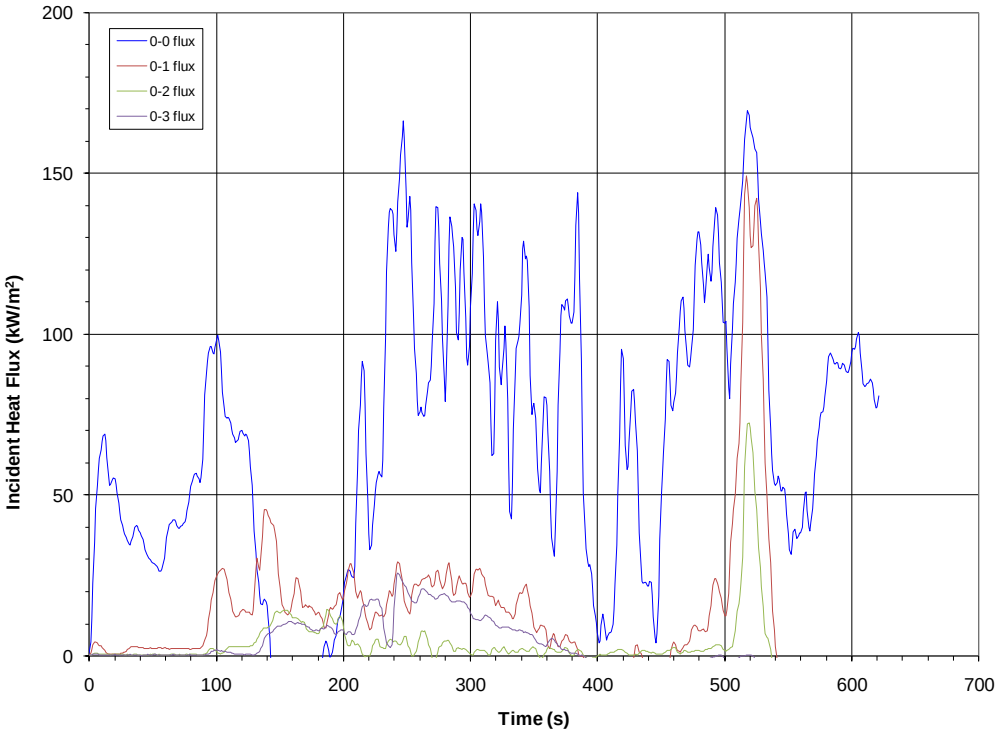

Figure 206 Incident heat flux at the pool DFTs on the North spoke in LNG Test 2.

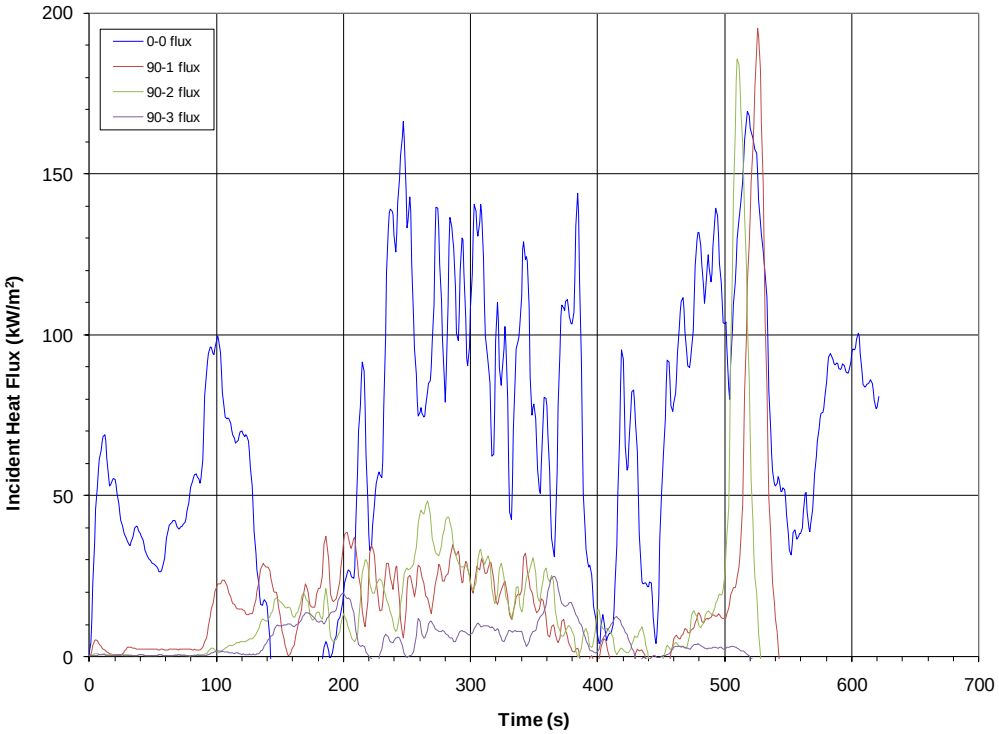

Figure 207 Incident heat flux at the pool DFTs on the East spoke in LNG Test 2.

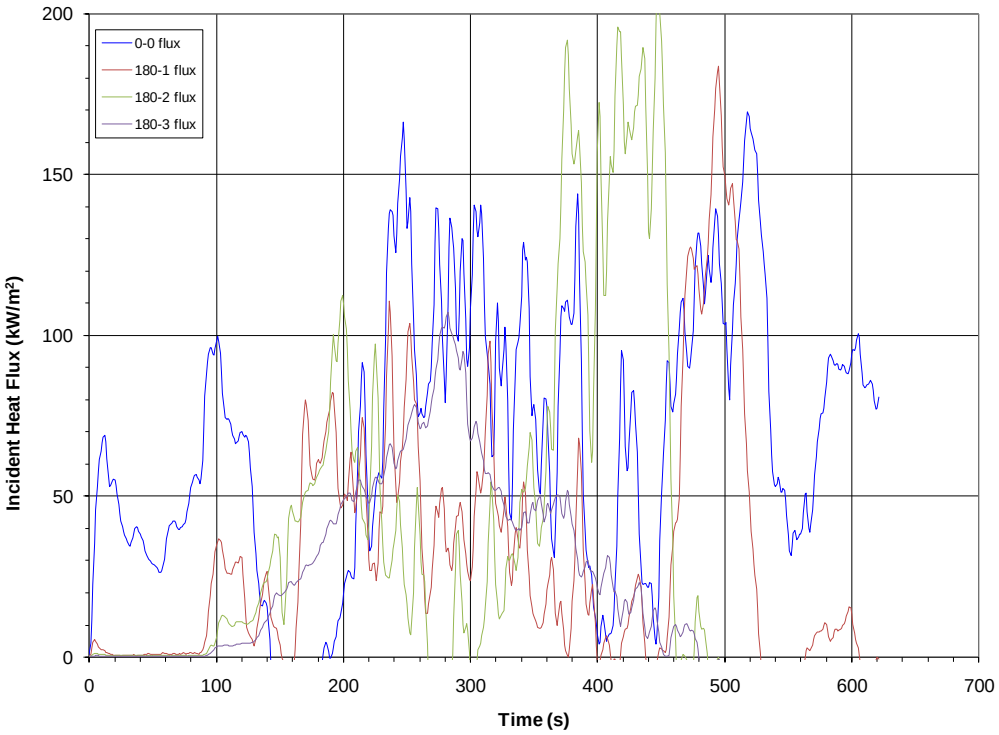

Figure 208 Incident heat flux at the pool DFTs on the South spoke in LNG Test 2.

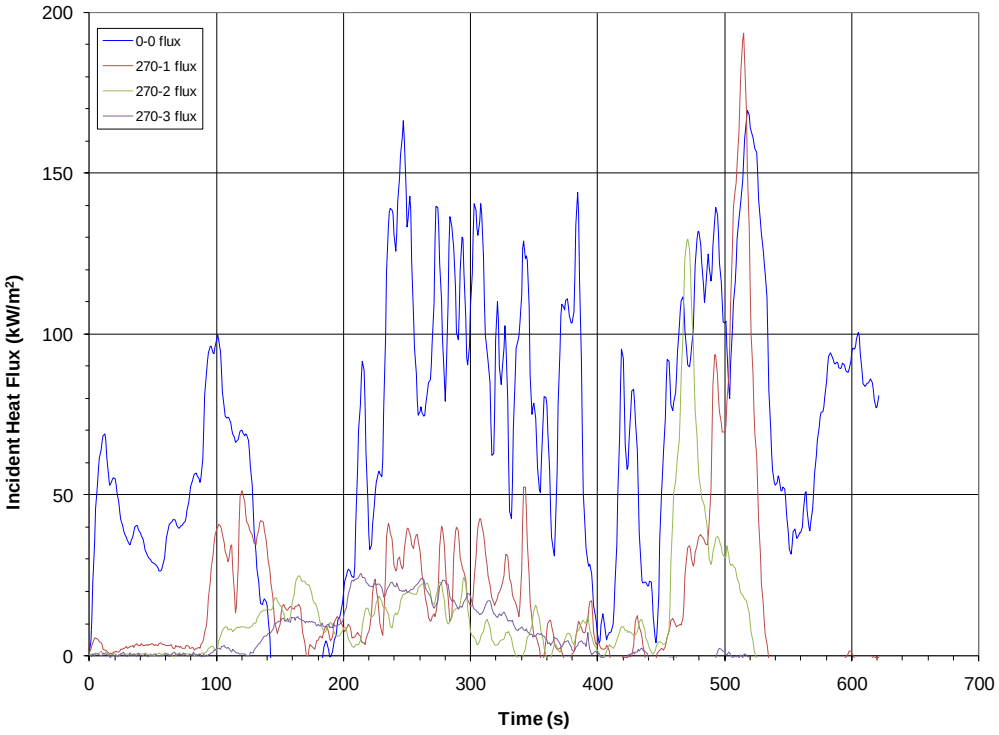

Figure 209 Incident heat flux at the pool DFTs on the West spoke in LNG Test 2.

DFT 8-1 is 8 ft above the diffuser and DFT 16-1 is 16 ft above the diffuser; they both face normal to the south and north directions. Figure 210 plots both sensing surface temperatures and the calculated heat flux from the DFTs. Note that the plates facing the south direction measured earlier and larger temperature increases. Peak diffuser DFT temperatures ranged from 900-970ºC and peak heat fluxes ranged from 160-180 kW/m^2. Figure 211 compares the incident heat flux from all of the diffuser DFTs.

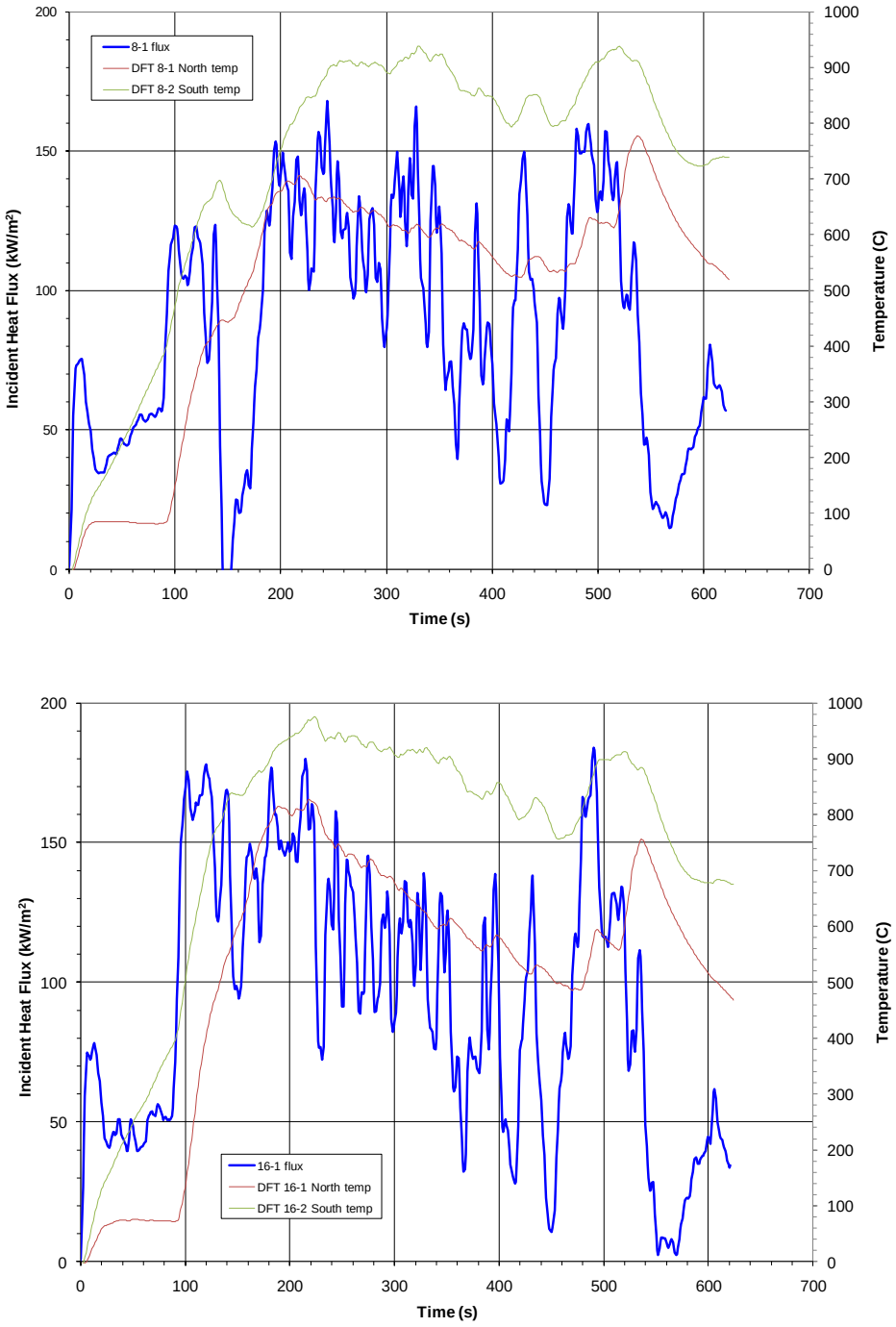

Figure 210 Plate temperatures and incident heat flux at diffuser DFTs in LNG Test 2.

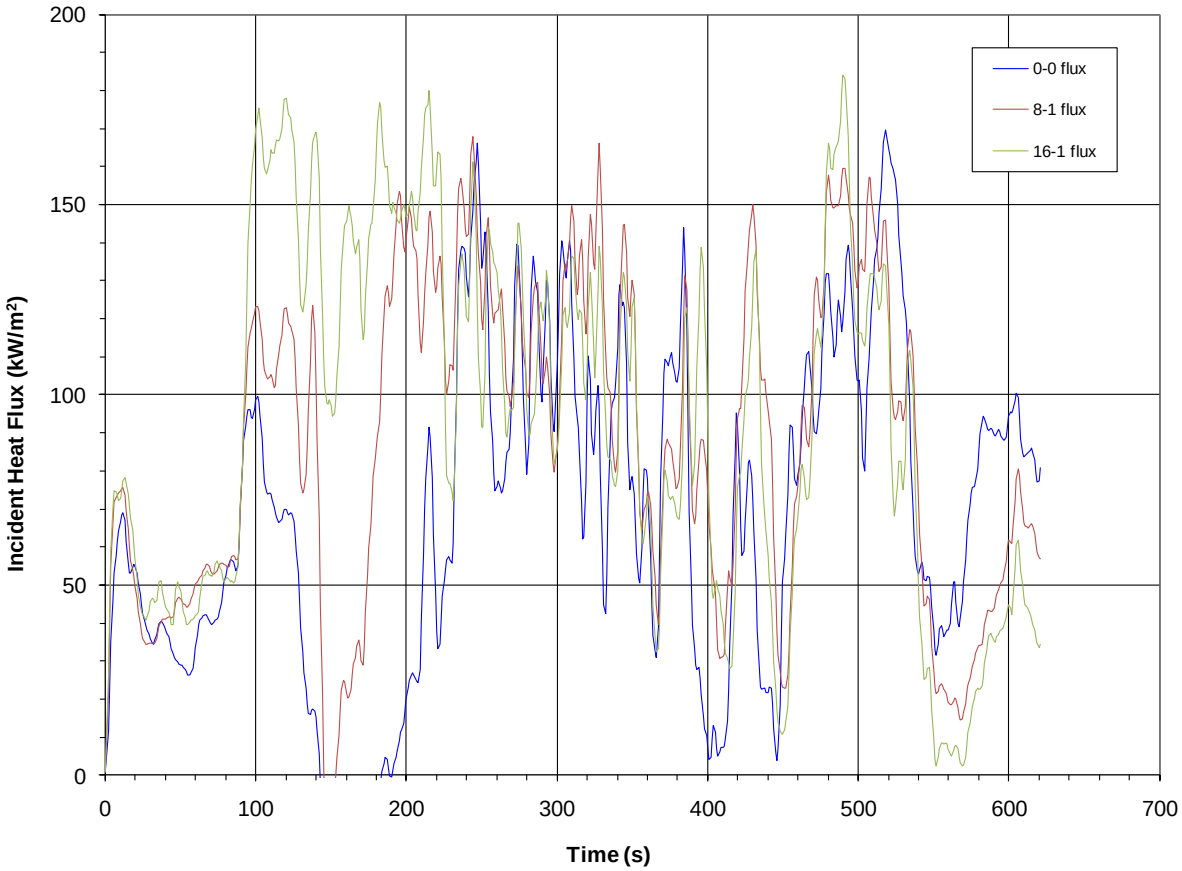

Figure 211 Incident heat flux at the diffuser DFTs in LNG Test 2.

7.9 Pool Water Temperature

Figure 212 presents the pool water temperatures as measured by the type-K thermocouples attached to the three DFT stands on the South spoke. The twenty-seven thermocouples from the other 9 DFT stands show very similar temperatures. The average water temperature of all thirty-six water thermocouples was approximately 1.5°C, and steady throughout the test.

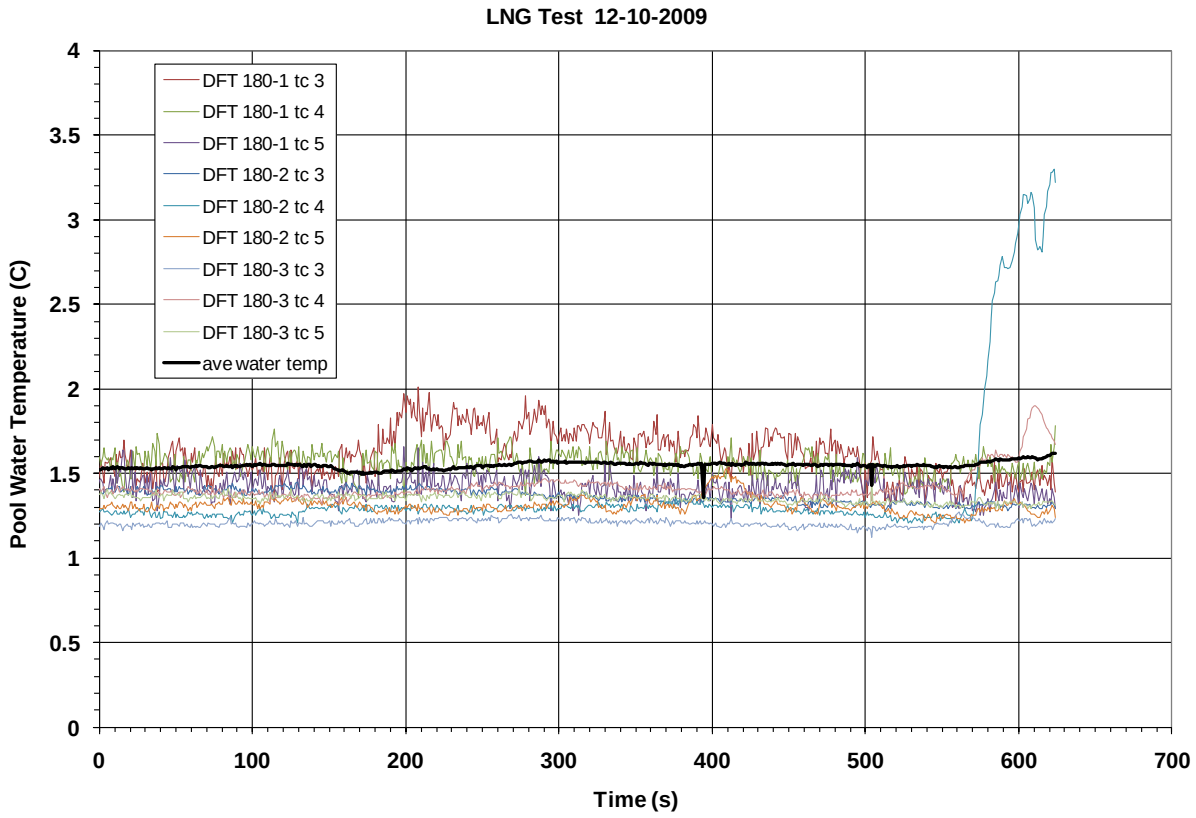

Figure 212 Pool water temperatures in LNG Test 2.

7.10 Flame Temperature

Figure 213 presents the temperatures as measured by the type-K thermocouples attached to a 16 ft tall rake located on top of the diffuser (note that the diffuser top surface is about 6 ft above the pool surface).

LNG likely splashed out of the 4-ft diameter hole at the top of the diffuser, as evident by the negative temperature measurements at rakes locations 2 and 3 during the reservoir discharge. Early in the test, while the rake was engulfed, rake temperatures ranged between 800-1000°C. Later in the test, as the fire moved south and attached to the berm, the thermocouple rake (16 ft tall) could be seen extending out of the flame zone.

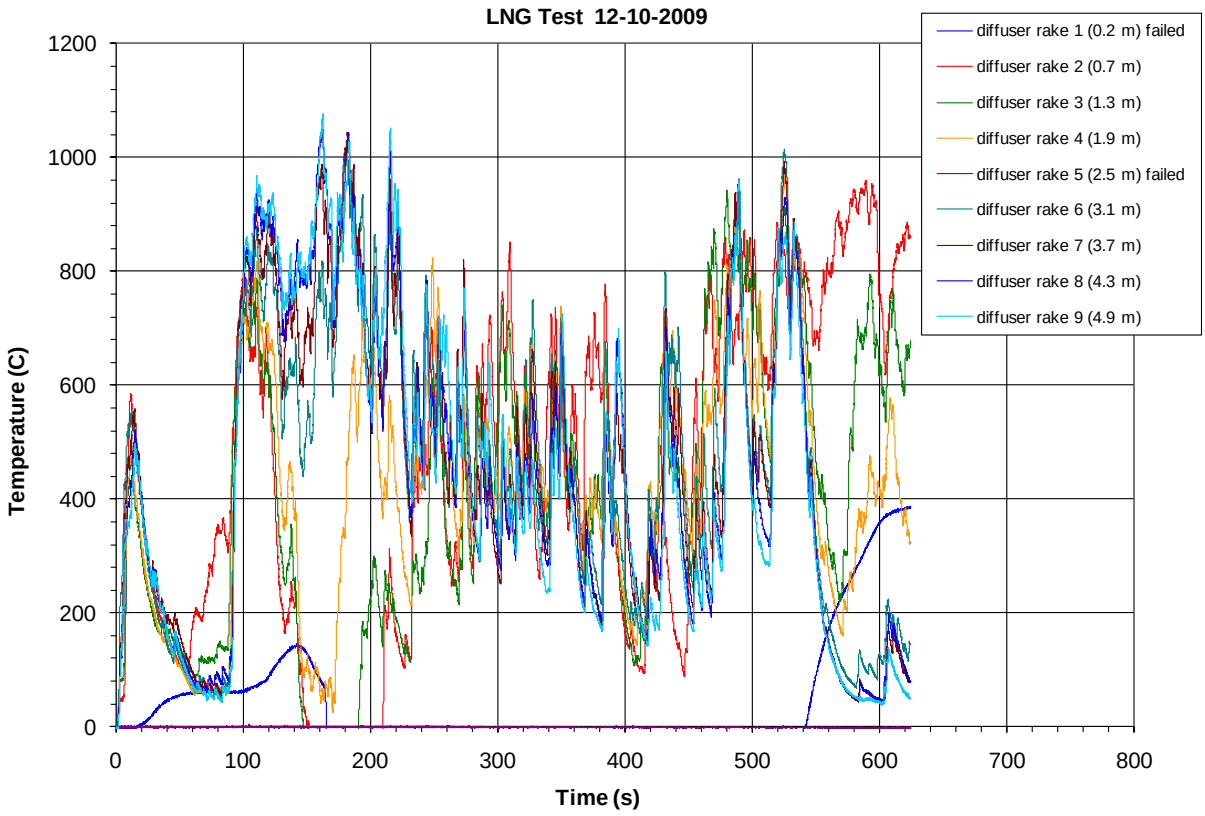

Figure 213 LNG flame temperatures from the diffuser thermocouple rake in LNG Test 2.

Figure 214 presents four images obtained at 420 s taken from the IR video cameras located on the East spoke. The South spoke camera failed to record after 120 s.

Figure 215 plots the temperatures from the East and South spoke IR cameras at 20 s intervals. Note the temperatures are calculated with the camera emissivity set to 1. Over the steady-state interval from 240-300 s, the East average IR-reduced temperature was 1386±29°C. Note this is 214°C greater than the average IR temperatures measured in LNG Test 1, also plotted for comparison.

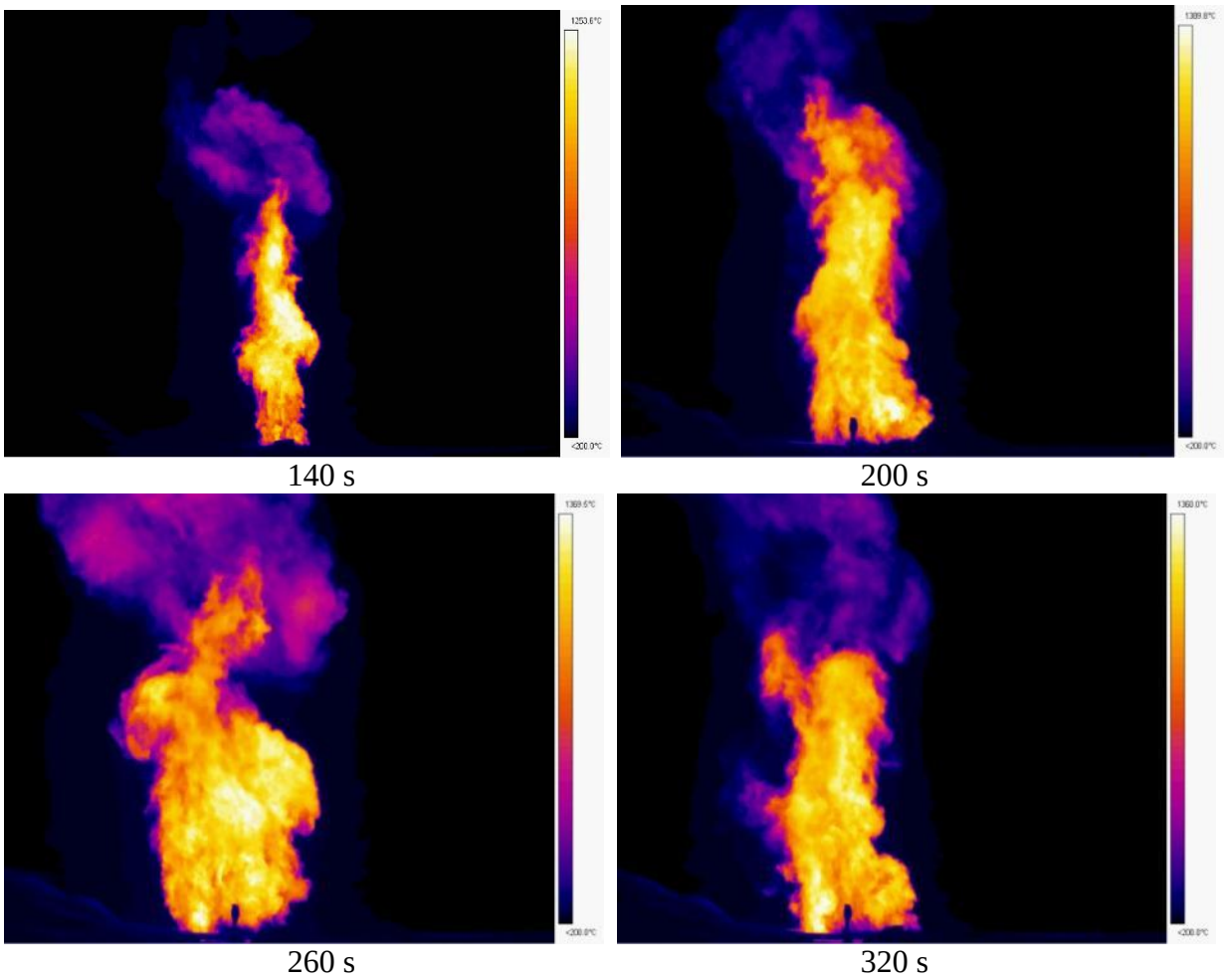

Figure 214 IR camera images from LNG Test 2.

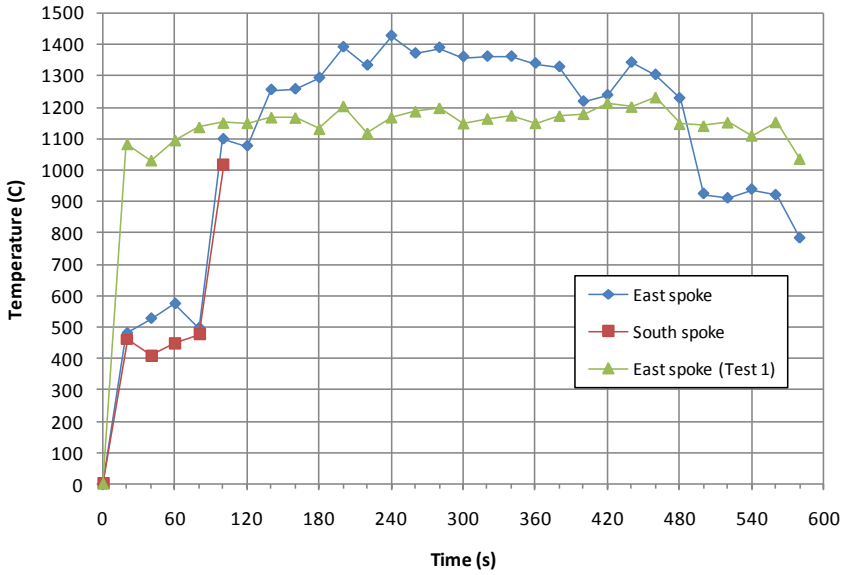

Figure 215 IR imaged-based temperatures in LNG Test 2.

7.11 Flame CG, Width, Height, and Area

The reduction of the video data to determine fire morphology (width, height, flame area, etc.), correct the radiometer data for atmospheric transmission effects, inform on the narrow-range radiometer "spot" results, and determine a time-dependent flame-average surface emissive power (SEP) from the wide-range radiometer data was performed in an identical manner as in LNG Test 1.

The flame plume horizontal center-of-gravity (CG) was determined to determine a time-dependent path length for use in later analyses, especially important in the correction of transmission losses for the narrow angle radiometers and also the average flame SEP analyses. The CG is calculated based on the calibrated video data from the cameras at each spoke. Refer to Figure 117 for the representative flame morphology depicting the CG location..

Figure 216 shows the flame plume CG as determined by data from the east and west cameras showing a shift (from pool center) toward the south camera as a result of the wind predominately from the north. A curve (drawn by fitting the data with regression analysis) showing the average of the east and west shift is also shown.

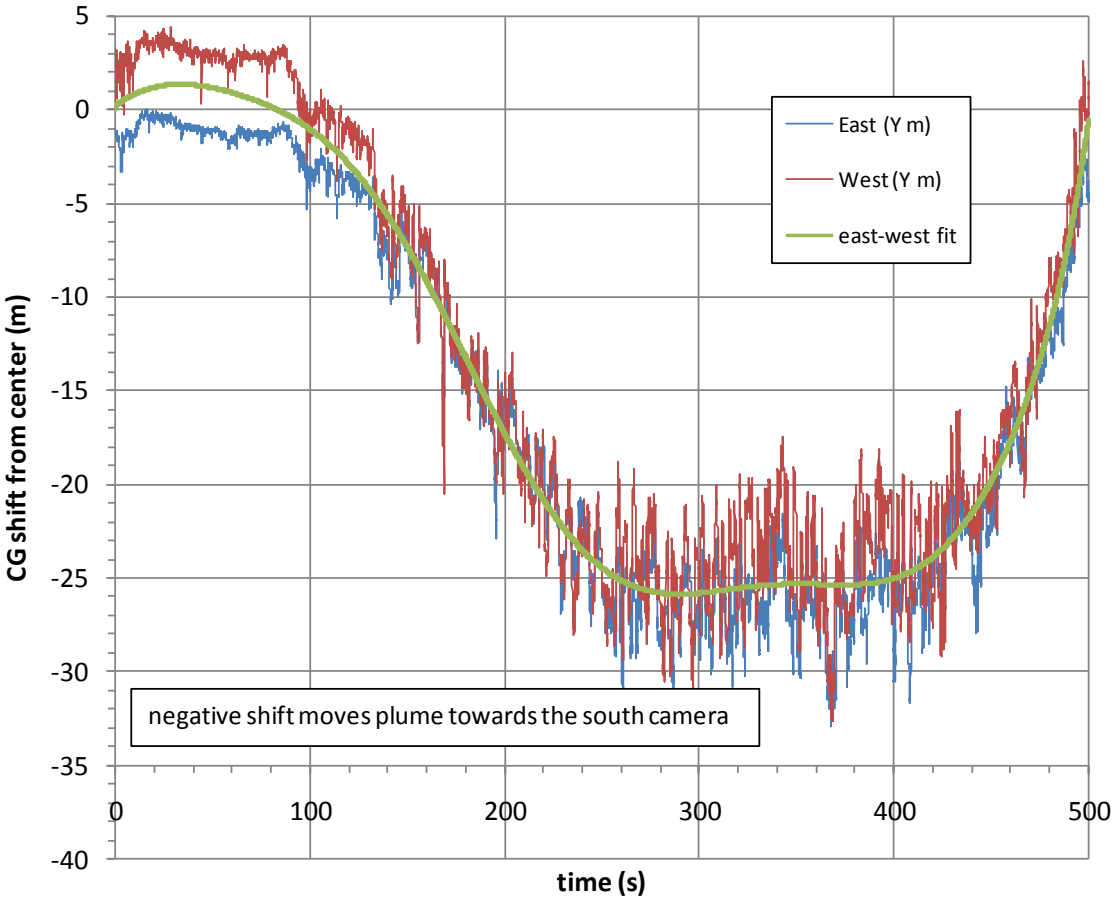

Figure 216 LNG Test 2 flame CG along the N-S axis.

Figure 217 shows the flame plume CG as determined by data from the north and south cameras showing a slight shift toward the east camera, again as a result of the wind predominately from the north as it interacted with the discharge pipe berm. A curve (drawn by fitting the data with regression analysis) showing the average of the east and west shift is also shown.

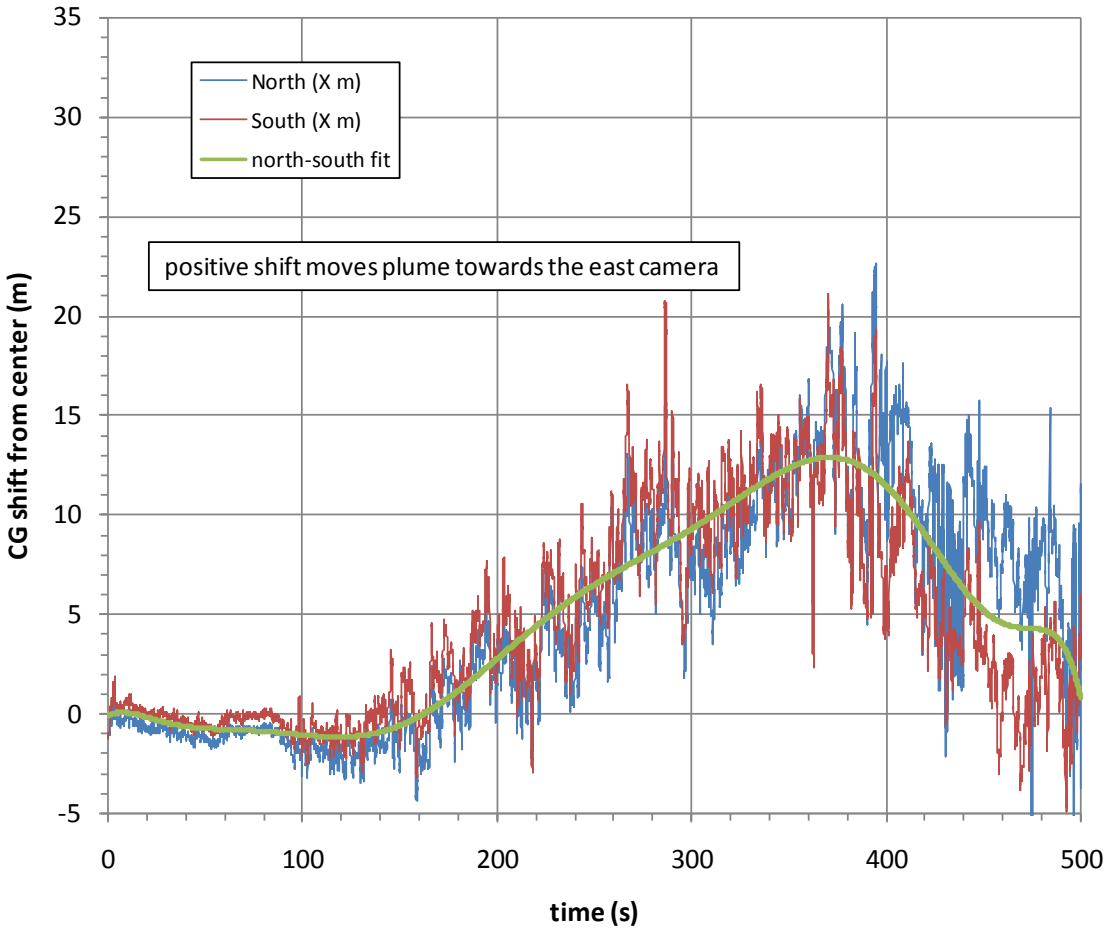

Figure 217 LNG Test 2 flame CG along the E-W axis.

Table 45 presents the average and standard deviation (between 250-300 s) of the shift in CG as determined from the video analyses.

Table 45 Average shift in LNG Test 2 CG at 250-300 s.

250-300 s	North (X m)	South (X m)	East (Y m)	West (Y m)
average	7.8	9.8	-26.5	-25.1
st. dev.	2.7	3.1	1.8	2.5

Figure 218 and Figure 219 present the flame height at the CG location and the peak flame height, respectively. Figure 220 and Figure 221 present the flame plume widths at both the CG height and at 15 m (an arbitrary choice) above the pool surface. Note that clouds that showed as fire (Figure 193) caused some intermittent false North widths at the CG height. Finally, the flame area as determined from each camera view is presented in Figure 222.

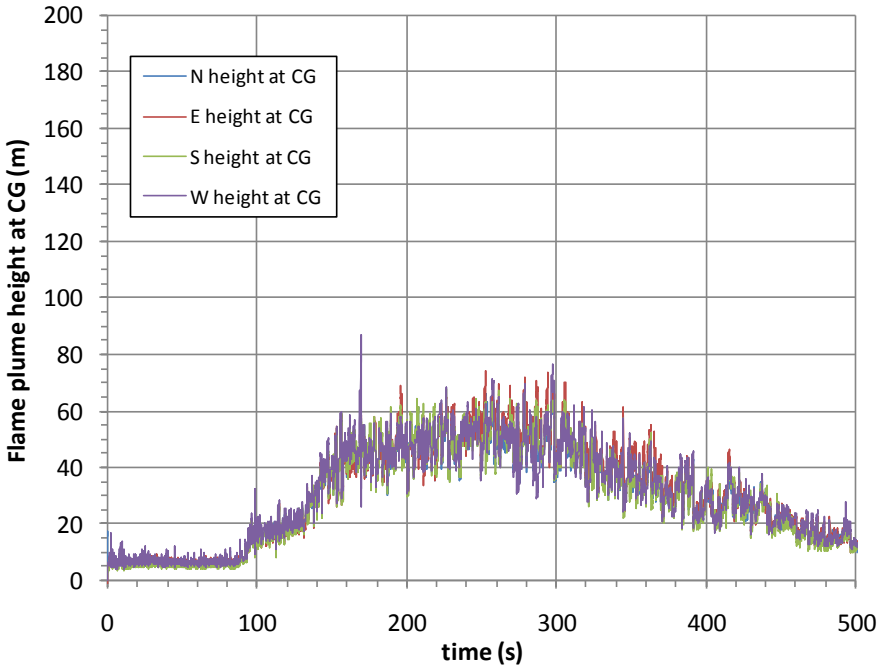

Figure 218 LNG Test 2 flame plume CG height.

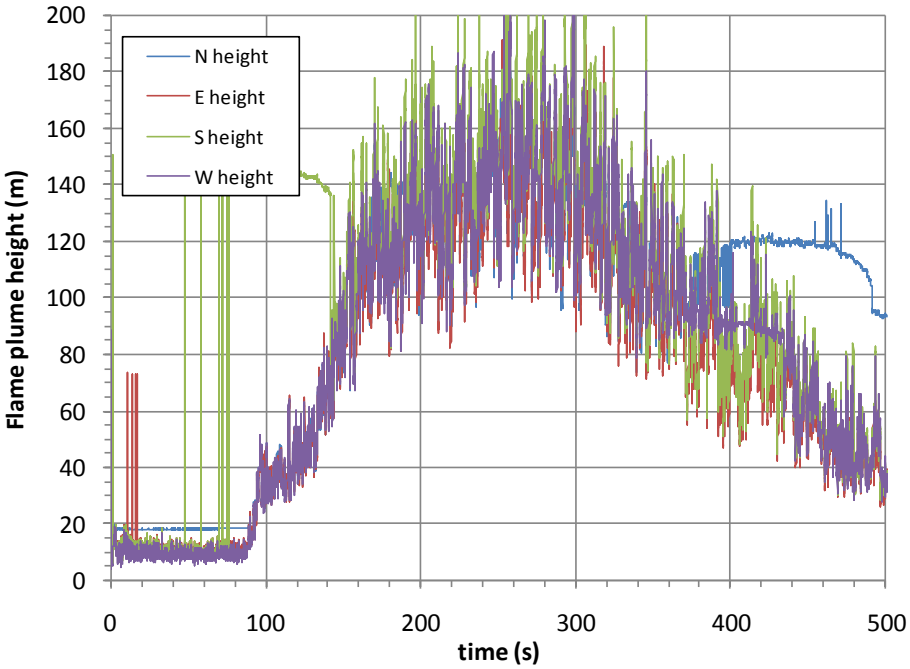

Figure 219 LNG Test 2 flame peak height.

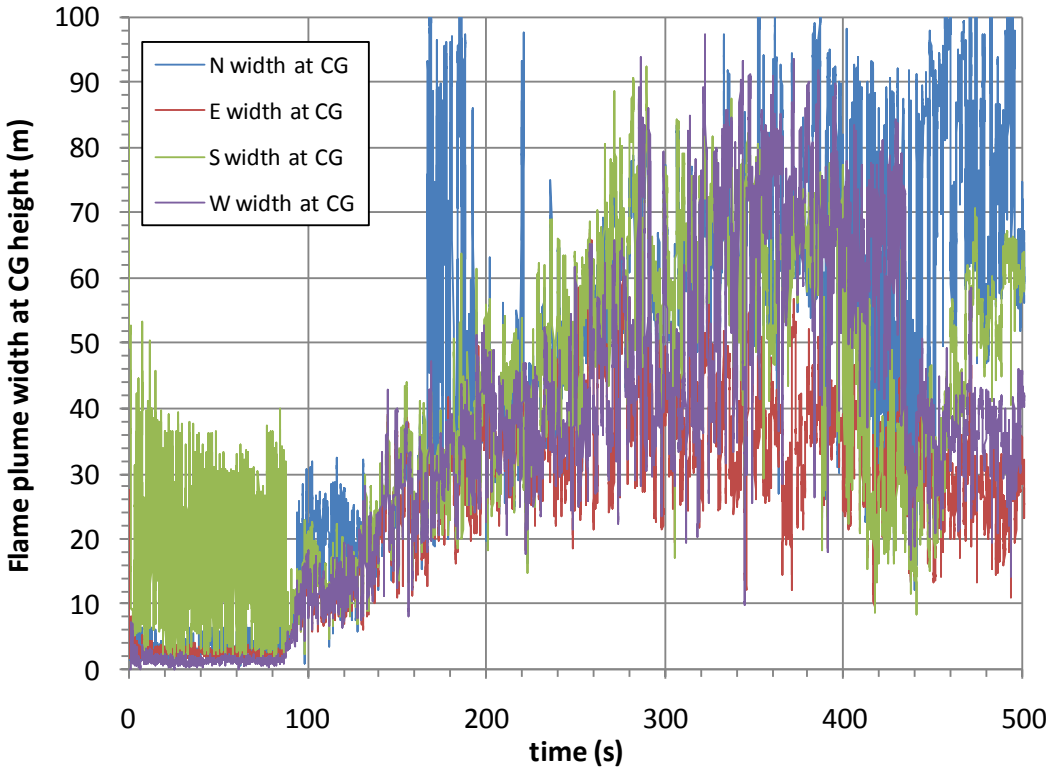

Figure 220 LNG Test 2 flame width at the CG height.

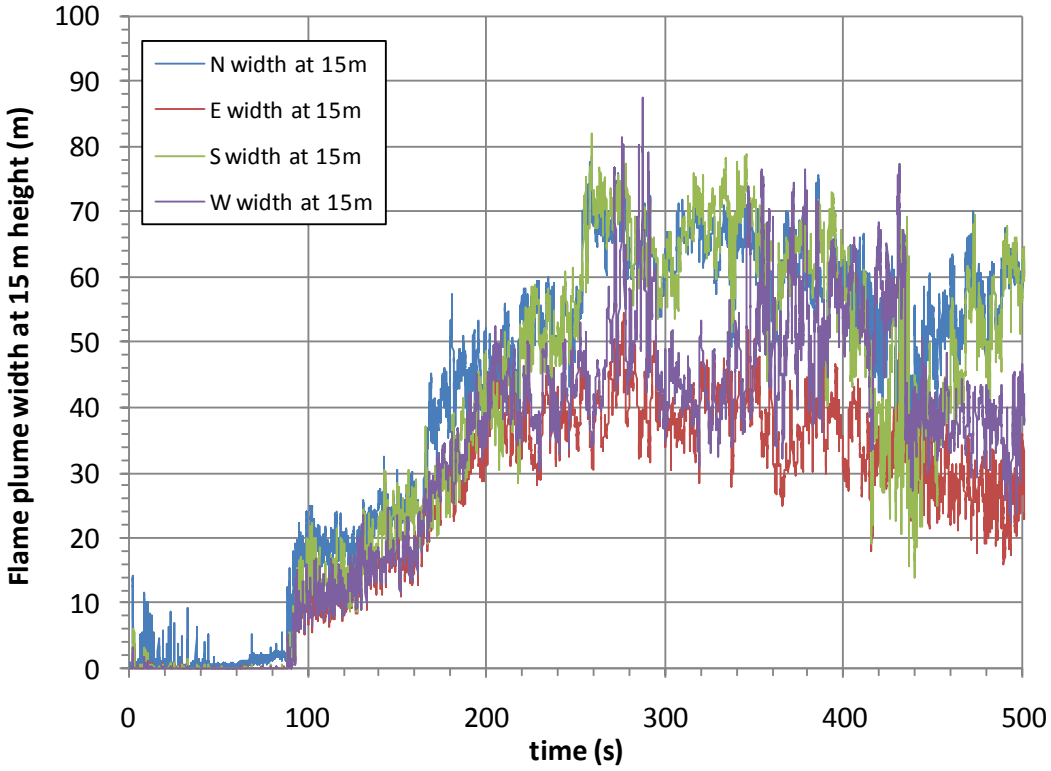

Figure 221 LNG Test 2 flame width at 15 m vertical height.

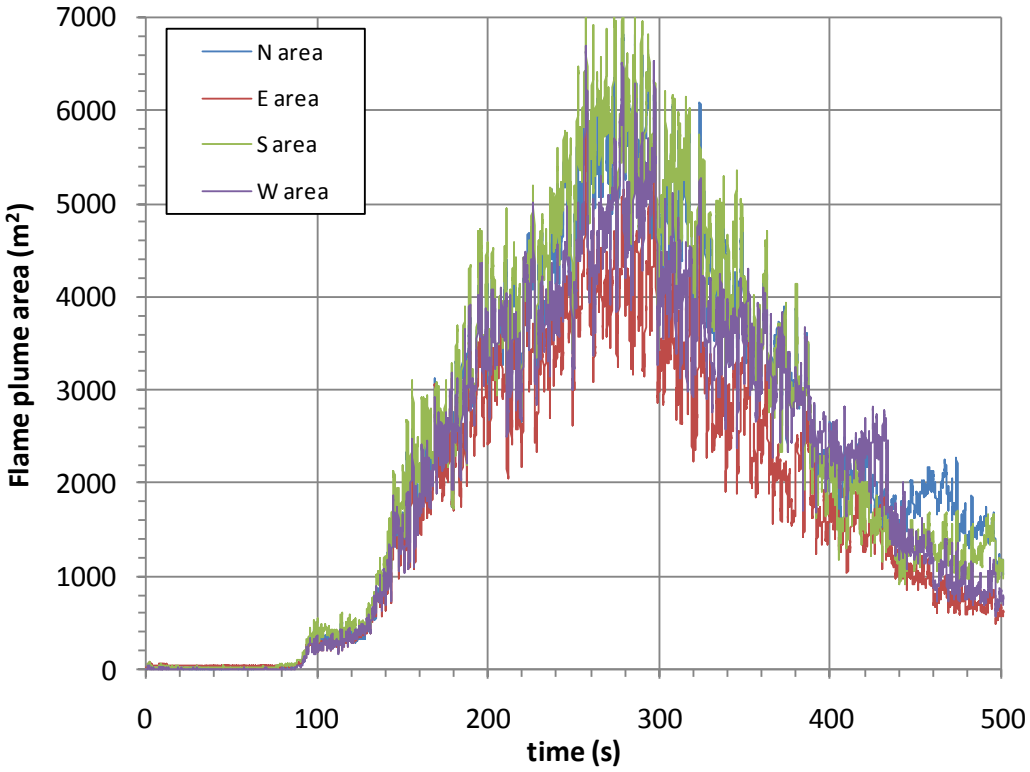

Figure 222 LNG Test 2 flame plume area.

Table 46 presents the average and standard deviation of the flame plume video results (widths and heights in m, area in m^2) during the interval between 250 and 300 s.

Table 46 LNG Test 2 flame plume average video analysis results at 250-300 s.

250-300 s	N width at CG	E width at CG	S width at CG	W width at CG	average width at CG
average	59.0	42.9	63.2	47.4	53.1
st. dev.	11.3	10.0	11.9	13.9	9.5
	N width at 15m	**E width at 15m**	**S width at 15m**	**W width at 15m**	**average width at 15m**
average	65.5	41.2	66.4	51.2	56.1
st. dev.	5.8	4.8	6.3	10.6	12.1
	N height at CG	**E height at CG**	**S height at CG**	**W height at CG**	**average height at CG**
average	50.3	55.4	52.3	50.8	52.2
st. dev.	6.2	7.5	6.5	9.2	2.3
	N height	**E height**	**S height**	**W height**	**average height**
average	140.4	139.7	156.3	148.3	146.2
st. dev.	19.6	20.0	24.3	22.5	7.8
	N area	**E area**	**S area**	**W area**	**average area**
average	5490	4094	5768	4865	5054
st. dev.	550	512	614	641	743

7.12 Atmospheric Transmission Effects on Radiative Measurements

As for LNG Test 1, MODTRAN (with a custom desert aerosol atmosphere model) was used to estimate the effects of atmospheric absorption on the radiometer measurements. The input parameters used for MODTRAN were measured just before the test with a local weather station and were recorded as follows:

Altitude: 1627 meters
Temperature: -4°C
Relative Humidity: 60%
Pressure: 12.19 psia (24.82 inHg)

The data were sampled evenly in wave number space (0.5 cm^{-1}) with a spectral range of 650 - 12500 cm^{-1} (~0.8-15.0 um) and at 8 horizontal path lengths. The MODTRAN calculated spectral transmission vs. path length for LNG Test 2 conditions is shown in Figure 223. The same methodology as described in LNG Test 1 was used to calculate the integrated average transmission as a function of path length and source temperature (1400K), shown in Figure 224. Slightly less transmission 1 (~0.01) occurred in Test 1 when compared to LNG Test 2.

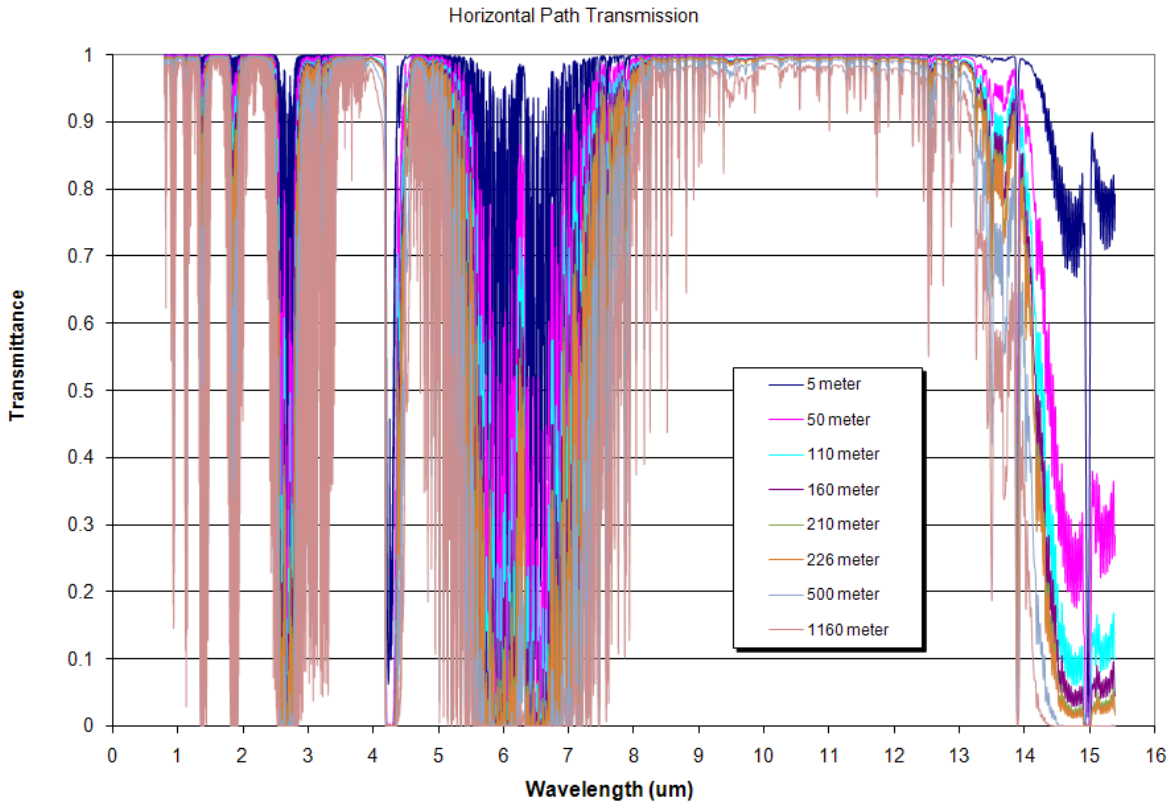

Figure 223 MODTRAN spectral transmission vs. path length for LNG Test 2.

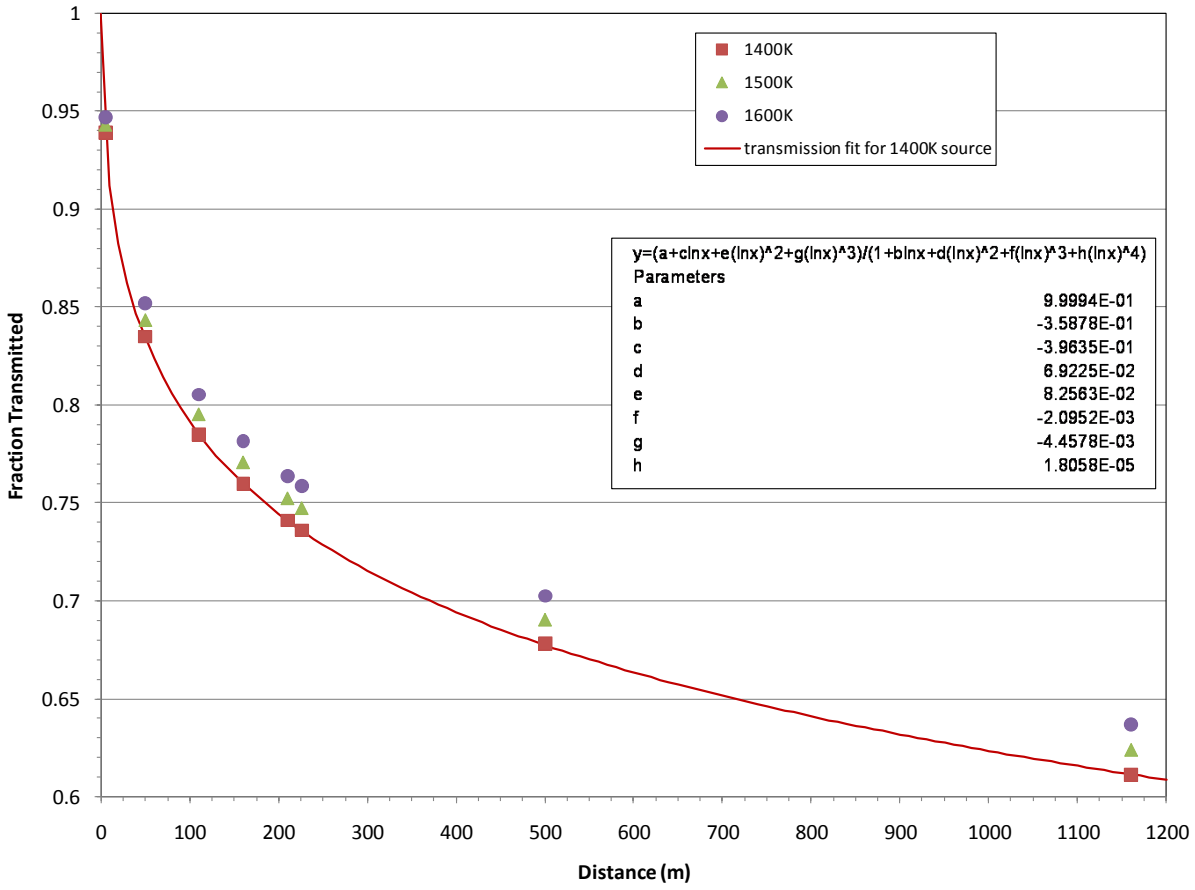

Figure 224 Integrated transmission vs. horizontal path length for LNG Test 2.

The fraction of energy transmitted to each instrument can now be estimated. Table 47 and Table 48 tabulate the distance from the flame CG to the instruments on the North-South and East-West spokes, respectively, at the times of data collection of the south spectrometer. These distances combined with the MODTRAN atmospheric transmission curve (drawn by fitting the data with regression analysis) yielded the transmission fractions for each gauge.

There was little variance in the CG shift from the pool center during the steady-state interval. Therefore, the fraction transmitted values at t = 258 s, also presented in Table 49, was used for correcting the radiometer data to obtain the average SEP values, as discussed in the following section.

Table 50 presents the average radiometer NV and WV heat flux data (units in kW/m^2) corrected by the transmission fractions (uncorrected data divided by the transmission fraction listed in Table 49) for the interval between 250-300 s.

Table 47 LNG Test 2 CG distance and transmission - North and South spoke gauges

time (s)	CG shift (m)	distance to flame CG (m)							fraction transmitted						
		south tow 1	south tow 2	south tow 3	south spec	north tow 1	north tow 2	north tow 3	south tow 1	south tow 2	south tow 3	south spec	north tow 1	north tow 2	north tow 3
0.00	0.0	110.7	159.9	209.8	227.7	109.9	159.8	209.6	0.785	0.760	0.741	0.735	0.785	0.760	0.741
145.80	-6.8	103.9	153.1	203.0	220.9	116.7	166.6	216.4	0.789	0.763	0.743	0.737	0.782	0.757	0.739
162.78	-9.6	101.1	150.3	200.2	218.1	119.5	169.4	219.2	0.791	0.764	0.745	0.738	0.780	0.756	0.738
179.52	-12.6	98.1	147.3	197.2	215.1	122.5	172.4	222.2	0.793	0.766	0.746	0.740	0.778	0.755	0.737
197.00	-15.7	95.0	144.2	194.1	212.0	125.6	175.5	225.3	0.796	0.768	0.747	0.741	0.776	0.753	0.736
212.48	-18.3	92.4	141.6	191.5	209.4	128.2	178.1	227.9	0.798	0.769	0.748	0.742	0.775	0.752	0.735
228.96	-20.6	90.1	139.3	189.2	207.1	130.5	180.4	230.2	0.799	0.770	0.749	0.743	0.773	0.751	0.734
242.70	-22.0	88.7	137.9	187.8	205.7	131.9	181.8	231.6	0.801	0.771	0.750	0.743	0.772	0.751	0.734
258.18	**-23.1**	**87.6**	**136.8**	**186.7**	**204.6**	**133.0**	**182.9**	**232.7**	**0.802**	**0.772**	**0.750**	**0.744**	**0.772**	**0.750**	**0.733**
273.66	-23.7	87.0	136.2	186.1	204.0	133.6	183.5	233.3	0.802	0.772	0.750	0.744	0.771	0.750	0.733
288.40	-23.9	86.8	136.0	185.9	203.8	133.8	183.7	233.5	0.802	0.772	0.750	0.744	0.771	0.750	0.733
325.62	-23.8	86.9	136.1	186.0	203.9	133.7	183.6	233.4	0.802	0.772	0.750	0.744	0.772	0.750	0.733
352.36	-23.8	86.9	136.1	186.0	203.9	133.7	183.6	233.4	0.802	0.772	0.750	0.744	0.772	0.750	0.733
377.34	-24.0	86.7	135.9	185.8	203.7	133.9	183.8	233.6	0.802	0.772	0.750	0.744	0.772	0.750	0.733
398.58	-23.8	86.9	136.1	186.0	203.9	133.7	183.6	233.4	0.802	0.772	0.750	0.744	0.772	0.750	0.733
418.30	-23.0	87.7	136.9	186.8	204.7	132.9	182.8	232.6	0.801	0.771	0.750	0.743	0.772	0.750	0.734
435.04	-21.4	89.3	138.5	188.4	206.3	131.3	181.2	231.0	0.800	0.770	0.749	0.743	0.773	0.751	0.734
467.76	-15.5	95.2	144.4	194.3	212.2	125.4	175.3	225.1	0.795	0.767	0.747	0.740	0.777	0.754	0.736
482.24	-10.9	99.8	149.0	198.9	216.8	120.8	170.7	220.5	0.792	0.765	0.745	0.739	0.779	0.756	0.738
499.74	-1.7	109.0	158.2	208.1	226.0	111.6	161.5	211.3	0.786	0.761	0.742	0.736	0.785	0.760	0.741
527.72	0.0	110.7	159.9	209.8	227.7	109.9	159.8	209.6	0.785	0.760	0.741	0.735	0.785	0.760	0.741

Table 48 LNG Test 2 CG distance and transmission - East and West spoke gauges

time (s)	CG shift (m)	distance to flame CG (m)						fraction transmitted					
		east tow 1	east tow 2	east tow 3	west tow 1	west tow 2	west tow 3	east tow 1	east tow 2	east tow 3	west tow 1	west tow 2	west tow 3
0.00	0.0	111.1	159.7	209.8	110.0	159.8	209.8	0.785	0.760	0.741	0.785	0.760	0.741
145.80	0.4	110.7	159.3	209.4	110.4	160.2	210.2	0.784	0.760	0.741	0.786	0.761	0.741
162.78	1.2	109.9	158.5	208.6	111.2	161.0	211.0	0.785	0.760	0.741	0.785	0.760	0.741
179.52	2.4	108.7	157.3	207.4	112.4	162.2	212.2	0.785	0.761	0.742	0.785	0.760	0.741
197.00	3.7	107.4	156.0	206.1	113.7	163.5	213.5	0.786	0.761	0.742	0.784	0.759	0.740
212.48	4.9	106.2	154.8	204.9	114.9	164.7	214.7	0.787	0.762	0.742	0.783	0.759	0.740
228.96	6.0	105.1	153.7	203.8	116.0	165.8	215.8	0.788	0.762	0.743	0.782	0.758	0.740
242.70	6.8	104.3	152.9	203.0	116.8	166.6	216.6	0.788	0.763	0.743	0.782	0.758	0.739
258.18	**7.7**	**103.4**	**152.0**	**202.1**	**117.7**	**167.5**	**217.5**	**0.789**	**0.763**	**0.744**	**0.781**	**0.757**	**0.739**
273.66	8.5	102.6	151.2	201.3	118.5	168.3	218.3	0.789	0.764	0.744	0.781	0.757	0.739
288.40	9.3	101.8	150.4	200.5	119.3	169.1	219.1	0.790	0.764	0.744	0.780	0.757	0.738
325.62	11.7	99.4	148.0	198.1	121.7	171.5	221.5	0.791	0.765	0.745	0.779	0.756	0.738
352.36	13.3	97.8	146.4	196.5	123.3	173.1	223.1	0.792	0.766	0.745	0.778	0.755	0.737
377.34	13.7	97.4	146.0	196.1	123.7	173.5	223.5	0.793	0.766	0.746	0.778	0.755	0.737
398.58	12.5	98.6	147.2	197.3	122.5	172.3	222.3	0.792	0.765	0.745	0.779	0.755	0.737
418.30	10.3	100.8	149.4	199.5	120.3	170.1	220.1	0.790	0.764	0.744	0.780	0.756	0.738
435.04	8.0	103.1	151.7	201.8	118.0	167.8	217.8	0.789	0.763	0.744	0.781	0.757	0.739
467.76	5.5	105.6	154.2	204.3	115.5	165.3	215.3	0.787	0.762	0.743	0.783	0.758	0.740
482.24	5.3	105.8	154.4	204.5	115.3	165.1	215.1	0.787	0.762	0.743	0.783	0.758	0.740
499.74	2.6	108.5	157.1	207.2	112.6	162.4	212.4	0.785	0.761	0.742	0.785	0.760	0.741
527.72	0.0	111.1	159.7	209.8	110.0	159.8	209.8	0.785	0.760	0.741	0.785	0.760	0.741

Table 49 Atmospheric transmission fraction for correcting LNG Test 2 radiometer data

spoke	tower 1	tower 2	tower 3
north	0.772	0.750	0.733
south	0.802	0.772	0.750
east	0.789	0.763	0.744
west	0.781	0.757	0.739

Table 50 LNG Test 2 radiometer data (corrected) for the interval between 250-300 s.

	narrow-angle radiometers							wide-angle radiometers		
spot height above pool (m)	15	30	55	85	120	55	55	55	55	55
nominal distance from pool center (m)	110	110	110	110	110	160	210	110	160	210
North spoke	**0 hfg 1**	**0 hfg 2**	**0 hfg 3**	**0 hfg 4**	**0 hfg 5**	**0 hfg 7**	**0 hfg 9**	**0 hfg 6**	**0 hfg 8**	**0 hfg 10**
average	275.2	283.4	306.4	197.4	56.9	326.7	324.5	20.9	12.6	8.4
st.dev.	19.9	37.5	43.8	91.8	65.5	47.5	30.5	1.6	0.9	0.6
South spoke	**180 hfg 1**	**180 hfg 2**	**180 hfg 3**	**180 hfg 4**	**180 hfg 5**	**180 hfg 7**	**180 hfg 9**	**180 hfg 6**	**180 hfg 8**	**180 hfg 10**
average	187.6	225.8	250.5	271.0	163.6			39.4	20.8	13.3
st.dev.	24.4	28.4	29.6	43.1	35.5			3.4	1.8	1.2
East spoke								**90 hfg 6**	**90 hfg 8**	**90 hfg 10**
average									13.3	8.6
st.dev.									1.2	0.7
West spoke								**270 hfg 6**	**270 hfg 8**	**270 hfg 10**
average								20.6	12.1	7.7
st.dev.								1.9	1.4	0.8

7.13 Flame Radiant Fraction

As was discussed in LNG Test 1, the 4π radiant fraction, χ_{rad}, can be estimated using Eq. 60:

$$\chi_{rad} = \frac{4\pi r^2 \left(q''/\tau\right)}{m_b h_c} \tag{60}$$

where r is the CG distance (m) from the fire, q''/τ is the wide-view heat flux (kW/m^2) corrected for the transmission loss (τ), and $m_b h_c$ is the average total heat release by combustion (m_b is the mass burning rate (kg/s, assumed equal to the reservoir mass flow rate) and h_c is methane heat of combustion (55687 kJ/kg)).

However, since the reservoir emptied prior to the fire achieving a steady-state (SS), the time-dependent reservoir mass flow rate could not be used to provide the mass burning rate, m_b. Three potential constant values of mass flow rate were reviewed. The first was the average discharge rate (~802 kg/s) during the interval when the discharge plugs were fully open (130-220 s). The other two mass flow rates were based on multiplying the SS regression rate of 0.14 kg/m^{2}s determined in LNG Test 1 by either the SS pool area (yielding an equivalent pool diameter of ~83m) or the fire area (from an equivalent fire diameter of 56.1 m), yielding 755 kg/s and 346 kg/s, respectively. It was decided that the latter was the most relevant (in addition to being conservative), and was used in the final analyses.

Figure 225 presents the time-dependent radiant fraction using the wide-view radiometer data from all spokes (corrected for transmission losses), shows the LNG mass flow rate from the reservoir, and the constant mass burning rate used in the analyses.

Table 51 presents the average radiant fraction from each gauge during the steady-state interval from 250-300 s. The listed standard deviation is due to the variability over the interval. The average radiant fraction from all measurements and one standard deviation is 0.24±0.08 (2 sigma).

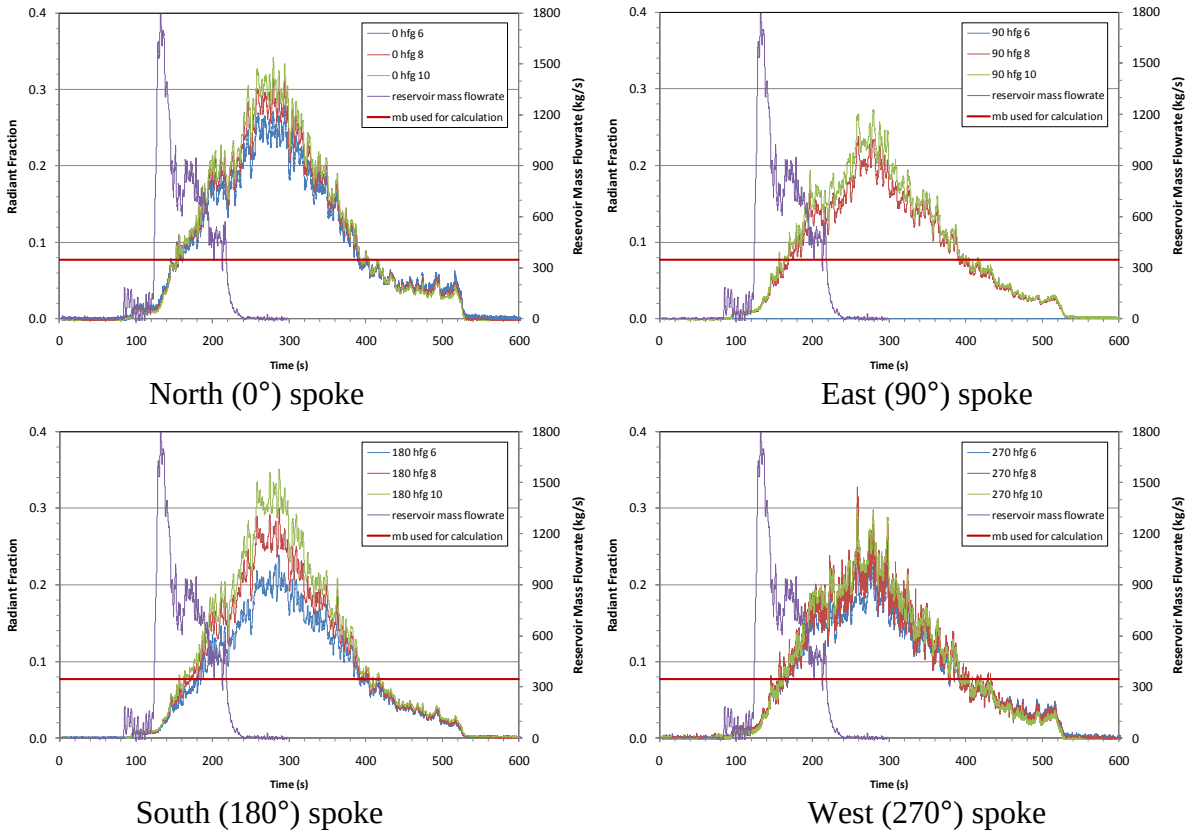

Figure 225 LNG Test 2 radiant fraction from the WV radiometers.

Table 51 LNG Test 2 Radiant Fraction

	Wide-View Heat Flux	Distance to CG	Radiant Fraction	
Duration 250-300s	kW/m^2	m	average	st.dev.
N Tower 1	20.9	133.0	0.24	0.02
N Tower 2	12.6	182.9	0.27	0.27
N Tower 3	8.4	232.7	0.30	0.30
S Tower 1	39.4	87.6	0.20	0.02
S Tower 2	20.8	136.8	0.25	0.25
S Tower 3	13.3	186.7	0.30	0.30
E Tower 1		103.4		
E Tower 2	13.3	152.0	0.20	0.20
E Tower 3	8.6	202.1	0.23	0.23
W Tower 1	20.6	117.7	0.19	0.02
W Tower 2	12.1	167.5	0.22	0.22
W Tower 3	7.7	217.5	0.24	0.24

7.14 Flame Surface Emissive Power

The video data was used in conjunction with the wide-view radiometers to determine a time-dependent flame surface emissive power (SEP). See the discussion in the LNG Test 1 Section 5.13 that provides some background theory on radiometers and the methodology used to determine the SEP.

Figure 226 and Figure 227 present the transmission corrected incident heat flux (green curve) from the wide-view radiometers on all spokes. These figures also show the view factor multiplier (blue curve) for the $E_{environment}$ term shown in Eq. (59). Finally, these figures also present the time-dependent overall flame SEP (red curve), the result of multiplying the transmission-corrected incident heat flux times the view factor multiplier.

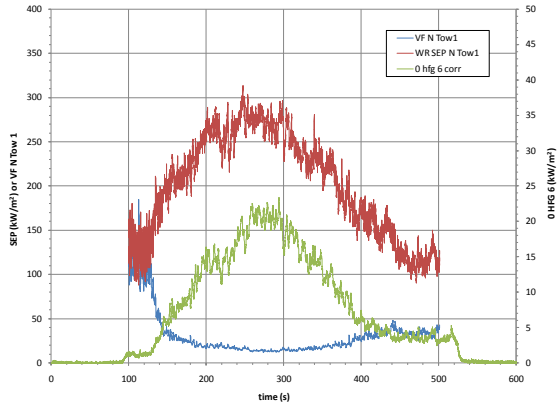

North Tower 1

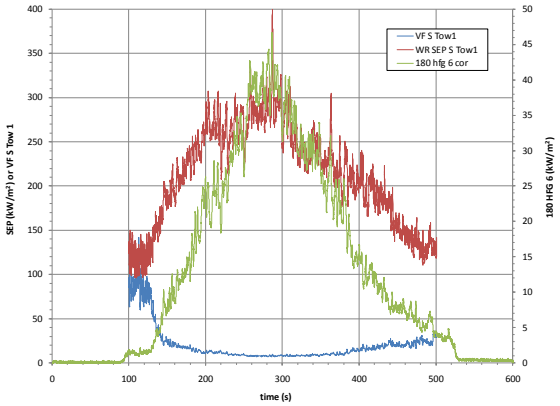

South Tower 1

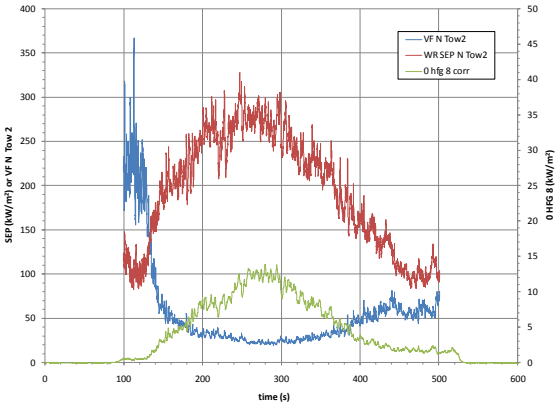

North Tower 2

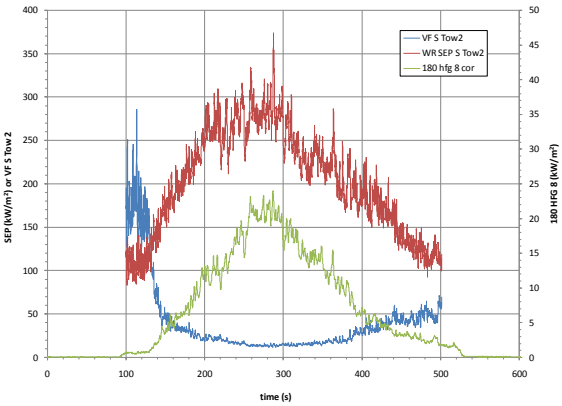

South Tower 2

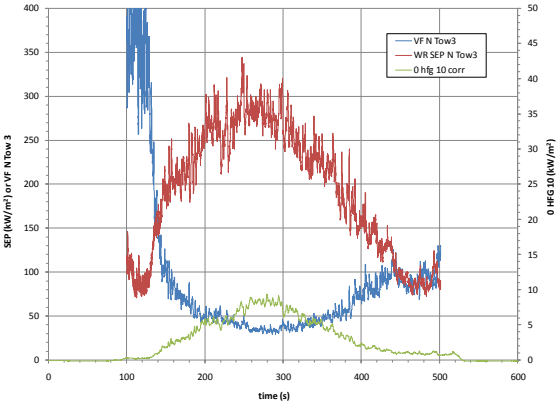

North Tower 3

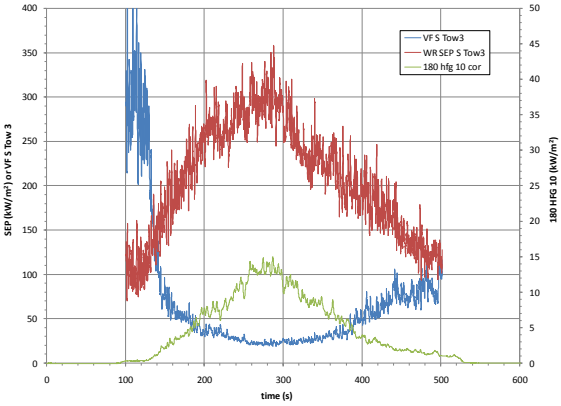

South Tower 3

Figure 226 SEP results from the North and South WV radiometers in LNG Test 2.

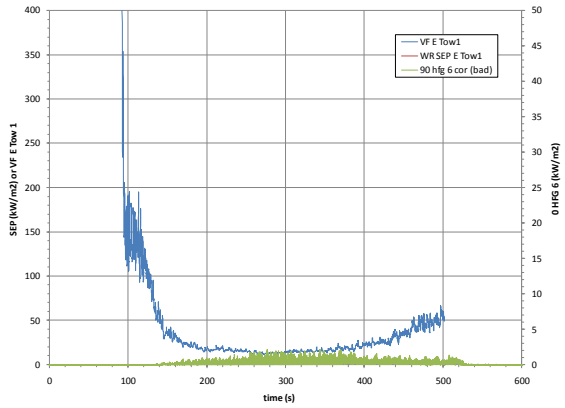

East Tower 1

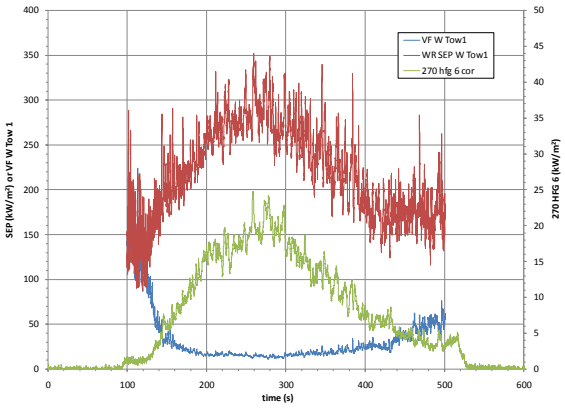

West Tower 1

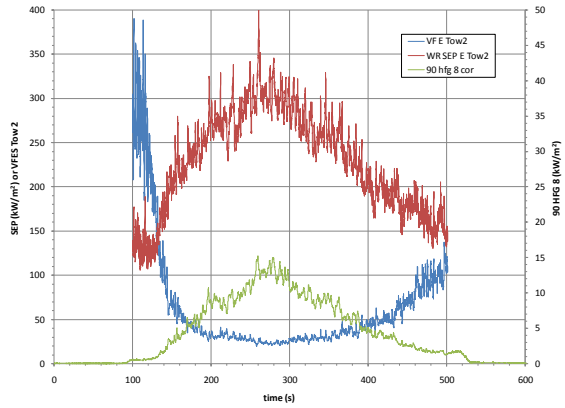

East Tower 2

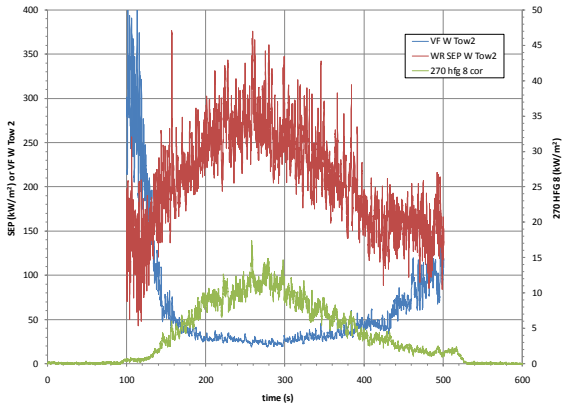

West Tower 2

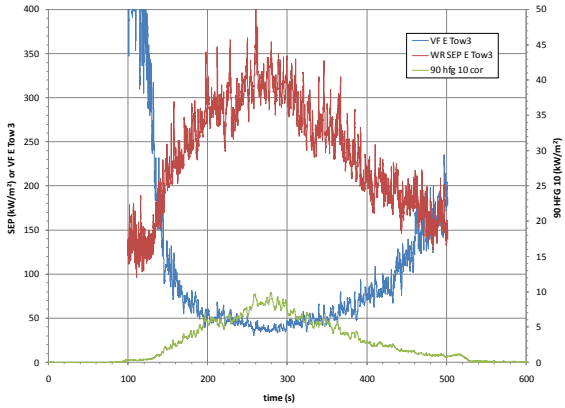

East Tower 3

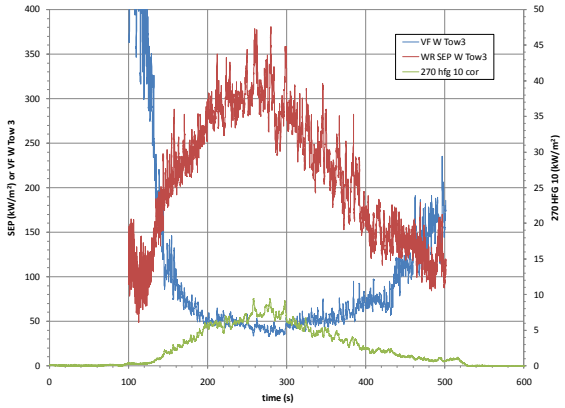

West Tower 3

Figure 227 SEP results from the East and West WV radiometers in LNG Test 1.

Table 52 presents the average and standard deviations over the interval from 250-300 s of the wide-angle incident heat flux (corrected for the atmospheric transmission loss), the view factor, and the flame SEP. **The average overall SEP is 286 ± 20 kW/m^2** (2 sigma) (average of the 11 individual SEP data points).

Table 52 LNG Test 2 heat flux (corrected), view factor, and flame SEP (250-300 s).

	Wide-View Heat Flux		View Factor		Surface Emissive Power	
Duration 250-300s	average	st.dev.	average	st.dev.	average	st.dev.
N Tower 1	20.9	1.6	13.6	1.1	283.4	11.8
N Tower 2	12.6	0.9	22.4	2.0	280.6	13.7
N Tower 3	8.4	0.6	33.9	3.1	284.3	15.5
S Tower 1	39.4	3.4	7.2	0.5	283.8	22.1
S Tower 2	20.8	1.8	13.3	1.0	276.0	19.8
S Tower 3	13.3	1.2	21.8	1.9	287.9	20.6
E Tower 1			13.1	1.1		
E Tower 2	13.3	1.2	22.6	2.0	298.6	19.5
E Tower 3	8.6	0.7	35.7	3.5	305.8	20.9
W Tower 1	20.6	1.9	14.3	1.3	292.6	25.8
W Tower 2	12.1	1.4	23.4	2.3	283.4	32.1
W Tower 3	7.7	0.8	35.5	3.8	271.4	23.8

7.15 Narrow-View Radiometer Analysis

The video analysis routines also determined a time-dependent "fill fraction" for each narrow-view radiometer, based on the nominal gauge parameters (gauge height, view angle, inclination angle, distance to pool center, and CG) in order to determine the validity of the gauge data.

Figure 228 and Figure 230 shows a video frame from the North and South spoke cameras at t = 233.5 s. Note the spot overlays representing the field of view for each North narrow-view radiometer show the gauges on the three towers nominally centered to view a height 55 m above the pool surface are no longer centered; this is because the distance from the gauges to the flame has changed from baseline as the flame CG shifts in time. Figure 229 and Figure 231 show the time-dependent fill fraction for each gauge on the North and South spoke.

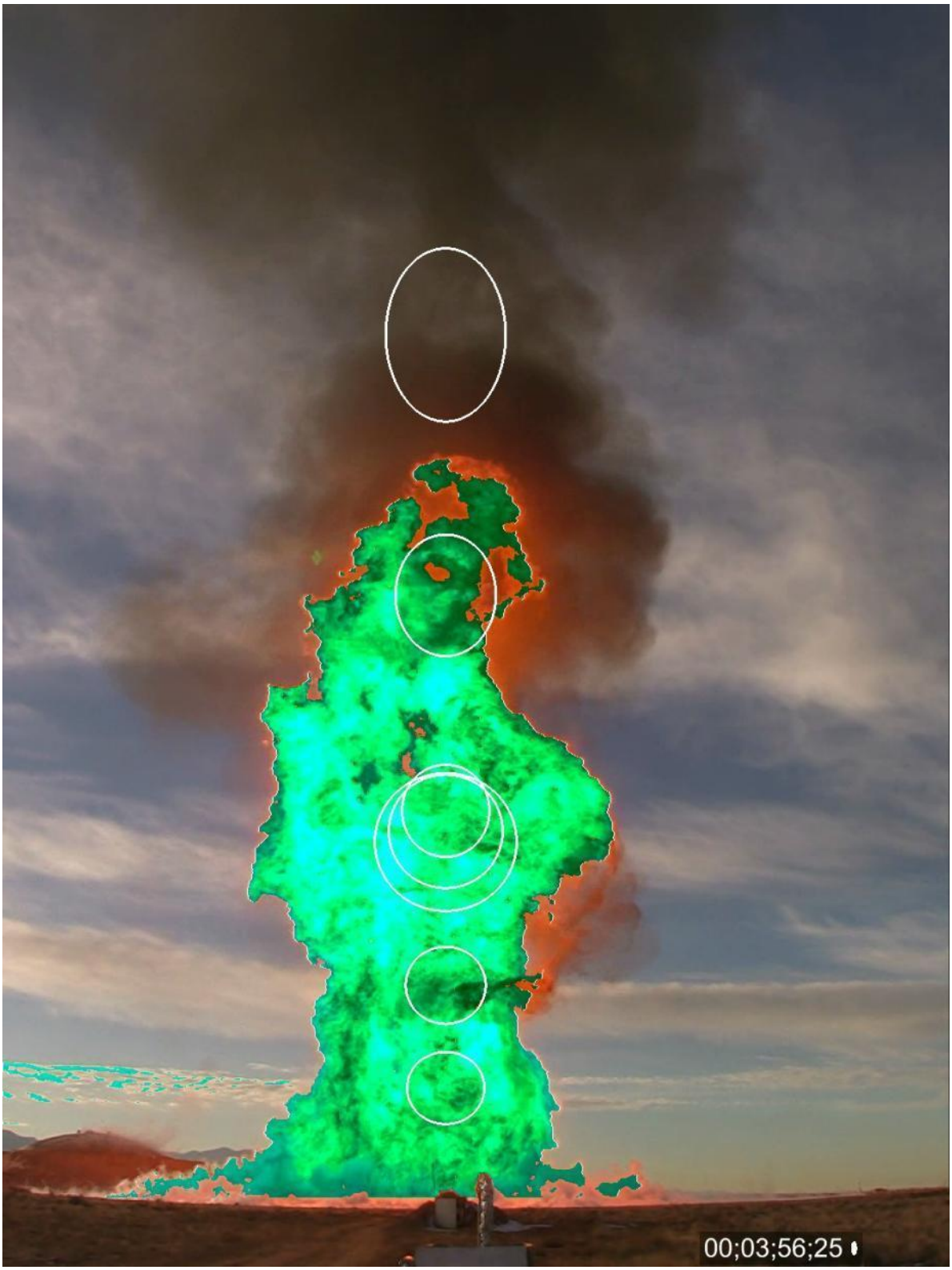

Figure 228 North spoke camera view with NV radiometer field of view overlay (t=233.5s).

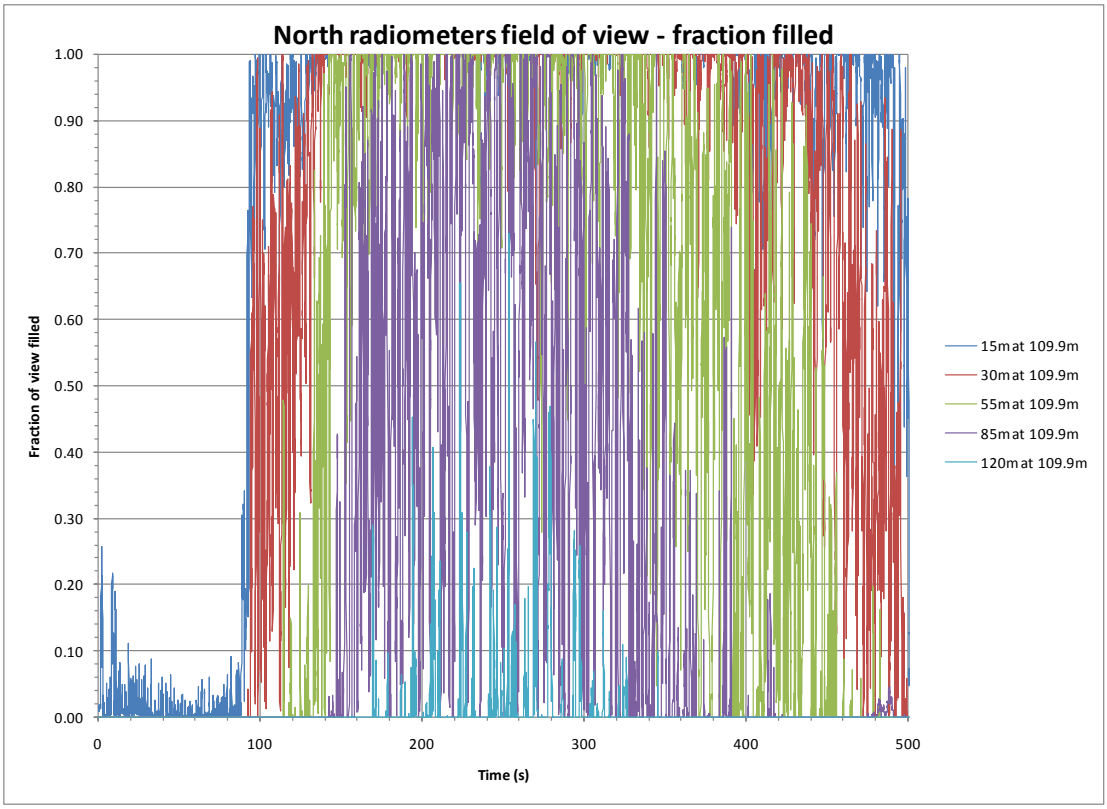

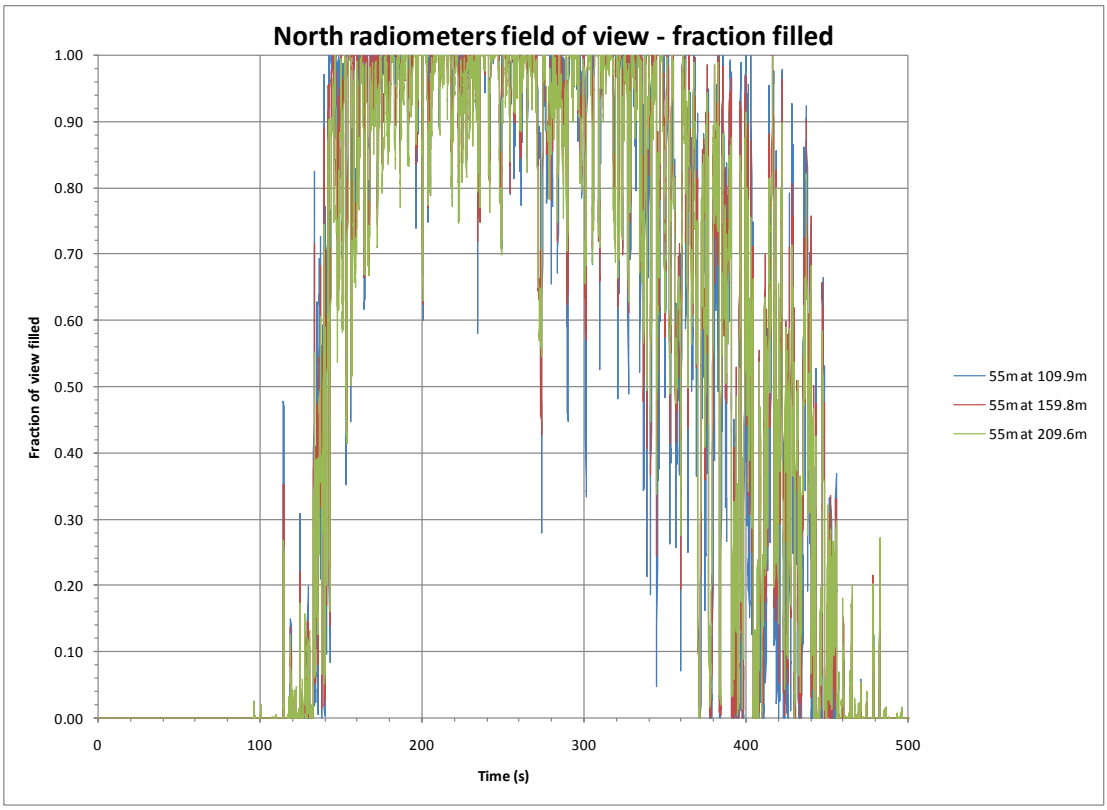

Figure 229 LNG Test 2 North HFGs fill fractions for the radiometer field of view.

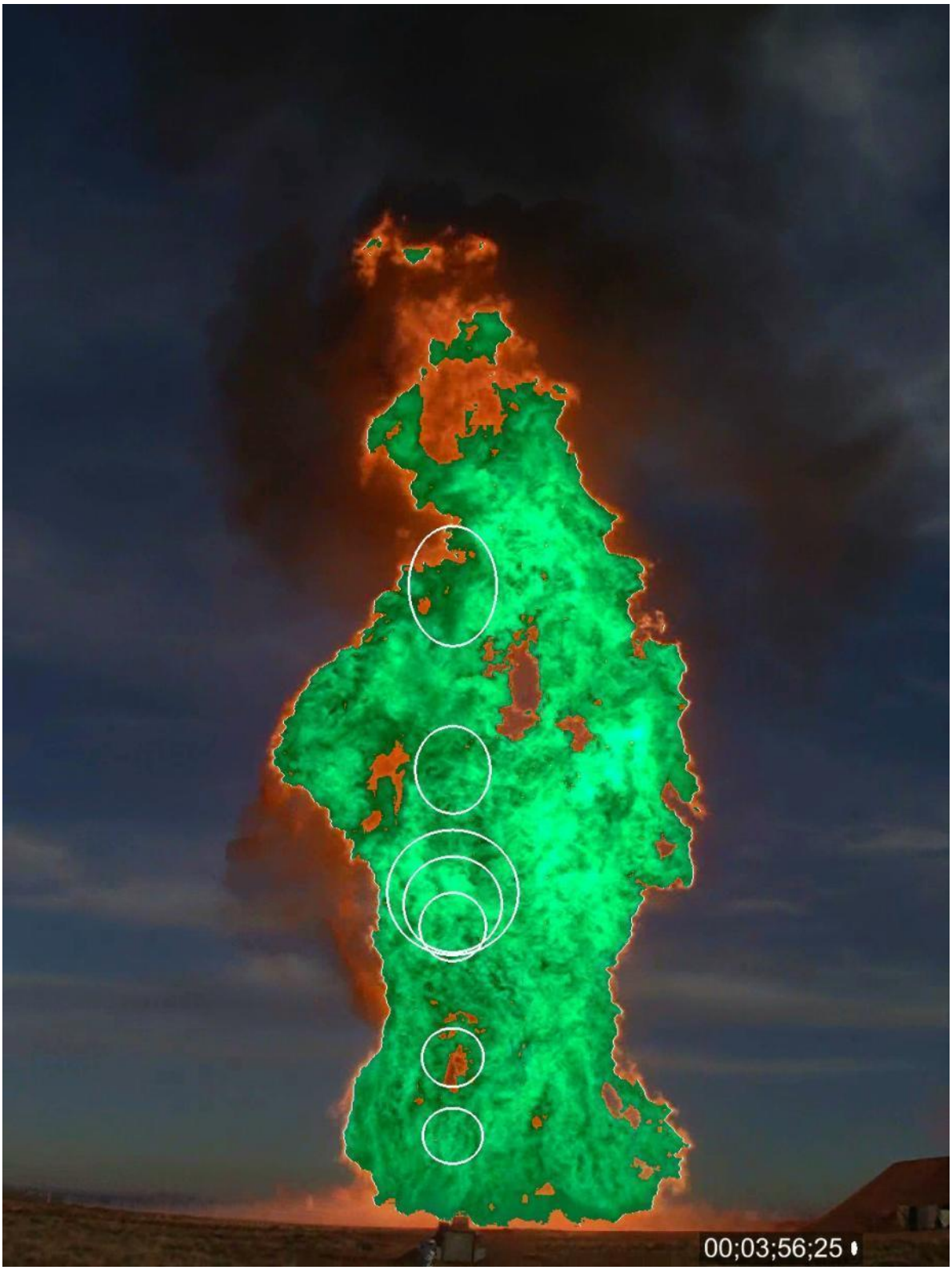

Figure 230 South spoke camera view with NV radiometer field of view overlay (t=233.5s).

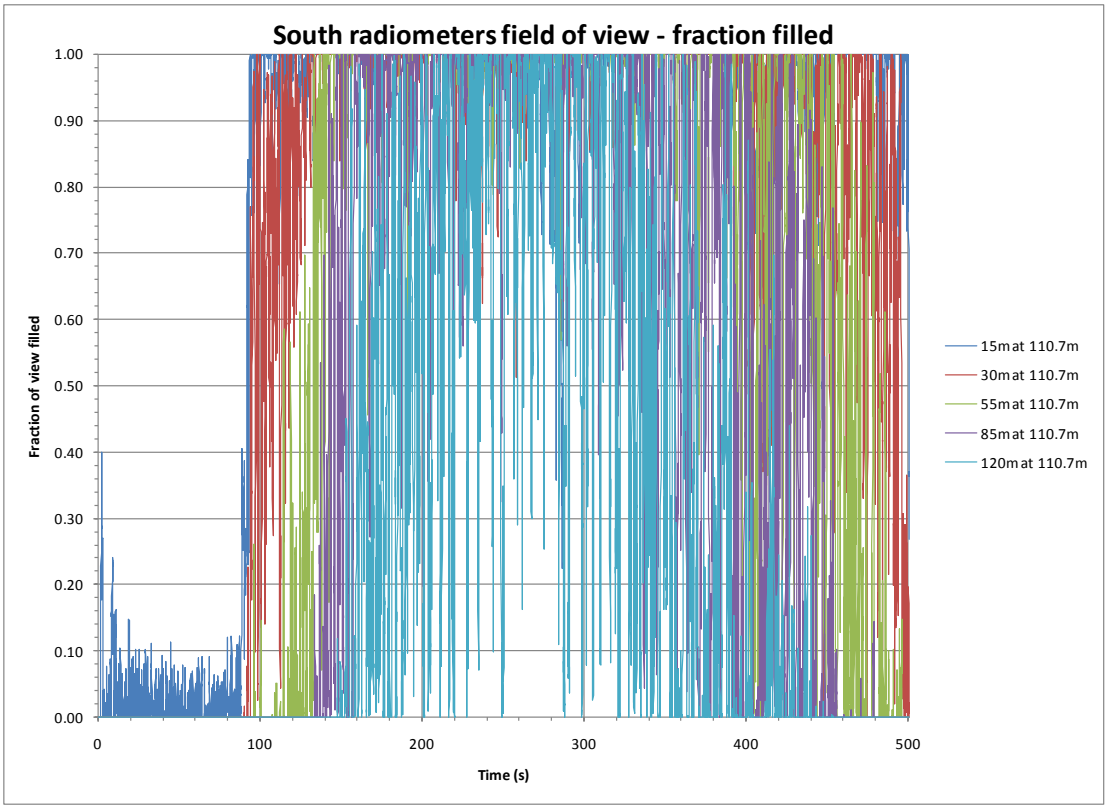

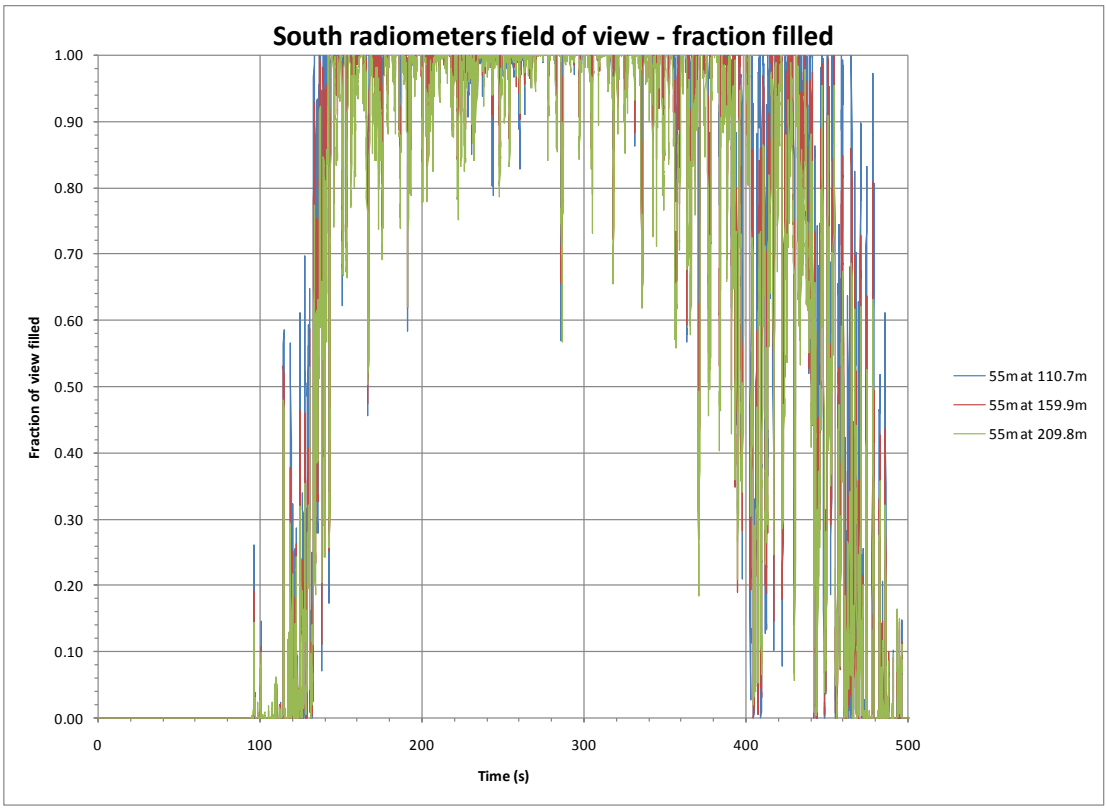

Figure 231 LNG Test 2 South HFGs fill fractions for the radiometer field of view.

Figure 232 compares the fill fraction to the heat flux (corrected for atmospheric attenuation) for the North and South gauges (HFG4, 85m height at 110.5m distance). Note that the as fill fraction changes a corresponding change in heat flux follows after a small delay (63.2% time constant for the HFGs is 35 ms). The embedded image is frame 7100, taking at ~237 s.

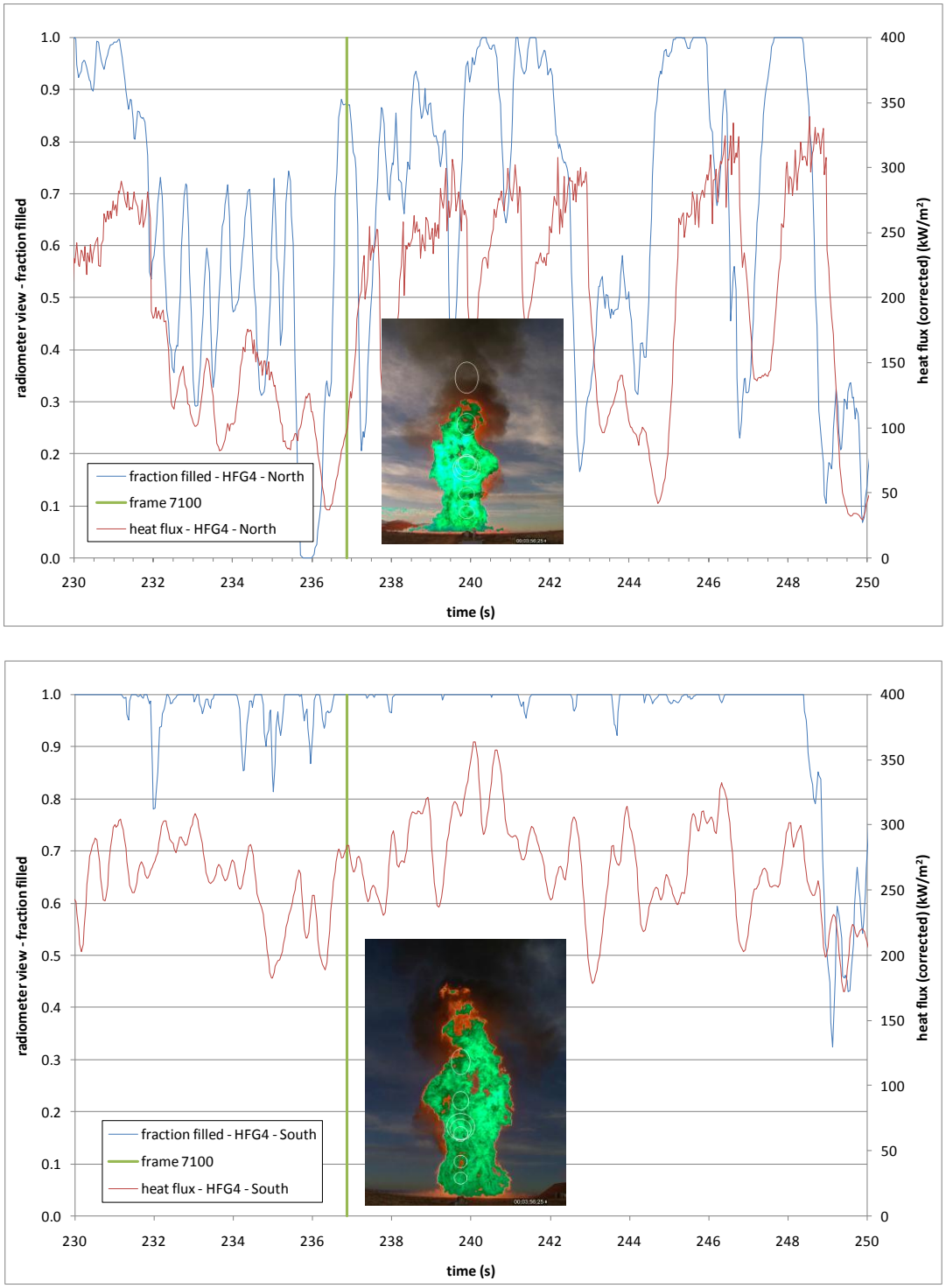

Figure 232 LNG Test 2 heat flux and fill fraction for North and South NV radiometers. (HFG4 at 85m height at 110.5m distance)

As mentioned earlier, lower flux values measured by the south narrow-view radiometer gauges (as compared to the north heat flux NV gauges) were likely due to the white smoke from small grass fires partially obscuring the gauge view. Figure 233 compares North and South NV radiometers incident heat flux (corrected for the transmission loss) that are focused at the same elevation point above the pool surface. A large difference is seen between the two measurements early in the test, especially for the gauges viewing the lower half of the fire (HFG1 and HFG2). After about 300 s, the videos show that the grass fires extinguish and the smoke clears, and the data shows better agreement. The North HFG3 gauge recorded peak fluxes in the range of 350 kW/m^2 for short periods of time during the steady-state interval.

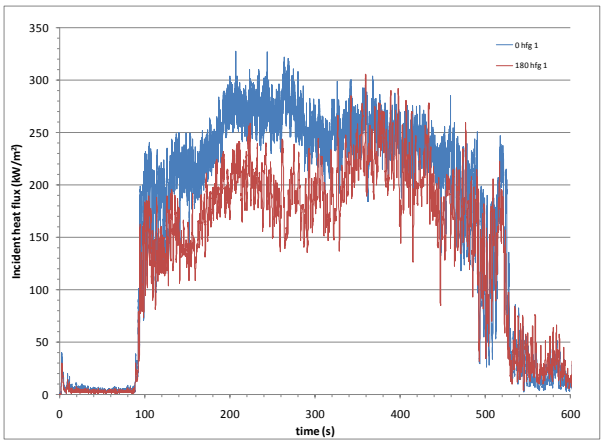

HFG 1 (15 m above pool)

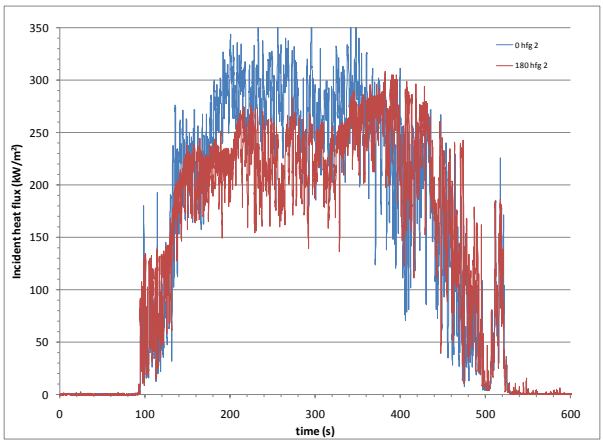

HFG 2 (30 m above pool)

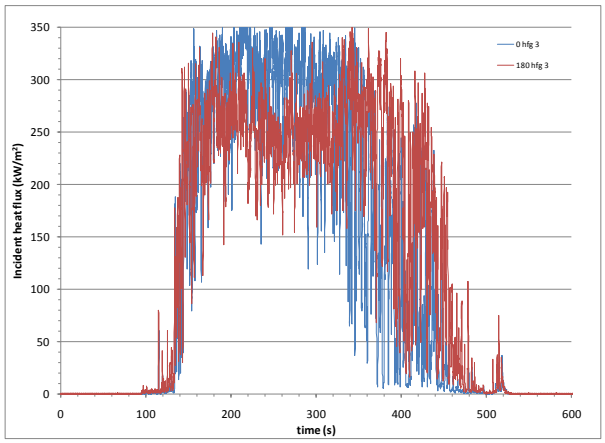

HFG 3 (55 m above pool)

Figure 233 Effects of grass fire smoke on South spoke NV HFGs in LNG Test 2.

Table 53 presents the average and standard deviation of the fill fraction over the 250-300 s interval for all gauges. Table 54 shows the North and South narrow-view radiometer heat flux data corrected for transmission losses and compares that to their respective fill fraction over the 250-300 s interval. For averaging purposes, valid data was obtained from all narrow-view gauges highlighted in Table 53, as their fill fractions were greater than 0.75 during the averaging interval.

Table 53 LNG Test 2 radiometers field of view – fill fraction

gauge #	fill fraction	North Towers		South Towers		East Towers		West Towers	
	250-300s	average	std.dev.	average	std.dev.	average	std.dev.	average	std.dev.
1	15m at 110.7m	0.99	0.03	0.94	0.13	0.22	0.20	0.51	0.26
2	30m at 110.7m	0.97	0.09	0.99	0.04	0.24	0.29	0.38	0.32
3	55m at 110.7m	0.95	0.10	1.00	0.02	0.20	0.32	0.22	0.31
7	55m at 159.9m	0.95	0.09	0.99	0.03	0.22	0.31	0.23	0.30
9	55m at 209.8m	0.94	0.09	0.99	0.04	0.23	0.28	0.25	0.28
4	85m at 110.7m	0.65	0.33	0.98	0.07	0.13	0.25	0.10	0.23
5	120m at 110.7m	0.10	0.19	0.84	0.25	0.02	0.06	0.01	0.03

Table 54 LNG Test 2 HFG fill fraction and corrected incident heat flux

fill fraction			0 hfg 1	0 hfg 2	0 hfg 3	0 hfg 4	0 hfg 5	0 hfg 6	0 hfg 7	0 hfg 8	0 hfg 9	0 hfg 10
spot height at distance		250-300s	15m at 110.7m	30m at 110.7m	55m at 110.7m	85m at 110.7m	120m at 110.7m	55m at 110.7m	55m at 159.9m	55m at 159.9m	55m at 209.8m	55m at 209.8m
	North	ave	0.99	0.97	0.95	0.65	0.10		0.95		0.94	
		sd dev	0.03	0.09	0.10	0.33	0.19		0.09		0.09	
	South	ave	0.94	0.99	1.00	0.98	0.84		0.99		0.99	
		sd dev	0.13	0.04	0.02	0.07	0.25		0.03		0.04	
	East	ave	0.22	0.24	0.20	0.13	0.02		0.22		0.23	
		sd dev	0.20	0.29	0.32	0.25	0.06		0.31		0.28	
	West	ave	0.51	0.38	0.22	0.10	0.01		0.23		0.25	
		sd dev	0.26	0.32	0.31	0.23	0.03		0.30		0.28	
HFG flux kW/m^2 transmittance corrected		250-300s	0 hfg 1	0 hfg 2	0 hfg 3	0 hfg 4	0 hfg 5	0 hfg 6	0 hfg 7	0 hfg 8	0 hfg 9	0 hfg 10
	North	ave	275.2	283.4	306.4	197.4	56.9	20.9	326.7	12.6	324.5	8.4
		sd	19.9	37.5	43.8	91.8	65.5	1.6	47.5	0.9	30.5	0.6
	South	ave	187.6	225.8	250.5	271.0	163.6	39.4		20.8		13.3
		sd	24.4	28.4	29.6	43.1	35.5	3.4		1.8		1.2
HFG flux / fill fraction kW/m^2	North	ave	277.4	290.8	323.3				344.8		344.0	
	South	ave	198.5	228.3	251.4	277.4						

Averaging the North spoke NV gauges (1,2,3,7,9) yields an incident heat flux of 303 ± 47 (2 sigma) kW/m^2. Averaging the South spoke NV gauges (1,2,3,4) yields an incident heat flux of 234 ± 72 (2 sigma) kW/m^2.

As discussed in Test 1, it is possible to adjust some of the gauges to account for the partial fill by dividing the average flux by the average fill fraction (for those gauges with fill fractions greater than 0.94). The adjusted values for the above gauges are also shown in Table 54.

Note that the highlighted gauges that see 100% flame (or are corrected to allow for this) and are corrected for transmission losses represent surface emissive power values.

The North spoke NV gauges (1,2,3,7,9) yielded a North "spot" average SEP of 316 ± 62 kW/m^2 (2 sigma).

The South spoke NV gauges (1,2,3,4) yielded a South "spot" average SEP of 239 ± 67 kW/m^2 (2 sigma).

Averaging all gauges with fill fractions ≥0.9 yielded a "spot" average SEP of 282 ± 101 kW/m^2 (2 sigma).

Figure 234 compares the "spot" SEP from the narrow view gauges HFG 1, 2, and 3 on the North spoke to the full-field "flame" SEP as calculated using the wide view heat flux gauge (HFG 6) and the video data from the North spoke. Both data sets were corrected for transmission losses. Results show good agreement and fall within the uncertainty of each method.

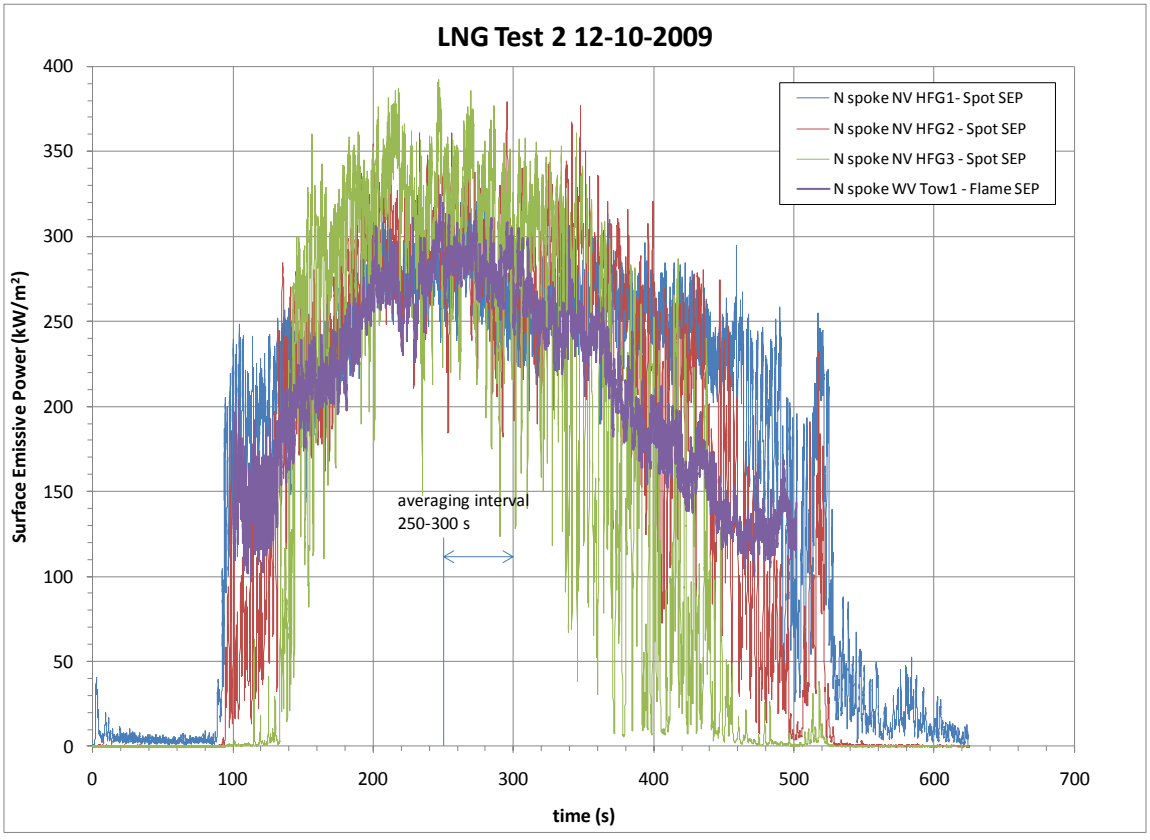

Figure 234 "Spot" SEP compared to the full-field "Flame" SEP in LNG Test 2.

7.16 LNG Spectra – Mid-Infrared

Although many spectrometers were fielded for the fire, only one of them acquired data throughout the test due to the position of the fire. There was very little wind, but the small amount present shifted the fire enough so that two of the spokes (45^o and 90^o) did not have the entire height of the fire within the vertical scan line of the spectrometer. The fire was shifted almost directly towards the 180^o spoke.

The unit 2 spectrometer was located on the 180^o spoke and it acquired data throughout the fire. The spectrometer was positioned on a tilt table, which obtained data from two different vertical scans (nominally 1-50 m and 50-100 m). The 50-100 m scan (tilt angle #2) did collect data throughout the fire which was not the case with the much smaller first LNG fire. In fact, the fire height actually exceeded the maximum height of the vertical spectrometer scan.

Triggering of the Spectrometer

The spectrometer software was configured to accept a total of 20 remote triggers during the fire. These 20 triggers were broken down into two groups of 10. In each group of 10, the spectrometer alternated between a low angle and high angle on the tilt table. Figure 235 shows experimentally acquired heat fluxes with the spectrometer triggers overlaid. The spectrometer triggers are shown as the black lines. Although all data were evaluated, only analysis of data acquired during the quasi-steady burning period (labeled as #7, 8, 9, 10) are included in this report. Triggers 7 and 9 were low elevation scans, while triggers 8 and 10 were high elevation scans. During each trigger at total of 1280 spectra were acquired which equates to 10 line scans since each line consists of 128 locations.

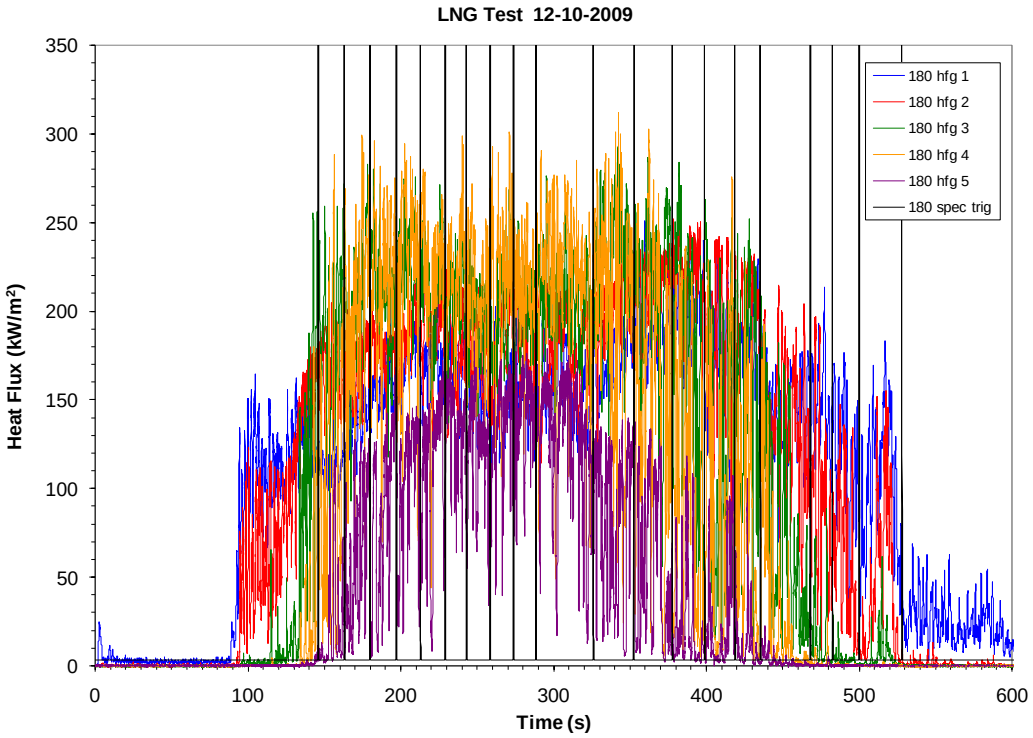

Figure 235 LNG Test 2 spectrometer trigger times.

Spectra as a Function of Height

Examples of the spectra collected at several heights during the four quasi-steady burning period triggers are shown in Figure 236. The lines represent the average of 10 spectra (~3.2 sec) at that location.

The scans (7, 9) taken for the low elevation (1-50m) are shown on the left and the high elevation scans (8, 10) are shown on the right of the figure. The variability in the intensity as a function of height is greater for the low elevation scans as the intensity tends to increase as a function of height above the fuel surface. The intensities are more consistent for the heights shown in the high elevation scans. It does not appear that the scan (maximum height of 103m) is reaching the top of the fire plume since the intensities are not decreasing as they would for decreased flame emission near the top of a fire.

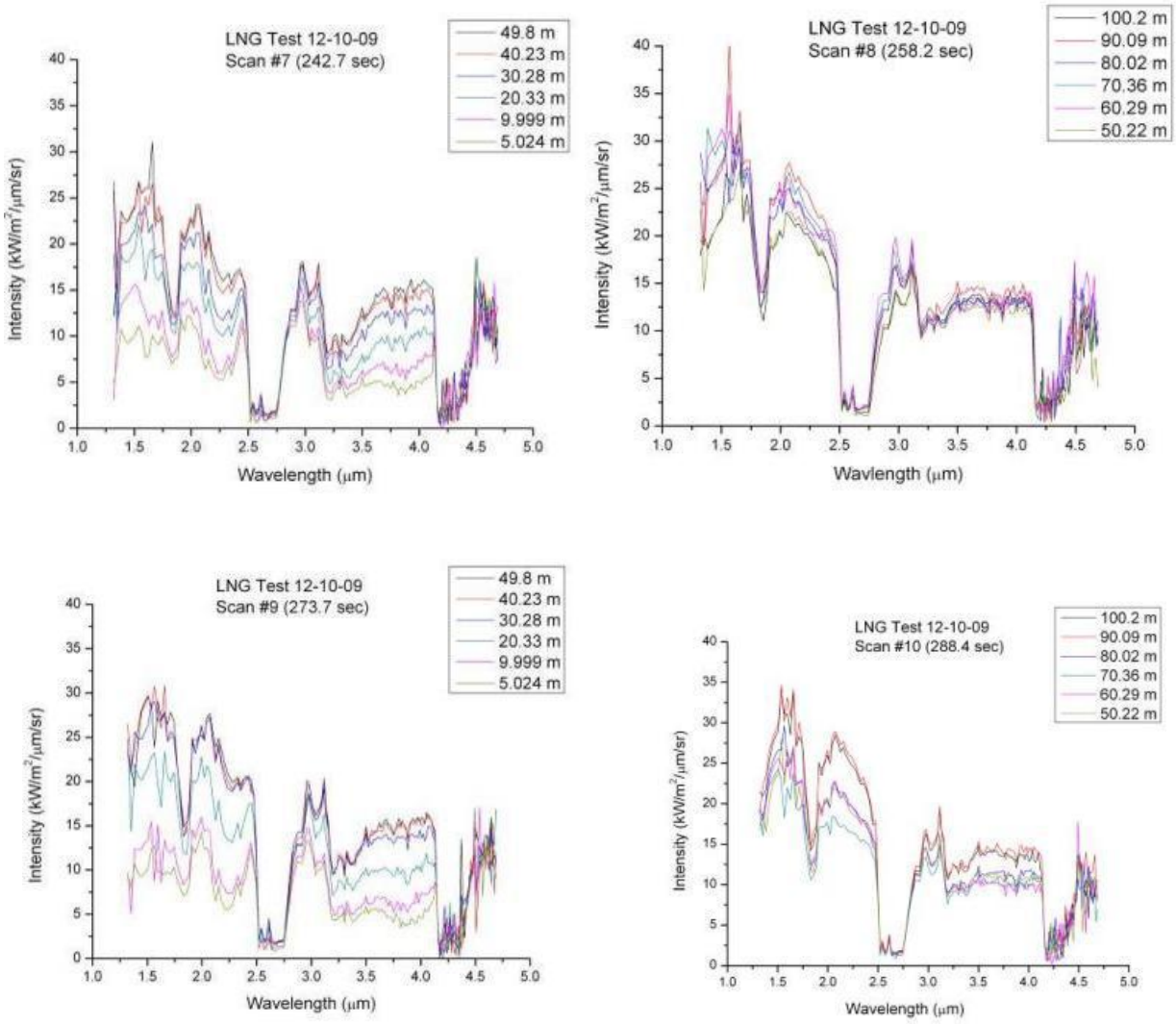

Figure 236 LNG Test 2 spectra at selected heights and times.

Figure 237 displays the spectra as a function of all heights for scans during the quasi-steady time period. These plots essentially present the same information as the plots in the previous figure

except that all 128 height locations are included instead of just a select few heights. This allows for a more complete assessment of the variability as a function of height to be made.

The dominant contributor to the thermal radiation is broadband emission by soot particles. There is likely some gas band emission from water, CO, and CO_2 but it is overwhelmed by the soot emission. In addition, the CO_2 emission is likely masked somewhat by the decreased sensitivity of the longer wavelength pixels (>4.3μm) in the array.

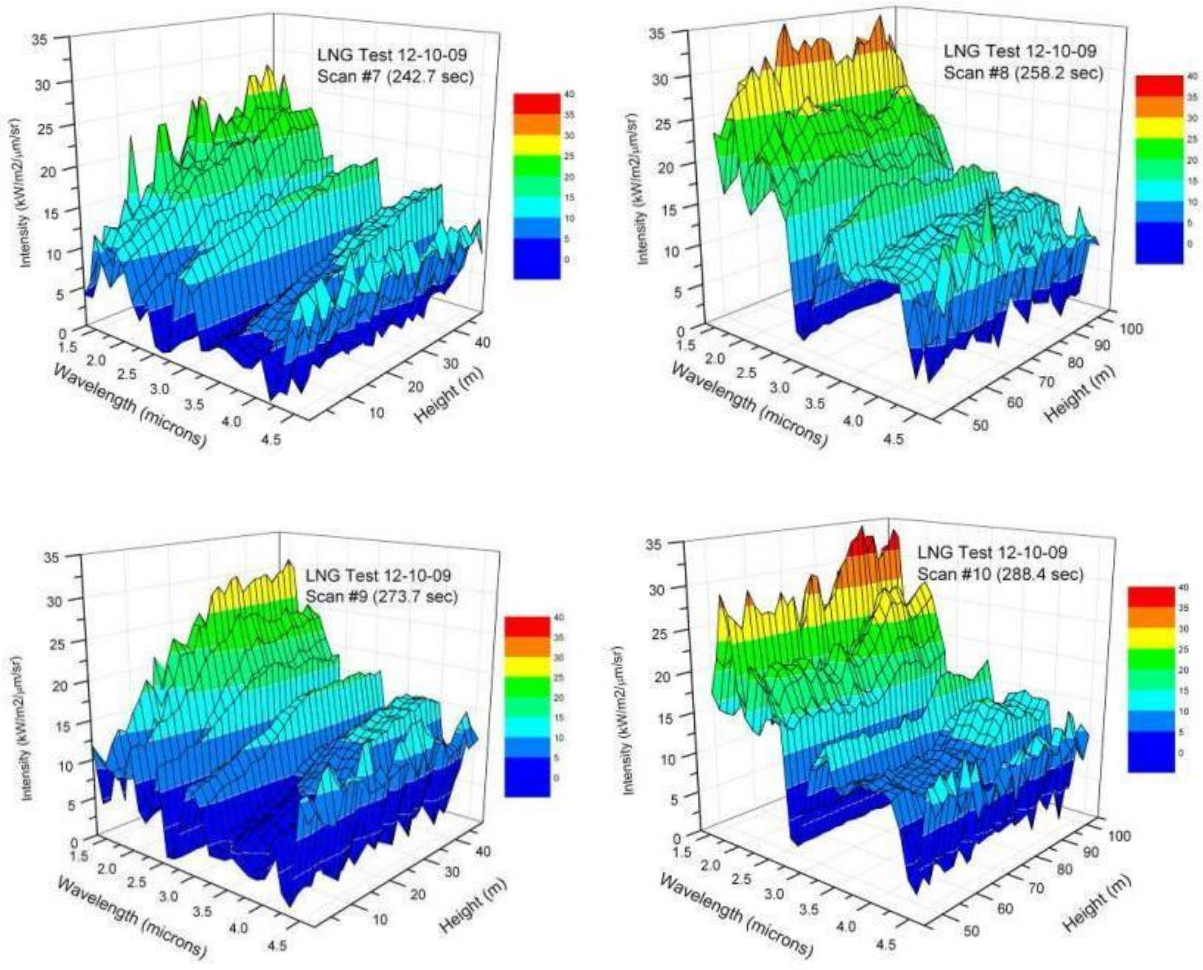

Figure 237 Wire mesh plots of LNG spectra in LNG Test 2.

It is evident that the features of the spectra seen in Figure 236 and Figure 237 allow for an evaluation of the spectral variation in thermal radiation as well as the variation as a function of height and time. These features are consistent with the paper by Raj [2007], such as the atmospheric absorption of thermal radiation by H_2O and CO_2 (1.87 μm, 2.7 μm, and 4.3 μm) in addition to the broadband soot emission in the spectra. Additional plots from other trigger times can be provided to further assess the variability as a function of time.

Surface Emissive Power from Acquired Spectra

Surface emissive powers were computed from all the acquired data by integrating the intensities over the wavelength range. These SEPs (not corrected for atmospheric attenuation or spectrometer wavelength limits, discussed later) are shown in Figure 238 and Figure 239 for the duration of the fire which provides insight into the transient variability in thermal radiation. At early times in the fire (scans 1 and 2), the SEPs are lower and there is a minimal increase with height at the low elevations and then the SEPs decrease with height at the higher elevations indicating the flame zone height is less than 100m. For the middle scans (5-10) the SEPs increase with height at the low elevations to a maximum value near 30-40m above the fuel surface, and then continue to fluctuate about a quasi-steady heat flux value for the higher elevations. Maximum uncorrected SEP measurements reach 170 kW/m^2. During this quasi-steady burning period there is no significant decrease in SEPs with a certain position in height which indicates that the flame height exceeds the maximum scan height of 103 m. For scans obtained after the quasi-steady burning period, SEPs increase with height and then decrease at some point due to the decrease in flame height as the fuel is consumed.

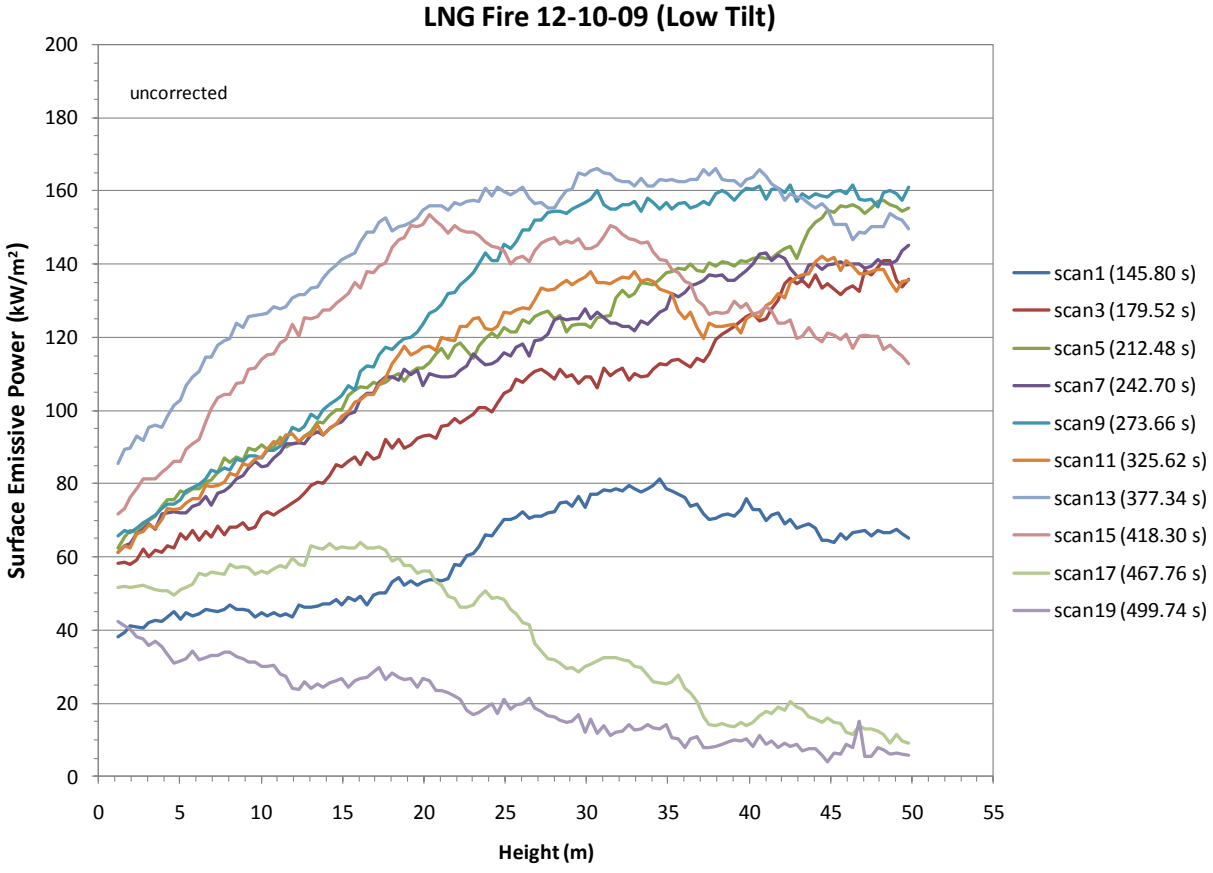

Figure 238 LNG Test 2 spectra-derived SEP (uncorrected) at low elevations.

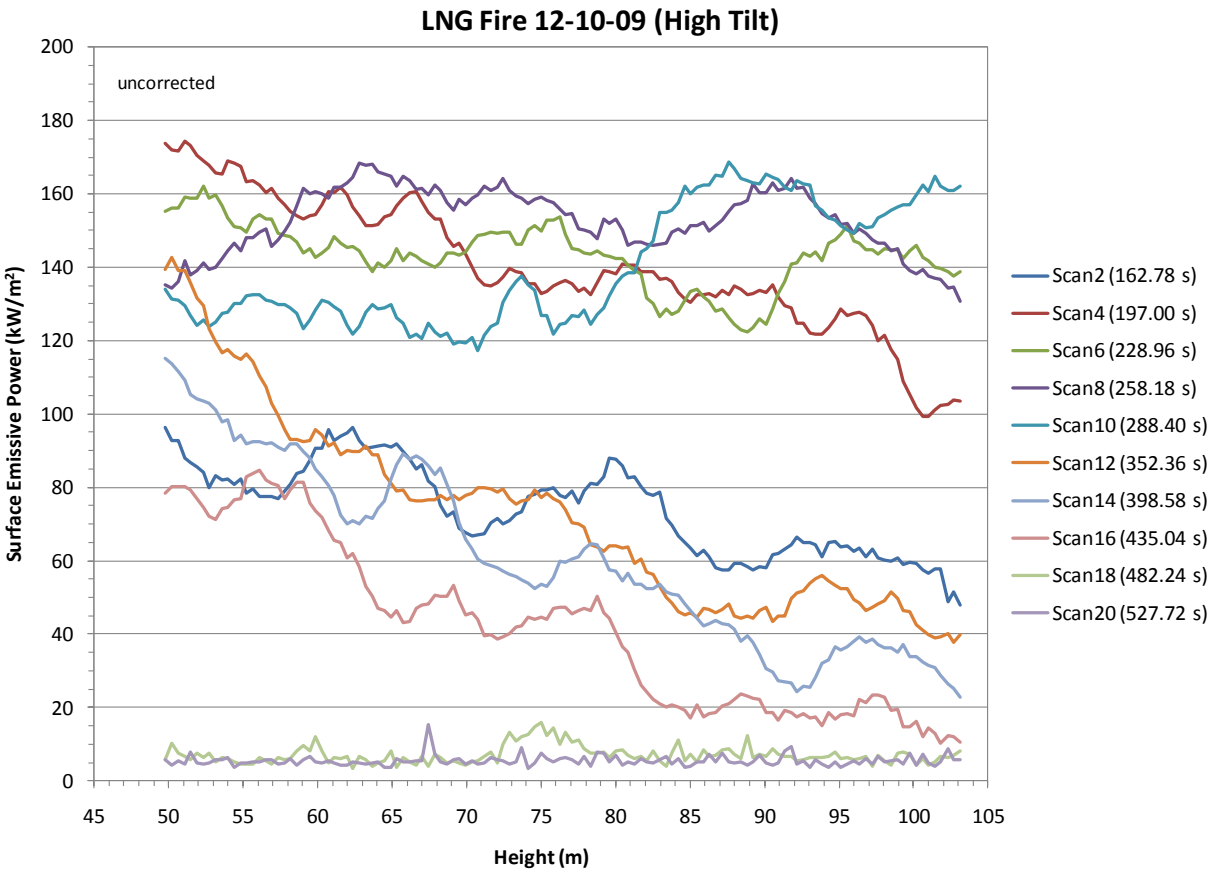

Figure 239 LNG Test 2 spectra-derived SEP (uncorrected) at high elevations.

Atmospheric Attenuation

The attenuation of thermal radiation by the atmosphere was calculated using MODTRAN; results are shown in Figure 240. The parameters for the day of the fire were as follows.

Distance L = 226 m
Ambient temperature = -4 C
Relative Humidity = 60%
Wind Speed = 1.5 m/s
Pressure = 12.19 psia (24.82 inch HG)

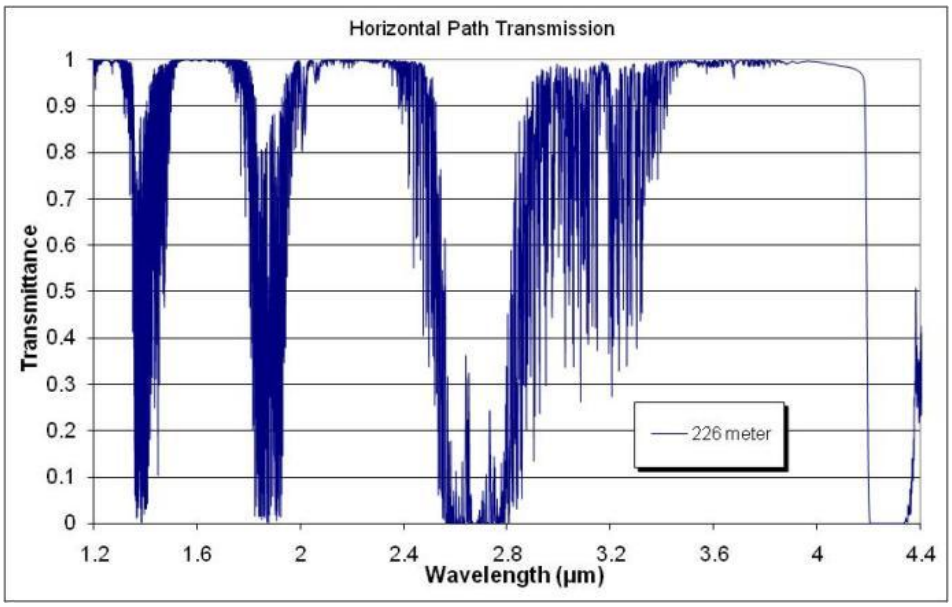

Figure 240 MODTRAN results for 226 m atmospheric transmission in LNG Test 2.

Gas Band Emission

Using the MODTRAN results above and infrared emission band data (Table 32) for typical gas band emission, bands that were free of gas band emission and atmospheric absorption (1.5-1.75 and 2.08-2.34 micron bands, 9 wavelengths in each band) were selected for further analysis of the temperature and emissivity. These bands were assumed to only contain emission from soot radiation.

Temperature and Emissivity Fits

The approximate temperature and emissivity of the flame zone was assessed by performing a two parameter fit of the thermal radiation to the Planck function in the bands that were determined to be free of atmospheric attenuation and gas band emission. The spectral radiation intensity (I_λ) emitted by the blackbody at any specific wavelength, λ can be obtained from Eq. (61):

$$I_{b\lambda} = \varepsilon_\lambda \left(\frac{C_1}{\lambda^5 \{ \exp(\frac{C_2}{\lambda T}) - 1 \}} \right) \tag{61}$$

where $I_{b\lambda}$ is the black body intensity, which depends purely on the temperature, T. C_1 and C_2 are the well-known first and second radiation constants. Note that the emissivity of the blackbody (ε_λ) is assumed to be 1.

Figure 241 compares T and ε fits to the spectra from scan 8 at two heights (100 m and 50 m). The fits are generally very good for the higher wavelength band (2.08-2.34 μm) since the atmospheric transmission is near 1. For the lower wavelength band (1.5-1.75 μm), there is slightly lowered transmission below 1.5 μm; therefore, the fit is not quite as good.

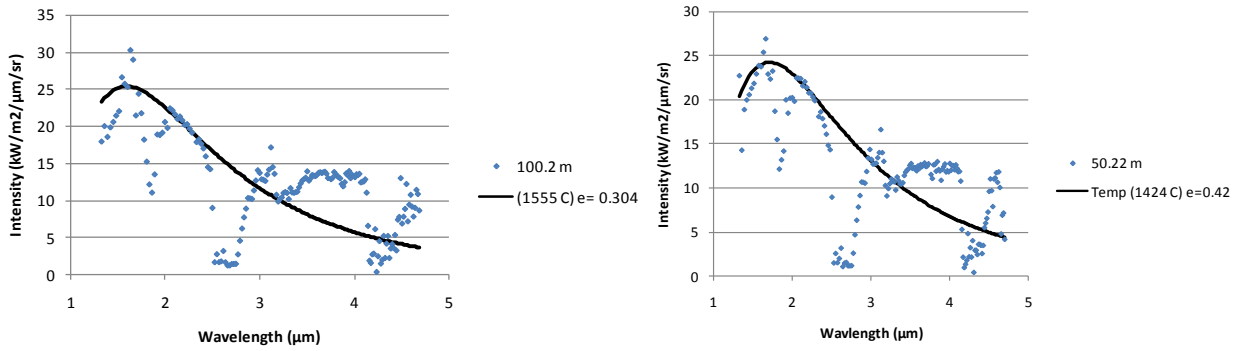

Figure 241 Comparison of T and ε fits of LNG Test 2 spectra (from scan 8).

Summary plots of the calculated temperature and emissivity of the fire for various heights in scans 7, 8, 9, and 10 are shown in Figure 242.

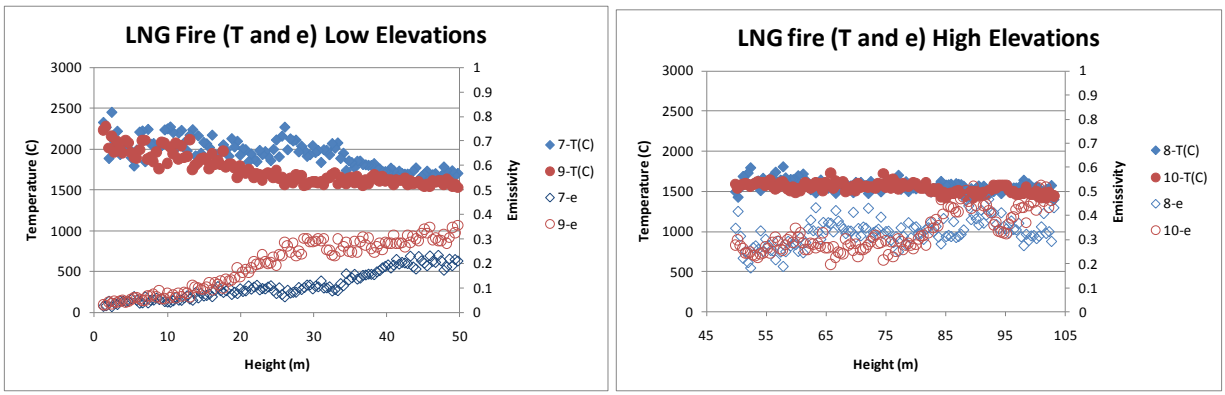

Figure 242 Estimate of temperature and emissivity vs. height (m) from LNG Test 2 spectra.

At low heights the calculated fire temperatures are highest (~2000°C) and the emissivity is lowest (~0.1). With increasing height, the temperature decreases and the emissivity increases. From a height of about 40 m to the top of the measurement region (~100 m) the temperature and emissivity are approximately constant. Table 55 provides average and standard deviation of the spectrometer-derived temperature and emissivity at the 4 scan times. The data in scans 7 and 9 for heights less than 40.2 m is not included in the averages, as discussed below. The overall average temperature and emissivity is 1600°C and 0.29, respectively.

Table 55 Spectrometer-derived average temperature and emissivity in LNG Test 2.

		Temperature (C)		**Emissivity**	
Scan # (time)	Height Range (m)	average	st.dev.	average	st.dev.
7 (242.7s)	40.2 - 49.8	1702	45	0.20	0.02
8 (258.3 s)	49.8 - 103.1	1566	69	0.33	0.05
9 (273.7 s)	40.2 - 49.8	1589	32	0.31	0.02
10 (288.4 s)	49.8 - 103.1	1542	61	0.33	0.09
	overall	**1600**	**71**	**0.29**	**0.06**

Figure 242 shows unrealistic calculated temperatures and emissivities near the base of the fire. The spectra, shown in Figure 236, look quite different below 30 m; this difference causes issues with the automated fitting process. Figure 243 shows a plot of the automated fits for a low and high elevation. The black dotted line was produced by assuming a blackbody temperature using the wavelength at the peak intensity (Weins formula states the wavelength at peak intensity = 2898 / source temperature in K). This yielded a fit that visually appears better than the automated one (blue line), resulting in a temperature of ~1850K and a corresponding emissivity of 0.08.

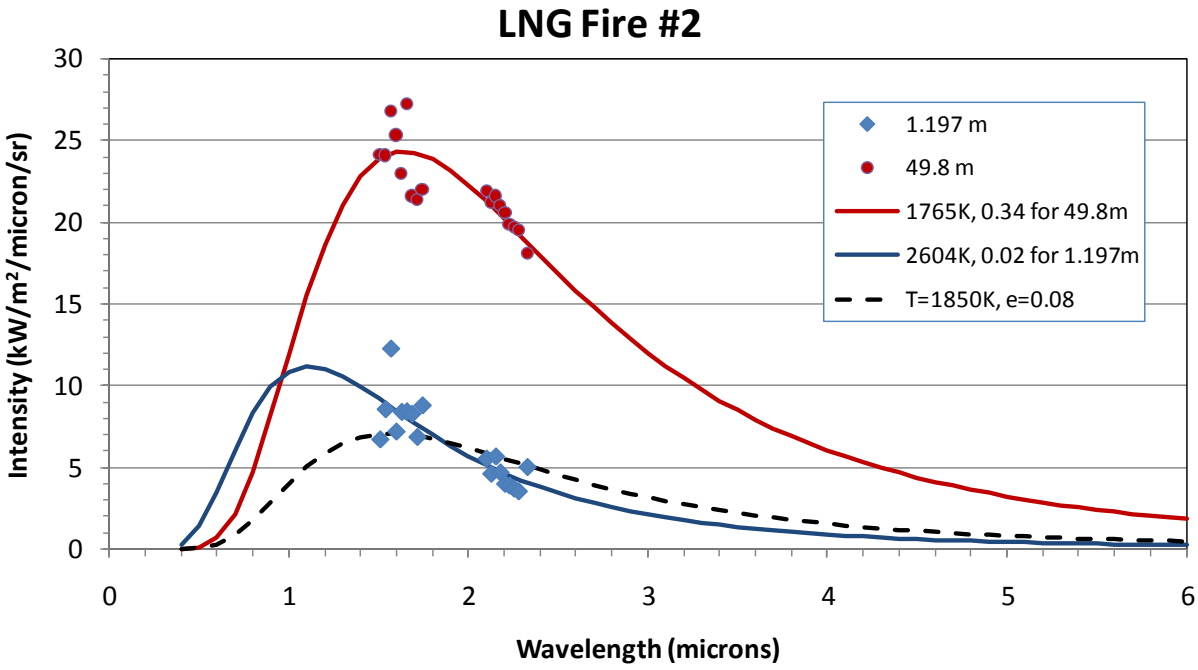

Figure 243 Automated fits for two elevations in LNG Test 2.

It was mentioned earlier that a white cloud formed on the water and surrounding ground. It appears that heat flux from the fire vaporizes water below. The vapor then encounters the cold LNG or hydrates which cause it to condense and form a white cloud near the base of the fire, obscuring part of the spectrometer field-of-view shown in Figure 244. The white cloud was very prominent during LNG Test 2. Such a white cloud will scatter rather than absorb radiation and indeed block the flame radiation coming from the base of the fire. The scattering is much greater for radiation having smaller wavelengths - that is why it appears white. This scattering explains reduced radiation coming from the base of the larger second fire test. In addition, this likely compromises the temperature/emissivity fits for data near the base of the fire, based on the reduced intensity from scattering and absorption.

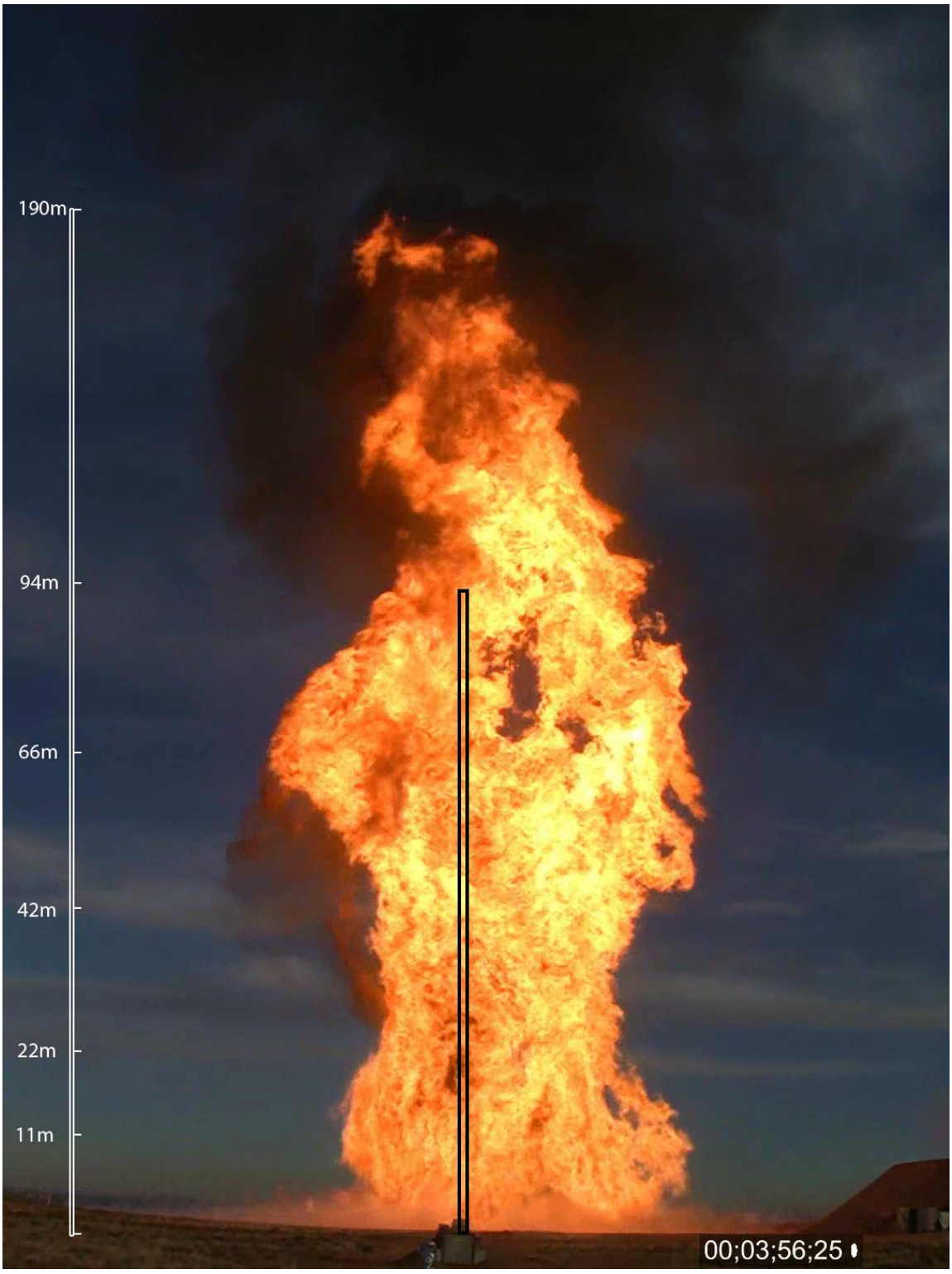

Figure 244 LNG Test 2 at ~236 s with spectrometer field-of-view overlay.

Assessment of attenuation/losses

Some insight into the acquired data can be obtained by analyzing the measured spectra and the idealized spectra obtained from the temperature and emissivity fit. These data can be used to assess how much of the total energy from the fire is attenuated by atmospheric absorption. Lastly, the idealized spectra can be used to gain insight into the comparison of the radiometer-derived surface emissive power with the surface emissive power calculated from the spectra.

As shown in Figure 245, the temperature and emissivity fit (T=1424 C, ε=0.42 as the smooth green line) for the spectrum at 50.22 m (symbols, scan8) was then multiplied by the transmission calculated from MODTRAN (gray line) for the experiment. The agreement between the fit and the actual measured emission when atmospheric losses are imposed is demonstrated. As seen, there is some difference in the values at longer wavelengths, but the fit can likely be used for assessing the amount of thermal radiation attenuated by the atmosphere.

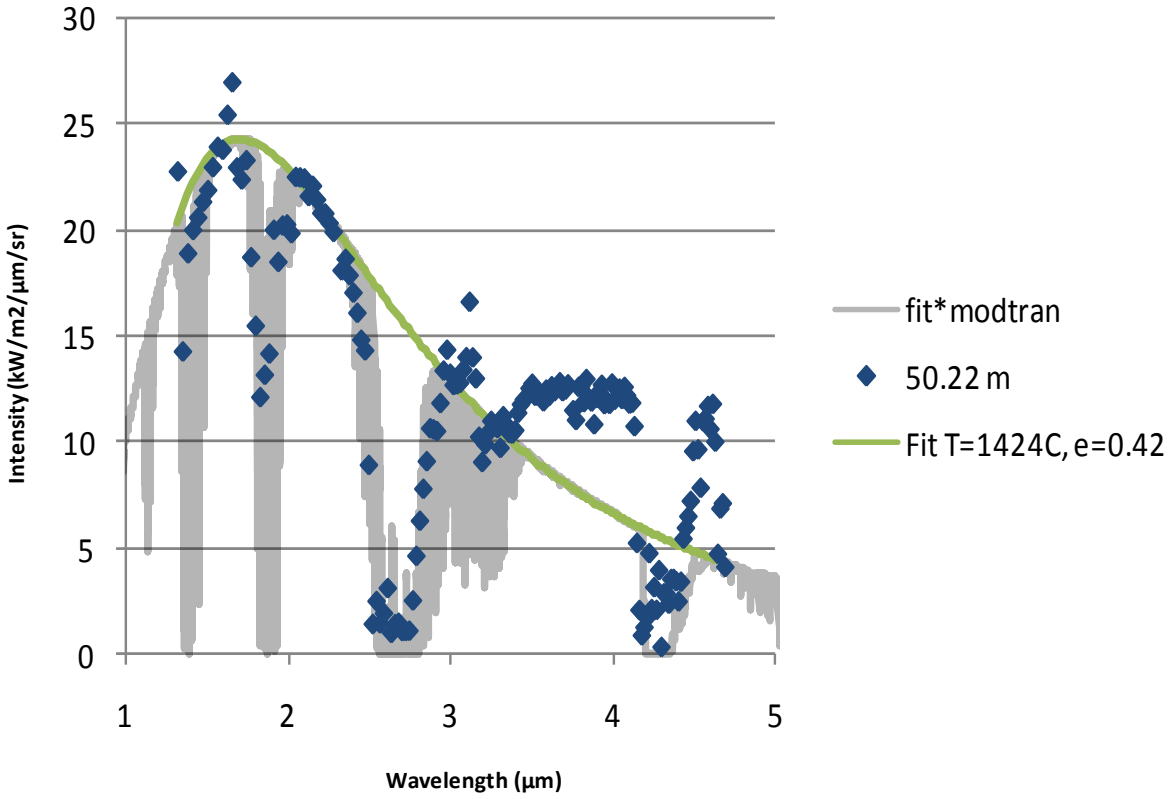

Figure 245 Comparison of the scan 8 measurement and two fits.

To assess the amount of radiation attenuated by the atmosphere in the spectrometer wavelength range of interest, a comparison of the integrated fit to the integrated fit accounting for atmospheric losses was made. To illustrate, Figure 246 shows the fit and the fit accounting for losses together. These curves were integrated to determine the fraction of energy that is lost due to atmospheric absorption to assess the empirical correlation used to correct the heat flux measurements for atmospheric absorption. A total loss of intensity of 22% over the spectrometer wavelength range was calculated. This evaluation was also performed over the entire wavelength range (0-15 µm) and the atmospheric attenuation was 22% as well.

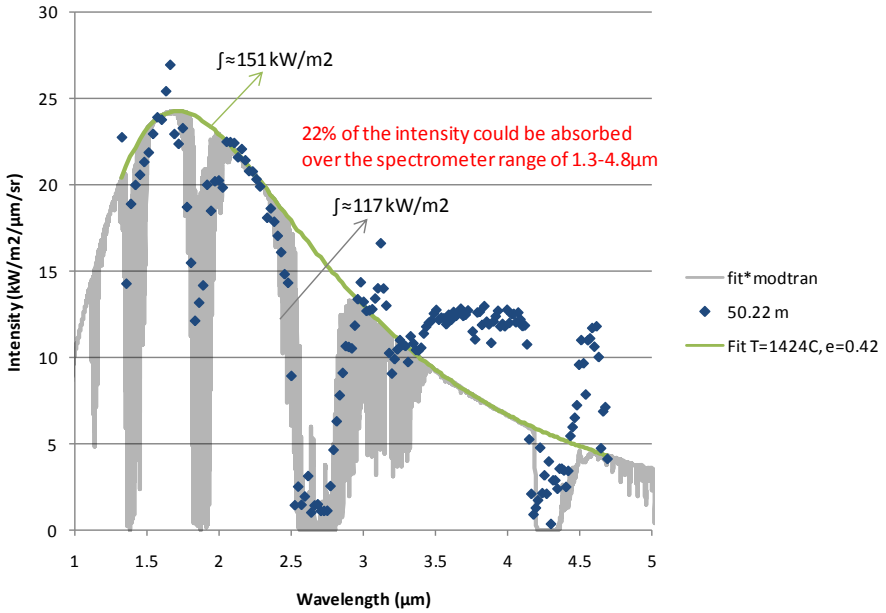

Figure 246 Assessment of the atmospheric attenuation in LNG Test 2.

Next, the idealized spectrum was used to gain insight into the spectral emission from the fire and how it might impact the comparison of surface emissive power calculated from the spectrometer measurements and obtained from the heat flux gauges. The idealized spectrum was integrated over the entire wavelength range and was then compared to spectrum integrated over just spectrometer range. Figure 247 displays the theoretical spectrum from the fit and that spectrum accounting for atmospheric attenuation. When the curves are integrated over the entire wavelength range (0-15 µm), it is determined that the approximately 22% of the emission is outside the spectrometer wavelength range. This suggests that the spectrometer surface emissive power values should be corrected by 22% before making comparisons with the narrow-angle heat flux gauges.

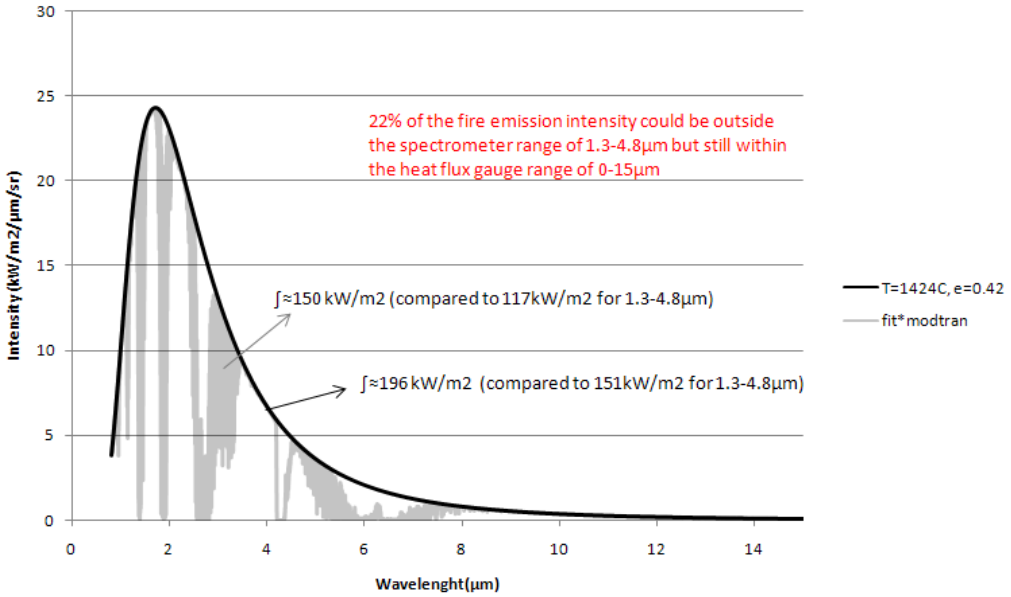

Figure 247 Assessment of the fire emission in LNG Test 2.

Comparison of Surface Emissive Power

As described in the sections above, the surface emissive power values calculated from the acquired spectra need to be corrected for losses due to atmospheric transmission (22%) and the limited spectral range (22%) to allow valid comparisons with the radiometer measurements. Figure 248 displays the comparison of the surface emissive power derived from the spectrometer and radiometer measurements (symbols slightly shifted from their nominal heights for easier viewing). A multiplier of 1.64 [(1/1-.22) x (1/1-0.22)] was used to correct the spectrometer data.

The agreement in the SEPs from both diagnostics is acceptable. Error bars on the radiometer measurements are an indication of the temporal variability of the heat fluxes measured by the radiometers. The data points represent a three second average of the high speed data and the error bars are one standard deviation. The extent of the error bars increases with height due to the fluctuations of the fire. These increased fluctuations are also evident in the spectrometer data above 50 m as the puffing of the fire is more pronounced at these higher elevations.

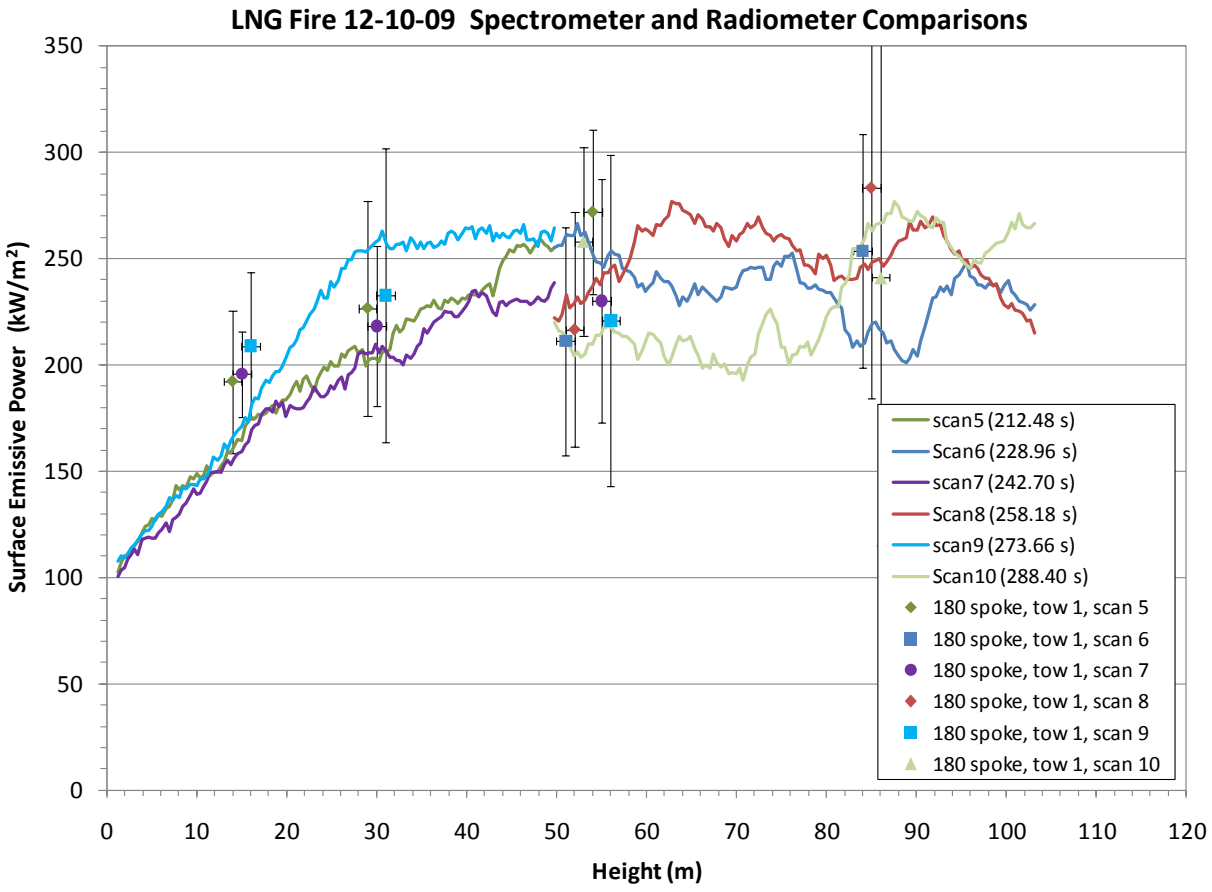

Figure 248 LNG Test 2 SEPs derived from spectrometer and radiometer measurements.

SEPs are low near the ground level, with approximate values of 100 kW/m^2. The SEP then increased steadily from 0 to 40 m and reached peak values approaching 275 kW/m^2. Note that the spectrometer was not able to scan past the top of the flame zone; thus, the SEP values do not begin to decline at some height.

7.17 LNG Spectra - Long Range, High Resolution

At the start of the test, just before the LNG was released, a flash bulb was illuminated on a pole just above the diffuser in the center of the pond. This flash proved a time stamp indication to align all of the instruments to a known time. The flash bulb was captured by the VNIR camera as shown in Figure 249. There is also a red circle in the VNIR image that has been superimposed to indicate the size and location of the FTIR FOV within the visible image.

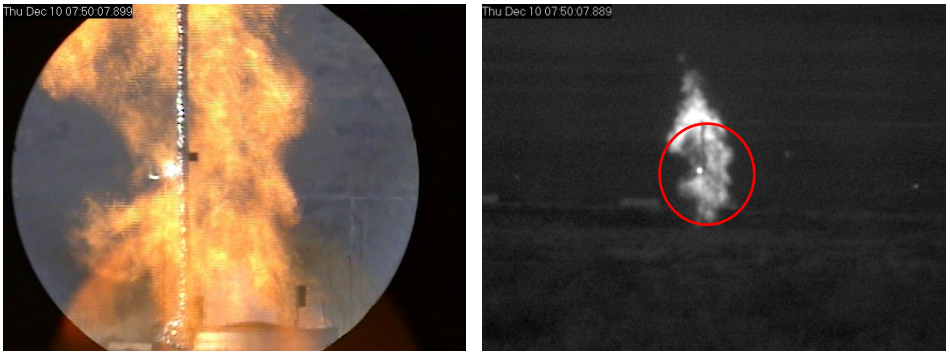

Figure 249 FTIR image of fiducial flash and VNIR bore sight view in LNG Test 2.

The exact time of the first flash was 7:50:07.8 AM. The propane burners were ignited 30.6 seconds prior to that at 7:49:37.2 AM. There was a small flame caused by the leaking of methane gas out of the diffuser that was ignited when the propane burners were lit. For analysis purposes, the ignition time of the burners was considered to be time zero. Figure 250 shows how the LNG pool fire visually looked from the location of the data acquisition trailer. The still image was taken with a standard digital camera.

Figure 250 LNG Test 2 fire view from the FTIR data acquisition trailer.

Hyperspectral Measurements

The hyperspectral data collected during the second LNG pool fire with the FTIR was spectrally sampled at 1 wave number. The spectral radiance at six different times throughout the LNG fire can be seen in Figure 251. The radiance measurements were averaged over approximately 0.25 seconds and were not corrected for the losses of the narrow telescope (~26%).

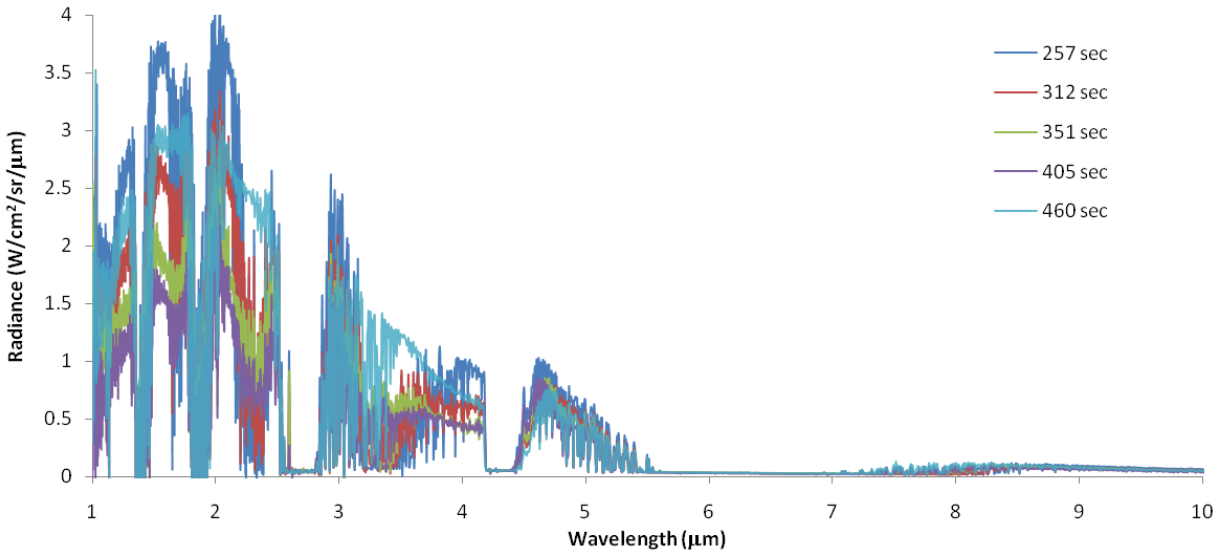

Figure 251 LNG Test 2 fire spectral radiance at selected times.

Signature Modeling (also see discussion in Section 5.14)

In order to predict the apparent radiance reaching the aperture of the FTIR, the source radiance has to propagate through the atmosphere. The same meteorological conditions that were previously mentioned were used as input parameters to MODTRAN in order to estimate the path transmission at the range of the FTIR.

Altitude: 1627 m
Horizontal Path: 1160 m
Ambient Temp: -4 C
Relative Humidity: 60%
Wind Speed: 1.5 m/s
Pressure: 12.19 psia (24.82 inHg)

The simulated path transmission for the test conditions can be seen in Figure 252. During the modeling effort it was noticed that there were spectral absorption features in the apparent radiance that were representative of methane gas. It is assumed that a small shell of methane gas, that had not yet ignited, existed around the fire causing additional radiometric absorption. The absorption features of methane can be seen in Figure 252, with the transmission of methane over an assumed 1 meter path for both a 1.6% and a 6.4% concentration.

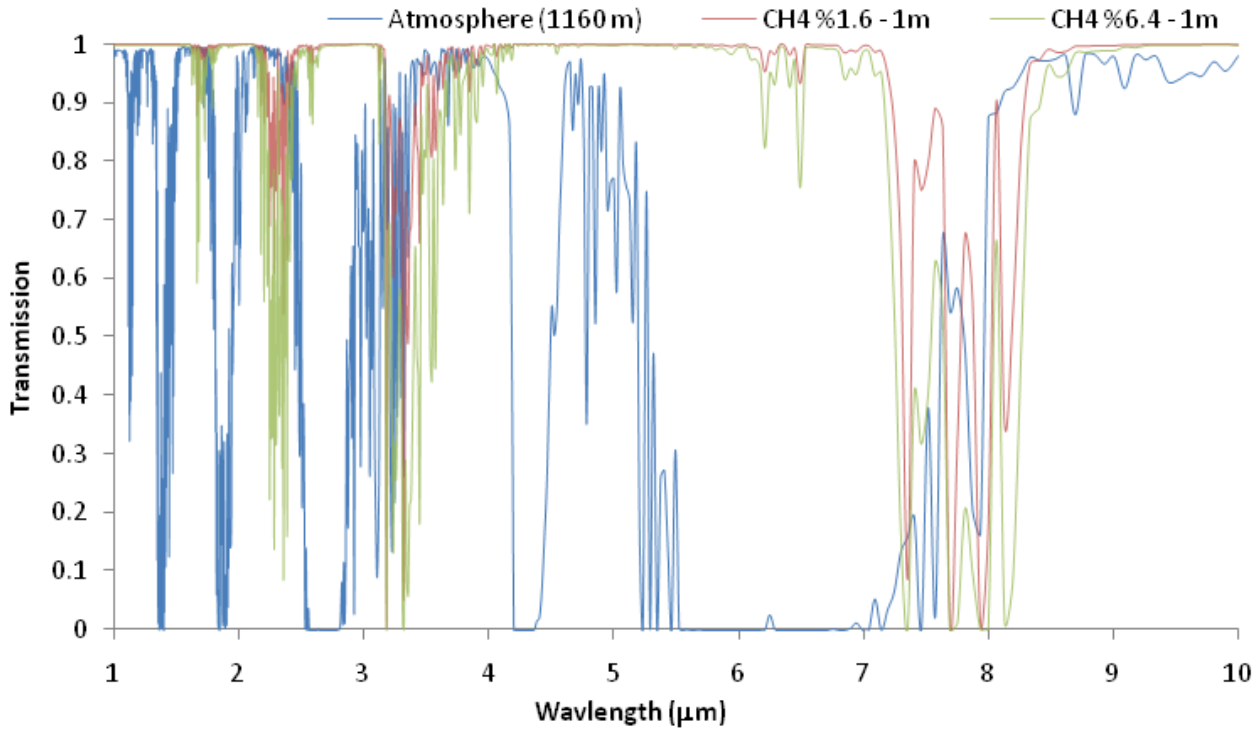

Figure 252 MODTRAN predicted path transmission for LNG Test 2.

The FLAMES code was again used to predict the source radiance for the second test. The output of the FLAMES code was again reduced by the predicted path radiance.

To more closely approximate the spectral signature, a two temperature linear mixing model was used to combine two separate FLAMES simulations. This allows for the simultaneous simulation of a hotter cleaner burning portion of the flame along with a cooler more soot filled portion.

Five different times were chosen during the second test to evaluate the flame properties from the spectral FTIR data. The results for the 5 different selected times can be seen below in Figure 253 through Figure 258. The height of the bore sight ranged from 10 m to 20 m above the pool surface, as shown in Figure 259.

For each time three images are shown, the left is the FTIR FOV, the center is the visible imager, and the right is the thermal imager (the halo in the FTIR image is caused by the beam splitter backside reflection). The spectral comparison of the FTIR measurements along with the simulated (modeled) data can be seen below the images. The curve labeled B is the data from the InSb detector and the curve labeled A is the data from the MCT detector. The table indicates the input parameters that were used for the modeled data. The length listed in each table is the depth of flame (10 m) assumed by the FLAMES code. The "Soot" in each figure (used to estimate the emissivity) is specified in optical density (OD) at wavelength of 2.5 um. Because the spectrometer was scanned up and down the flame, the location of the spectral measurement is indicated by a red circle in the visible image and a black circle in the thermal image.

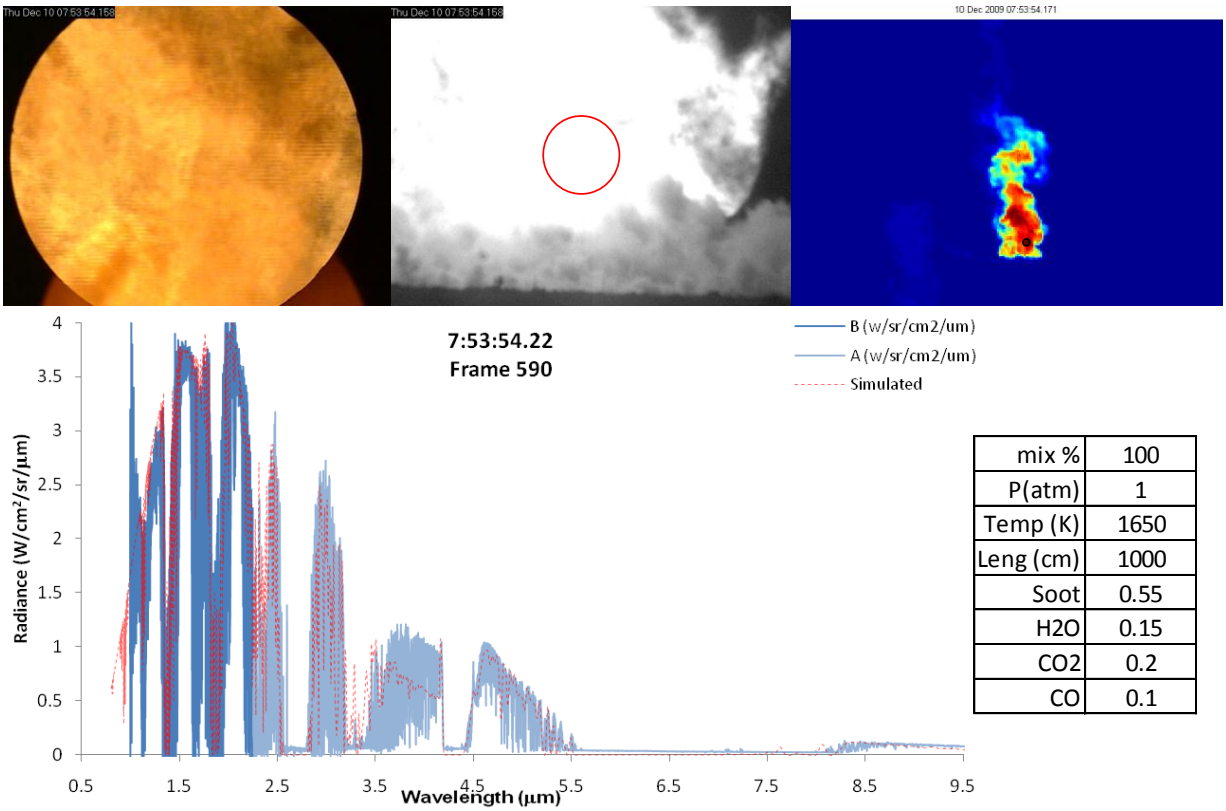

Figure 253 LNG Test 2 fire spectral analysis at 257 s.

In order to get the modeled radiance to fit the measured data better, a short path of CH4 was modeled to account for some absorption that was observed but otherwise unaccounted for. A much better fit of the data is determined (Figure 254, focusing on the 2.25-3.55 micron range shown in Figure 253) when assuming a 1 meter path of 6.4% methane just outside of the flame.

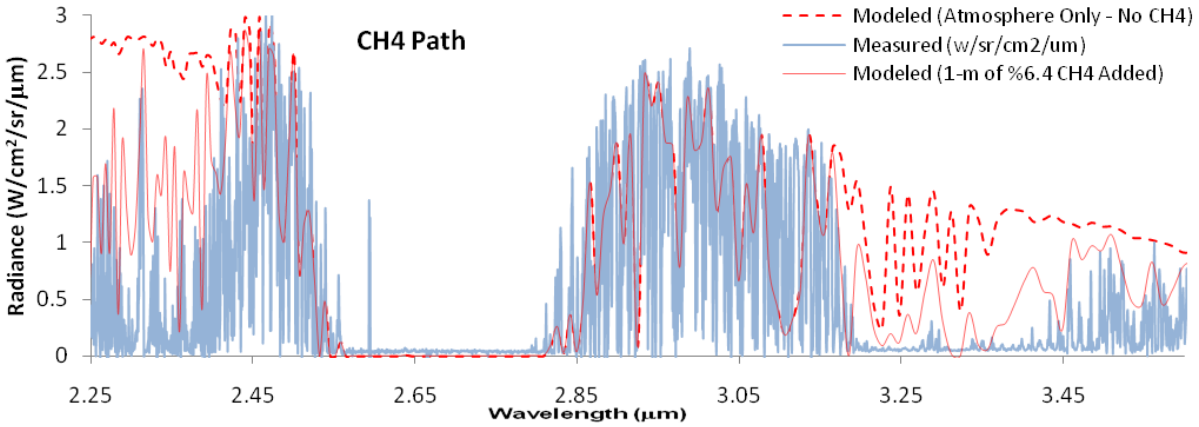

Figure 254 CH4 gas absorption contribution in LNG Test 2.

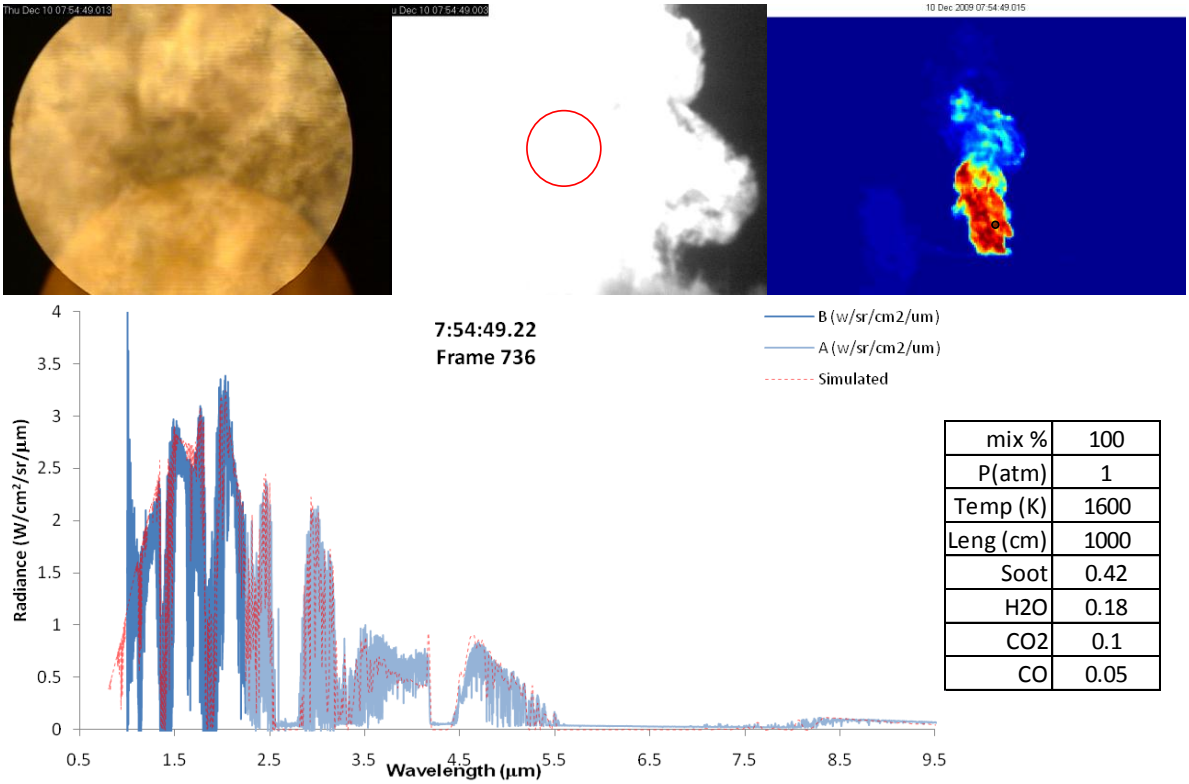

Figure 255 LNG Test 2 fire spectral analysis at 312 s.

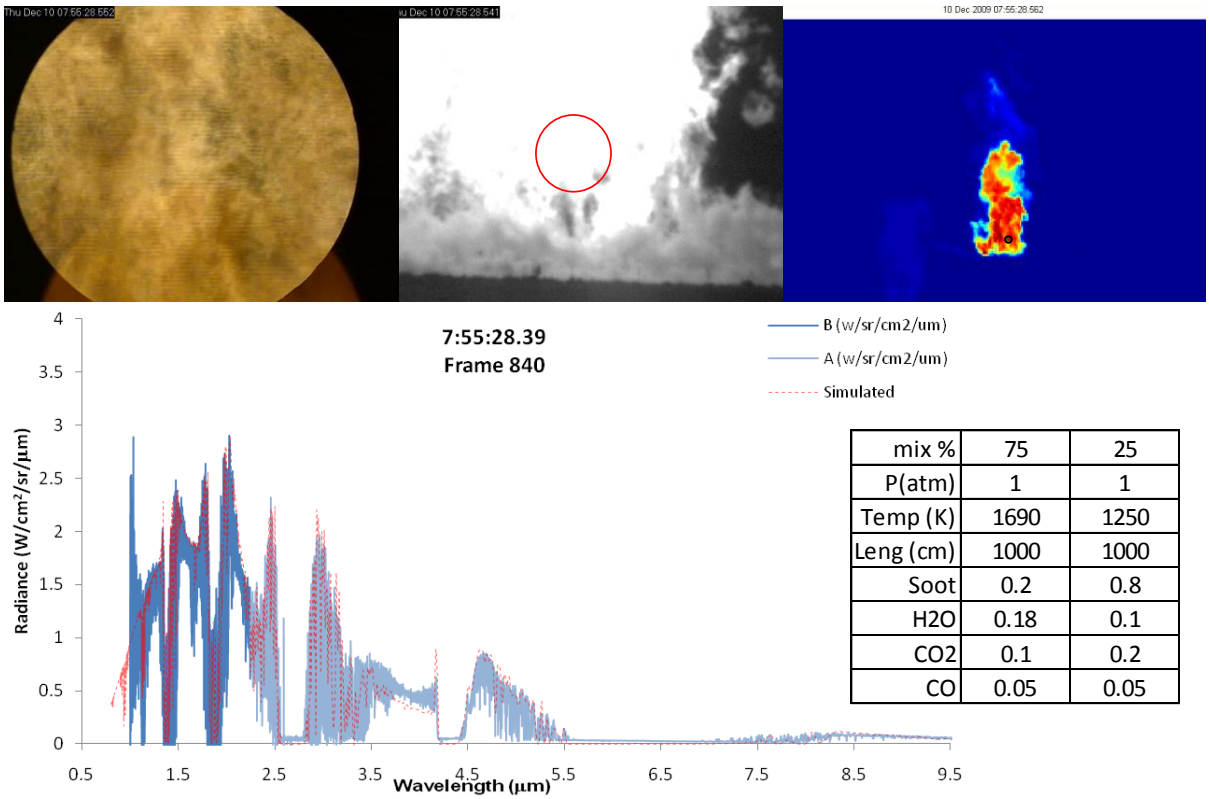

mix %	75	25
P(atm)	1	1
Temp (K)	1690	1250
Leng (cm)	1000	1000
Soot	0.2	0.8
H2O	0.18	0.1
CO2	0.1	0.2
CO	0.05	0.05

Figure 256 LNG Test 2 fire spectral analysis at 351 s.

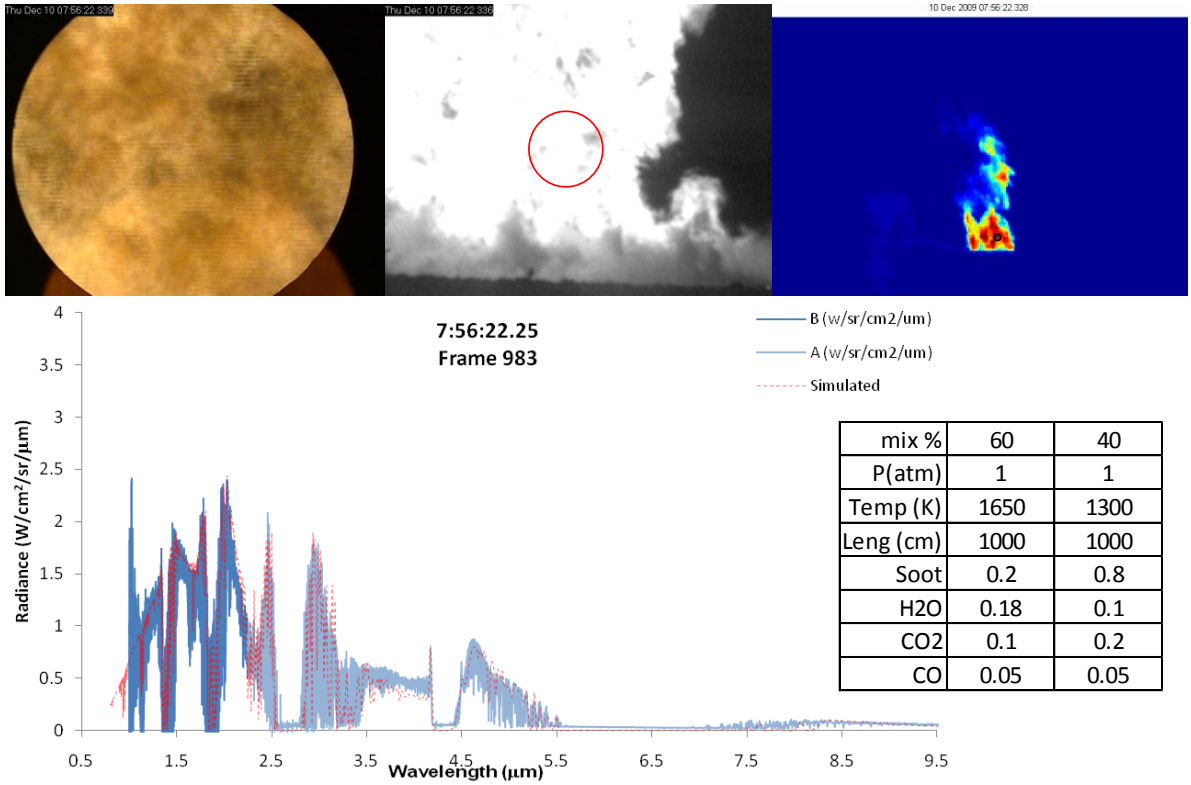

mix %	60	40
P(atm)	1	1
Temp (K)	1650	1300
Leng (cm)	1000	1000
Soot	0.2	0.8
H2O	0.18	0.1
CO2	0.1	0.2
CO	0.05	0.05

Figure 257 LNG Test 2 fire spectral analysis at 405 s.

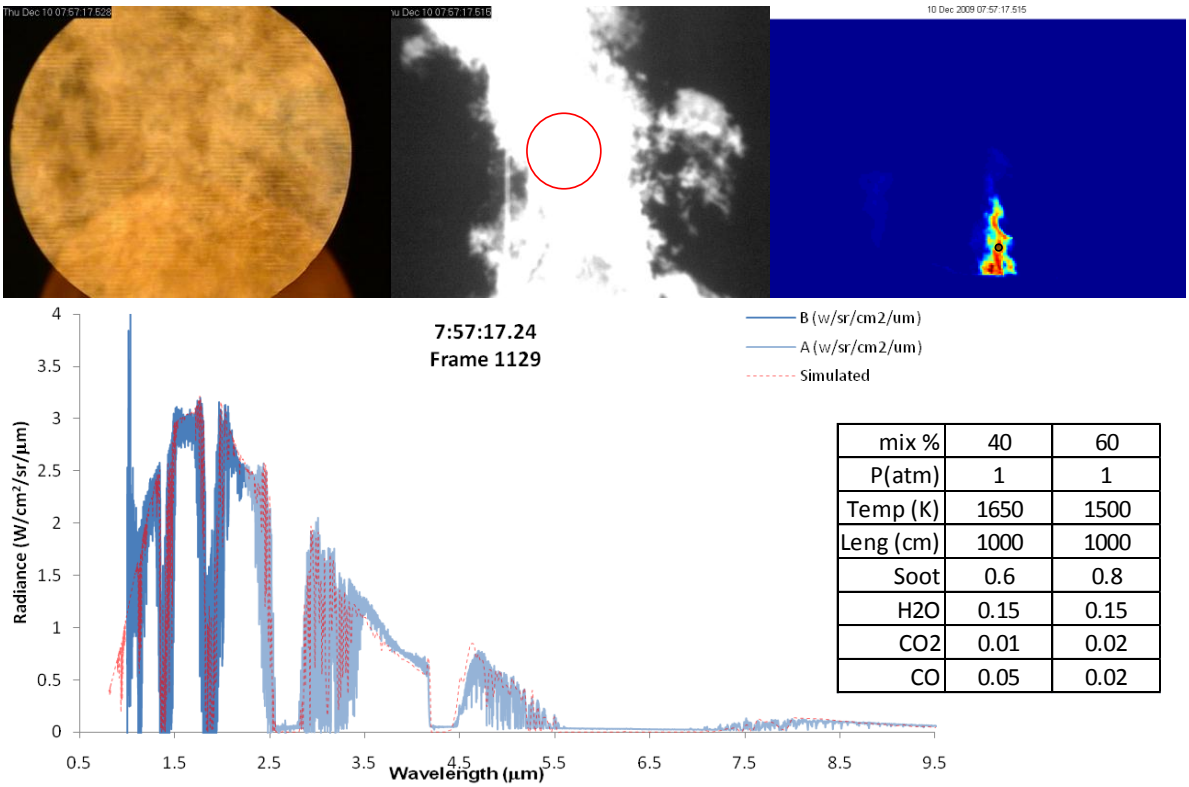

Figure 258 LNG Test 2 fire spectral analysis at 460 s.

The average source temperature and emissivity (based on mixture fractions) as derived from fitting the FLAMES model to the data is given in Figure 259 for the selected times and bore sight heights above the pool. The average CH4% is the percent methane assumed in the 1 meter path just outside of the flame, chosen to achieve the best fit. The emissivity is calculated with Eq. (62) using the soot optical density (OD),

$$\varepsilon = 1 - e^{-OD} \tag{62}$$

Time (s)	Average Temperature (C)	Average Emissivity	Average CH4 (%)	Boresight Height (m)
257	1377	0.42	6.40	10
312	1327	0.34	6.40	15
351	1307	0.30	3.20	10
405	1237	0.36	6.40	10
460	1287	0.51	0.00	20
average	1307	0.386	4.48	13

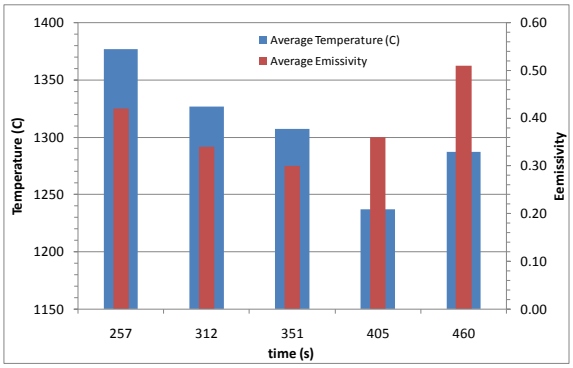

Figure 259 LNG Test 2 derived temperature, emissivity, and CH4 path concentration.

7.18 LNG Test 2 – End of Spill

An interesting phenomenon occurred near the end of the spill. The flames slowly moved into the North and East regions of the spill as shown in Figure 260. After the flames died out, a fairly thick whitish layer of what is believed to be a combination of ice and methane hydrates covered most of the water where fire was not seen on top of the spreading LNG pool for the majority of the test. The ice/hydrate layer remained on the water pool for many hours after the test.

Figure 260 Phenomena at end of LNG Test 2.

7.19 LNG Test 2 - Post-test Operations

The purpose of the post-test operations is to reduce the concentration on methane (CH_4) gas in both the reservoir and the discharge pipes (while minimizing air infiltration) until the concentration of methane is below flammability limits for any amount of air ingress. The addition of the liquid nitrogen (LN_2) cooling spray ring allowed a quite different approach as to what was used after Test 1. The basic approach was to spray LN_2 (-196°C) into the reservoir and monitor gas concentrations. In theory, the relatively hot walls (-160°C) vaporizes the LN_2; this cold gas essentially performs a very slow "plug" lift of the warmer methane gas and, as the bottom of the reservoir fills with nitrogen gas, the methane gas is pushed out of the partially open roof vents.

At the end of the drain the reservoir was placed in a static condition. All LNG discharge valves were closed (but not sealed as the membranes/gaskets were intentionally broken during the lift). The dome vent dampers were closed, the mixing fans were turned on to ensure the reservoir was fully-mixed and non-flammable (fuel-rich) and then turned off (note that there was air ingress during the reservoir drain). Both sample points in the reservoir (HIGH above the suspended ceiling and LOW below) indicated 0% O_2 and 100% CH_4 after mixing. All LNG discharge pipes were continuously purged with nitrogen from the onsite LN_2 bulk storage trailer with integral vaporizer.

For the next five hours, a small fire was anchored to the diffuser as the methane was pushed out of the three LNG discharge pipes by the nitrogen purge ($3ft^3$/min/pipe).

A LN_2 trailer (containing 6444 gallons) was connected to the LNG fill line and commenced filling the well at 1:14PM. When filling the well, increased flames were initially seen due to the higher nitrogen flow rate (caused by leakage at the plug/flange interfaces), then the flames went out and a decreasing heat signature was observed. LN_2 sprays commenced after the well was filled. Reservoir vents were opened periodically to limit the reservoir differential pressure (DP) below ~1 inch water column (w.c.).

At ~2:30PM, methane started to decrease below 100% indicated concentration at the LOW measurement point. At ~3:30PM, methane started to decrease below 100% at the HIGH measurement point (note there is only one instrument, a sampling system is used to select the individual sample lines). LN_2 spray continued until the LOW side measured 13.4% CH_4 and the HIGH side measured 15.4% CH_4 (both sides measured 0% O_2.) At ~6:02PM, LN_2 spray operations were stopped, the vents and the LNG discharge valves were fully opened, and the remaining LN_2 in the well flowed through the pipes and onto the water pool. Figure 261 and Figure 262 provide the post-test reservoir gas and wall temperatures, respectively. Figure 263 provides the oxygen and methane measurements in addition to showing the liquid level in the reservoir well and the reservoir DP.

It took ~5 hours to place the reservoir in a safe condition. Less than one trailer of liquid nitrogen (~600,000 ft^3 total) was required to purge the reservoir (100,000 ft^3) that was essentially filled with 100% methane gas at the end of the drain.

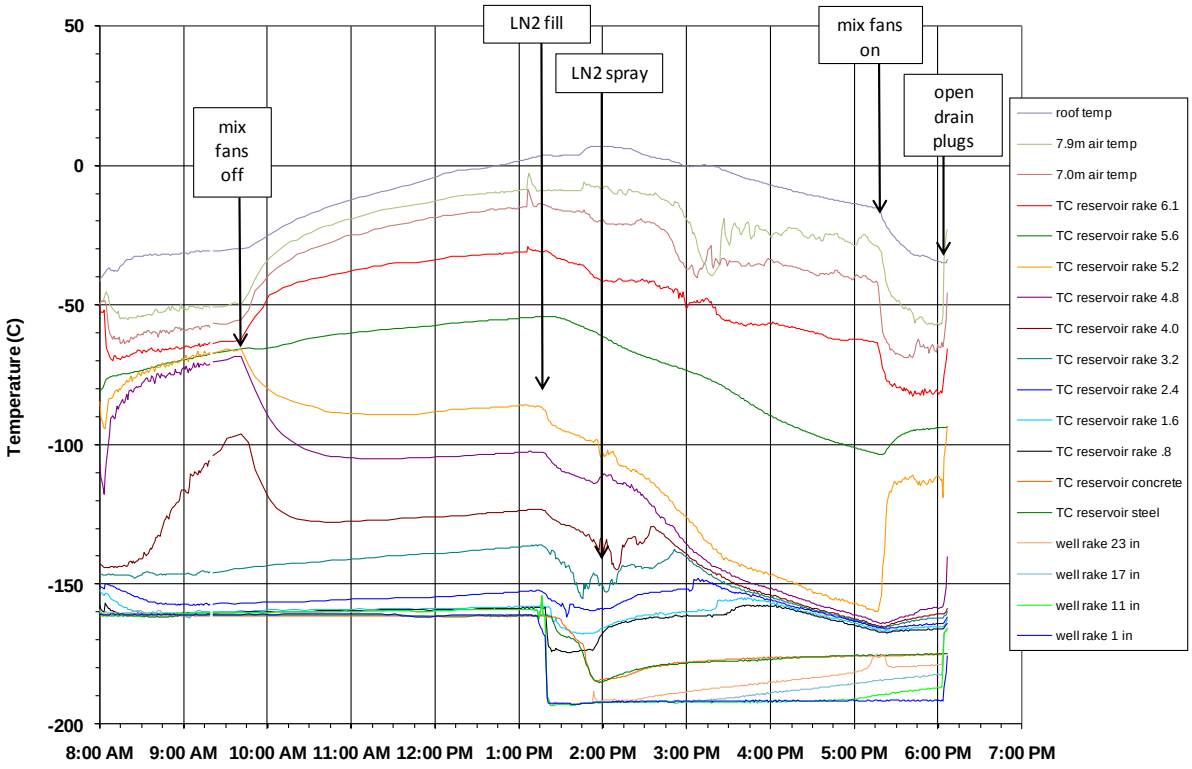

Figure 261 Post-test reservoir gas temperatures in LNG Test 2.

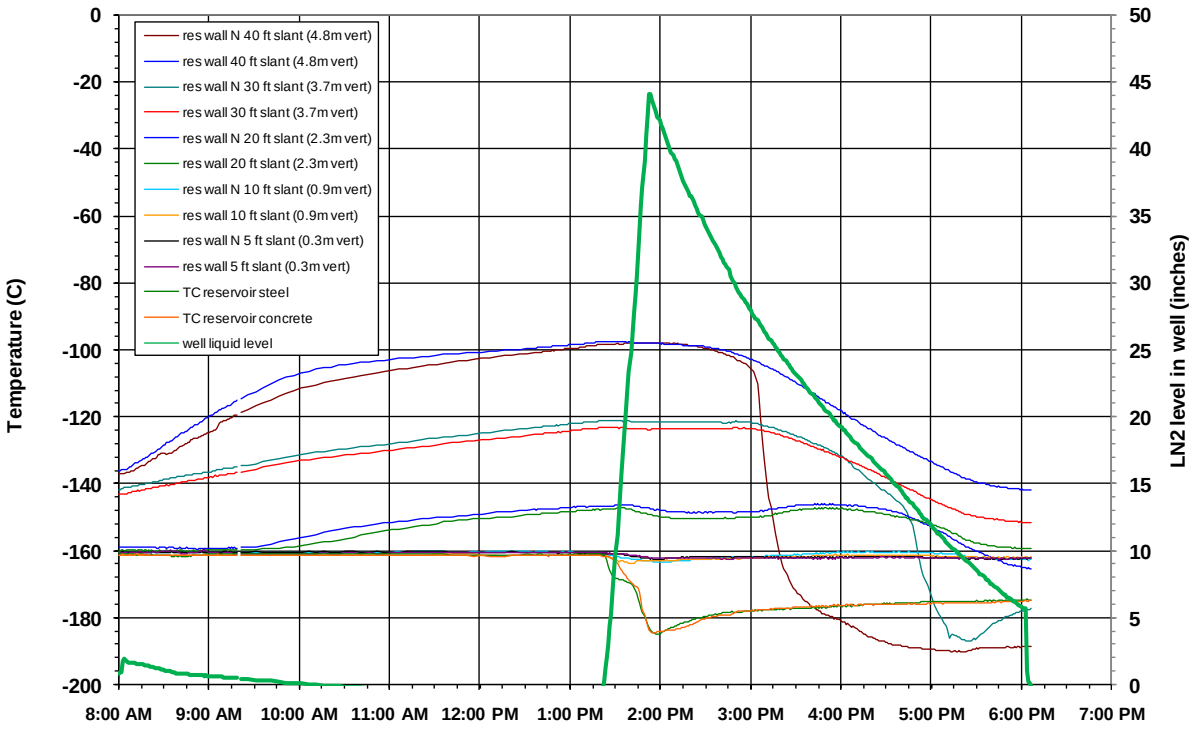

Figure 262 Post-test reservoir wall temperatures in LNG Test 2.

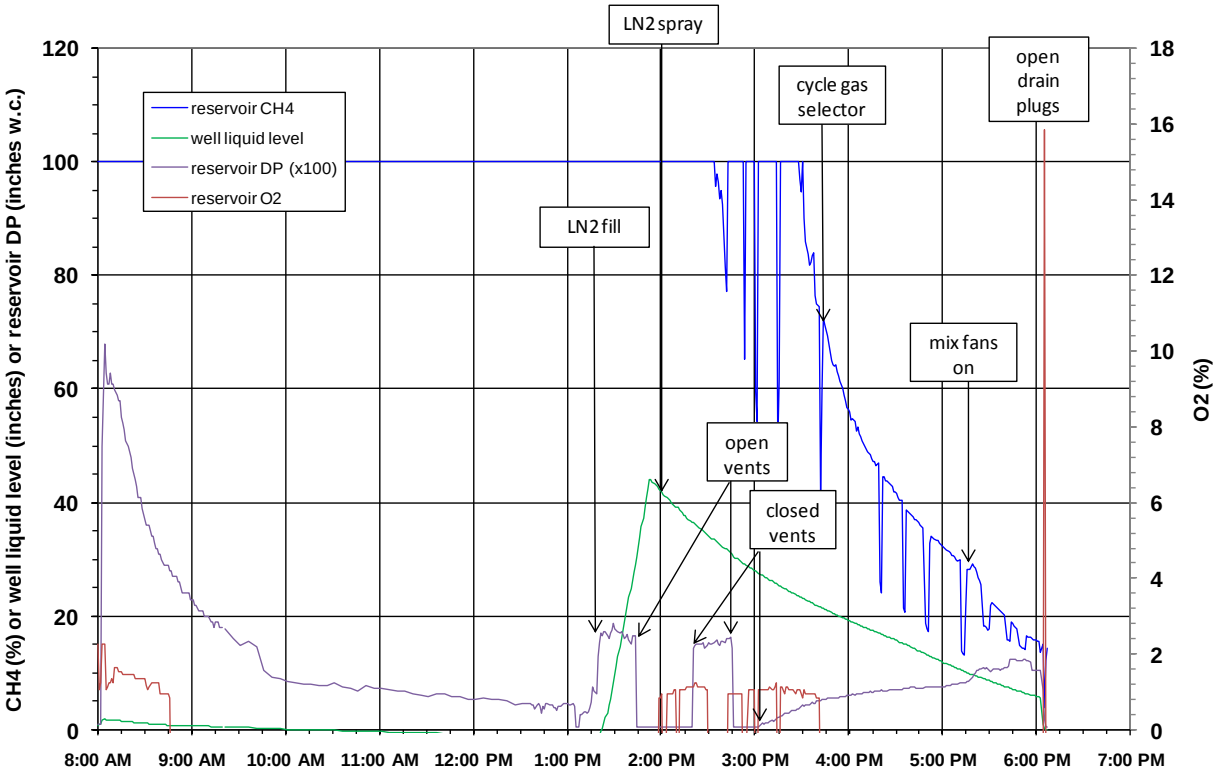

Figure 263 LNG Test 2 post-test reservoir gas, liquid level, and DP measurements.

A confined space entry into the reservoir was performed the following week. Figure 264 and Figure 265 show a layer of ice on all subzero temperature surfaces. With the discharge pipes and roof vents open, a steady supply of water vapor allowed a continuous buildup of ice.

Figure 264 Inside reservoir showing dropped ceiling panels after LNG Test 2.

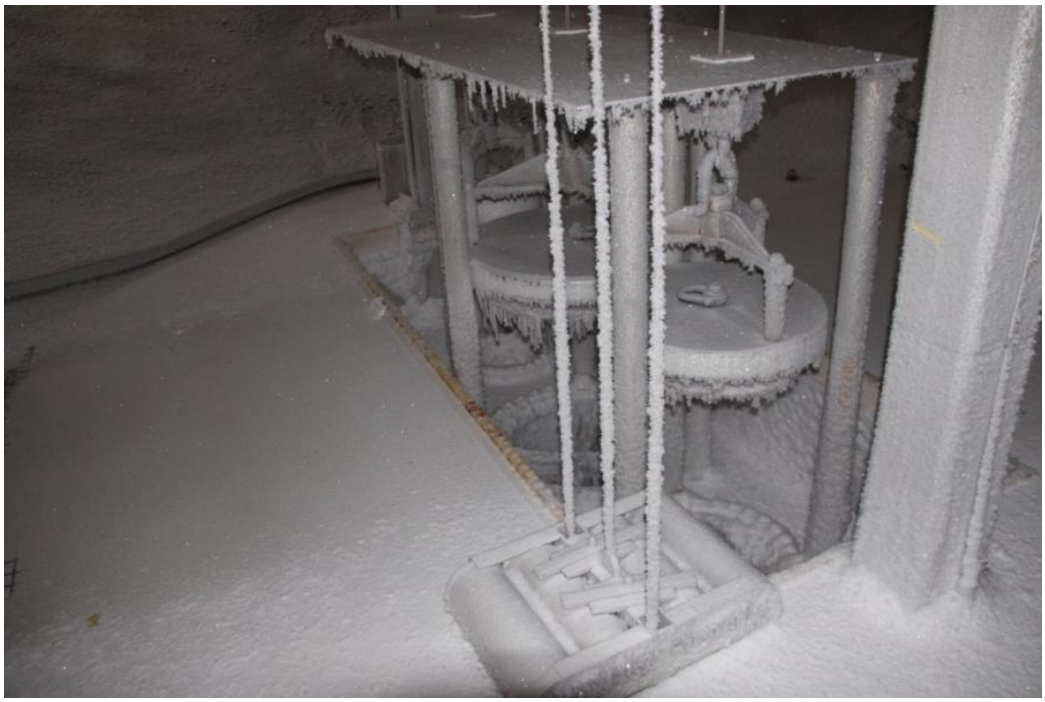

Figure 265 Inside reservoir showing intact ice dam at well after LNG Test 2.

Inspection of the ice dam showed a solid, robust sheet of ice firmly attached to the floor and well dam. Very fine glazing cracks were embedded in the sheet. It appears that the ice dam and new plugs seal were intact and functioned as intended. It is now suspected that the cause of the high loss rate during filling was due to cracks in the polyurethane foam insulation that were formed during the course of three thermal cycling events to cryogenic temperatures. These cracks likely extended over a large area on the reservoir inside surface and allowed the LNG to directly contact the compacted dirt, yielding high heat flux and increased boil-off.

If this is indeed the cause (that can be confirmed by removing some of the shotcrete and inspecting the foam), industry sources (SIGTTO) have suggested that an internal liner composed of Triplex (certified to stop LNG leaks and used as the secondary barrier in membrane-type GTT MK III design LNG tankers) laid on top of the shotcrete would fix the problem.

7.20 LNG Test 2 Summary

With the exception of high boil-off, all test operations, including the reservoir cool down, the fuel loading, the test conduct, and the post-test safing of the reservoir, were very successful. Measured reservoir flow rates during discharge were close to two-phase flow predicted values. Test conditions were ideal, and validation data was obtained for the surface emissive power and the flame plume view factor goals (H/D). Due to the limited amount of fuel, a steady-state LNG pool area was not achieved while discharging LNG; therefore, a mass loss rate could not be calculated.

About 198.5 m^3 (52,500 gallons) were discharged in ~144 s through the three discharge pipes.

The measured average flow rate during the partial open period (83 s to 123 s) was 0.16 ± 0.14 m^3/s (2550 ± 2260 gpm). At the start of the fully open period the flow rate increased to about 3.78 m^3/s (60000 gpm) for a short interval (~10-15s).

The average flow rate during the fully opening period (130 s to 220 s) was 1.91 ± 0.84 m^3/s (30300 ± 13350 gpm). During the fully open period, the average mass discharge rate was ~802 kg/s, based on a methane density of 420 kg/m^3.

The spreading LNG pool area continuously increased during the discharge interval, reaching an equivalent circular diameter of ~83 m at the end of the spill. The fire did not attach to the leading edge of the spill; hence the effective fire diameter was smaller than the spreading LNG pool diameter. The flame did appear to be attached (anchored) to the diffuser and the discharge pipe berm.

The average wind speed was 1.6±0.2 m/s at 324±9 degrees (magnetic north). There was very little flame tilt; however, the wind did appear to drag the plume toward the south. During the steady-state duration (250-300 s) used to determine average test values, the average flame width at 15 m above the pool was 56.1±12.1 m and the average flame height was 146.2±7.8 m.

Equation 1, a mass loss rate of 0.147 kg/m^{2}s, a reacting flame diameter, and appropriate atmospheric conditions were used to determine a Q* value of 0.85 and an estimated H/D ratio of 2.9. The reacting diameter was assumed to be the measured flame width (W) of 56.1 m (at 15 m above the pool), yielding a burn rate of 363 kg/s. The measured height (H) of 146.2 m yielded a measured H/W ratio of 2.6.

The average of all narrow view (spot) radiometers on the North and South spokes with field-of-view fractions greater than 0.94 yielded a spot-average steady-state (between 250-300 s) surface emissive power of 282±101 kW/m^2. The average flame surface emissive power (SEP), determined by correlating view factor information from video analysis with the wide-angle radiometer data, yielded an average overall flame SEP of 286±20 kW/m^2.

A smoke mantle was not evident. There were a few instances when small amounts of smoke were seen during the production of large scale vortices that "rolled up" from the base of the flame when the fire exhibited a puffing behavior.

Surface emissive power derived from spectroscopy data correlated well with the radiometer derived data. Surface emissive power was lowest near the ground level, with approximate values of 100 kW/m^2. The surface emissive power then increased steadily as the spectrometer scanned from 0 to 40 m above the pool, and then the SEP was fairly constant until the spectrometer reached its maximum height of ~102 m, with measured peak values approaching 275 kW/m^2. The 2-temperature model of the spectra correlated extremely well to the measured spectra, yielding an average flame temperature of 1307ºC and emissivity of 0.39.

In LNG Test 2, a very prominent white cloud formed on the water and surrounding ground. It appears that heat flux from the fire vaporizes water below. The vapor then encounters the cold LNG or hydrates which cause it to condense and form a white cloud near the base of the fire. Such a white cloud will scatter rather than absorb radiation and indeed block the flame radiation coming from the base of the fire. The scattering is much greater for radiation having smaller wavelengths; that is why it appears white. This scattering explains the reduced radiation and the low inferred emissivity coming from the base of the fire.

8 Effect of Pressure on Radiation and Smoke Shielding

The data acquired in this work is expected to find application at coastal sites at sea level with a nominal ambient pressure of 14.7 psia. The tests were conducted in Albuquerque, NM with a nominal ambient pressure of 12.2 psia, which is approximately 17% lower than at sea-level. An important question is the potential differences between surface emissive power measurements made in Albuquerque and surface emissive power that would occur in a sea-level fire.

At the current time, there is no data known to the authors that directly correlate surface emissive power as a function of pressure for large, optically thick, fully turbulent fires relevant to the current study. Further, it is well known that soot plays a large role in thermal radiation from fires, and that soot formation and transport relative to high temperature flame sheets are still active areas of research. As a result, a definitive statement about the pressure dependence of surface emissive power cannot be made at this time. However, estimates can be made for models based on physics assumptions about the important phenomena.

Based on these estimates there is reason to believe that pressure does not significantly affect surface emissive power and the distance above the pool at which a 'smoke mantle' shield forms on the outer portion of the flame, that is, where smoke, or cooled soot, provides a reduction in the externally radiated heat flux. The physical basis for this assertion is as follows.

Thermal radiation that contributes to surface emissive power is generated in the high temperature flame sheets. Emission is proportional to the fourth power of temperature (or fifth power if temperature dependent properties are taken into account). Thus, the source of the radiation is in the high temperature flame sheets. Within the flames sheets there are two sources of emission, gas-band emission and soot emission. Flame temperatures are weakly dependent on pressure for pressures near ambient. Thus the gas emission will not change between Albuquerque and sea-level.

For large turbulent fires, in which there are many, many individual flame sheets, it can be idealized that the divergence of the radiant intensity goes to zero, i.e., the radiation vector becomes 'saturated' after passing through many flame sheets (that are the same for this idealization). In this case, the radiant intensity is proportional to the emission divided by the absorption. Both emission and absorption are proportional to soot concentration to the first power. Thus, in ratio, the radiant intensity is independent of soot concentration, although strongly dependent on the temperature of the soot. The soot temperature is related to the gas temperature, which as previously noted does not change significantly with pressure.

Data from laminar pool fires also suggests that pressure does not strongly affect soot production. Data obtains by McCrain and Roberts [Combustion and Flame 140 (2005) 60–69] suggests that for methane flames local peak values of soot volume fraction scales with pressure as $p^{1.2}$, however path-integrated soot volume fraction values indicated no pressure dependence at 65% of the flame height, and as $p^{0.6}$ at 85% of the flame height. This potentially indicates that pressure dependent scaling is not the correct scaling parameter for soot production due to obtaining

different powers at various locations of the flame. The scaling relation must be validated by comparing to pool fires that are in the fully turbulent regime since heat and mass transfer characteristics are very different than laminar flames. Thus, the scaling rule should be able to predict information about ‘large-scale’ turbulent fires from information obtained at ‘small-scale’ performed under elevated pressure. In order to validate the above mentioned scaling dependence such comparison is necessary.

Additionally, the magnitudes of the heat flux measured in this test series compared to earlier studies at sea-level strongly suggest that the surface emissive power in the unshielded part of the flame is independent of the pressure over the range between Albuquerque and sea-level.

Note that the smoke layer which acts as a radiation shield by absorbing the emission from the flaming regions of the fire before re-emitting it to the surroundings could possibly depend on pressure as indicated by McCrain and Roberts since the amount of energy absorbed in the smoke layer will be directly dependent on the soot concentration. However, as previously noted, pressure dependence has not been substantiated for optically-thick turbulent pool fires.

Thus, the aforementioned provides indications that surface emissive power in the unshielded parts of the flame for large LNG flames is independent of pressure. In other words, in the unshielded parts of the flame the surface emissive power of the test in Albuquerque would be identical to that had the test been run at sea-level.

9 Conclusions and Recommendations

The Government Accountability Office (GAO), in report GAO-07-316, recommended that the Secretary of Energy ensure the Department of Energy (DOE) incorporate key issues identified in their report into DOE's current LNG study, including large scale LNG fire testing. DOE tasked Sandia National Laboratories (SNL) to perform a set of experiments to improve the understanding of the physics and hazards of large LNG spills on water with concurrent fires.

The above described experiments and resulting data and analyses describing flame height, smoke production, and burn rate for large LNG spills due to accidental and other events fires met that goal. These large scale spreading LNG pool fire experimental datasets, combined with small scale gas burner experiments, will support pool fire model development and validation for extrapolation to a scale of a potential LNG spill of 200-400 m or larger in diameter to better represent the fire behavior of spills postulated from current and future LNG carriers.

Some highlights of the Sandia small-scale gas burner experiments and two large-scale spreading LNG pool fire experiments are listed below.

Small-scale Gas Burner Tests

The reduced-scale experiments, burning methane gas in the FLAME test cell at the Thermal Test Complex, measured flame height at various flow rates to provide data for flame height correlations in fully turbulent fires burning lightly sooting fuels. One of the deficiencies of historical data with gas burners is that due to the small size of burners used (< 1 m) the fires were not fully turbulent. Turbulence affects flame height and the Sandia tests utilized the largest gas burner to date (3 m diameter) such that the tests were fully in the turbulent regime. Four separate methane experiments yielded twenty two sets of flame height vs. fuel flow rate data.

A flame height correlation as a function of a dimensionless heat release rate (e.g., Q*) was developed to support recommendations on flame height for very large LNG pool fires (~1000 m diameter). The data collected show:

1. The correlation estimates the H/D for a 200-400 m diameter LNG fire to be approximately 1.5-1.1 (with decreasing H/D for increasing diameter).
2. These values are a similar to current flame height correlations for large spills.

Large-scale Pool Fire Tests

Two pool fire experiments were completed, obtaining fires from LNG spills with diameters of approximately 21 m and 83 m. Extensive sets of fire data were collected for each test. Numerous cameras, spectroscopic diagnostics, and heat flux sensors were used to obtain heat flux data from the resulting fires. The spreading pool fire area was photographed with the aid of gyroscopically stabilized cameras deployed in U.S. Air Force helicopters.

The data collected showed some unique and unexpected results in that the fire diameter was not the same as the spreading pool diameter (as had been assumed in previous analyses to date). We

now understand that for spills on open water, the flames will not anchor to the leading edge of the spreading LNG pool, limiting the diameter of the flame to something less than the spreading pool diameter. The data collected also showed the following:

1. While the 21 m spill had a flame width similar to the spill diameter, this may have been influenced by the tilted flame. The 83 m spill had an approximately 56 m flame width at 15 m above the water surface.
2. The flame length to diameter ratio was ~3.4 for the 21 m spill (the flame height correlation developed from the small-scale burner tests predicted an H/D of 4.1, a difference of 18%).
3. The height to diameter ratio was ~2.6 for 83 m spill (reacting fire portion was ~56 m) (the flame height correlation developed from the small-scale burner tests predicted an H/D of 2.9, a difference of 8%).
4. The burn rate measured in the 21 m spill test was 0.147 kg/m^2s, but no value was able to be calculated for the 83 m spill test.
5. The average overall surface emissive power (SEP) was 277 kW/m^2 and 286 kW/m^2 for the 21 m and 83 m spill tests, respectively.
6. The smoke generation and smoke shielding found for smaller LNG fires on land did not occur. A smoke mantle was not evident in either test.

The data collected further showed that in both very light and significant cross-winds the flame will stabilize on objects projecting out of the fire, suggesting that the ship itself will act as a flame anchor. If the flame was anchored to the leading edge of the spill, a scenario possible if the spill occurred in a confined region or harbor, the results might be different. A large anchored fire in the range of 100 m in diameter may produce more smoke shielding. An experiment to develop this new information would improve model development and enhance understanding of fires in congested areas such as inner harbors or berthing areas.

10 References

Berk, A., Acharya, P.K., Bernstein, L.S., Anderson, G.P., Chetwynd, J.H., and Hoke, M.L., "Reformulation of the MODTRAN® band model for higher spectral resolution", in the SPIE Proceeding, Algorithms for Multispectral, Hyperspectral, and Ultraspectral Imagery VI, Vol. 4049 (2000).

AIChE 1992, *Guidelines for Hazard Evaluation Procedures*, 2nd Ed., Center for Chemical Process Safety of the American Institute of Chemical Engineers, 1992.

Beck, J. V., "Users Manual for IHCP1D," a Program for Calculating Surface Heat Fluxes from Transient Temperatures Inside Solids, Beck Engineering Consultants Co., Okemos, Michigan, 48864, October 30, 1999.

Berk, A., Acharya, P.K., Bernstein, L.S., Anderson, G.P., Chetwynd, J.H., and Hoke, M.L., "Reformulation of the MODTRAN® band model for higher spectral resolution", in the SPIE Proceeding, Algorithms for Multispectral, Hyperspectral, and Ultraspectral Imagery VI, Vol. 4049 (2000).

Bernstein, L. et al., Non-Equilibrium High-Altitude Rocket Plume Signature Model, *Proceedings of the 1990 IRIS Specialty Group on Targets, Backgrounds, and Discrimination*, January 1990.

Blanchat, T., "Memo of Record for Commissioning Tests at the Thermal Test Complex, Liquid and Gas Fuel Testing in the FLAME/RH Facility." March 2006.

Blumm, J., Lindemann, A., and Niedrig, B., "Measurement of the thermophysical properties of an NPL thermal conductivity standard Inconel 600," Presented at the 17th European Conference on Thermophysical Properties, Bratislava, Slovakia, 5-8 September 2005, High Temperatures - High Pressures, 2003/2007, volume 35/36, pages 621-626.

Coleman and Steele. *Experimentation and Uncertainty Analysis for Engineers*, Wiley & Sons, 1999.

Cooper, P., "Comments on the detonability of gasses in the reservoir in the Large Scale LNG Experiment," Sandia National Laboratories internal memo, November 14, 2008.

Delichatsios, M. A., *Combustion and Flame,* 33, p. 12, 1993.

Doebelin, E. O., Measurement Systems- Application and Design, Fourth Edition, McGraw-Hill Publishing Company, 1990.

GAO Report to Congressional Requesters, GAO-07-316, "MARITIME SECURITY Public Safety Consequences of a Terrorist Attack on a Tanker Carrying Liquefied Natural Gas Need Clarification", February 2007.

Heskestad, G., “Fire Plumes,” SFPE *Handbook, 2nd ed.*, National Fire Protection Association, 1995.

Heskestad, G., *Fire Safety Journal*, 5, p. 103, 1983.

Hightower, M. et. al., “Guidance on risk analysis and safety implications of a large liquefied natural gas (LNG) spill over water”, SAND2004-6258, Sandia National Laboratories, Albuquerque, NM, 2004.

Incropera and DeWitt, *Fundamentals of Heat and Mass Transfer, 2nd ed.*, Wiley & Sons, 1981.

Jensen, R., “Seismic Analysis of the LNG Reservoir,” Sandia National Laboratories internal memo, May 13, 2008.

Kearney, S. P., “Temporally resolved radiation spectra from a sooting, turbulent pool fire,” *Proceedings of International Mechanical Engineering Congress and Exposition*, November 11-16, 2001, New York, NY.

Keltner, N. R., “Directional Flame Thermometers - A Tool for Measuring Thermal Exposure in Furnaces and Improving Control,” Interflam 2007, September 2007, University of London, Royal Holloway College, UK.

Luketa, A., “Thermal hazard distance from a fireball from LNG reservoir,” Sandia National Laboratories internal memo, October 21, 2008a.

Luketa, A., “Calculated dispersion distances for the large scale LNG tests,” Sandia National Laboratories internal memo, April 9, 2008b.

Luketa, A., Hightower, M., Attaway, S., “Breach and safety analysis of spills over water from large liquefied natural gas carriers,” SAND2008-3153 Sandia National Laboratories, Albuquerque, NM, 2008.

Luketa, A. “Recommendations on the prediction of thermal hazard distances from large liquefied natural gas pool fires on water for solid flame models,” SAND2011-0495, Sandia National Laboratories, Albuquerque, NM, 2011.

McCrain, L. L., and Roberts, W. L., “Measurements of the soot volume field in laminar diffusion flames at elevated pressures”, Combustion and Flame, Volume 140, Issue 1-2, January 2005.

Mathews, F., “Estimated Hazard Distances From An Unexpected But Possible Burn Within The Reservoir During The Large Scale LNG Experiment,” Sandia National Laboratories internal memo, October 22, 2008.

Melof, B., “LNG Explosion Hazards,” Sandia National Laboratories internal memo, December 1, 2008.

Moorhouse, J. "Scaling criteria for pool fires derived from large scale experiments." *I. Chem.E.*

Symposium Series, 1982: 165-179.

Nakos, J. T., "Uncertainty analysis of thermocouple measurements used in normal and abnormal thermal environment experiments at Sandia's Radiant Heat facility and Lurance Canyon burn site," SAND2004-1023, April 2004, Sandia National Laboratories, Albuquerque, NM.

Nakos, J. T., "Uncertainty analysis of steady state incident heat flux measurements in hydrocarbon fuel fires," SAND2005-7144, December 2005, Sandia National Laboratories, Albuquerque, NM.

PSM 29 CFR 1910.119, *Process Safety Management of Highly Hazardous Materials*, Occupational Safety and Health Administration, July 1, 2007.

PHS, Preliminary Hazard Screening, Sandia National Laboratory Primary Hazard Screening PHS Number: SNL07A00147, Large-Scale LNG Tests, 2008.

Pritchard, M. J., and T. M. Binding. "FIRE2: A new approach for predicting thermal radiation levels for hydrocarbon pool fires." *Sym. major hazards onshore and offshore*, 1984: 491-505.

Raj, P. K. "Experiments involving pool and vapor fires from spills of liquefied natural gas on water." Arthur D. Little, 1979.

Raj, P. K., LNG Pool Fire Spectral Data and Calculation of Emissive Power, *Journal of Hazardous Materials*, 142, pg. 720-729, 2007.

Ricks, A. J., "Characterization of air flow in New FLAME / Radiant Heat," Sandia internal memo to T. Blanchat, April 19, 2006a.

Ricks, A. J., "Gas Burner Flow Characterization Study," Sandia internal memo to T. Blanchat, March 20, 2006b.

Romero, V. J., Sherman, M. P., Johnson, J. D., Dempsey, J. F., Edwards, L. R., Chen, K. C., Baron, R. V., and King, C. F., "Development and validation of a component failure model," paper AIAA2005-2141, *46th AIAA/ASME/AHS/ASC Structures, Structural Dynamics, and Materials Conference*, April 18-21, 2005, Austin, TX.

SBM, Safety Basis Manual, Issue A, Sandia National Laboratories, September 30, 2008.

Sutton, M. A., Orteu, J-J, and Schreier, H. W., "Image Correlation for Shape, Motion and Deformation Measurements: Basic Concepts, Theory and Applications," Springer Science+Business Media, LLC, New York, NY, 1st edition, 2009.

Thomas, P.H. "The size of flames from natural fires." *9th Int. Combustion Symposium*, 1963: 844-859.

Vela, Iris; Chun, Hyunjoo; Wehrstedt, Klaus-Dieter; Schönbucher, Axel, "Thermal radiation of di-tert-butyl peroxide pool fires - Experimental investigation and CFD simulation," *Journal of Hazardous Materials*, 1, 167, 2009, 105–113.

Zukoski, E. E., *Fire Safety Science - Proceedings of the First International Symposium*, Hemisphere, New York, 1984.

Appendix A Reservoir Construction Drawings

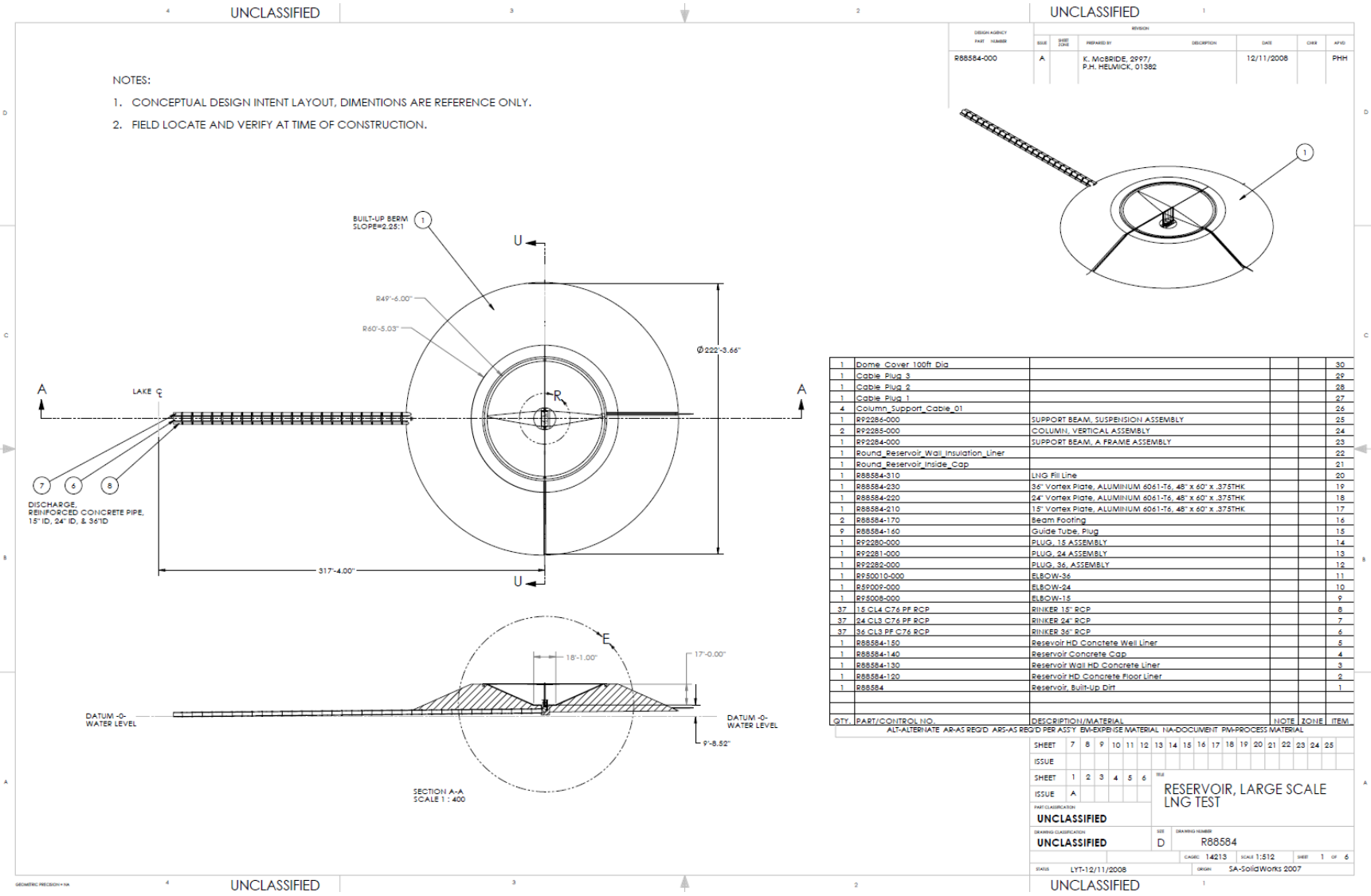

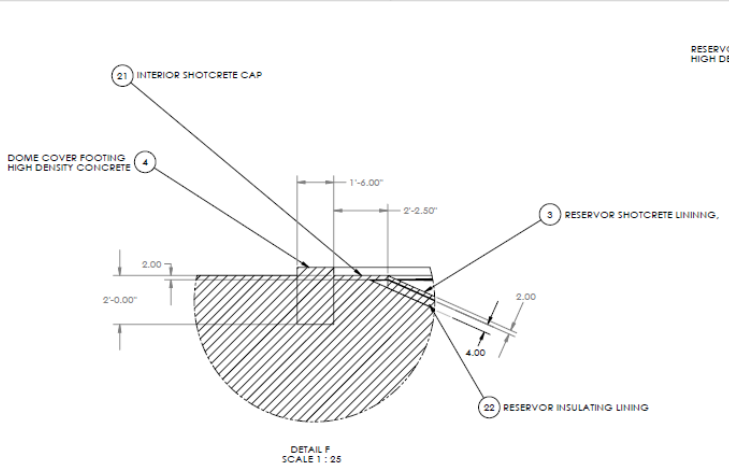

DETAIL F
SCALE 1 : 25

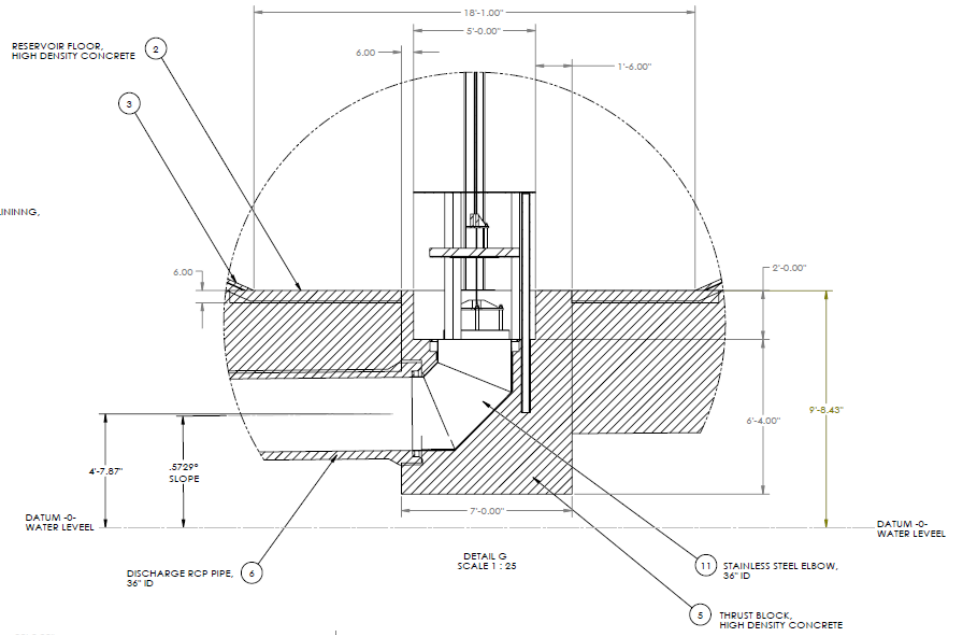

DETAIL G
SCALE 1 : 25

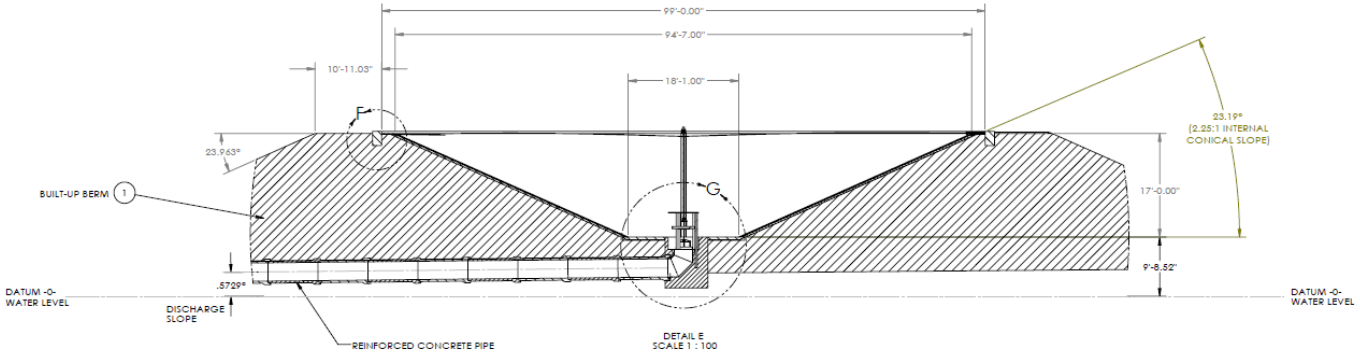

DETAIL E
SCALE 1 : 100

DRAWING NUMBER
R88584
DRAWING CLASSIFICATION
UNCLASSIFIED
SIZE D | CAGE/C 14213 | SCALE 1:512
SIZE A | SHEET 2 OF 6
STATUS LYT-12/11/2008

UNCLASSIFIED

UNCLASSIFIED

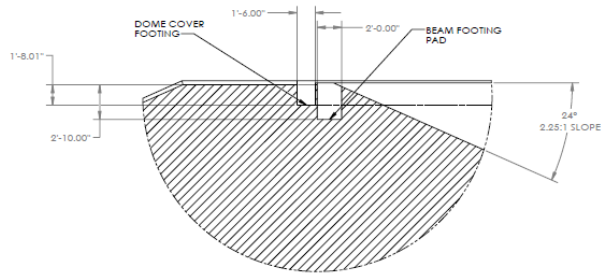

DETAIL K
SCALE 1 : 50

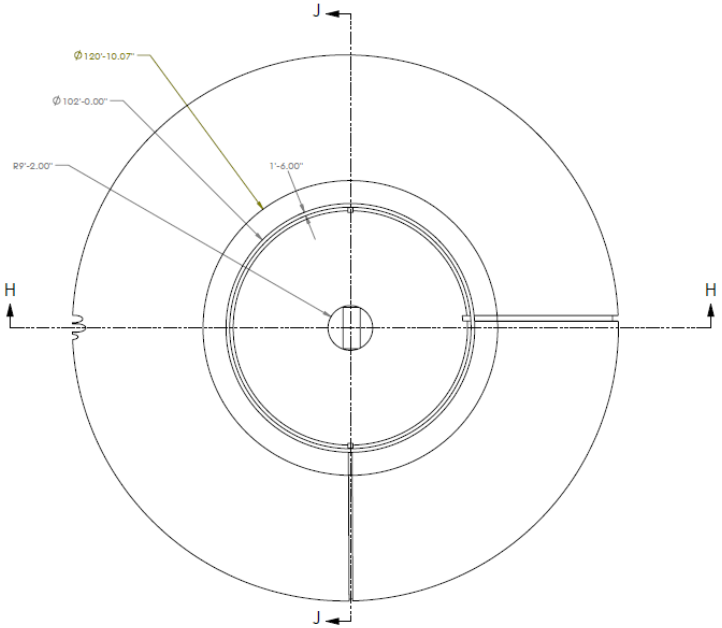

DETAIL: RESERVOIR
BUILT-UP DIRT

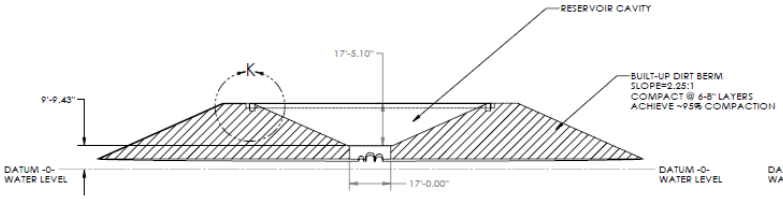

SECTION J-J
SCALE 1 : 250

VIEW ROTATED
90° FOR CLARITY

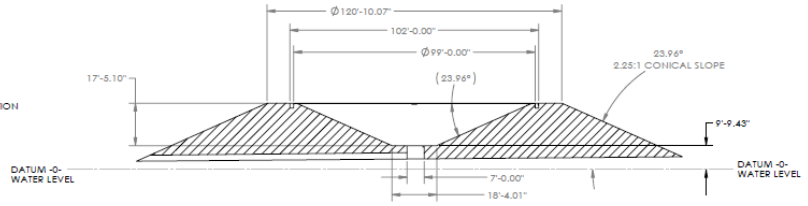

SECTION H-H
SCALE 1 : 250

DRAWING NUMBER
R88584
DRAWING CLASSIFICATION
UNCLASSIFIED
SIZE D
CAGE# 14213
SCALE 1:384
ISSUE A
SHEET 3 OF 6
STATUS LYT-12/11/2008

UNCLASSIFIED

UNCLASSIFIED

UNCLASSIFIED

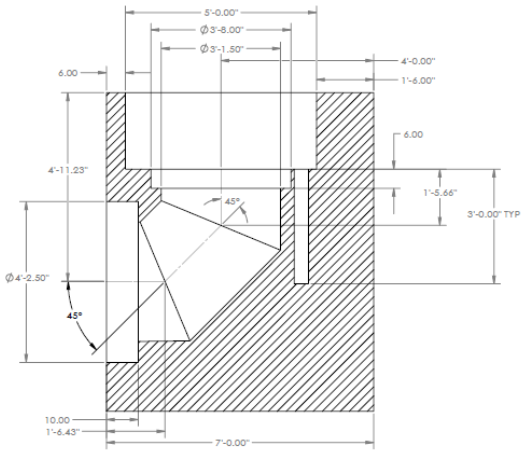

DETAIL: THRUST BLOCK
SECTION M-M

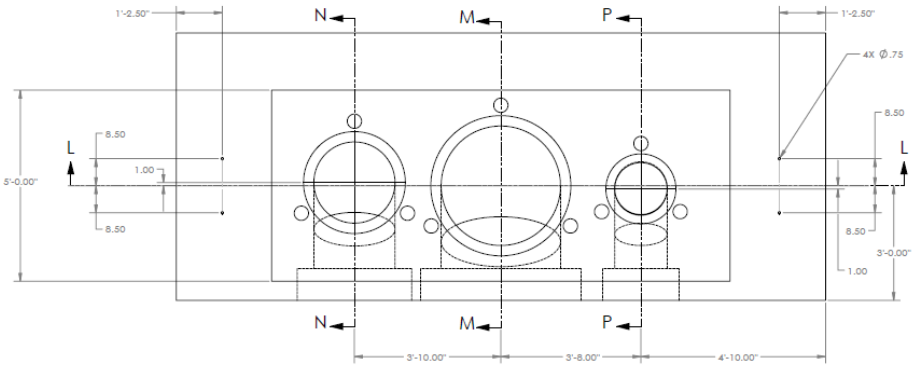

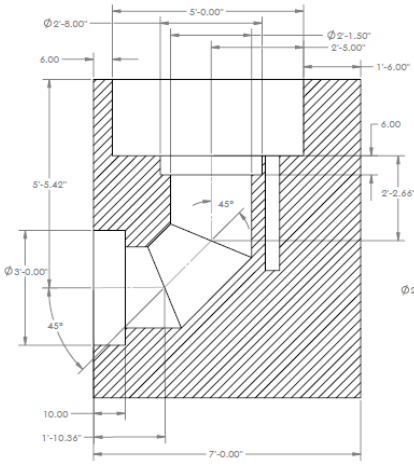

DETAIL: THRUST BLOCK
SECTION N-N

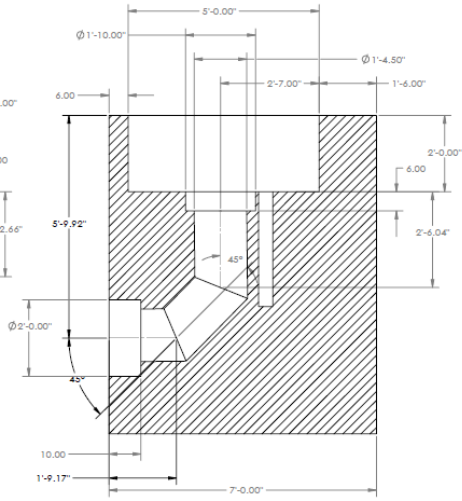

DETAIL: THRUST BLOCK
SECTION P-P

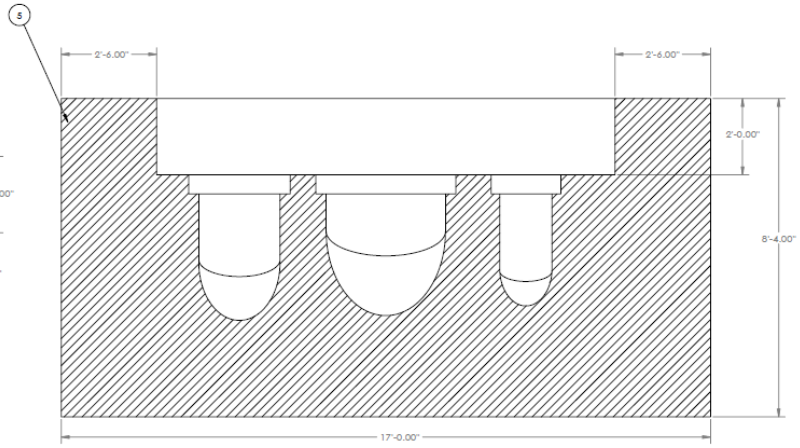

DETAIL: THRUST BLOCK
SECTION L-L

DRAWING NUMBER	R88584
DRAWING CLASSIFICATION	UNCLASSIFIED
SIZE D	CAGEC 14213 SCALE 1:16
	ISSUE A SHEET 4 OF 6
STATUS	LYT-12/11/2008

UNCLASSIFIED

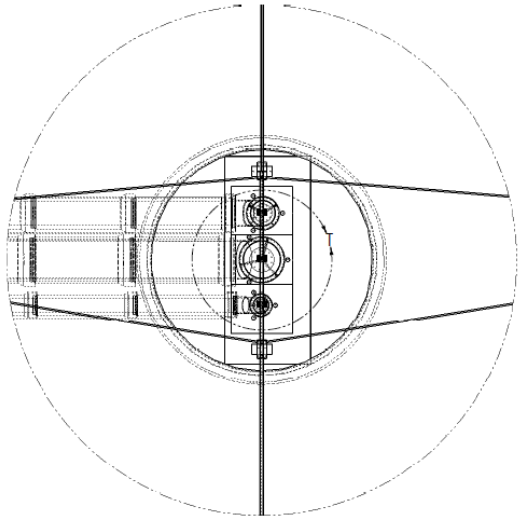

DETAIL R
SCALE 1 : 50

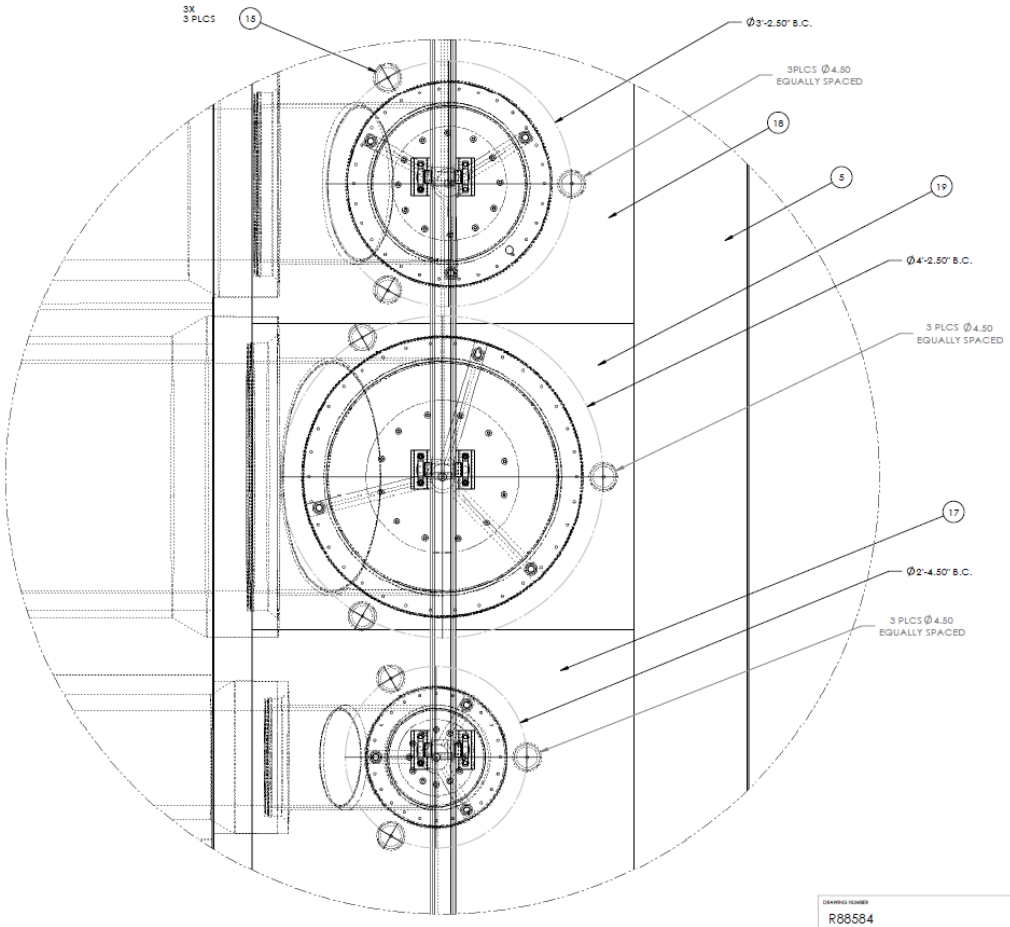

DETAIL T
SCALE 1 : 8

DRAWING NUMBER	R88584		
DRAWING CLASSIFICATION	UNCLASSIFIED		
SIZE D	CAGEC 14213	SCALE 1:16	
	ISSUE A	SHEET 5 OF 6	
STATUS	LYT-12/11/2008		

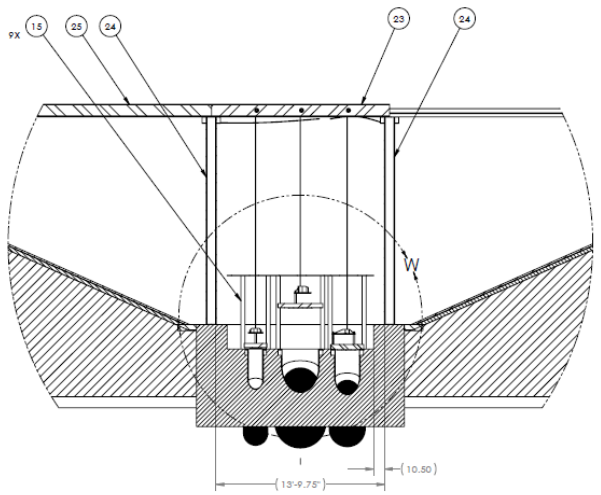

DETAIL V
SCALE 1 : 50

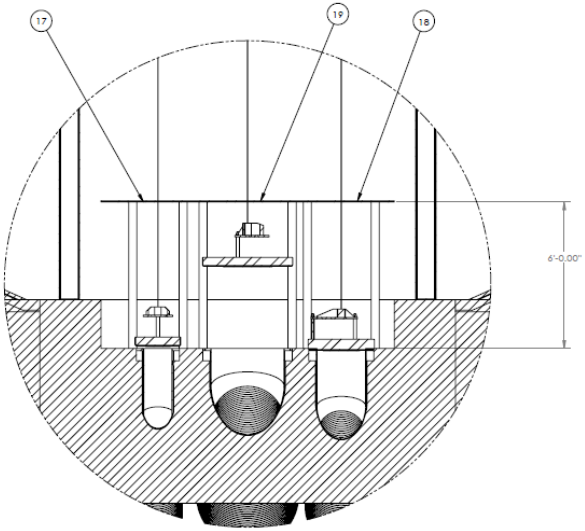

DETAIL W
SCALE 1 : 25

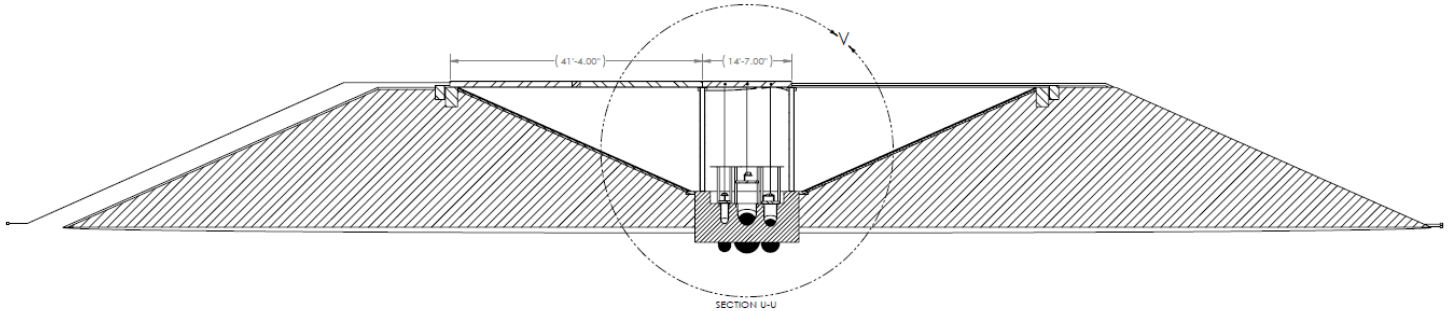

SECTION U-U
SCALE 1 : 100

DRAWING NUMBER	R88584		
DRAWING CLASSIFICATION	UNCLASSIFIED		
SIZE D	CAGEC 14213	SCALE 1:16	
	ISSUE A	SHEET 6 OF 6	
STATUS	LYT-12/11/2008		

Appendix B Field Alignment of the Radiometers

The radiometers were mounted to fixtures on towers located at varying distances from the center of the pool with a requirement that gauges on different towers view the same spot (vertical and azimuthally) on the fire plume. The fixture (or mount) for the radiometer was a machined hollow cylinder that held a radiometer (essentially 1 inch diameter copper slug containing a thermopile) to the tower, allowed movement in both the horizontal and vertical directions for alignment purposes, and then was locked in place after alignment. To ensure accurate alignment the following tools and procedure was used.

Tools:

1. 3x9 power rifle scope
2. Digital level 0.05° resolution
3. Mechanical mount (MM) for digital level

Procedure:

1. Install rifle scope in radiometer mount on tower (not shown). Rotate radiometer mount left to right to align the rifle scope cross hairs to center on the diffuser (center of the test pool). This yields an accuracy of +/- 3 minute of angle (~1/20th of a degree) left to right. Tighten screws that control rotation.
2. Remove rifle scope.
3. Install radiometer into radiometer mount on tower (not shown).
4. Place mechanical mount with attached digital level onto radiometer (which protrudes from the radiometer mount).
5. Tilt mechanical mount until level reads required angle +/- 0.1°. Tighten screws that control tilt.

The mechanical mount is constructed such that it slips over the outer housing of the radiometer and mounts normal to the face of the radiometer (Figure 1). This will allow direct reading of the digital level tilt angle. A bubble level is attached to ensure the mount is not rotated when the assembly is tilted to the desired angle (Figure 2 and 3).

Figure 1 Attachment to radiometer housing.

Figure 2 MM side view.

Figure 3 MM top view.

Appendix C Camera Calibration and Image Analysis

Image Analysis Background

Extensive MatLab programs were developed to reduce the video data to determine fire morphology (width, height, flame area, etc.). In addition, the video analyses provide information to allow corrections of radiometer data for atmospheric transmission effects, inform on the narrow-view radiometer "spot" results, and determine a time-dependent flame-average surface emissive power (SEP) from the wide-range radiometer data.

Camera calibration and image scaling are required to properly derive fire width, height, flame, area, radiometer fill ratio, and wide-range radiometer scaling data for SEP calculations. In order to scale each image correctly, the base line camera calibration for each camera was updated based on the distance between the camera and horizontal center-of-gravity (CG) of the flame plume for the corresponding image frame. The CG (a term commonly used in video analysis to denote the center of area of an image) is calculated based on the calibrated video data from the cameras at each spoke. Figure 1 provides a diagram of a representative flame outline showing the CG, CG shift from pool centerline, flame height, CG height, and flame width at the CG height.

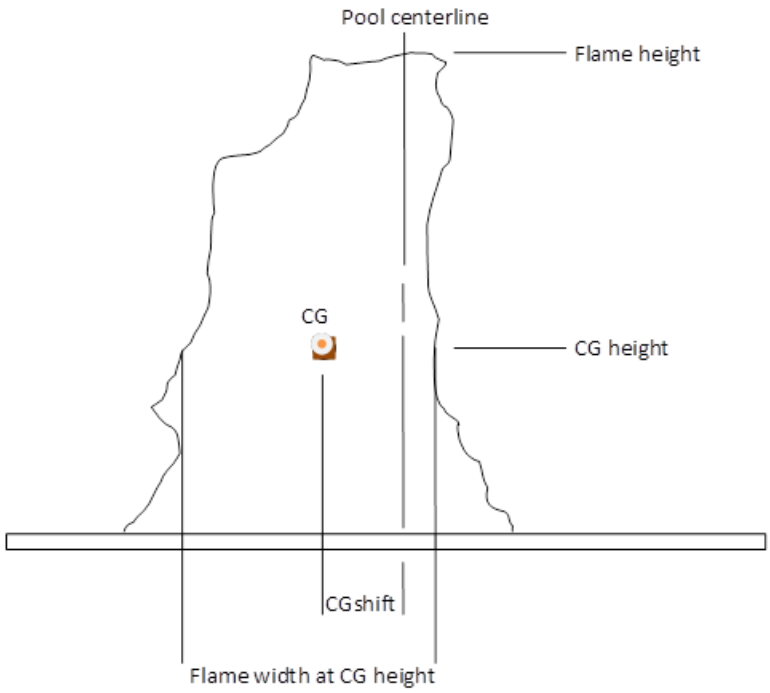

Figure 1 Representative flame morphology.

Camera Calibration

Camera calibration is the process in where the specific intrinsic and extrinsic parameters of the camera system are estimated. The intrinsic parameters are specific to each camera and are comprised of the center of the image sensor plane and its skew, horizontal and vertical focal lengths, and the lens distortions. The extrinsic parameters define the relative position and

orientation of the camera in the real world. In essence, the intrinsic and extrinsic parameters define how to relate the acquired imagery from each camera to the real world.

The highly accurate calibration of a computer vision system is quite complex. Consequently, tradeoffs and assumptions are applied to simplify the calibration problem to be consistent with level of accuracy required from the system. For a detailed treatise on calibrating a computer vision system, refer to chapters 2, 3, and 4 in Sutton et al. [2009].

For the wide field of view spoke cameras, the intrinsic camera parameters definitions that were used are based on a pin-hole projection camera model. A simplified pinhole camera is shown in Figure 2. Note how images are inverted as they pass through the focal point (pinhole).

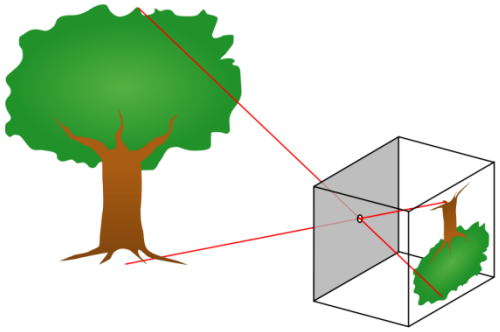

Figure 2 Basic Pinhole Camera[1]

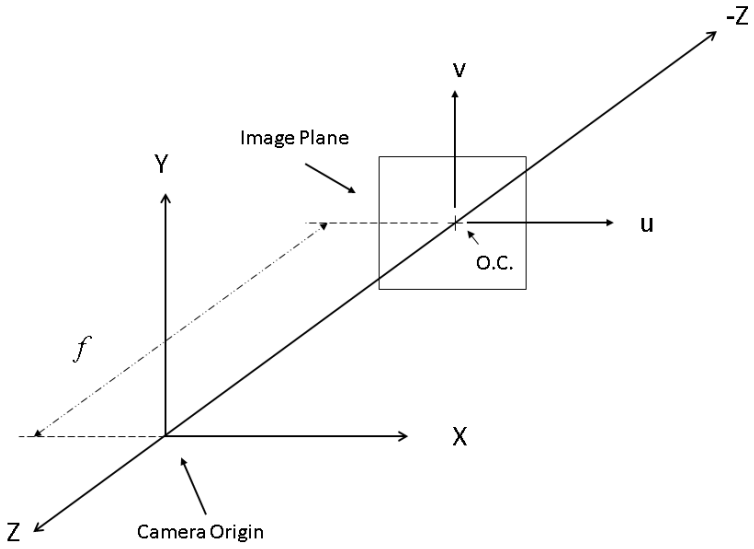

Figure 3 Basic pin-hole camera model

[1] Image source: http://en.wikipedia.org/wiki/File:Pinhole-camera.svg

The pin-hole projection camera model as shown in Figure 3 is shown in one of its most simplified forms where the Z-axis coincides with the optical axis of the camera and the sensor plane. In addition, the image sensor plane is placed in front of the camera's origin (i.e., focal point), which prevents images from being inverted. It is shown here to give the reader a basic sense of the pin-hole model. However, the transformation matrices shown in this appendix closely follow the definitions provided by Sutton, et al. [2009] on pages 27 thru 33.

The primary reason for calibrating a camera system is to be able to relate image coordinates to world coordinates for the purpose of making measurements. Image coordinates are related to world coordinates using three principal transformations matrices. They are:

1.) The Sensor-to-Camera transformation matrix (usually called the Camera Matrix) relates the camera's sensor plane (i.e., points in the image) to the camera's coordinate frame. This transformation includes the intrinsic parameters such as the center of the image sensor plane and its skew, horizontal and vertical focal lengths, and the lens distortions.
2.) The Camera-to-World transformation matrix relates the camera's position and orientation to world coordinate system (i.e., the camera's extrinsic parameters).
3.) The Sensor-to-World transformation matrix relates the image coordinates (i.e., sensor plane coordinates) to world coordinates; it is combination of the Sensor-to-Camera and Camera-to-World matrices.

To simplify the calibration process the following assumptions have been made:

1.) The sensor plane skew and lens distortions will be considered negligible and will not be considered.
2.) The base camera position and orientation will consist of its position relative to the pool's center and will be tilted in one axis only (i.e., the cameras were tilted up to capture the entire height of the flame).

The Camera Matrix is defined as:

$$C = \begin{bmatrix} f_x & f_s & c_x & 0 \\ 0 & f_y & c_y & 0 \\ 0 & 0 & 1 & 0 \end{bmatrix}$$

Where:
$f_x = focal\ length\ in\ x$
$f_y = focal\ length\ in\ y$
$f_s = 0$
$c_x = camera\ sensor\ center\ in\ x$
$c_y = camera\ sensor\ center\ in\ y$

The Camera Matrix parameters, f_x , f_y , f_s , c_x , c_y , shown above are in pixel units.

For a camera system where sensor skew is being considered, the terms f_x , f_y , f_s , c_x , c_y , shown above are defined to include the effects of sensor skew. The term f_s is shown to preserve the form

of the Camera Matrix. The value of f_s has been has been set to zero based on assumption (1) that sensor skew is negligible.

Let the Camera-to-World transformation matrix (2) be defined as:

$$T_{cw} = \begin{bmatrix} R_{11} & R_{12} & R_{13} & t_x \\ R_{21} & R_{22} & R_{23} & t_y \\ R_{31} & R_{32} & R_{33} & t_z \\ 0 & 0 & 0 & 1 \end{bmatrix}$$

Where:

$R_{11}\ thru\ R_{33} = the\ rotation\ matrix\ representing\ the\ orientation\ of\ the\ camera$
$t_x, t_y,\ and\ t_z = The\ position\ of\ the\ camera\ relative\ to\ pool\ center$

When assumption (2) is accounted for, the Camera-to-World matrix simplifies to:

$$T_{cw} = \begin{bmatrix} 1 & 0 & 0 & 0 \\ 0 & \cos(\alpha) & -\sin(\alpha) & -camHeight \\ 0 & \sin(\alpha) & \cos(\alpha) & camDistance \\ 0 & 0 & 0 & 1 \end{bmatrix}$$

Where:
$\alpha = the\ tilt\ angle\ of\ the\ camera$
$camHeight = the\ vertical\ position\ of\ the\ camera$
$camDistance = the\ horizontal\ position\ of\ the\ camera$

The value *camHeight* can be thought as the height above of pool where the camera axis intersects the vertical axis rising from the pool center. The *camDistance* represents the distance between the camera and the vertical plane being imaged. The shortest vector between the camera's position and the vertical plane of the flame being imaged is assumed to be normal to the vertical plane being imaged. In general the normal vector from the plane being imaged to the camera lies horizontally along the ground. The tilt angle, α, is assumed to be angle between the camera's sensor plane and the vertical plane of the flame being imaged. During the calibration process, the surveyed position of each camera relative to the pool center is used to evaluate the *camDistance* parameter.

When each image sequence is analyzed, the *camDistance* parameter gets updated for each image in the sequence based on the CG of the flame in world space. In other words, the Camera-to-World matrix is updated to account for the relative position of the camera to the vertical plane of the flame (camDistance) where the distance between the camera and the vertical plane of the flame is given by CG flame for the image frame being analyzed.

Both the Camera matrix and the Camera-to-World matrix are shown in homogenous form; and when multiplied together, form the Sensor-to-World transformation matrix. The Sensor-to-World matrix is updated (as noted above) based on the flame CG when determining fire morphology.

Camera Calibration Process

Before analyzing any of the image sequences, each camera was calibrated based on pre-test calibration images. To determine the vertical intrinsic parameters of each spoke camera, a tethered linear array of helium balloons was deployed prior to reservoir fill operations. The array consisted of an 8' diameter balloon at a height of 460' above the diffuser with 26" diameter marker balloons at 100' spacing on the tether (starting at 50' below the 8' diameter balloon). A 10' leader followed the last 100' section and was attached from the lower most marker balloon to the main tether anchored at the top of the diffuser. This 10' leader provided for full visibility of the lowermost marker balloon from all camera angles. The total height of the 8' main balloon was 460' above the top of the diffuser. Three guy lines attached to the large balloon and anchored at the pool perimeter helped stabilize the balloons during image acquisitions. The horizontal intrinsic parameters for each spoke camera were determined using poles positioned at known distance near the edge of the pool. See Figure 4 for a calibration image with extracted calibrations points.

The known vertical locations of the balloons and their corresponding location in the image along with the known horizontal positions of the poles and their corresponding locations in the image provide the minimum information necessary to calibrate each camera. Given that each spoke camera was tilted up so that the full extent of the plume height could be captured and the fact the balloons themselves were moving, the vertically dependent calibration parameters required minimization.

The evaluations of each spoke camera's intrinsic and extrinsic parameters were determined by minimizing f_y , c_y , α , and *camHeight*. The angle α and *camHeight* are referred as the "inclination angle" and "look-at point" in the `genCameraMatrixParams.m` MatLab script (see Image Analysis Procedure section).

The `genCameraMatrixParams.m` MatLab script uses MatLab's `fminsearch` function to call the `evalCameraCalMatrix_minSearchFN.m`, where the Camera and Camera-to-World matrices are iteratively evaluated by the `fminsearch` function.

Figure 4 Calibration image showing the extracted calibration points

Image Analysis Procedure

The first steps in analysis process were to calibrate the cameras and to segment the area of the flame in all of the images captured be each camera. This was done by thresholding the red channel of each image to produce a binary image of the fire area. The binary images from each camera were then used by each of the subsequent analysis programs, including the program for deterring CG, to derive fire morphology. The Global Coordinate System used for flame CG is provided in table below:

Global Coordinate System Relative to Pool Center				
Direction	North	East	South	West
Spoke	0	90	180	270
Axis	+X	+Y	-X	-Y

A list of each MatLab script (in alphabetical order) and its function is shown below:

1. assembleCameraMatrices.m– camera calibration
2. calcArea.m – calculate fire area
3. calcCenterOfGravity.m – calculate fire CG
4. calcHeightWidth.m – calculate fire height and width
5. calcPnts.m - calculate point data
6. calcPrcntRadFill.m- calculate narrow-view radiometer fill data
7. calcPxls.m - calculate pixel data
8. calcViewFactorRatio.m – calculate SEP from wide-view radiometer data
9. copyImages.m - copy images for evaluation at discrete times for documentation purposes and code verification
10. countRowPixels.m - called by scripts 18, 19, and 27 during the image segmentation process
11. createNotificationFile.m
12. evalCameraCalMatrix_minSearchFN.m– camera calibration
13. findRowBoundry.m - called by scripts 18, 19, and 27 during the image segmentation process
14. genCameraMatrixParams.m – camera calibration
15. genHTML.m
16. generateNewCamDist.m - determines the camDistance parameters to update the camera calibration matrices for each frame
17. patchDataFiles.m - correct data effected by bad image frames
18. processFireArea.m
19. processFireArea_North.m – correct for bad images in image sequence
20. runArea.m – calculate fire area
21. runCalcCenterOfGravity.m – calculate fire CG
22. runCalcHeightWidth.m – calculate fire height and width
23. runCalcPrcntRadFill.m- calculate narrow-view radiometer fill data
24. runCalcPrcntRadFill_to_GenCalCheckImages.m
25. runProcessFireArea.m - segmentation process for individual sequences
26. runProcessFireArea_South.m – correct for bad images in image sequence
27. runViewFactorRatio.m– calculate SEP from wide-view radiometer data.

DISTRIBUTION

EXTERNAL DISTRIBUTION

Christopher J. Freitas
Program Manager, Natural Gas Storage, Pipeline Reliability, and LNG
Office of Oil and Natural Gas
United States Department of Energy

Bob Corbin
Director, Oil and Gas Global Security and Supply
Office of Oil and Natural Gas
United States Department of Energy

Jeff Petraglia
NNSA/SSO

SANDIA INTERNAL DISTRIBUTION

MS0384	D. B. Dimos, 1500
MS1139	D. L. Miller, 1530
MS1135	R. D. Watkins, 1532
MS1135	T. K. Blanchat, 1532
MS0821	A. Luketa, 1532
MS1135	J. M. Suo-Anttila, 1532
MS1135	A. Ricks, 1532
MS1135	S. Gomez, 1532
MS0836	S. R. Tieszen, 1532
MS1139	T. J. Miller, 1535
MS1139	B. Demosthenous, 1535
MS1104	Margie Tatro, 6200
MS0735	John Merson, 6730
MS0751	R. P. Jensen, 6731
MS1108	Juan Torres, 6351
MS1108	M. M. Hightower, 6351
MS1146	R. B. Simpson, 1384
MS1141	P. H. Helmick, 1385
MS0729	R. A. Deola, 4133
MS0406	J. A. Mercier, 5717
MS0899	Technical Library, 9536 (electronic copy)


Sandia National Laboratories